Universität Paderborn

Lehrstuhl für Anorganische Chemie

Syntheses of Ruthenium Complexes for Studies on Water Oxidation and their Immobilization Approaches

---

Dissertation

Vorgelegt von

HATICE SÖYLER

Zur Erlangung des akademischen Grades eines

DOKTORS DER NATURWISSENSCHAFTEN (DR. RER. NAT.)

Vorsitzende: Prof. Dr. Sabine Fechner

Prüfer der Dissertation: 1. Prof. Dr. Matthias Bauer

2. Prof. Dr. Gerald Henkel

Die Dissertation wurde am 29.10.2018 an der Universität Paderborn eingereicht. Die mündliche Prüfung erfolgte am 07.12.2018.

Für meinen Ehemann,

meine Eltern

und meine Geschwister.

“But what will they burn instead of coal?” asked Pencroft.

“Water,” replied Harding.

… Water will be the coal of the future.” [1]

EIGENSTÄNDIGKEITSERKLÄRUNG

Hiermit versichere ich, dass ich den vorliegenden Masterarbeit mit dem Titel:

„Syntheses of Ruthenium Complexes for Studies on Water Oxidation and their Immobilization Approaches“

selbständig verfasst und keine anderen als die angegebenen Hilfsmittel benutzt habe. Alle Passagen, die aus der Literatur oder aus anderen Quellen wörtlich oder sinngemäß übernommen wurden, sind kenntlich gemacht. Ich versichere, dass die hier vorliegende Arbeit in gleicher oder ähnlicher Fassung noch nicht Bestandteil einer Studien- oder Prüfungsleistung war.

Datum: 29.10.2018 ……..

HATICE SÖYLER

KURZZUSAMMENFASSUNG

In den letzten zwei Jahrzehnten hat die Herstellung und Entwicklung neuer MOF-Systeme auf Basis von Übergangsmetallen enorm zugenommen, was auf ihre exzellenten Eigenschaften zurückzuführen ist. Metallorganische Gerüstverbindungen (engl. *metal organic frameworks, MOFs*) bestehen aus anorganischen Knotenpunkten (engl. *secondary buildung units, SBUs*) und den organischen Bausteinen, den sogenannten Linkern, die als Verbindungselemente zwischen den Knotenpunkten fungieren. Sie zeichnen sich durch sehr hohe innere Oberflächen und eine enorme Porosität aus. Durch Variation der anorganischen Knotenpunkte und der Brückenliganden kann die Porengröße gezielt festgelegt und die Porenabstände anwendungsspezifisch optimiert werden. Aufgrund ihrer die Zeolithe übertreffenden Eigenschaften eignen sich MOFs sehr gut für den Einsatz im Bereich der Gasspeicherung, für Trennverfahren, Katalyse sowie in der Sensorik.

Im Fokus dieser Doktorarbeit steht die Entwicklung neuer, auf Ruthenium basierender UiO-68 MOF Systeme. Insbesondere steht die Synthese von Komplexen mit langen Rückrat-Systemen, die Zugang zu großporigen MOF Systemen bieten sollen. Durch den Einbau aktiver Komplexe für die katalytische Wasseroxidation sollen stabile Systeme für zukünftige technische Anwendungen erhalten und die Auswirkungen der Linker-Größe sowohl auf die Geometrie des MOF-Gitters als auch auf die Porengröße und Porosität erforscht werden.

Um detaillierte Informationen zu strukturellen und elektronischen Veränderungen (Oxidationsstufen) der katalytisch aktiven Spezies zu erhalten, sollen die elektrochemischen und optischen Eigenschaften detailliert erforscht werden. Die katalytische Aktivität soll anschließend durch Wasseroxidationsexperimente untersucht werden.

ABSTRACT

Within the last two decades, a lot of efforts were made concerning the production and development of new MOF systems based on transition metals due to their excellent properties. Metal-organic frameworks are built up from inorganic nodes *(secondary building units, SBUs)* and organic building blocks, called linkers, which act as connecting elements between the nodes. They are characterized by very high internal surface areas and by an enormous porosity. By varying the inorganic nodes and the bridging ligands, the pore size can be exactly defined and optimized for specific applications. Because of these properties that surpass those of the structural similar zeolites, MOFs are very well suited for gas storage, separation processes, catalysis and in the sensors.

The main focus of this PhD thesis is the development of new UiO-68 MOF systems in which ruthenium complexes are implemented. By installing active complexes for the catalytic water oxidation, it should be able to obtain stable systems for future technological applications. The effects of linker size on both the geometry of the MOF lattice as well as the pore size will be explored.

In order to get detailed information about structural and electronic changes (oxidation states) of the catalytically active species, the electrochemical and optical properties will be studied in detail. The catalytic activity will finally be investigated by water oxidation experiments.

DANKSAGUNG

An dieser Stelle möchte ich mich bei einigen Personen bedanken, die mir mit Rat und Tat zur Anfertigung dieser Doktorarbeit geholfen haben. Ein ganz bedeutender Dank geht an Prof. Dr. Matthias Bauer, der mir in jeder Phase dieser Arbeit vollstes Vertrauen entgegenbrachte und mir Freiheit während des gesamsten Forschungsprojektes gewährte. Jederzeit stand er mir mit kritischer, aber stets konstruktiver Rückmeldung beratend zur Seite, was maßgeblich zum Gelingen dieser Arbeit beitrug. Des Weiteren gab er mir die Möglichkeit, an wissenschaftlichen Konferenzen teilzunehmen, die mir zu wertvollen Anregungen verhalfen und mein Verständnis durch zahlreiche Diskussionen erweiterten. Durch die Teilnahme an Messzeiten, unter anderem am ESRF, eröffnete er mir den Zugang zu einem neuen Forschungsfeld der Röntgenspektroskopie, was mir Einblicke in komplexere Arbeitsprozesse verschaffte. Ich danke ihm für die interessante Themenstellung und die guten Arbeitsbedingungen.

Ein weiterer besonderer Dank geht an Herrn Prof. Dr. Henkel, der sich bereit erklärte, das Zweitgutachten dieser Arbeit zu übernehmen. Vielen Dank für die mühevolle Erstellung des Zweitgutachtens. Auch danke ich ihm für die umfassende freundliche Unterstützung und Beratung während meiner gesamten Studienzeit an der Universität Paderborn, die ich zum großen Teil in der Anorganischen Chemie im AK Henkel verbringen durfte.

Bei Frau Karin Stolte möchte ich mich für die Aufnahme von zahlreichen NMR-spektroskopischen Messungen bedanken. Herrn PD. Dr. H. Egold danke ich für die wertvollen Diskussionen bezüglich spektroskopischer Fragen. Bei Frau M. Busse und Frau C. Gloger bedanke ich mich für die Durchführung der Elementaranalysen. Dr. Heinz Weber gilt ein freundliches Dankeschön für die Durchführung der massenspektroskopischen Messungen und die unterhaltsamen sowie lehrenden Pausen. Bei Dr. Roland Schoch möchte ich mich für die Ausführung und Auswertung der Röntgenstrukturanalysen herzlichst bedanken. Ein weiteres Dankeschön geht an Dr. Adam Neuba zum einen für die Durchführung der cyclovoltammetrischen Messungen und zum anderen dafür, dass er mir mit seinem Fachwissen und seiner beruflichen Erfahrung stets zur Seite stand. Dem AK Tiemann gebührt ein recht herzlicher Dank für die Durchführung der XRD- und BET-Messungen. Danken möchte ich nicht zuletzt meinen Kollegen und Mitarbeitern des AK Bauers, die mich während der ganzen Promotionszeit hilfreich unterstützt haben. An dieser Stelle sind auch die zahlreichen Seminare,

Diskussionen und Gespräche zu erwähnen, die wesentlich zur Fertigstellung dieser Arbeit beigetragen haben.

Mein größtes Dankeschön gilt an meine Eltern, die mir dieses Studium überhaupt erst ermöglicht haben. Ich danke euch nicht nur für die finanzielle Unterstützung während meines Studiums, sondern auch für den moralischen Rückhalt während der gesamten Zeit. Nicht zuletzt möchte ich mich bei meinen Geschwistern und, vom tiefsten Herzen, bei meinem Ehemann Emrah bedanken. Danke, dass du mir stets die nötige Kraft gegeben hast, trotz aller Zweifel und Frustrationen im Leben durchzuhalten und weiterzumachen.

PUBLICATIONS

H. Söyler, L. Burkhardt, L. Qinghua, A. Neuba, M. Bauer: Tuning the Reaction Kinetics of Ruthenium Water Oxidation Catalysts by Introducing π-Extended Ligands, manuscripts in progress.

H. Söyler, A. Neuba, R. Schoch, M. Bauer: Steric Effects of Substituted Polydentates on Water Oxidation Activity, manuscripts in progress.

H. Söyler, L. Burkhardt, A. Neuba, M. Bauer: The Influence of H-bonding Interactions of Carboxylic Acid Groups on the Water Oxidation Performance, manuscripts in progress.

CONFERENCE CONTRIBUTIONS

Speech

15th Ferrocene Colloquium at the Johannes Gutenberg University, Mainz **2017**.
"Ruthenium Catalysts Containing Extended Ligands for Water Oxidation".

Poster

15th Ferrocene Colloquium at the Johannes Gutenberg University, Kiel **2016**.
"Developement of new Ru@MOFs as Water Oxidation Catalysts".

48th Annual Meeting of German Catalysis, Weimar **2015**.
"New Ru-complexes for induction of defects in UiO-68 MOFs and their application in water oxidation reactions".

Participation

International Conference on *Coordination Chemistry*, Paderborn **2015**.
International Conference on *Coordination Chemistry*, Heidelberg **2018**.

LIST OF ABBREVIATIONS

TON	Turnover number
TOF	Turnover frequency
WOC	Water Oxidation Catalyst
OEC	Oxygen Evolving Complex
Mn	Manganese
Ca	Calcium
PSII	Photosystem II
MeOH	Methanol
THF	Tetrahydrofurane
DMSO	Dimethyl sulfoxide
MeCN	Acetonitrile
HCl	Hydrochloride acid
HAc	acetic acid
PSI	Photosystem I
CO_2	Carbon dioxide
NASA	National Aeronautics and Space Administration
FTO	Fluorine-doped tin oxide
tpy	Terpyridine
bpy	Bipyridine
dcbpy	2,2′-bipyridine-5,5′-dicarboxylic acid
tpdc	Triphenyldicarboxylate
sal	Salphen
phen	Phenanthroline
4-pic	4-picoline (4-methylpyridine)
i.e:	In other words
Cp^*	Pentamethylcyclopentadien
UiO	University of Oslo
PCET	Proton-Coupled Electron Transfer
EXAFS	Extended X-ray Absorption Fine Structure
EPR	Electron Paramagnetic Resonance
Asp 61	Asparaginic acid
D1-His 337	Histidin

CP43-Arg	Arginin
P680	Pigment 680
NADP	Nicotinamide Adenine Dinucleotide Phosphate
Tyr_Z	Tyrosine
CAN	Cer(IV) ammonium nitrate
HOTf	Ttrifluormethanesulfonic acid
NHE	Normal hydrogen electrode
WO	Water oxidation
HOMO	Highest Occupied Molecular Orbital
LUMO	Lowest Occupied Molecular Orbital
CV	Cyclic Voltammetry
SWV	Square Wave Voltammetry
DFT	Density Functional Theory
WNA	Water Nucleophilic Attack
I2M	Intramolecular mechanism
SBU	Secondary Building Unit
MOF	Metal-Organic Framework
IUPAC	International Union of Pure and Applied Chemistry
PSM	Post-synthetic modification
PSE	Post-synthetic exchange
BDC	Benzene dicarboxylate
Vs.	versus
IRMOF	Isoreticular Metal-Organic Framework
HKUST	Hong Kong University of Science and Technology
ZIF	Zeolitic Imidazolate Framework
as	As-synthesized
BET	Brunauer-Emmett Teller
XRD	X-ray diffraction
TGA	Thermogravimetric Analysis
TG	Thermogravimetry
GeV	Giga-electron-volt
FTIR	Fourier Transform Infrared Spectroscopy
GC-MS	Gas Chromatography Mass Spectroscopy
ESI-MS	Electrospray Ionization MS

MS/MS	Tandem mass spectrometry
M-O	Metal-oxo
s	Singlet
d	Doublet
dd	Doubledoublet
t	Triplet
m	Multiplet
J	Coupling constant [Hz]
ν	Wavenumber [cm^{-1}]
δ	Chemical shift [ppm]
λ	Wavelength [nm]
ε	Extinction coefficient [$M^{-1}cm^{-1}$]
Å	Angstrom

TABLE OF CONTENT

CHAPTER 1

Aim of the thesis

Since the industrial revolution of the late 18th and 19th centuries, the concepts of modernization rapidly spread to the rest of the world. During this period, modernization became a term often equated with industrialization, economic and financial growth, social and environmental developments. James Watt (*1736-†1819) was one of the key figures in transforming the world from one based on agriculture to one based in engineering thanks to his invention of the first modern steam engine.[2] Over the years, electric power replaced steam and water power in factories, moving the society into the age of high-technology, in which larger amounts of carbon dioxide were released into the atmosphere. This trend continues today and is more pronounced in developing countries such as China[3] or India[4], which are in their earliest stages of industrialization. Up to now, the strong demand for energy could be only satisfied by burning fossil fuels such as coal, oil and natural gas. Because modernization is an ongoing process and fossil fuels are finite resources, it seems to be only a question of time when the world's carbon budget will be totally consumed. Besides, carbon dioxide is known as the main product of fuel combustion responsible for climate change including the impacts of global warming. Considering that population is continuously growing and available resources are limited, the importance of planning future energy supply based on renewable and sustainable resources becomes clear.

The main renewable energy sources are wind power, hydropower, geothermal energy, solar energy, biomass and biofuels.[5-9] Besides those technologies, one promising alternative comes from hydrogen fuel cells, which combine excellent application performance with environmental benefits.[10] Currently, hydrogen is mainly used as fuel in the American space program thanks to its high energy density. Since the 1950s, the National Aeronautics and Space Administration (NASA) uses liquid hydrogen to launch the space shuttles, while hydrogen fuel cells power the shuttle's electrical systems, producing heat and pure water clean enough to supply the shuttle crew with drinking water.[11]

Depending on the application, many types of fuel cells exist which work according to the same principle: a typical fuel cell consists of an anode and a cathode, at which the chemical reactions

take place. The electrodes contain catalysts that activate the fuel to undergo redox reactions producing protons and electrons, the latter creating the electric current. The positively charged hydrogen ions permeate across the electrolyte to the cathode, where they react with oxygen anions to produce pure water. The fundamental principle of a fuel cell is illustrated in Figure 1. As long as a fuel cell is supplied with hydrogen and oxygen, it will generate electricity.[12]

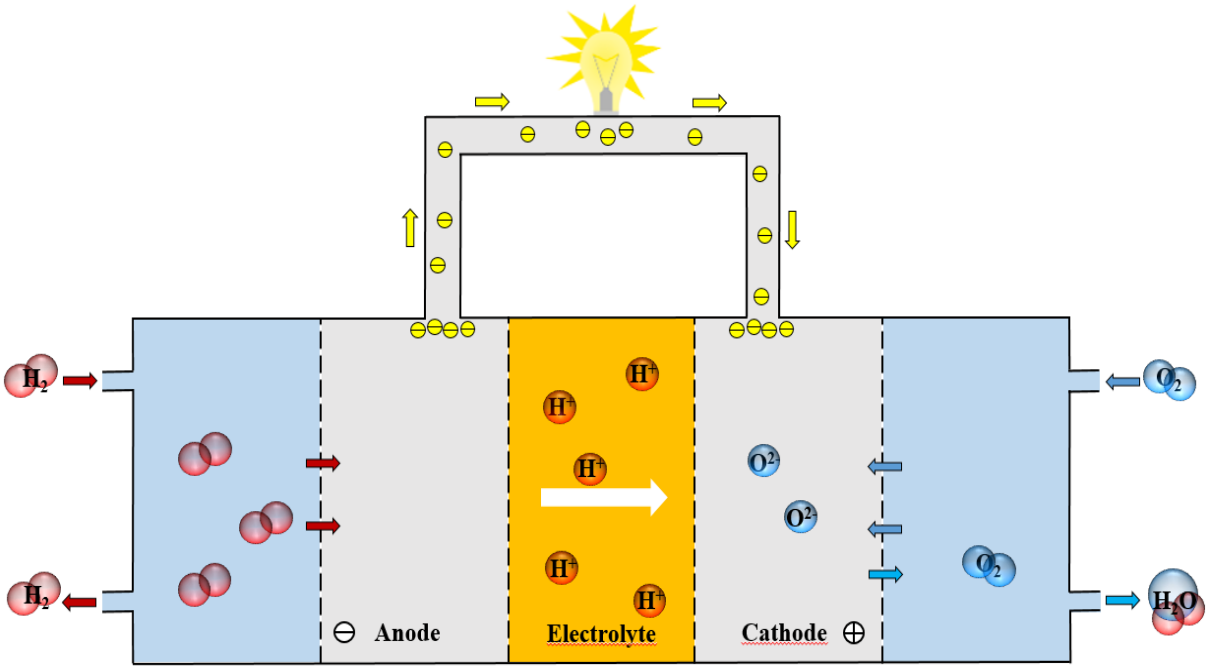

Figure 1. Schematic presentation of a fuel cell.

The major problem with using hydrogen as an energy source is that the reactants introduced into the fuel cell do not occur naturally as a gas. Because the water-splitting process into its elements does not occur spontaneously, the generation of hydrogen and oxygen in pure form requires more energy than it takes to make electricity. Consequently, different approaches were adopted for large-scale hydrogen and oxygen production. For hydrogen, one of the most favoured and widely used methods in industry is steam reforming[13], in which hydrocarbons such as methane are converted into hydrogen. Because this technology is limited to fossil fuels associated with CO_2 release into the atmosphere, more environmentally friendly alternatives are required in terms of global warming.

Another popular method for the production of hydrogen and oxygen is electrolysis of water.[14] Like fuel cells, electrolyzers consist of electrodes, at which water is separated into its elements by generating an electric current. Hydrogen produced by electrolysis is of high quality ensuring no greenhouse emissions by gaining electricity from renewable energy sources. Nevertheless, this strategy is too expensive for industrial use to compete with conventional energy resources.

One appealing solution for future energy needs comes from the field of catalysis, where catalysts based on transition metals are developed to create water-splitting reactions including water oxidation and water reduction.[15-17] The ideal catalyst system should be capable of both molecular oxygen and hydrogen production. In reality, each half reaction is too complex and needs to be investigated and optimized independently in order to realize practical overall water splitting. Due to the fact that the oxidation part is the limiting key step of water-splitting, which demands more energy to generate one molecule of oxygen by transferring four electrons and four protons from two water molecules[18, 19], this work focuses on artificial water oxidation systems.

In recent years, different metal-derived molecular catalytic systems have been designed for water oxidation. The development of homogeneous catalysts was found to be useful in terms of elucidation intermediates during the catalytic mechanism, which is quite difficult to realize in heterogeneous systems due to their complex surface structures. A remarkable breakthrough came with the discovery of fast mononuclear ruthenium complexes reported by SUN et al.[20] which worked at a rate comparable to that found in nature, where water splitting is catalyzed by a manganese-calcium cluster located within Photosystem II (PSII).[21-26] Due to the remarkable stability of higher oxidation states and the excellent chemical robustness of homogeneous ruthenium complexes under harsh acidic conditions under which water oxidation reaction is performed, the development of water oxidation catalysts (WOCs) containing similar structural motifs gained growing attention recently.

Inspired by the oxygen-evolving complex (OEC) of nature, whose protein environment is surrounded by oxygen rich ligands including hydroxyl, phenol and carboxylate ligands, future catalyst design is focused on the introduction of negatively charged ligands, which were proven to decrease the redox potentials, thus stabilizing the high-valent states of ruthenium. However, ligand dissociation and oxidative decomposition were found to be the main deactivation pathways in homogeneous catalysis, which are mostly attributed to the experimental conditions. One relatively new and promising approach to achieve WOCs with long-term stability is to combine the benefits of homogeneous and heterogeneous catalysis such as high catalytic performances and easy catalyst separation. Following this idea, the first MOF-based ruthenium catalyst containing a 2,2’:6’,2’’-terpyridine (tpy) backbone was prepared by JOHNSON et al. in 2017, which was grown directly on fluorine-doped tin oxide (FTO) substrates capable of oxidizing water electrochemically with a Faradaic efficiency of 82 %.[27] Following this strategy, the structure of the catalyst was stabilized by preventing the formation of catalytically

active nanoparticles, which usually takes place when the pure catalyst is used in homogeneous WO. The structure of the Ru-doped UiO-67 is schematically shown in Figure 2.

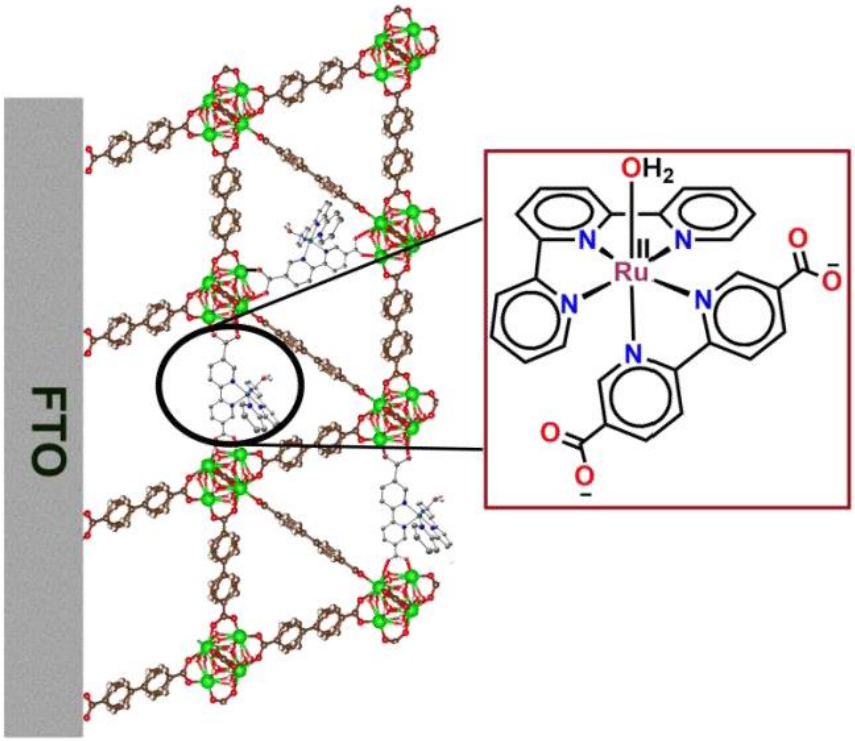

Figure 2. Schematic illustration of the structure of a well-known ruthenium-based water oxidation catalyst, $[Ru(tpy)(dcbpy)OH_2](ClO_4)_2$, incorporated into FTO-grown thin films of UiO-67, termed UiO67-$[RuOH_2]$@FTO. Reprinted from Ref. [27].

In the present case, the MOF structure was created *via* post-synthetic exchange (PSE) by mild reaction of the ruthenium catalyst $[Ru(tpy)(dcbpy)OH_2](ClO_4)_2$ with zirconium metal-organic framework UiO-67, in which the zirconium nodes are connected to bipyridine ligands functionalized with carboxylic acid groups. Considering the fact that heterogeneous catalyst systems are linked to many advantages, one aim of this thesis was the synthesis of highly crystalline three-dimensional MOF structures, which can be doped with ruthenium water oxidation catalysts prepared within the framework of this study. By introducing π-extended bridging ligands into the 3D framework, it is attempted to enlarge the pore size of the MOF in order to enhance the rate of diffusion of the water reactants to the catalytic sites (ruthenium) within the pores. Additionally, the high surface area of a MOF offers an excellent base for enhanced reactant and product storage.

The class of UiO MOFs[28-33], especially UiO-66 and UiO-67, have been widely examined due to their easy scaling-up, high chemical as well as thermal stability, while the synthesis of UiO-68 is challenging since the organic linker is not commercially available. Inspired by the

experimental complexity of UiO-68 and the lack of active Ru@MOFs, experiments on MOFs were focused on the synthesis and optimization of UiO-68 by varying conditions of pressure, temperature, reaction time, crystallization vessel and synthesis additives in this work.

CHAPTER 2

Dissertation Structure

This thesis is categorized into ten main chapters involving a brief overview of the literature regarding the biological water oxidation and the developments of homogeneous ruthenium catalysts up to date (**Chapter 3**), followed by **Chapter 4** which provides insight into the different synthetic strategies of metal-organic frameworks and the general characterization methods for such porous materials. **Chapter 5** was introduced to highlight the structural ligand requirements needed to fulfill the key goals of this study, and to briefly demonstrate the health risks associated with the synthesis of the desired final ligands. The preparation of the ligands used for complex syntheses (**Chapter 7)** are presented in **Chapter 6**, including the main challenges associated with the syntheses stages. The experimental results and their interpretations are summarized in the results and discussion section, which is divided into following chapters:

Chapter 8: Mononuclear ruthenium(II) complexes have been prepared and examined concerning their potential catalytic applications. The structural conformation of the complexes are provided by NMR spectroscopy and electrospray ionization mass spectrometry (ESI-MS). The electrochemical and optical properties are monitored by cyclic and square-wave voltammetry (CV, SWV). With the results gained from previous studies on single-site ruthenium WOCs, a better understanding is obtained for the electron-transfer processes induced by such complexes in chemically-driven water oxidation.

Chapter 9: In this chapter, the catalytic performances of the catalysts in homogeneous water oxidation are investigated using cerium(IV) ammonium nitrate as oxidant. The results are compared with those of other published studies. The differences in activity are discussed in terms of the electronic and steric properties of the substituents with a proposed reaction mechanism based on DFT calculations.

Chapter 10: Generally, MOFs constructed from longer organic linkers produce larger pores, which can form interpenetrating[34] structures making such materials less stable towards specific

applications. However, considering the benefits of large pores in catalytic reactions, several attempts were made to find a reproducible and controllable synthetic route to develop the UiO-68 type Zr-MOF including the effect of reaction solvent time, exchange solvents and activation time. From these results, no general rule can be applied for the MOF synthesis, but it can help to control framework collapse in future works. Adsorption and diffraction studies have been performed to explore the relationship between structure and properties in UiO-68 type MOFs. In order to study the reactivity of the obtained materials, immobilization approaches were carried out pre- and post-synthetically.

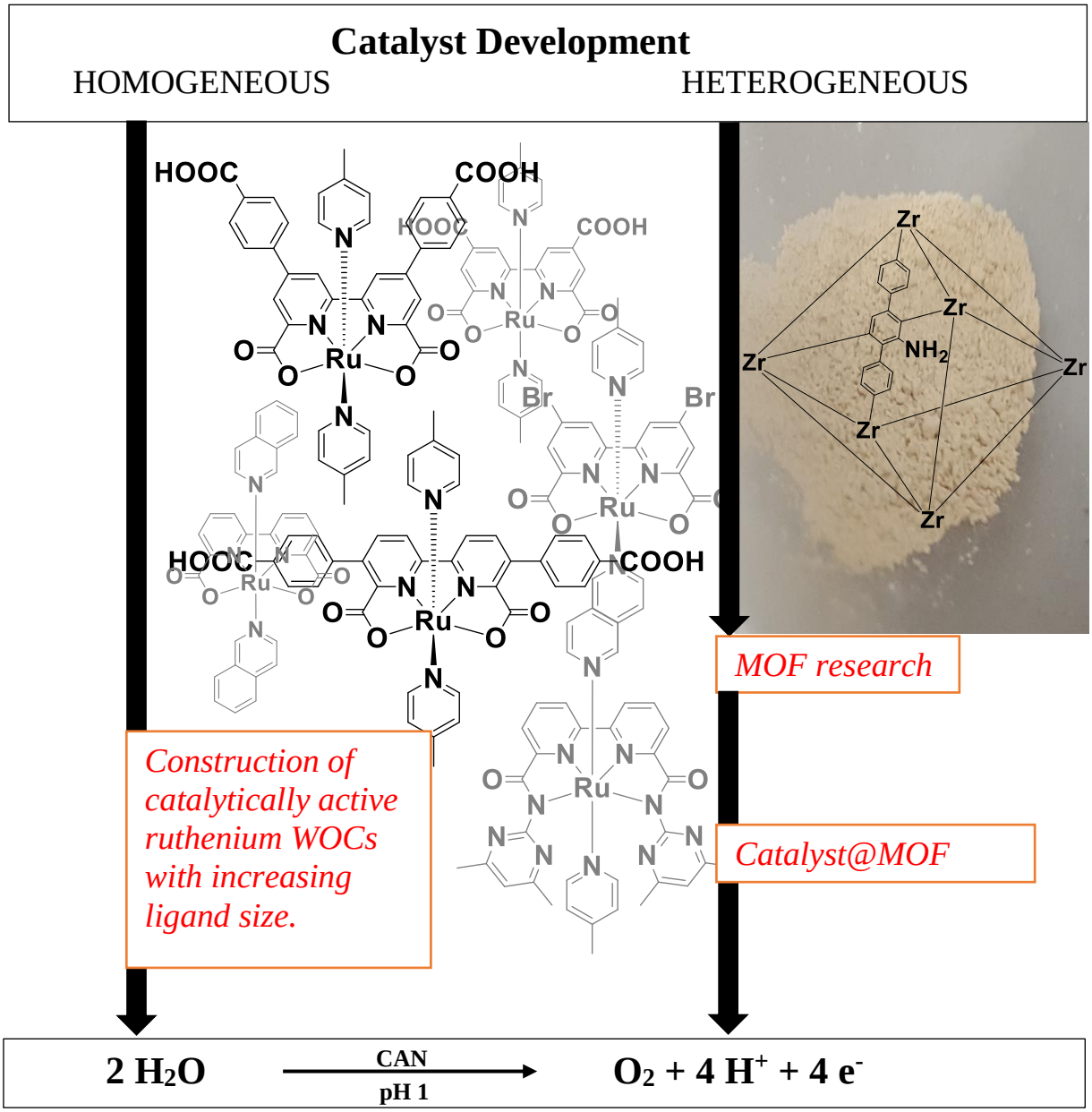

Figure 3. Schematic overview of the dissertation structure involving key stages of ruthenium WOCs.

CHAPTER 3

Literature Review

3.1 Worlds Energy Demand – An Outlook.

The demand for cheap and environmentally friendly energy resources is continuously rising especially in view of the global warming crisis[35-39], which has led to groundbreaking successes in the field of artificial water splitting. Inspired by the survival strategies of nature where a Mn-Ca cluster within the oxygen-evolving complex (OEC) located in photosystem II (PSII) of cyanobacteria, algae and plants catalyzes light-induced water splitting, intense efforts are ongoing towards the imitation of this *'super catalyst'* aiming to solve the energy problems of the future. In order to design systems with catalytic activities comparable to that of PSII, a thorough mechanistic understanding for the whole water splitting process is necessary which is divided into two half reactions: catalytic proton reduction and catalytic water oxidation, the latter being the more challenging half reaction due to the fact that water oxidation is highly energy-demanding and requires the transfer of four electrons to generate molecular oxygen. In thermodynamic terms, water oxidation occurs at 0.82 V in pH 7.0 and 1.23 V in pH 1.[40] The nature uses proton-coupled electron transfer (PCET) to couple the electron and proton transfer, and avoids the formation of unwanted high-energy intermediates. In artificial photosynthesis, high overpotentials have to be overcome which can be realized using suitable water oxidation catalysts (WOCs).[41]

$$4\,H^+ + 4\,e^- \rightarrow 2\,H_2;\; E° = 0.0 - (0.059\ \text{pH})V \qquad \text{(Equation 3.1)}$$

$$2\,H_2O \rightarrow O_2 + 4\,H^+ + 4\,e^-;\; E° = 1.23 - (0.059\ \text{pH})V \qquad \text{(Equation 3.2)}$$

$$2\,H_2O \rightarrow O_2 + 2\,H_2;\; E° = 1.23\,V \qquad \text{(Equation 3.3)}$$

In order to establish artificial photosynthesis as a *'green'* approach to renewable energy, molecular WOCs working under *'green'* conditions need to be designed. If this could be done in future, natural sources such as water and sunlight would be the only needed reaction partners for clean energy production.

3.2 Natural Photosynthesis – The Oxygen Evolving Center.

In order to mimic the key functions of photosynthetic water oxidation, a full understanding of all biologicial steps in PSII is essential. The protons and electrons released from two molecules of water are transferred to photosystem I (PSI) to reduce CO_2 to carbohydrates. In order to understand the water-splitting mechanism, several attempts were undertaken to determine the structure of the OEC and its chemical environment. Due to the structural complexity of the PSII, which was found to consist of 20 protein subunits, 35 chlorophylls, 12 carotenoids, 25 integral lipids and one chloride ion per monomer, different crystal structures have been obtained from two species of thermophilic cyanobacteria to exactly clarify the protein environment and get a full picture of the catalytic active manganese centre.[25, 42]

In 2001, the first crystal structure of PSII was obtained by ZOUNI et al.[21] from the cyanobacterium *Synechococcus elongatus* at 3.8 Å resolution using X-ray analysis which showed good structural agreements with the model previously suggested by HASEGAWA et al.[43] (1999) and PELOQUIN et al.[44] (2000). Although they were able to determine the spatial structure of the PSII complex and proposed a *'3 + 1'* arrangement of the manganese ions in the OEC, the positions of some protein subunits could not be clearly identified due to the limited resolution. In order to analyze the PSII structure in more detail, crystals of PSII could be isolated from *Synechococcus vulcanus* by KAMIYA and SHEN in 2003.[22] Refined crystal structure at 3.7 Å resolution yielded new information about the arrangement of protein subunits and cofactors, including β-carotenes located near the metal centre. Electron density map calculations supported the idea that D1-His337, D1-Asp189 (or D1-His190) and D1-Tyr73 could serve as ligands for the Mn cluster. In contrast to the structure of ZOUNI et al., in which the central Mn ion was protruded toward the luminal surface of the membrane, KAMIYA et al. favoured a cluster of four manganese which were approximately in the same plane. Although the new crystal structure provided additional insights for the surrounding coordination sphere of the Mn cluster, the mechanism of water-splitting of PSII remained still unknown.

In subsequent years, the resolution was increased to 3.5 Å by FERREIRA et al.[23] (2004), 3.0 Å by LOLL et al.[24] (2005) and 2.9 Å by GUSKOV et al.[25] (2009). However, it is thanks to FERREIRA'S work that nearly all amino acid side chains were successfully assigned revealing all the major cofactors and subunits of PSII from *T. elongates* (Figure 4). Based on the PSII crystal structure, the OEC was revealed as a Mn_4Ca^{2+} cluster, in which three of the manganese ions form a Mn_3CaO_4 cuboid. The forth *'dangler'* Mn ion was suggested to be bounded to a corner μ_4-oxide ion within the small domain as proposed in earlier studies (PELOQUIN et al., 2000). With the identification and positioning of the Ca^{2+} within PSII, FERREIRA et al. were now able

to develop a structural model for the OEC active site which was in good agreement with theoretical predictions obtained by X-ray fine structure (EXAFS), electron paramagnetic resonance (EPR), computational studies by SPROVIERO et al.[45, 46] (2005) and by site-directed mutagenesis studies performed by DEBUS and DINER (2001).[47-50] This was the first time that calcium was regarded as an integral part of the OEC cluster.

Finally, the crystal structure obtained at a resolution of 1.9 Å by KAMIYA et al.[26] in 2011 revealed the full structure of the catalytic manganese center for the first time containing four Mn and one Ca atoms as well as five oxygen and four water molecules involved within water oxidation reactions (Figure 5). Due to the better quality of the electron density map, the arrangement of all amino-acid residues coordinated to the Mn-Ca cluster could be precisely determined which provided a basis for analysing and understanding the water-splitting reactions within PSII in detail. In addition to the ligands directly coordinated to the metal ions, the structure of the second coordination sphere was determined by X-ray crystallography. It was found that the cluster was surrounded by D1-Asp 61, D1-His 337 and CP43-Arg 357 that are being presumed to maintain the cubane structure by stabilizing the different oxidation states (III and IV) of manganese. Although the crystal structure o PSII determined by FERREIRA et al. provided no substantial information about the protein environment, it confirmed earlier models and helped to formulate realistic chemical schemes for the water splitting reaction based on the insights gained to this point.

A plausible mechanistic explanation came in 1970, when KOK et al.[51] introduced a five-step reaction cycle, in which the OEC undergoes a sequential ($S_0 \rightarrow S_4$) abstraction of four electrons and protons from two molecules of water to generate one molecule of oxygen. As illustrated in Figure 6, the catalytic oxidation of water involves five different oxidation states of the manganese cluster, known as the S-state cycle, which is initiated by the absorption of visible light by P680, excited to P680* and rapidly transfers an electron to the nearby primary electron acceptor of PSII, pheophytin, within a few picoseconds. In the following steps, the electron is translocated across the thylakoid membrane to reduce $NADP^+$ to NADPH. The oxidized P680, $P680^+$, is a strong oxidizing agent which abstracts an electron from a tyrosine residue, Tyr_Z (Y_Z), which in turn abstracts an electron from a Mn-bound water substrate. The O-O bond formation is taken place at the final step of the S-state cycle *via* a nucleophilic attack of a calcium-bound water molecule on the high electron-deficient oxo species Mn^V=O. This way, the oxo becomes highly electrophilic (oxyl radical), which allows a nucleophilic attack by the oxygen of a second substrate water coordinated to the coordination sphere of Ca^{2+}.[51] When

four electrons are transferred, the OEC retrieves its electrons by oxidizing two molecules of water to one molecular oxygen.

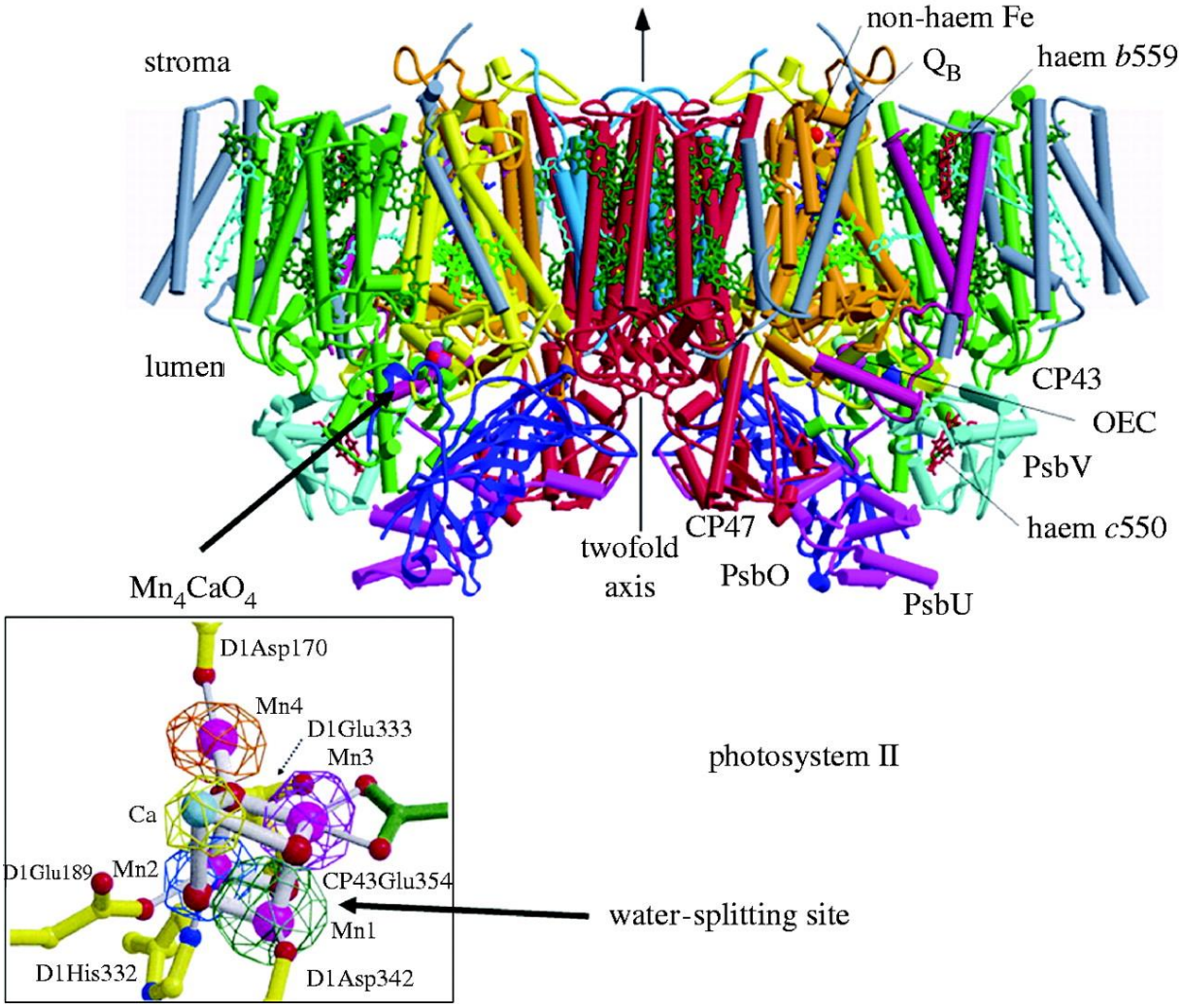

Figure 4. Side view of the protein structure of Photosystem II and the crystal structure of the OEC determined by X-ray diffraction analysis at 3.5 Å by FERREIRA et al. (2004) isolated from the cyanobacterium *Thermosynechococcus elongatus*. Reprinted from Ref. [51].

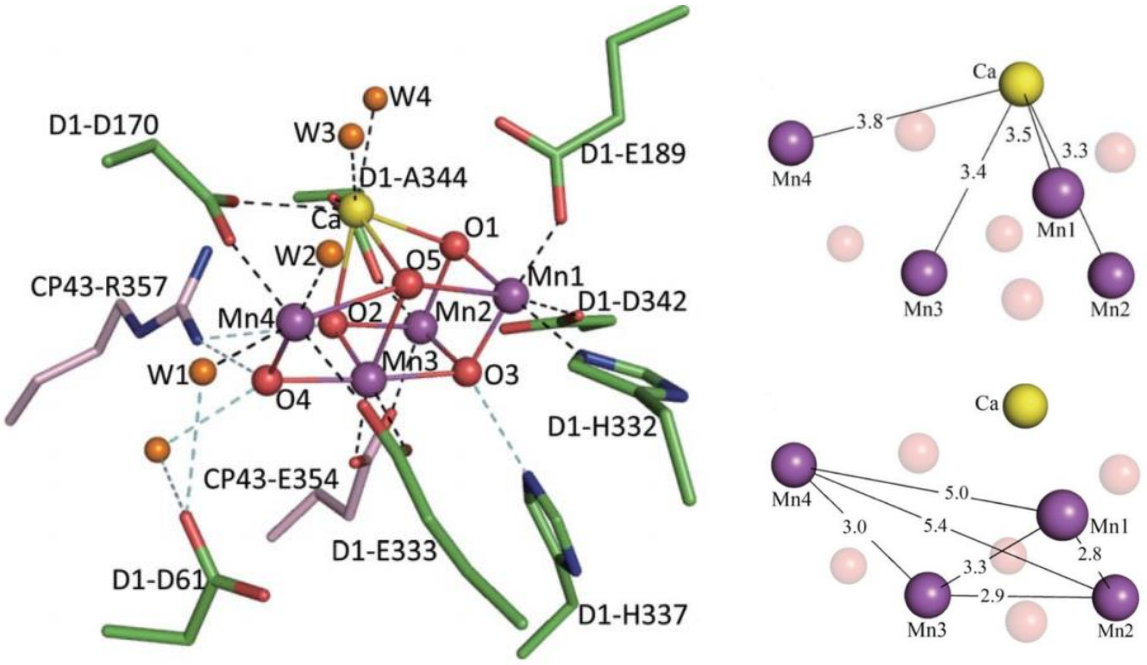

Figure 5. Crystal structure from X-ray-diffraction analyses at 1.9 Å by KAMIYA and UMENA (2011). Reprinted from Ref. [26].

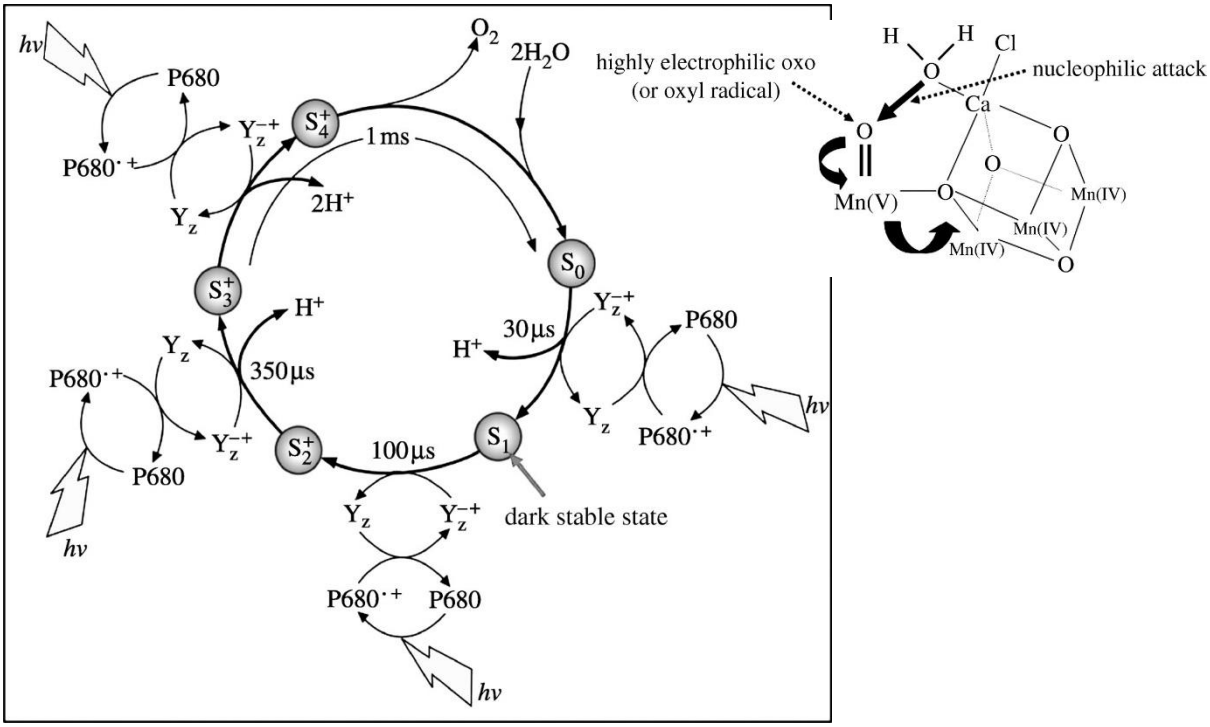

Figure 6. Left, the S-state cycle of KOK. Right, proposed mechanism of the O-O bond formation step in PSII. Reprinted from Ref. [51].

A variety of homogeneous water oxidation catalysts based on transition metals such as iridium[52-67], ruthenium[68-77], manganese[78] and cobalt[79-81] have been synthesized and tested in water oxidation reactions. Since the oxidation of water in PSII is induced by light, the question is why chemically-driven water oxidation is still preferred over photo-induced water oxidation.

The conditions for light-induced water oxidation catalysis are diverse and must be continually optimized for each system (pH, buffer, concentrations of different components, light source etc.), artificial photosynthetic systems containing less components are required for water-splitting in order to reduce the influence of the parameters on the catalytic activity. A two-component system consisting of a sacrificial oxidant instead of a photosensitizer and a suitable catalyst can be driven chemically to catalyze water oxidation by electron abstraction from the water oxidizing complex forming a high-valent oxidation state as the *'true'* active species. The shift from photocatalytic to chemical conditions brings more benefits to the water oxidation reaction in defining the catalytic system. A commonly used oxidant is cerium(IV) ammonium nitrate (CAN), which is a strong one-electron oxidant ($E_{1/2}$ = 1.61 *vs*. NHE).[82] CAN has the advantage that it is commercially available, inexpensive, excellently soluble in water and stable even under extreme acidic conditions (pH < 1.0). It has weak absorption in the UV-vis region, which allows spectroscopic study on catalytic processes. Furthermore, the cerium concentration can be easily varied in order to achieve optimum performance for each catalytic system. However, *in-situ* formed hydrolysis products as well as cerium(III) oxide produced by the reduction of cerium(IV) may interact with the *'true'* catalyst during the water oxidation process, thus quickly deactivating the catalytic reaction.[83-86]

$$4\,Ce^{\mathrm{IV}} + 4\,e^{-} \rightarrow 4\,Ce^{III} \qquad \text{(Equation 3.4)}$$

$$2\,H_2O\ +\ 4\,Ce^{\mathrm{IV}} \rightarrow O_2 + 4\,H^{+} +\ 4\,Ce^{III} \qquad \text{(Equation 3.5)}$$

$$4\,[Ru^{III}(bpy)_3]^{3+} + 4\,e^{-} \rightarrow 4\,[Ru^{II}(bpy)_3]^{2+} \qquad \text{(Equation 3.6)}$$

Besides CAN, $[Ru^{III}(bpy)_3]^{3+}$ can be applied as a milder oxidant ($E_{1/2}$ = 1.26 vs. NHE)[87] in both, neutral and slightly basic media, avoiding dramatic decomposition of the investigated molecular WOCs if they are unstable under acidic conditions. However, one of the main disadvantages to the use of Ru-type oxidants are their tendency to chemical decomposition and their expensive synthesis route.

3.3 Artificial Photosynthesis – Molecular Water Oxidation Catalysts.

Since the discovery of the *'blue dimer'* by MEYER'S group in the early 1980's (TON = 13.2, TOF = 4.2×10^{-3} s^{-1})[88, 89], ruthenium-based molecular water oxidation catalysts are known as highly active when using CAN as chemical oxidant. The low catalytic performance was firstly attributed to the μ-oxo bridge, which made the complex less resistant towards oxidative degradation and resulted in inactive monomeric species. After this discovery, the range of catalysts based on ruthenium was significantly enlarged by translating the key features of the OEC into the WOCs. The most important factors regarding synthesis, structure, properties, mechanism and catalytic performance are summarized in the following.

(1) The ideal catalyst should operate at low overpotentials in order to facilitate rapid electron transfer from the WOC to the oxidant. By lowering the redox potential of a catalyst, it is possible to drive the catalytic reaction with oxidants possessing lower redox potentials, which are generally used in light-driven WO.

(2) A long-term chemical durability of WOCs is essential to increase the catalyst efficiency. In case of ruthenium, highly stable metal species with various oxidation states can be generated and detected even under strongly acidic conditions required for WO, underlying the enormous stability of ruthenium catalysts and their promising potential for catalytic applications.

(3) The use of inexpensive and insensitive materials allows the preparation of the desirable complexes in large scale. Considering that structural changes of a WOC strongly influences its properties and catalytic performance, systematic modification of the ligands is one major challenge to get a better understanding for the mechanistic processes involved in oxygen evolution. Therefore, a simple and inexpensive synthesis route for homogeneous catalysts is required.

The first series of mononuclear ruthenium WOCs were reported by THUMMEL et al.[90] in 2005, which gave turnover numbers ranging from 50 to 580, showing that the catalytic performance was depending on the nature of the ligands directly linked to the metal centre in axial position and their chemical behavior during the catalytic cycle. More importantly, these results showed that one ruthenium centre was catalytically active enough to drive the oxidation of water. Based on this knowledge, SUN and coworkers developed a WOC that worked extremely quickly at a rate comparable to that of photosystem II (TOF = 469 ± 4 s^{-}).[20] By varying the axial ligands, they developed a new family of fast mononuclear ruthenium WOCs containing negatively charged backbone ligands, such as carboxylate groups, which were found to stabilize the high valent redox-states of the catalytically active metal species by lowering their overpotentials.

The variation of both, the ligand architecture and the substituents directly coordinated to the metal centre opened up new doors in the design of WOCs based not only on ruthenium but also on other transition metals such as iridium, manganese, cobalt, copper or iron. Despite their low toxicity, low cost of production and simple way for synthesis, water oxidation proved challenging when using these catalysts, which is primarily due to oxidative ligand degradation in acidic aqueous media, followed by rapid catalyst deactivation. In the following section, the most well-known non-ruthenium WOCs will be shortly introduced to outline the importance and suitability of ruthenium for water oxidation.

3.3.1 Non-ruthenium water oxidation catalysts.

In order to mimic the natural catalyst in PSII, BRUDVIG et al. designed the first synthetic homogeneous dimer based on Mn-terpy. Oxygen evolution was observed when using hypochlorite or oxone as oxidant.[91] Later a $[Mn_2(H_2O)_2(mcbpen)]^{2+}$ complex was reported by MNKENZIE et al.[92, 93], which exhibited a TON of up to 15 000. To date, no manganese catalysts exist that are able to generate dioxygen from water using CAN or $[Ru(bpy)_3]^{3+}$ in reactions, highlighting the influence of the proper geometrical arrangment on water oxidation.

The first cobalt-based water oxidation catalyst was published by BERLINGUETTE et al.[94], who synthesized a Co(II) complex containing a pentadentate ligand and one water molecule in the sixth position. Even though they suggested that the catalytic current corresponding to water oxidation was molecular in origin, they did not rule out the possibility that the catalytic activity could stem from molecular fragments formed *in-situ* during catalysis.

In 2013, SAKAI et al.[95] reported different substituted Co-based oxygen evolving catalysts with porphyrin backbones exhibiting turnover numbers from 89 up to 122 in photogenerated water oxidation. Highly active iron-based homogeneous catalysts bearing tetradentate nitrogen ligands with two triflate ions in *cis*-position were designed by COSTAS and coworkers, which yielded a TON > 1000 and a TOF of 838 h^{-1} when using different oxidizing agents.[96] Interestingly, no oxygen was generated when the triflates were positioned in *trans*-configuration. These values obtained are the highest so far reported for WOCs based on first-row transition metals.

A soluble copper-bipyridine water oxidation electrocatalyst was developed by MAYER et al.[97] which is considered as the most rapid homogeneous copper catalyst, with a TOF of ~100 s^{-1}. Molecular water oxidation catalysts containing iridium as centers were found to show a comparable high catalytic activity towards water oxidation. Well-known examples include the bis-aquo complex of BERNHARDT et al.[98], the Cp^* substituted one of CRABTREE et al.[56] and the

iridium catalyst bearing a carbenetype donor-ligand prepared by ALBRECHT and coworkers[99]. All compounds were tested in Ce^{IV}-driven water oxidation with the highest turnover number of nearly 10 000 for the iridium catalyst of Albrecht's workgroup.

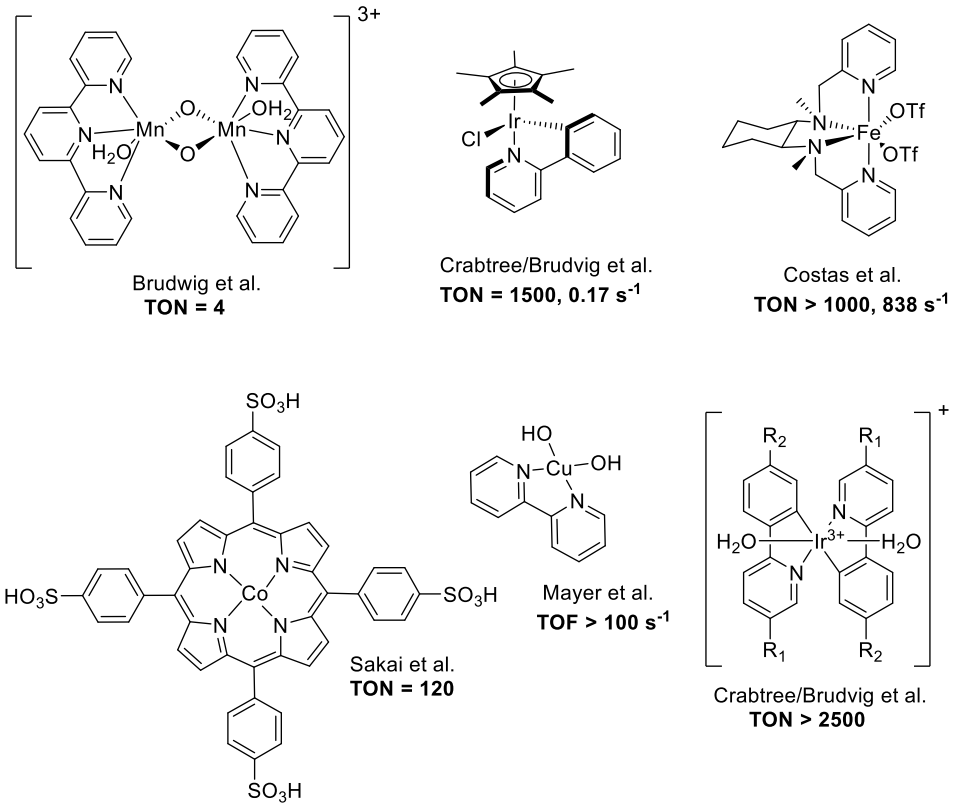

Figure 7. Molecular structures of non-ruthenium water oxidation catalysts.

3.3.2 Ruthenium water oxidation catalysts.

Based on the knowledge that dinuclear ruthenium complexes showed higher tendency towards structural decomposition, recent studies have focused on the preparation of mononuclear ruthenium complexes, which were successfully proven to be potential candidates with the best features for water oxidation. Compared to multinuclear systems, mononuclear WOCs are characterized by simple ligand design and facile manipulation of the structural properties. Additional information gained from mechanistic insights with dinuclear ruthenium complexes indicated that not both metal cores were involved in the O-O bond formation step, which will be detaily discussed in the following sections, confirming once more the benefits of mononuclear ruthenium complexes. Instead of fully reviewing the history, this section will summarize only the previous results that are related to the theme of this thesis.

3.3.2.1 Ruthenium (non-) aqua complexes for water oxidation.

Some selected examples for Ru WOCs are shown in Figure 8 in order to illustrate the diversity of structural motifs in catalytic systems, including changes in the axial and equatorial positions. The first examples were reported by THUMMEL and coworkers[100], which contain two axially bounded pyridine ligands as illustrated by complex 2. Small variations in the axial position have shown that substituent effects have a big influence on the catalytic activity, decreasing from $-CH_3$ to $-CF_3$ to $-NMe_2$. The decrease of the catalytic activity was attributed to the electron-withdrawing nature of the trifluoromethyl groups at the axial positions, while the catalytic drop in the dimethylamino-substituted complex was due to the protonation of the amino group in strongly acidic reaction conditions (pH 1), thus changing its electronic properties from a strong electron-donor to a strong electron-acceptor molecule. Thanks to x-ray strucrural analysis, it could be shown that the aqua ligand in complex 2 was stabilized by H-bond formation with the un-coordinated napththyridine nitrogen.

A charge-neutral complex was designed by ÅKERMARK et al.[101] containing an anionic tridentate ligand bounded through imidazole and phenolate moieties to the ruthenium centre as illustrated by complex 3. Mechanistic investigation revealed that complex 3 underwent ligand exchange of 4-picoline with water through a WNA pathway in order to enter the catalytic cycle of water oxidation. Using $[Ru(bpy)_3]^{3+}$ as sacrificial oxidant, a TON of 4000 was obtained, which suggested that the involvement of ligands with negatively charged groups led to high-valent metal species at low overpotentials. Nevertheless, to this finding was not given much attention at that time, so that the search of new ruthenium complexes was ongoing.

Important steps in clarifying the mechanism of water oxidation were made by MEYER et al.[102-108], who synthesized the first series of Ru WOCs containing an aqua ligand in the axial position. Complex 4 gave rise to a TON of 320 when using CAN in acidic conditions. Upon decorating the bi- and tridentate ligands of complex 4 with various electron-withdrawing and donating substituents, a variety of ruthenium WOCs possessing different electronic properties were isolated and tested in water oxidation reactions. These results supported the reported process of ligand exchange with water and confirmed the formation of an aqua species $[Ru^{II}\text{-}OH_2]^{2+}$ as the real catalyst. Further investigations made by BERLINGUETTE et al.[109, 110] and YAGI et al.[111] impressively showed that the conversion to the aqua form also took place when the axial aqua ligand in complex 4 was replaced by a chloride-ion, experimentally corresponding to an induction time required for the chloride-aqua exchange during the initial phase of oxygen evolution. Furthermore, it could be demonstrated that ligand variation on the bipyridine or on the terpyridine unit shows opposite effects on both, the catalytic activity and the catalytic

stability expressed in TOF and TON, respectively. Similar substituent effects were also observed for a number of mononuclear ruthenium WOCs with polypyridine ligands, as illustrated in the examples of SAKAI et al.[112], which showed a tendency for the O_2-evolving activity to rise as the electron-donating ability of the substituents was increased.

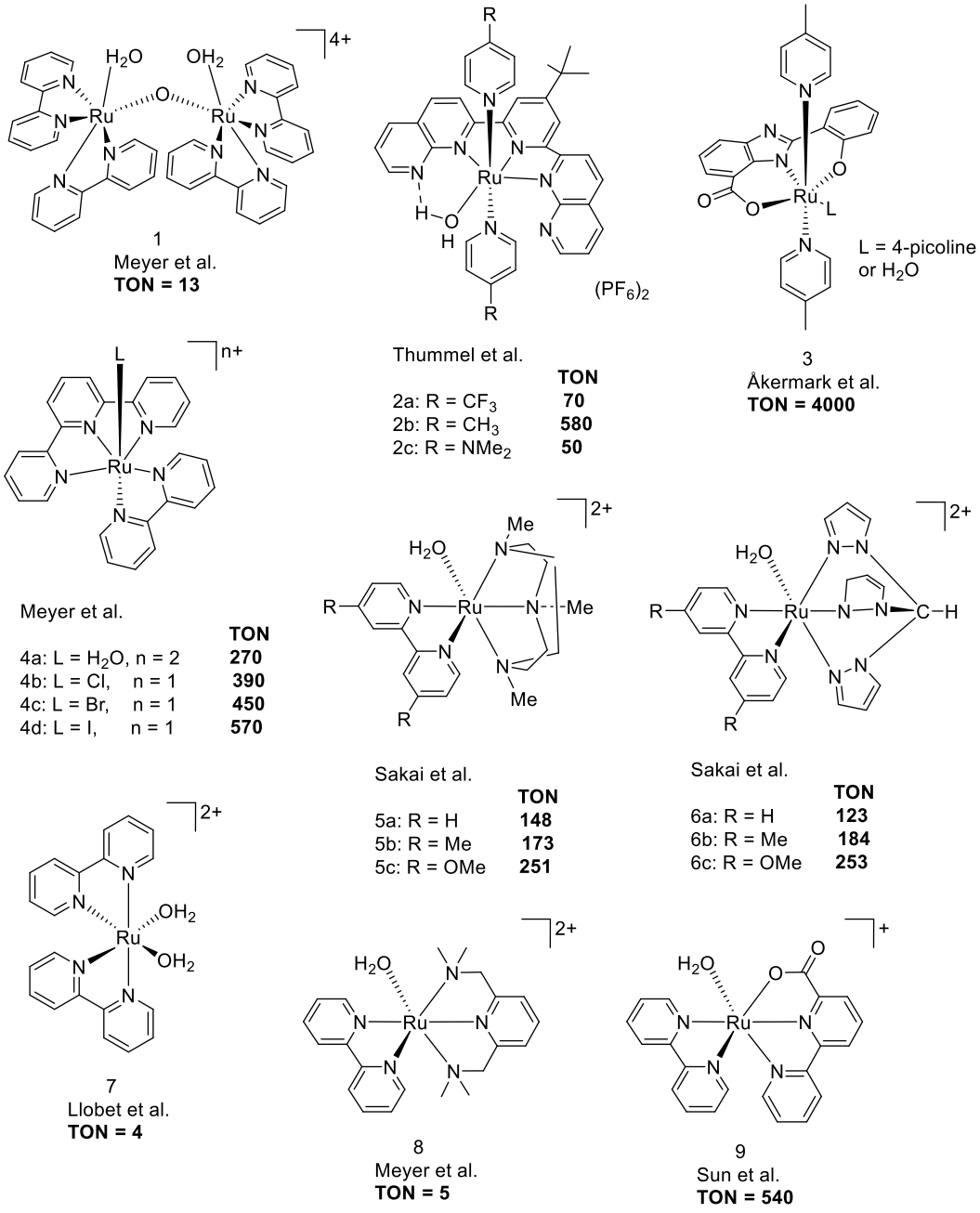

Figure 8. Molecular structures of mononuclear ruthenium aqua complexes for water oxidation.

In the knowledge that non-aqua ruthenium catalysts underwent rapid aqua conversion into the real active catalyst, complex 7 was designed containing two ligand-bound water molecules in order to investigate the relation between chemical structure and activity. Suprisingly, the *cis*-$[Ru(bpy)_2(H_2O)_2]^{2+}$ showed higher activity under catalytic conditions, with a TON = 4, than

trans-$[Ru(bpy)_2(H_2O)_2]^{2+}$ with a TON = 1.[113] One explanation for this observation was that both isomers were following different reaction mechanism when oxidized. Based on EPR analysis, an H-bond-stabilized dimer, structural similar to that find in the blue dimer, was proposed as the real catalytic species. Considering that this radical coupling mechanism was responsible for activity involving both coordinated oxygens, it appears likely that the dimer structure can only be formed by the *cis*-isomer, explaining the non-linear concentration dependence of the oxygen evolution rate.

Using the example of complex 8 formed by a tridentate ligand and containing two robust σ-donating tertiary amine groups, SUN et al. prepared a more active catalyst by introducing an anionic carboxylate ligand in complex 9, thus decreasing the energy barrier for the release of O_2.[75] Earlier studies by ÅKERMARK et al. reported similar results, clearly showing that these findings can be applied to a variety of mononuclear ruthenium complexes in order to design structures with enhanced catalytic properties.

Besides the influence of substituents, ligand type and trans–cis effects, a further ligand effect on the catalytic activity that should not be underestimated is the geometric arrangement of the aqua ligand. For this purpose, complexes of the type $[Ru(NNN)(N)_2(L)]$ were synthesized by THUMMEL and coworkers that allow a direct comparison to the mononuclear WOCs of the type [Ru(NNN)(NN)(L)].[114] The molecular structures of the complexes are shown in Figure 9.

As illustrated by complexes 4, 10-14, the $[Ru(NNN)(N)_2(L)]$ type compounds show higher activity than their [Ru(NNN)(NN)(L)] analogues, which can be attributed to the position of the exchangeable ligand. As evident from their TON values, axially or equatorially bound chloride ion as well as the steric demands of the surrounding ligands (4-pic, bpy) within the complex cause blockade of the catalyst's active site, thus making the preactivation step to the aqua complex more difficult or even impossible. However, when the chloride ion is attached to the equatorial plane, the sterical blockade appears to be lifted resulting in notable water oxidation performances.

A significant effect on catalytic ativity was observed when comparing complexes 10, 11 and 14 of the $[Ru(NNN)(N)_2(L)]$ type. The reduced activity in these complexes was found to correlate with the geometric arrangement and bulkiness of the surrounding ligands, which are located close to the exchangeable ligand, leading to an increase of the sterical hindrance to the approaching ligand exchange reaction. In order to further invesigate this effect, complexes 15-17 were synthesized by small modifications of the phenanthroline ligand. As assumed, with additional steric effects of methyl groups, the TON decreased systematically from complex 15 to complex 16 to complex 17. The same effect was observed for complex 18 and complex 19,

by which it could be shown that the the catalytic activity was dependent on the steric hindrance of the proximal benzyl ring connected to the bipyridyl ligand. Compared to complex 4b, the catalytic activity of complex 18 is reduced by a factor of 6, giving a TOF of 10 x 10^{-4} s^{-1} and a TON of 66. Extending the bpy ligand by two phenyl rings even led to a total deactivation as shown for complex 19.

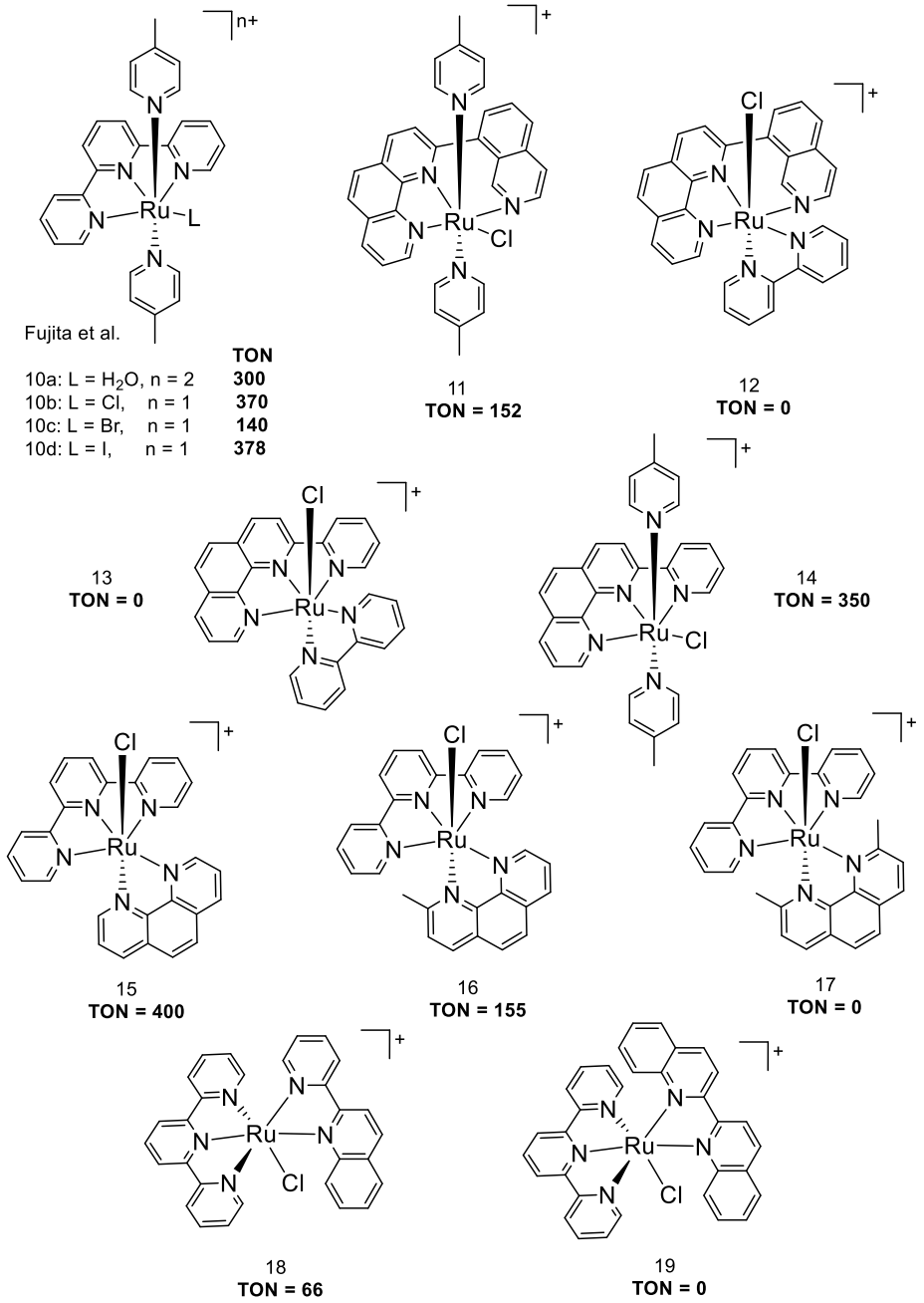

Figure 9. Molecular structures of ruthenium complexes of the type [Ru(NNN)$(N)_2$(L)] and [Ru(NNN)(NN)(L)].

One another important influencing the catalytic activity was intramolecular hydrogen-bonding, as shown in Figure 10, underlying the role of ligands in catalytic water oxidation. LLOBET and

coworkes have synthesized two isomers with fluoro substituents on the bpy ligand, showing that H-bonding networks found in type 21 complexes lead to a strong stabilization of all potential species generated along the catalytic cycle of water oxidation.[115]

Compared to the un-functionalized complex 4a, the presence of fluorine groups results in an increase of the $Ru^{III/II}$ couple for complex 20 and complex 21, as expected for substituents with electron-withdrawing abilities. The almost identical, higher redox couples corresponding to the oxidation of Ru^{II} to Ru^{IV} (0.54 V *vs*. 0.56 V) and Ru^{IV} to Ru^{V} (1.68 V *vs*. 1.69 for 20 and 21, respectively) suggest that the arrangement of the fluorine groups has no marked effect on the electronic structure of the metal centre. Based on the structural similarity of both Ru catalysts, the different catalytic activities were therefore due to the interaction of the F atom with the nearby aqua ligand through hydrogen-bonding, thus stabilizing the $[Ru^{III}\text{-}OOH]^{+}$ species and slowing down the process of O_2 release, as also confirmed by theoretical studies.[115]

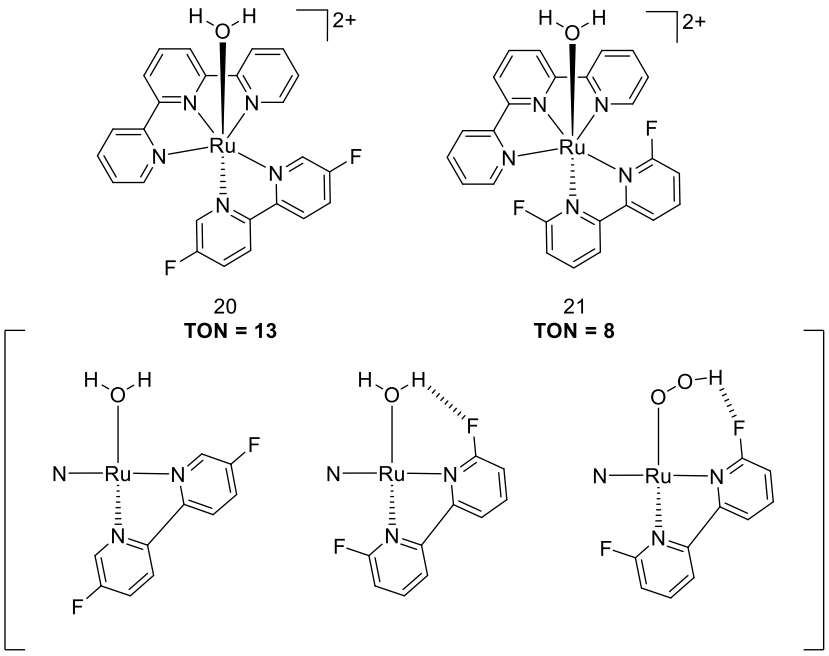

Figure 10. Schematic illustration of intramolecular hydrogen-bonding interactions in ruthenium complexes.[115]

Inspired by the fact that electronic effects as well as inter- and intramolecular H-bonding groups have a strong effect on the kinetics of the catalytic process, THUMMEL et al. recently designed a ruthenium water oxidation catalyst containing a bipyridine glycoluril ligand, complex 22, which works at a rate that is ~5 times higher than the parent complex $[Ru(tpy)(bpy)H_2O]^{2+}$.[116] Confirmed by X-ray crystallographic data analysis, intermolecular hydrogen bonding could be observed between the C=O group and the bound aqua ligand, which was believed to stabilize

the catalyst leading to a significantly higher TON of 833. Both, the electron-donating ability of the glycouril group and the formation of higher intermediates at low redox potentials further provided a major contribution in increasing catalytic activity. At pH 1, electrochemical studies revealed evidence of higher oxidation states at 1.6, 1.41 and 0.83 V for the redox couples $Ru^{V/IV}$, $Ru^{IV/III}$ and $Ru^{III/II}$, respectively. In fact, all these complexes described above already possess one axially or equatorially coordinated water molecule, or they form the active catalytic aqua species during the initial proton-coupled electron transfer by ligand-exchange.

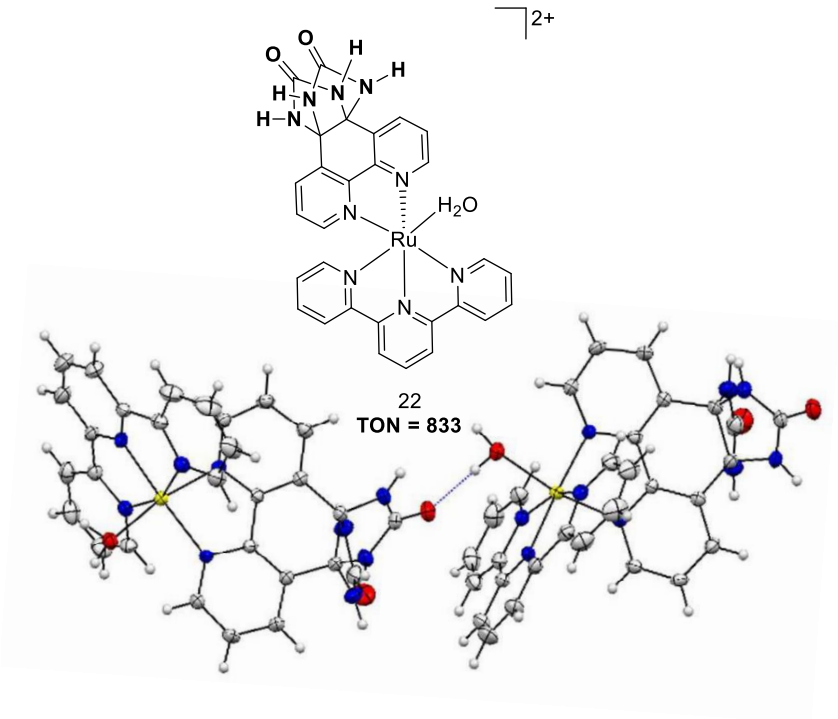

Figure 11. Top, molecular structure of complex 22. Bottom, intermolecular hydrogen bonding between C=O oxygen of bpg ligand and the coordinated water molecule. Reprinted from [116].

The development of active non-aqua Ru WOCs is attributed to the work of THUMMEL et al.[117], who reported a series of tetradentate ligands in single-site Ru complexes. On replacing the bypiridyl unit by phenanthroline (phen), a new door was open for the the design of more robust and rigid Ru catalysts. As shown in Figure 12, the resulting complexes exhibit low to moderate activity, depending on the substituents attached to the phen-bounded pyridine ligand. While complex 23a gave rise to a TON of 416, the low TON of 186 for complex 23c was due to the protonation of the amino groups under acidic conditions, thus inducing an opposite effect onto the system and acting as electron-withdrawing groups. Additionally, the bulkiness of the ligands was found to affect the water oxidation activity negatively in the same way as the analogues mononuclear ruthenium complexes containing polypyridine ligands depicted in Figure 9. As a

result, the incoming water molecules is blocked for the approaching coordination to the Ru centre, which prevents the formation of the active high-valent Ru species. Based on this knowledge, it is not surprising that the introduction of steric effects by ring extension led to less water oxidation activity, as illustrated by complex 24. Taking into account that several factors can influence the catalytic cycle, the clarification of the mechanism pathway of water oxidation is one major aim of research, especially regarding the future design of catalysts based on ruthenium and other transition metals. Mechanistic aspects of the catalytic O-O bond formation will be discussed in section 3.3.3.

In previous studies, much work has been done on varying the axial ligands of ruthenium catalysts as well as investigating substituent effects, but less in studying the equatorial influences. Therefore, current studies focused on the synthesis of Ru WOCs modified in the equatorial plane in order to enhance the catalytic properties even more. Examples include the positively charged complex of ÅKERMARK et al.[118] containing a dicarboxamide ligand (complex 27), the charge-neutral complex of RICHMOND et al.[119] based on a biisoquinoline dicarboxylic acid ligand (complex 28) and the complex of SUN et al.[120] with the strongly electron-donating and planar carbazoledicarboxylate ligand (complex 29), as can be gathered by Figure 12. A comparison of the catalytic performances reveals a correlation between water oxidation activity and equatorial effects. Features, which can stabilize the Ru center at high redox states allow water oxidation to proceed efficiently. However, inducing non-planarity and rigidity in the equatorial coordination sites displays the reverse effect, *i.e.* drop of the catalytic activity.

The continuous search for neutral mononuclear Ru WOCs of the type 25, 28 and 29 can be traced back to the work of Licheng Sun, undoubtedly consider as a pioneer in the field of catalytic chemistry. Thanks to his excellent work, experimental methods for the isolation of high valence intermediates have been developed and subsequently supported by theoretical calculations. The very simple ligand design including a bipyridine moiety, the easily available ruthenium precursor $Ru(DMSO)_4Cl_2$ and various pyridine axial ligands enabled a systematic investigation of complexes 30 (TON_{max} = 2010, TOF = 32 s^{-1}), 31 (TON_{max} = 11300, TOF = 303 s^{-1}) and 32 (TON_{max} = 61300, TOF = 286 s^{-1}). Based on earlier results, SUN made use of the strong electron-donating ability of carboxylate groups, which were known to lower the potential required for fast WO. Using cerium(IV) as sacrificial oxidant, initial turnover numbers up to ~62000 were determined, proving the efficiency and robustness of such complexes (Figure 13).

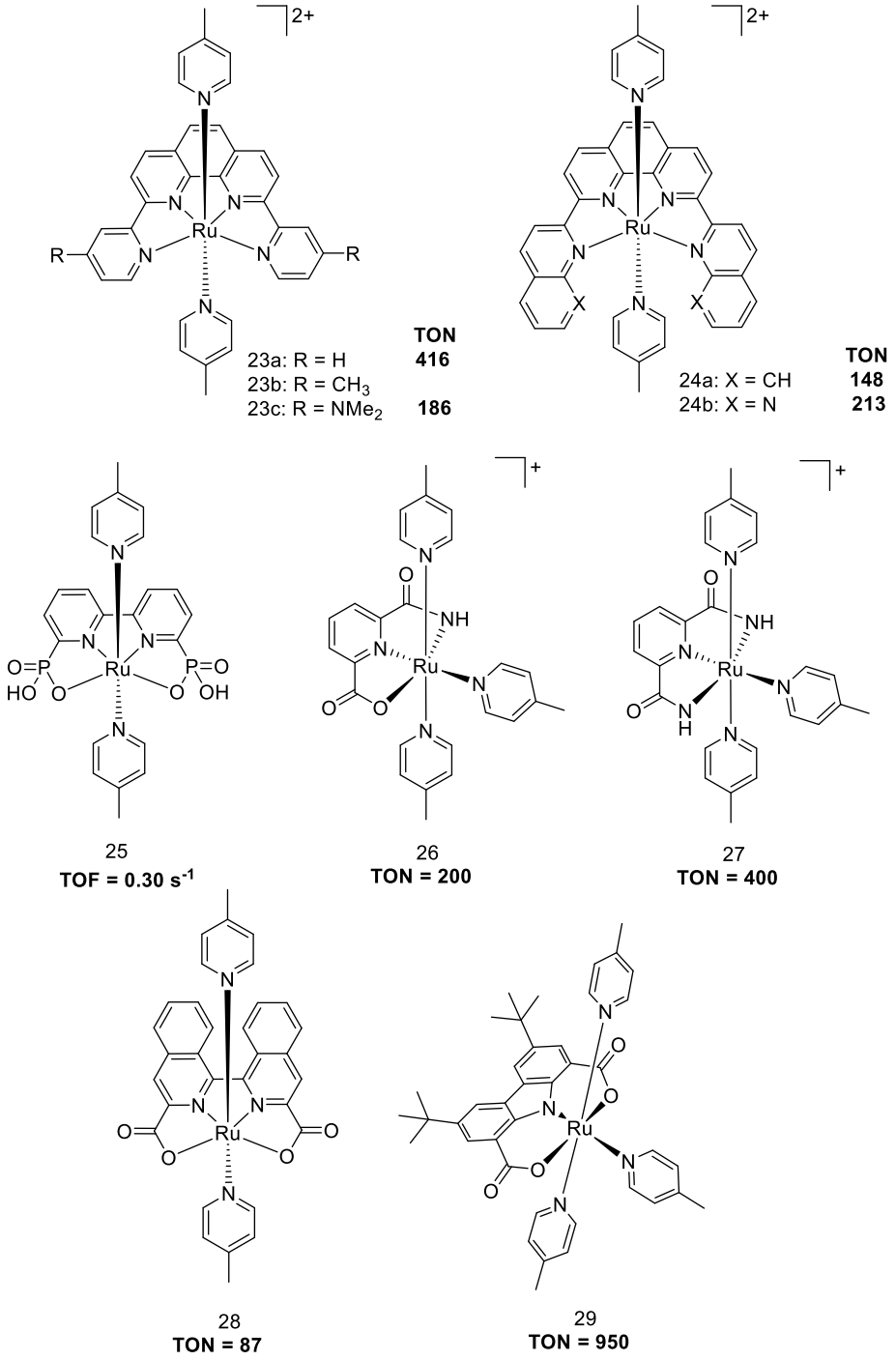

Figure 12. Molecular structures of mononuclear non-aqua ruthenium complexes for water oxidation.

However, one drawback of the [Ru(bda)(L)$_2$] catalysts is their limited water solubility, which makes the use of co-solvents necessary. SUN et al. observed that a strong coordinating co-solvent such as acetonitrile showed a dramatic influence on both, solubility and reactivity by coordination to the metal centre. By using less coordinating organic solvents such as trifluoroethanol, the catalytic stability of a given ruthenium system could be significantly

increased. For catalyst 32, replacement of acetonitrile by trifluoroethanol gave rise to a TON of 62 000[74], thus even exceeding the TON of 55 000, which was regarded as the highest value since developing the first catalysts based on ruthenium. The results demonstrated that the choice of the solvent plays a major role in the catalytic water oxidation process, especially those, which show no affinity for the Ru binding site. However, $Ru(bda)(L)_2$ type complexes and their derivatives are still the best ruthenium WOCs known to date.

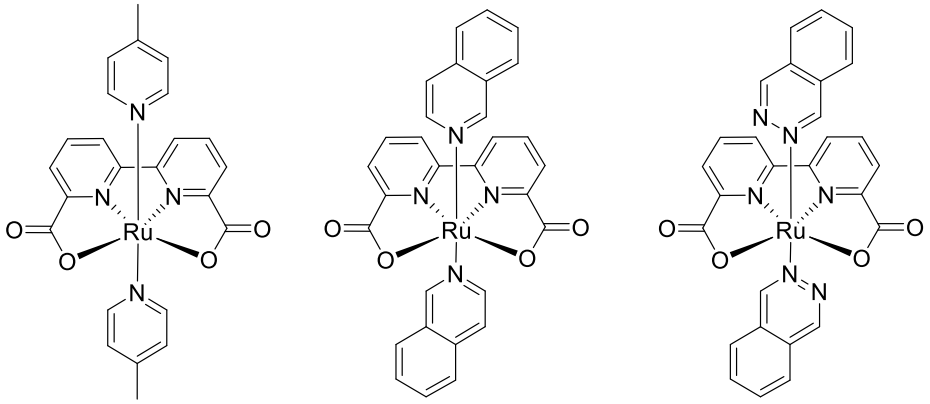

Figure 13. Molecular structures of ruthenium WOCs 30-32.

With the aim of achieving higher efficiency, several modifications have been made at the axial binding site of mononuclear ruthenium complexes. Under the same catalytic conditions, Ru-bda catalysts with extended π-systems at the axial position showed improved stability and performance towards WO. Accordingly, the isoquinoline ligand in complex 31 shows much higher TON and TOF values compared to complex 30 containing the 4-picoline ligand. This is due to non-covalent attractive interactions between two axial isoquinolines, also called π-π stacking[121], which reduce the barrier for the radical coupling I2M. Moreover, introducing a strong electron-donating ligand enhances longevity and durability properties for O_2 generation, an initial assumption that was later confirmed by DFT calculations, which were performed to investigate the Gibbs free energy of reaction in pH 0 aqueous solution as a function of HOMO energy of the ligand in the gas phase. Therefore, it is complex 32 with the axial phthalazine ligands being far more robust than all the other ligands applied within the Ru-bda family.

Understanding the mechanisms behind the catalytic water oxidation enables to develop the ideal catalyst for future applications. Previous studies and reports have shown that it is possible to easily tune the mechanism pathway of WO only by changing the nature of the coordinated ligands and thus the properties of the complex. Hence, the next section will give a brief

overview of the main classes of reaction pathways postulated for ruthenium complexes on the basis of photophysical (UV-vis), electrochemical (CV/SW) and standard analytical methods (NMR, mass).

3.3.3 Mechanistic Insights – WNA *vs*. I2M.

Currently one of the most debated questions is the critical O-O bond formation during the catalytic cycle to release molecular oxygen. In general, there are two possible pathways for the oxidation of water (Figure 14). First, the water nucleophilic attack (WNA) on a metal-oxo unit (M-O), and second, the interaction of two M-O units (I2M). The majority of homogeneous ruthenium WOCs generate oxygen *via* the WNA mechanism[76, 101, 113, 122-125], which is also known to take place in the oxygen-evolving complex of PSII.

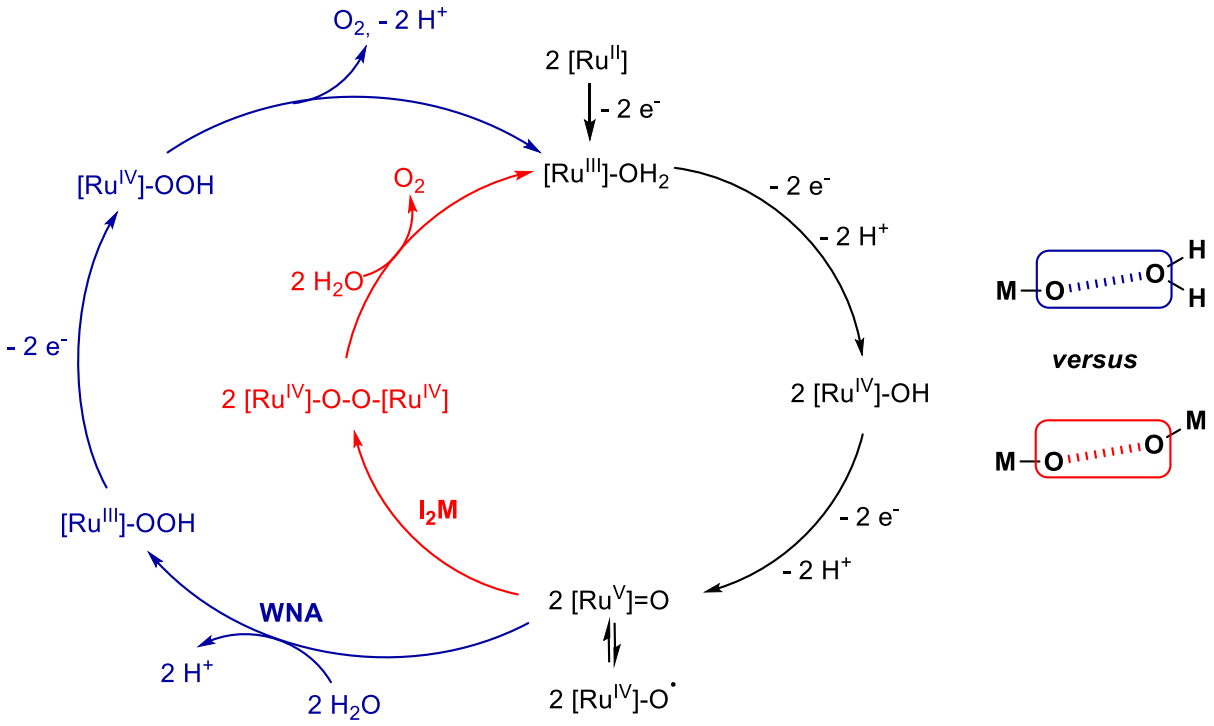

Figure 14. Possible mechanistic pathways for the key O-O bond formation step.

In case of WNA, an unbound free water molecule precipitates in the formation of the O-O bond. As a result, the metal centre undergoes several oxidation states to generate a hydroperoxide species, triggering the release of O_2 by hydrogen abstraction.

For I2M[126, 127], two mono-radical M-O units have to couple to each other, either intra- or inter-molecularly, yielding a peroxo intermediate which subsequently eliminates one O_2 molecule. To make the O-O bond step possible, most of the metal complexes which enter the catalytic

cycle of both reaction pathways often function as pre-catalysts that needed to be activated by dissociation of one labile ligand (axial or equatorial) and coordination of one water molecule, both taking place simultaneously. One example is the dinuclear Ru-Hbpp water oxidation catalyst of LLOBET[128, 129], by which O-O bond formation proceeds intramolecularly through this mechanism. However, the most famous example of mononuclear ruthenium complexes is the Ru(bda) family of Sun, which catalyze chemically-driven water oxidation by an intermolecular interaction between two complexes.

Pioneering studies have shown that mechanistic switching from one path to the other, usually from I2M to WNA, can be realized by slight modification of the ligands. For example, inducing rigidity or non-planarity in the equatorial plane were found leading to a drop of the catalytic activity with a preference for the WNA mechanism. Diffusion-limited systems also catalyze water through the water nucleophilic attack pathway.[130-133] The un-substituted catalyst 30 follows a second order reaction, while substitution with bromine, dibromine and nitro at the para-position of the bda-ligand results in a totally different kinetic behavior, which is primarily due to the increased electron-withdrawing character of the substituents.[134]

CHAPTER 4

Metal-Organic Frameworks

A relatively novel class of microporous materials are called metal-organic frameworks (MOFs), which combine the benefits of inorganic and organic chemistry. In general, MOFs are built up from metal ions or clusters, also known as secondary building units (SBUs), which are linked by organic bridging ligands.[135-137]

The crystalline products are formed during MOF synthesis through ligand exchange processes within solution, as will be described in section 4.4. MOFs are characterized by enormously high surface areas, high porosity and flexible tunability of their properties. Due to the easy variation of the organic linkers, the pore size can be exactly defined and optimized for specific applications. To keep the porous structure of MOFs, the use of rigid ligands containing multiple binding sites is necessary. Thanks to their properties which surpass those of the structural similar zeolites, MOFs are qualified for gas storage, separation processes, catalysis and for chemical sensing. At the beginning of this chapter, key terms used throughout this thesis will be briefly explained to give a better understanding of the current context.

4.1 Terminology for MOFs.

MOF = Metal-organic framework. According to IUPAC (International Union of Pure and Applied Chemistry), MOF is a *'Coordination Polymer (or alternatively Coordination Network) with an open framework containing potential voids.'* [138]

SBU = secondary building units. The term *'secondary building unit'* was originally used in zeolite chemistry, this concept was later introduced to MOFs. In general, SBUs are described as metalcarboxylate clusters that are linked by organic linkers. These nodes can be built up from different clusters of metal oxides or single metal ions, which can undergo post-synthetic metal exchange.

PSM = Post-synthetic modification. The term *'post-synthetic modification'* contains every possible change in a MOF following its synthesis. This procedure is used to develop MOF structures that cannot be generated by direct synthesis. Typically, post-synthetic

transformations require the presence of reactive functional groups on bridging linkers, which can be directly converted into other functional groups under mild experimental conditions. If this is done before the functionalized linker is incorporated into the MOF, this process is called pre-synthetic modification.

Interpenetration = Interpenetration takes place when large pores in MOFs accommodate a second network or subnetwork. This process occur mainly during MOF formation.

MOF Digestion = MOFs are insoluble in both organic and inorganic solvents. Digestion refers to the breakdown of the covalent bonds between organic linkers and SBUs into free (unbound) carboxylic acid linkers that can be detected by NMR.

4.2 A new wonder material – MOF-5.

Since the first MOF was discovered, the field of research based on MOFs was enlarged over the past years.[139-144] In this context, MOF-5, also called IRMOF-1, is one of the best-known examples representing a highly stable and crystalline metal-organic framework, which was first discovered by YAGHI et al.[137] in 1999. The structure of MOF-5 is formed from tetrahedral Zn_4O nodes which are bridged by 1,4-benzenedicarboxylate (BDC) as organic linkers. MOF-5 is characterized by its exceptional surface area of 2900 m^2/g, high porosity, temperature (up to 300 °C) and chemical stability even upon total removal of all solvent molecules trapped in the MOF pores in high vacuum. The solvothermal synthesis technique (in DMF as solvent, at temperatures between 90-105 °C for 18-24 h) is the most widely used method for preparing MOF-5.

MOF-5 is formed by the reaction of $Zn(NO_3)_2 \cdot 6\ H_2O$ and 1,4-benzenedicarboxylic acid (BDC) (Figure 15). Its framework consists of $[Zn_4O]^{6+}$-clusters in octahedral subunits, which are connected to BDC linkers (Figure 16). The highly crystalline product is resistant to dry air, but it decomposes in moist air by protonation of the Zn_4O SBUs.

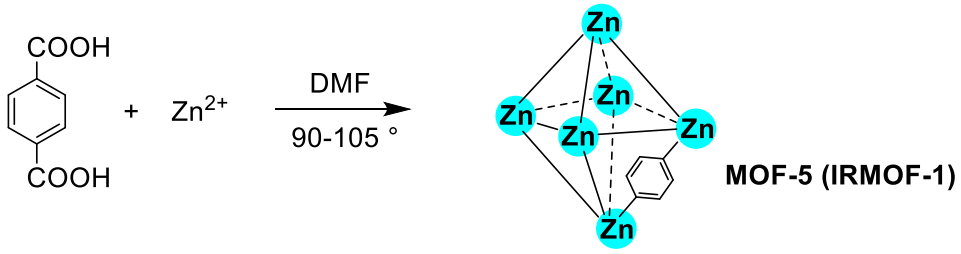

Figure 15. Synthetic route of MOF-5 (IRMOF-1).

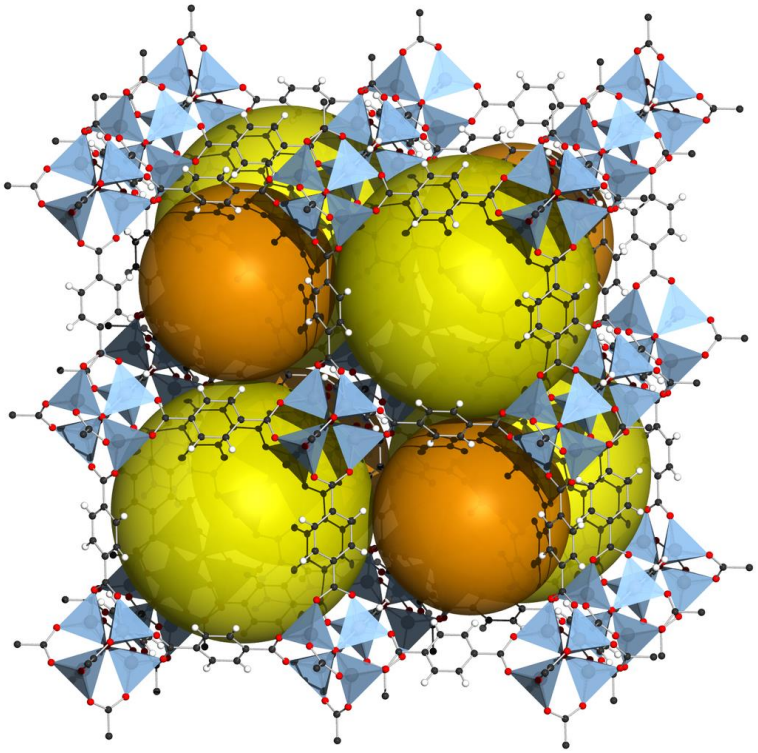

Figure 16. 3D structure of MOF-5 (IRMOF-1). Reprinted from Ref [137].

A considerable disadvantage of MOFs is their tendency to collapse structurally upon thermal or physical treatment.[145-149] Therefore, the most compelling challenge regarding MOF synthesis is the introduction of linkers with increased sizes and lengths, which are rigid enough to survive both, a possible network collapse and a general phenomenon occurring in self-assembled systems that is known as framework interpenetration.[150, 151] In other words, interpenetration often leads to reduced pore size, thus limiting the pore space in MOFs. Based on these finding, future work focused on the installation of longer organic linkers into MOF scaffold to enhance stability by controlling interpenetration through linker conformation. Recently, a new class of MOFs based on zirconium was discovered at the University of Oslo, commonly known as UiO-MOFs, which displayed unique properties thanks to the highly charged and oxygen-affine zirconium atoms at the nodes.[33, 152]

4.3 UiO MOFs.

Three newly synthesized Zr-MOFs, including UiO-66, UiO-67 and UiO-68, were synthesized only by extending the starting linker bdc-linker by one or two phenyl units (Figure 17). According to expectations, both the surface area as well as the pore volume were increased upon extending the length of the organic linker. UiO-MOFs are the best examples clearly

showing that tailoring the pore environment, which is especially required for catalytic applications, is feasible at optimized synthesis conditions.[153, 154]

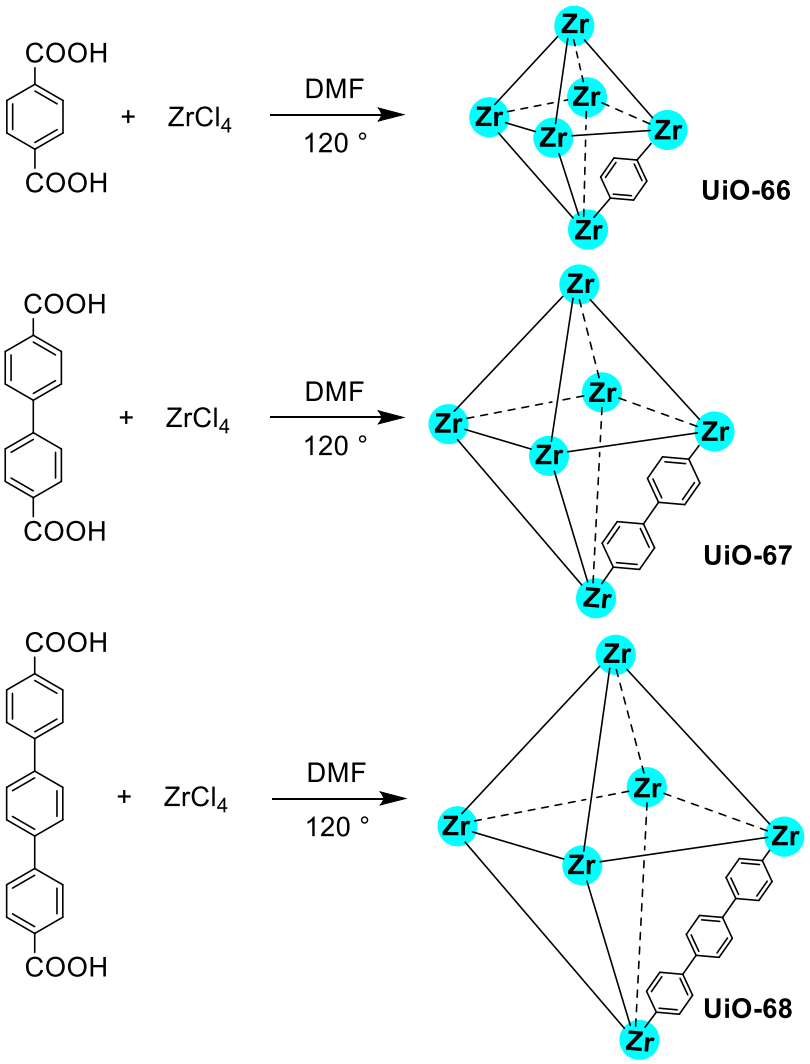

Figure 17. Synthesis reactions of UiO-MOFs (UiO-66 and UiO-68).

The SBUs of UiO-66 consist of six Zr(IV), whereby each zirconium ion is surrounded by eight oxygen atoms resulting in a square antiprismatic coordination geometry. Each SBU is coordinated with 12 carboxylate linkers.

UiO-66 has a cubic structure, in which octahedral cages close to 11 Å are connected to tetrahedral cages close to 8 Å in a 1:2 ratio through a small triangular window close to 6 Å. UiO-66 is stable in various organic solvents (benzene, acetone, ethanol, DMF), upon washing in boiling water and in air up to 375 °C. The specific surface area was determined to be 1147 m^2/g. Replacing bdc with 4,4'-biphenyldicarboxylate (bpdc) or 1,1':4',1''-terphenyl-4,4''-dicarboxylic acid (tpdc) gives rise to a calculated surface area of 3097 m^2/g and 4000 m^2/g, respectively. However, reproducibility is one of the most serious limiting factors of

MOFs. As a result of the increased linker size, pristine 68 and its derivatives are difficult to reproduce. Thus each MOF synthesis requires product-specific conditions. The following sections will provide an overview of the standard synthesis methods of MOFs.

4.4 Strategies of MOF synthesis.

There is no common rule for the synthesis of MOFs. Parameters such as reaction time, temperature, concentration of the reactants and reaction pressure relate to the final product. Starting from the same starting materials, different synthetic methods can result in different network structures.

4.4.1 Conventional heating.

Conventional heating methods can be divided into two major types: solvothermal and non-solvothermal. According to the definition of RABENAU[155], solvothermal reactions are performed in closed vessels such as autoclaves or closed glass flasks under autogenous pressure by heating above the boiling point of the solvent. In a typical solvothermal synthesis, the reactants are dissolved in the reaction solvent, commonly DMF, and mixed together before transferring to a preheated autoclave. A typical synthesis is kept for 24 h until MOF precipitation is finished. The crystalline product is filtered off and washed with low boiling point solvents to remove both, unreacted reactants and guest solvent molecules. The isolated materials are then activated by heat and vacuum treatment.[156]

Non-solvothermal heating includes reactions below or at the boiling point of the solvent. MOF-5, MOF-74, MOF-177, HKUST-1 and ZIF-8 are the most prominent examples which precipitate out of the solution at room temperature.[157-159] In general, aprotic polar formamides are preferred as reaction solvents due to their excellent dissolution power required for the hydrophilic metal salts and hydrophobic aromatic acids, which prevents the formation of two-phase systems and long reaction times.

4.4.2 Other strategies of MOF synthesis.

Traditional heating is not always the most suitable method for MOFs. For example, microwave irradiation[160] provides much faster processes requiring minutes rather than hours. No additional solvents or equipment are needed for further isolation and purification of the products, enabling higher yields than conventional methods.

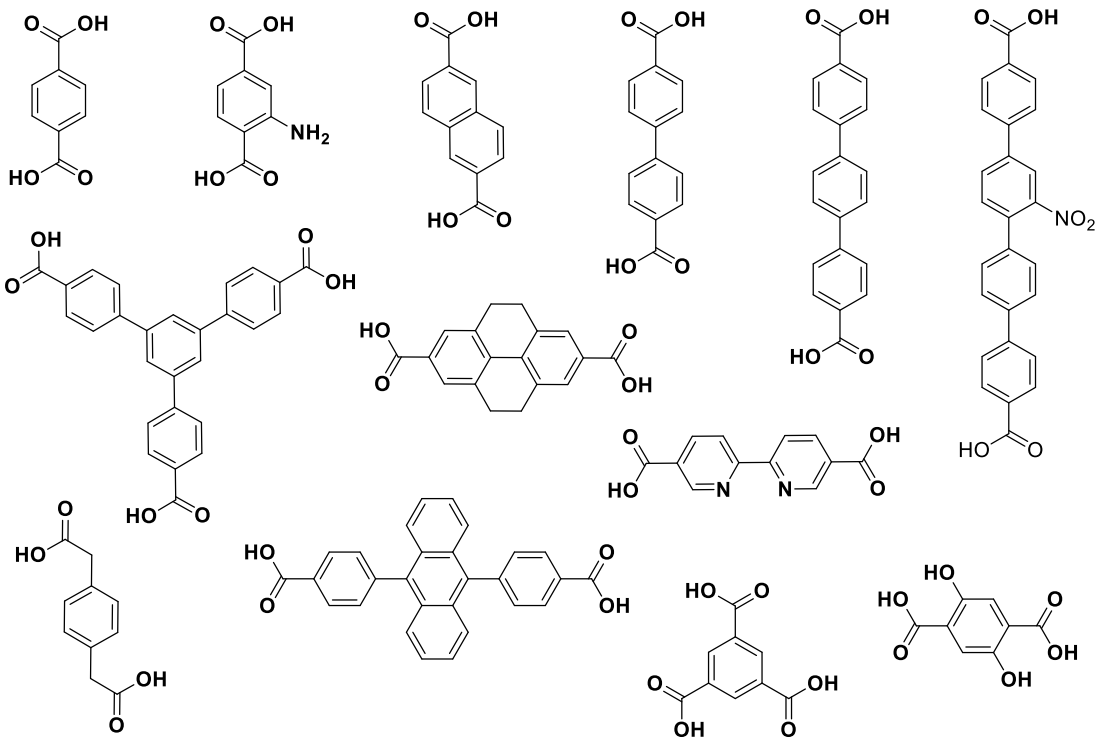

Figure 18. Molecular structures of selected organic linkers used or MOF synthesis.

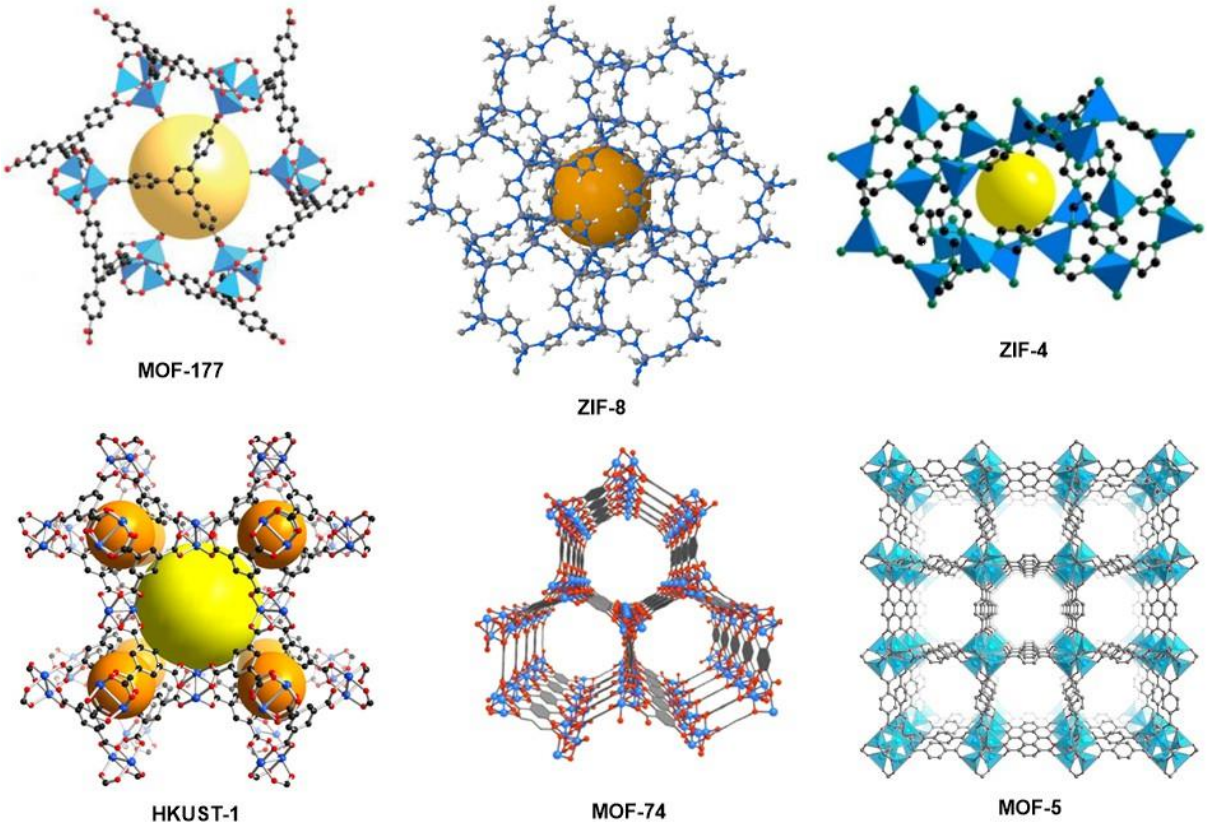

Figure 19. 3D structure of MOFs obtained from non-conventional syntheses. Reprinted from [168-173].

Another promising method is electrochemical MOF synthesis[161-163], which promises shorter reaction times at low temperatures and gives the opportunity to manipulate the reaction conditions during MOF formation, for example by controlling the oxidation state of the metal upon changing the appropriate voltage. Several Zn-based MOFs were synthesized using the electrochemical route and firstly reported by BASF in 2005.[164]

The use of a mechanochemical synthesis on a microporous MOF was first reported in 2006 by JAMES et al., when the preparation of $Cu(INA)_2$ was described.[165] The main benefit of sonochemical procedure is that it works under mild conditions (solvent-free, lower than 30 °C), product is isolated at very short times (10-60 min), both avoiding dramatic network collapse. The by-products formed can be easily removed out of the pores by thermal activation. A relatively new synthetic route is based on sonochemistry[166], combining environmental and economic benefits with reaction conditions, which is usually carried out at a frequency of 20 kHz. Using this method, MOF-5 was synthesized with greater material properties.[167]

In order to obtain information about the structural and physical properties of MOFs like porosity, surface area and thermal stability, different characterization techniques are employed including powder X-ray diffraction (P-XRD), nitrogen adsorption/desorption isotherms according to the Brunauer-Emmett-Teller (BET) model, thermogravimetric analysis (TGA), aqueous stability tests and MOF digestion. The operating principles of these methods will be introduced in the following sections.

4.5 Characterization of MOF materials.

The main focus of this chapter lies on understanding the principles of characterization techniques for MOFs, which represents one main part of this work.

4.5.1 Powder X-ray diffraction (P-XRD).

P-XRD[174] is a wide-ranging analysis method which gives detailed information about the structure, porosity, polymorphism, phase composition, crystallite size and residual stress of powders, solids and liquids. A powder diffraction pattern is an image of scattered intensity as a function of the Bragg-scattering angle (2θ).[175]

As a result of the regular arrangement of the atoms, a crystalline material produces a diffraction pattern of well-defined Bragg peaks (reflexes), while increased lattice disorder leads to a broadening of these reflexes correlating to an amorphous or nano-sized material. Since each material produces a unique diffraction pattern, the identification of a compound whose three-

dimensional structure is unknown is done by comparing the experimental diffractogram with a database of similar diffraction (fingerprint) patterns.

In general, there are two different processes which can generate x-ray photons: one is x-ray tube and one is synchroton radiation, the former commonly used as fast alternative in laboratories. Despite the high costs and elaborate equipment, synchroton radiation offers enormous advantages over conventional x-ray source thanks to the brightness of the photon source associated with shorter measuring times, the tunability of x-ray wavelengths and the continuous distribution of photon energy up to giga-electron volts (GeV) involving a wide spectral range from infrared to hard x-rays.[176-179]

The fundamental principles of x-ray diffraction is based on the interaction of x-ray photons of specific energy with atoms and electrons in matter. When x-rays interact with the surface of a sample, part of the waves will be absorbed, transmitted or scattered. Besides being coherent and incoherent, scattering events can be divided into elastic and inelastic processes dependent on whether an energy change of the wave has taken place or not after being scattered.

In case of elastic scattering, also called Rayleigh scattering[180], the total kinetic energy of the colliding particles remains unchanged, while the direction of the photon's wave vector is reversed. From the point of view of classical physics, the incident electromagnetic wave induces oscillation in the atom bound electrons, which produces secondary electromagnetic waves of the same frequency as that of the oscillation. Whereas, when scattering is inelastic (subdivided into Compton or Raman scattering), the photon looses part of its energy due to Bremsstrahlung driven by energy transfer from the photon to the sample by excitations.[181] However, coherent elastic (Bragg) scattering processes are of most interest for diffraction purposes. Thanks to the regular repeating arrangement of atoms in a lattice, crystalline samples are able to diffract light. Scattering of x-rays from these atoms generates a regular array of spherical waves propagating in all directions. As shown in Figure 20, a diffraction pattern is produced only when waves scattered from two different planes are in phase and interfere constructively. In other words, diffractions peaks only occur when the geometrical conditions of Bragg's law, expressed as

$$n \cdot \lambda = 2 \cdot d_{hkl} \cdot \sin\theta \qquad \text{(Equation 4.1)}$$

are satisfied.[181] Hereby, θ is the angle of incidence of the X-ray, and 2θ the angle between the incident beam and the detector, λ is the wavelength of the incident X-ray beam, n is any integer and known as the order of reflection, while d represents the spacing between the atomic planes, corresponding to the Miller indices d(h, k, l).[181]

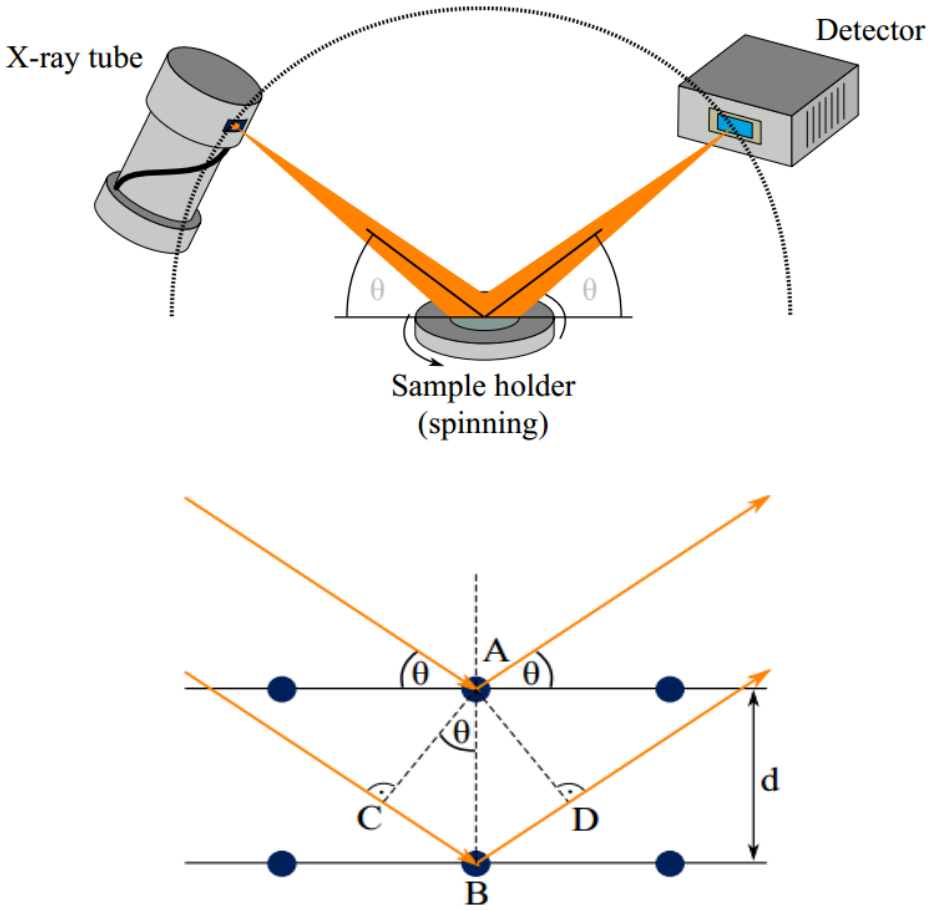

Figure 20. Top, geometric representation of Bragg-Brentano *θ-θ* geometry. Bottom, schematic presentation of Bragg's law. Reprinted from [181].

The so-called Bragg-Brentano[182, 183] configuration is the most commonly used instrumental arrangement for powder diffraction experiments, which can be driven in two different scan modes. In a traditional θ-2θ scan, the x-ray source remains fixed while the sample is slightly rotated by the angle θ in the x-ray beam and the detector moves by 2θ, allowing a full scan of the crystallite. The main disadvanages of this method are that in some cases, the sample can fall out of the holder during the rotating process, the flattening process induces a preferred orientation at the sample surface, and the handling and analysis of some samples can be limited due to their air sensitivity and strong surface electrostatic interactions. Alternatively, the sample is fixed while both the x-ray source as well as the detector are moved by the angle θ simultaneously (*θ-θ* geometry), as schematically shown in Figure 20 (top). If the wavelengths of x-rays are similar to the distance between atoms, the peak positions will provide information about the crystal lattice.

4.5.1.1 Evaluation of XRD data.

After having discussed how diffracted patterns are constructed, several examples of x-ray diffractograms will be given from differently structured samples to understand XRD interpretation (Figure 21, left). The analysis of diffraction patterns is quite difficult due to several factors. Besides instrumental parameters such as X-ray beam size, detector resolution or imperfect focusing, the quality of Bragg peaks is strongly influenced by the sample itself (strain, finite size, fluctuations in lattice spacing etc.).[184]

Usually, solids can be divided into crystalline and amorph, producing either a sharpsymmetrical or a broadened peak. Peak broadening is mostly related to the thermal and chemical instability of the samples upon the activation process to remove all solvent molecules out of the pores, which is literature-known and regarded as one of the greatest challenges associated with MOF characterization. In this work, framework collapse was clearly observed by a color change from white to shining yellow when samples were dried under vacuum, even at room temperature. This phenomenon is probably due to a small amount of solvent molecules trapped within the pores quickly escaping by external pressures. Furthermore, slow linker exchange during MOF synthesis can lead to defects and destabilization of the resulting MOF. Since excess of modulators are added to improve the crystallinity, the competition with the MOF's bridging ligands for coordination to the SBUs can result in less ordered and robust structures, which tend to collapse in solvent-free medium. In the best case, the amorphous component will overlap on existing crystalline patterns. Additionally, uncontrolled synthetic conditions such as rapid cooling and heating, or precipitation of the product will significantly increase the amount of amorphous impurities. Another source of error is the preparation of the sample as mentioned before. Since particles in a powder tend to lie flat on the surface, preferred orientation of individual crystallites will lead to some intensified and some reduced reflections. In order to minimize such effects, the samples need to be ground repeatedly to fine prior to measurement.

4.5.2 Nitrogen physisorption.

The determination of the specific surface area of a crystalline powder is achieved by physical adsorption of a gas (adsorbate) on the solid surface (adsorbent). The fundamental interacting force of physical adsorption is caused by van-der-Waals forces between the gas, usually nitrogen, and the surface, which depends on the pressure and temperature. The surface area can be calculated from the number of adsorbed molecules in the monolayer.[185]

According to IUPAC, the physisorption isotherms can be divided into six types, which are shown in Figure 21 (right). For microporous materials such as MOFs, the most widely used

method for the measurement of the surface area is the Brunauer-Emmett-Teller (BET) method. Typical BET isotherms are indicated in types II and IV.

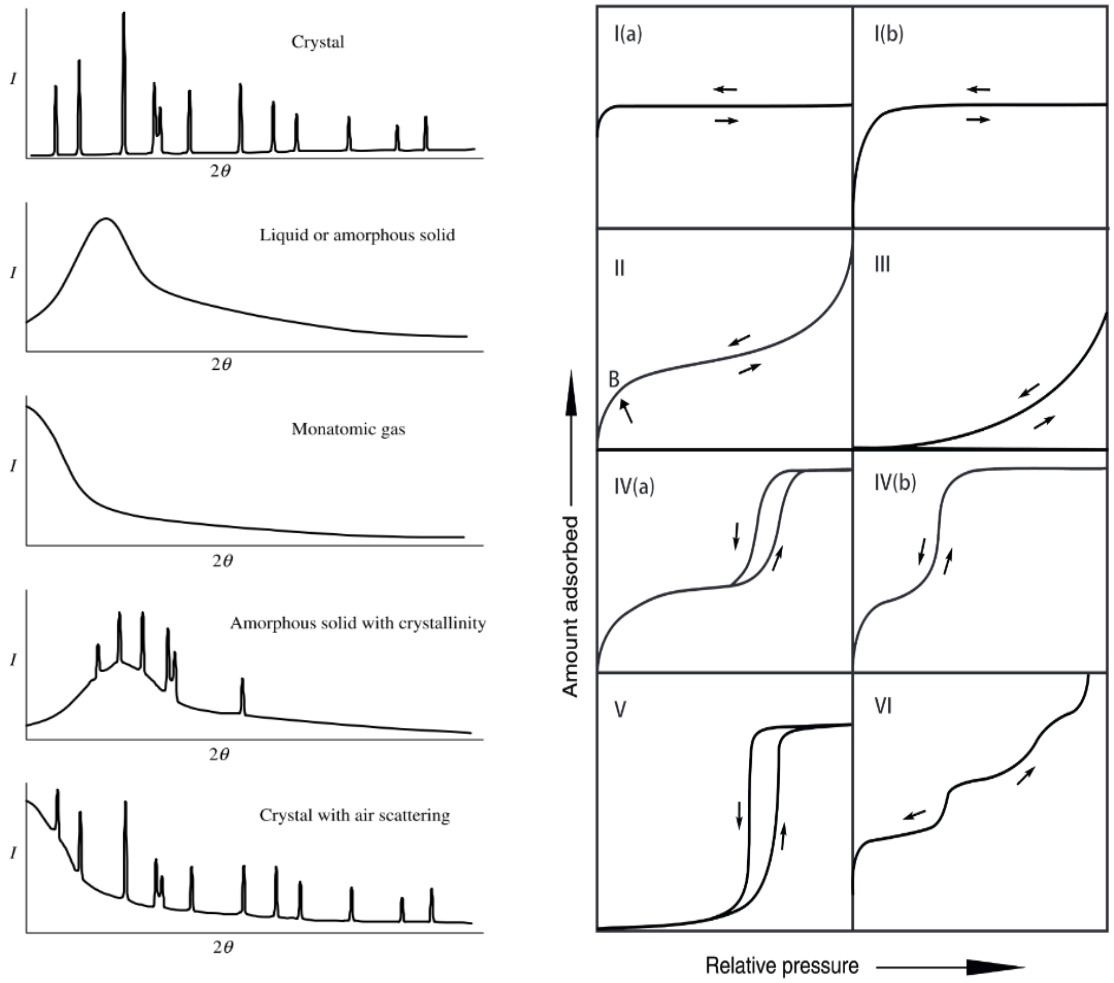

Figure 21. Left, influences of ordered and disordered matter on diffraction pattern of MOFs. Reprinted from Ref. [184]. Right, classification of physisorption isotherms. Reprinted from Ref. [185]: *Type I isotherms are observed for microporous solids; type II isotherms are given by nonporous or macroporous adsorbents; type III isotherms are representative of nonporous macroporous solids; type IV isotherms are characteristic for mesoporous adsorbents; type V isotherms are observed for water adsorption on hydrophobic microporous and mesoporous adsorbents; type VI isotherms represent layer-by-layer adsorption on a uniform nonporous surface, for example graphitized carbon.*[185b]

4.5.2.1 Calculation of surface area from BET method.

The classical methods to determine surface characteristics (specific surface area S_{BET}, pore volume, Ø pore size**)** are based on the model of Brunauer-Emmett-Teller and Langmuir. However, the latter gives rise to values of S_{total} much larger than those obtained from the BET model, especially when microporous materials are used. Considering that the adsorption model of Langmuir is limited only to one monolayer of adsorbate, the always higher value for the Langmuir surface area is attributed to the size and number of gas molecules adsorbed over the first layer on the surface of the adsorbent, while the BET model - in theory - considers multilayer formation.[186] Hence, the BET equation is a kind of extension of the Langmuir model. The resulting BET equation is expressed by

$$\frac{p}{n_a(p_0-p)} S_{total} = \frac{1}{n_m C} + \frac{(C-1)}{n_m C}\frac{p}{p_0} \qquad \text{(Equation 4.2)}$$

With p = the equilibrium pressure, p_0 = the saturation pressure of adsorbates at the temperature of adsorption and n_a = the adsorbed gas quantity. These are the measured inputs, while the monolayer capacity (n_m) and the BET constant (C) are calculated factors according to

$$n_m = \frac{1}{gradient - intercept} \qquad \text{(Equation 4.3)}$$

$$C = 1 + \frac{gradient}{intercept} \qquad \text{(Equation 4.4)}$$

The determination of these values is done by plotting the BET equation as an adsorption isotherm typically at p/p_0 between 0.05-0.35. From the resulting linear plot, n_m and C are calculated as Equation 4.3 and Equation 4.4, respectively. Finally, the total surface area can be determined using

$$S_{BET,total} = \frac{n_m N_s}{V} \qquad \text{(Equation 4.5)}$$

Herein, N_s is the Avogadro's constant and V is defined as the molar volume of the adsorbate gas. The specific surface area S_{BET} is then calculated using

$$S_{BET,total} = \frac{S_{BET}}{sample\ mass} \qquad \text{(Equation 4.6)}$$

4.5.3 Thermogravimetric analysis

For specific applications, the chemical stability of MOFs must be known to exlude thermal degradation during their use. Thermogravimetric analysis (TGA) or shortly thermogravimetry (TG) is one conventional method which enables the measurement of the mass change of the sample as a function of increasing temperature or as a function of time (isotherm) under given conditions.[187]

The most common application of TG is the analysis of pharma materials to check their solubility, purity and their point of thermal decomposition. When coupled with other analytical techniques such as FT-IR, MS or GC-MS, various volatile compounds can be easily detected and identified to understand decomposition mechanisms.

Generally, a thermogravimetric analyser consists of a microgram balance equipped with a platinum pan that contains 10-20 mg of the sample, a thermocouple to measure the temperature and an autosampler.[188] The shape of a thermogravimetric curves provide information on the chemical composition, which can be classified into seven different types according to their shapes.[189]

4.5.3.1 Interpretation of TGA data

In general, a TG curve is characterized by two temperatures, $T_{initial}$ and T_{final}, which represent the starting of decomposition temperature and the lowest temperature at which the process of mass loss has been completed, respectively. TGA curves are classified into seven types.[189]

Typically, the first weight loss is often recorded immediately at the beginning of heating and is assigned to the desorption process of free water and solvent molecules left within the system. If there is no decomposition, there will be no change in weight. For a single stage decomposition, the thermogram shows an initial long gradual plateau which indicates the high thermal stability of the sample up to a certain temperature, followed by a second sharp drop in weight corresponding to the structural decomposition. However, if stable intermediate products are formed during heating, a multi-stage decomposition scheme will be obtained due to the stepwise release of organic ligands. A gain in mass is observed when the sample reacts with atmospheric nitrogen or oxygen, while the decomposition reaction of previously formed oxidation products at higher temperatures gives a characteristic shape of the thermogram as illustrated in [189].

CHAPTER 5

Ligand Design and Motivation

This chapter gives a short summary about the main motivational factors concerning motivation and design of the complexes discussed in this thesis. Thus, the opening of this chapter includes a discussion of the structural requirements of the ligands and catalysts prepared in this work to enhance the catalytic properties. Also, it is of main interest to explain to what extent these homogeneous systems can be adopted into the field of heterogeneous catalysis. The closing section is dedicated to limitations of carboxylate ligands involving their synthesis, purification, characterization and crystallization as well as synthetic risks regarding MOF synthesis.

5.1 Linker requirements

Having in mind the design of environmental-friendly catalysts, it was primarily of main interest to develop water-soluble ligands and catalysts, while maintaining the excellent catalytic properties of reported ruthenium WOCs for the production of molecular oxygen from water. Therefore, this work mainly focused on the incorporation of water-soluble functional groups, particularly of carboxylic acid groups, into the ligand backbone of SUN'S reference system.

Thinking one step ahead, the presence of bindings groups such as carboxylic acids enables access to MOFs. Thus, extension of the π-conjugated ligand system of SUN's ruthenium system should open the door to MOFs with large pores and high specific surface areas, enabling MOF-driven water-splitting. This was achieved by extending the conjugated π-system of the bda-ligand at the 4- and 5-positions. Carboxylate, phosphonate or sulfonate groups are the commonly used building groups for MOF synthesis due to their coordinative flexibility. However, by comparison with phosphonate and sulfonate ligands, carboxylate groups are known to bind stronger to the SBUs, thus resulting in highly porous materials. To enable the coordination of the resulting Ru WOCs to the zirconium nodes of the SBUs, carboxylic acid groups were incorporated into the equatorial plane of the novel ruthenium ligands, as shown in Figure 22.

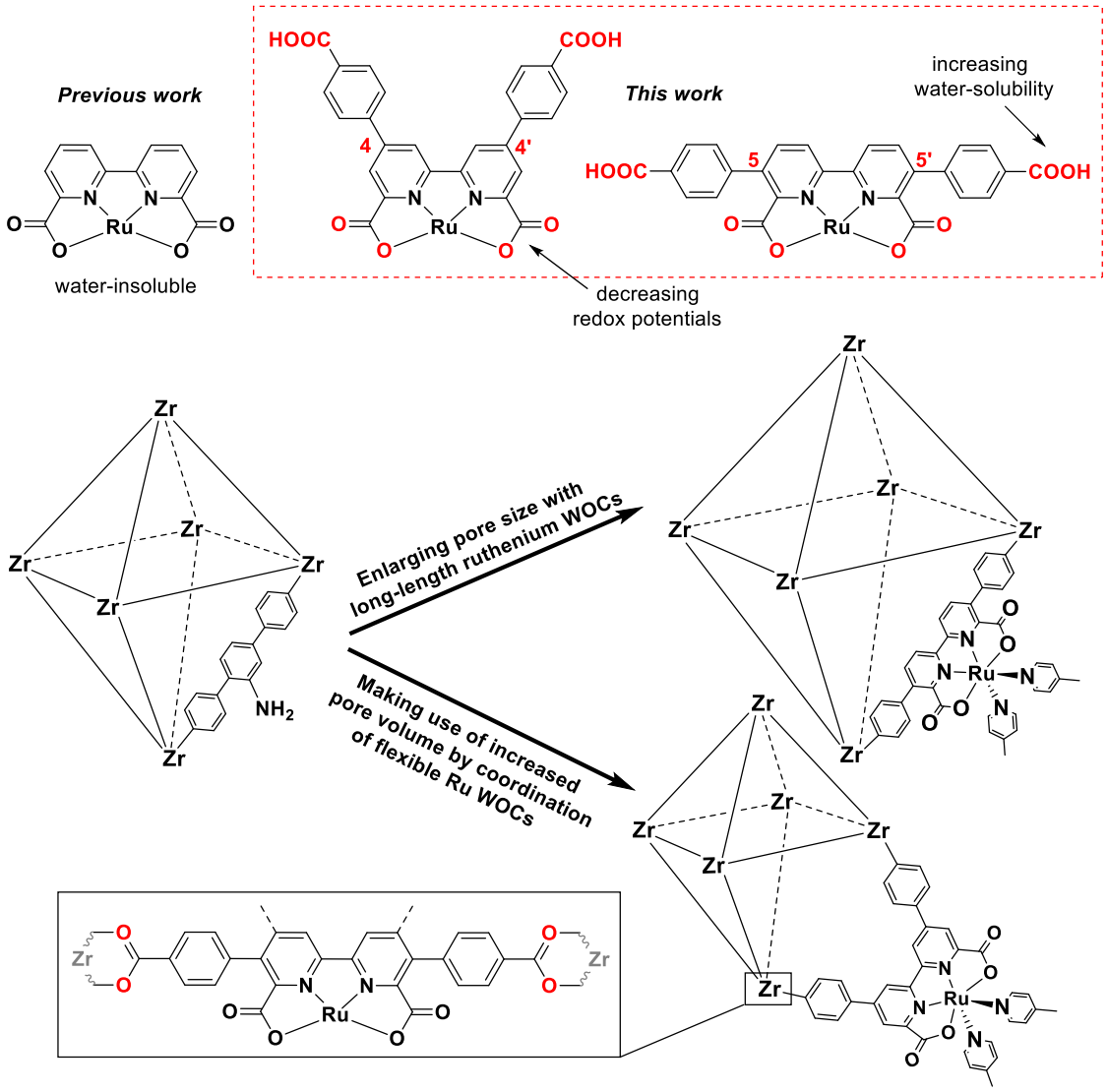

Figure 22. Linker requirements of homogeneous and heterogeneous Ru WOCs prepared during this thesis.

Hence, the presence of carboxylic acid groups offers a promising way to heterogenize catalysts, combining the benefits of homogeneous and heterogeneous catalysis and fulfills a number of requirements described in section 3.3. Considering that the catalytic water oxidation reaction will be conducted under highly acidic conditions, both the homogeneous as well as the heterogenized catalyst systems should be stable towards reaction conditions and the resulting decomposition processes.

Since the position of substituents at the equatorial plane is a key factor for the functionality and catalytic performance of WOCs, carboxylic acid groups which are close enough may be able to interact internally, producing intramolecular H-bonding. Therefore, investigations of the substituent positions (3 and 3', 4 and 4' of the bda ligand) are envisaged to study their influence on the O_2 release, as shown in Figure 23. Here, substitution at the 5 and 5' positions of the bda

ligand was ignored which was believed to have no influence on the interactions due in large part to the spatial shielding of the groups.

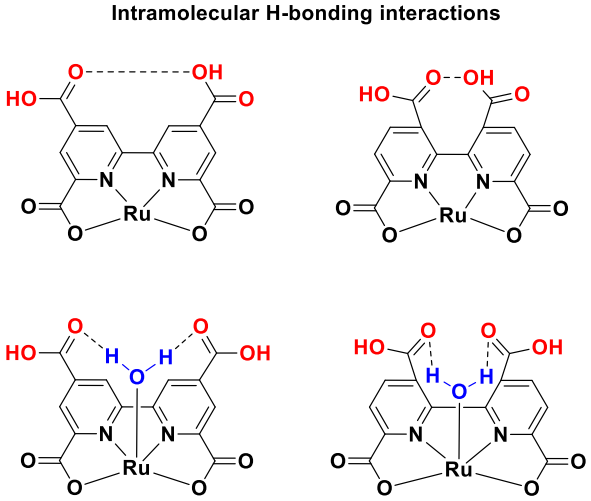

Figure 23. Possible intramolecular hydrogen bonds within ruthenium WOCs bearing carboxylic acid groups.

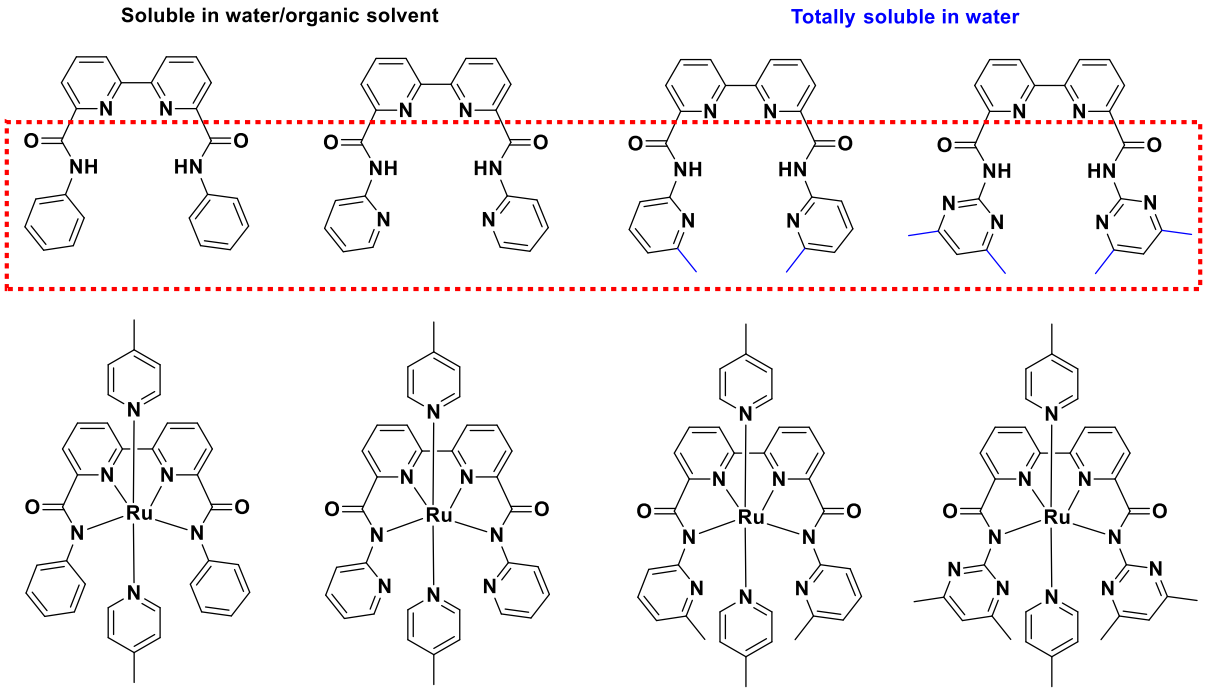

Figure 24. Molecular structures of Ru WOCs based on carboxamide ligands prepared during this thesis.

Pursuing the construction of robust ruthenium water oxidation catalysts, a closer look at recent studies in the literature on single-site water oxidation catalysts revealed that modification of the carboxylate groups, which directly coordinate to the ruthenium centre, is one alternative strategy to improve the catalytic activity of the complexes. Worth mentioning at this point is a recent study by ÅKERMARK et al., who found that replacing the carboxylate units to amide moieties apparently offered access to an even more active and stable catalyst.[118] According to their work, this might be due to the presence of the labile carboxylate unit which tends to undergo decarboxylation in higher oxidation states, thus rapidly deactivating the catalyst. More remarkably, the incorporation of the carboxamide functionality enabled H_2O oxidation to be driven by the mild chemical oxidant $[Ru(bpy)_3]^{3+}$ which was attributed to the significantly lower redox potentials.

Due to the lack of robust ruthenium WOCs, a part of this work was focused on the development of charge-neutral ruthenium(II) WOCs containing different polypyridine ligands with the aim of enhancing the catalyst durability (Figure 24). The synthesis of these ligands was achieved by replacing the carboxylate units of the original bda ligand with two amide groups. By increasing the bulkiness of the surrounding ligands, it is attempted to study the effect of the steric hindrance on the structure and reactivity towards water oxidation. Considering that steric bulkiness close to the ruthenium centre is known to affect the approaching water, all ligands and complexes presented in this part are important examples for ruthenium WOCs modified at the equatorial plane to understand and interpret the relationship between structure, stability and catalytic activity.

5.2 Limitations and synthetic risks

5.2.1 Synthesis of carboxylic acid linkers

The design of water-soluble ruthenium catalysts for homogeneous catalysis has proven challenging, which is attributed to the following factors:

(1) The direct substitution of carboxylic acid groups onto the benzene ring is not possible and requires a two step process involving the substitution and oxidation of a methyl group. In some cases, oxidation of the $-CH_3$ group was not as easy as expected, even when using the strong oxidizing agent $KMnO_4$. Instead, more toxic reagents such as chromium trioxide (CrO_3) has to be included into the synthesis. Since chromium compounds are known to be highly toxic and cause cancer in animals and humans, its regular use is linked to number of major health problems and requires a high level of protection for its intended use in working areas.

(2) A further problem is attributed to the high reactivity of carboxylic acids including nucleophilic substitution reactions at the carbonyl carbon, where the nucleophile hydroxyl group is replaced by functional groups such as acid chlorides, amides, esters, acid anhydrides or thioesters. Due to the sensitivity for acid/base-catalyzed reactions, the direct conversion of intermediates containing free carboxylic acid groups required the application of protecting groups, which prevented the formation of unwanted side-reactions but extended the synthesis pathway.

(3) Another strong negative feature of carboxylic acid groups lies in their ability to undergo decarboxylation by heating. This makes the drying of the ligands and complexes during thermal treatment under vacuum conditions much more difficult.

(4) The exceptional high boiling points and water solubility of carboxylic acids are in large part attributed to H-bonding interactions with like molecules and water. However, this significant advantage of water-solubility, which is essential for catalytic water oxidation, turns at the same time to a disadvantage associated with less solubility in organic solvents, in which most of organic reactions are conducted. In particular, the use of polar aprotic solvents are of great importance when considering cross-coupling reactions, which are key reactions of this work.

(5) Probably the most complicated task is the chromatographic separation of complexes functionalized with carboxylic acids, which is particularly attributed to the small number of solvent selection due to the limited solubility of the complexes in organic solvents. In addition, the polar carboxylic acid groups are able to interact with the column. As a consequence, all ruthenium complexes give bright-band fractions on the chromatographic column (SiO_2, alumina, reversed-face) and need to be separated very carefully. In order to improve the handling of such molecules, all ligands and complexes have been modified to survive the required reagents and chemical environments to which they were exposed.

5.2.2 Procedure of MOF synthesis

The most challenging aspects of preparing MOFs is the use of autoclaves or pressure vessels such as Schott flasks to build up pressure (Figure 25). Since the solvent used for MOF synthesis, usually DMF, is heated near its boiling point, prolonged exposure to high temperatures for several days can cause the reaction vessel to rupture. If an autoclave was used, the pressure inside of the reactor had to be calculated beforehand and special precautions were taken in the lab to avoid explosion. Alternatively, MOF reactions were carried out in a round bottom reaction flask in order to study the effects of pressure on the MOF formation and its properties.

Figure 25. Various crystallization techniques used for MOF synthesis.

RESULTS AND DISCUSSION

CHAPTER 6

Experimental Part

6.1 Class 1: π-extended carboxylic acid ligands.

The choice of the ligand is important for the catalytic efficiency of a catalyst. Considering that the active site for water oxidation is in the equatorial plane generating the common oxo-species Ru^{V}=O of both possible reaction pathways, modification of the ligand backbone is expected to have a significant electronic effect on the metal center. Based on the reported synthetic methods, possible synthetic routes were designed for the development of the π-extended carboxylic acid ligands L1 and L2 starting from the same starting molecule 2-amino-6-methylpyridine.

6.1.1 Synthetic limitations for the preparation of L1.

Different synthetic routes were investigated for the preparation of the extended ligand L1, all of which involved the introduction of methyl substituents into the 6 and 6’ positions of the bpy ligand. Intitially, it was attempted to prepare L1 by the reaction of methyl-4-formylbenzoate, butane-2,3-dione and piperidine. Method I was developed primarily to eliminate synthesis steps, thus saving both costs and working time (Figure 26).

Method I.

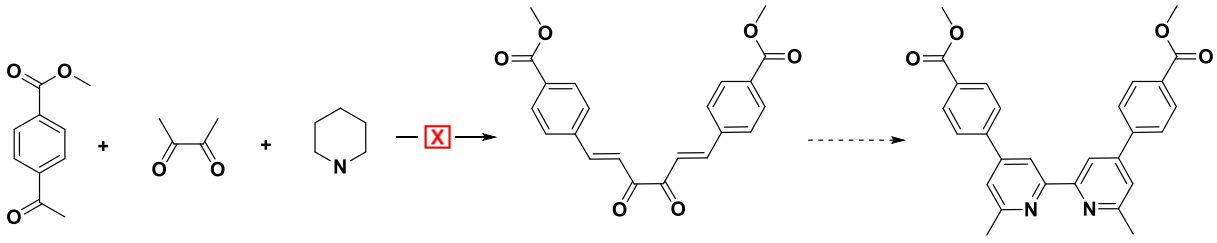

Figure 26. Synthesis scheme of dimethyl 4,4’-(6,6’-dimethyl-[2,2’-bipyridine]-4,4’-diyl)dibenzoate by the Knoevenagel-Dübner Condensation.

After work-up, the desired ligand could not be obtained which is attributed to the keto-enol tautomerism of butane-2,3-dione due to stabilization of the enol by intramolecular hydrogen

bonding. Thus, the ketone carbonyl carbon is nucleophilically attacked by the enol, resulting in the formation of the undesirable β-hydroxy carbonyl compound.

Method II.

A new method was adopted for the synthesis of ligand L1 upon the Suzuki coupling of 4-methoxyphenylboronic acid with 4,4'-dibromo-6,6'-dimethyl-2,2'-bipyridine, which is readily prepared in a six-step procedure from 6-amino-2-methylpyridine. This method is very promising because 4,4'-dibromo-6,6'-dimethyl-2,2'-bipyridine is strongly activated toward C-C bond formation.

Suzuki coupling of 4-methoxyphenylboronic acid with 4,4'-dibromo-6,6'-dimethyl-2,2'-bipyridine was found to proceed in high yields. Residual amounts of DMF were easily and completely removed by washing the crude product several times with petroleum ether. ESI-MS analysis revealed highly pure product.

In the next synthetic step, hydrolysis was performed to selectively convert the methyl esters to carboxylic acid groups. Generally, hydrolysis of methyl esters is realized in aqueous acidic or basic medium. Compared to alkaline hydrolysis, acid hydrolysis is reversible and does not go to completion. Thus, alkaline hydrolysis was the preferred method to produce the desired carboxylate compound, since this process is irreversible and ends up in the formation of the corresponding alcohol and the salt of the acid. The carboxylic acid itself is formed upon subsequent addition of a strong acid to the reaction mixture (Figure 27). Inspired by the different solubility behaviour of KOH in protic solvents, conversion of the methyl esters into carboxylic acids was achieved by saponification using a potassium hydroxide solution in methanol (5.5 mol/l) under very mild conditions (40 °C). The ^{1}H spectra of the reaction intermediates are shown in Figure 28.

The last step involves the oxidation of the methyl groups by the mild and non-toxic potassium permanganate. Unfortunately, neither $KMnO_4$ nor acidic CrO_3, which are both very strong oxidising agents, were able to oxidize the methyl groups into carboxylic acids. A drawback of such reactions is the poor oxidation resistance of the starting compound towards the harsh experimental conditions. In the case of the oxidation with $KMnO_4$, this was primarily attributed to the low solubility of the reactant in water. In positive ion mode, only one but intense peak at m/z = 425 was observed, which is clearly assigned to the starting molecule demonstrating its unreactivity towards methyl oxidation under the selected experimental conditions (Figure 29). However, only very small traces of mono- and dioxidation products can be detected in negative mode, displaying a mass peak around *m/z* = 453 and a weak peak at *m/z* = 483.

Table 1. Solubility behaviour of KOH in protic solvents.

Solvent	Solubility of KOH
Isopropanol	14 g / 100 g (28 °C)
Ethanol	40 g / 100 g (25 °C)
Methanol	55 g / 100 g (28 °C)
Water	121 g / 100 g (25 °C)

An attempted oxidation using chromium oxide resulted in a change of the solution color to green, indicating the formation of chromium(III) oxide. Nevertheless, no product could be isolated from the green solution upon addition of water, which suggests that the starting compound might get decarboxylated or even decomposed during the oxidation process due to its acid-sensitivity and thermal instability.

Similar results were obtained when oxidation of the methyl groups was performed using SeO_2 to produce the corresponding aldehyde, followed by subsequent oxidation to the carboxylic acid. Again, the conversion failed which led to the design of an alternative route for the synthesis of L1 by returning back to 4,4'-dibromo-6,6'-dimethyl-2,2'-bipyridine.

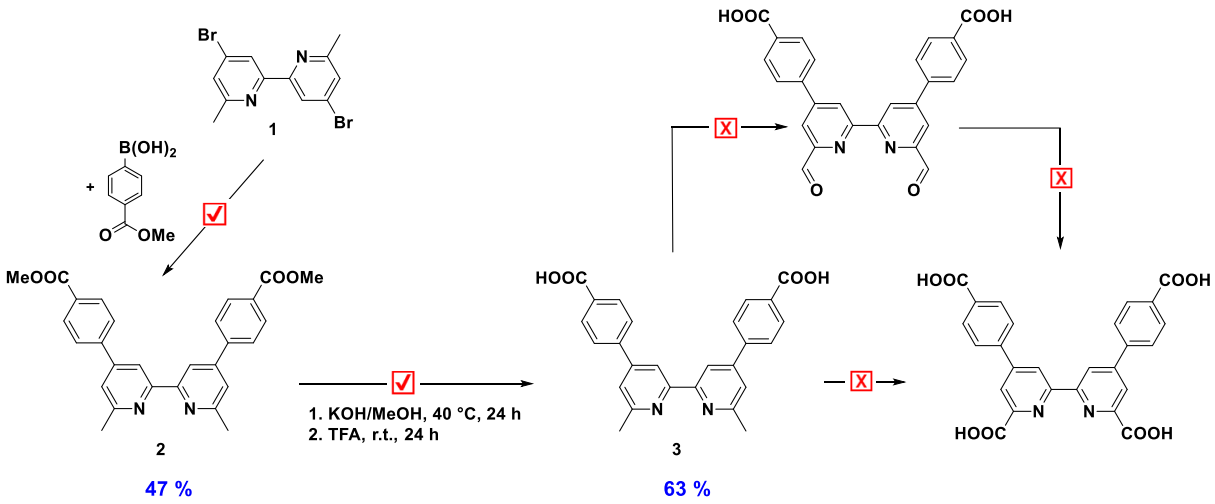

Figure 27. Unsuccessful attempts at the synthesis of ligand L1.

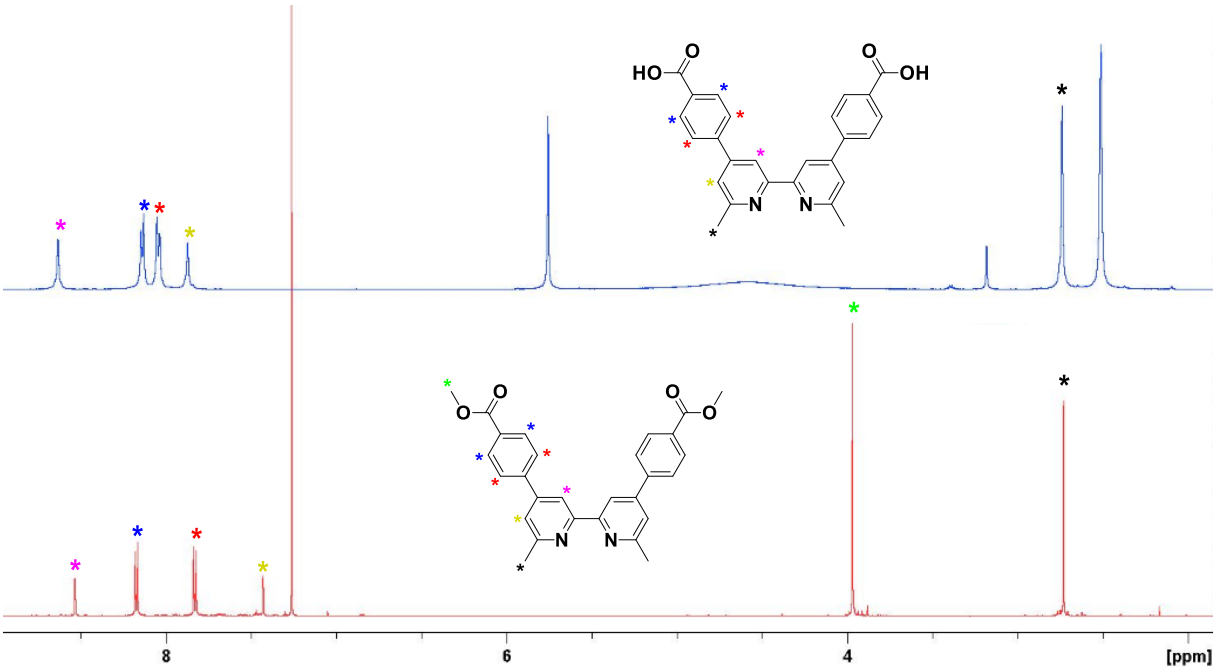

Figure 28. ^{1}H NMR spectrum of ligands 2 and 3.

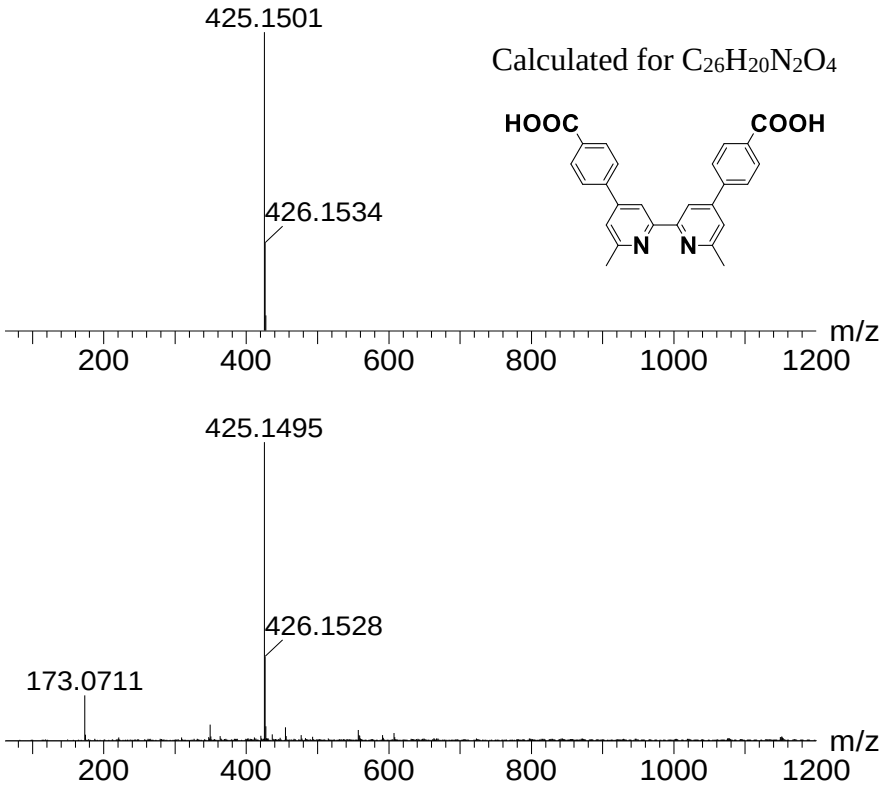

Figure 29. ESI-MS spectrum of a reaction solution containing unconverted ligand 3.

Method III.

After having tested various procedures with limited success, a new approach for methyl oxidation was developed promising high conversion rates and subsequent high yields of the product and its reaction intermediates. In the following, the synthetic steps will be introduced and discussed in detail. In summary, the novel synthetic route involves the oxidation of the methyl groups at an earlier step of synthesis, followed by esterification of the carboxylic acid groups in order to increase the solubility of the di-methylated 4,4'-dibromo-[2,2'-bipyridine]-6,6'-dixarboxylate in organic solvents, which facilitates the separation of the products formed in the Suzuki coupling using DMF as solvent generally preferred for coupling reactions. Final saponification drive the reaction toward the desired carboxylated ligand L1. This method was found to work faster and more efficiently (Figure 30).

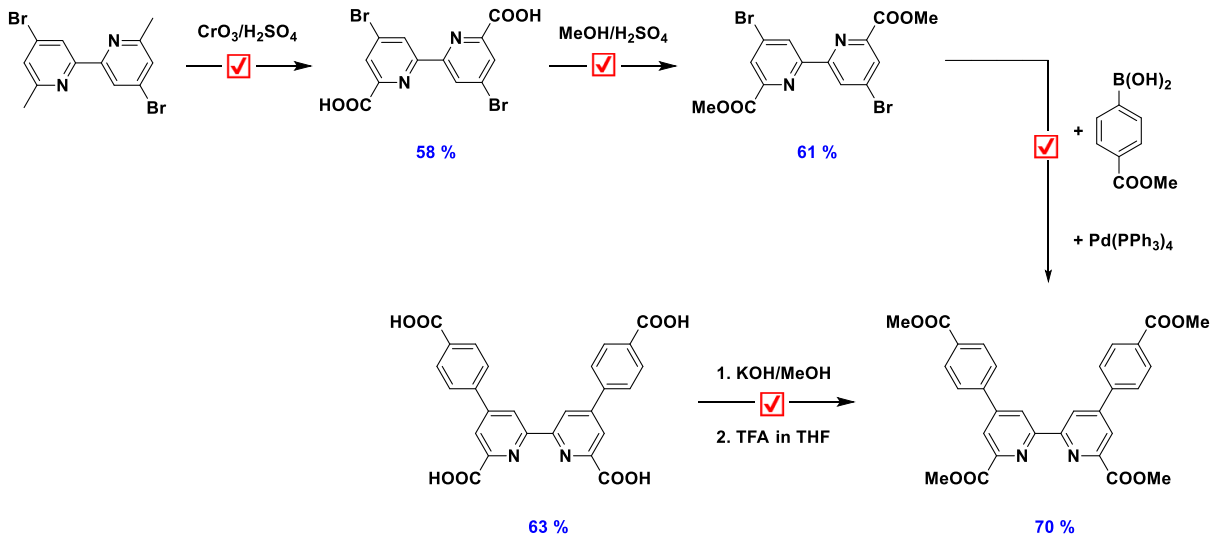

Figure 30. Successful synthesis of L1 *via* oxidation and esterification.

6.1.2 Optimized synthetic route to ligand L1.

Typically, the synthesis of extended ligands require a multi-step process. The most efficient synthetic methods to build large structures from simple precursors are catalytic cross-coupling reactions mostly mediated by palladium, nickel or copper complexes. The most widely used methods are the Suzuki-Miyaura, Stille, Negishi, Kumada, Sonogashira, Heck and Buchwald-Hartwig couplings. In general, these reactions require organic halides (-I, -Br, -Cl) able to simply undergo metal-halogen exchanges in the transmetallation step of the catalytic cycle. If more than one type of halogen atom is present in one molecule, the major product will be formed by the most reactive group, derived from reactivity series, thus leading to a mixture containing the mono- and disubstituted products. Therefore, achieving high product selectivity

was one major challenge of this work, which was proven by tuning synthetic conditions. For L1, all intermediate steps were performed under optimized reaction conditions, which has shortened the preparation time of each step, reduced the number of by-products and increased the yield of the purified carboxylate ligand. The general synthesis scheme of ligand L1 is summarized in Figure 31. The preparation of 6,6'-dimethyl-2,2'-bipyridine represents the first product of a cross-soupling process, which was prepared in two steps *via* bromination and nickel-catalyzed reductive homocoupling of 2-bromopyridines. Afterwards, the *N*-oxid was made by utilizing peracid as the oxidising agent, followed by nitration with a mixture of HNO_3/H_2SO_4 a. In a next step, the nitro groups were converted by treating with acetyl bromide to afford the bromo-*N*-oxid compound. The *N*-oxid function was then removed by the reaction with PBr_3. Due to the fact that carboxylate groups are often not tolerated in Suzuki cross couplings, originally performed with $Pd(PPh_3)_4$, the methyl groups of 4,4'-dibromo-6,6'-dimethyl-2,2'-bipyridine were esterified with methanol under acidic conditions. The final saponification step yielded the carboxylated ligand L1 in 63 % (Figure 31).

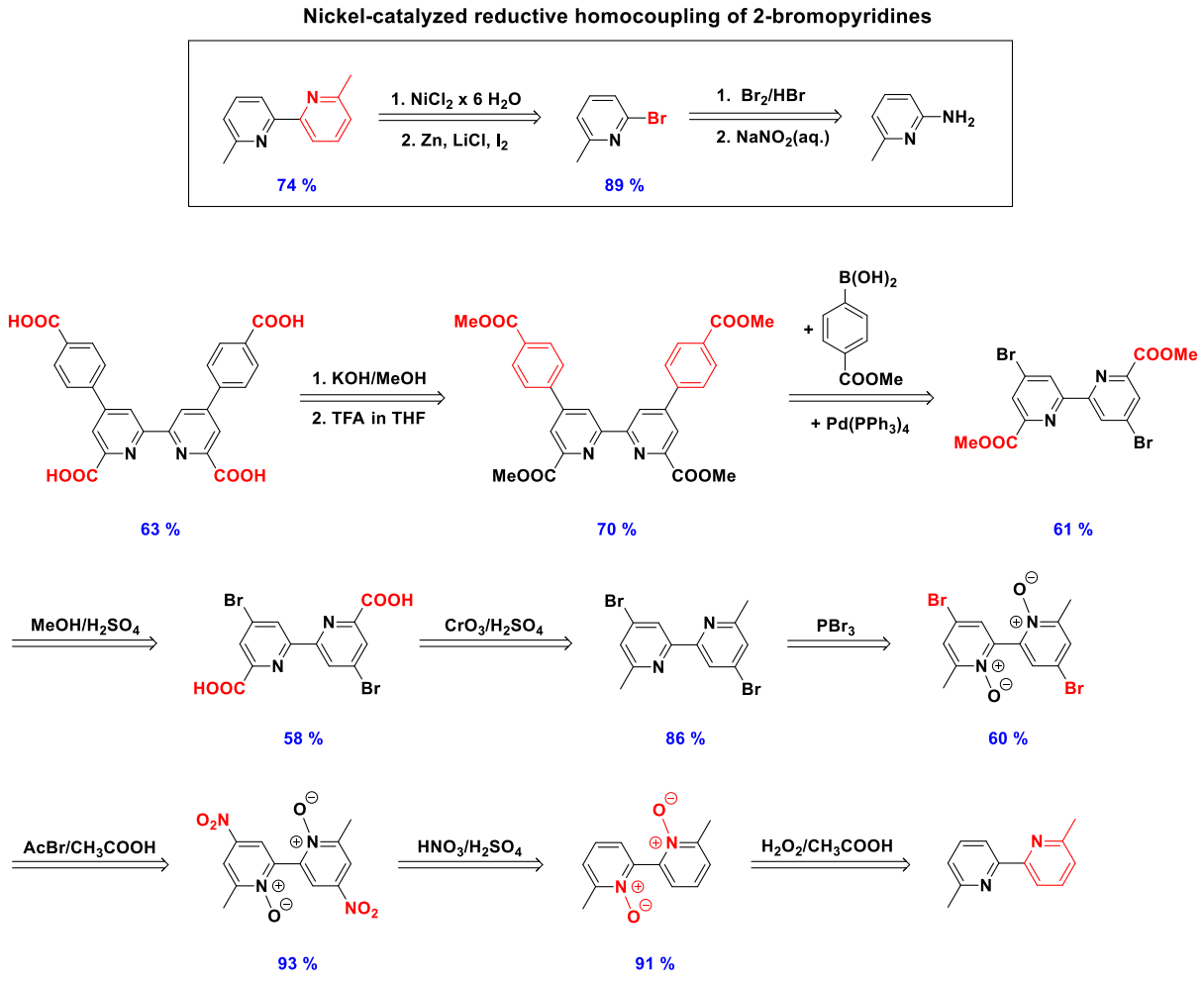

Figure 31. Full retro-synthesis scheme of ligand L1.

6.1.2.1 6-bromo-2-methylpyridine.

3-bromo-2-methylpyridine was synthesized through the bromination of pyridine and is traditionally used to synthesize 6,6'-dimethyl-2,2'-bipyridine. However, despite the simplicity of the reaction, the synthetic conditions have to be strictly controlled over the whole reaction time. The main reason for that is that diazonium salts are instable at temperatures above 5°C in aqueous solution. If the mixture is warmed or just let stand over time, decomposition will occur explosively. To generate the diazonium cation, an aqueous solution of $NaNO_2$ is slowly added to the reaction mixture containing the aniline compound in HBr, which is previously cooled down to -20°C. The subsequent decomposition of the diazonium salt releases molecular nitrogen and a highly reactive pyridine radical, which undergoes radical bromination in the presence of molecular Br_2. After extraction with diethylether, a dirtybrown oil was obtained.

As shown in Figure 32, ^{1}H NMR of the oil revealed clean product. The brownish color of the product is due to unreacted bromine in solution, which can be removed by washing the reaction mixture with sodium thiosulfate. Alternatively, the oily residue can be fractionally distilled (exp. 70 ° C, 8 mbar) to get the product as colourless to pale yellow liquid (Yield: 89 %). However, it was found that small impurities with bromine did not affect the next reaction step.

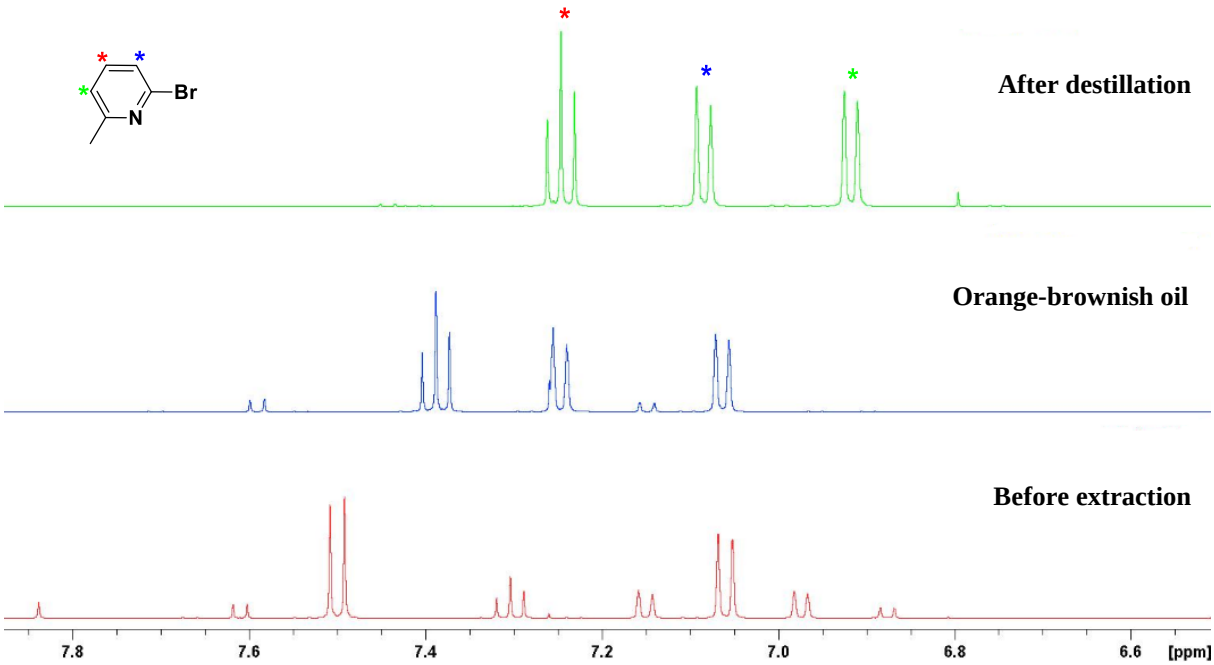

Figure 32. ^{1}H NMR spectrum of 6-bromo-2-methylpyridine after different work-up procedures. *The methyl protons are located at 2.23 ppm.*

6.1.2.2 6,6'-dimethyl-2,2'-dipyridine.

6,6'-dimethyl-2,2'-dipyridine is commercial available but expensive. There are some published methods for the synthesis of this compound starting from 6-bromo-2-methylpyridine using bistriphenylphosphinedichloronickel, $Pd(OAc)_2$ or $NiCl_2 \cdot 6\ H_2O$. In the following, the synthetic alternatives were tested for their suitability and compared in terms of yield and costs.

Table 2. Price of 6,6'-dimethyl-2,2'-dipyridine and price of starting materials.

Reagent	Price from commercial source
6,6'-dimethyl-2,2'-dipyridine	136 €/g, Sigma Aldrich
6-bromo-2-methylpyridine	30 €/g, Sigma Aldrich
6-amino-2-methylpyridine	0.24 €/g (calculated from 100 g), Sigma Aldrich
$NiCl_2 \cdot 6\ H_2O$	5.20 €/g (calculated from 5 g), Sigma Aldrich
$Pd(OAc)_2$	110 €/g (calculated from 500 mg), Sigma Aldrich
$NiCl_2(PPh_3)_2$	4.10 €/g (calculated from 10 g), Sigma Aldrich

The first synthetic method is a commonly known and used procedure, which is often used for the preparation of biaryls and bipyridines by homocoupling of aryl halogenides (chlorides, bromides, iodides). However, when used this procedure, 30 mol% of $NiCl_2(PPh_3)_2$, 100 mol% of Et_4NI and excess of zinc dust are required to reduce and activate the nickel precursor for the coupling of two molecules of 6-bromo-2-methylpyridine. Although the synthesis of this nickel catalyst is done under phosphine-free conditions, the preparation of the nickel precursor requires large amounts of triphenylphosphine, which makes it's separation by chromatography necessary. Using this method, the coupling product is only obtained in very low yields (33 %).

The homocoupling of aryl halides by using $Pd(OAc)_2$ as catalyst in DMF in the presence of a base, typically K_2CO_3, and isopropanol as reductive agent to regenerate the palladium Pd(0) is another alternative of the Ullmann reaction to produce biaryls and biheterocycles. The mechanism is supposed to occur *via* two oxidative additions, followed by a reductive elimination. Compared to the first method, the yield of the product after purification by flash

chromatography using *n*-Hexan:EtOAc (7:1) is slightly higher (40 %), but requires forcing reaction conditions such as high reaction temperature (110 °C) and the addition of water to increase the solubility of the base, which induces a slowdown of the reaction. Hence, the major problems associated with the synthesis of 6,6'-dimethyl-2,2'-dipyridine are long reaction times, low product yields as well as large excess of catalysts and ligands.

To improve the yield of 6,6'-dimethyl-2,2'-dipyridine, another synthetic route was explored. This simple and efficient method includes the homocoupling of two halopyridines using 5 mol% of $NiCl_2 \cdot 6\ H_2O$ in DMF and Zn-LiCl as reducing agent. Generally, the complete reaction is conducted at 70 °C over a period of 3 h. According to the literature[190], the product can be isolated in 78 % by column chromatography. In this work, impurities and reaction by-products were removed by precipitation from *n*-hexane. Evaporation of the organic phase afforded the desired homocoupling product in 84 %, shortend working hours and prevented the use of external ligands.

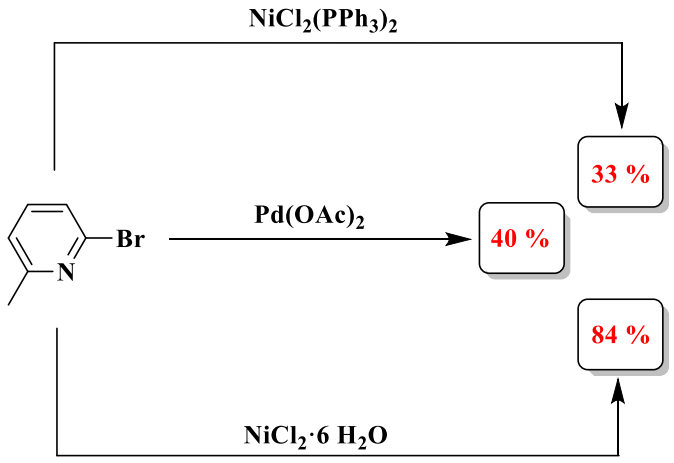

Figure 33. Yield improvement of 6,6'-dimethyl-2,2'-dipyridine by various synthetic methods.

6.1.2.3 6,6'-dimethyl-2,2'-dipyridyl di-*N*-*N'*-oxide.

The di-*N*-oxide of 2,2'-bipyridine is prepared by oxidation of the bipyridine with peracetic acid, which is always generated *in-situ* from glacial acetic acid and hydrogen peroxide due to its instability. Peracids themselves are weakly acidic due to their much higher pKa of 8.2, thus the reaction rate is accelerated by acetic acid whose pK_a value is 4.8. The oxidation with peracetic acid is an environmentally benign method for the preparation of *N*-oxides because water is the only by-product.

6.1.2.4 6,6'-dimethyl-4,4'-dinitro-2,2'-dipyridyl di-*N*,*N'*-oxide.

The nitration of the di-*N*-oxide has proved extremely difficult and was found to proceed under only very drastic conditions. Attempts to nitrate the di-*N*-*N'*-oxide by 65 % nitric acid were always unsuccessful. This behaviour is ascribed to the π-electron deficiency of the pyridines, which is believed to attenuate its reactivity with electrophiles such as the nitronium ion. Replacing concentrated sulfuric acid with oleum did not significantly improve the nitration process, since the product was obtained only in 1 % yield. The best method to obtain 6,6'-dimethyl-2,2'-dipyridyl di-*N*-*N'*-oxide in very high yields was the use of fuming HNO_3.

Table 3. Various attempts for nitration of 6,6'-dimethyl-2,2'-dipyridyl di-*N*-*N'*-oxide.

Entry	**Scale mmole**	**Reaction conditions**	**Results**
1	2	H_2SO_4/KNO_3, 80 °C, 48 h	-
2	2	H_2SO_4/HNO_3, 0 °C → 70 °C, 24 h	-
	2.2	H_2SO_4/HNO_3, 0 °C → 80 °C, 24 h	-
	2.2	H_2SO_4/HNO_3, 0 °C → 90 °C, 24 h	-
	2.4	H_2SO_4/HNO_3, 0 °C → 100 °C, 24 h	-
3	1	Oleum/HNO_3, 0 °C → 110 °C, 24 h	1 %
4	11	H_2SO_4/HNO_3(fum.) 0 °C → 70 °C, 6 h	93 %

In order to avoid the oxidation of the methyl groups with subsequent decarboxylation at the 2 and 2' positions during nitration, which is well-known to occur for the oxidation of naphthyridones at high temperatures, the electrophilic aromatic substitution reaction was carried out at 70 °C. The reaction is driven by the regeneration of the aromaticity, which is achieved by rapid loss of a proton producing the nitro product.

In Table 3, different experimental approaches are summarized for the nitration under different conditions. The results clearly show that nitration is simplified using concentrated sulfuric acid and fuming HNO_3 including shorter reaction times at low temperatures, which was found to increase the yield of the desired product dramatically.

6.1.2.5 6,6'-dimethyl-4,4'-dibromo-2,2'-dipyridyl di-*N*,*N*'-oxide.

Heating of the corresponding nitropyridine *N*-oxide compound with acetyl bromide and acetic acid ends up in a mixture containing the major di-brominated and mono-brominated products. Due to the similar chemical properties, a separation of the mixture into both compounds was not possible. Attempts to convert this crude product mixture in the next step without any further purification gave access to the desired product, but in very low yields. Interestingly, increasing the temperature of the reaction by just 10 degrees celsius substantially reduced the formation of the unwanted mono-product, as evident from the ^{1}H NMR signals shown in Figure 34.

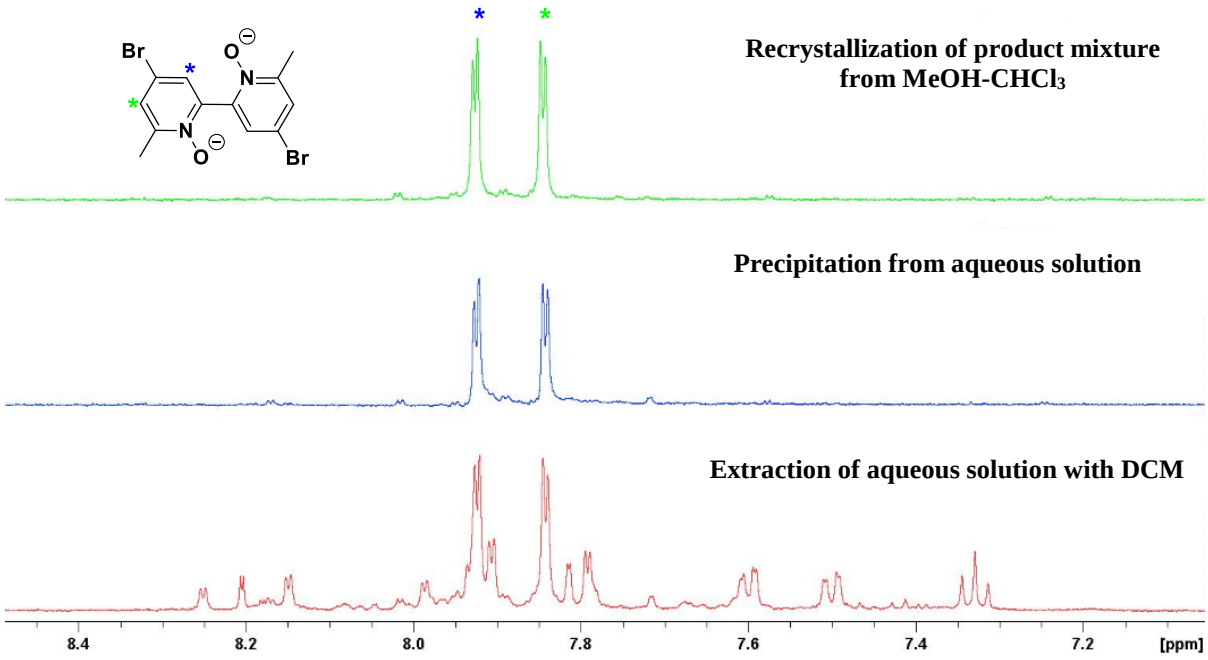

Figure 34. Proton NMR of 6,6'-dimethyl-4,4'-dibromo-2,2'-dipyridyl di-*N*,*N*'-oxide after different work-up procedures. *The methyl protons are located at 2.36 ppm.*

Pure product has been collected by precipitation from aqueous solution with 16 M NaOH, which resulted in almost quantitative conversion to the di-bromo compound with 93 % isolated yield, while extraction of the aqueous layer with dichloromethane revealed a small number of impurities in proton NMR, which could be assigned to the mono-substituted product. Alternatively, purification of the crude product by recrystallization from MeOH-$CHCl_3$ also gave access to clean product.

6.1.2.6 4,4'-dibromo-6,6'-dimethyl-2,2'-bipyridine.

Cleavage of the *N*-oxide bonds was achieved using PBr_3, while the formation of the strong P=O bond is the driving force for the reaction. The crude product is purified by sublimation to remove less volatile impurities.

6.1.2.7 4,4-dibromo-2,2-dipyridyl-6,6-dicarboxylic acid.

The oxidation of the methyl groups in 4,4'-dibromo-6,6'-dimethyl-2,2'-bipyridine using CrO_3 is initiated by the formation of chromic acid, which is the true active reagent. The *in-situ* formation of Cr(III) is indicated by a color change to green. The oxidation to the carboxylic acid is accomplished by the addition of water, which triggers the oxidation of the *in-situ* formed aldehyde intermediate.

6.1.2.8 Dimethyl-4,4'-dibromo-2,2'bipyridine-6,6'-dicarboxylate.

The next step is the esterification of the carboxylic acid groups using a mixture of H_2SO_4/MeOH. This reaction is well-known as Fisher esterification. The acid works as catalyst, triggering the protonation of the carbonyl group of the carboxylic acid, which is subsequently attacked by the alcohol. After proton transfer, water is eliminated to produce an oxonium-ion intermediate. Finally, deprotonation of the positively charged oxygen leads to the ester product. Since the reaction is reversibel, the position of equilibrium can be pushed to the right by using excess of methanol or removing water.

6.1.2.9 Dimethyl 4,4'-bis(4-(methoxycarbonyl)phenyl)-2,2'-bipyridine-6,6'-dicarboxylate.

The key step in the synthesis of L1 is the Suzuki coupling[191] of dimethyl-4,4'-dibromo-2,2'bipyridine-6,6'-dicarboxylate with the respective boronic acid. In order to reduce the number of synthesis steps, 4-methoxycarbonylphenylboronic acid was used as coupling reagent (Figure 35).

The introduction of methoxy groups was found to increase the solubility of the product in organic solvents and thus facilitated the work-up. More importantly, the presence of identical functional groups enables their direct conversion into the corresponding carboxylic acids in a one pot procedure.

The Suzuki-Miyaura coupling is divided into 3 fundamental reaction steps including oxidative addition, transmetallation and reductive elimination. In this reaction, palladium in a basic environment is the catalyst. First, oxidative addition of the halide with Pd(0) gives the bromo-

palladium intermediate, in which Pd is in the oxidation state +2. In basic environment, ligand exchange occurs, generating the corresponding hydroxyl-palladium complex, which then undergoes transmetallation with the boronic acid. The final reductive elimination re-generates the palladium(0) catalyst and provides the desired cross-coupled product in very high yields (70%).

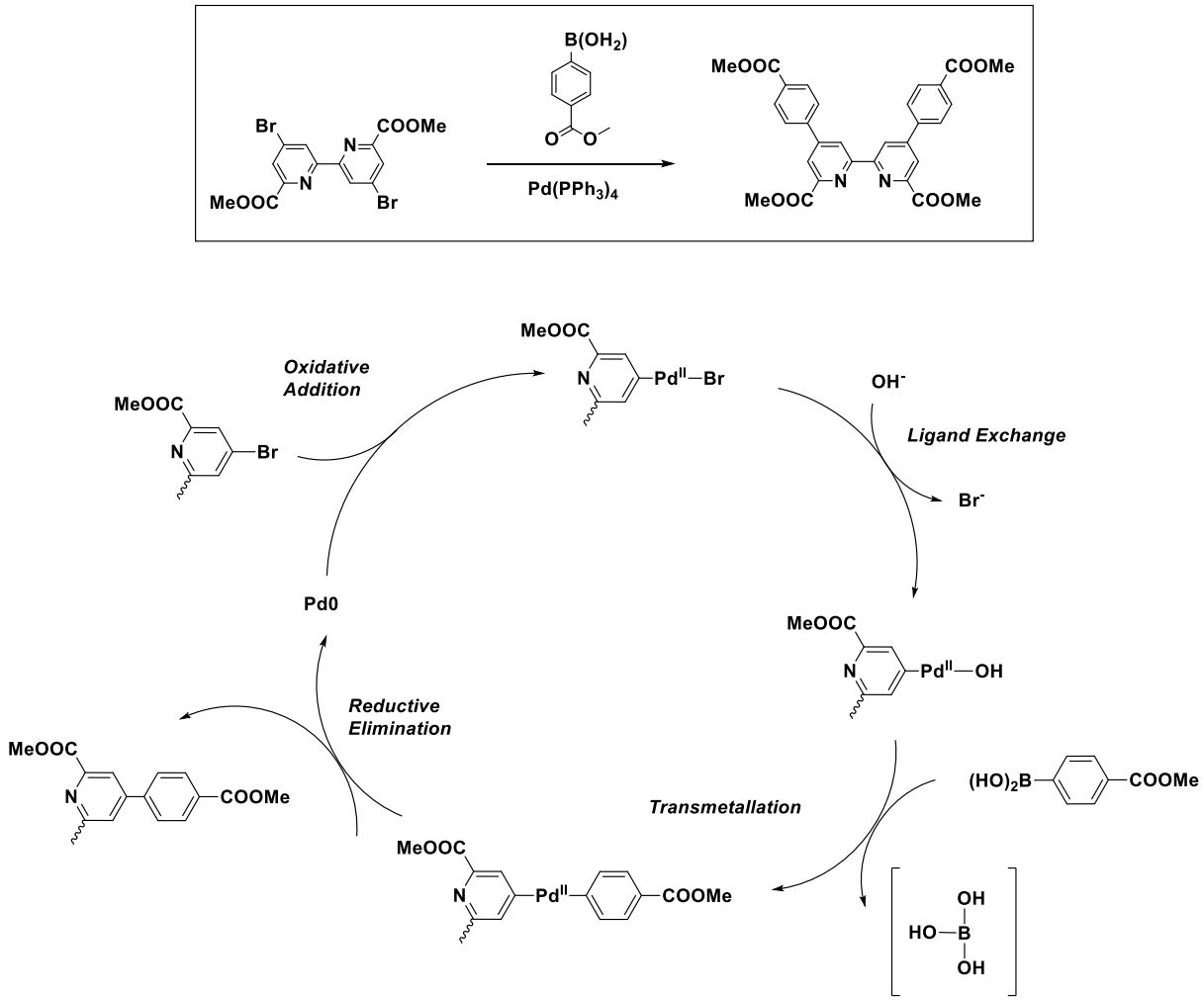

Figure 35. The catalytic cycle of Suzuki-Miyaura cross-coupling.

6.1.2.10 6,6'-dimethyl-2,2'-bipyridine-4,4'-dibenzoic acid.

The last step of L1 synthesis involves the conversion of the aforementioned ester into the carboxylic acid by hydrolysis in the presence of methanolic KOH. Following quenching by addition of water and acidification of the aqueous layer leads to precipitation of the desired acid.

Figure 36. [1]H NMR spectra of L1 and its reaction intermediates.

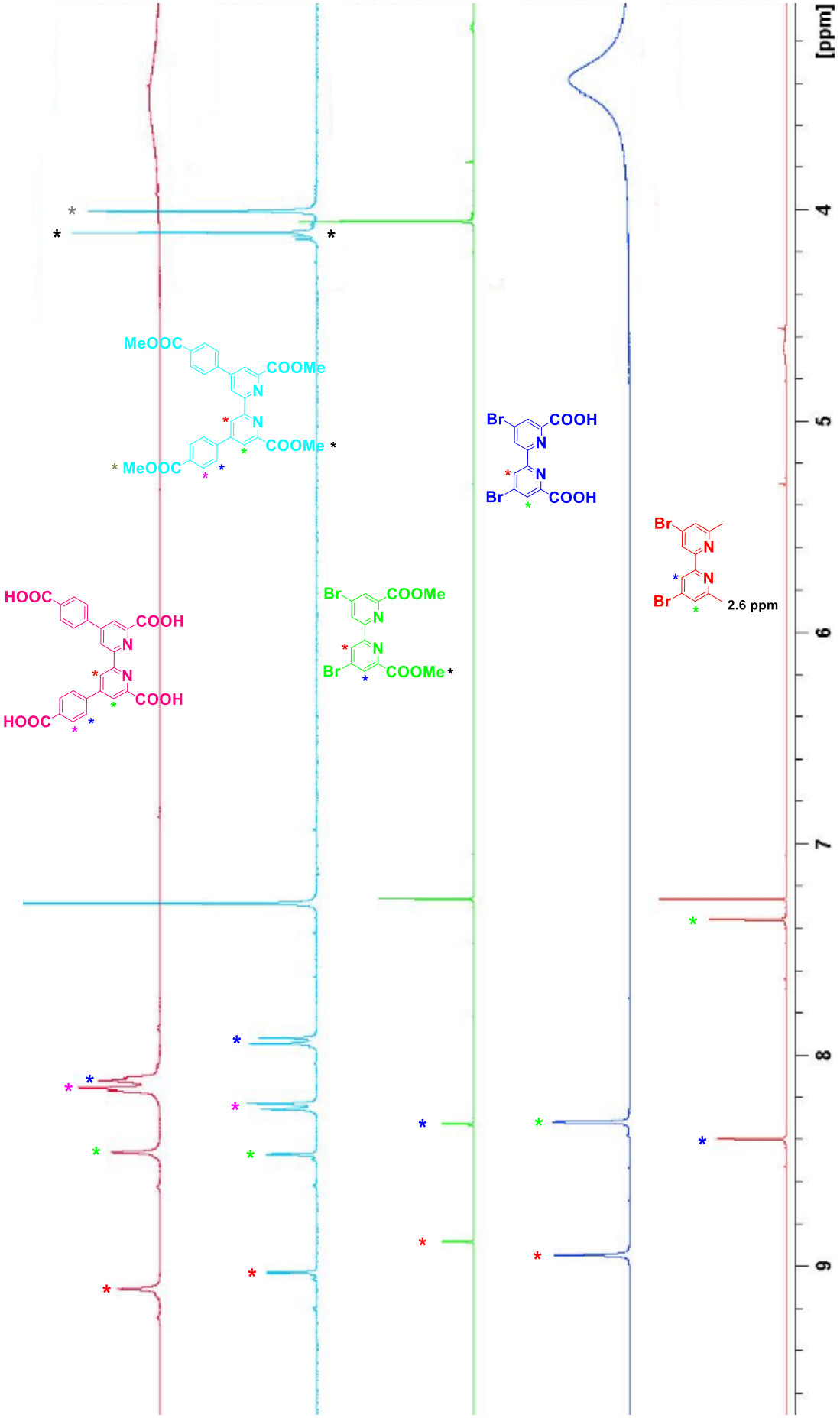

6.1.3 Optimized synthetic route to ligand L2

Starting from 2-amino-6-methylpyridine, the linear ligand L2 was prepared in 7 steps by using the Pd-catalyzed Suzuki and Stille cross-couplings (Figure 37). First, 6-amino-3-bromo-2-methylpyridine was prepared in excellent yields by bromination of the starting molecule with NBS. Next, the amino group was converted into a diazonium group and subsequently reacted with bromine to give the dibromo-substituted compound. This was treated with *in-situ* generated iodotrimethylsilane to undergo halogen exchange forming 3-bromo-6-iodo-2-methylpyridine. The following Stille coupling reaction between hexabutylditin and iodopyridine forms the linear ligand analogue of the symmetric 4,4'-dibromo-6,6'dimethyl-2,2'bipyridine bearing terminally bound 5,5'-dibromo groups.

The second key step involves a Suzuki-Miyaura, by which the π-conjugation of the bpy unit was extended by additional phenyl rings. After saponification and subsequent oxidation with $KMnO_4$, the synthesis of L2 was completed.

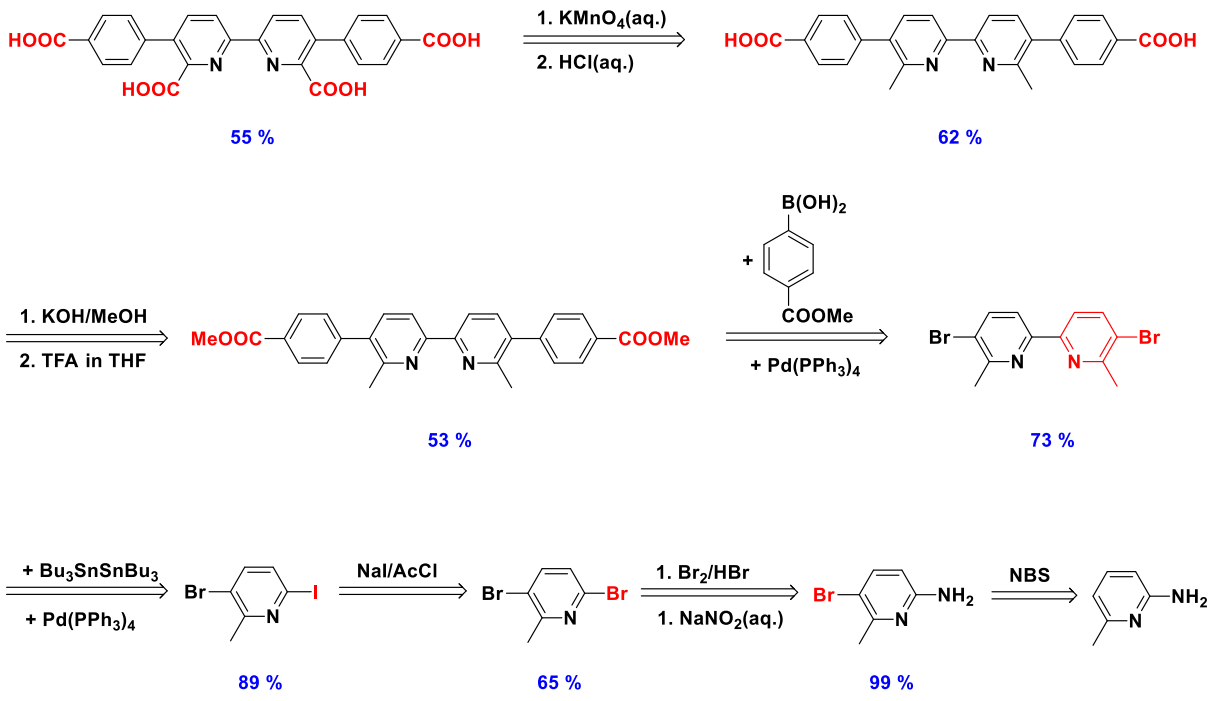

Figure 37. Full retro-synthesis scheme of ligand L2.

6.1.3.1 5-bromo-6-methylpyridin-2-amine.

2-amino-6-methylpyridine was substituted with NBS, which enables the metal-free one-pot strategy for the synthesis of the corresponding bromo product under very mild conditions involving short reaction time, simple work-up and excellent yields.

The amino group of the starting molecule is strongly activating, thus directing the bromo substituent in ortho- and para position in electrophilic aromatic substitution reactions. In addition, the methyl group also works as an activator. However, compared to the methyl group, the amino group contains unshared electron pairs outside the aromatic ring, which makes it more activating. Hence, the bromine is directed to the position para within the molecule.

6.1.3.2 3,6-dibromo-2-methylpyridine.

3,6-dibromo-2-methylpyridine was prepared in analog to the synthesis of 6-bromo-2-methylpyridine. After work-up, a brownish-red oil was obtained which was attributed to free bromine.

^{1}H NMR of the crude product, which was obtained as red solution from extraction with DCM revealed two major peaks in the aromatic region, whereby the proton shifted downfield to 7.6 ppm is assigned to the proton at the carbon C-3 being the most electron-rich carbon compared to the proton at C-2. Purification of the oily product by either a) SiO_2 column using EtOAc/*n*-Hexan (1:10, v:v) or b) dissolving in *n*-Hexan to separate the insoluble oily brown residue gives no significant differences in proton spectra (Figure 38).

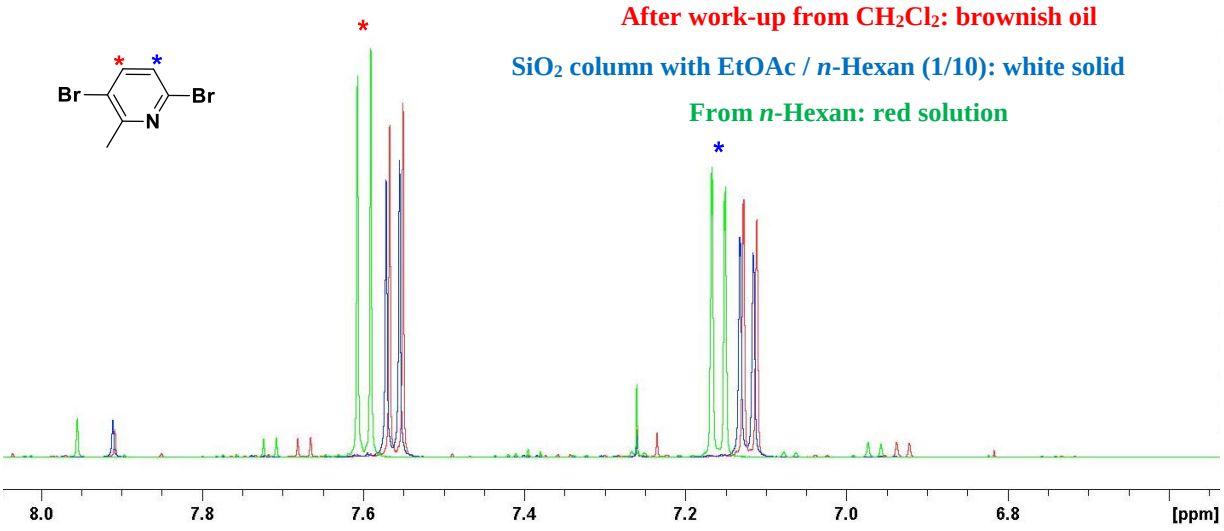

Figure 38. ^{1}H NMR spectrum of 3,6-dibromo-2-methylpyridine after different work-up procedures.

Therefore, halogen exchange was performed with both, solid and liquid 3,6-dibromo-2-methylpyridine.

6.1.3.3 3-bromo-6-iodo-2-methylpyridine.

The synthesis of 3-bromo-6-iodo-2-methylpyridine was performed using sodium iodide and acetyl chloride which undergoes a SN_2 reaction to exchange the bromide for iodide. This reaction is known as Finkelstein reaction (Figure 39).

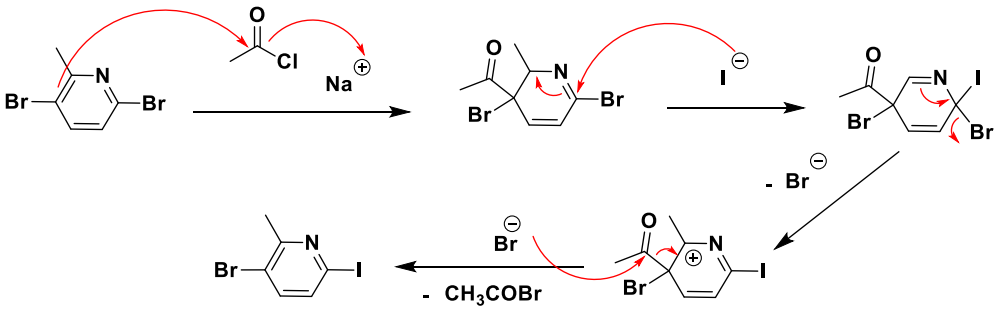

Figure 39. The mechanism of the Finkelstein reaction.

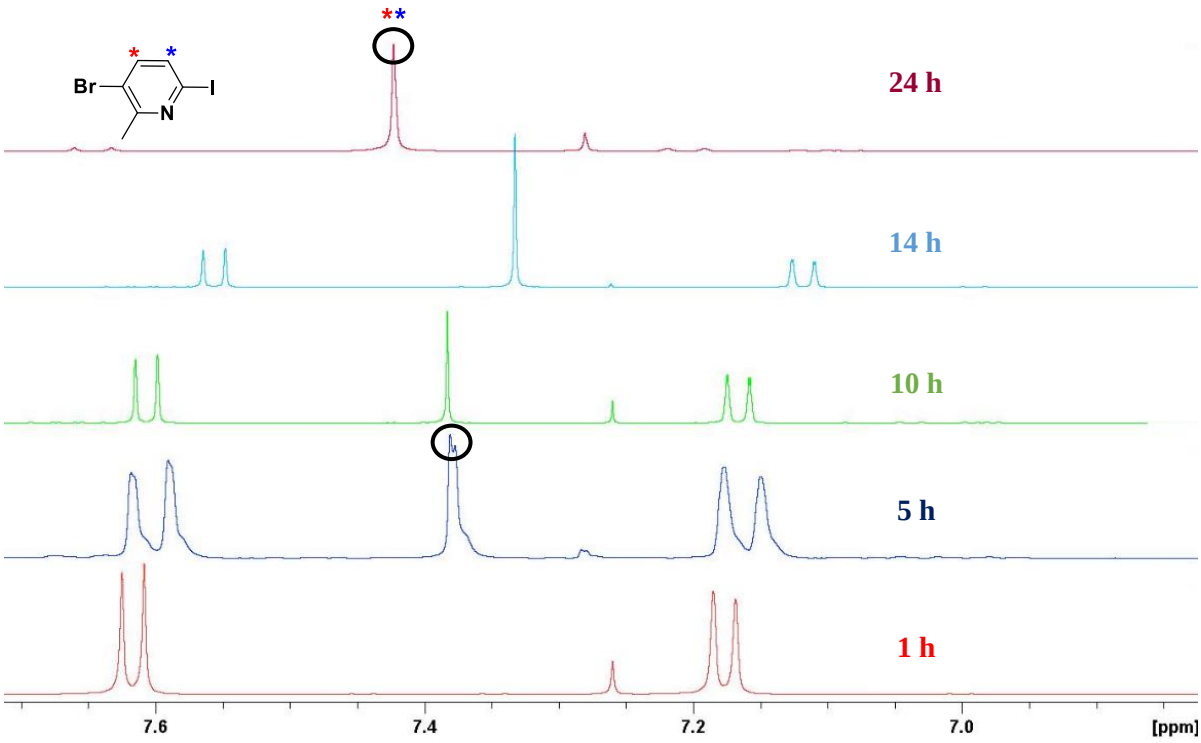

Figure 40. ^{1}H NMR spectrum of 3-bromo-6-iodo-2-methylpyridine at various reaction times.

As evident from Figure 40, the reaction has to be carried out over a longer period of time. Considering that the Finkelstein reaction is an equilibrium reaction, quantitative conversion of 3,6-dibromo-2-methylpyridine to 3-bromo-6-iodo-2-methylpyridine was achieved by controlling the reaction time. Otherwise, educt cannot be separated from the product due to

their similar structural and chemical properties. Increasing reaction time results in increased acetyl bromide formation, which is the main by-product of the reaction. Because acetyl bromide is released and removed as soon as it was formed during reaction time, the equilibrium is shifted instantaneously towards the side of the product to replace the volatile component, according to LeChatelier. After refluxing for 24 hours, the starting material is completely converted into the product. Interestingly, the product shows only one single peak in the aromatic region, which is due to similar proton chemical shifts (Figure 40).

6.1.3.4 5,5'-dibromo-6,6'-dimethyl-2,2'-bipyridine

The reaction of the iodinated precursor with hexabutylditin is only one example of the (intramolecular) Stille reaction.[192] As can be seen from Figure 42, the organotin compound is formed *in-situ* in the presence of palladium catalyst by transferring a trialkylstannyl group onto the aromatic core upon iodide release. Thanks to the symmetry of the product, the resulting aryltrialkyltin intermediate does not need to be isolated, thus enabling the synthesis to proceed in a one-pot reaction. The observed selectivity of the coupling is attributed to the enhanced reactivity of the 2-position compared with position 5.

Nevertheless, toxic by-products of tin based reactions are not unusual but can be removed by different work-up procedures. In this case, Bu_3SnI is fully separated by adding methanol to the crude product, which creates the polar Bu_3SnOH being excellently soluble in MeOH and methyl iodide that remains in solution. The product precipitates from the organic solution as white crystalline product in highly pure quality as confirmed by ^1H NMR spectra (Figure 43).

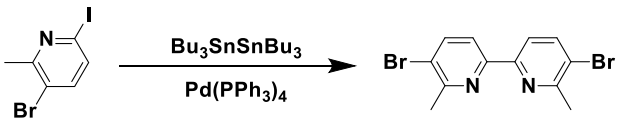

Figure 41. The synthesis of 5,5'-dibromo-6,6'-dimethyl-2,2'-bipyridine starting from 3-bromo-6-iodo-2-methylpyridine *via* Stille cross-coupling.

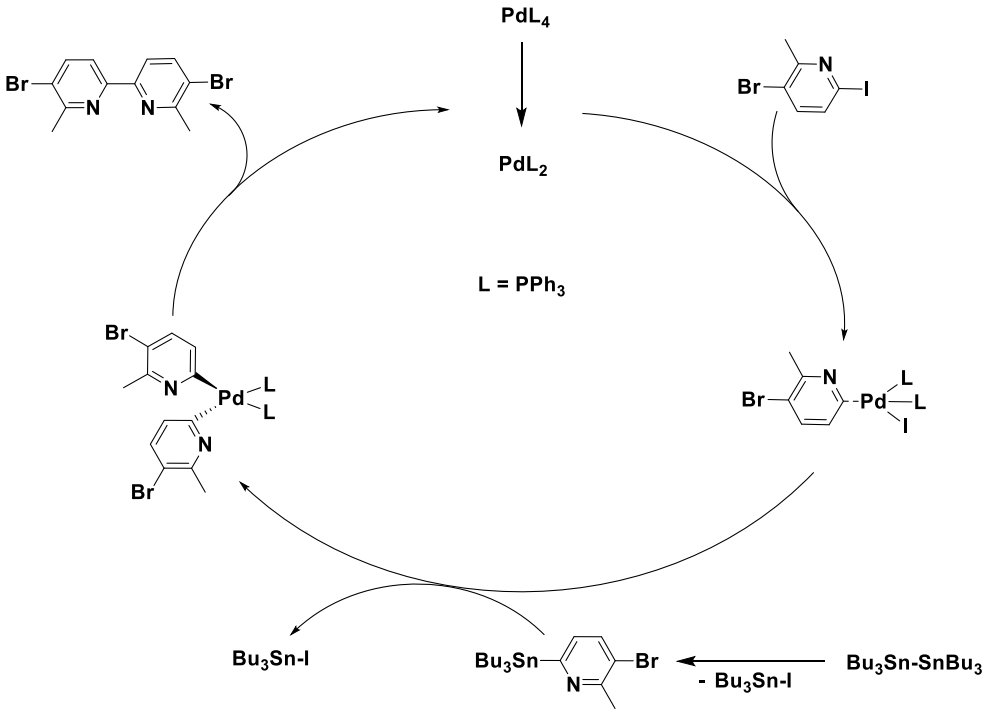

Figure 42. The catalytic cycle of Stille cross-coupling.

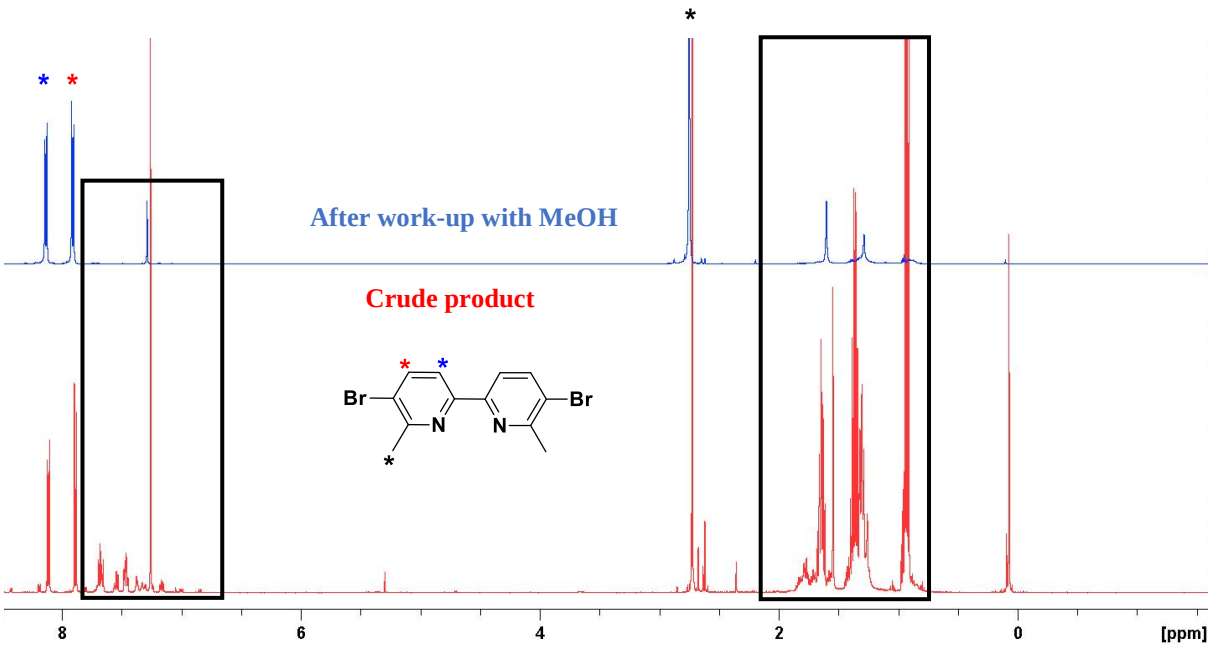

Figure 43. ^{1}H NMR spectrum of 5,5'-dibromo-6,6'-dimethyl-2,2'-bipyridine.

6.1.3.5 Dimethyl 4,4'-(6,6'-dimethyl-[2,2'-bipyridine]-5,5'-diyl)dibenzoate.

Since oxidation of 5,5'-dibromo-6,6'-dimethyl-2,2'-bipyridine with different types of oxidizing agents did not lead to the corresponding carboxylic acid, the backbone of ligand L2 was developed by first extending the ligand backbone at the 5, 5'-positions, followed by oxidation of the methyl groups. Mass spectrometric analysis of products from different approaches involving oxidation with CrO_3 and $KMnO_4$ under different conditions revealed that, in both cases, the methylated educt was recovered again intactly. Oxidation reactions are often very complex, including several intermediate steps. Considering that oxidation of the methyl groups in 4,4'-dibromo-6,6'-dimethyl-2,2'-bipyridine with chromium trioxide was fast and straightforward in nearly quantitative yields, the failure to oxidize the 5,5'-dibromo analog in a similar manner was attributed to the nearby presence of the electronegative bromine atoms, which are believed to block the coordination site, at which binding of the oxidizing agent occurs, followed by rearrangement to first generate the aldehyde intermediate and subsequently reacting to give the corresponding carboxylic acid. Thus, the oxidative reaction was limited by the structural requirements of 5,5'-dibromo-6,6'-dimethyl-2,2'-bipyridine.

Dimethyl 4,4'-(6,6'-dimethyl-[2,2'-bipyridine]-5,5'-diyl)dibenzoate was prepared to the procedure described in section 6.1.1.9 by coupling 5,5'-dibromo-6,6'-dimethyl-2,2'-bipyridine with 4-methoxycarbonylphenylboronic acid. Compared to the Stille coupling, Suzuki coupling requires the addition of a base to activate the boronic acid. The following steps of the catalytic cycle are similar to that of other coupling reactions.

Crystals suitable for single crystal X-ray diffraction were obtained by slow evaporation of cyclopentane into a chloroform solution containing the complex. The ligand crystallizes in the triclinic space group P1 and the following unit cell parameters: a = 7.268(2), b = 7.280(2), c = 11.022(3) Å, α = 99.056(5), β = 95.820(6), γ = 108.743(5)°. As shown in Figure 44, both pyridine rings of the bpy lie almost perfectly coplanar to each other, while the nitrogen atoms N1 and N1A are arranged to be in opposite sites of the C1-C1A bond. The distance between the pyridine rings is 1.49 Å, which is comparable to that found for the distance of the phenyl rings in biphenyl (1.48 Å). The angle C12-C7-C6 [122.41(15)°] is significantly greater than C8-C7-C6 [118.56 (15)°] which is certainly due to the steric repulsion between the C1 methyl group and the terminal phenyl ring, while the distance between the pyridine and the phenyl ring was determined to be 1.49 Å. As can be obviously seen, both phenyl rings are non-coplanar with the central bipyridine ring, twisting out of plane by 31.80 and 29.81°.

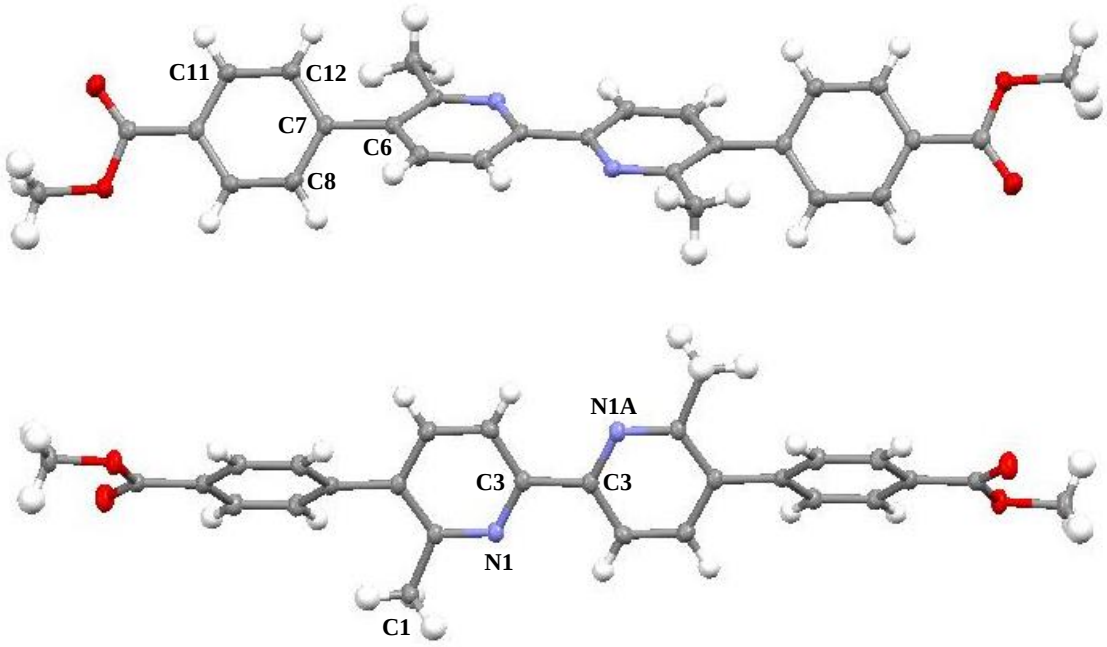

Figure 44. The molecular structure of the title compound, showing 50% probability displacement ellipsoids and the atom-numbering scheme.

6.1.3.6 4,4'-(6,6'-dimethyl-[2,2'-bipyridine]-5,5'-diyl)dibenzoic acid.

Subsequent saponification of the ester in KOH in MeOH provides the desired dibenzoic acid. The mechanism was already discussed in section 6.1.2.10.

6.1.3.7 5,5'-bis(4-carboxyphenyl)-[2,2'-bipyridine]-6,6'-dicarboxylic acid.

The last step involves the oxidation of the methyl groups to carboxylate acid groups. The oxidation was performed under well-known conditions using $KMnO_4$ in neutral medium. The initial purple color of the solution disappears within 24 hours. At the same time, a brown precipitate is observed which is attributed to *in-situ* formed MnO_2 indicating a positive reaction. After cooling, filtration over celite, and acidification with 1 M hydrochloride acid to pH 1-2, the desired carboxylated ligand L2 was isolated.

Under neutral conditions, the strong oxidizing agent Mn^{+7} being only stable in alkaline medium is reduced to Mn^{+4}. Upon addition of HCl, water-soluble potassium benzoate is converted into the corresponding carboxylic acid, which rapidly comes out of aqueous solution in the form of a snow-white precipitate.

However, a further single peak around 8.0 ppm was observed in proton NMR in a wide pH range (1-9), which showed no correlation between proton and carbon atoms of the compound, as consistent with 2D NMR spectroscopy. Therefore, the product was washed several times

with different organic solvents to separate the unknown impurity. Unfortunatly, the signal has remained the same after each wash.

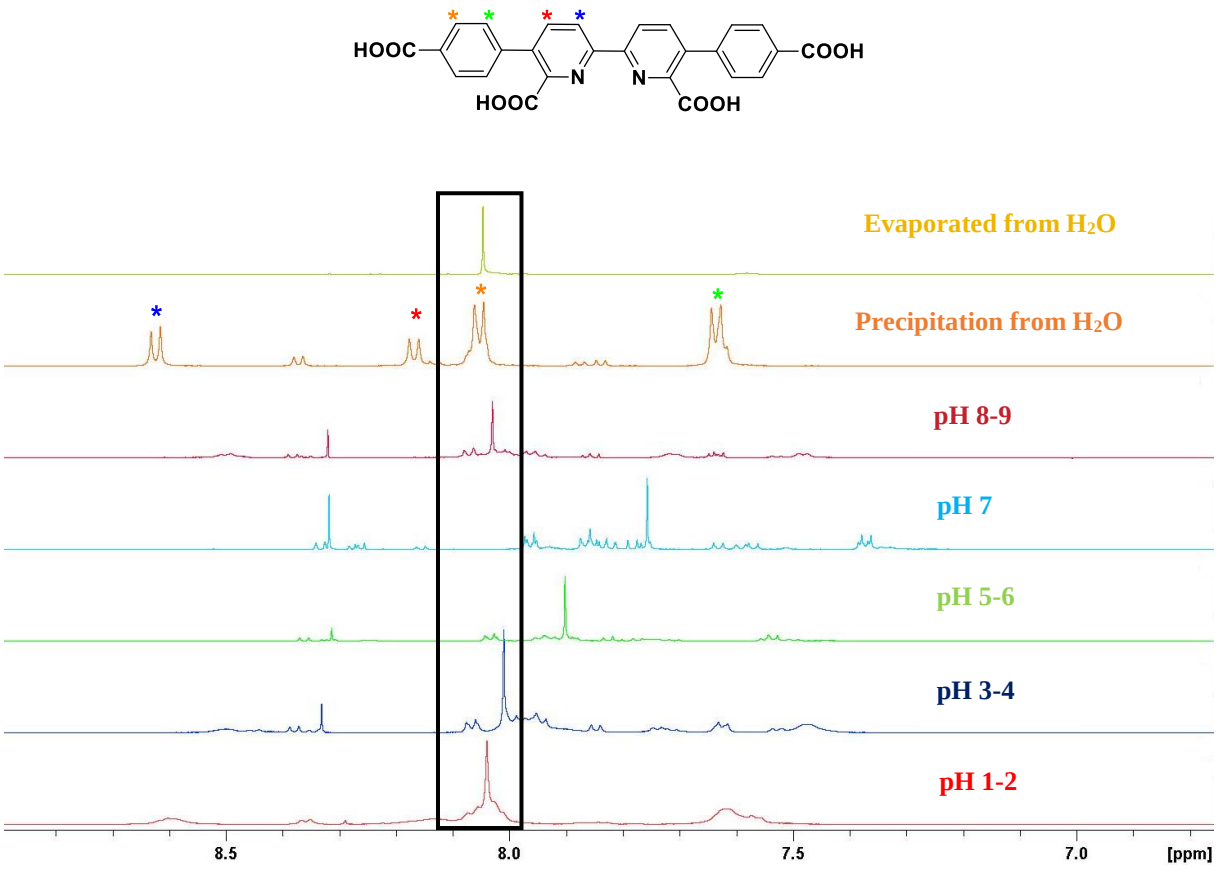

Figure 45. ^{1}H NMR spectra of aqueous solutions containing L2 at different pH values.

Finally, L2 was refluxed in water for several hours, followed by hot filtration to remove undissolved white solid. Surprsingly, the white precipitate was attributed to pure ligand, while evaporation of the aqueous solution gave acces to a second crop of a white solid, corresponding to the single still unknown peak (Figure 45).

6.2 Class 2: Tetradentate carboxylic acid ligands.

6.2.1 Synthetic preparation and structural assignment.

After having synthesized the long-sized goal compounds L1 and L2, the question being looked into here was whether extension of the π-conjugated system led to an additional drop of the catalytic activity compared to the reference system. In this connection, special attention was paid to the synthesis of ligands bearing substituents directly coordinated to the equatorial bipyridine rings to investigate the change in catalytic performance and kinetic behaviour.

Moreover, studies which focused on the effects of the axial coordinating ligands showed that attaching electron-withdrawing substituents to the aromatic rings of the pyridines led to an improved catalytic activity. Thus, it was of main interest to study the electron-withdrawing effect on the equatorial ligand plane. For this purpose, the ligands L3-L6 were synthesized, while ligand L4 was obtained as reaction intermediate in the synthesis of L1 and used to study the electronic effects of bromo substituents. The synthesis of the ligands L3 and L4 was achieved by oxidation of the methyl groups with chromium trioxide. The mechanism is discussed in section 6.1.2.7. Isolation of ligand L5 was accomplished starting from 2,4-dimethylpyridine, which was reacted to 4,4',6,6'-tetramethyl-2,2'bipyridine by a palladium on carbon catalyzed Suzuki-Miyaura coupling according to the method reported in the literature.[193] Oxidation of phenanthroline by $KMnO_4$ under basic conditions gave access to ligand L6, with carboxylic acid groups attached to the 3, 3'-positions of the bda-ligand (Figure 46).[194]

As shown in Figure 47, oxidation of phenanthroline under basic conditions gives access to two major products, 2,2′-bipyridyl-3,3′-dicarboxylic acid and 4,5-diazafluoren-9-one. Both products can be isolated from 1,10-phenanthroline-5,6-quinone either by its oxidation to the dicarboxylic acid or by a rapid benzyl-benzilic acid ring contraction of the quinone to form the unwanted by-product. Fortunately, an excess of $KMnO_4$ was found to favour the oxidation reaction rather than the ring contraction, which is necessary to oxidize not only the phenanthroline backbone but also the additional methyl groups at the 6,6'-positions. In addition, the low oxidation potentials of the chinon thermodynamically favors the oxidation of the methyl groups. ^{1}H NMR analysis of crude products after work-up of the reaction at different reaction times revealed that oxidation first takes place at the phenanthroline backbone. It was found that full oxidation of 1,10-phenanthroline-5,6-quinone to ligand L6 could only be achieved by refluxing the reaction mixture overnight. To suppress the competitive ring contraction reaction, the concentration of the base can additionally be decreased, thus preferable turning the reactivity towards the desired pathway.

The Pd/C-calayzed coupling of two molecules of 2,4-dimethylpyridine is similar to the Suzuki coupling reaction involving the oxidative addition of an aryl halide followed by *in-situ* halide metathesis and the formation of the tetrahedral intermediate, the transmetalation step, the reductive elimination to generate the Pd(0) species and the final regeneration of the Pd/C catalyst by precipitation, which can be separated from organic reaction solution by simple filtration. The oxidation of 4,4',6,6'-tetramethyl-2,2'-bipyridine to ligand L5 is an effective single-step method using aqueous nitric acid as oxidizing agent under solvothermal conditions (160 °C, 36 h). Considering that oxidation of one methyl group through traditional methods

(CrO_3, $KMnO_4$) generates large quantities of hazardous waste and requires a permanent control of the experimental conditions, the solvothermal oxidation approach is a less harmful alternative to produce compounds with more than two carboxylic acid groups.

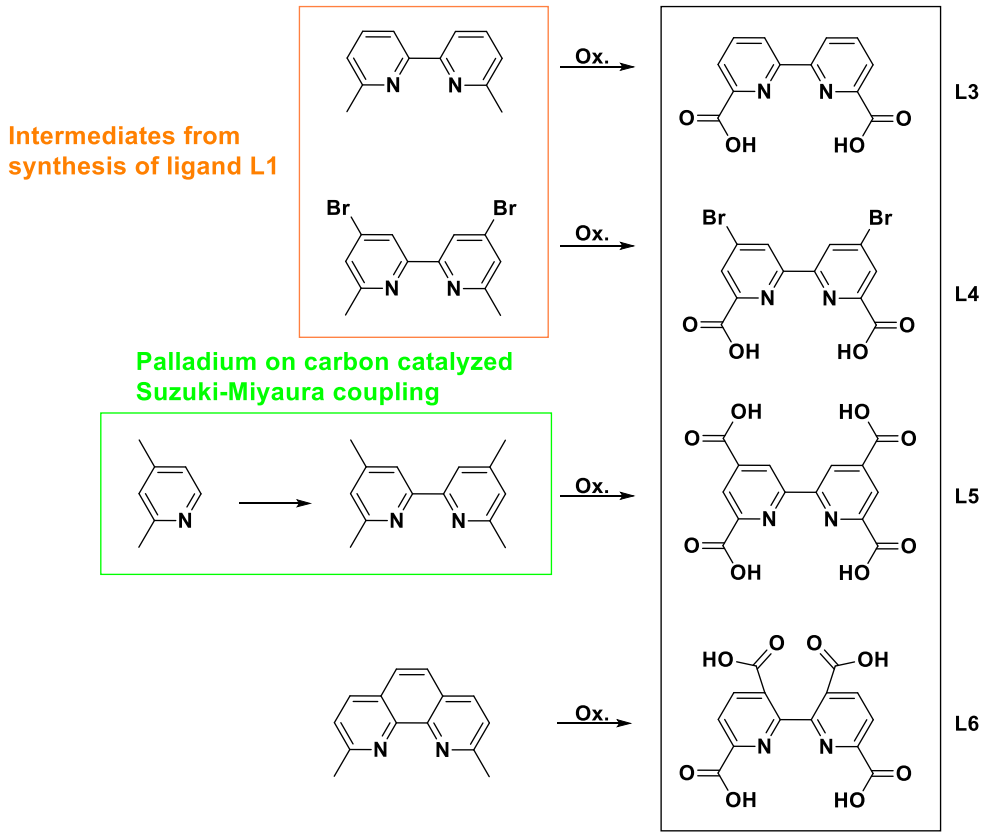

Figure 46. Preparation of ligands L3-L6 *via* oxidation.

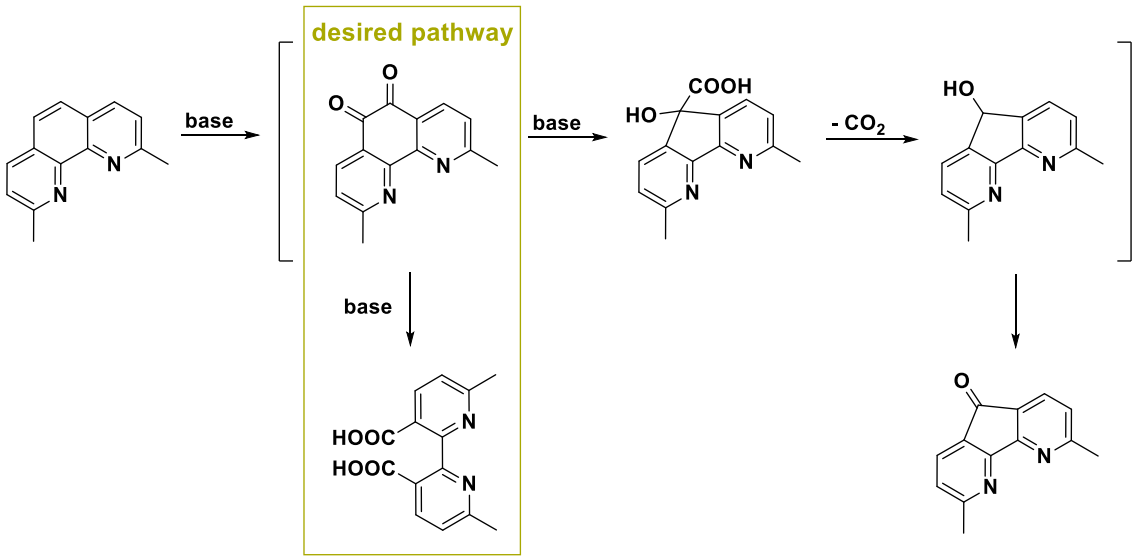

Figure 47. Oxidation of phenanthroline by $KMnO_4$ under basic conditions.

Due to the fact that carboxylic acid protons undergo a rapid proton exchange with protons of water present in solution, the peak width of carboxylic protons is depending on the rate of exchange and the sample concentration, even in non-polar solvents such as DMSO. Since ligands L3-L6 are formed upon addition of aqueous solutions of an acid, the proton NMR peaks of water at around 3 ppm are attributed to the synthetic conditions, as evident from Figure 48.

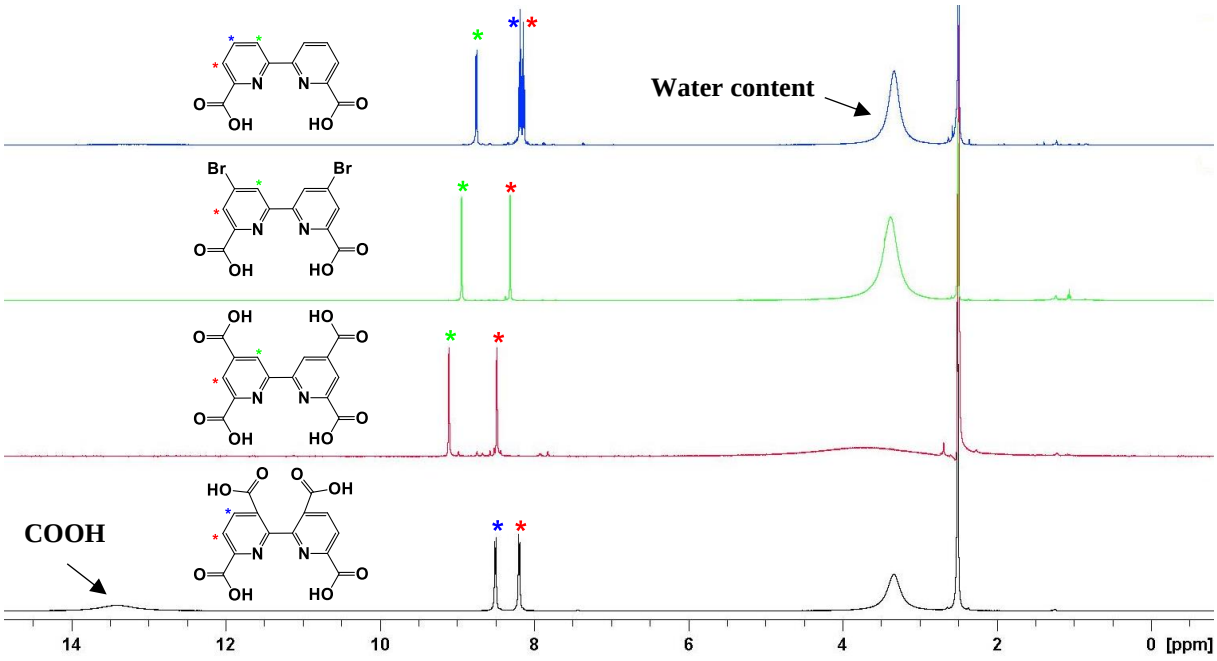

Figure 48. ^{1}H NMR spectra of ligands L3-L6.

6.3 Class 3: Tetradentate dicarboxamide ligands.

The synthesis of the following ligand class involves a one-pot reaction, in which the carbonyl moieties of the starting carboxylic acid are replaced by amide moieties through *in-situ* acid chloride formation. The most synthetically important source of chloride ions is thionyl chloride ($SOCl_2$), which reacts with carboxylic acids to produce the corresponding acyl chloride by eliminating the gaseous SO_2 and HCl. The reaction is driven by the change of the reaction entropy ΔS. Considering that the carbon centre of acyl chlorides are highly electron deficient, they tend to react more quickly with nucleophiles and are good starting materials for the preparation of carboxylic acid derivatives such as esters, amides and anhydrides, some of which are more easily formed from the acyl chloride than directly from the carboxylic acid.[195]

Upon subsequent addition of an amine to the reactive acyl chloride, a series of ligands with substituents of different steric properties were successfully synthesized, as shown in Figure 49.

With exception of 2-amino-4,6-dimethyl pyrimidine, all other amine precursors have been obtained from commerically available sources. The preparation of the pyrimidine was carried out under basic aqueous conditions using guanidine nitrate, an excess of acetylacetone in the presence of sodium carbonate, while the reaction was carried out in a polar solvent (H_2O) at heating (100 °C) for 24 h. The occurrence of a positive reaction was indicated by the formation of a brown suspension.

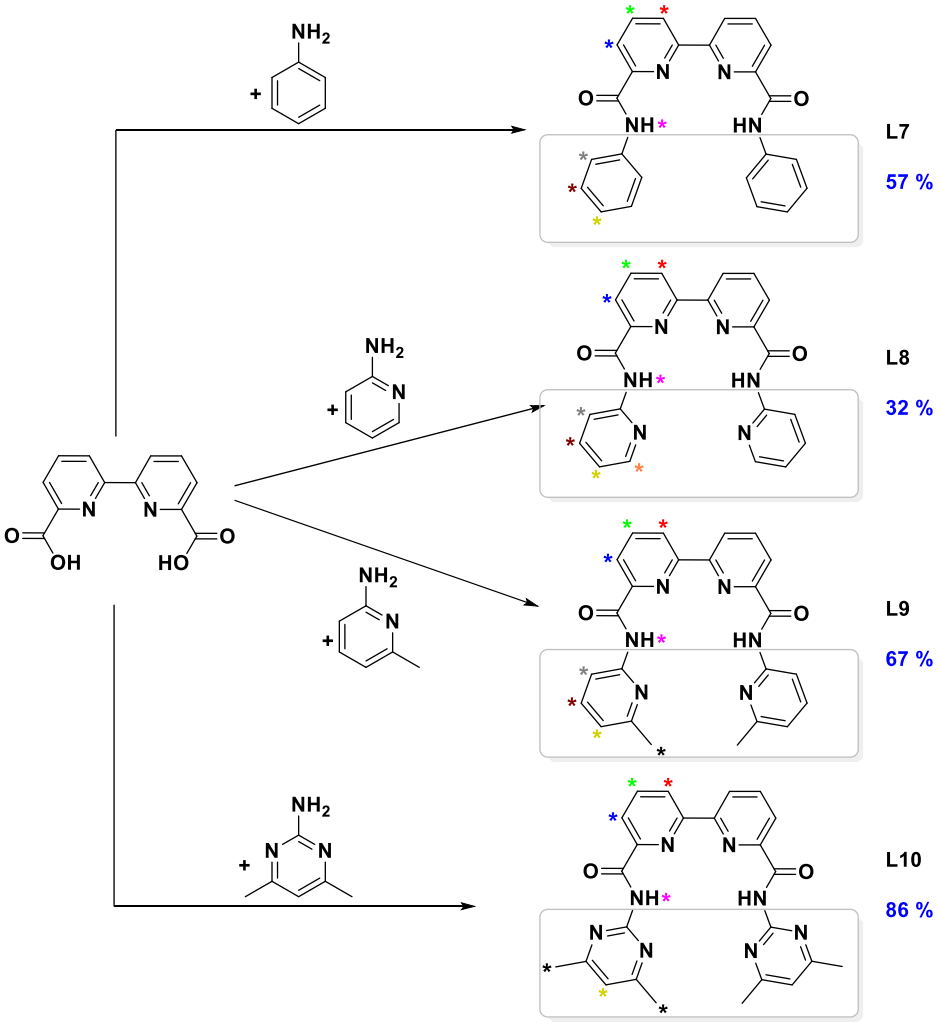

Figure 49. Synthetic route for the preparation of ligands L7-L10.

6.3.1 Characterization of ligands L7-L10.

The overall ^{1}H NMR spectra of the ligands L7-L10 are shown in Figure 50. Because of the symmetry in each of the molecules always sets of protons are observed in the ^{1}H spectra, not only for the aromatic protons but also for the protons of the methyl groups in L9 and L10. By way of reminder, the introduction of functional groups close to the central ruthenium atom were found to increase the sterical hindrance as illustrated by the complexes 11-19 and thus reduced

the probability of water coordination, O-O bond formation and oxygen release. Therefore, the systematical modification of the ligands L7-L10 by additional methyl groups should help determine whether catalyst stability induced by the amide moieties or steric effects of the surrounding ligands have a bigger influence on the catalytic activity of the catalysts.

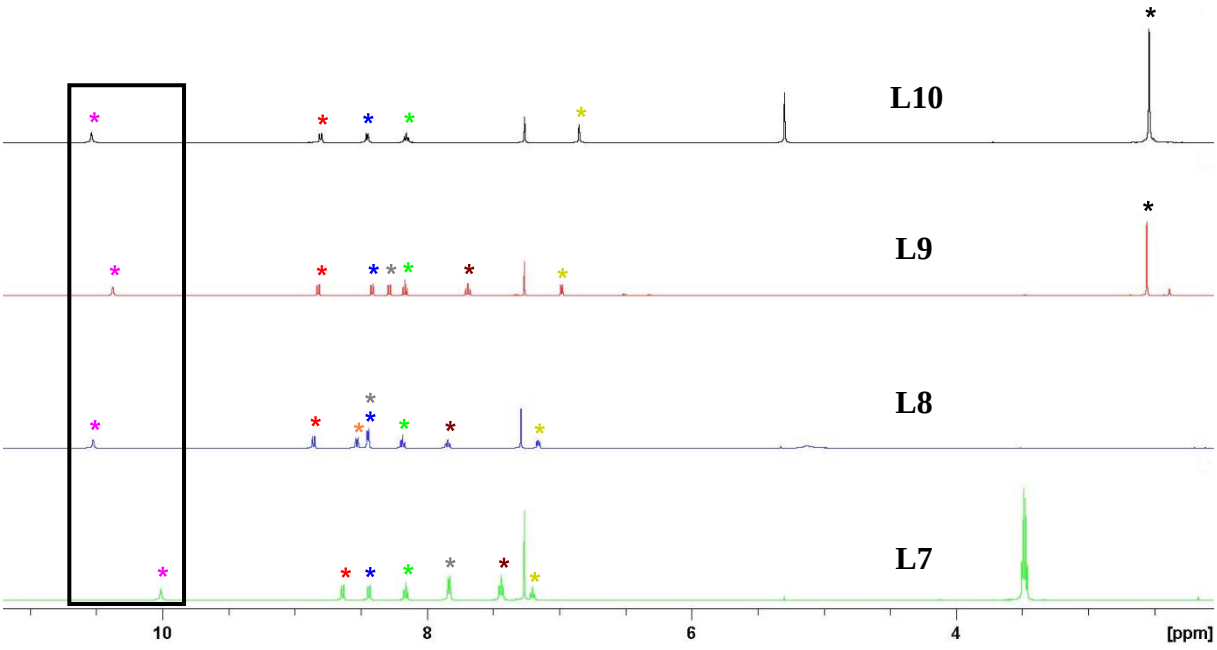

Figure 50. ^{1}H NMR spectra of ligands L7-L10. *The chemical shifts illustrated above correspond to the proton signals of the ligands L7-L10 marked in color in Figure 49.*

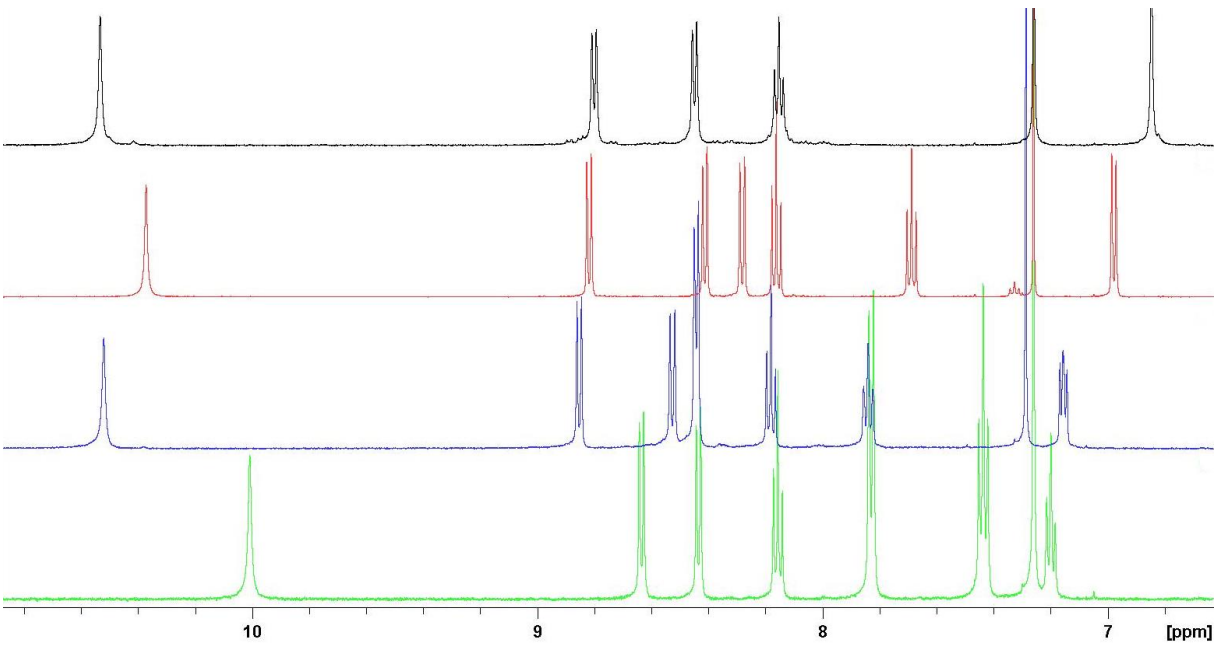

Figure 51. Enlarged view of aromatic regions of ligands L7-L10.

Figure 51 represents the enlarged view of aromatic regions of ligands L7-L10. A comparison of the ^{1}H spectra of the ligands reveal a strongly downfield shifted proton signal between 10-11 ppm, which is characteristic for the presence of amide NH protons. This is further supported by studies on ^{15}N-HMBC NMRs that give rise to a doublet splitting deriving from one bond ^{15}N-^{1}H spin coupling. A representative ^{15}N-HMBC spectrum is shown exemplarily in Figure 52. In addition, the carboxamide N-H protons tend to have ^{15}N chemical shift values of about 130-140 ppm. In case of ligand L10, this is observed at 132 ppm.

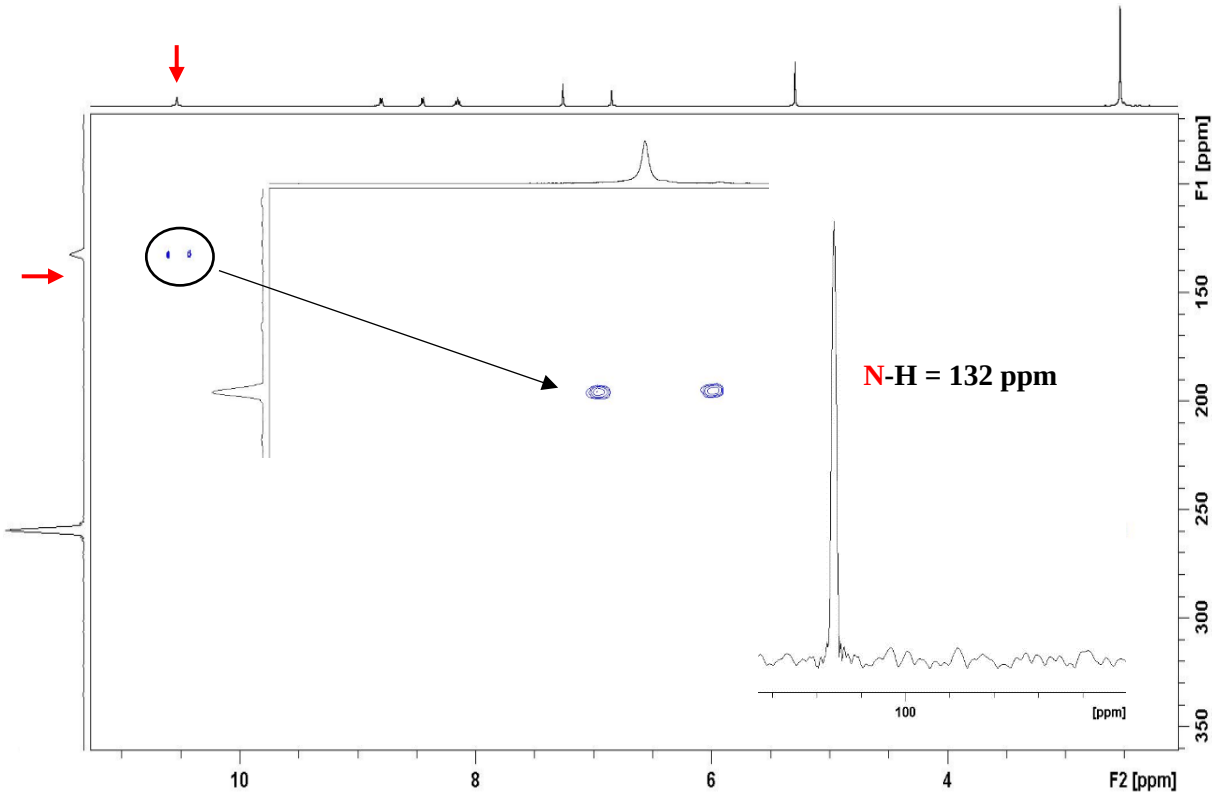

Figure 52. ^{15}N-HMBC spectrum of ligand L10.

The ^{13}C-NMR spectrum of L10 shows ten signals altogether, which is in excellent agreement with the number of carbon atoms present in the molecule. Considering that L10 contains 24 carbons but only shows 10 signals turns out that there is symmetry in this molecule and its analogs. In general, carbonyl carbons appear between ~160-180 ppm in ^{13}C NMR. This is observed for the ligands L7-L10, which show a strongly deshielded signal above 160 ppm. Carbons to which the methyl groups are attached appear in the most downfield region around 170 ppm, which is due to the presence of the nearby electronegative nitrogen atoms, pulling electron density away from the carbon atoms and thus increasing the chemical shift. The same effect is observed for the methyl groups, which appear most upfield at 24 ppm (Figure 53).

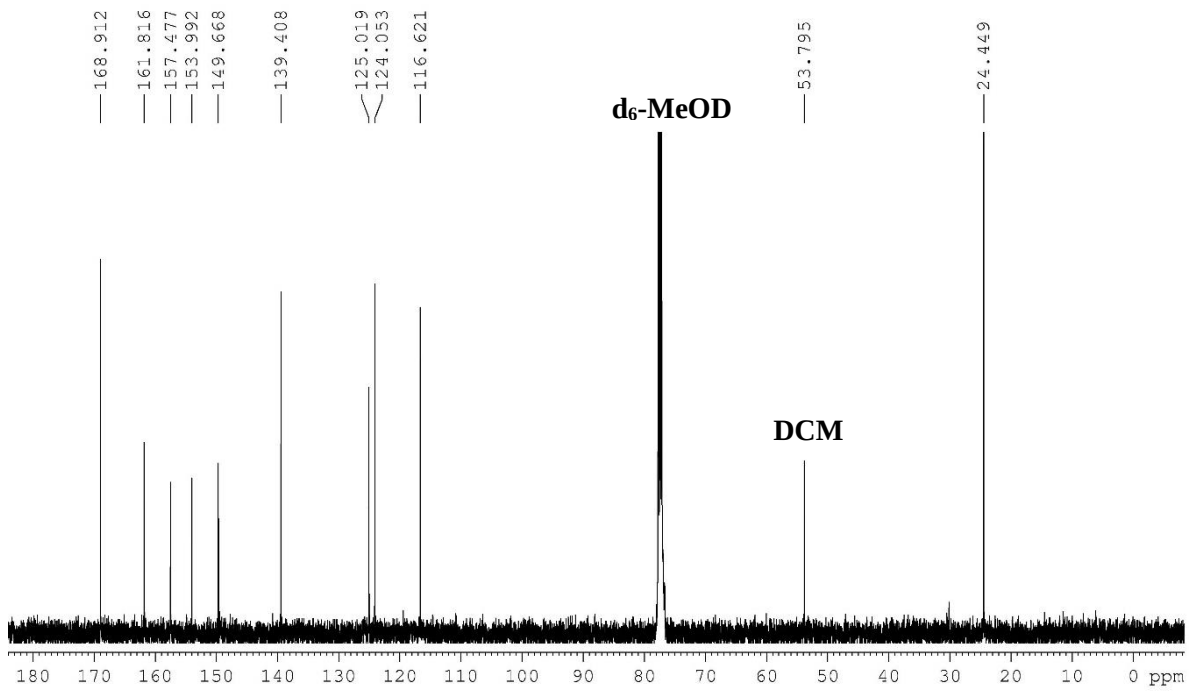

Figure 53. ^{13}C spectrum of ligand L10.

In order to find more evidence for the presence of the carboxamide moiety, infrared sprectroscopy was performed in the spectral range of 200-4000 cm^{-1}. As expected, the IR spectra of the ligands are quite similar due to their structural similarity. Considering that the only difference is the nature of the substituents attached to the amide motif, an interpretation of the major IR absorption bands was taken place with the help of representative examples L7 and L9 since L8 and L10 contain the same repeating structural motifs.

A comparison between L7 and L9 reveals that there is one broad absorption band around 3300 cm^{-1} (3348 cm^{-1} in L7, 3365 cm^{-1} in L8, 3332 cm^{-1} in L9 and 3367 cm^{-1} in L10), which is characteristic for the N-H stretching mode in secondary amides. By comparison, N-H stretches of primary amines show two absorption bands in the 3300-3000 cm^{-1} region. The carbonyl stretching vibtration of the C=O-NH moiety appears around 1700 cm^{-1}, while the peak around 1500 cm^{-1} was attributed to a N-H bending vibration.

Typically, the N-H wag of secondary amines and amides are less intensive, thus the bands around 700 cm^{-1} were attributed to the N-H wagging vibration. In general, the C-N stretching vibration is observed as medium or strong bands in regions that are overlapped by the bands of other functional groups. However, the C-N stretching vibrations were found around 1300 and 1100 cm^{-1}, which are in good agreement to the reported values in literature (C–N stretch from 1335-1250 cm^{-1} and 1250–1020 cm^{-1} for aromatic and aliphatic amines, respectively).[196]

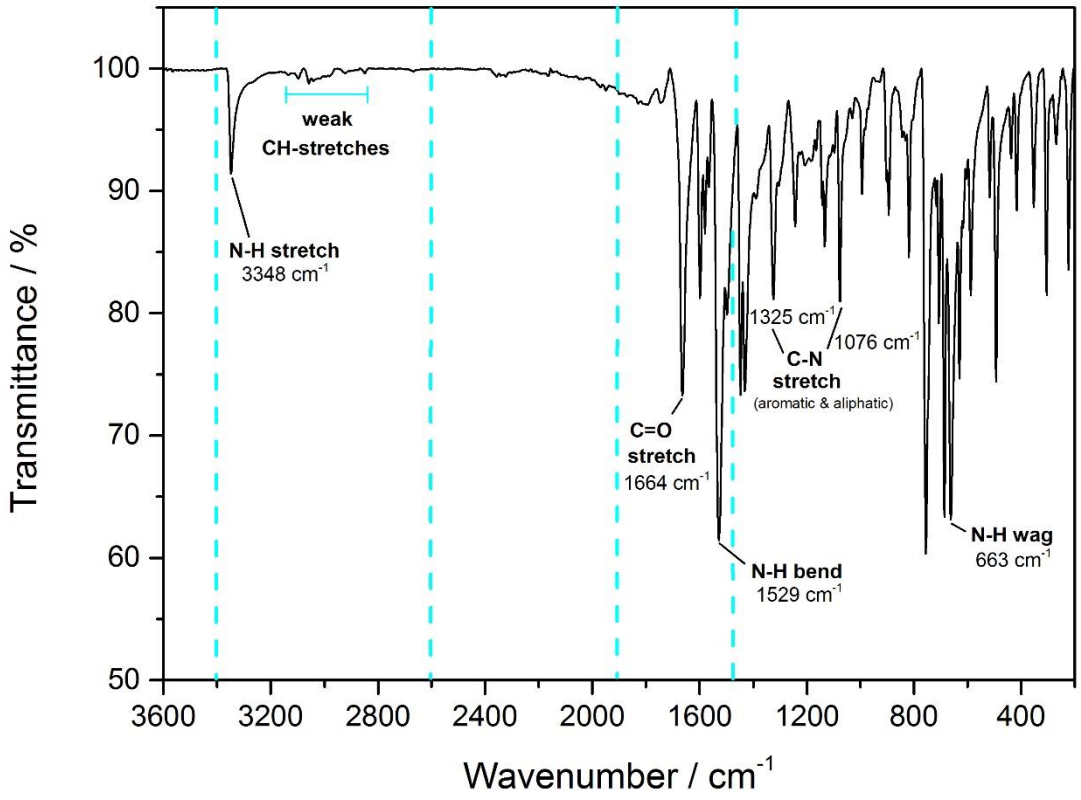

Figure 54. IR spectrum of ligand L7.

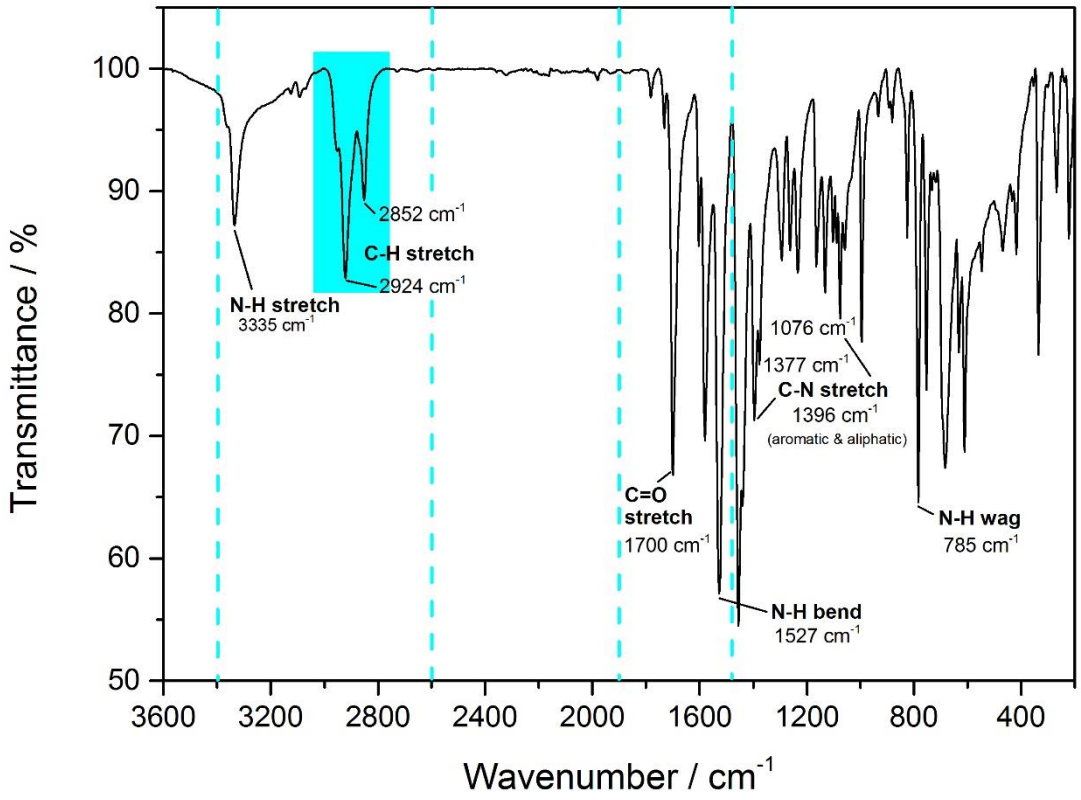

Figure 55. IR spectrum of ligand L9.

In case of ligand L9, two additional bands located at 2850 and 2920 cm^{-1} were assigned to stretching vibrations of the methyl groups (Figure 55). Compared to ligand L7 (Figure 54), this region is missing or only very weakly pronounced which is due to the absence of C-H stretches of the alkyl groups within this molecule. Considering that the N-H stretching absorption is more or less sensitive to hydrogen-bonding interactions, inter- as well as intramolecular, these factors can lead to a shift of the above mentioned absorptions.

CHAPTER 7

Complex Synthesis

A commonly used starting material for other ruthenium(II) complexes is dichlorotetrakis(dimethy1 sulfoxide)ruthenium(II), $Ru(DMSO)_4Cl_2$, which is well known for its stability in air. In this chapter, some important points regarding the synthesis of $Ru(DMSO)_4Cl_2$ are summarized, since the formation of this compound is strongly depending on the reaction temperature, the purity of both the solvent DMSO and the starting molecule $RuCl_3 \cdot H_2O$ and the time of reflux. Moreover, its crystal structure has been determined by X-ray structure analysis, clearly showing the bonding properties in this compound. Due to the fact that $Ru(DMSO)_4Cl_2$ is the source material for all ruthenium(II) complexes reported in this work, a general synthesis concept will be introduced for the development of Ru complexes containing carboxylate and amide moieties in their equatorial ligand backbone.

7.1 Preparation of $Ru(DMSO)_4Cl_2$.

The synthesis of the precursor $[Ru(DMSO)_4C1_2]$ is relatively straightforward and is a useful alternative starting material to $RuCl_3 \cdot H_2O$.[197] As shown in Figure 56, it is prepared by the reaction of $RuCl_3 \cdot H_2O$ in DMSO. Thanks to the lability of the DMSO ligands, their replacement by other strong coordinating ligands, such as pyridines, is relatively simple.

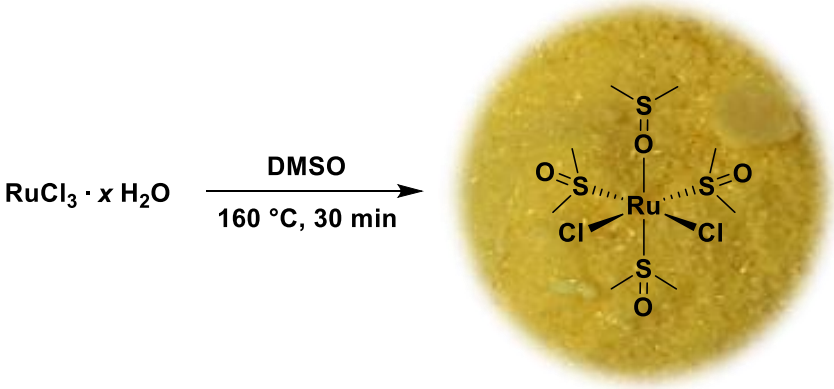

Figure 56. Synthesis of ruthenium precursor $[Ru(DMSO)_4C1_2]$.

Gentle refluxing of the starting dark solution containing ruthenium trichloride is one of the most important synthetic aspects, to which special attention has to be paid in order to avoid some *'burning'* of the reaction mixture. Considering that reaction intermediates formed *in-situ* during $[Ru(DMSO)_4C1_2]$ synthesis are extremely air-sensitive, all starting compounds need to be used after complete drying under nitrogen atmosphere, since commercially available $RuCl_3$ always contains an undefined amount of water molecules. A positive reaction is confirmed by a slow color change of the reaction mixture from deeply greenish-black to slightly yellow to a clear brownish-orange solution.

The ^1H spectrum of $[Ru(DMSO)_4C1_2]$, which was recorded directly from the reaction mixture, is complex and due to the coordination of the DMSO ligands being either S-bonded or O-bonded. Lastly, the crystal structure of $[Ru(DMSO)_4C1_2]$ shown in Figure 57, which was obtained from an acetone/DMSO solution, reveals that three of the four DMSO molecules are S-bonded to the metal centre in a facial configuration, while the last one is O-bonded. NMR analysis revealed that the methyl proton resonance of S-bonded Me_2SO were located in the downfield region. The ligands are symmetrically arranged around the central ruthenium atom, corresponding to a nearly octahedral geometry. The Ru-O bond distance is 2.133 Å, while average values of 2.259 Å and 2.428 Å were found for Ru-S and Ru-Cl, respectively.

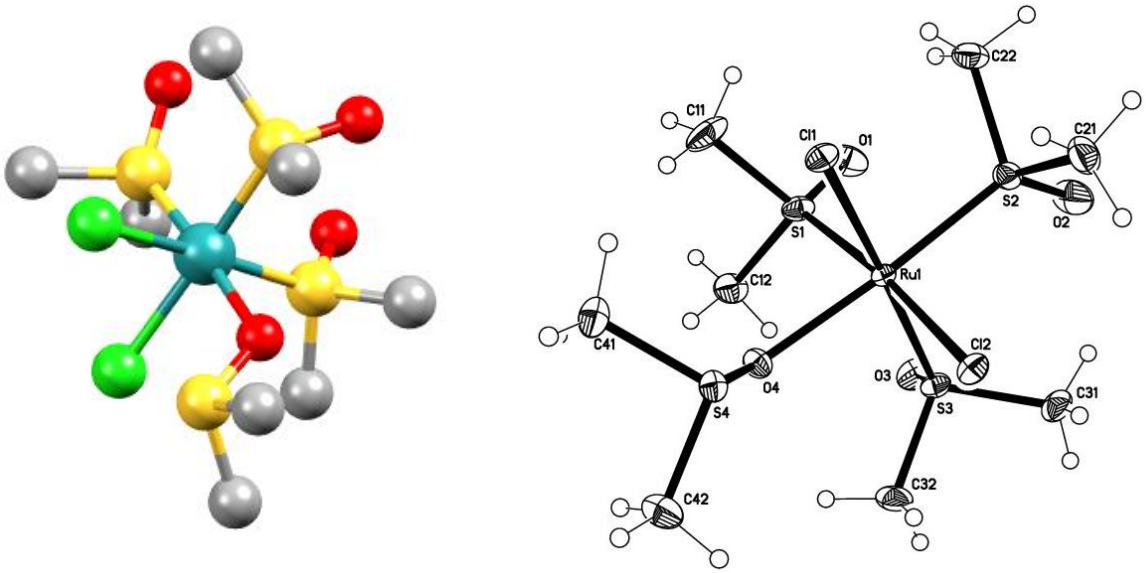

Figure 57. Crystal structure of $[Ru(DMSO)_4C1_2]$, showing 50% probability displacement ellipsoids and the atom-numbering scheme.

7.2 General synthesis scheme of Ru(II) complexes.

The desired ruthenium complexes containing carboxylate (Figure 58) and amide moieties (Figure 59) were synthesized from the respective carboxylic acid by refluxing a solution of ligand, $Ru(DMSO)Cl_2$ and Et_3N overnight.

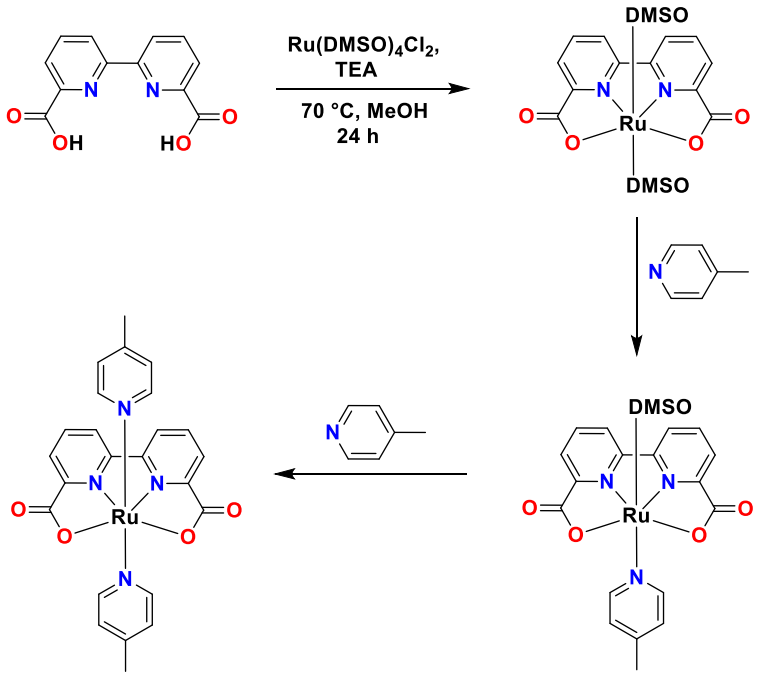

Figure 58. Synthesis scheme of Ru WOCs containing negatively charged carboxylate ligands.

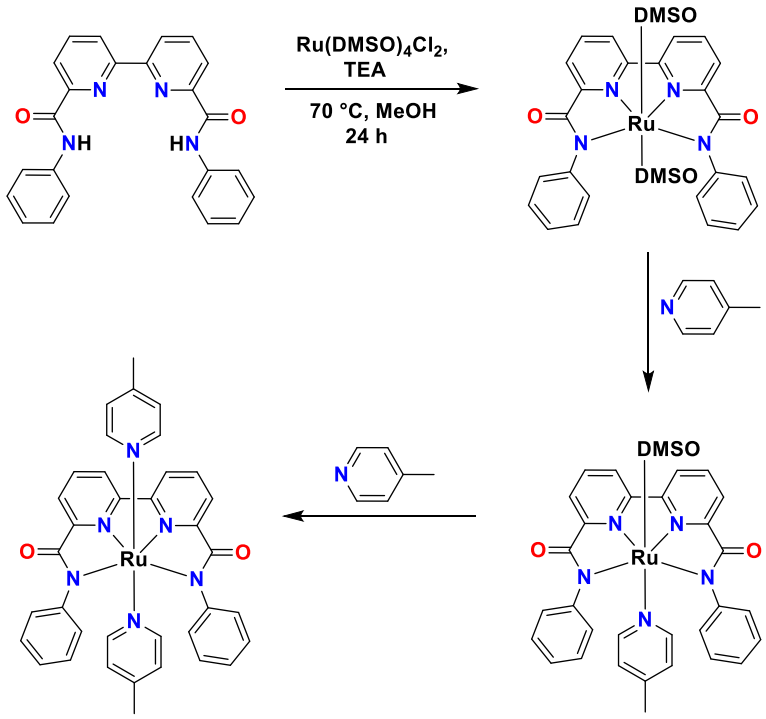

Figure 59. Synthesis scheme of Ru WOCs containing polydentate nitrogen ligands.

To this solution was added 4-picoline and the resulting solution was further refluxed for 48 h. This afforded all ruthenium complexes as red solids in good to moderate yields. Table 4 gives an overview of all ligands and ruthenium complexes prepared during this thesis.

Table 4. List of Ru complexes prepared in this work.

L1 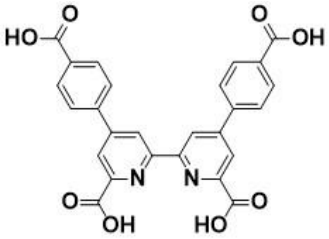	**K1** 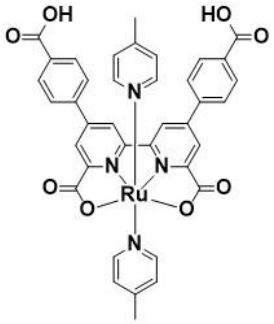	**K2** 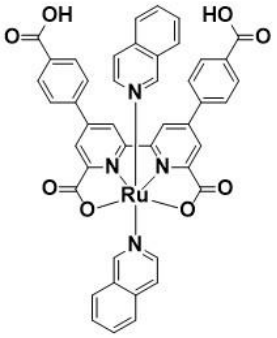
	K3 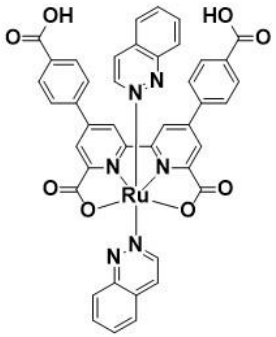	
L2 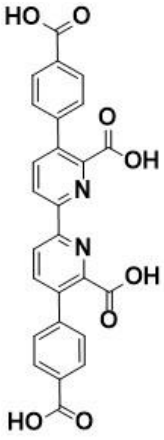	**K4** 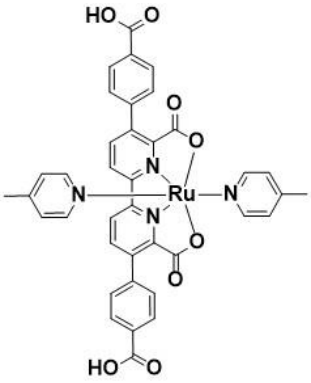	**K5** 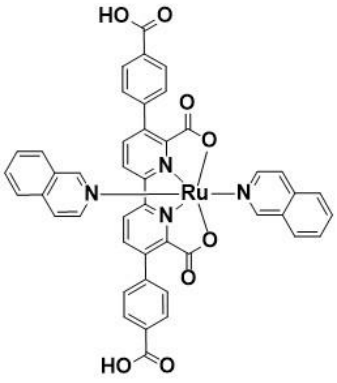
	K6 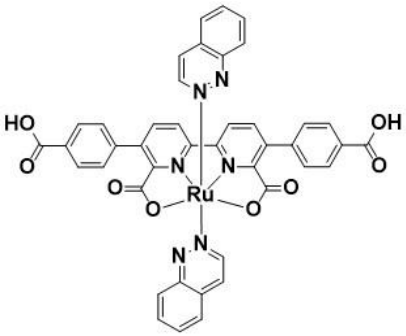	

L3 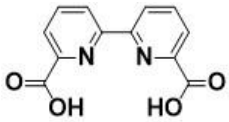	**K7** 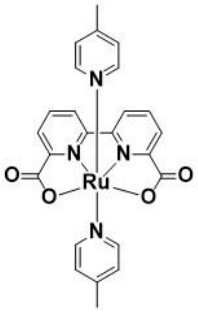	**K8** 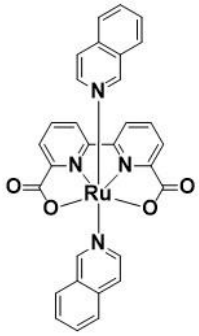
	K9 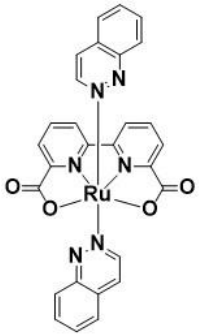	
L4 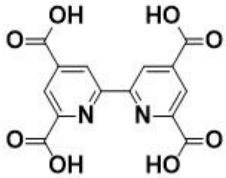	**K10** 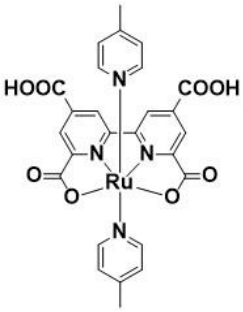	**K11** 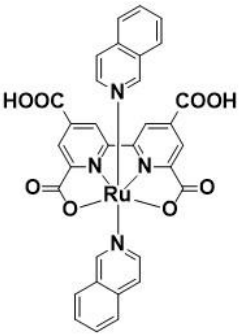
L5 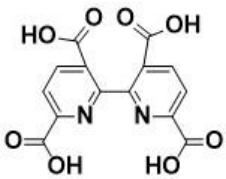	**K12** 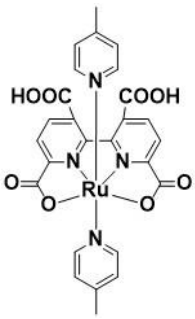	**K13** 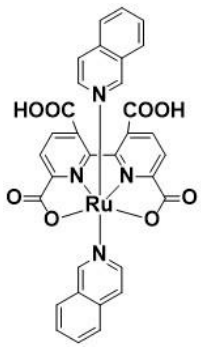

L6

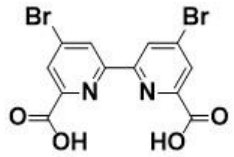

K14

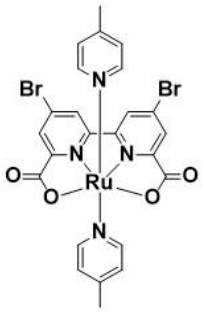

K15

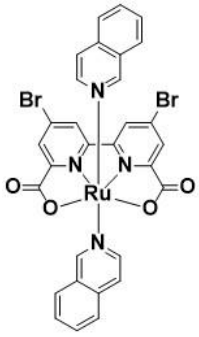

L7

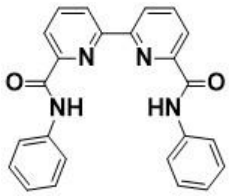

K16

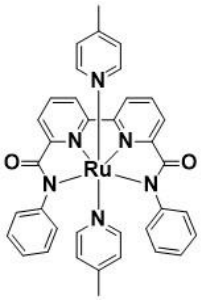

L8

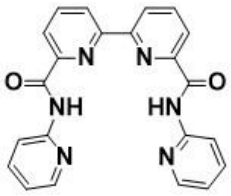

K17

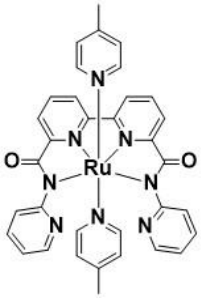

L9

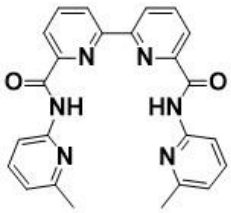

K18

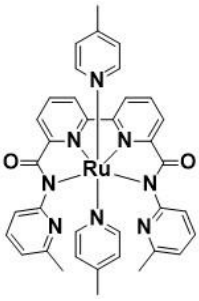

L10

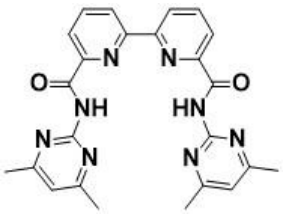

K19

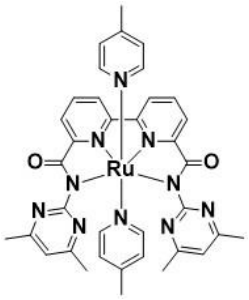

CHAPTER 8

Characterization

A relatively simple, fast and routine method to determine the structure of an organic compound is NMR spectroscopy including ^{1}H, ^{13}C, ^{15}N, DEPT, COSY, HMBC, HMQC etc.

Ruthenium has two magnetically active quadrupolar isotopes, ^{99}Ru and ^{101}Ru. Although the receptivity of ^{99}Ru is only half of that of ^{101}Ru, it is preferable to observe ^{99}Ru due to its lower quadrupole moment, which compensates for the difference in receptivity between the two isotopes (4.614 MHz *vs.* 5.171 MHz).[198] Nevertheless, not every compound is perfectly suited for NMR examinations due to the fact that transition metals have multiple potential oxidation states. For example, amongst all current oxidation states, ruthenium +III can not be measured by conventional NMR methods because of its paramagnetism. All other states (-II to VIII) are diamagnetic or only contain a small amount of paramagnetism, whereby the strength of this effect is dependent on the formal molecular charge at the ruthenium site. Characteristic for paramagnetic ruthenium compounds are broad signals in ^{1}H NMR, which is the main problem of all ruthenium complexes prepared within the framework of this doctoral thesis. Addition of small amounts of ascorbic acid into the deuterated solutions was found to improve the sharpness of the the NMR signals, which is attributed to the reduction of the central Ru^{3+} ion to diamagnetic Ru^{2+}.

Important information on structure, mechanisms and catalytic as well as electrocatalytic behaviour can be gained from electrochemistry and UV-vis analysis. While infrared spectroscopy was applied to identify specific functional groups in the molecules, UV-vis spectroscopy is helpful in studying mechanistic details and electronic transitions causing visible color changes, which result in characteristic absorption spectra. Information on electron transfer processes including the stability of oxidation states and the reactivity are obtained by voltammetry (CV, SWV). Only the combination of all these data gives a full picture of the structural and functional features of the catalysts. All measurements were performed under the same conditions as for the chemical water oxidation reaction in order to give the closest possible comparison.

8.1 Characterization of K1 and K4.

8.1.1 Structural confirmation by NMR, IR spectroscopy and ESI-MS.

In this chapter, the structural, electrochemical and optical properties of K1 and K4 will be investigated to ensure that the water oxidation reaction is only triggered by the catalysts themselves. Due to the structural similarity, K1 and K4, which only differ in their ligand topology are directly compared to each other. In solid forms, both complexes are sufficiently stable to be handled under ambient conditions. Upon exposition to air for several hours, analysis of ^{1}H NMR spectra reveals a structural change, which is indicated by broad proton signals in the aromatic region. Considering that broadening of NMR signals can be attributed to a paramagnetic center due to the presence of an unpaired electron which induces fast magnetic relaxation, it is presumed that oxidation of Ru^{2+} occurs under air. Similar behaviour is observed for solutions containing the corresponding catalyst, wherein the color of the solution changed from red to green when exposed to air for several hours (Figure 60). This process could be speeded-up by bubbling the solution with oxygen gas, resulting in a dark-green solution.

Analysis of the green aqueous solutions containing the corresponding catalyst display a signal at around *m/z* = 770, clearly indicating that oxidation was achieved even by molecular oxygen dissolved in solution. Considering that water molecular dissociates rapidly at the $[Ru^{III}]^{+}$ state during the ionization process, the active intermediate is proposed to be $[Ru^{III}\text{-}OH_2]^{+}$ at this state.

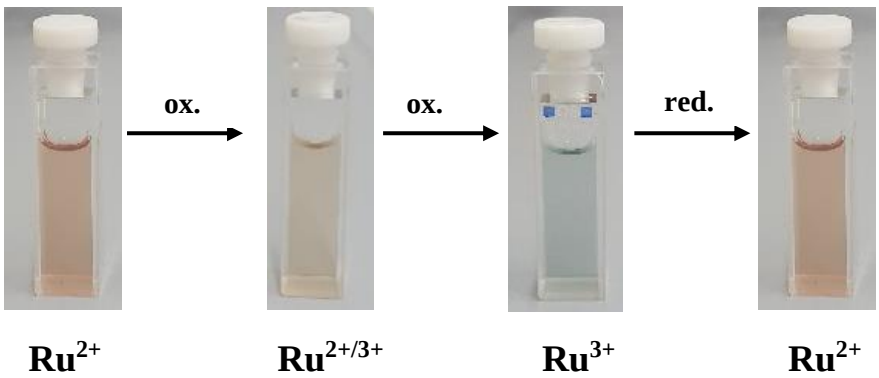

Figure 60. Time-dependent color change of a solution containing the corresponding catalyst.

By adding a small amount of ascorbic acid to the *'green'* samples, the paramagnetic species could be promptly reduced to the diamagnetic species, conversely turning the color of the solution back to red and again displacing sharp peaks in proton NMR. As evident from the ^{1}H spectra of reduced K1 and K4, both complexes display sets of equivalent protons in the

aromatic region, which is consistent with their C_{2v} symmetry (Figure 61). Another approach to overcome the problem of line broadening is to warm the samples to speed up the exchange rate, creating significantly sharper peaks as can be seen in Figure 64. The temperature decrease resulted in a broadening and shifting of the resonances in the spectrum, which suggested the presence of an equilibrium between the initial ruthenium(II) complex and a new complex where the central ruthenium atom is oxidized to Ru^{3+}. Interestingly, it was found that protons close to the terminal carboxylic acid groups were most affected by the phenomenon of peak broadening. The ^{1}H NMR of complex K1 shows six sets of signals in the aromatic region (Figure 62). Six protons can be assigned to one singlet at 2.29 ppm which represents the protons of the methyl groups of the picoline ligands. Four sets of four doublets at 7.07 ppm, 7.75 ppm, 8.02 ppm and 8.15 ppm are assigned to the aromatic protons of the picoline ligands and of the phenyl groups. The single peaks at 8.39 and 9.18 ppm are assigned to aromatic ring proton resonances of the bipyridine moiety. Similar magnetic behaviour was oberseved for complex K4, which shows nearly identical resonance peaks located at 2.28 ppm for the methyl protons, the peaks at 7.06 ppm and 7.99 ppm are attributed to the aromatic protons of the picoline ligands, while the protons of the phenyl rings at the 5,5'-positions are found to be at 7.40 ppm and 7.69 ppm (Figure 63). The aromatic protons of the central bipyridine ligand are located at 7.84 ppm and 8.46 ppm.

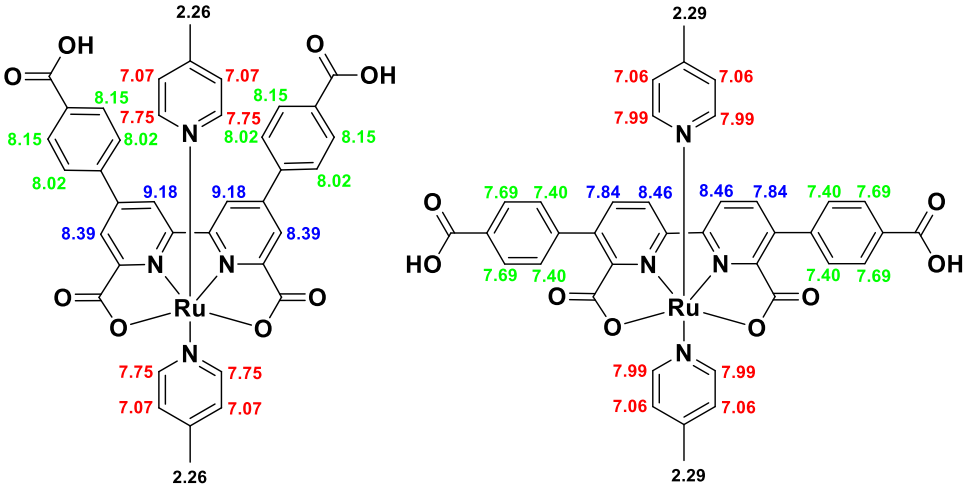

Figure 61. Correct nuclei correlations in K1 and K4 based on two-dimensional NMR spectra (COSY, HMBC and HMQC etc.)

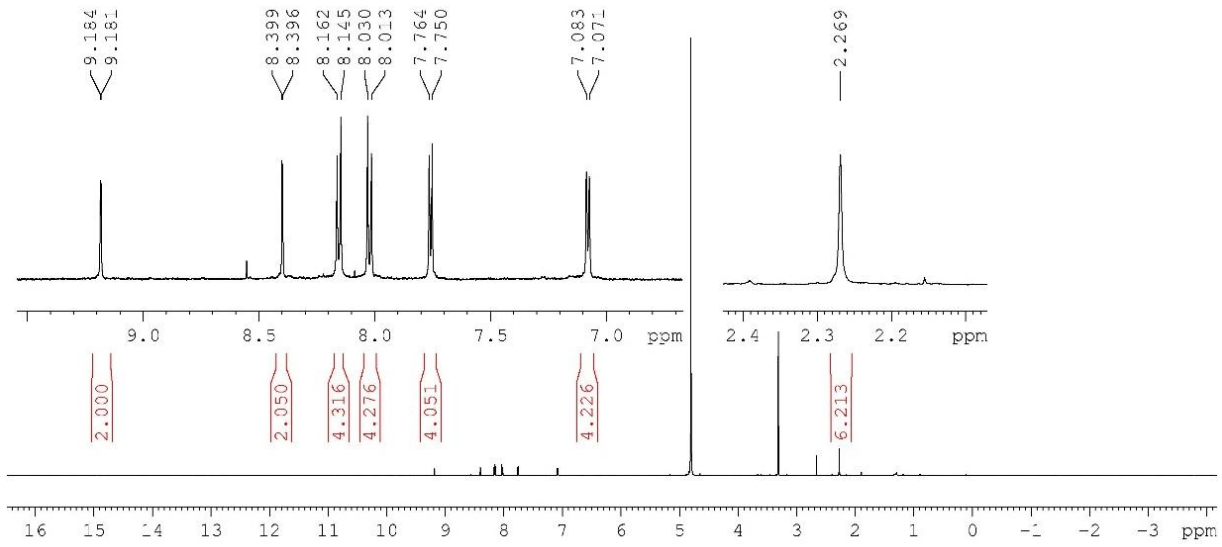

Figure 62. ^{1}H NMR spectrum of complex K1.

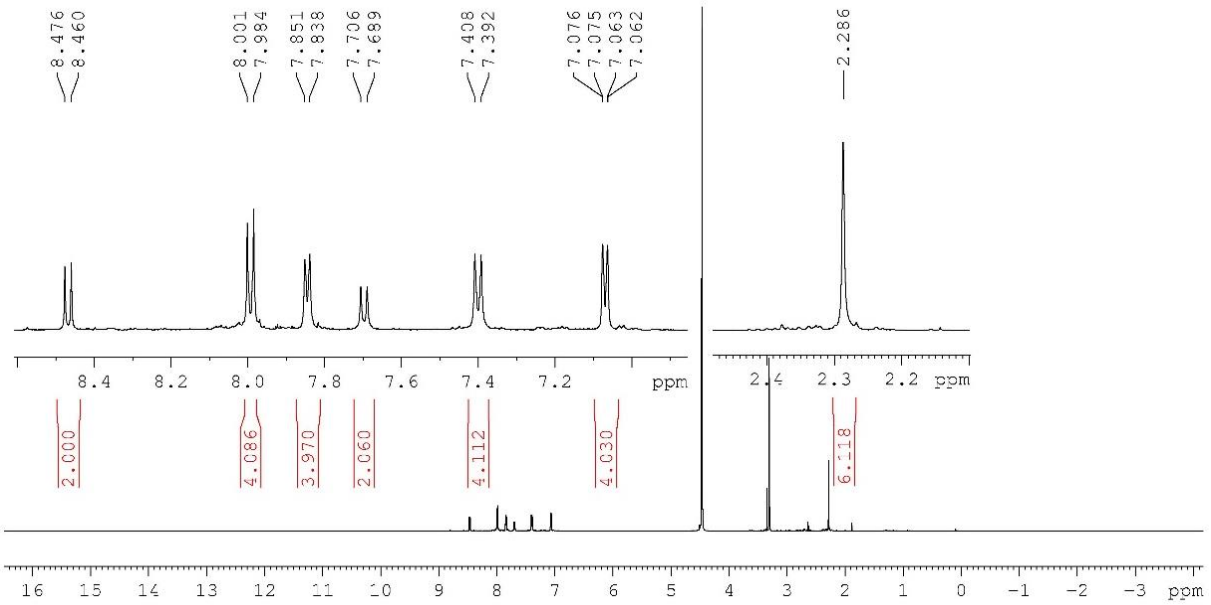

Figure 63. ^{1}H NMR spectrum of complex K4.

To investigate the effects of catalysis conditions on the catalyst stability, an aqueous solution of DCl (pH 1) was added to K4 at T = 333 K and NMR spectra were recorded after different time of exposure. As shown in Figure 65 and Figure 66, paramagnetically-shifted proton resonances were found to appear at 15, 19 and 33 ppm, the most upfield at -5.9 ppm. Though line broadening and unpredictable resonance shifts make the interpretation of these paramagnetic NMR spectra more complex, the results obtained so far allow to conclude that the ruthenium centre has to be in equilibrium between the oxidation states Ru^{2+} and Ru^{3+}, since strong negative shifts of proton signals in the ^{1}H NMR are generally attributed to paramagnetism.

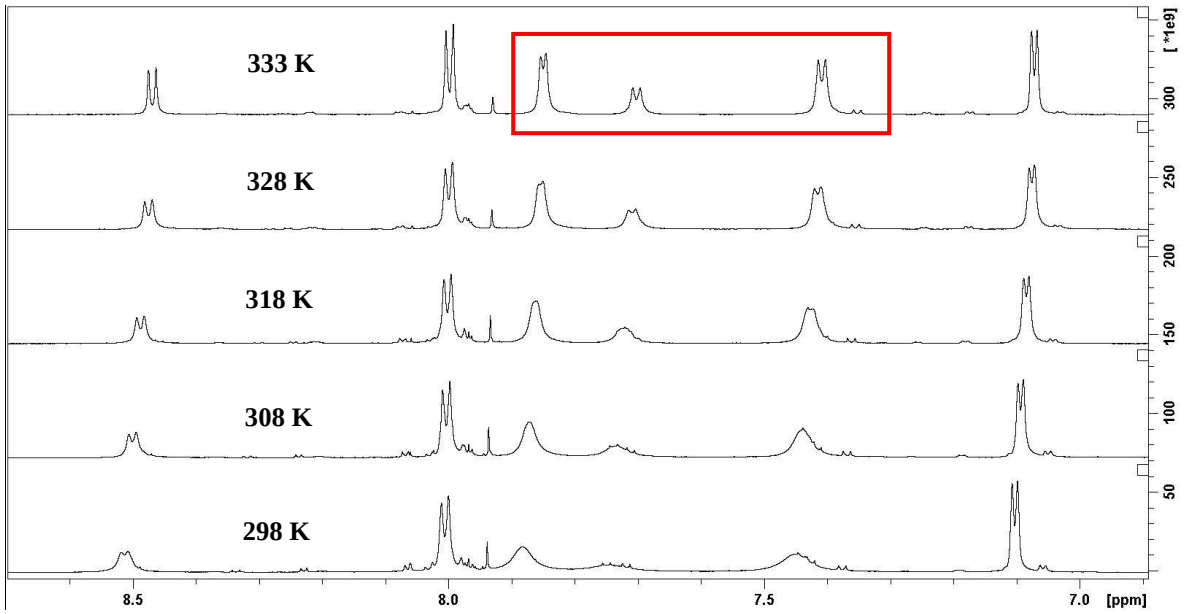

Figure 64. ^{1}H NMR spectra of complex K4 at temperatures between 298-333 K.

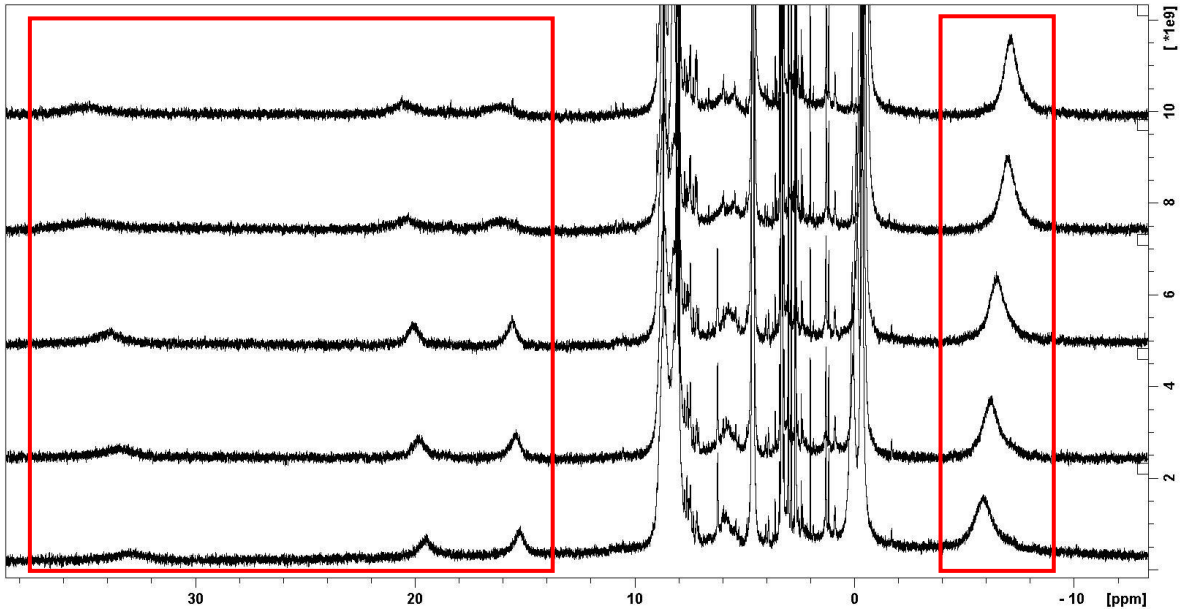

Figure 65. ^{1}H NMR spectra of complex K4 in the presence of aqueous solutions of DCl (pH 1) recorded at 10 min intervals after each addition.

Furthermore, to verify the presence of bounded and unbounded carboxylate groups, infrared spectroscopy was performed revealing characteristic absorption bands for the presence of carboxylic acid groups in K1 (Figure 67) and K4 (Figure 68). Typically, carboxylic acids are characterized by two main absorption features in the infrared, which can shift to higher or lower frequency, depending on the strength of the hydrogen-bonding interactions.

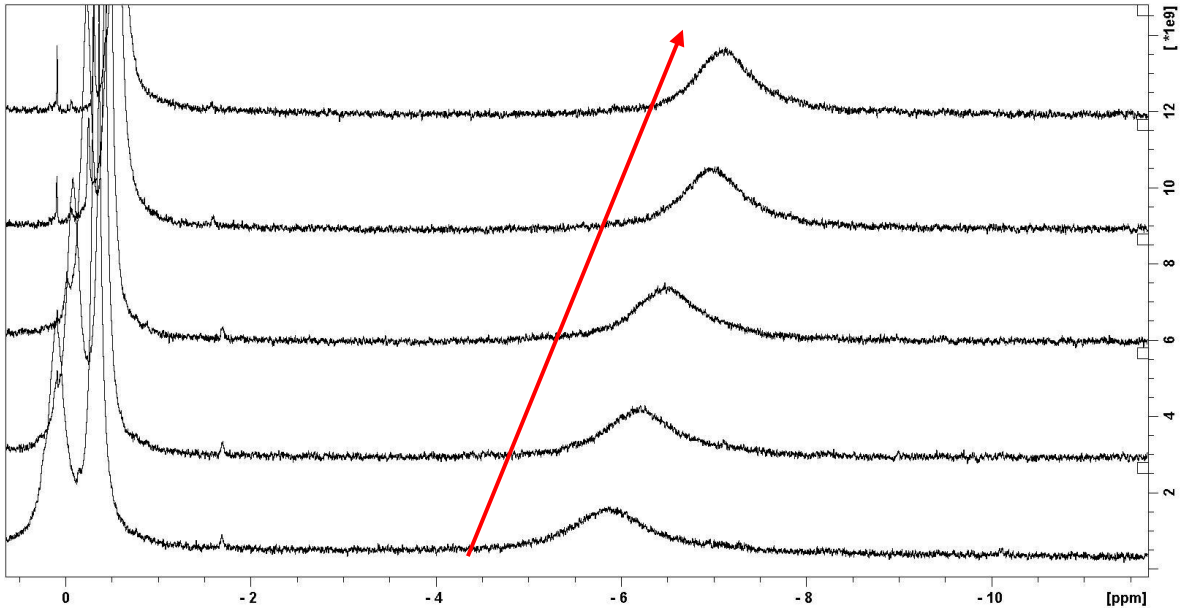

Figure 66. ^{1}H NMR spectra of paramagnetic K4 showing strong negative ^{1}H shifts**.**

In the region between 2500 and 3700 cm^{-1}, a very strong and broad O-H stretching absorption is observed, which is due to the existence of hydrogen-bonded carboxylic acid dimers. By comparison, the alkyl C-H stretches of the axial picoline ligands located at 2944 and 2979 cm^{-1} are hidden in complex K4 due to its extended O-H stretching zone, which can be seen as small peaks protruding near 2921 and 2854 cm^{-1}. The signal around 1600 cm^{-1} corresponds to the carbonyl groups stretching vibration of the H-bonded dimer. Other characteristic vibrational absorptions present in the molecules are marked in the spectra, clearly indicating the presence of carboxylic acid groups.

Generally, the detection of *in-situ* generated ruthenium species is very difficult to achieve with standard analytical methods which is primarily attributed to the increased reactivity of high-valent ruthenium-oxo complexes rather than to their instability. Often theoretical calculations assist in the interpretation of experimental data, which provide a detailed mechanistic picture of the reaction steps in the catalytic cycle. Against this background, it seemed interesting to study the electron-transfer ability of the catalysts K1 and K4 in solution by mass spectrometric analysis.

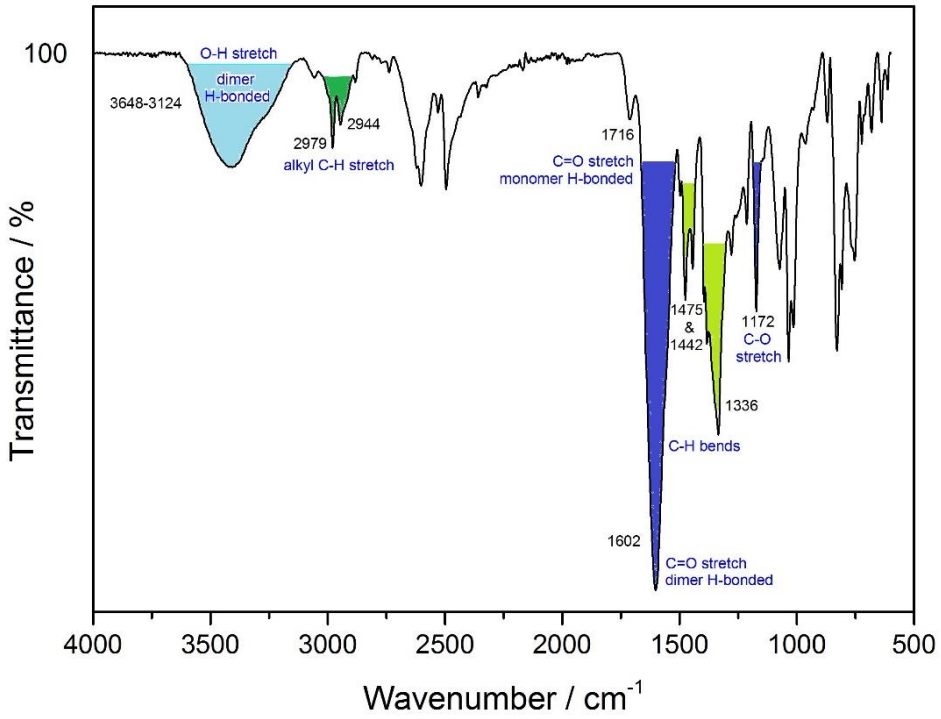

Figure 67. IR spectrum of complex K1.

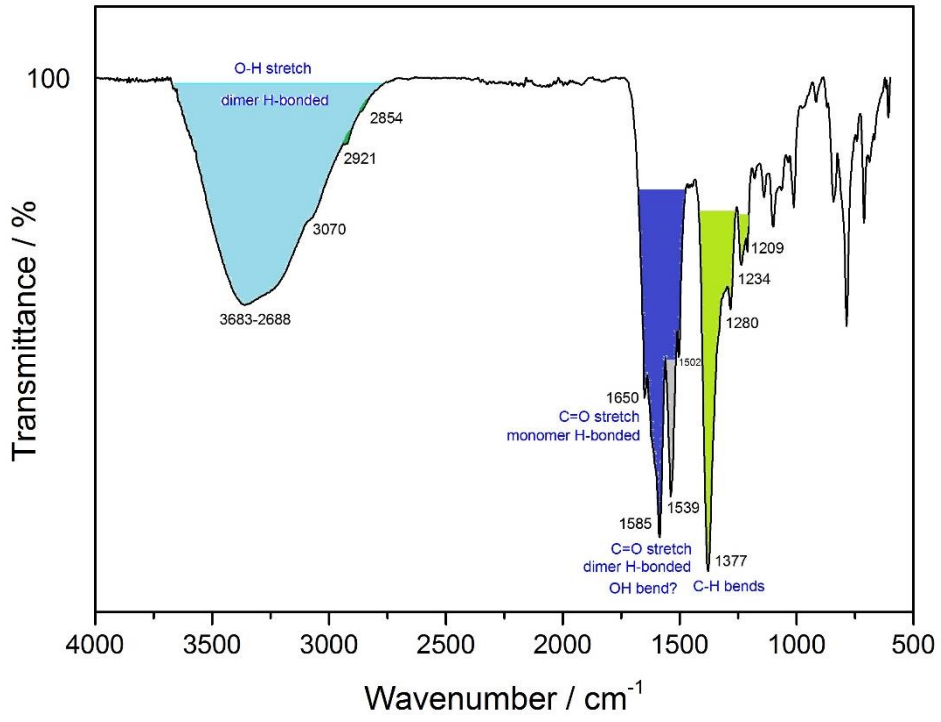

Figure 68. IR spectrum of complex K4.

ESI measurement of catalyst solutions gave support to the idea that oxidation of the central ruthenium ion was triggered by the solvent water. At pH 7, a dominant peak at *m/z* = 771 was observed corresponding to $[M+H]^+$ ions, while the peak at *m/z* = 793 was clearly assigned to the sodium adducts. No high mass peaks were observed, indicating that the water oxidation

reaction should be only triggered by catalytically active ruthenium species generated *in-situ* during catalytic reaction. As shown in Figure 71, a closer look to mass spectrometric analysis revealed a weak mass peak found around *m/z* = 787, which goes along with the oxidation of the ruthenium center to Ru^{3+} as evident from the mass peak at *m/z* = 770. Interestingly, the same mass signals were obtained when ionization was performed with red solutions containing the respective catalyst in the presence of an acid (pH 1), suggesting that PCET are involved. Contrary to the generally accepted idea, it could be concluded that water coordination did not require ligand exchange to produce the active species for water oxidation. Instead, addition of water took place at the Ru(III) state resulting in the appearance of the mass signal around *m/z* = 787, which indicates the formation of the seven-coordinated intermediate $[Ru^{IV}\text{-}OH]^{+}$. This species could only be detected when catalysts K1 and K4 were exposure to water for several hours, which was even stable over several days or weeks. In Figure 72 and Figure 73, the experimental and calculated isotope patterns of *in-situ* formed ruthenium species are shown for comparison, which were recorded in aqueous solutions (H_2O/pH 1) containing the respective catalyst (K1 or K4). However, these intermediates are not stable after the addition of cerium(IV). Instead, the mass peaks rapidly disappear which is attributed to the much faster reaction rates of both complexes that are beyond the sensitivity of the MS. Based on these findings, an initial mechanism path was proposed starting from Ru(II), at which the nucleophilic attack of water takes place upon oxidation to Ru(III), followed by rapid deprotonation to give the Ru(IV) intermediate. Since ruthenium in the oxidation state +5 is mainly postulated as key intermediate that trigger O-O bond formation, the hydroxo species is supposed to undergo further oxidation to Ru(V).

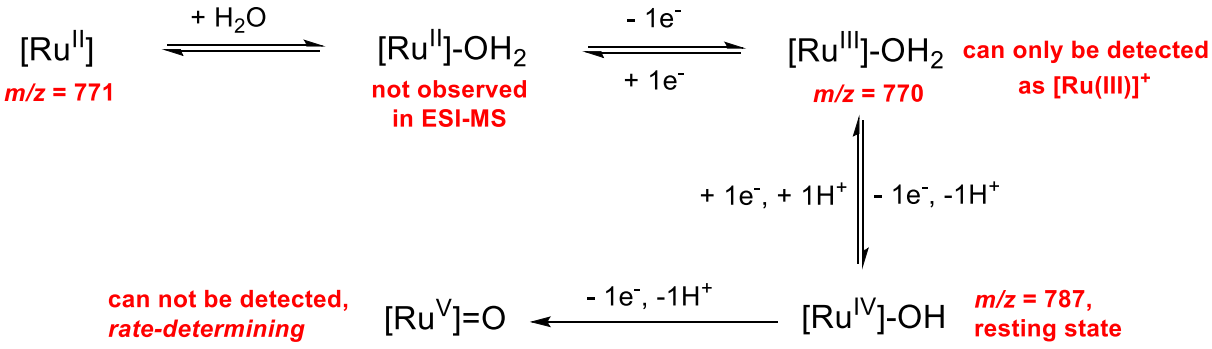

Figure 69. Proposed mechanism pathway for the initial phase of water oxidation triggered by K1 and K4.

The latter could not be detected because of fast water oxidation, indicating that Ru(V)=O could be a rate-limiting intermediate. Although the mechanism pathway presented in Figure 69 seems so simple, in reality the initial steps of water oxidation are very complex and poorly explored.

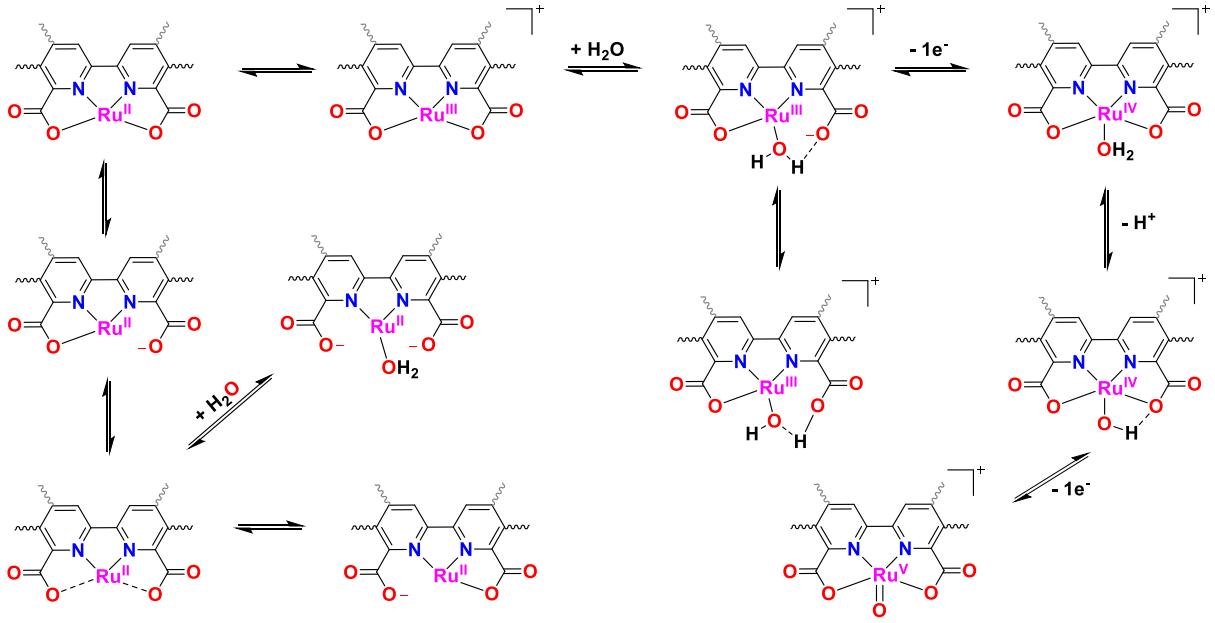

Figure 70. Proposed ruthenium species formed during the initial step of water oxidation. *The dashed lines indicate bonds that are simultaneously formed and broken in the transition state.*

This is due to the high flexibility of the labile carboxylate groups in solution, that are directly coordinated to the central ruthenium atom and allow incoming water molecules to bind early in the catalytic cycle, "leading to a combination of equilibria" [199] involved in dynamic behavior of ruthenium complexes, especially in the oxidation states +2 and +3, as evident from Figure 69. More importantly, the presence of dangling carboxylate groups (Figure 70) are believed to be the main factor to switch from a WNA-type mechanism to the radical coupling mechanism I2M.

Concerning K1 and K4, the results obtained from mass spectrometric analysis suggest the existence of a dangling carboxylate group to generate active high-valent ruthenium species since no ligand dissociation was observed for these intermediates. Therefore, computational studies have been carried out on transition state structures with bonded and non-bonded dangling carboxylate groups. The latter was supposed to coordinate to a single water molecule, which originates from the solvent water. For improved comparability, same was done for the reference system Ru-bda. The results of theoretical studies will be presented in chapter 9.

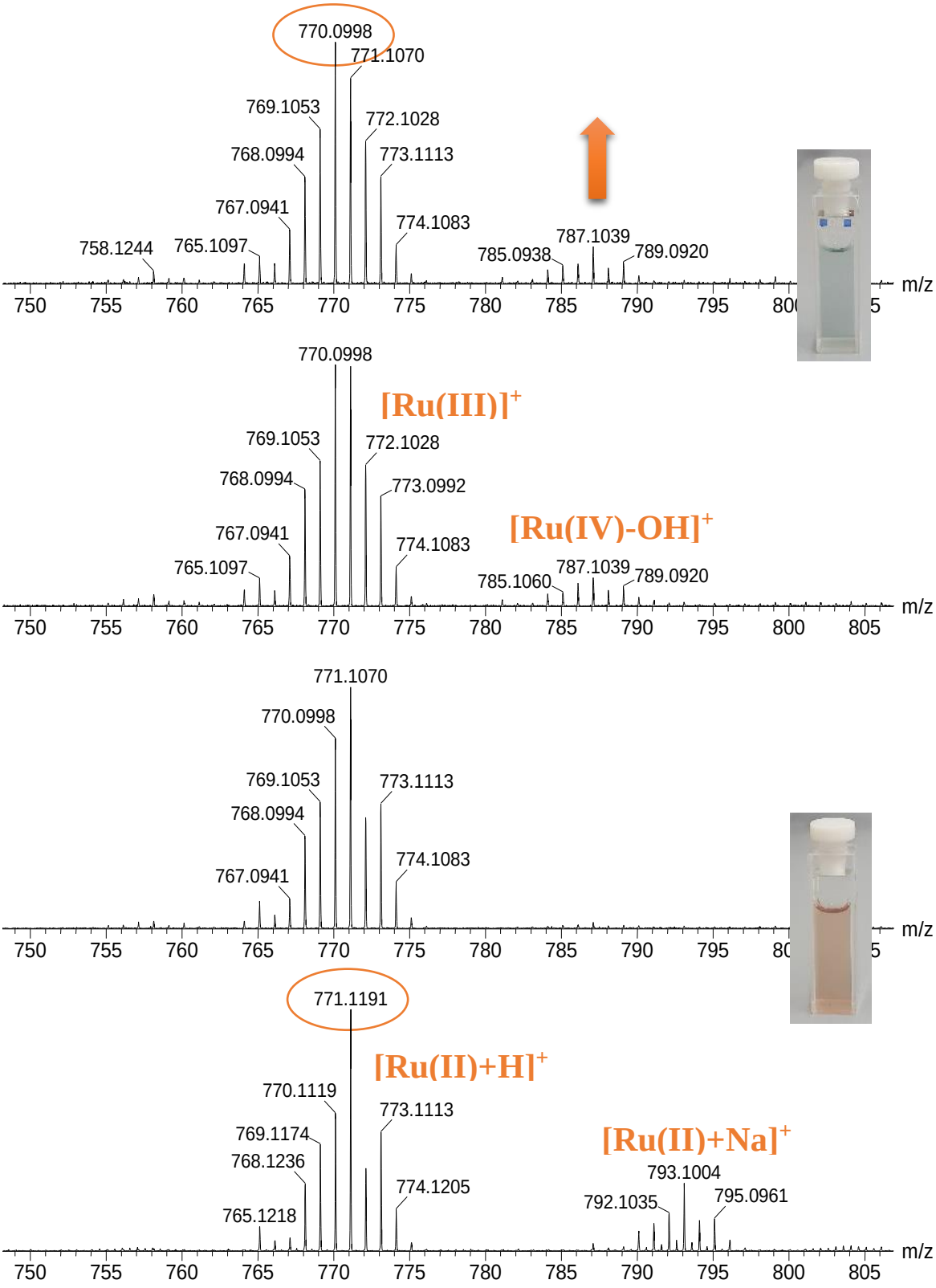

Figure 71. ESI-MS analysis of red and green solutions containing K4 in pure H_2O.

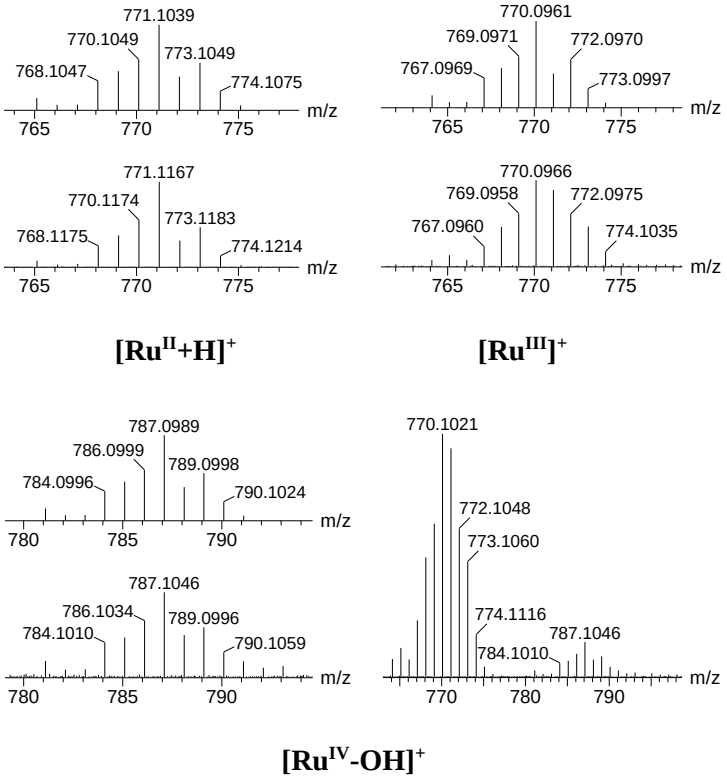

Figure 72. ESI-MS analysis of aqueous solutions (H_2O/pH 1) containing Ru complex K1: experimental isotope pattern (bottom), calculated (top).

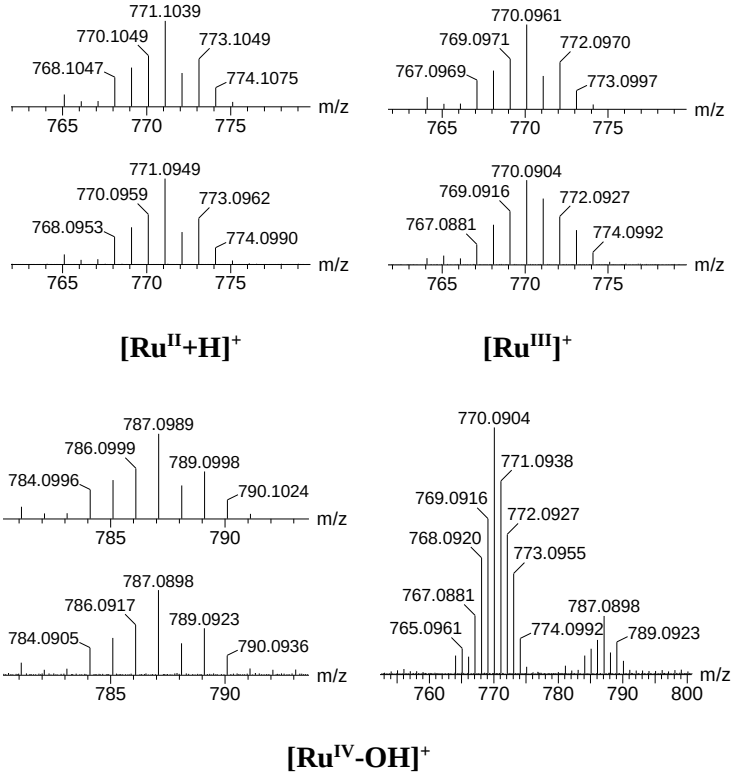

Figure 73. ESI-MS analysis of aqueous solutions (H_2O/pH 1) containing Ru complex K4: experimental isotope pattern (bottom), calculated (top).

8.1.2 Electrochemical and optical properties in of K1 and K4 in aqueous solution.

Having confirmed the structural assignment of K1 and K4, the next step was to find spectroscopic evidence for one-electron-one-proton transfer processes supposed to be involved in the catalytic water oxidation of both catalysts.

8.1.2.1 Electrochemical studies.

To provide first insights into the capability of the complexes to catalyze the oxidation of water, aqueous electrochemical investigations were carried out, which revealed promising results concerning their ability to stabilize high-valent states of ruthenium. Thanks to the excellent solubility of the complexes in water, voltammograms were recorded in aqueous solutions containing the respective catalyst without the addition of organic co-solvents. The use of pure water is essential since it offers a '*green*' method to realize overall water-splitting. Nevertheless, the interpretation of cyclic voltammograms (CVs) obtained from water solutions is quite difficult which is due to the presence of the high background current in water. This is why square wave voltammetry (SWV) measurements were performed for each sample that led to better pronounced peaks, providing detailed information on the redox-driven events (Figure 74).

The results of the CVs recorded at pH 1 are shown in Figure 75. By comparison, K4 exhibits a higher catalytic current than K1, indicating that the catalytic activity of K4 may be slightly higher than that of K1. At the reverse scan, a reduction peak is observed at around ~0.5 V, which was electrochemically generated at E > 1.1 V and corresponds to the reduction of molecular O_2. In comparison to a blank measurement without catalyst, the current for both complexes strongly increases after reaching the $Ru^{(IV)}/Ru^{(V)}$ step, suggesting that water oxidation is triggered by the Ru(V) intermediate.

The SWVs of the catalysts reveal three redox events around 0.6 V, 0.9 V and 1.2 V *vs*. NHE, which are assigned to the oxidation events Ru(II/III), Ru(III/IV) and Ru(IV/V), respectively. Different from the voltammogram in H_2O, the voltammogram in DMSO for example only displays one reversible peak. Considering that the onset of oxygen evolution seems to start at ~1.2 V (*vs.* NHE), cerium(IV) ammonium nitrate should be powerful enough to oxidize water to O_2 in the presence of one of these catalysts. The corresponding electrochemical data of K1 and K4 are summarized in Table 5.

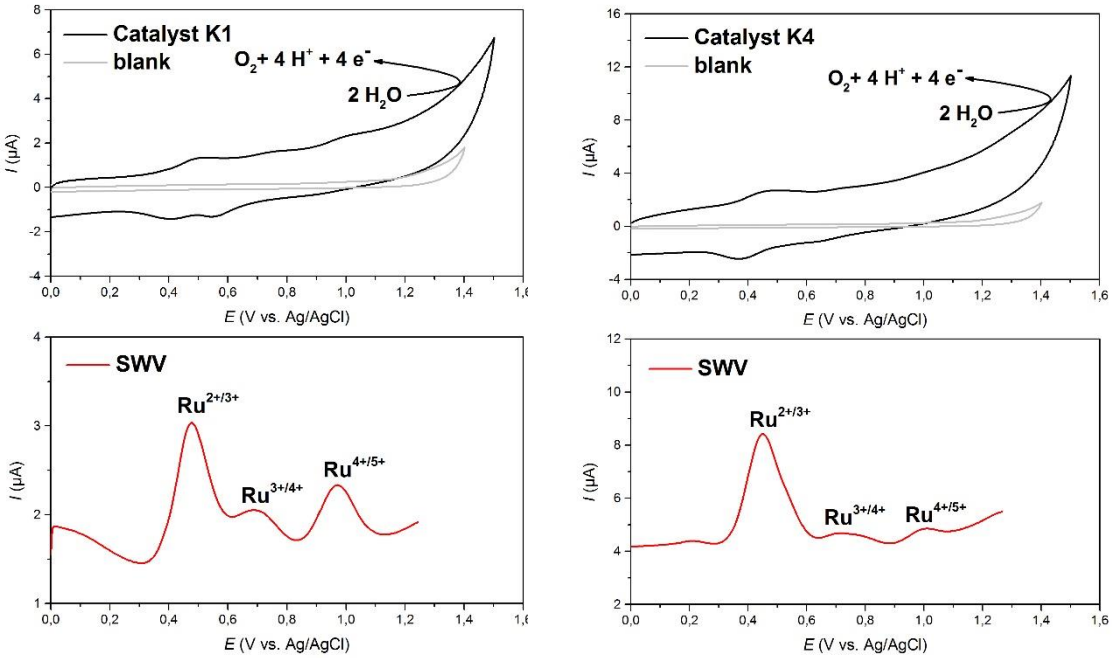

Figure 74. Cyclic voltammograms of complex K1 and K4 (1 mmole/L) (blue) with a corresponding blank measurement (grey) and the corresponding SWV (red) in water/pH 1 (0.1 M HOTf). *At pH 1, three redox states that can be assigned to the oxidation states* $Ru^{2+/3+}$, $Ru^{3+/4+}$ *and* $Ru^{4+/5+}$. *At pH 7, the reversible peak is centered at 0.39 V (0.60 V vs. NHE) and 0.43 V (0.64 V vs. NHE) for K1 and K4, respectively.*

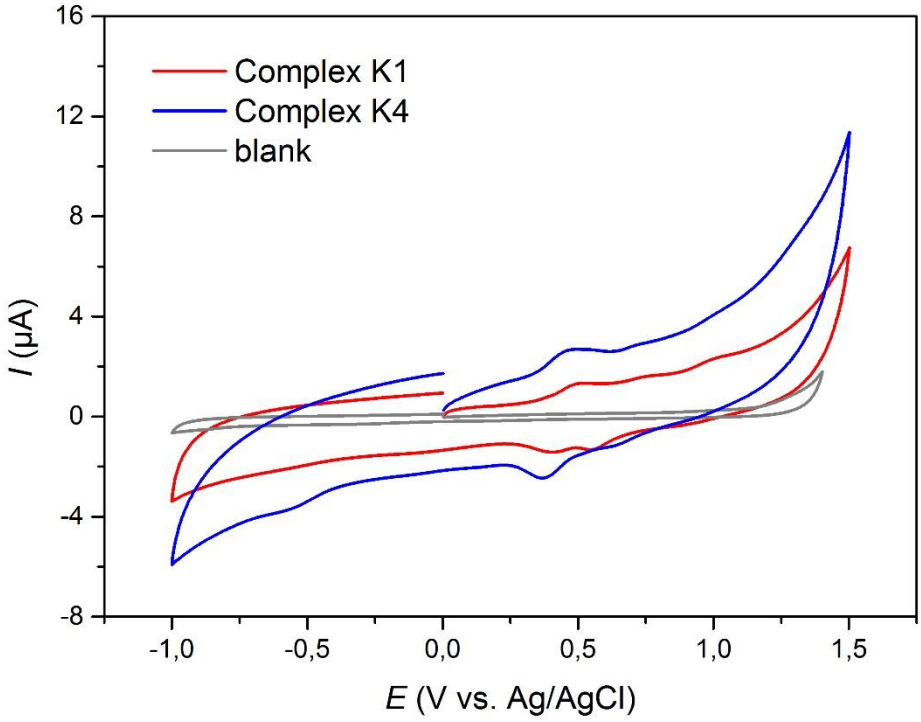

Figure 75. Electrochemical comparison of K1 and K4.

To study the effect of the pH on the electrochemical behavior of K1 and K4, experiments were also conducted with catalyst solutions at pH of 7.0. As can be clearly seen in the case of K1 (Figure 76), the same three redox couples are observed at neutral conditions. More remarkably, they are found to shift toward more positive potentials at pH 1. Due to the fact that the redox potentials decreased with increasing pH, it could be concluded that sequential $1H^+/1e^-$ PCET processes might be involved in water oxidation.

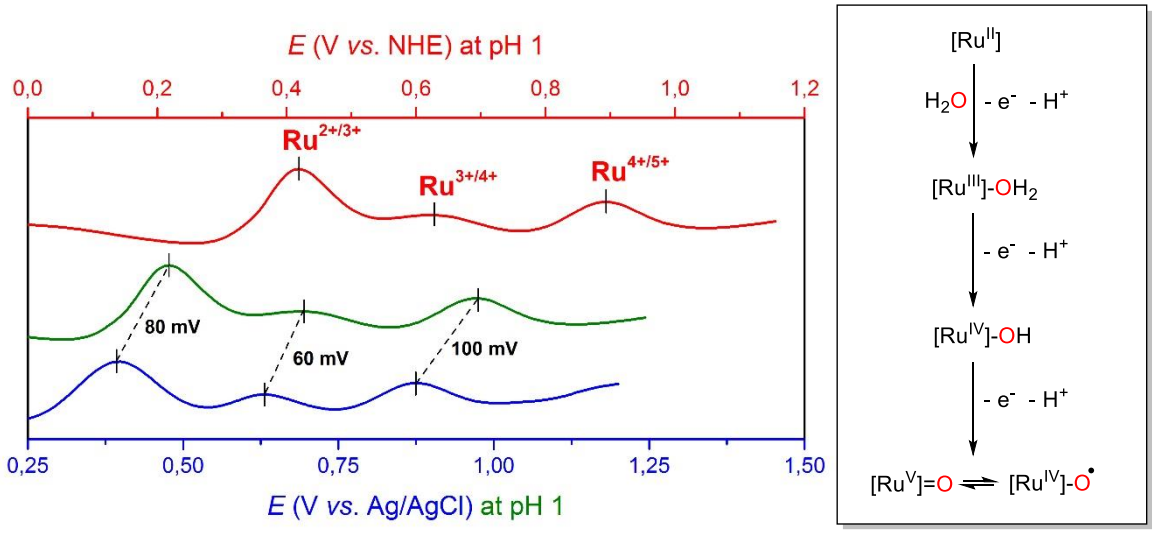

Figure 76. The influence of pH on oxidation potentials exemplarily shown for K1.

Table 5. Summarized electrochemical data of K1 and K4.

Complex	**$E_{1/2}$ $Ru^{2+/3+}$**	**$E_{1/2}$ $Ru^{3+/4+}$**	**$E_{1/2}$ $Ru^{4+/5+}$**
K1[a]	0.67 (0.60)	0.89 (0.84)	1.17 (1.08)
K4[a]	0.65 (0.64)	0.92 (0.89)	1.20 (1.17)
Ru-bda(pic)[b]	0.60	1.07	1.25

[a] $E_{1/2}$ values taken from SWV and converted to V *vs*. NHE using $E_{1/2}$ Ag/AgCl = 0.209 V *vs*. NHE. *$E_{1/2}$ values measured at pH 7 are given in brackets. Conditions: [catalyst] = 1 mmole/L dissolved in water/pH 1.0 (HOTf). [b] values taken from [73].*

In spite of the great difficulties in synthesizing the isoquinoline analogs of K1 and K4, which was mainly due to the increased aromaticity of the axial ligands related to less solubility, K1-isoq could be successfully prepared. The resulting CVs and SWVs of this complex show

that addition of the acid is essential and gives rise to the catalytic current (Figure 77). Compared to its picoline analogue, the redox events of the isoquinoline substituted complex are slightly lower appearing at 0.65, 0.81 and 1.08 V (*vs.* NHE) for $Ru^{2+/3+}$, $Ru^{3+/4+}$ and $Ru^{4+/5+}$, respectively.

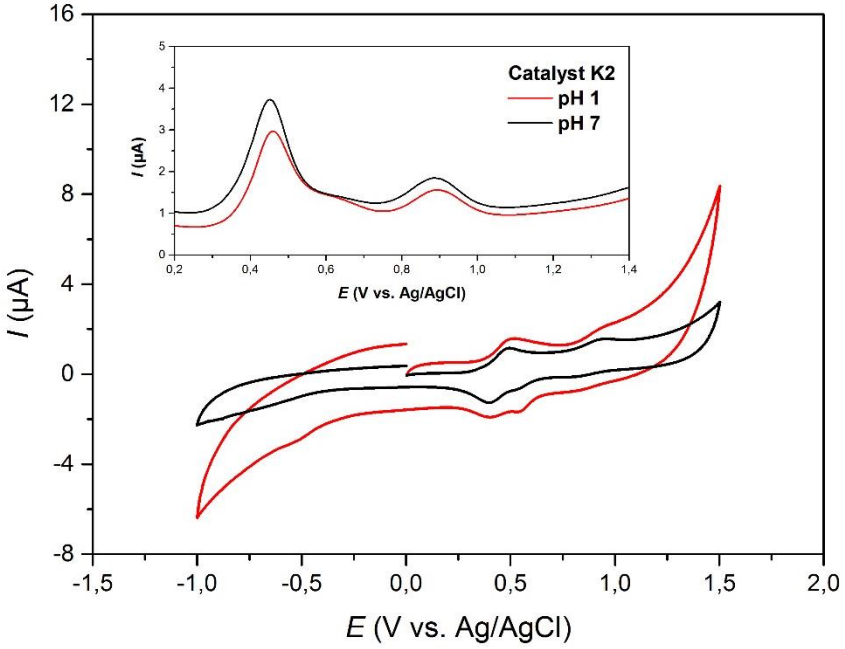

Figure 77. CV- and SW voltammogram of complex K2 (1 mmole/L) measured at pH 1 (red) and pH 7 (black).

By combining all the experimental data obtained so far, the redox processes of K1 and K4 at pH 1 are supposed to come from the coordination of one water molecule initiating the reaction sequence $[Ru^{II}] \rightarrow [Ru^{III}\text{-}OH_2]^+ \rightarrow [Ru^{IV}\text{-}OH]^+ \rightarrow [Ru^{V}]^+$ before water oxidation. The values for the redox potentials are in good agreement with values reported for ruthenium complexes of similar type.[73] More importantly, the redox peaks of Ru(III/IV) and Ru(IV/V) couples of the new catalysts appear at remarkably lower potentials. Considering that reported systems make use of co-solvents to increase solubility, the generation of their high-valent oxo-species at more positive potentials is believed to result from the competition of the organic solvent with the water molecule for the same binding site.

At the oxidation state +II, the water is most likely only weakly bound to the complex, which is a possible explanation for the absence of this species in ESI-MS. Considering that each oxidation step enhances the stabilization of the Ru-O bond to water, the formation of the high-valent Ru(IV) species where the seventh coordination site is occupied by an additional hydroxo ligand is believed to be the real active catalytic intermediate. In order to find any evidence for the presence of Ru^{5+}, UV-vis spectroscopy and redox titrations were performed using CAN as strong oxidant.

8.1.2.2 Optical properties.

UV-vis spectra of K1 and K4 were studied in pure H_2O and are shown in Figure 78. It is worth-mentioning that the position of the UV absorption bands of both catalysts are compared with well-known literature data which permit assignment of the electronic absorption bands to specific ruthenium species. Since spectroscopic analyses of K1 and K4 is conducted under identical conditions, smallest differences in chemical, electronic and structural properties can be exploited to gain detailed information about the catalytic behavior of these systems.

The UV/vis spectra were recorded at pH of 1.0 and 7.0, since cerium (IV)-driven water oxidation experiments are mostly conducted under strongly acidic conditions, which is explained by the fact that cerium solutions in acidic media are stronger oxidizing agents. Further advantages include its excellent solubility in water in solid form, while its consumption can be accompanied by the fading of its orange color to pale yellow. As a result of their similar molecular structures, the absorption bands of both complexes are nearly identical, typically appearing as broad spin-allowed MLCT absorptions.

At pH 7, absorption bands are observed at 272 nm and 325 nm for K1 and K4, respectively, which are ascribed to bda-$\pi \rightarrow$ bda-π^* transition. According to previous reports[131], the bands between 425 and 555 nm can be explained by MLCT transitions of the $Ru^{II} \rightarrow$ bda. Comparison of the UV-vis spectra shows that there is a remarkable difference in optical properties. Catalyst K4, carrying the extended conjugated π-electron system at the bpy acceptor ligand on the 5,5'-positions shifts the optical absorption of the intraligand bands into the visible spectral range. One possible explanation for this could be the delocalization of π-electrons, which might place more electron density on the central ruthenium atom when the extended π-conjugated systems is substituted in para-position with regard to the ruthenium atom.[200] This small but marked structural difference could heavily influence the catalyst activation towards catalytic applications.

During the measurements, a visual color change was observed from red *via* yellow to green when solutions of complexes were exposed to water for several hours. Analysis of these solutions revealed that oxidation to Ru(III) was slowly triggered over time even in the absence of oxidizing agent, giving rise to broad bands at 708 nm and 704 nm for K1 and K4, respectively. As the reaction progresses, the intensity of these new absorptions gradually increase and that of Ru(II) complexes decrease till they completely disappear for K1 as well as for K4. Considering that mass analysis of green solutions of these solutions gave parent peaks at m/z = 770 and the same greenish solutions give rise to bands around 700 nm in UV/vis, the results clearly confirm the presence of Ru^{3+} species. More importantly, this finding is a strong

indication that nucleophilic addition of water already occurs at the Ru^{III} state, which is thanks to the electron-withdrawing character of the carboxylate groups that lower the energy of the LUMO and thus enables the first oxidation of Ru at ambient conditions. Interestingly, the Ru^{3+} bands differ according to their intensity, expressed in the molar extinction coefficient, which could give a hint about the stability and robustness of the linear catalyst.

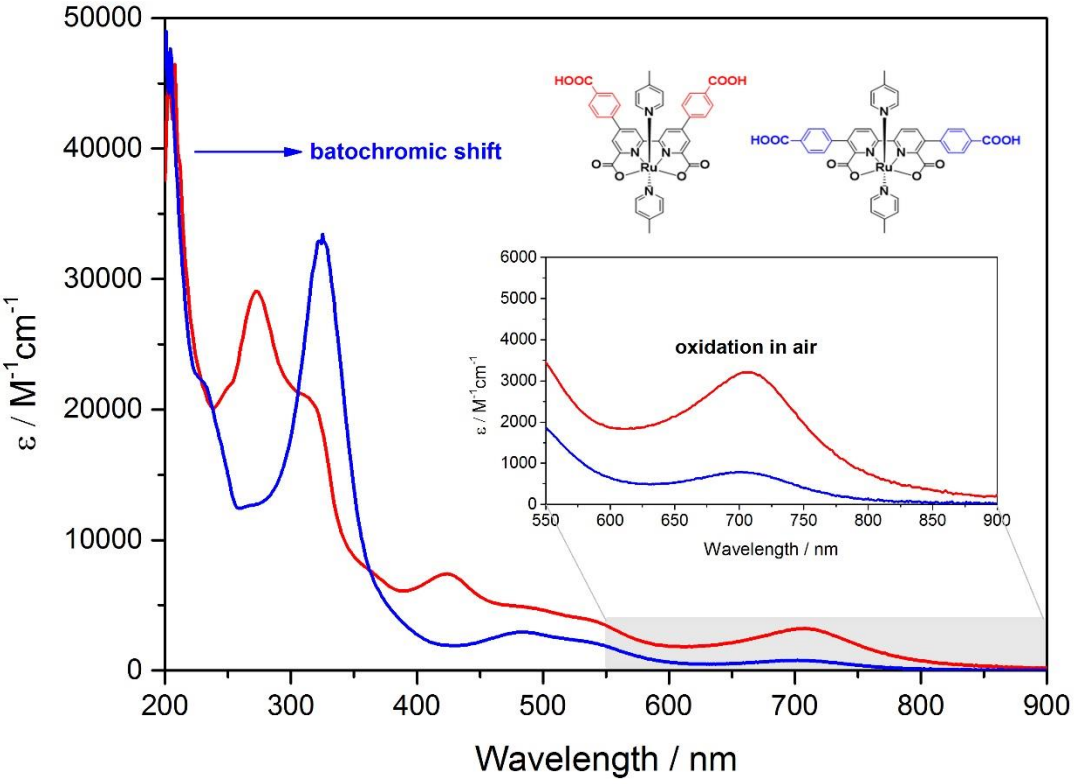

Figure 78. UV-vis spectra of K1 (red) and K4 (blue) in pure water.

The spectra shown in Figure 78 were recorded directly after dissolving the solid complexes in pure and freeze-pumped water. Considering that NMR spectroscopy revealed evidence for diamagnetic as well as paramagnetic ruthenium centers, the results suggest that both complexes are able to slowly undergo spontaneous air oxidation to form stable high-valent ruthenium(III) compounds not only in water but also in solvent-free environment by atmospheric oxidation. Changes in the oxidation state of the central metal atom were indicated by changes in the color of the respective solutions, first from deep red to reddish-yellow, for which it was assumed that the oxidation was not completed for all Ru^{2+} centres. Therefore, measurements were performed after different periods of time. The results are shown in Figure 79 and Figure 80, while the results of UV-vis measurements for K1 and K4 are listed in Table 6.

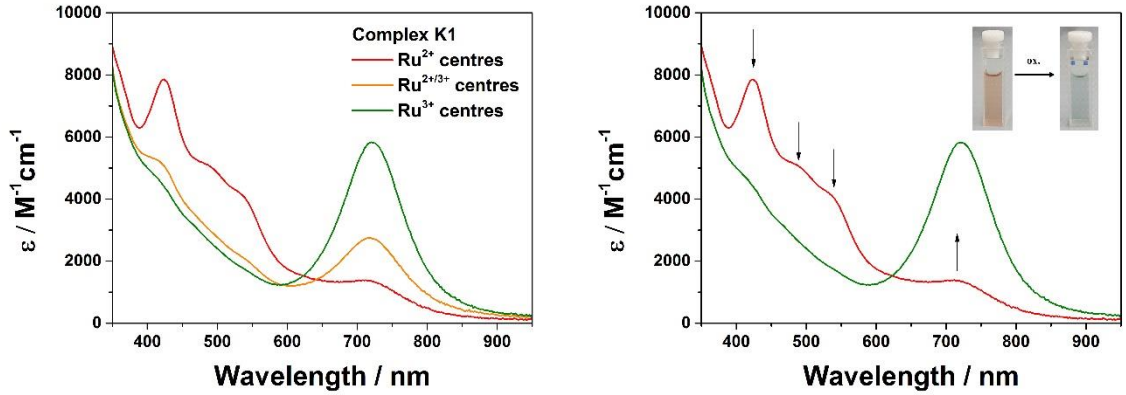

Figure 79. UV-vis spectra of K1 (10^{-5} M) recorded in pure water.

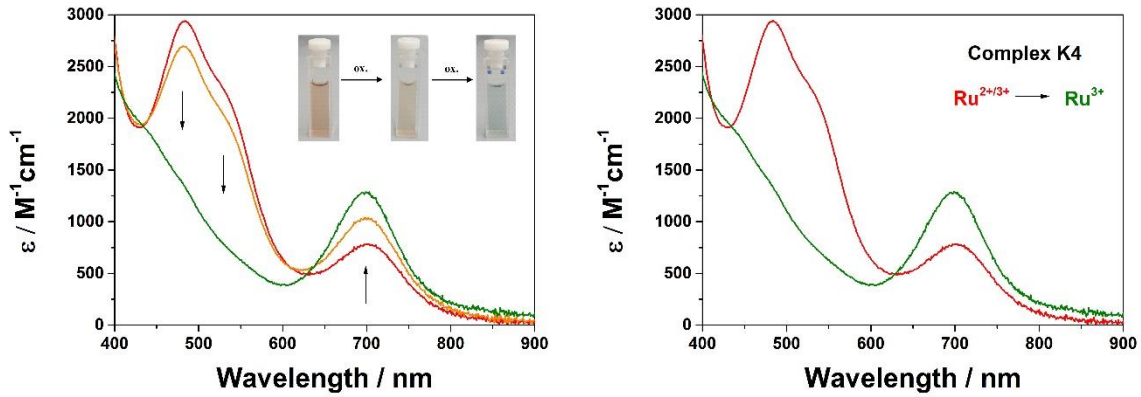

Figure 80. UV-vis spectra of K4 (10^{-5} M) recorded in pure water.

When catalysts were exposed to air overnight, the color of the solutions slowly turned to green indicating the generation of ruthenium(III), which goes along with the increase of the absorption band around 700 nm and the total disappearance of the MLCT bands. A further oxidation to the +4 oxidation state could not be accomplished by oxygen.

In order to realize complete oxidation of higher oxidation states (of ruthenium to Ru^{IV} and Ru^{V}), titration experiments were conducted using CAN as strong oxidizing agent. In a typical experiment, different equivalents of oxidant were added to acidic solutions (pH 1, HOTf) containing the respective catalyst, in which all ruthenium centres were proven to be in the Ru^{3+} oxidative state. The results will be presented in the following section.

Table 6. Summarized optical data of K1 and K4.

Complex	λ_{max} [nm]	ε [$M^{-1}\,cm^{-1}$]	classification
K1	272	29067	bda-π → bda-π*
	422	7409	Ru-d → bda- π*
	708	5820	Ru^{3+}-species
	590	2634	Ru^{4+}-species
K4	325	33429	bda-π → bda-π*
	481	2932	Ru-d → bda- π*
	704	1266	Ru^{3+}-species
	577	1325	Ru^{4+}-species

8.1.2.2.1 UV-vis redox titrations with CAN.

Knowing that higher oxidation states of ruthenium are very difficult to detect and require a highly complex equipment, the implementation of the corresponding titration experiments with '*green*' solutions of K1 and K4 was all the more exciting, especially against the background that most of the ruthenium WOCs reported in the literature give no hint for oxidation of the metal centre. The results of UV-vis redox titrations using CAN are shown in Figurs 81-82. In both cases, the conversion to the +4 state was achieved by the stepwise addition of CAN, giving rise to a new band at 590 nm and 577 nm for K1 and K4, respectively. The generation of the Ru^{4+} bands goes along with the decrease of the absorption bands around 700 nm. The assignment of these new bands to Ru^{4+} is unambiguous that agree extremely well with literature data reported by WÜRTHNER et al.[131], who were inspired by the works of CONCEPCION et al. [132] revealing spectral changes at very similar wavelengths, for which a dinuclear Ru^{4+}-species was postulated (Figure 83). An increase in the addition of CAN up to 12 equiv. lead to no further changes in the absorption spectra since analysis of the final solutions by ESI-MS gave no hint to *in-situ* formed Ru^{5+}-species.

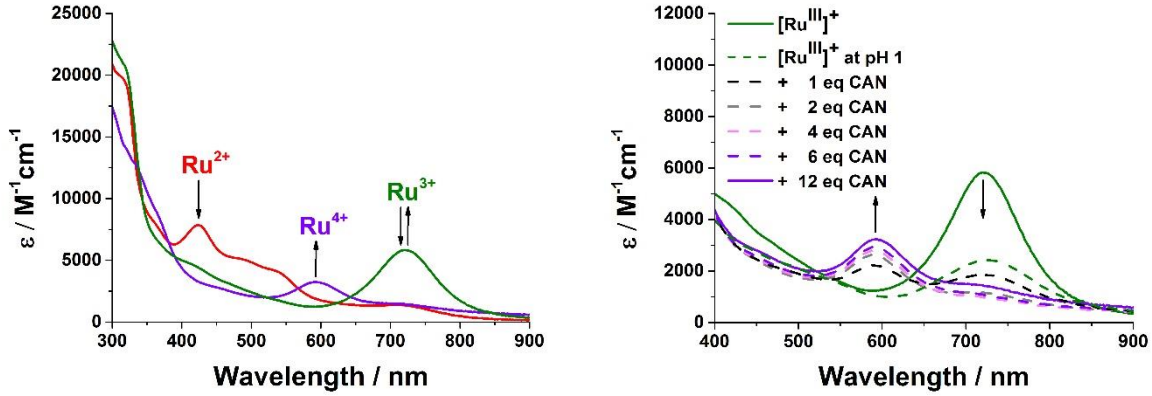

Figure 81. UV-vis spectra recorded in the process of the redox titration of K1 with cerium(IV) ammonium nitrate as oxidant.

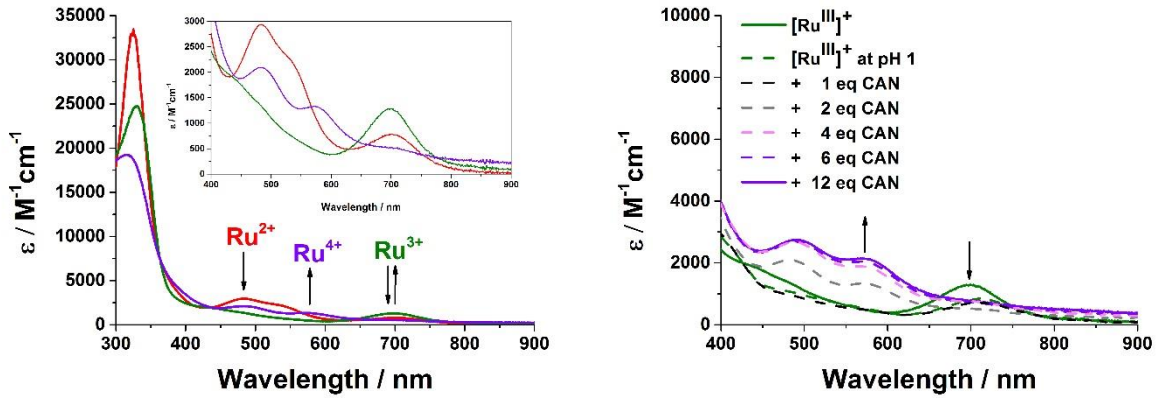

Figure 82. UV-vis spectra recorded in the process of the redox titration of K4 with cerium(IV) ammonium nitrate as oxidant.

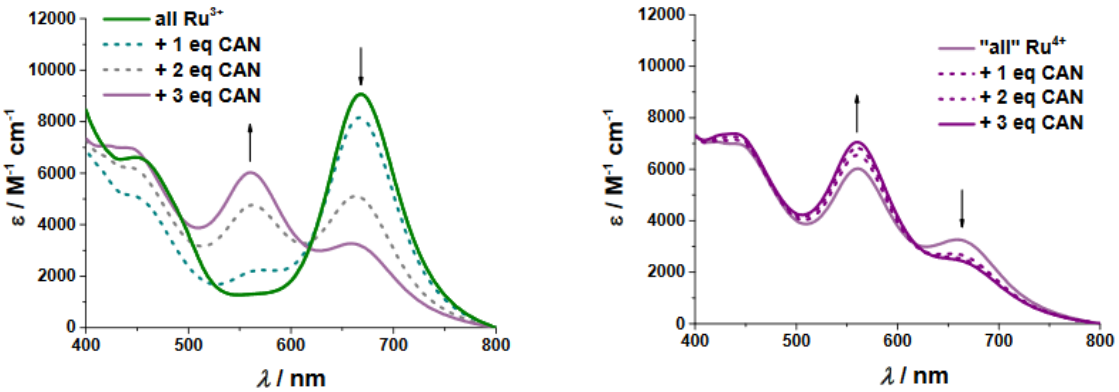

Figure 83. Spectral changes in the process of redox titration of WÜRTHNER's complex with cerium(IV) ammonium nitrate as oxidant. Reprinted from Ref [131].

A closer look at time-dependent UV-vis spectra of both complexes revealed the existence of isosbestic points, clearly confirming that the active ruthenium species, which are responsible for mediating O–O bond formation, are only generated by the catalyst itself under the influence of the oxidizing agent. In the presence of ascorbic acid, oxidized ruthenium is reduced from Ru^{4+} to Ru^{3+} to Ru^{2+}, which indicates the reversibility of the redox processes (Figure 84). In summary, it was successfully confirmed that complete oxidation of all Ru^{3+} centres can just be accomplished by the addition of CAN.

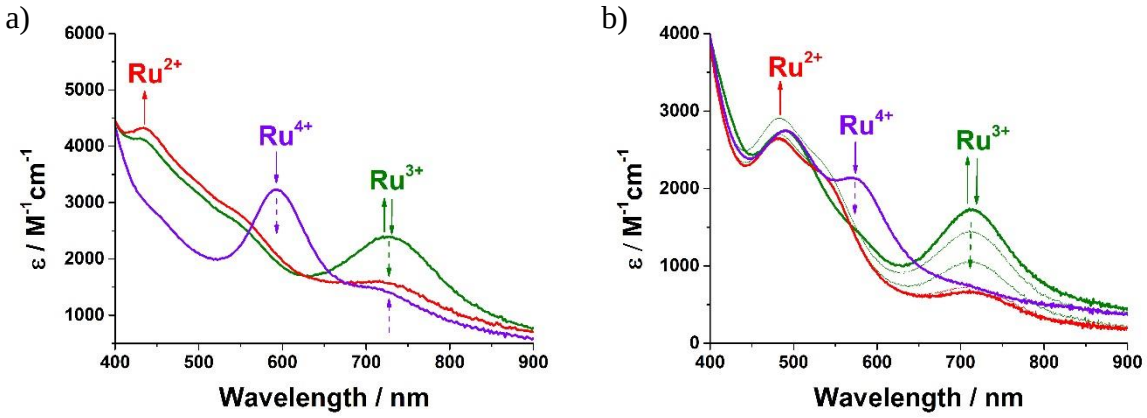

Figure 84. Redox titration with ascorbic acid with solutions containing a) K1 and b) K4, in which all ruthenium centres were supposed to be in the Ru^{4+} oxidative state.

The results obtained so far provide evidence that the structure of K1 and K4 is able to undergo reversible changes under very mild oxidative conditions ($Ru^{2+} \leftrightarrow Ru^{3+}$), generating the *'true'* catalytically active ruthenium species.

8.1.2.2.2 Spectroelectrochemistry of ruthenium redox states.

UV-visible spectroelectrochemical studies were performed to add evidence for stepwise conversion of all ruthenium centres first to Ru^{3+} followed by Ru^{4+}. Noting that catalyst K1 displayed much sharper peaks during cerium(IV)-driven titration experiments than catalyst K4, the latter was used for spectroelectrochemistry in order to assign its Ru oxidation states more precise.

As shown in Figure 85, the results are in perfect agreement with those measured for the macrocycle of WÜRTHNER et al., who were able to demonstrate that increasing the potential from 607 to 1227 mV gave access to spectral band formations with the maximum located at 550 and 668 nm, corresponding to Ru^{3+} and Ru^{4+}, respectively. More importantly, these events were found to occur simultaneously as previously described in section 8.1.2.3.

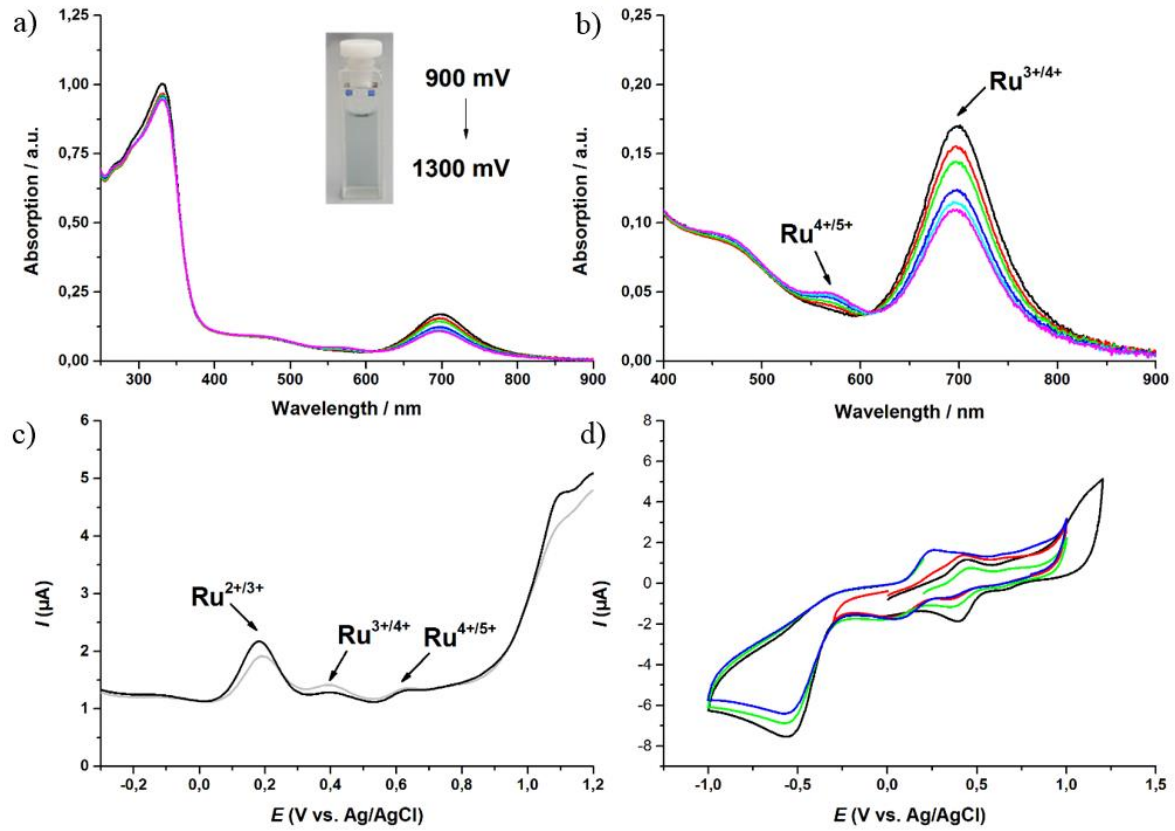

Figure 85. a) Spectroelectrochemistry of *'green'* solution containing K4 (10^{-5} M/10 mL) in water/pH 1. b) large view c) the corresponding SWV's and d) CVs.

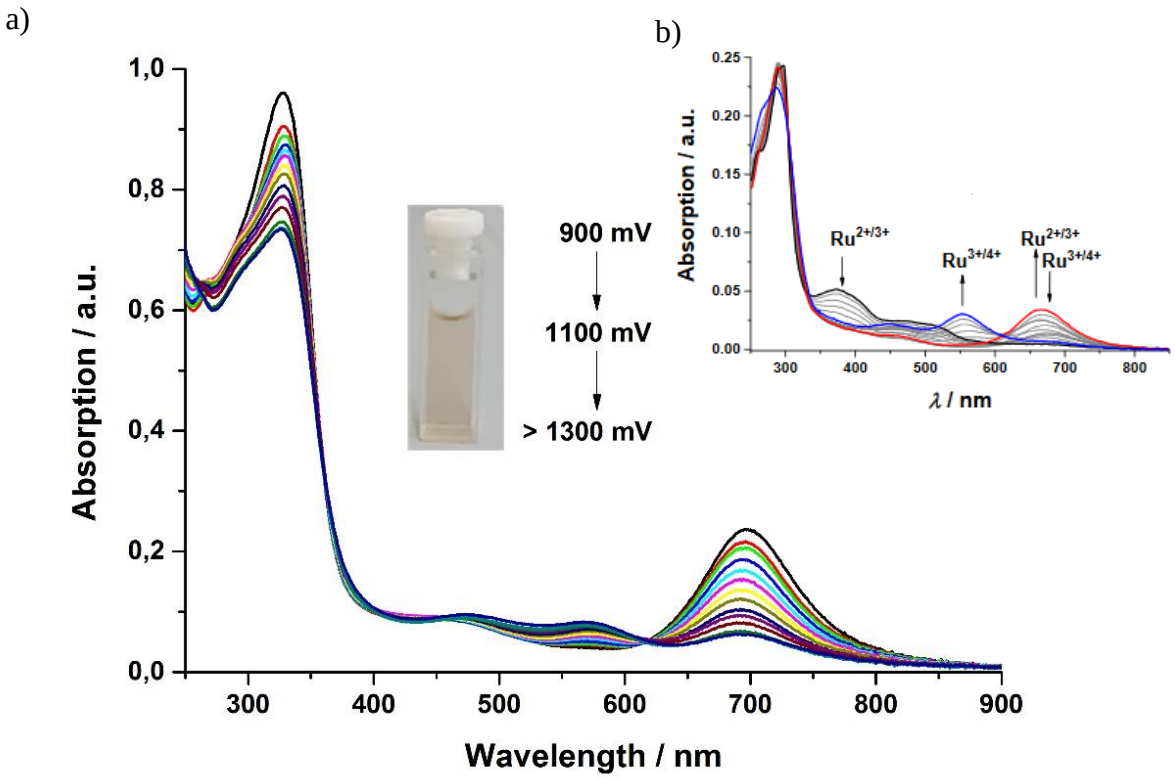

Figure 86. a) Spectroelectrochemistry of *'yellow'* solution containing K4 (10^{-5} M/10 mL) in water/pH 1. b) Spectroelectrochemistry of $[Ru(bda)bpb]_3$ (c = 0.1 mM) in 1:1 TFE/water pH 1. Reprinted from Ref [131].

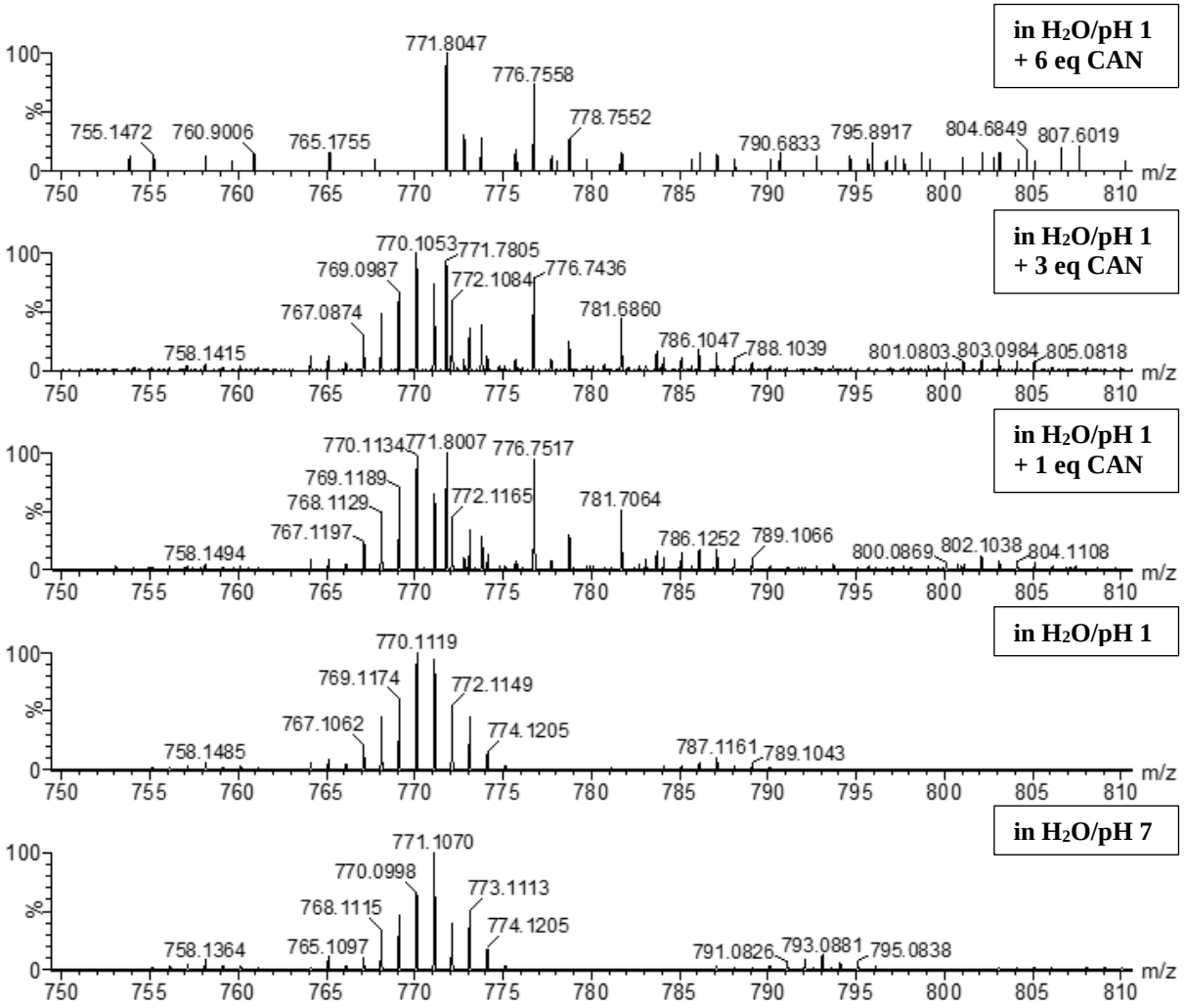

Figure 87. ESI-MS spectra of K4 in H_2O/pH 1 after addition of different equiv. of CAN.

The same was observed for catalyst K4, showing a new band at 570 and 696 nm when the potential was increased from 0.9 to 1.3 V, which were attributed to Ru^{3+} and Ru^{4+}, respectively. When spectroelectrochemistry was performed *versus* $Ag/AgNO_3$ with yellow solutions, in which the linear complex is between the oxidation states +2 and +3, the absorption bands became more pronounced, as shown in Figure 86. A further increase in the potential from 1.3 to 2.5 V revealed no change in the absorption spectrum. After reaching the $Ru^{4+/5+}$ redox couple, oxidation of water occurs at such a fast rate that *in-situ* generated Ru^{5+}-species cannot be detected sprectroscopically. Based on this finding, ruthenium at the oxidation state +5 was presumed as the rate-determining intermediate of the catalytic cycle. This was additionally supported by ESI measurements of the catalyst with different equivalents of CAN (Figure 87). While ESI-MS in positive mode shows a single peak corresponding to the catalyst in the oxidation state +2, addition of trifluoromethane sulfonic acid to adjust the pH to 1.0 gave rise to a new mass signal at around *m/z* = 770 (Ru^{3+}). This peak decreases upon addition of CAN

till it completely diminishes when [CAN] was increased to 6 equivalents. Under the same experimental electrospray conditions, the peak at *m/z* = 787 corresponding to ruthenium at the oxidation state +4 seems to be weakly stable at pH 1 but unstable when a strong oxidant was added. Thus, neither Ru^{3+}- nor Ru^{4+}-species cannot be observed after final catalysis. This suggests that catalyst decomposition is the main source for the loss of the water oxidation activity.

8.2 Comparison with complexes K7-K15.

The development of ligands bearing carboxylic acid and bromo groups directly attached to the equatorial bipyridine unit was essential to study the effect of the additional phenyl groups in K1 and K4, the influence of H-bonding interactions and the effect of electron-withdrawing groups on both the catalytic performance and stability. On the next pages, only the most important factors contributing to the catalytic activity of the complexes will be discussed.

8.2.1 Electrochemical and optical properties of K7-K15.

The synthesis of the complexes K7-K15 is similar to that of K1 and K4, but the replacement of the axial methylpyridine ligands by ligands with increased aromaticity, isoquinoline or phthalazine, proved to be difficult in terms of purification and further characterization of the molecules. Same could be observed not only for ligand modification in the axial but also in the equatorial plane. Especially those which possess carboxylic acid groups at the 3,3'-positions of the bda-ligand displayed broad peaks in the ^{1}H NMR, probably deriving from strong inter- and intramolecular H-bonding interactions. Hence, a clear confirmation of the structural assignment of complexes K3-K6, K13 and K15 was provided by mass analysis, while an indepth study of the electrochemical and optical properties revealed precious information concerning the catalyst's capability of catalyzing water oxidation.

For better clarity, cyclic voltammograms of complexes where the axial positions were occupied by the same pyridine ligands will be compared with each other. Table 7 summarizes the redox values taken from the corresponding SWVs, which were converted to V *vs*. NHE using $E_{1/2}$ Ag/AgCl = 0.209 V *vs*. NHE. The pH dependence of the redox potentials is presented in Figure 90 and Figure 91. Based on the initial results, a possible reaction sequence for the water oxidation process was proposed.

At pH 1, complexes K7, K8, K10-K12 show three redox events in the region of +0.5 V to +1.3 V (*vs*. NHE), while K13 displays two broad redox waves. The first reversible peaks from

+0.5 to +0.8 V (*vs*. NHE) are assigned to $Ru^{II}/[Ru^{III}\text{-}OH_2]^+$ redox couples. The redox peaks found in the potential range from +0.8 to +1.1 V (*vs*. NHE) correspond to the oxidation of $[Ru^{III}\text{-}OH_2]^+$ to $[Ru^{IV}\text{-}OH]^+$. Another redox wave appearing between +1.1 and +1.3 V (*vs*. NHE) is assigned to the Ru^{IV}/Ru^{V} redox couples, after which the catalytic current of the complexes strongly increases, thus affirming that Ru^{V} triggers the oxidation of water. A remarkable difference was found when comparing the intensity of the catalytic current (Figure 88), showing an increase in the following order: K10 < K7 < K12. Considering that a catalytic current occurs after $[Ru^{V}=O]^+$ is generated, the strength of the current might give an indication of the catalytic efficiency of the complexes as potential catalysts for oxidation of H_2O to O_2.

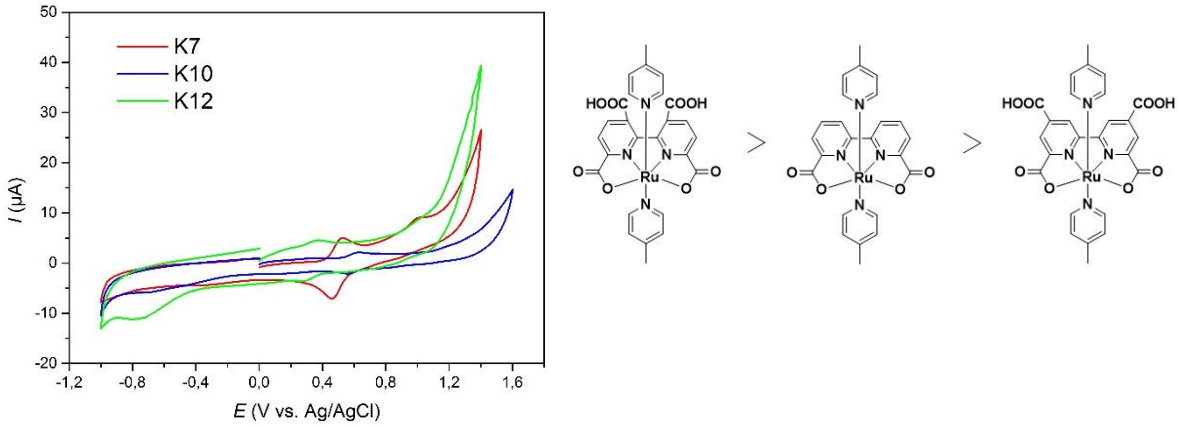

Figure 88. Cyclic (CV) voltammograms of complexes K7, K10 and K12 (1mmole/L) at pH 1 (0.1 M HOTf). *Conditions: K7 was measured in water/MeCN (1:1, v:v, pH 1) due to less solubility, while K10 and K12 were performed in water/pH 1, scanning rate = 100 mV* s^{-1}*, working electrode = Ag/AgCl / 3 M KCl.*

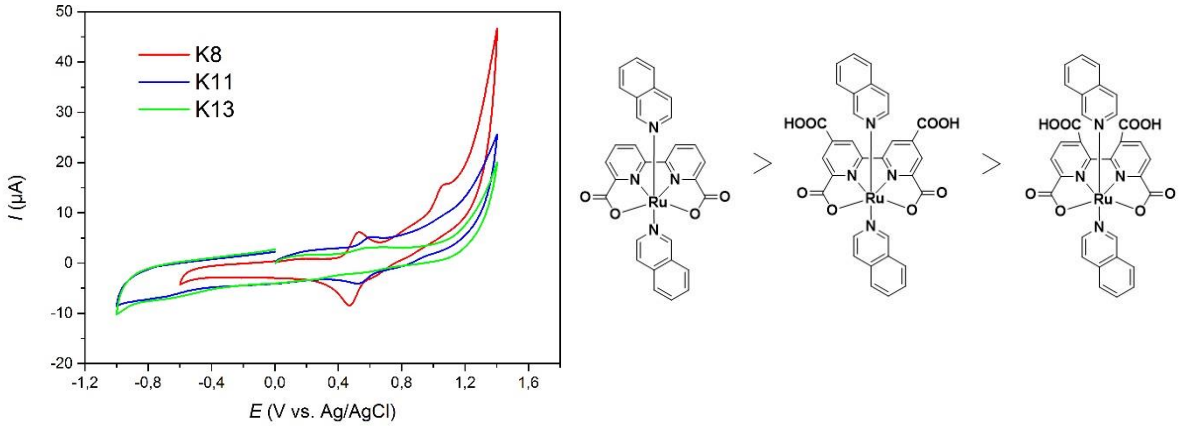

Figure 89. Cyclic (CV) voltammograms of complexes K8, K11 and K13 (1mmole/L) at pH 1 (0.1 M HOTf). *Conditions: K8 was measured in water/MeCN (1:1, v:v, pH 1) due to less solubility, while K11 and K13 were performed in water/pH 1, scanning rate = 100 mV* s^{-1}*, working electrode = Ag/AgCl / 3 M KCl.*

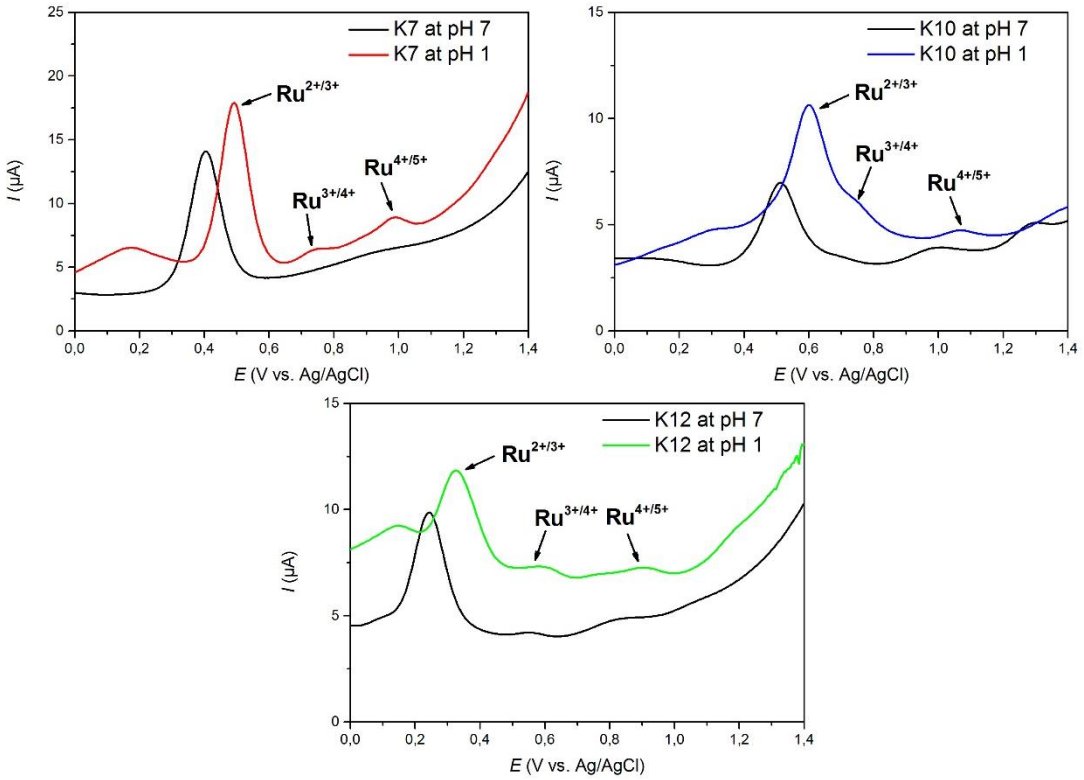

Figure 90. SWVs of complexes K7, K10 and K12 (1mmole/L) in acidic (0.1 M HOTf, pH 1, colored curves) and neutral medium (black curves).

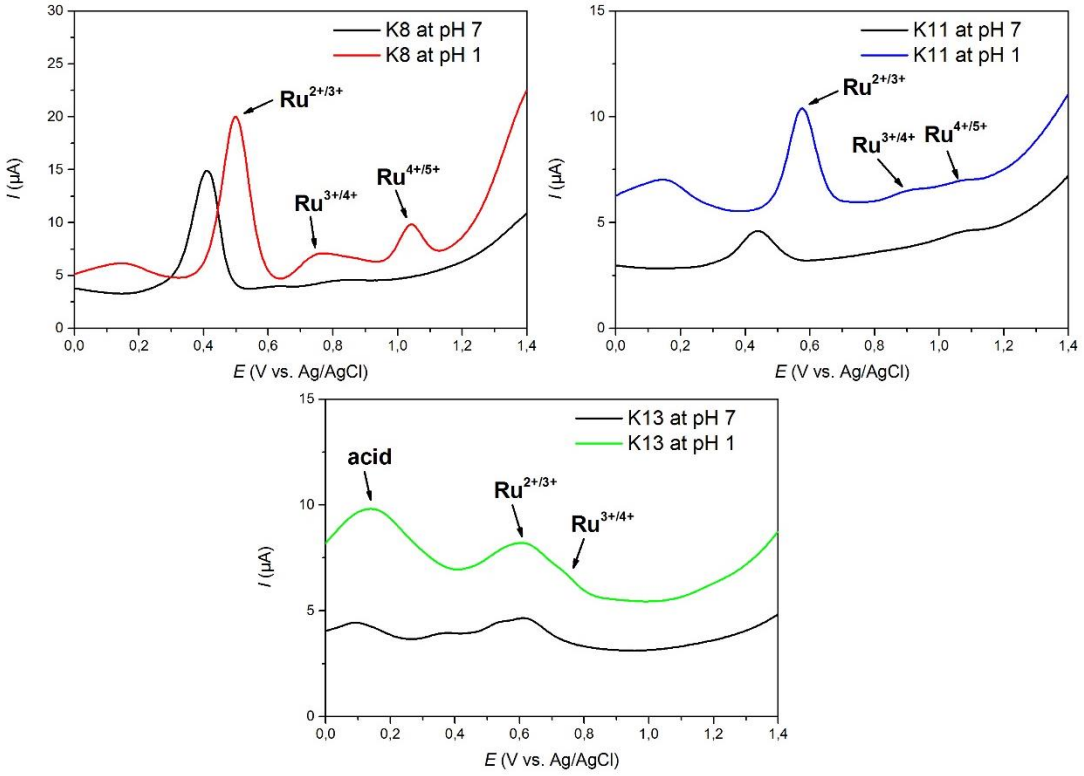

Figure 91. SWVs of complexes K8, K11 and K13 (1mmole/L) in acidic (0.1 M HOTf, pH 1, colored curves) and neutral medium (black curves).

By comparison, the isoquinoline analogues occur at slightly higher potentials in the CV measurements, a trend, which is also observed for the Ru-bda(pic)$_2$ and Ru-bda(isoq)$_2$ catalysts reported by SUN et al. As evident from SWV curves, increasing the pH value from 7 to 1 results in an anodic shift of the reversible oxidation potential of the Ru^{II}/Ru^{III} couple, indicating that PCET processes are involved as already observed for K1 and K4.

Within the isoquinoline family, K8 exhibits the highest catalytic current, followed by K11 and K13. At the reverse scan, a reduction peak was observed between -0.7 and -0.8 V, which can be attributed to the reduction of molecular O_2 electrochemically generated at E > 1.2 V (Figure 89). An overview of the electrochemical properties of the above mentioned complexes are given in Table 7.

Table 7. Summarized electrochemical data of title compounds.[a]

Complex	$E_{1/2}$ $Ru^{2+/3+}$	$E_{1/2}$ $Ru^{3+/4+}$	$E_{1/2}$ $Ru^{4+/5+}$
K7	0.69	0.93	1.18
K10	0.79	0.95	1.26
K12	0.53	0.79	1.10
K8	0.69	0.95	1.24
K11	0.77	1.09	1.28
K13	0.80	0.93	-
Ru-bda(pic)[b]	0.60	1.07	1.25
Ru-bda(isoq)[b]	0.63	1.09	1.27

[a] $E_{1/2}$ values taken from SWV and converted to V *vs*. NHE using $E_{1/2}$ Ag/AgCl = 0.209 V *vs*. NHE. Conditions: [catalyst] = 1 mmole/L dissolved in water/pH 1.0 (HOTf). [b] values taken from [73].

Surprisingly, K12 containing ligand L5 in its backbone exhibits remarkable low redox potentials, which are nearly completely hidden in the isoquinoline substituted complex K13 despite having the same ligand system. Due to the similar molecular structures of the complexes, this remarkable difference is proposed to stem from a combination of the following

factors: the positions of the carboxylic acid groups and the increased aromaticity of the axially bounded isoquinoline ligands in K13. The resulting complex is strongly affected by its poor solubility in water, which increases the electrochemical cell potentials of K13 compared to its analog pyridine system.

UV-vis spectra of K7, K8 and K10-K13 were studied in (MeCN)-H_2O mixtures, which are shown in Figure 92a. In general, the absorption bands of the complexes are nearly identical, which is again due to their similar structural features. The two types of absorption bands around λ_{max} = 250 and 260 nm are assigned to the absorption of bda–π → bda–π* electron transition. The strong absorption bands located at λ_{max} = 342, 379 and around 400 nm are assigned to the MLCT band due to the transition from the d-orbital of Ru to the π*-orbital of the bda ligand.

Obviously, the absorption bands of complexes containing carboxylic acid groups are slightly shifted toward longer wavelengths, which is due to the presence of electron-withdrawing substituents on the bda-ligand. More interestingly, there are two additional bands present at λ_{max} = 667 and 696 nm for K7 and K10, respectively, which are clearly assigned to *in-situ* generated catalytically active Ru^{3+}-species (Figure 92b). For comparison, these findings are consistent with previous results from UV-vis studies on K1 and K4, where the formation of Ru(III) species was indicated by the appearance of absorptions bands at λ_{max} = 722 nm (K1) and 697 nm (K4).

Particularly notable is the fact that K10 as well as K1 containing the substituents at the 4,4'-positions of the bda-ligand display the most pronounced Ru^{3+}-bands when compared to all other systems discussed above. Considering that in both complexes the substituents are bound in para-position with regard to ruthenium and are expected to place more electron density on the central ruthenium atom, the observation of these strong bands around 700 nm suggest that electronic effects might lead to more easily available high-valent ruthenium intermediates. Nevertheless, it is not possible to provide more precise information, since mechanistic processes involved in catalytic water oxidation are known to be very complex due to the variety of parameters influencing the catalytic reaction steps.

a)

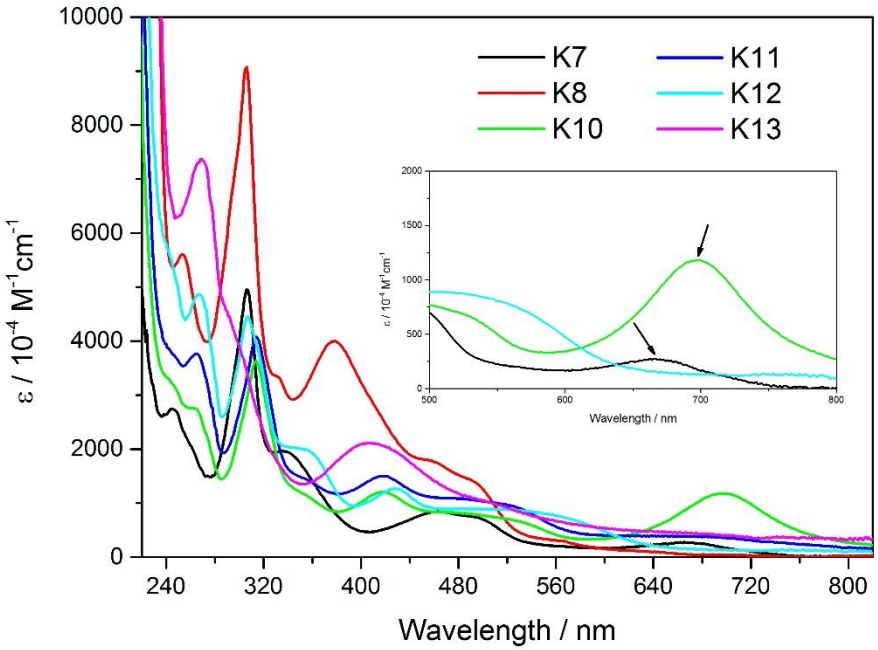

b)

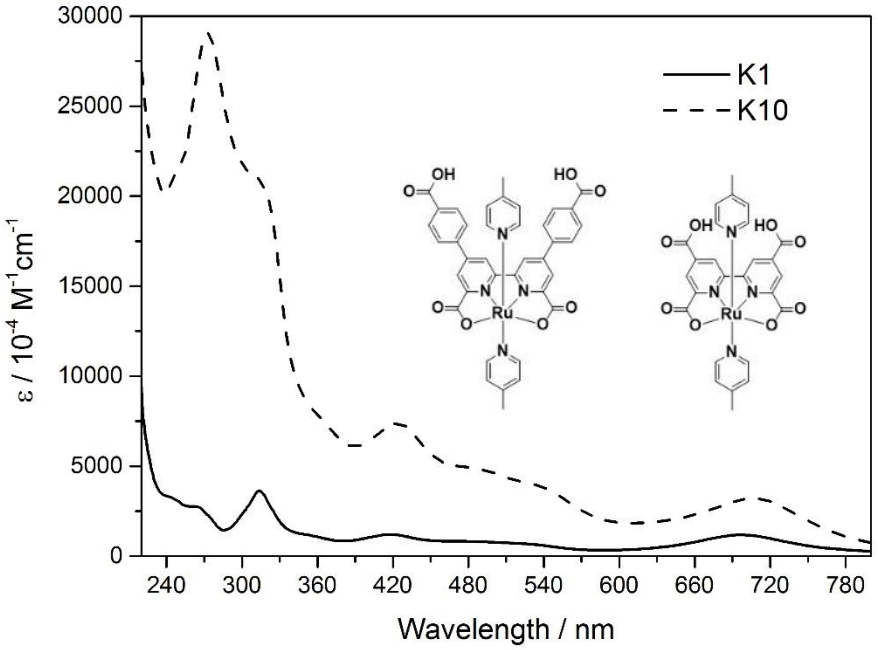

Figure 92. a) Electronic absorption spectra of title compounds (10^{-5} mol/l) recorded either in MeCN-H_2O (for K7, K8) or in pure H_2O (for K10-13). b) Comparison of UV-vis spectra belonging to K1 and K10.

Having confirmed the catalytic features of ruthenium complexes based on carboxylic acids, a closer look was taken at the bromo substituted complex K14. At pH 7, electrochemical measurements of K14 bearing two Br substituents at the bda-ligand revealed three redox waves from +0.7 V to +1.1 V (*vs*. NHE), which are in line with the reaction sequence $Ru^{II/III} \rightarrow Ru^{III/IV} \rightarrow Ru^{IV/V}$. However, at pH 1, one broad redox wave was observed around +0.8 V (*vs*. NHE). As obvious from the SWVs of K14, addition of acid leads to a shift of the reversible redox wave towards more positive potentials from +0.7 to 0.8 V (*vs*. NHE), while the peak potentials corresponding to $Ru^{3+/4+}$ and $Ru^{4+/5+}$ move towards more negative potentials (Figure 93). Hence, only one broad peak is observed in acidic pH range. Comparing with the un-substituted complex K7, the catalytic current of K14 is significantly lower and indicates a lower efficiency than that of K7, while the CV curves of the dicarboxylated complex K10 and K14 are only slightly different and indicate comparable activities.

Worth-mentioning at this point is a recent study by LIU et al.[134], who synthesized a series of similar Ru-bda catalysts with bromine and nitro modification at the 4,4'-positions on the equatorial ligand. The results of water oxidation experiments and measured kinetics revealed that substitution of the bda-ligand at the para-position results in a dramatic shift of the reaction order from second to first order, which corresponds to a change of the O-O bond formation mechanism from the I2M pathway to the WNA pathway. In addition, studies on catalytic water oxidation showed that the mechanism of O-O bond formation directly correlates with the catalytic activity. Considering that the un-substituted bda-complex K7 proceeds *via* an I_2M mechanism, substitution on the bda-ligand seems to have a significant effect on the reaction barrier, or else water oxidation by K7 would probably occur through a *'nucleophilic attack'* by the ever present solvent water.

Kinetic studies[134] at different catalyst loadings suggested that water oxidation by the bromo catalyst might proceed through both mononuclear and dinuclear pathways, which could be confirmed by the slope value of ~1.8 from linear fitting of the plot ln[(Rate)] vs. ln[(cat.)]. By comparison, the kinetic order value of the dibromo analog was 1.6, which implies higher propensity to a water nucleophilic attack reaction, while the un-substituted Ru-bda catalyst preferentially follows a second-order reaction process as evident from its slope value of ~2.1. The low kinetic order of the dibromo catalyst was attributed to the increasing number of the electron withdrawing groups attached to the molecule, thought to dramatically lower the WNA reaction barrier. Nevertheless, all these findings do not mean that water oxidation will only proceed through one of the above mentioned reaction paths. Rather, a mechanistic switch is to

be expected due to the more complex interactions and dynamics of the catalysts in aqueous solutions.

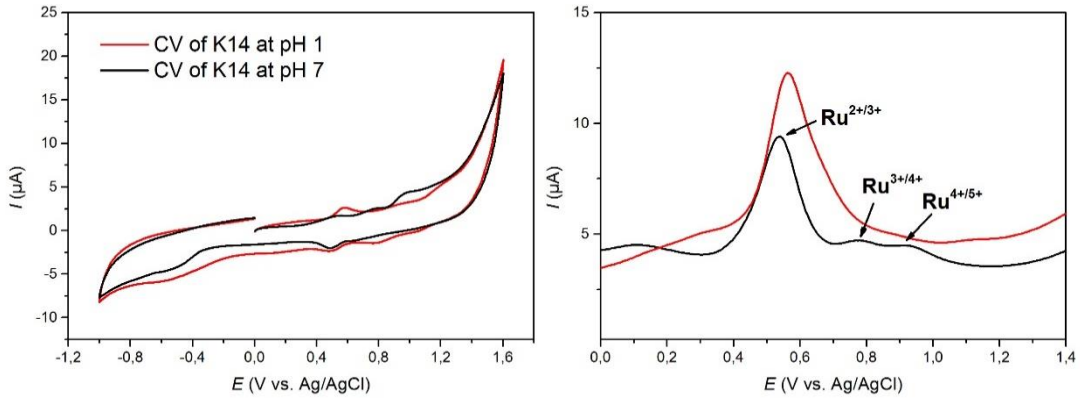

Figure 93. Left, cyclic- and right, square wave voltammograms of K14 (1 mmole/L) in acidic (0.1 M HOTf, pH 1, red curves) and neutral medium (black curves).

A comparison between K10 and K14 revealed similar features, which possess electron-withdrawing groups at the same positions on their equatorial ligand backbone. The CV voltammograms illustrated in Figure 94 show a similar trend under the same experimental conditions, probably signaling water oxidation activities at approximately identical reaction rates. The redox potentials corresponding to the high-valent ruthenium-oxo species move toward more negative redox potentials upon acidification of the catalyst solutions to pH 1. This leads to a significant broadening of the Ru^{II}/Ru^{III} redox wave, overlapping the Ru^{III}/Ru^{IV} and Ru^{IV}/Ru^{V} redox couples as can be gathered from Figure 95. Considering that K14 performs water oxidation *via* the WNA mechanism, a similar mechanistic trend is proposed for the dicarboxylated catalyst K10.

The same trend was observed for the high-valent ruthenium intermediates of complex K9, in which the axial ligands of K7 were replaced by phthalazine ligands. Compared to its pyridine and isoquinoline substituted analogs K7 and K8, K9 shows one asymmetric broad peak at 0.95 V (*vs.* NHE) at pH 1 belonging to the redox couples Ru^{III}/Ru^{IV} and Ru^{IV}/Ru^{V}, while the SWVs of K7 and K8 revealed three single peaks for each transition, which were clearly separated. An explanation for this difference is that reactive ruthenium species, which are easier to retrieve, might be able to speed up the electron transfer in the oxygen evolution process before the catalyst would undergo several types of deactivation.

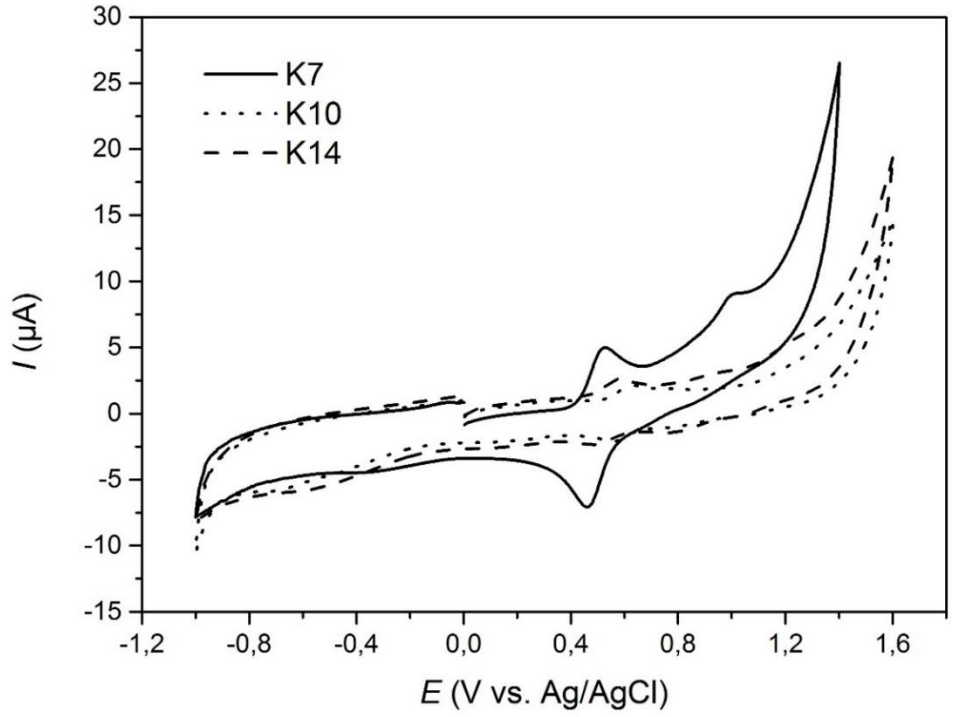

Figure 94. Electrochemical comparison between complexes K7, K10 and K14.

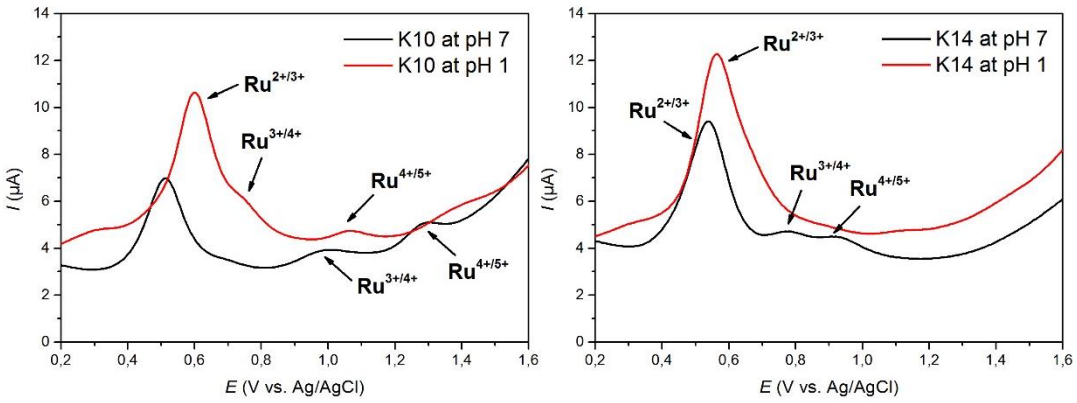

Figure 95. SWVs of complexes K10 and K14 (1 mmole/L) in acidic (0.1 M HOTf, pH 1, red curves) and neutral medium (black curves).

Although spectroscopic data provide useful information on the potential applications of the catalysts for water oxidation, only the results of kinetic experiments, as well as theoretical simulations can offer more comprehensive explanations into the processes involved. However, considering that several groups work on the development of Ru WOCs structurally very similar to those designed in the course of this doctoral thesis, the results herein are believed to give additional support in understanding water oxidation catalysts.

8.3 Comparison with complexes K16-K19.

8.3.1 Electrochemical and optical properties of K16-K19.

The characterization of the complexes K16-19 was accomplished by NMR spectroscopy, mass analysis, FT-IR, CV/SWV and UV-vis spectroscopy. Since the central Ru^{2+} atom in complexes K16-K19 undergo easy oxidation to Ru^{3+}, again small amounts of ascorbic acid had to be added to solutions containing the respective catalyst, which gives the appearance of complete disappearance of the unpaired electron and thus allows paramagnetic proton signals to disappear in the background noise. Taking into account that the addition of the reducing agent gives rise to further signals in the non-aromatic region of the proton NMR, it is obvious that spectra of pure complex signals cannot be obtained. Moreover, adding a large amount of ascorbic acid was found to overwhelm the signals of the target compound, thus finding the right balance between the substance to be oxidized and the reducing agent is of additional importance.

The proton NMR spectrum of K16, K18 and K19 are shown in Figure 98. Considering that chemically equivalent protons induce one signal in the ^1H spectrum, the number of proton signals obtained for these complexes indicates molecular symmetry within the molecules. Unfortunately, characterization of complex K17 was found to be very difficult and could only be identified by mass spectrometric analysis, as presented in Figure 99.

The N-H proton signal usually located between 10-11 ppm in the ligands L7-L10 is a useful indication to prove whether or not complex formation occurred, since coordination of ruthenium through the nitrogen atoms of the carboxamide unit is accompanied by the disappearance of the amide N-H protons in the ^1H spectrum (Figure 96). In addition, this coordination induces a marked downfield shift from 132 (N-H) to 233 ppm (N-Ru) for the resonance of the N atom, which is attributed to the reduced electron density on the nitrogen atom when attached to ruthenium. In Figure 97, this is exemplarily shown for ligand L10 and its corresponding ruthenium complex K19.

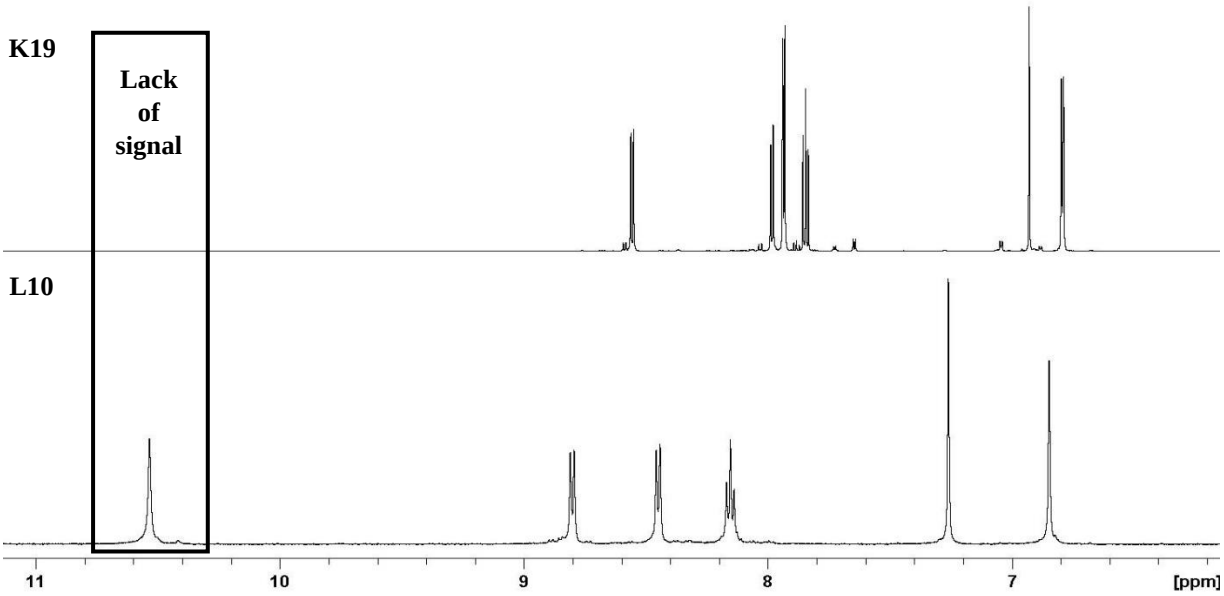

Figure 96. ^{1}H NMR spectra of ligand L10 and its corresponding complex K19.

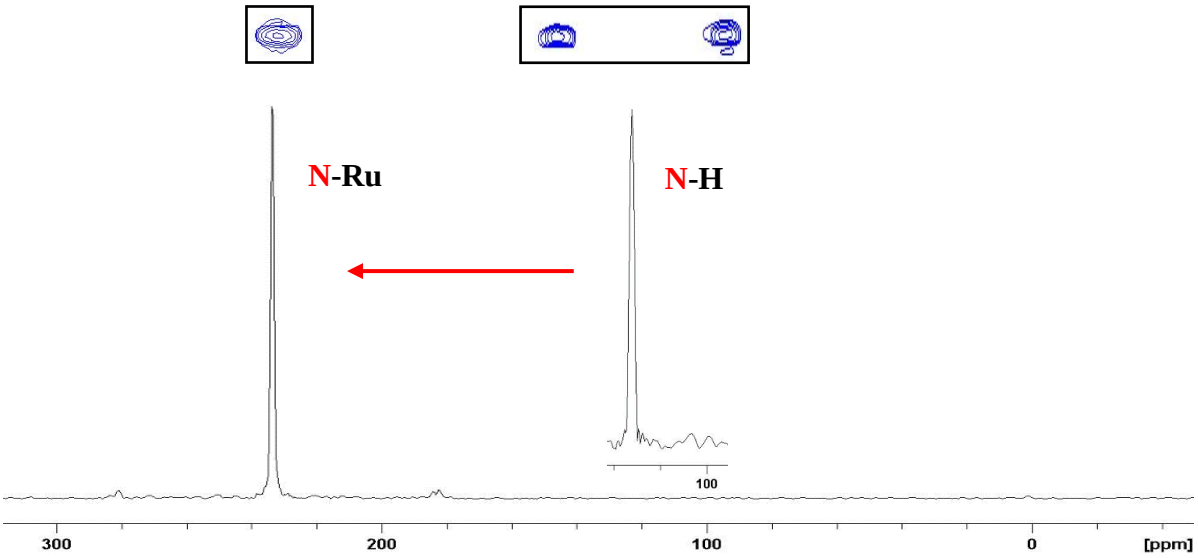

Figure 97. ^{15}N NMR spectra of ligand L10 and its corresponding complex K19.

As evident from Figure 98, the experimental mass spectra of the complexes K16-19 recorded in the positive ion ESI mode consist of similar fragmentation patterns, which were attributed to the sequential dissociation of the pyridine ligands in the axial positions (- *m/z* = 94). To clearly confirm that the selected complex was the only source of fragmentation, ionization products were monitored by MS/MS techniques in positive ion mode. As expected, the resulting MS/MS spectrum first displayed one major peak corresponding to the complex injected, which rapidly disappeared upon fragmention to give product ions only deriving from the selected ruthenium complex. Since no higher isotopic peak pattern of ruthenium was detected or generated in the

electrospray ionization process, the peaks around *m/z* = 700 are supposed to be the key species for catalytic water oxidation.

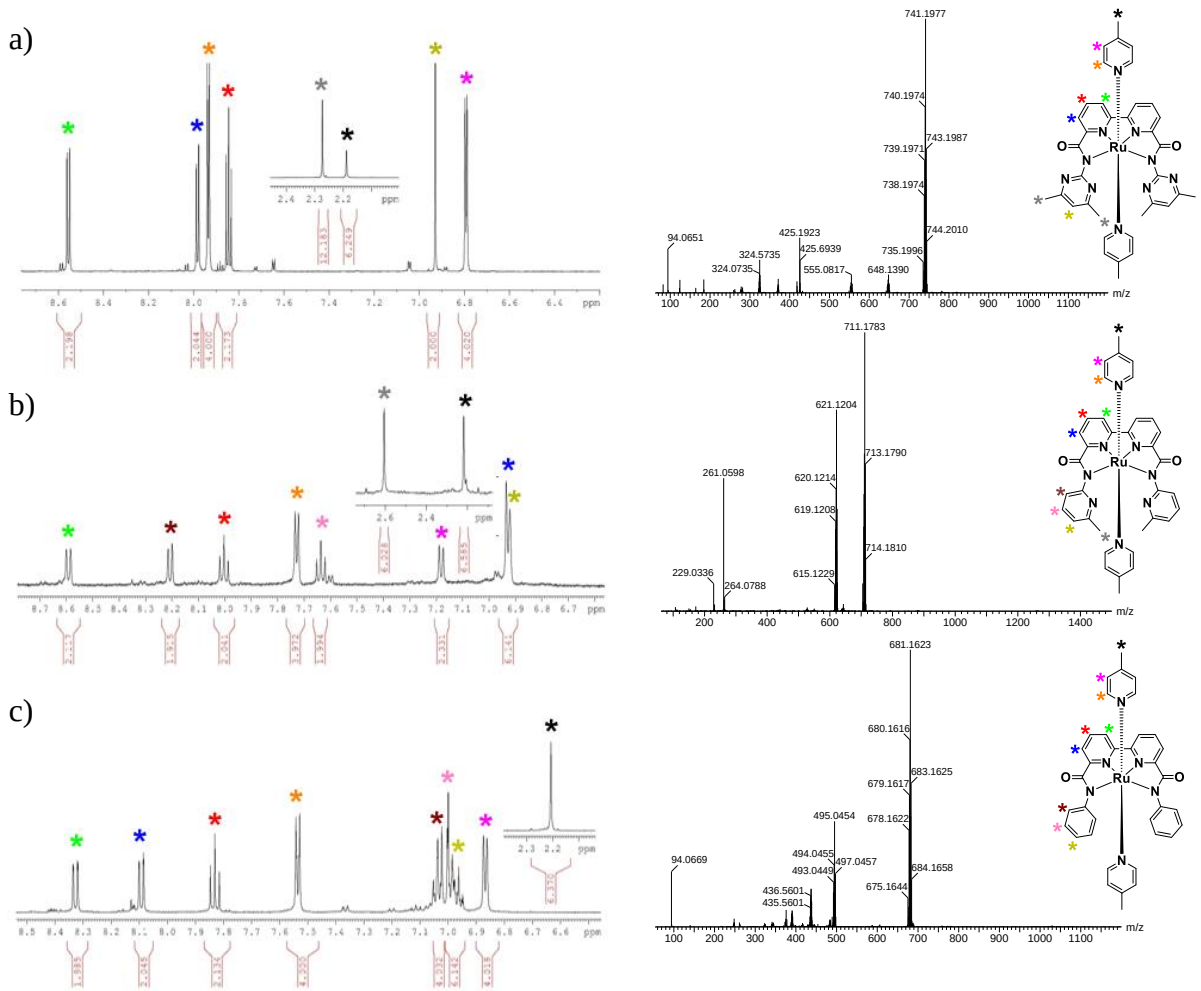

Figure 98. ^{1}H NMR spectra of a) K19, b) K18 and c) K17. *The corresponding mass spectra are shown in the right.*

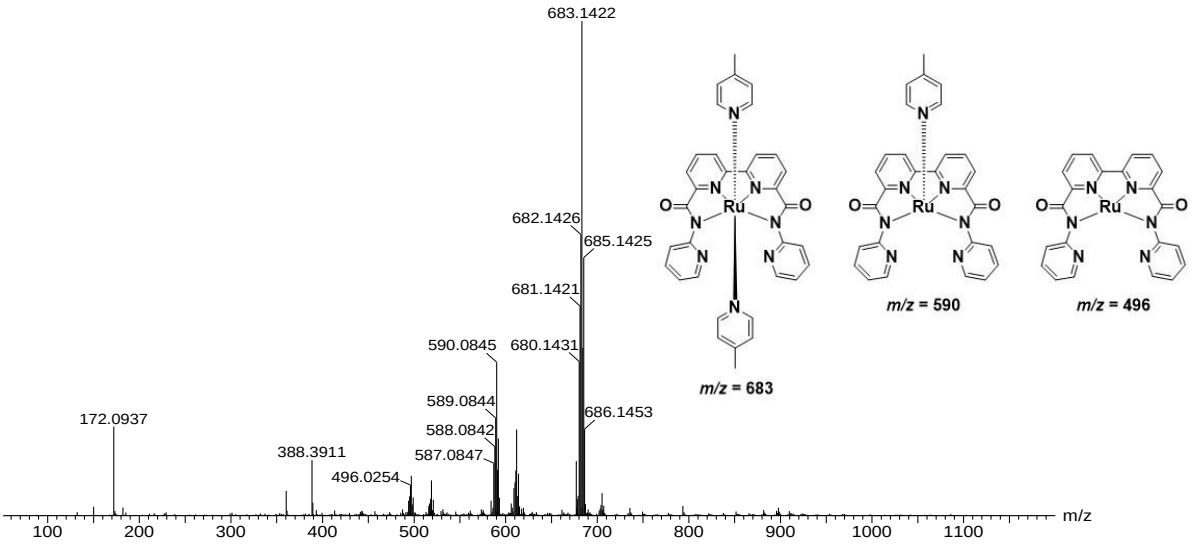

Figure 99. ESI-MS spectrum of complex K16.

In order to gain more detailed information about the electron transfer dynamics, cyclic and square wave voltammetry experiments were performed using a glassy carbon disk as working electrode and Ag/AgCl / 3 M KCl as reference electrode with MeCN/H_2O solutions (1:1 volume ratio, 1 mL) containing the respective catalyst (10^{-5} M). Considering that the solubility of the complexes is dramatically decreasing in the order K19 > K18 > K17 > K16, the addition of an organic solvent was essential in terms of solubility enhancement and comparability. Acetonitrile was used here due to its broad acceptance as co-solvent for a variety of active ruthenium complexes.

However, in spite of the stability of high-valent ruthenium-oxo species, their detection can be very difficult which is due to their high reactivity and very short lifetime with respect to further oxidation to the key ruthenium-oxo species to release molecular oxygen. Particularly, the use of water as solvent for electrochemical measurements can render the interpretation of the results difficult, which is primarily due to its high background current. This is why SWV was the preferred method to identify redox potentials of the complexes K16-K19 if there was any evidence. As illustrated in Figure 100, all complexes display three consecutive redox couples, which are located at around + 0.68, + 0.92 and + 1.25 V on average (*vs*. Ag/AgCl) and can be assigned to the oxidation sequence $Ru^{2+/3+} \rightarrow Ru^{3+/4+} \rightarrow Ru^{4+/5+}$. Table 8 gives a summary of the redox potentials of complexes K16-K19.

Table 8. Summarized electrochemical data of K16-K19.

Complex	**$E_{1/2}$ $Ru^{2+/3+}$**	**$E_{1/2}$ $Ru^{3+/4+}$**	**$E_{1/2}$ $Ru^{4+/5+}$**
K16	0.62	1.01	1.45
K17	0.67	0.92	1.13
K18	0.80	0.90	1.22
K19	0.62	0.84	1.20

Amongst complexes K16-K19, the water solubility increases with the number of methyl groups present in the molecule. As a result, complexes K18 and K19 are excellently soluble in water and show comparable electrochemical behaviour, possessing three redox couples in the region between 0.6 and 1.2 V, the latter being in good agreement with the water-oxidation reaction occurring at 1.23 V *vs.* NHE. Considering that water is essential to form high-valent ruthenium

species by addition of one water molecule to the central ruthenium atom, the solubility of an active catalyst system plays a major role in detecting such species spectroscopically, since ruthenium complexes in pure organic solvents give rise to only one single sharp redox peak corresponding to the first oxidation from Ru^{2+} to Ru^{3+}.

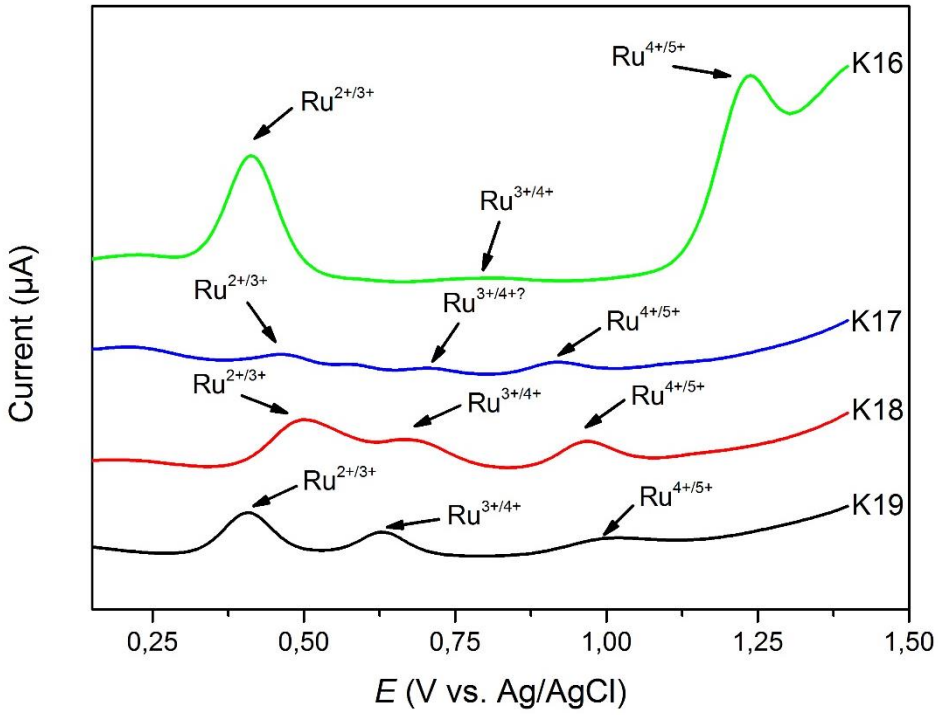

Figure 100. SWVs of complexes K16 (green), K17 (blue), K18 (red), K19 (black) (1 mmole/L) in acidic (0.1 M HOTf, pH 1, red curves).

By comparison, the redox potentials of K19 are noticeably lower than that of K18 and can be ascribed to the increased number of methyl groups, which suggests that water oxidation triggered by K19 might proceed at faster rates than with K18. Remarkably, the aniline substituted complex K16 shows a dramatic shift of the $Ru^{4+/5+}$ redox couple towards higher redox potentials, while the redox peaks of complex K17 appear only very weakly.

Worth-mentioning at this point are studies on polypyridyl-based ruthenium complexes by THUMMEL et al.[100], which showed a marked difference in catalytic stability attributed to the presence of unbound or weakly bound nitrogen atoms that most likely underwent protonation when water oxidation was carried out under acidic conditions (pH 1). Consequently, this was found to exert an electron-withdrawing effect rather than electron-donating and thus lowered the stability of the respective catalyst. Considering that complexes K16-K19 also contain unbound *N*-donors, the same effect might also reduce the catalytic efficiency of these complexes (Figure 101).

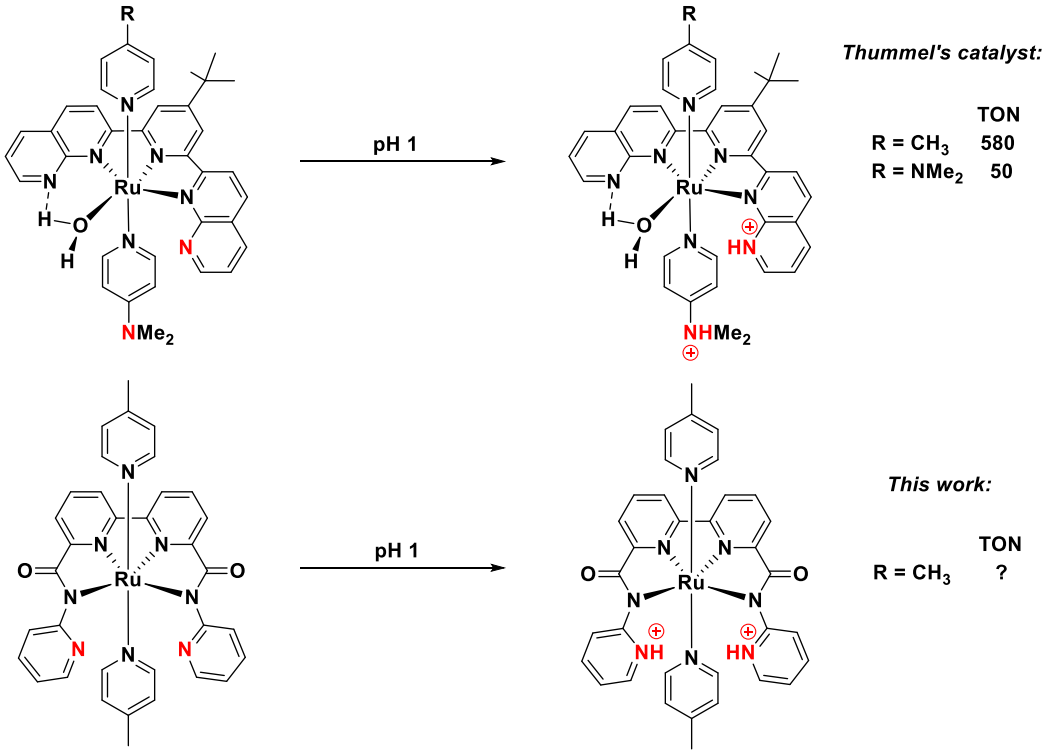

Figure 101. Proposed protonation process of *N*-substituents during water oxidation experiments.

During electrochemical studies, a color change of the catalyst solution from deeply to slightly red was observed when measurements were conducted with K18 and K19 in pure water at pH 1. A closer look at the reaction flask revealed that this was due to precipitation of the protonated complex, which could be fed back into solution again by adding few drops of acetonitrile. In order to study the effect of solvent on the electrochemical behavior, CVs of the excellently water-soluble complex K19 were also carried out in organic solutions. The results are presented in Figures 102-104. In fact, the cyclic voltammograms plotted against applied potential of ferrocene clearly show that the existence and appearance of the redox potentials are strongly depending on the solvent. More remarkably, the CV of K19 measured in pure water only shows one single reversible couple at 0.55 V (*vs*. NHE), while the addition of acid (pH 1) gives access to high-valent oxidation states.

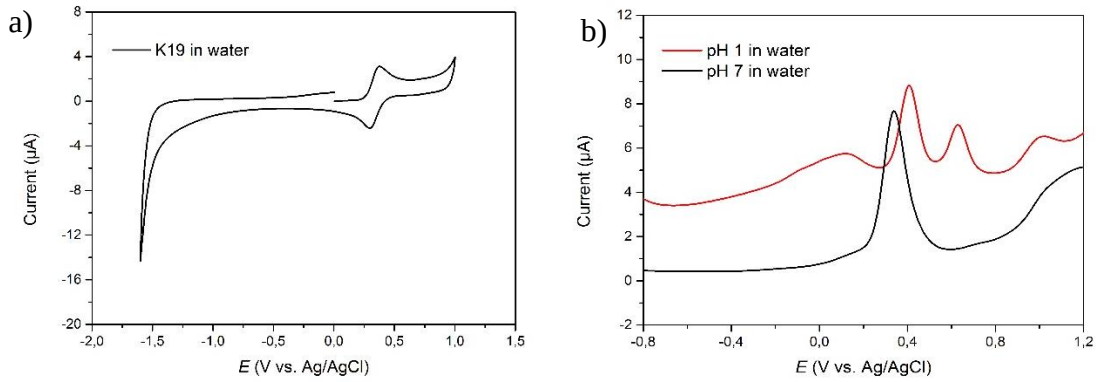

Figure 102. a) CV curve of complex K19 in pure water and b) its corresponding SW curves in acidic (red) and neutral medium (black).

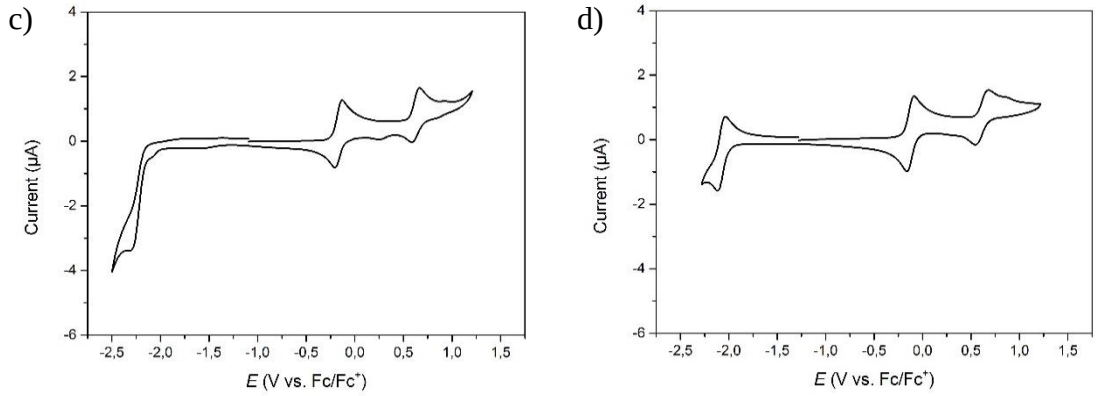

Figure 103. CV curves of complex K19 in c) DCM and d) MeCN.

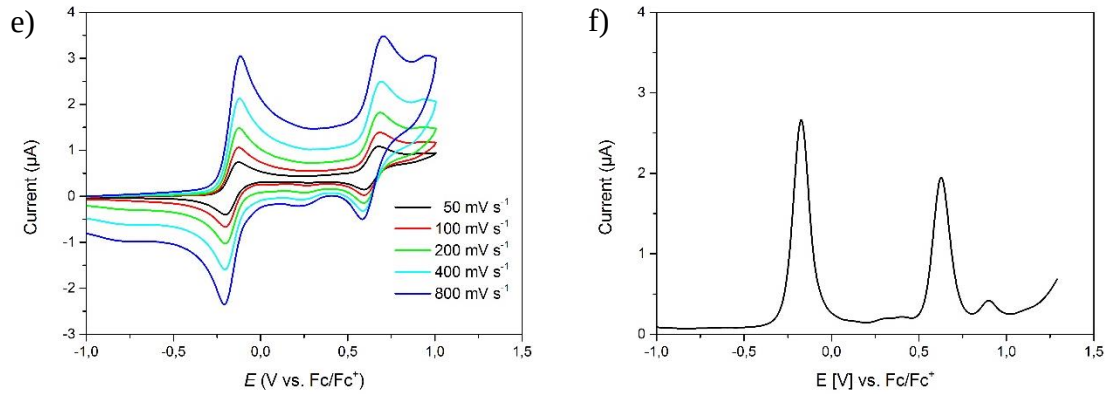

Figure 104. CVs of complex K19 at different scan rates varying from 50 to 800 mV s^{-1} in e) DCM and f) the corresponding SW curve.

CV curves at different scan rates varying from 50 to 800 mV s^{-1}, which were measured in DCM and MeCN solutions, are shown in Figures 104 and 105. A comparison revealed that using the more strongly coordinating solvent acetonitrile gave rise to three redox couples in the CV and SWV spectra, while measurements in dichloromethane revealed only two redox peaks.

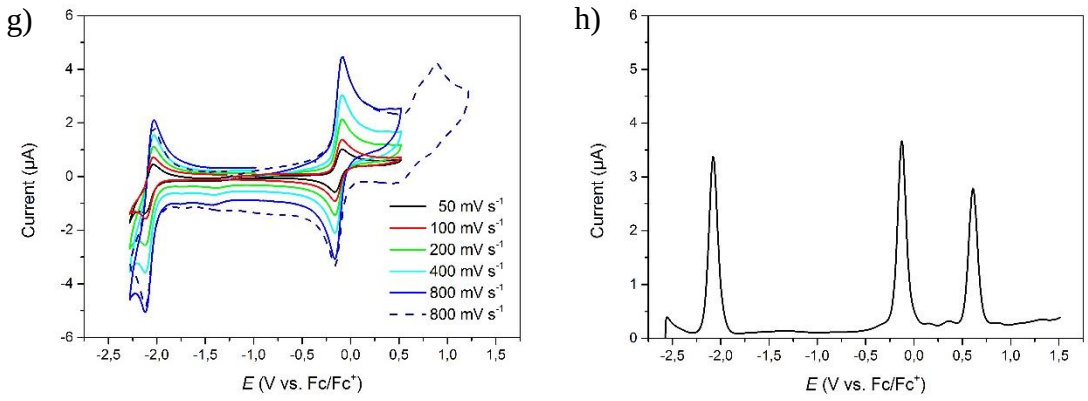

Figure 105. CVs of complex K19 at different scan rates varying from 50 to 800 mV s^{-1} in g) MeCN and h) the corresponding SW curve.

The appearance of this phenomenon is unknown, but it is believed that the strongly coordinating character of MeCN could facilitate the access to ruthenium-MeCN-aqua intermediates. However, the use of pure water seems to be more efficient in terms of catalytic water oxidation, which is due to the low oxidation potenials compared to those obtained in organic media.

Regarding the electrochemical properties of K17, protonation of the pyridine nitrogens might have influenced the catalyst solubility in such a manner that even a mixture of MeCN/H_2O was less capable of re-dissolving the precipitate. Hence, the redox pair transitions of K17 appear very weakly. Under the same experimental conditions, the aniline-substituted complex K16 displays three widely diverging redox peaks. Considering that K16 is more soluble in the organic than in the aqueous phase, its high overpotential for the oxygen evolution reaction is believed to arise from the central ruthenium atom strongly coordinated by acetonitrile ligands due to its π-accepting ability, largely inhibiting the coordination of water and O-O bond formation.

To further confirm complex formation, infrared spectroscopy was performed and the spectra obtained were compared with those of the corresponding ligands, as evident from Figure 106. Considering that infrared spectroscopy is useful to determine functional groups with characteristic IR bands, the absence of certain reactive groups can help to identify the final product. In the following, the results will be examplarily discussed for L9 and K18. In uncomplexed state, the IR spectrum of ligand L9 shows a broad band above 3200 cm^{-1}, which correponds to the N-H stretch of the amide units. As expected, these vibrations almost completely disappear when the N-H nitrogens are coordinated to the ruthenium(II) center. Moreover, complexes K18 and K19 show additional C-H stretching vibrations above 2800 cm^{-1}, which can be attributed to the presence of methyl substituents that are missing in complexes without alkyl groups.

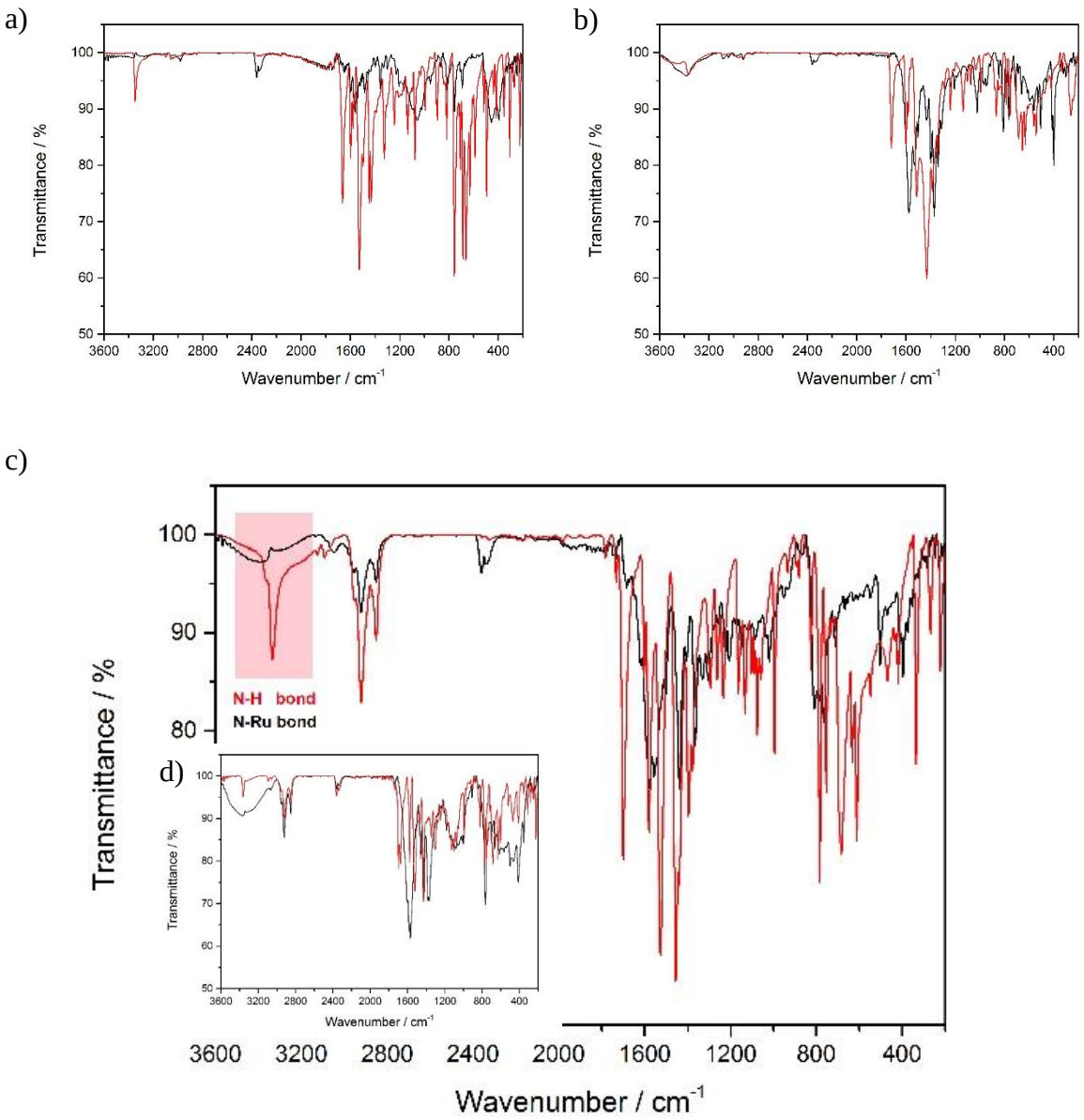

Figure 106. Comparison of IR spectra of ligands L7-L10 (red curves) with complexes a) K16, b) K17, c) K18 and d) K19 (black curves).

Finally, the optical properties of the complexes were studied by UV-vis spectroscopy in MeCN:H_2O (v:v, 1:1) containing 10^{-5} mol/L of catalysts (Figure 107). By comparison, all complexes show characteristic absorptions due to their similar molecular structures. The two obviously absorptions bands at ~250 nm and ~300 nm are assigned to bda-π → bda-π^*. The higher energy metal-to-ligand and charge transfer (MLCT) bands at around 400 nm are assigned to Ru-d → bda-π^*. However, there was no evidence for Ru^{3+}- or Ru^{4+}-species, which is certainly due to the stable Ru-N bond. By comparison, ruthenium(II) complexes containing negatively charged carboxylate ligands provided detection of high-valent ruthenium species, which was proposed to arise from the lability of the Ru-O bond located in the equatorial framework of these complexes, facilitating the access to the corresponding aqua complex due to the non-

bonded dangling oxygen atoms of the carboxylate groups. By replacing the dangling bonds by more stable ones for example nitrogen atoms, the catalyst stability was seemingly increased as desired, but at the same time could decreased the catalytic performance of the systems. Thus, it was of main interest to investigate the relationship between bond strength in the equatorial ligand plane and catalytic properties of complexes K16-K19 in water oxidation experiments.

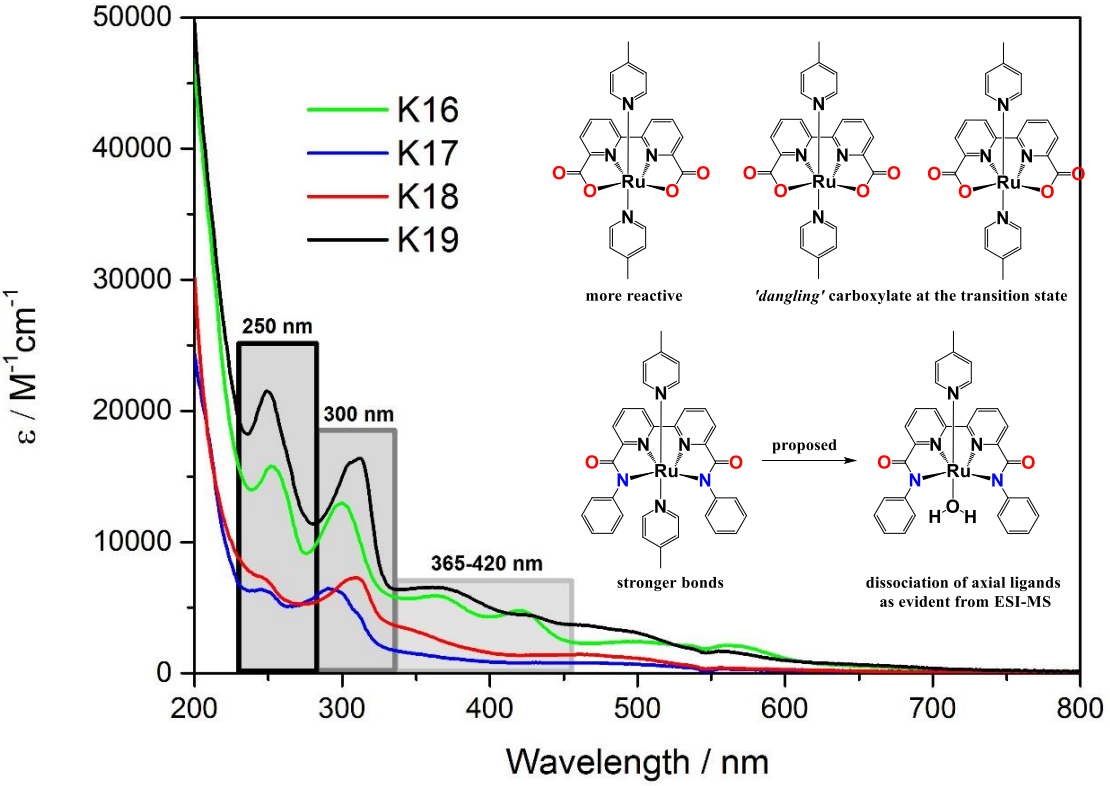

Figure 107. UV-vis spectra of complexes K16-K19 (10^{-5} mol/l) recorded in MeCN/H_2O (1:1, v:v, 3 mL).

8.3.2 Single crystal X-ray.

Colorless and red crystals suitable for X-ray diffraction were obtained by slow diffusion of cyclopentane into dichloromethane solutions containing the respective ligand and catalyst at room temperature. Due to the very similar molecular structure of the ligands, bond length data as well as atom angles of ligand L7 and ligand L9 are nearly identical which is evident from Table 9 and Table 10. Moreover, single crystal X-ray diffraction confirmes the symmetry present in the ligands as previously suggested by ^{1}H NMR spectroscopy.

Ligand 7 crystallizes in the orthorhombic space group Pbca and the following unit cell parameters: a = 9.24, b = 9.94, c = 21.8 Å, α/β/γ = 90 °, while ligand L9 crystallizes in the monoclinic space group P2 1/n with unit cell parameters a = 11.6, b = 6.09, c = 15.1 Å, α/γ = 90 ° and β = 106.1 °. As shown in Figure 108 and Figure 109, the central bipyridine unit is planar and has a trans configuration. In both ligands, the distance between the bipyridine ring and the amide-carbonyl is 1.50 Å. By comparison, the distance N(2)-C(6) [1.348 Å] in L7 is slightly shorter than the distance between N(2)-C(7) [1.354 Å] in L9, while the angle of N2-C6-N2 was determined to be 113.11 ° being significantly smaller than the angle found in L7 [118.59 °] for C12-C7-N2. This difference is due in part to the lone pair repulsion interaction of the N1- and N2-nitrogen lone pairs and also to the bulkiness and mutual repulsion of the alkyl substituents of the terminal pyridine rings.

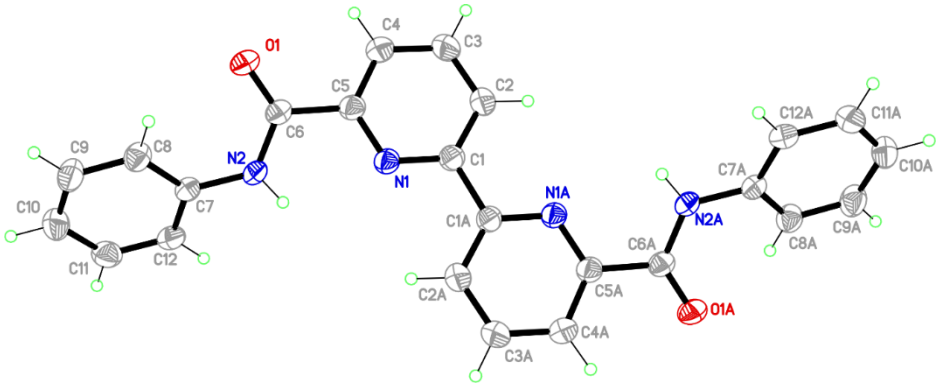

Figure 108. Crystal structure of ligand L7, showing 50% probability displacement ellipsoids and the atom-numbering scheme.

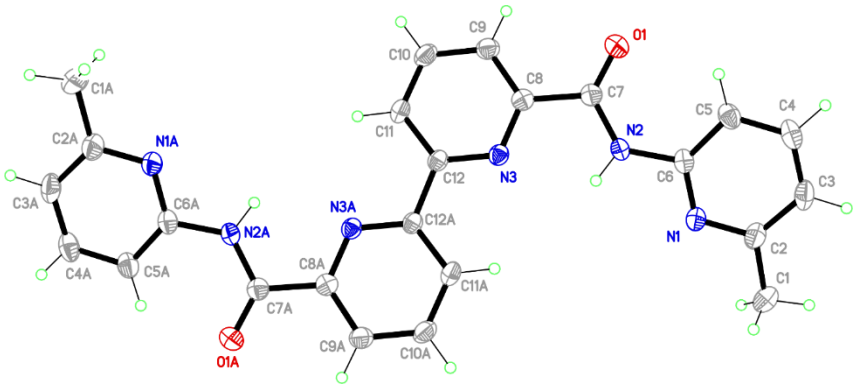

Figure 109. Crystal structure of ligand L9, showing 50% probability displacement ellipsoids and the atom-numbering scheme.

The crystal structure of complex K19 is shown in Figure 110. It crystallizes in the orthorhombic space group $P2_12_12_1$ and the following unit cell parameters: a = 11.46, b = 16.0, c = 19.1 Å, α/β/γ = 90 °. The central ruthenium is hexacoordinated by a bidentate *N,N'*-chelating 2,2'-bipyridine ligand, two amide nitrogen donors and two axially bounded pyridine ligands. The Ru1-N11 distance of 2.167 Å is considerably longer than the Ru1-N30 distance of 2.095 Å and the Ru1-N13/N12 distance of 1.941 Å due to the steric crowding by the dimethyl pyrimidine substituents attached to the amide nitrogens. Hence, upon binding to ruthenium, the flexibility of the ligand converts to a rigid and robust structure that offers a good stability to the ruthenium system.

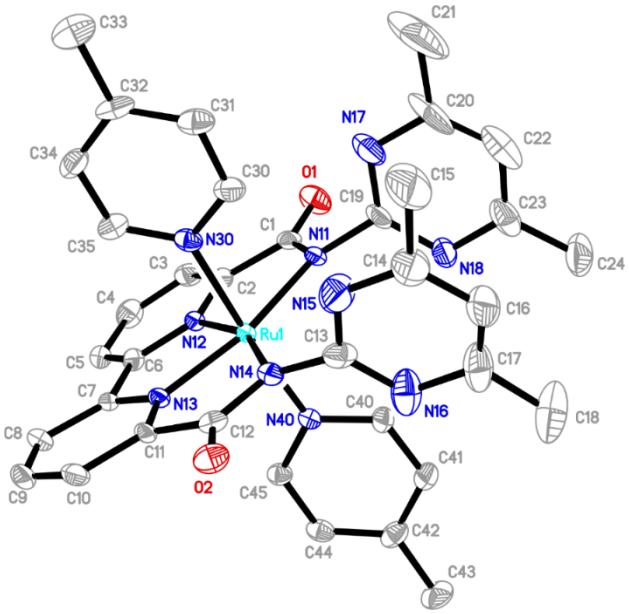

Figure 110. Crystal structure of complex K19, showing 50% probability displacement ellipsoids and the atom-numbering scheme.

Table 9. Selected bond lengths [Å] and angles [°] for L7.

Atom-Atom	Bond length [Å]	Atom-Atom-Atom	Angles [°]
C(1)-N(1)	1.3411(15)	**N(1)-C(1)-C(1A)**	116.23(13)
N(1)-C(5)	1.3366(15)	**C(2)-C(1)-C(1A)**	121.44(14)
N(2)-C(6)	1.3486(15)	**N(1)-C(5)-C(6)**	117.14(10)
N(2)-C(7)	1.4159(15)	**C(4)-C(5)-C(6)**	119.42(11)
C(1)-C(1A)	1.487(2)	**C(6)-N(2)-C(7)**	125.50(10)
C(5)-C(6)	1.5038(16)	**C(8)-C(7)-N(2)**	121.50(11)
O(1)-C(6)	1.2276(14)	**C(12)-C(7)-N(2)**	118.59(11)
		O(1)-C(6)-N(2)	124.96(11)
		O(1)-C(6)-C(5)	120.24(11)
		N(2)-C(6)-C(5)	114.78(10)

Table 10. Selected bond lengths [Å] and angles [°] for L9.

Atom-Atom	Bond length [Å]	Atom-Atom-Atom	Angles [°]
O(1)-C(6)	1.2200(18)	**C(6)-N(1)-C(2)**	118.28(14)
N(1)-C(2)	1.329(2)	**C(7)-N(2)-C(6)**	128.23(13)
C(1)-C(2)	1.345(2)	**N(1)-C(2)-C(1)**	116.54(15)
N(2)-C(7)	1.502(3)	**C(3)-C(2)-C(1)**	122.02(15)
N(2)-C(6)	1.3548(19)	**N(1)-C(6)-N(2)**	113.11(13)
N(3)-C(12)	1.4088(19)	**C(5)-C(6)-N(2)**	122.74(14)
N(3)-C(8)	1.3388(18)	**O(1)-C(7)-N(2)**	125.03(14)
C(7)-C(8)	1.3400(18)	**O(1)-C(7)-C(8)**	121.43(13)
C(12)-C(12A)	1.505(2)	**N(2)-C(7)-C(8)**	113.54(12)
	1.485(3)	**N(3)-C(8)-C(7)**	116.98(13)
		C(9)-C(8)-C(7)	119.80(13)
		N(3)-C(12)-C(12A)	116.66(15)
		C(11)-C(12)-C(12A)	121.48(16)

Table 11. Selected bond lengths [Å] and angles [°] for K19.

Atom-Atom	Bond length [Å]	Atom-Atom-Atom	Angles [°]
Ru(1)-N(12)	1.937(4)	**N(12)-Ru(1)-N(13)**	81.35(17)
Ru(1)-N(13)	1.941(4)	**N(13)-Ru(1)-N(14)**	77.45(17)
Ru(1)-N(40)	2.095(4)	**N(12)-Ru(1)-N(14)**	158.79(16)
Ru(1)-N(30)	2.095(4)	**O(1)-C(1)-N(11)**	127.0(5)
Ru(1)-N(14)	2.155(4)	**O(1)-C(1)-C(2)**	120.0(5)
Ru(1)-N(11)	2.167(4)	**N(11)-C(1)-C(2)**	113.1(5)
N(11)-C(1)	1.342(7)	**O(2)-C(12)-N(14)**	127.9(5)
N(11)-C(19)	1.417(7)	**O(2)-C(12)-C(11)**	119.3(5)
N(14)-C(12)	1.350(7)	**N(40)-Ru(1)-N(11)**	88.71(17)
N(14)-C(13)	1.406(6)	**N(12)-Ru(1)-N(40)**	91.57(18)
O(1)-C(1)	1.243(7)	**N(40)-Ru(1)-N(30)**	174.55(18)
O(2)-C(12)	1.240(6)	**N(40)-Ru(1)-N(14)**	90.04(19)
C(1)-C(2)	1.509(7)	**N(17)-C(19)-N(11)**	116.7(5)
C(11)-C(12)	1.506(7)	**C(3)-C(2)-C(1)**	125.8(5)
		C(2)-N(12)-Ru(1)	121.1(3)
		C(12)-N(14)-C(13)	119.9(5)
		N(13)-C(11)-C(12)	113.4(4)
		C(1)-N(11)-Ru(1)	114.1(3)
		C(19)-N(11)-Ru(1)	128.4(4)

CHAPTER 9

Water Oxidation – Catalysis by CAN

9.1 Artificial Water Oxidation: Apparatus, Conditions and Theoretical Background

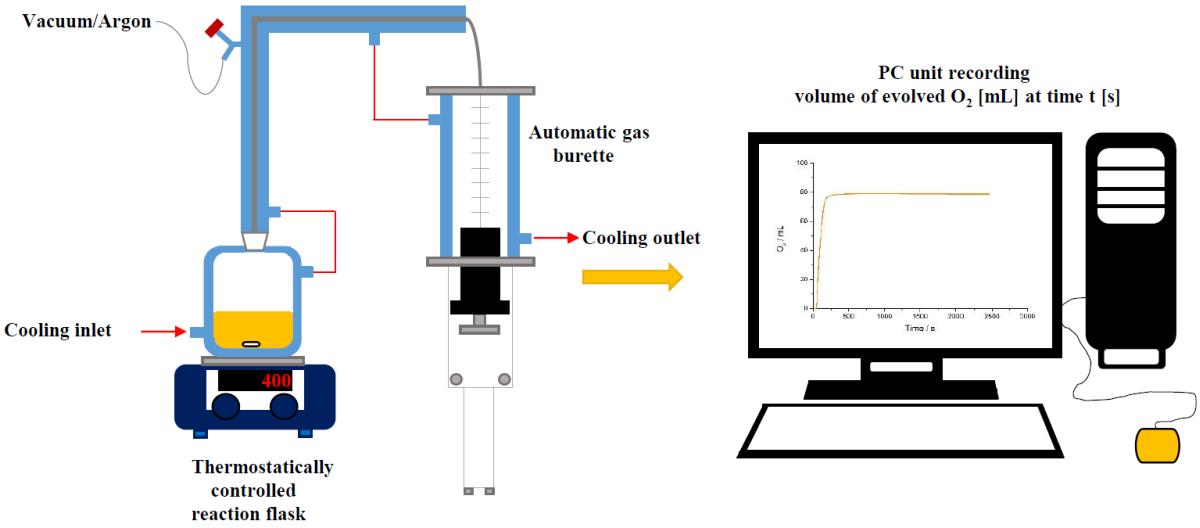

Figure 111. Schematic illustration of water oxidation apparatus.

Volume measurements in the chemically-driven water oxidation were performed with the apparatus shown in Figure 111. The main components include a temperature controlled reactor and an automatic gas burette (GASMESS-5-CONT) for measuring gas volumes, which was connected to the reactor by a glass condenser. The thermostatically controlled reaction flask, the glass condenser as well as the measurement cylinder were all maintained at 25°C. Changes in volume of evolved oxygen during catalysis were recorded by a pressure sensor, while the process within the reactor was controlled isobarically by the gas burette. The pressure inside the reactor was hold constant by the movement of the piston in the gas burette, which compensated the volume change. This change of volume of evolved gas at time t was then recorded by a PC unit.

A typical reaction was performed in a 100 mL double-walled glass reactor, which was loaded with an aqueous Ce(IV)-CF_3SO_3H solution (initial pH = 1.0, 14 mL). Subsequent injections of 1 cm^3 of water containing the respective catalyst (10^{-4} mol/L) promptly triggered the evolution of oxygen, as evidenced by the formation of gas bubbles. Under vigorous stirring, the evolved

oxygen was recorded over time until the reaction reached a plateau, indicating catalyst deactivation. To confirm that the amount of evolved gas was attributed to the generation of oxygen, an aliquot of the gas headspace was taken out of the reaction vessel and injected into the gas chromatograph to determine the gas composition at the end of the catalytic reaction (Figure 112).

Headspace before catalytic reaction	→	Argon
Headspace without catalyst	→	Ce^{IV} + HOTf
Headspace after catalytic reaction	→	Ce^{IV} + HOTf + cat.

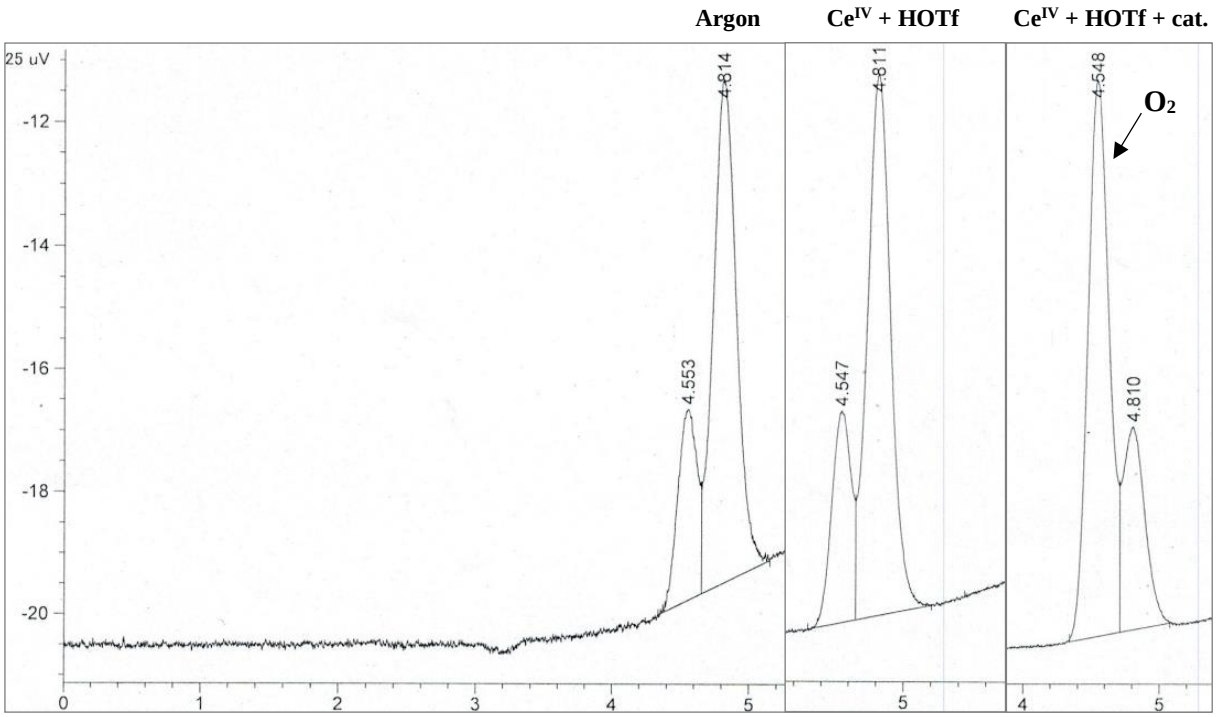

Figure 112. Headspace-GC analysis of the gas volume before and after the catalytic reaction.

9.1.1 Calculation of catalytic stability and catalytic activity

The measurement of the total dioxygen production was a little bit complex, since addition of the catalyst solution immediately triggered the release of oxygen even during injection time. To avoid loss of volume, especially in the initial phase in which gas formation was strongest, the volume and time data were recorded shortly before the catalyst solution was injected. Considering that the injection of the catalyst-water solution also generates its own gas volume, corresponding to the vapour pressure of the solution at the temperature of the measurement, this value needs to be subtracted from all measured gas volumes to obtain the true value. This

was done by a blank experiment, which was carried out by addition of the water solvent with no catalyst to the CAN solution. The amount of oxygen was determined using the ideal gas law, which is widely accepted and used in the literature for the calculation of the TON:

$$pV = nRT \qquad \text{(Equation 9.1)}$$

With R = 8, 3144598(48) J mol^{-1} K^{-1}, T = 298, 15 K, p = 1 atm = 1, 01325·10^5 Pa, V = evolved volume of oxygen and n = the number of oxygen molecules in mole. Assuming that 3·10^{-6} mol of starting catalyst produces a volume of 15 mL oxygen during catalysis, n is calculated as follows:

$$n = \frac{pV}{RT} = \frac{1{,}01325x10^5\ x\ 0{,}015}{8{,}3144598\ x\ 298{,}15}\ \frac{Pa\ x\ L}{J\ mole^{-1}\ K^{-1}\ x\ K} \qquad \text{(Equation 9.2)}$$

Using $1\ Pa = \frac{kg}{m\ s^2}$; $1\ J = \frac{kg\ m^2}{s^2}$, the ideal gas law is simplified to the following equation:

$$n = \frac{pV}{RT} = \frac{1{,}01325x10^5 x\ 0{,}015}{8{,}3144598\ x\ 298{,}15}\ \frac{kg\ x\ L\ x\ mole\ x\ K\ x\ s^2}{m\ s^2\ x\ kg\ m^2 x\ K} \qquad \text{(Equation 9.3)}$$

$$n = \frac{pV}{RT} = \frac{1.519{,}875}{2.478{,}95618}\ \frac{L\ x\ mole}{m^3} = \frac{1{,}519\ 875}{2.478{,}95618} mole = 0{,}00061\ mole \qquad \text{(Equation 9.4)}$$

Finally, the TON can be calculated according to

$$TON = \frac{moles\ of\ oxygen}{moles\ of\ catalyst}\ \frac{mole}{mole} = \frac{6{,}1x10^{-4}}{3{,}0x10^{-6}} mole \approx 200 \qquad \text{(Equation 9.5)}$$

The initial TOF was measured at the beginning of the water oxidation curve, which corresponds to the point at which the slope of the curve is at its maximum.

$$TOF = \frac{TON}{time\ [s]} \qquad \text{(Equation 9.6)}$$

Unfortunately, many publications wrongly use the TON value to define the catalytic activity of a catalytic system. However, the turnover number of a system does not provide any information on the catalytic activity. In general, the TON is defined as *'the number of moles of a substrate that a mole of catalyst can convert before becoming in-activated'*[201], which means that the TON value can be used to determine the catalyst stability.

Ideally, a catalyst should be characterized by its infinite turnover number, but in reality homogeneous catalysts rapidly undergo catalyst decomposition and deactivation pathways due

to the experimental conditions in water oxidation or interactions of catalyst intermediates with reaction partners present in the reaction solution. Hence, the term turnover frequency (TOF) was used in the following to refer to the catalytic performance.

9.1.1.1 Oxygen evolution by catalysts K1 and K4.

A detailed understanding of the critical O-O bond formation step, which is currently accepted to proceed through two main types of mechanisms, is required to improve the properties of Ru-based WOCs. Probably the most significant example for examining the catalyst's preference for one specific reaction mechanism is presented in the [Ru(bda)L_2] family reported by SUN et al., which show a dramatic change in reaction kinetics upon slight variation or substitution of the Ru-bound ligands. Slight modification at the equatorial plane near the Ru center, at which the formation of the critical O-O bond occurs, gave access to more active ruthenium catalysts which clearly shows that even slight structural changes can enhance the system's efficiency towards fast water oxidation. Hence, it was of main interest to study the effects of large-sized ruthenium WOCs on the reaction pathway by introducing additional π-accepting character on the bda side. Moreover, the introduction of carboxylic acid groups was necessary to ensure complete solubility.

Under the same catalytic conditions, catalysts K1 and K4 displayed different catalytic performances for water oxidation. First oxygen evolution experiments were carried out with solutions containing 10^{-4} M of catalyst. As evident from Figure 113, complex K4 shows higher catalytic performance but looses its activity after merely 15 minutes as observed by the fast growth rate in the initial phase of water oxidation, abruptly followed by a slow phase and finally extending into the steady state probably due to catalyst deactivation. However, catalyst K1 reaches very slow convergence. K1 and K4 showed only modest TONs of 188 and 494. Considering that the stability of a complex is measured in terms of its turnover number, the TON of K4, which is nearly 3-fold higher than that of K1, highlights the robustness of the linear catalyst in oxidative environment. No starting complexes could be observed at the end of the catalytic reactions which appear to confirm that catalyst degradation was the origin of performance decay.

Despite fairly similar catalytic features, the catalysts show marked differences in activity. Under the same catalytic conditions ([cat.] = 2.2 x 10^{-4} M, [CAN] ~5000 eq), K1 exhibits a turnover frequency of 0.2 s^{-1} while K4 shows a remarkable TOF of 6 s^{-1} in organic solvent-free medium. By comparison, this value is significantly greater than those of analogous [Ru-bda]-type WOCs which contain neutral ligands known to date, only operating with the use of co-solvents. Due

to the fact that the geometrical arrangement of the terminal benzoic acid moieties is the only difference between both catalysts, the better performance of K4 is primarily attributed to the linearity of its ligand backbone.

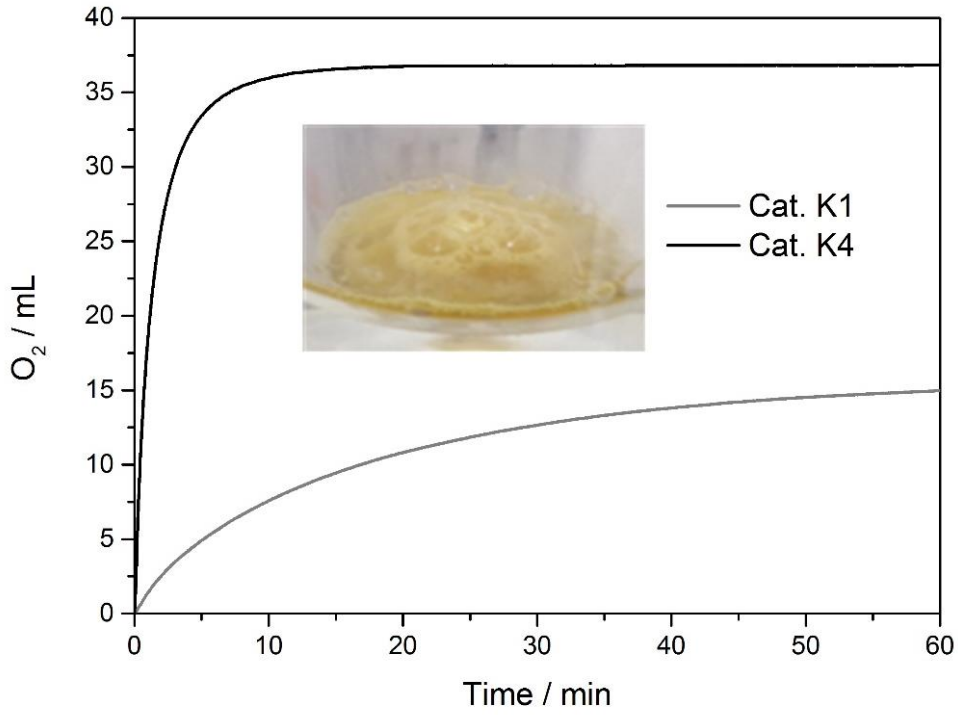

Figure 113. Oxygen evolution curves of the first 60 min of the catalysis with K1 (grey) and K4 (black). *Conditions: 200 µM of catalyst in 0.1 M HOTf (15 mL) containing CAN (~ 5000 eq.) at 25 °C.*

A closer look to the literature revealed similar observations for systems based on rhenium capable of reducing CO_2 to CO, which showed dramatic changes in activity depending on whether the phenylethynyl are attached to the 4,4'- or 5,5'-positions of the acceptor ligand.[200] This was due to the delocalization of π-electrons, which was believed to place more electron density on the central ruthenium atom when the extended π-conjugated systems were substituted in para-position with regard to the Ru atom, thus heavily influencing the catalysts activation towards catalytic applications. Based on these results, it was concluded that less electron density at the metal center might lead to an increase of the electrophilic nature of ruthenium to undergo attack by water, lower the energy needed to form the O-O bond and accelerate O_2 release, as observed for the case of K4. Since catalysts having more or less electron density around the Ru centre tend to operate *via* different reaction pathways, kinetic studies were carried out to provide insight into the mechanism for the critical O-O bond formation.

9.1.1.2 Kinetics of K1 and K4.

In order to study the reaction pathway of the catalysts and to further examine whether a mechanistic change of the reaction kinetics occurs upon slight variation of the equatorial ligand backbone, water oxidation experiments were performed at different catalyst loadings. Assuming that the maximum O_2 formation is equal to the consumption of CAN, initial rates of O_2 evolution were calculated by linear fitting the data from 6-90 s (Figures 114-116).

Evaluation of the data from 6 to 90 s show that the slope of the regression line for the oxidation of water triggered by K1 is significantly different from that of K4 (Figures 118-119). No data were collected in the first 5 s, which is due to the induction time period varying with catalyst loading.

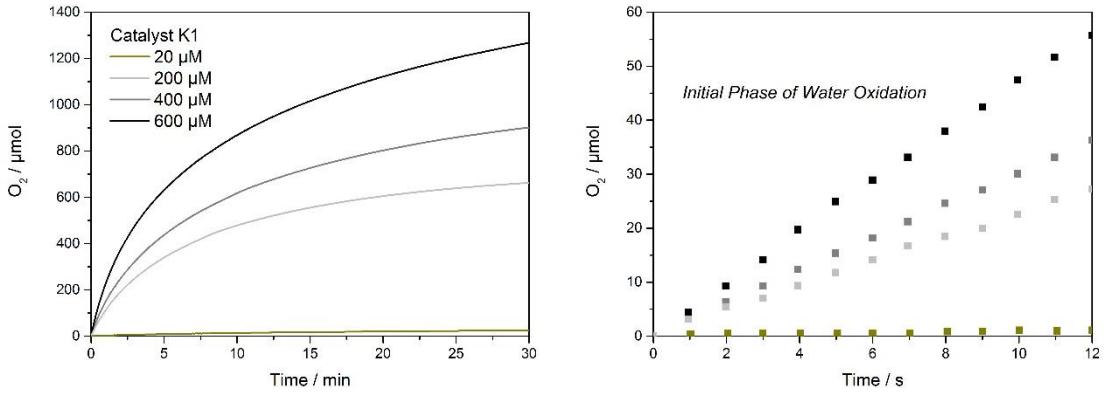

Figure 114. Left, plots of O_2 evolution versus time at various concentration of K1. Right, initial phase of water oxidation within the first 12 seconds.

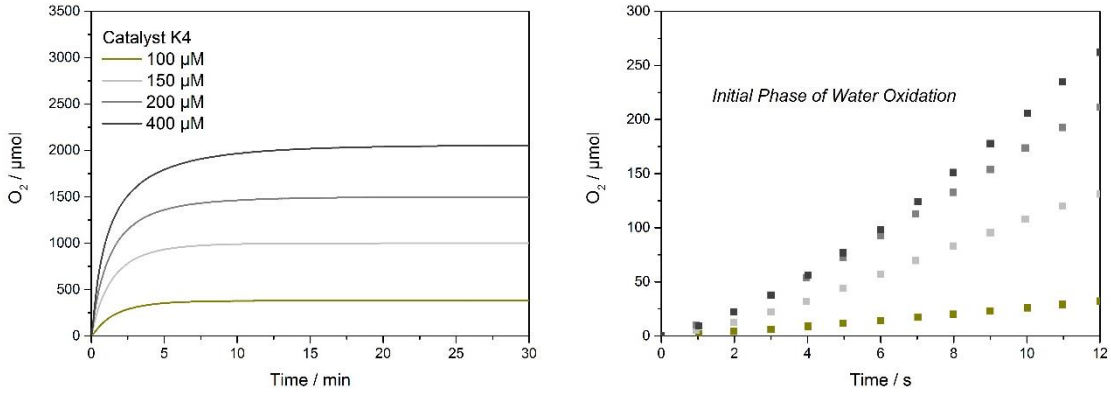

Figure 115. Left, plots of O_2 evolution versus time at various concentration of K4. Right, initial phase of water oxidation within the first 12 seconds.

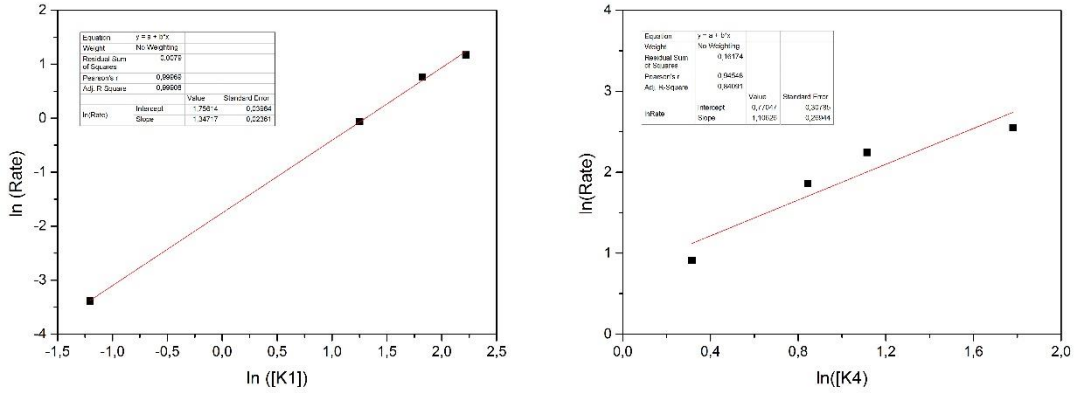

Figure 116. Left, plots of ln(Rate) vs. ln([K1]). Right, plots of ln(Rate) vs. ln([K4]). *Initial rate of O_2 evolution plotted as a function of the concentration of catalyst K4. Rates of O_2 evolution were calculated from the slopes of linearly fitted O_2 evolution plots in the period 6-90s.*

Remarkably, the color of the reaction solution immediately turned colorless at high catalyst concentrations. Simultaneously, the catalytic reaction stopped which was indicated by the flat section of the oxygen evolution curve. It could be observed that further addition of CAN to colorless solutions helped trigger the evolution of oxygen, from which it could be concluded that the catalyst was still active in solution and that CAN was the limiting factor under these conditions for water oxidation. More interestingly, pH testing of both solutions showed that there was a significant difference in acidity. While solutions containing a large excess of cerium(IV) were orange-yellow and pulled the pH near neutrality, which was primarily due to the presence of aqueous Ce^{4+}-ions, reaction solutions containing high concentrations of the respective catalyst still remained in a highly acidic state, as at the start of catalysis. Considering that cerium rapidly dissolves in concentrated aqueous acid solutions to form solutions containing colorless Ce^{3+}-ions, which in large part exist as $[Ce(H_2O)_9]^{3+}$ complexes[202], the decolorization of the orange solution after final catalysis was attributed to the conversion of all Ce^{4+}-ions to Ce^{3+}-ions, while a large excess of Ce^{4+}-ions seem to turn the color back to orange-yellow. However, the change in the pH value from pH 1 to pH 7 was unexpected, since both solutions should generate large amounts of hydrogen ions (H^+) combined with the production of molecular oxygen in the presence of a suitable redox catalyst. Finding a possible explanation for this different behaviour was quite difficult since mass spectra recorded for both solutions were superimposed by signals belonging to CAN and gave no experimental evidence for the formation of ruthenium species. Hence, it was speculated that, if CAN concentration was high enough, complex interactions between Ce^{3+}-, Ce^{4+}-ions and *in-situ* formed ruthenium species must lead to an increase of the pH. A closer look at the

literature[193] revealed that photochemical water oxidation experiments under neutral conditions led to a drop of the pH value from pH 7 to pH 3, which was supposed to be responsible for the termination of water oxidation. They postulated that with increasing acidity, the onset potential of the catalytic curve increased, which led to the deactivation of the catalytic system. Thus, similar might explain the rapid termination of the oxidation reaction in decolorized reaction solutions.

Figure 118. Analysis of pH after CAN-driven catalysis.

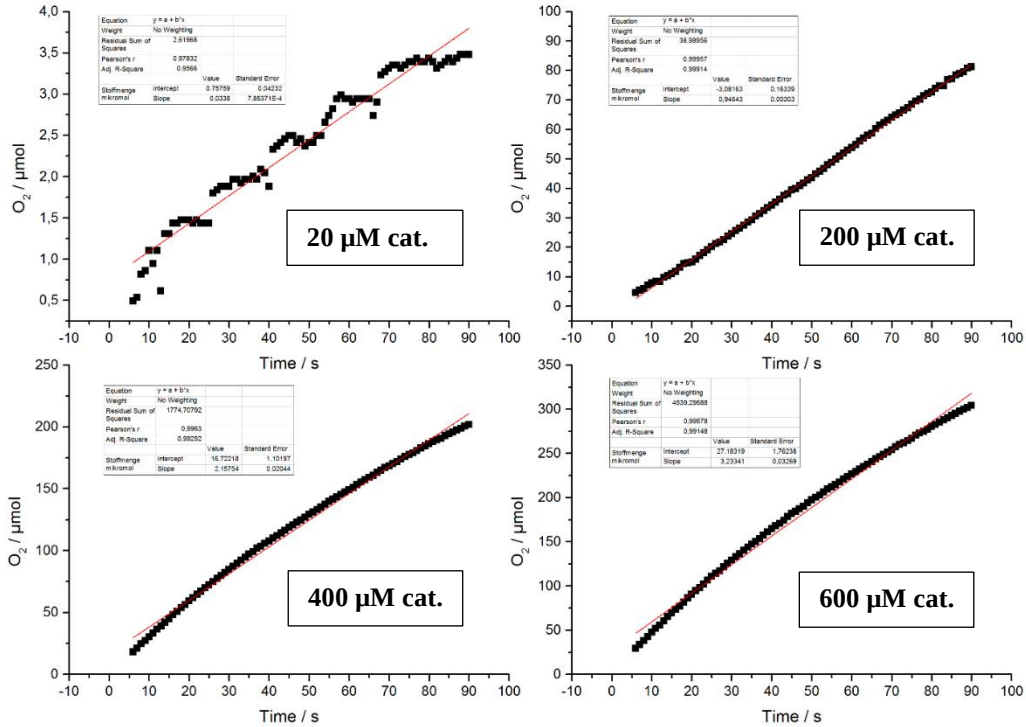

Figure 119. Oxygen evolution curves between 6-90 s after injection of K1 at different catalyst loadings (20-600 µM) and the corresponding linear regression fits.

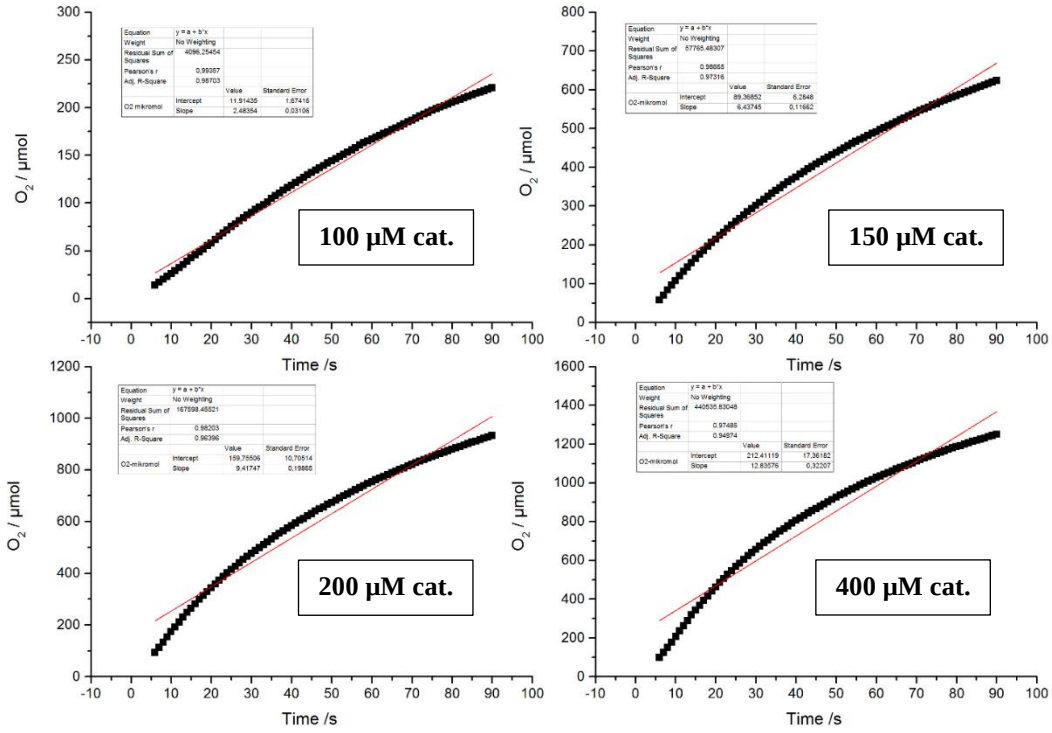

Figure 120. Oxygen evolution curves between 6-90 s after injection of K4 at different catalyst loadings (100-400 µM) and the corresponding linear regression fits.

The initial rates for K4 show a linear dependence on catalyst concentration. The slope of ~1.1 indicates that K4 has a higher propensity to proceed *via* a mononuclear water nucleophilic attack reaction for the O-O bond formation rather than a bimolecular coupling pathway. By comparison, the slope value of K1 is ~1.4, being higher than that of K4. This result implies that K1 follows not a normal water nucleophilic attack pathway. Hence, a mechanistic switch from WNA to I2M cannot be excluded for the case of K1 at this point.

9.1.1.3 Theoretical studies by DFT.

Density functional theory (DFT) calculations is useful to understand the catalytic behaviors of Ru-bda complexes. The purpose of the theoretical study here is to explore the configurations of intermediates and energetics of unit reactions involved in the catalytic water oxidation pathway. In order to describe the surroundings of the aqueous medium accurately, an explicit water molecule was included as an acceptor of hydrogen bonding for each polar hydrogen (aqua or hydroxyl group) when the geometry of ruthenium intermediates was simulated. Detailed information on theoretical calculations are given in Chapter 12. For calculations, catalyst K4 was renamed as K2.

In Figure 121, simulated structures of the ruthenium complexes K1 and K2 are shown, while Figure 122 represents the corresponding molecular orbital energy diagrams. For clarity, the divalent state was also optimized for the reference compound Ru-bda. Considering that computational studies on ruthenium species formed in the initial step of water oxidation has only been poorly explored, calculations on the Ru(II) state of K1 and K2 were essential since aqueous solutions containing the respective catalyst revealed significant changes in their optical properties. Thus, slight differences in orbital energies can drastically influence the water oxidation ability of these catalysts and can help understand the mechanisms responsible for oxygen release.

As introduced at the beginning of this thesis, the increase of the π-accepting character by adding electron-withdrawing groups at the meta- and para-positions of the original bda-ligand is expected to lower both π* and π-orbital energies. Initial calculations on the splitting energies of the d-orbitals show that both octahedral ruthenium complexes show similar π and π* orbital energies (Figure 121). By comparison, the π-orbitals of the reference complex Ru-bda, which is structurally very similar to K1 and K2, are remarkably higher in energy. Thus, the electronic influence of the functional groups attached to the bda ligand in the π-extended ruthenium catalysts appear to play a major role in decreasing the LUMO energy level. Considering that ruthenium WOCs exhibiting stronger π-acceptor capabilities are able to switch the water oxidation mechanism from I2M to WNA, the initial results for the divalent states give first hints about potential mechanistic processes involved in the early stages of water oxidation. Knowing that Ru-bda operates *via* a bimolecular pathway (I2M), the lowering of the LUMO levels in K1 and K2 could shift the water oxidation mechanism towards WNA.

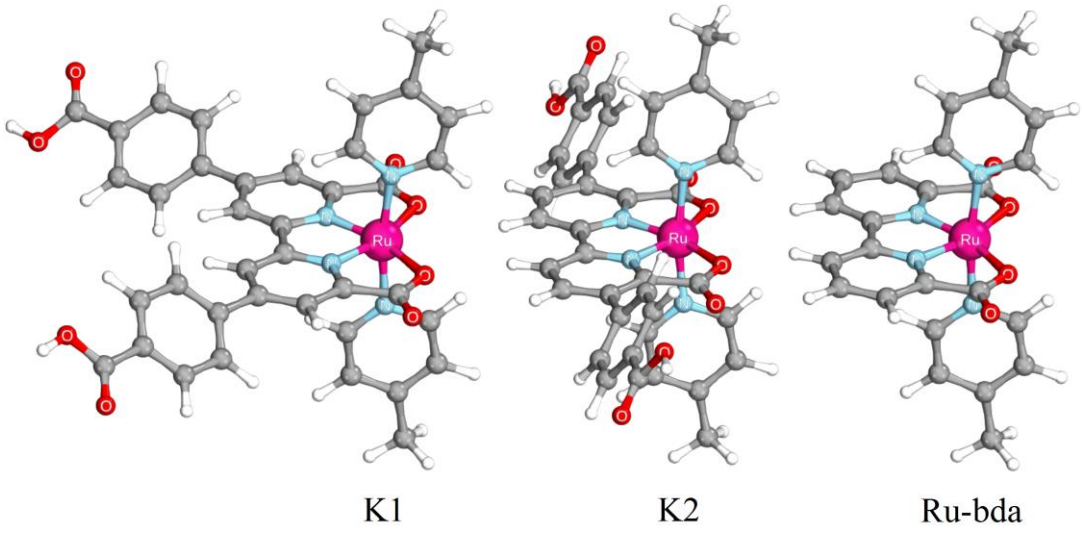

Figure 120. Optimized structures of ruthenium complexes K1, K2 and Ru-bda in the oxidation state +2.

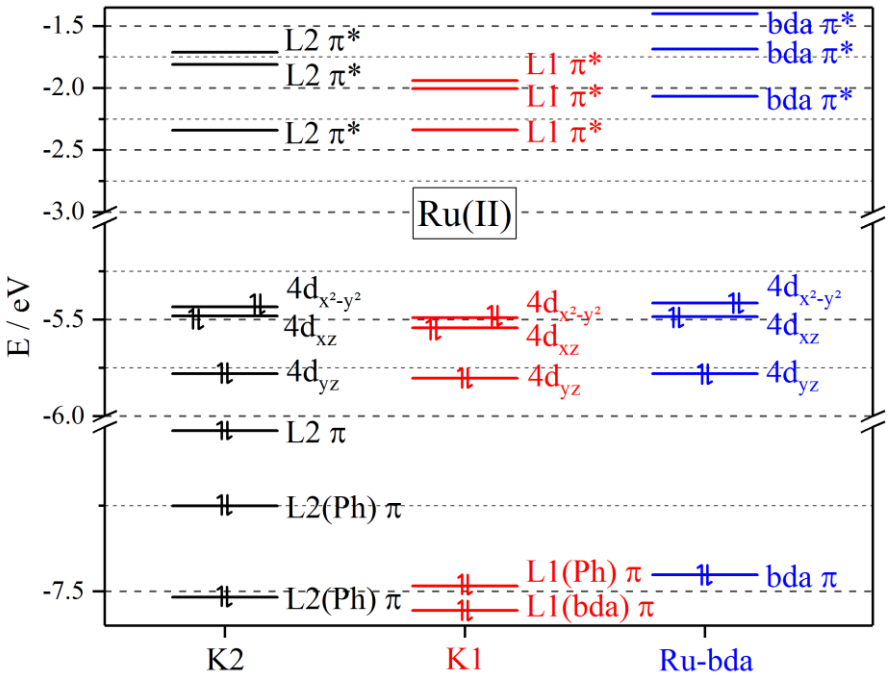

Figure 121. Schematic energy diagram of K1, K2 and Ru-bda in the oxidation state +2.

Further oxidation reactions of K1 and K2 undergoing PCET processes at ~1.23 V *versus* NHE result in the formation of the key $[Ru^{V}=O]^{+}$-species. Although ruthenium WOCs can operate *via* different catalytic paths, depending on the properties of the complex, they all have in common that they generate the reaction intermediate $Ru^{V}=O$. Once this state is reached, O-O bond formation could occur at the Ru-O intermediate by the water nucleophilic attack path. Hence, the electronic structures of the corresponding $Ru^{V}=O$ species were studied by density function theory calculation and the results are shown in Figure 122 and Figure 123, representing the simulated structures of the ruthenium complexes of K1 and K2 in the oxidation state +5 and the corresponding molecular orbital energy diagrams, respectively.

According to DFT calculations, the ligand orbital of K2 is higher in energy than the d-orbital of both, K1 and Ru-bda. This was very interesting to observe since there was no significant difference in electronic properties of K1 and K2 in the Ru^{II} state, while the electronic structure of the active Ru^{V} species appears to control the process of oxygen release. The catalytic performance of K2 is much worse that that of the linear catalyst K1, while kinetic measurements reveal that K2 catalyzes the O-O bond formation through not a normal water nucleophilic attack pathway. Even though no plausible information can be deducted from the results of the energy levels, they show that the geometrical arrangement of the surrounding ligands have a certain influence on the mechanistic route of the catalytic cycle.

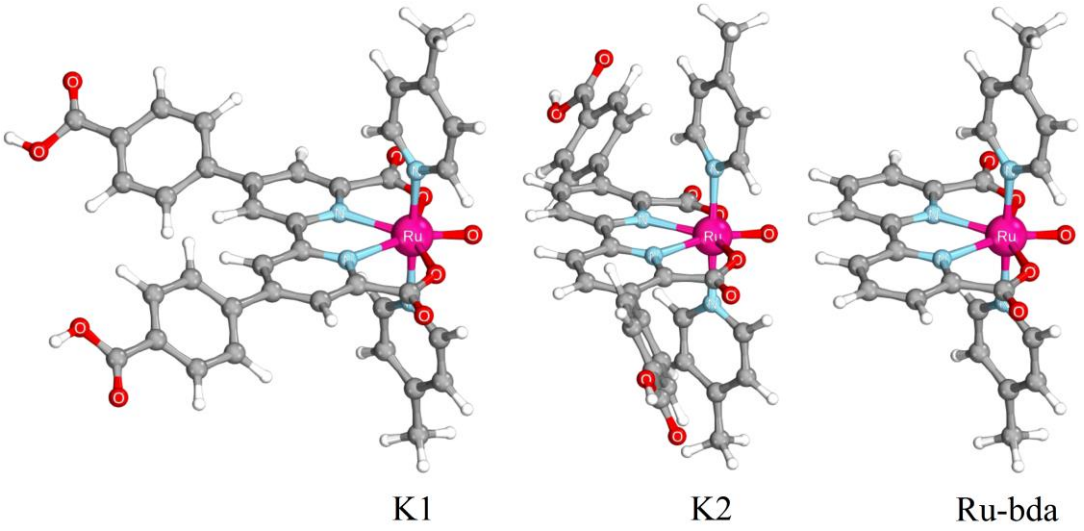

Figure 122. Optimized structures of ruthenium complexes K1, K2 and Ru-bda in the oxidation state +5.

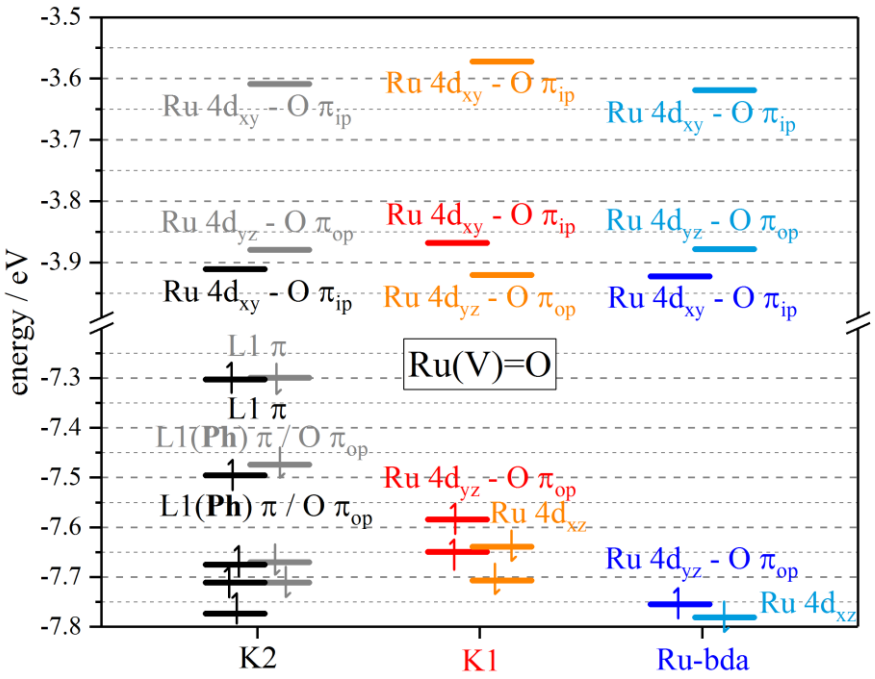

Figure 123. Schematic energy diagram of K1, K2 and Ru-bda in the oxidation state +5.

Hence, the question is why the Ru-bda preferable undergoes the radical bimolecular pathway while most of other Ru complexes *via* the WNA pathway. There is a general agreement that the tendency of a catalyst to follow one of two possible reaction paths is mainly determined by the radical character on the O atom of Ru^{V}=O. According to this, catalysts which favour the I2M pathway exhibit LUMO energy being not too close to the HOMO of the substrate water ($HOMO_{water}$ = -8.16 eV)[203], while the opposite trend is observed for catalysts preferring the WNA pathway: low spin density on the O atom and a low LUMO level of the Ru^{V}=O. However,

this could not be confirmed in the case of K1 and K2. Analysis of the spin density located at the oxygen atom of Ru^{V}=O of K1, K2 and Ru-bda revealed that the spin density of all three systems were always similar to each other, as shown in Table 12. For that reason, activation energies for the WNA barrier were calculated with systems, in which the terminal carboxylic acid groups were replaced or even totally removed in order to study the inductive withdrawing effect on the reaction kinetics. Considering that energy transition states reached during the chemical process of water oxidation are associated with the activation barriers or activation energies, DFT data give information about the general preference of a catalytic system to one of the possible mechanisms.

Table 12. Calculation of the spin population by the method of Loewdin.

	Ru	**O**
K1	0,476201	0,541854
K2	0,477128	0,546768
K1-DC	0,475779	0,542137
K2-DC	0,476361	0,547544
K1-COOH	0,476778	0,541121
K2-COOH	0,475915	0,548542
Ru-bda	0,48347	0,538818
K10	0,478281	0,539975

The corresponding calculated transition state energies for the WNA barrier are presented in Figure 124. A comparison between K1 and K2 revealed that the activation barrier for the water nucleophilic attack was significantly lower for the carboxylated linear ruthenium complex than for its angled analogue K2. According to DFT, K1 produced an activation energy of 81,75 kJ/mol, while extending the π-conjugated system of the bipyridine at the 5,5'-positions appear to reduce the overall reorganization energy of forming the transition state enabling a lower activation barrier of 67,84 kJ/mol for the water nucleophilic attack. By comparison, the reference complex Ru-bda exhibited an activation energy of 83,50 kJ/mol, which is quite

similar to that of K1. These results are in good agreement with kinetic water oxidation experiements performed with K1, which resulted in a reaction order of ~1.4. This implies that the catalytic process of K1 does not follow neither a normal first-order nor a second-order reaction and thus suggests that catalyst K1 possibly undergoes both reaction paths, the bimolecular coupling and the water nucleophilic attack reaction. Interestingly, the WNA path was found to be energetically less favourable when the terminal carboxylic acid groups were completely removed in K2 (87,22 kJ/mol *vs*. 67,84 kJ/mol). This finding was remarkable since K1-DC, differing only in the geometrical arrangement of the phenyl rings, resulted in a lower WNA activation barrier, while there was no significant difference in energy compared to its carboxylated analogue K1 (81,86 kJ/mol *vs*. 81,75 kJ/mol).

From these results, it could be concluded that full removal of the carboxylic acid groups generally end up in higher transition state energies, showing that the incorporation of electron-withdrawing groups was essential to reduce the barrier for WNA by decreasing the redox potentials, especially of the high-valent ruthenium states as shown in Table 5, which are the key steps in the the O-O bond formation.

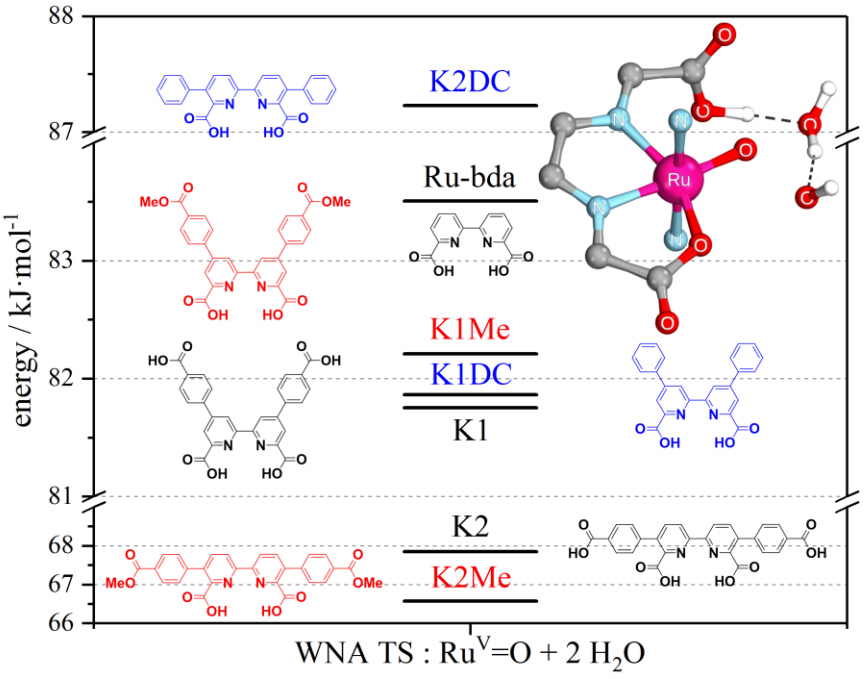

Figure 124. WNA-Transition state energies of target complexes.

More interestingly, the same complexes containing ester instead of carboxylic acid groups showed opposite trends in their behaviour. While the linear catalyst K2-Me gave an activation energy of 66,56 kJ/mol and thus showed a slightly higher preference for the WNA mechanism compared to its carboxylated analogue K2 (66,56 kJ/mol *vs*. 67,84 kJ/mol), K1-Me produced

an activation energy of 82,20 kJ/mol which evidently seems to favor the same mechanism as Ru-bda. In general, the energy values within the linear family differ strongly depending on the substituents attach to the linear ligand backbone, while K1 and its derivatives show only minimal differences in energy. Then, another question comes: what is the reason for the change of the catalytic processes, is it the addition of the terminal phenyl rings at different positions of the original bda-ligand since this was the only difference in the structures of K1 and K2 which could influence the rigidity and the steric hindrance within the molecules. Therefore, DFT calculations were performed on optimized structures of catalyst K10.

Table 13. HOMO-LUMO energies of target complexes.

Energy [eV]	**K2**	**K1**	**Ru-bda**	**K2-DC**	**K1-DC**	**K2-Me**	**K1-Me**	**K10**
HOMO	-8,10	-8,63	-8,53	-7,74	-8,33	-8,02	-8,55	-8,81
LUMO	-2,12	-2,24	-2,01	-1,86	-1,86	-2,07	-2,17	-2,60
HOMO -LUMO	5,97	6,39	6,57	5,88	6,46	5,95	6,37	6,20

Table 14. Calculated energies of WNA transition states.

	K2	**K1**	**Ru-bda**	**K2-DC**	**K1-DC**	**K2-Me**	**K1-Me**	**K10**
Educt	-2454,1	-2454,1	-1615,4	-2077,1	-2077,2	-2532,6	-2532,6	-1992,3
WNA TS	-2606,8	-2606,8	-1768,2	-2229,9	-2229,9	-2685,4	-2685,4	-2145,1
DE /Eh	0,02	0,03	0,03	0,03	0,03	0,02	0,03	0,02
/ eV	0,70	0,84	0,86	0,90	0,84	0,68	0,85	0,65
/kcalmol^{-1}	16,21	19,53	19,95	20,84	19,56	15,91	19,64	15,07
/kJmol^{-1}	67,84	81,75	83,50	87,22	81,86	66,56	82,20	63,07

According to DFT, the activation energy of K10 was calculated as 63,07 kJ/mol and thus has the lowest activation barrier for the WNA mechanism among all ruthenium catalysts listed in Table 14. Compared to catalyst K1, there is a significant difference in energy of 20 kJ/mol (63,07 kJ/mol *vs*. 81,75 kJ/mol). Due to the fact that kinetic studies on K2 revealed a first-order reaction and Ru-bda follows a bimolecular coupling reaction, the activation barrier of K10 strongly suggests a WNA pathway, which is in good line with the proposed path of catalyst K14 (or Ru-2br), also possessing electron-withdrawing groups on the bda-ligand.

From these data, it can be concluded that *(i)* even the introduction of carboxylic acid groups into Ru-bda leads to a decrease of the activation energy from 83,50 kJ/mol to 63,07 kJ/mol, thus switching the O-O bond formation pathway from I2M toward WNA and *(ii)* there is a correlation between the geometrical arrangement of the surrounding substituents and the catalytic performance. It is believed that K1 and K2 (K4) predominantly trigger O_2 evolution *via* a water nucleophilic attack on a Ru^{V}=O intermediate. This is primarily due to the ever present water in which the catalysts are dissolved that is supposed to suppress the interaction of two Ru-O radicals. Nevertheless, parts of K1 molecules are believed to follow a bimolecular I2M reaction, as evident from kinetic measurements discussed before.

9.1.2 Oxygen evolution by K7, K8, K10-K13.

As already mentioned, theoretical investigations revealed that modification of catalyst Ru-bda at the 4,4'-positions by carboxylic acid groups drastically influenced the activation barrier towards WNA. This was studied by oxygen evolution experiments. To ensure data comparability amongst all complexes, the catalytic conditions remained the same $[(NH_4)_2[Ce^{IV}(NO_3)_6]$ as oxidant (~5000 equiv.), HOTf (trifluoromethanesulfonic acid, 14 mL, pH 1), [catalyst] = 2.2 x 10^{-4} M]. The resulting plots of oxygen evolution experiments are presented in Figure 125 and Figure 127.

As evident from the O_2 release curves, all complexes show high catalytic performance within the first five minutes of water oxidation as indicated by the fast growth rate. However, this is abruptly followed by a slow phase into a steady state. Again, in some cases, the deactivation of the catalyst goes hand in hand with the simultaneous bleaching of the orange cerium solution, indicating that all cerium(IV) was consumed, while the catalyst was presumed to be still active (Figure 126). After a second addition of cerium(IV) to the colorless solution, oxygen evolution was repeated, supporting the idea that the turnover numbers are limited by the amount of cerium(IV). To evaluate the highest catalyst durability, the concentration of the respective catalysts, K7 and K8, was decreased, while maintaining the amount of oxidant. Due to the fact

that no starting complex could be isolated at the end of the catalytic reaction, catalyst degradation was supposed to be the origin of performance decay. The resulting TON and TOF values are summarized in Table 15.

By contrast, the isoquinoline substituted catalysts show better catalytic stability than the picoline analogs, which decreases in the order K8 > K11 > K13, being in total agreement with their catalytic electrochemical catalytic current. The, in general, better catalytic activity of the isoquinoline catalyst family is due to π-stacking interactions between two axial isoquinolines, which are known to reduce the barrier for the O-O bond formation.

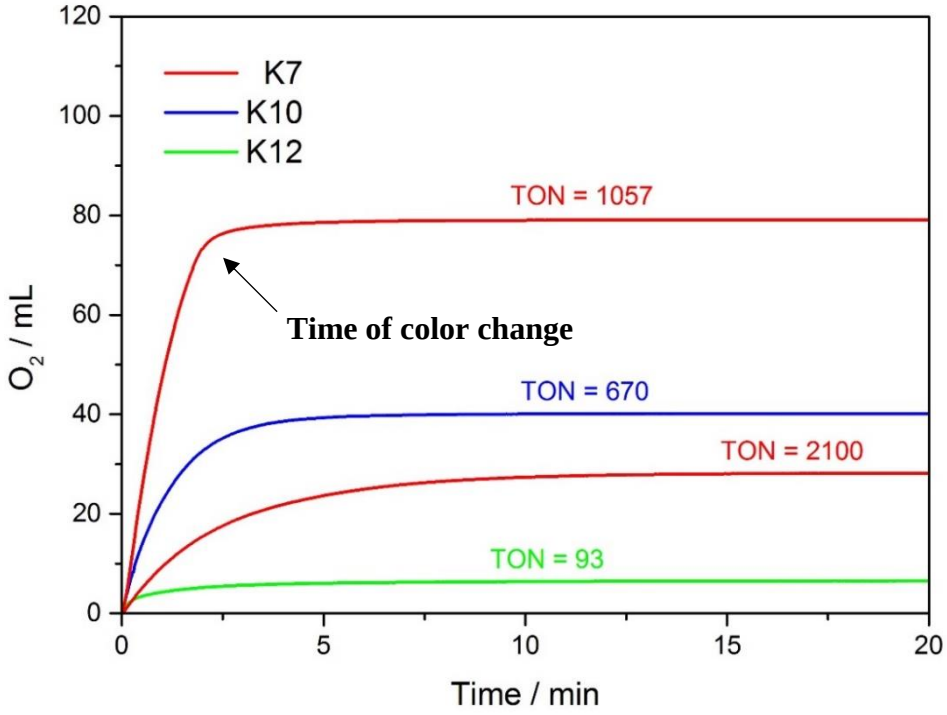

Figure 125. Plots of oxygen evolution with K7, K10 and K12 (10^{-4} M). *Conditions: 0.1 M HOTf (14 mL) containing CAN (~ 5000 eq.) at 25 °C. [Cat.] is varied depending on the color of the cerium(IV) solution.*

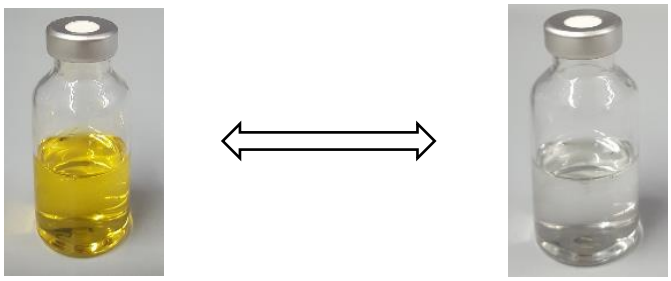

Figure 126. Color change after final catalysis depending on [CAN].

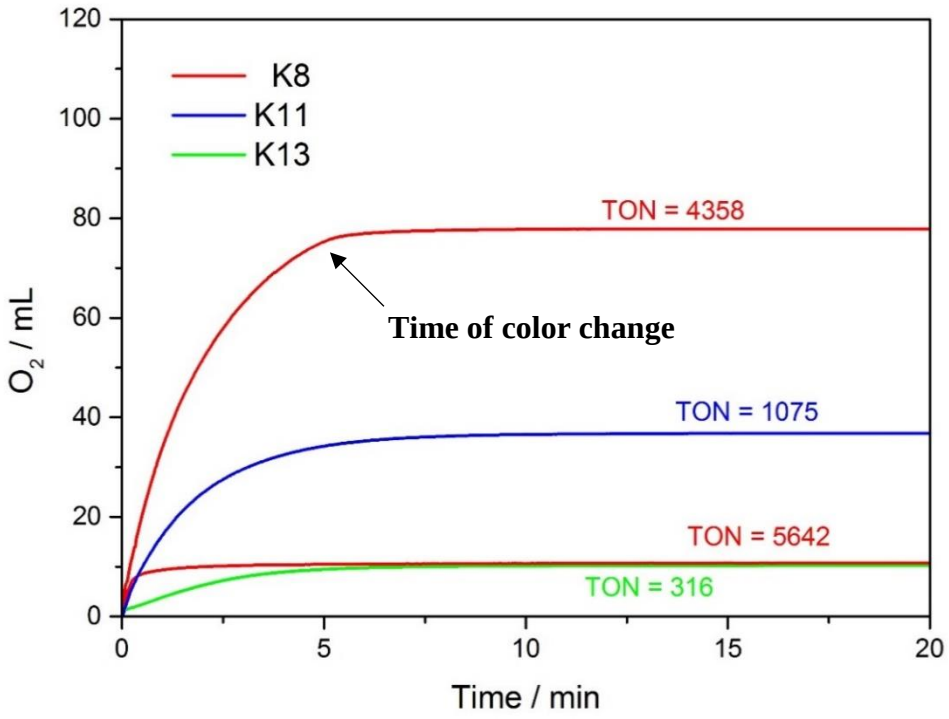

Figure 127. Plots of oxygen evolution with K8, K11 and K13 (10^{-4} M). *Conditions: 0.1 M HOTf (14 mL) containing CAN (~ 5000 eq.) at 25 °C. [Cat.] is varied depending on the color of the cerium(IV) solution.*

Moreover, it has to be noted that the catalytic activity of the -COOH subtitiuted isoquinoline complexes K11 and K13 are nearly identical, while K8 exhibits a remarkable TOF of 162 s^{-1} under the same experimental conditions. Considering that the stability of a complex is measured in terms of its turnover number, the increase in stability upon replacement of the ligands picoline by the more aromatic isoquinoline highlights the robustness of these catalysts in oxidative environment.

Within the picoline family, K7 displays the best catalytic performance with a TOF of 13 s^{-1}, while the TOF of K10 is two times higher than that obtained for K12 (9.09 s^{-1} *vs.* 4.88 s^{-1}). Due to the fact that the geometrical arrangement of the carboxylic acid moieties in K10 and K12 is the only structural difference between these catalysts, the lower catalytic activity of K12 probably indicates a potential stabilization of the ruthenium peroxide species due to H-bonding interactions between the neighboring carboxylic acid groups or the incoming water molecule.

Table 15. TON and TOF values calculated for K7, K8, K10-K15.[a]

Complex	TON_{max} O_2	TOF_{max} O_2 [s^{-1}]
K7	2105	13.0
K10	670	9.09
K12	94	4.88
K14	315	3.54
K8	5743	162
K11	1075	14.5
K13	316	19.9
K15	700	4.99
Ru-bda[b]	2010	19-32
Ru-isoq[b]	8360	236-303

[a] Values calculated according to *pV = nRT* and *TON / time per unit*. [b] values taken from [73].

Interestingly, the dibromo catalysts K14 and K15 bearing either axially bounded 4-picoline or isoquinoline ligands show remarkable better stability compared to the -COOH 3,3'-substituted complexes K12 and K13, while a slight shift of the substituent position from 3,3' to 4,4' results in a dramatic change of the catalytic properties. Here, catalysts K10 and K11 show higher catalytic activity and better catalytic stability than their bromo-substituted analogs K14 and K15 (Figure 128). This finding confirms the initial assumption that molecular interactions between two neighboring substituents can be crucial in terms of developing stable and active catalytic water oxidation systems.

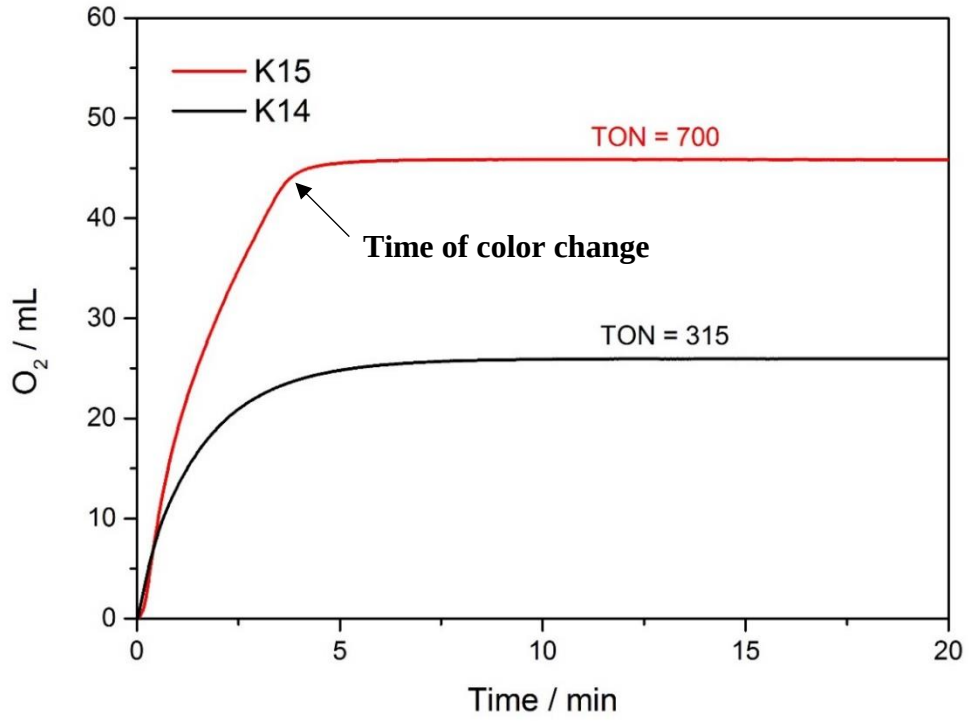

Figure 128. Plots of oxygen evolution with K14 and K15 (10^{-4} M). *Conditions: 0.1 M HOTf (14 mL) containing CAN (~ 5000 eq.) at 25 °C.*

In summary, the results show that replacing the H-atoms of the Ru-bda catalyst in general lead to the formation of less efficient ruthenium WOCs. Nevertheless, compared to analogous charge-neutral [Ru-bda]-type WOCs known to date which only operate with the use of co-solvents, these values are significantly greater and can be optimized by variation of the catalyst concentration.

The catalytic properties of K10 are in good agreement with the DFT results, which suggested that K10 is more reactive than catalyst K2 due to its lower WNA energy barrier (63,07 kJ/mol *vs*. 67,84 kJ/mol). This was confirmed by oxygen evolution experiments, showing that K10 was better in stability and higher in activity (670 *vs.* 494, 9.09 s^{-1} *vs.* 6 s^{-1}).

For complexes K10, K12 and K14, it is proposed that the complex molecules react with the solvent water with which it collides much more frequently than with another complex (I2M) at high dilution, thus operating *via* the WNA path. Since it is assumed that the influence of the conjugation effect of isoquinoline is more pronounced than the electronic effects of substituents attached to the equatorial ligand backbone, the mechanism path of K11, K13 and K15 are believed to follow both reaction paths. Computational study on the mechanism of these catalysts are ongoing.

However, it has to be noted that differences in the measured catalyst performance are often specific to a given system, and results may be different in other systems. Particular emphasize

should be placed on the role of the catalyst concentration, since variation of [cat.] was generally found to result in improved catalytic properties. Thus, finding the optimum conditions of water oxidation catalysis is one major important part for defining the *'true'* TON and TOF values of a given catalyst system.

9.1.3 Oxygen evolution by Ru catalysts based on carboxamides.

The plots of oxygen evolution experiments of the complexes K16-K19 bearing the novel carboxamide ligands are shown in Figure 129. Initially, replacing the carboxyl groups by amide moieties should increase the stability of the complexes, thus avoiding dramatic catalyst degradation and enabling longer catalyst durability.

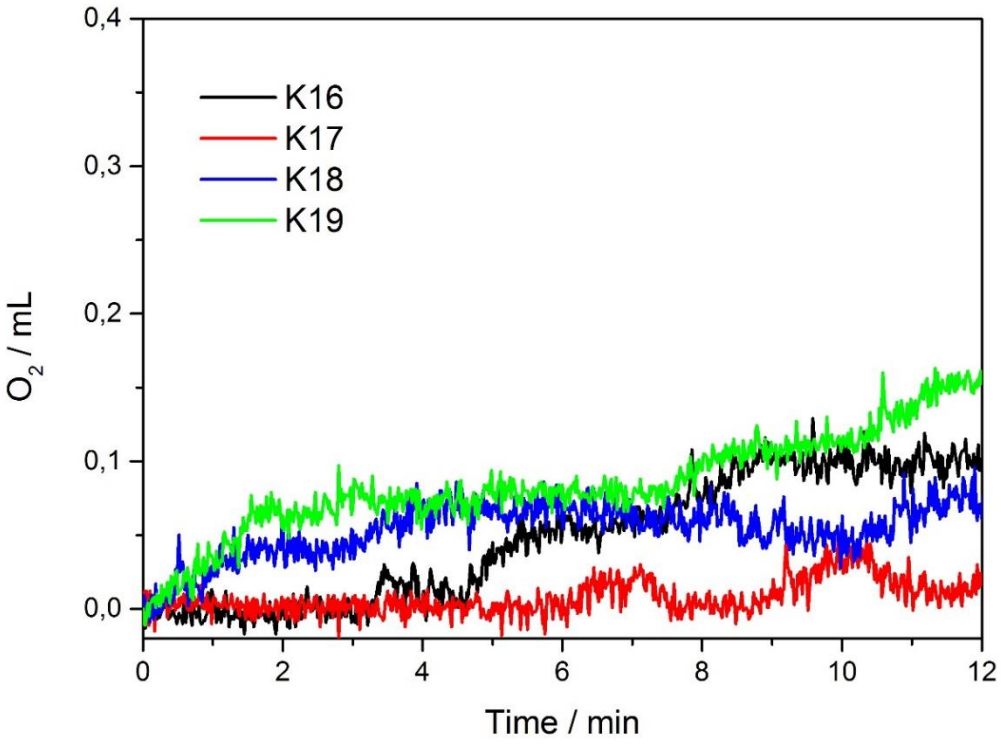

Figure 129. Plots of oxygen evolution with ruthenium complexes K16-K19.

Unfortuately, the oxygen production by these complexes are negligible low, the reason why TON and TOF values could not be calculated. Although they show a slight increase at the beginning of the cerium(IV)-induced water oxidation reaction, they are not able to compete with ruthenium complexes containing dangling carboxylic acid groups in their equatorial ligand backbone. Moreover, it is proposed that the sterical hindrance within the complexes permits the coordination of water molecules and thus slows down the release of oxygen. In summary, the synthesized ruthenium complexes appear to be unsuitable for the catalytic oxidation of water.

CHAPTER 10

MOF Synthesis and Immobilization – UiO68

10.1 Synthesis of MOF linker H_2tpdc-NH_2.

UiO-68-NH_2 was synthesized for the first time by the Working Group of P. Behrens[33] who reported the isolation and first X-ray crystal structure of a zirconium based metal-organic framework. In this work, the goal was to synthesize UiO-68-NH_2 according to the known procedure to fully describe the analytical properties which were not investigated by BEHRENS et al. in 2010.

As shown in Figure 130, the MOF linker H_2tpdc–NH_2 was synthesized in two steps from 2,5-dibromaniline and 4-(methoxycarbonyl)-phenylboronic acid by a palladium-catalyzed Suzuki-Miyaura cross-coupling, followed by saponification of the diester. Because of the sensivity of the palladium catalyst $Pd(PPh_3)_4$, the coupling was carried our under an argon atmosphere by using standard Schlenk techniques. The final product was isolated as a yellow solid, which was highly stable in air.

10.1.1 Characterization of MOF linker, H_2tpdc-NH_2.

Dimethyl-2'-amino-[1,1';4',1"-terphenyl]-4,4"-dicarboxylate could be successfully prepared in very high yields from the coupling of two molecules of boronic acid and the corresponding haloaromate under basic conditions using palladium acetate as catalyst. This reaction was also carried out in DMF using $Pd(PPh_3)_4$ as catalyst and potassium hexafluorophosphate as base. However, the esterified product was obtained in only 10 % yield in a prolonged reaction time of 3 days, while replacing the catalyst by $Pd_2(dba)_3$/tri-tert-butylphosphine gave no yield. Fortunately, the $Pd(OAc)_2$-catalyzed coupling reaction ended up in an excellent yield of 74 % after purification. The ^{1}H NMR of the final product is illustrated in Figure 131.

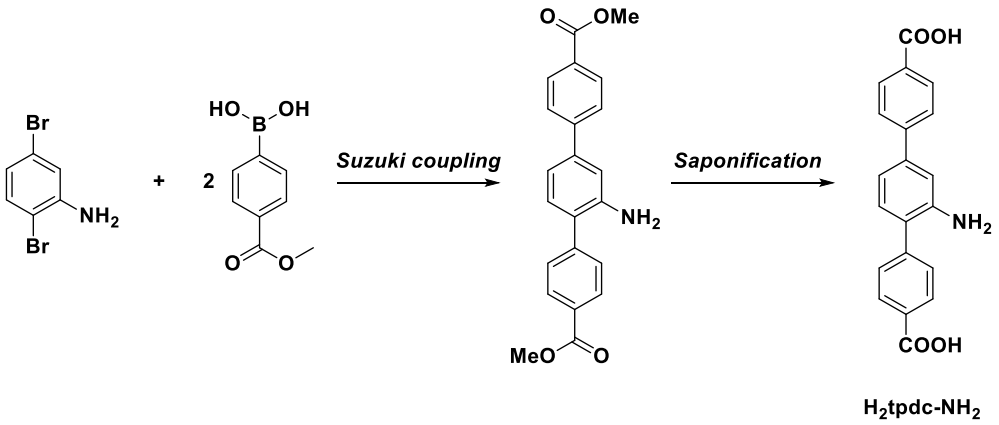

Figure 130. Schematic synthesis route of H_2tpdc preparation.

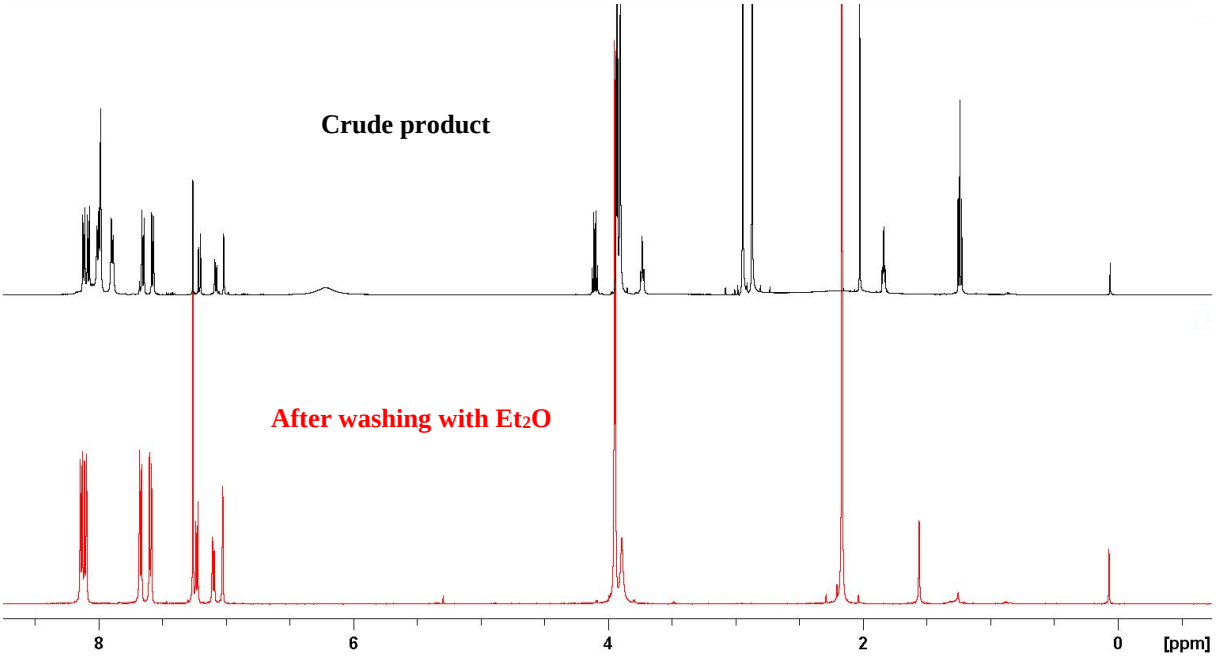

Figure 131. ^{1}H NMR of dimethyl 2'-amino-[1,1':4',1''-terphenyl]-4,4''-dicarboxylate in $CDCl_3$.

As can be gathered from the Figure 132, the product is symmetric resulting in four sets of doublets at 8.10 ppm, 8.14 ppm, 7.67 ppm and 7.59 ppm which can be assigned to two equivalents aromatic protons of the terminal phenyl rings. Because the protons attached to the phenl ring in the middle of the molecule are not chemically equivalent, three different signals can be observed in the range of 7 ppm. Considering that the molecule is not fully planar and the terminal groups can rotate around its own axis, the methyl groups of the ester functionality split up into two different sets of three equivalent protons at 3.94 ppm and 3.95 ppm. The amino group was found as broad singulett at around 4 ppm, typical chemical shift for amine protons.

The oxidation of the diester to 2‘-amino-[1,1’;4’,1”-terphenyl]-4,4”-dicarboxylic acid was performed with MeOH/KOH under acidic conditions. The product yield was maximized by optimized work-up techniques up to 92 %.

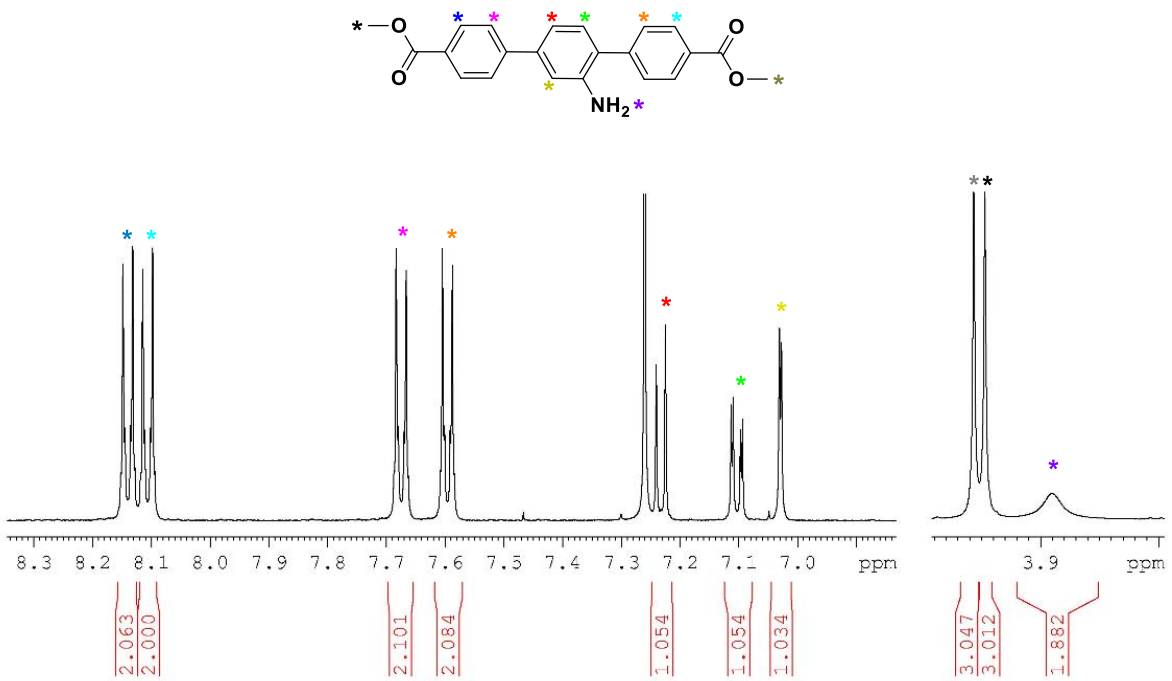

Figure 132. Correct nuclei correlations in dimethyl 2'-amino-[1,1':4',1"-terphenyl]-4,4"-dicarboxylate based on two-dimensional NMR spectra.

As shown in Figure 133, the methyl groups in the non-aromatic field of the ^{1}H spectrum have totally disappeared, instead, a broad signal occurs at 13 ppm with an integrated value of nearly two due to the presence of two carboxylic acid groups.

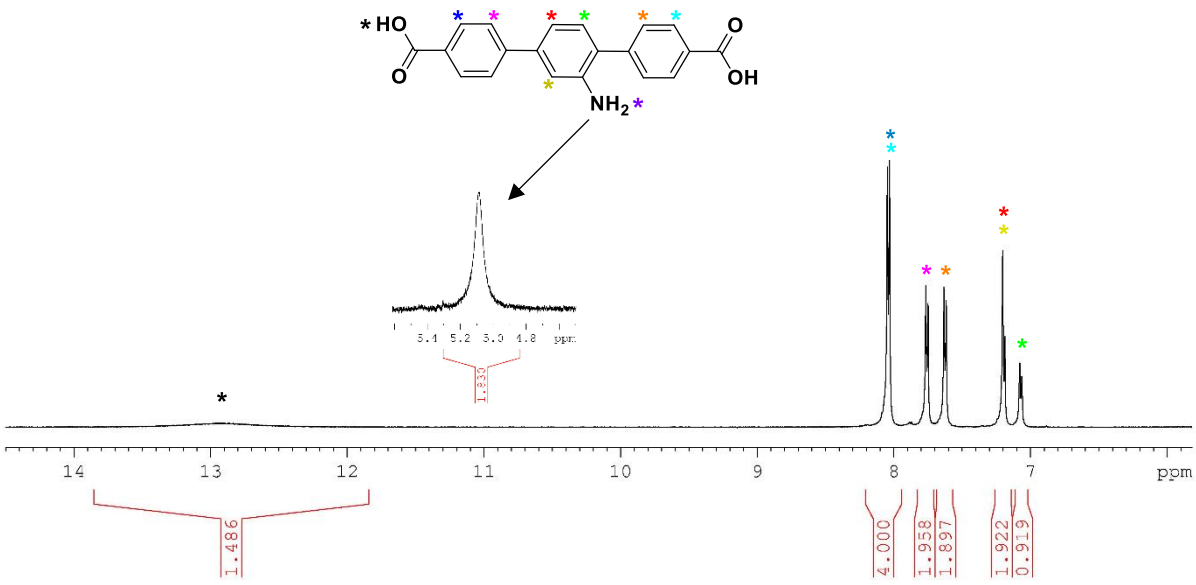

Figure 133. ^{1}H NMR of 2’-amino-[1,1’;4’,1”-terphenyl]-4,4”-dicarboxylic acid.

The structures have been also confirmed by ^{13}C NMR spectroscopy. The quaternary carbons of the carboxyl and ester groups appear at higher chemical shifts at around 170 ppm, which typically lie in the range of 160-180 ppm.

10.2 Synthesis of UiO-68 MOF.

The best results for surface area and pore properties were achieved when equimolar amounts of the reactants were mixed together and the MOF syntheses were performed at 70 °C for 72 h. As described in literature, benzoic acid was added in excess of 30 equivalents for modulating the size and morphology of the crystallites.

In a typical procedure, 0.06 g $ZrCl_4$ and 0.970 g benzoic acid were fully dissolved in DMF by sonicating. Then 0.102 g of the pre-prepared organic linker was added and treated by sonication, followed by the addition of 0.021 mL of water that proved to be essential for the formation of the well-ordered Zr-tpdc-NH_2. The reaction mixture was sealed and transferred into a pre-heated oil bath at 70 °C. After MOF precipitation was finished (Figure 134), the white solid was first washed with DMF, then with ethanol to remove all unreacted linker molecules or solvent molecules from the pores. All synthesized MOFs have been dried under high vacuum prior to chemical and physical analysis.

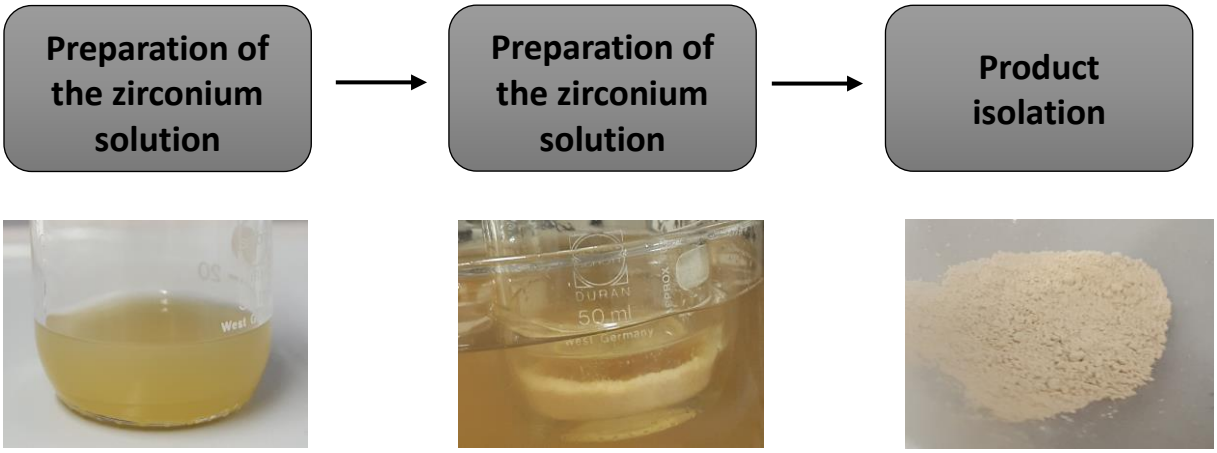

Figure 134. Reaction process of UiO-68-NH_2.

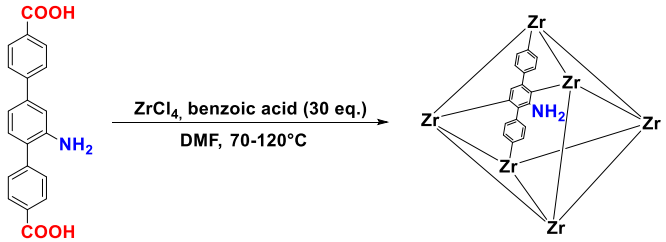

Figure 135. Schematic synthesis route of of UiO-68-NH_2.

10.2.1 Characterization of MOF products.

At the beginning of this research project on metal organic frameworks, the primary focus was rapidly synthesizing the amino-functionalized MOF UiO-68 based on well-known synthesis methods, followed by immobilization the ruthenium catalysts K1 and K4 within the MOF using either pre- or postsynthetic modifiication techniques. To realize this idea, much more MOF material is required, thus large-scale production of UiO-68 was of great importance. Alternatively, the synthesis can be repeated several times until the desired quantity has been obtained. Unfortunately, it quickly became clear that the re-synthesis of MOF products was fraught with many problems and pitfalls, which was due to following factors: the volume of the reaction vessel since decreasing or increasing the volume will affect the pressure inside the vessel, time of reaction, the volume of the solvent which can influence the rate of precipitation, and the cooling rate since fast cooling can produce amorphous MOF materials. Another factor considerably influencing the formation of the networks is due to the process conditions of MOF washing after final precipitation, which is needed to activate the MOF by removing guest molecules (DMF molecules, modulator, excess of organic linker) from all pores. Excess of modulator molecules containing polar functional groups can also act as bridging linkers and cause defects by strongly binding to the SBU's, while large amounts of solvent during the washing procedure can lead to a collapse of the network structure. In this context, the type of the washing solvent also plays an important role in determining the MOF quality, since solvents with low boiling points (acetone, THF, DCM, *n*-Hexan) will be more easily removed from the pores with less heat as compared with solvents with high boiling points (ethanol, DMF, toluene, MeCN), which thus reduces the probability of producing some defects within the pores and minimizes the impact of the destabilizing forces upon drying. Furthermore, the influence of the pressure and temperature on the stability of the MOF is enormous, since drying the final products either at atmospheric pressure, by heating or in vacuum is primarily correlated to destabilization and collapse of the resulting porous products. This structural damage can be observed due to a marked color change. Finally, well-ordered, highly porous MOF structures are often damaged by losing their excellent properties after long-term exposure to air, which limits their industrial large-scale use. All these factors mentioned above are interacting and thus cannot be controlled independently of each other.

For that reason, the first task was developing the simplest possible synthesis approaches for the preparation of UiO-68 by varying several experimental parameters in order to get a feel for a controllable MOF growth. In the most cases, a yellow to white product precipitated during the MOF synthesis. To analyze the quality of each product in terms of crystallinity and surface

properties, the obtained material had to be characterized and identified by MOF digestion, XRD and nitrogen adsorption.

In order to determine the optimal conditions of UiO-68-NH_2 preparation in this study, the volume of the solvent was varied from 45 to 100 mL, temperature was varied from 70 to 120 °C and the reaction time was varied in the range of 24 h to 6 days. The first experiments were conducted in a simple glass bottle (Schott flask) with a volume of 50 mL. Unlike organic polymers, MOFs are insoluble in any solvents. Therefore, all products were first characterized by MOF digestion to confirm the incorporation of the bridging ligand.

A typical NMR digest experiment of MOF material was performed by solving a small amount of the washed solid in a solution of CsF/D_2O/d_6-DMSO. Due to the high affinity of zirconium for fluoride ion, the bonds between inorganic zirconium nodes and organic carboxylic acid ligands are cleaved, which allows the detection of the bridging ligands in solution. Upon addition of an aqueous CsF solution to a white suspension of MOF UiO-68-NH_2 in d_6-DMSO, the color of the mixture instantly turns to a shiny yellow, which corresponds to the color of the free unbound MOF linker. In Figure 136, ^{1}H spectra recorded for MOFs from different synthesis approaches are presented in comparison.

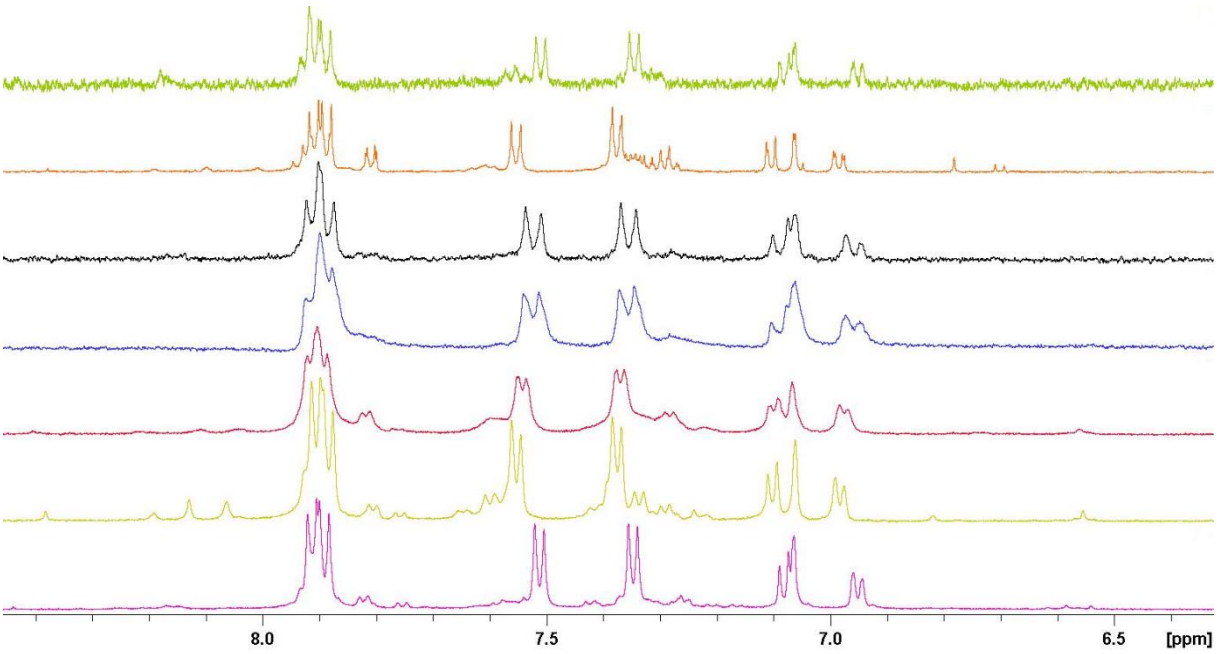

Figure 136. ^{1}H NMR spectra of different UiO-68-NH_2 MOF materials from NMR digestion.

As evident, the purity of the MOF products is strongly depending on the interaction of the experimental parameters during the synthesis and activation step. ^{1}H NMR integral analysis of spectra black, purple and blue revealed no changes in the structure of the linker molecules, while the rest of the spectra directly showed minimal additional signals within the aromatic

range, that could be attributed to contamination of the materials or defects in the framework and considered as main sources for pore-blocking as well as pure surface quality. In addition, it was found that these signals could not be removed by repeated washing, suggesting that they are strongly bounded to the MOF structure.

By comparison, a relatively pure spectra is presented in Figure 137. The spectrum obtained by digestion is in line with the spectrum of the pure ligand. Furthermore, the NMR shows that the MOF is free of guest molecules because no reaction solvent, in this case DMF, or modulator molecules were observed in the spectrum after washing the MOF several times with ethanol.

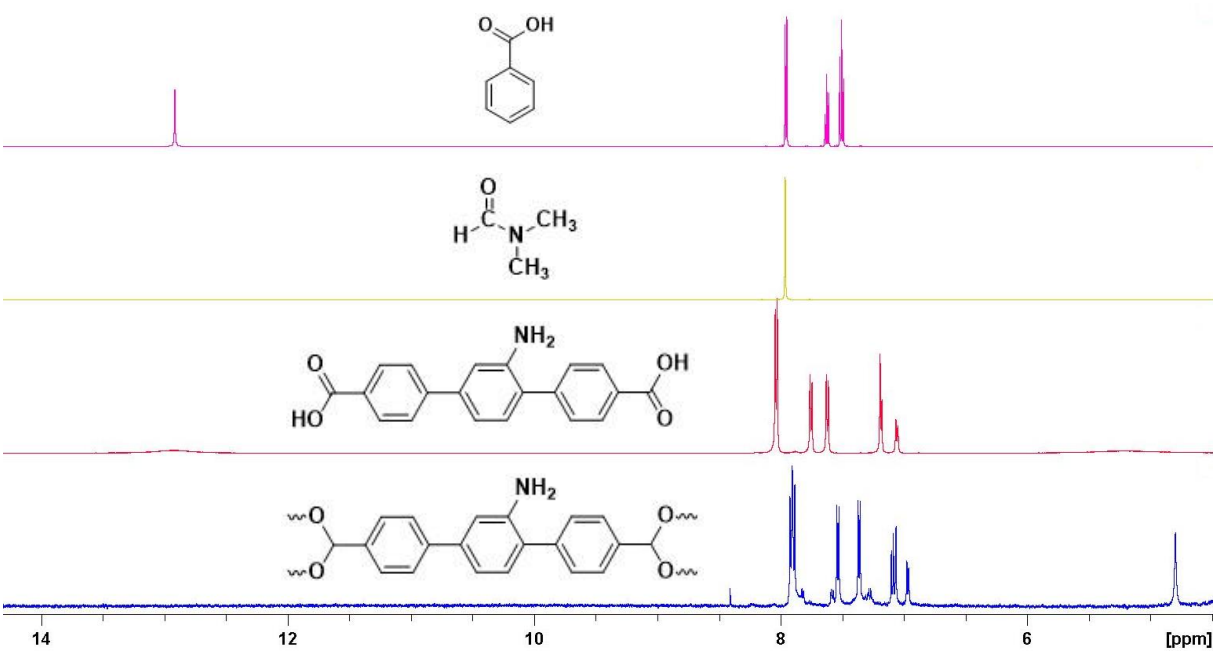

Figure 137. Characterization of UiO-68-NH_2 by MOF digestion. *The red spectrum represents the chemical shifts of unbound, free MOF linker molecules, while the blue ^1H spectrum was recorded after MOF digestion.*

The digestion method was used for each MOF sample, which offered a quick alternative to get information on the structure since bright peaks in the diffraction pattern as well as low specific surface ares generally referred to ^{1}H NMR spectra containing undefined peaks with any residual contamination.

Typically, the XRD pattern of porous materials show characteristic peaks with different intensity depending on the reaction parameters. In order to highlight this relation, MOF syntheses were carried out under varied experimental conditions.

First of all, the influence of the reaction temperature on the MOF product was investigated since most MOF syntheses were carried out overnight at one selected temperature. Thus, numerous synthetic attempts have been made at 70 °C and 120 °C while maintaining the principal

conditions as described at the beginning of this section. Following, the corresponding XRD spectra are presented in Figure 138 and Figure 139.

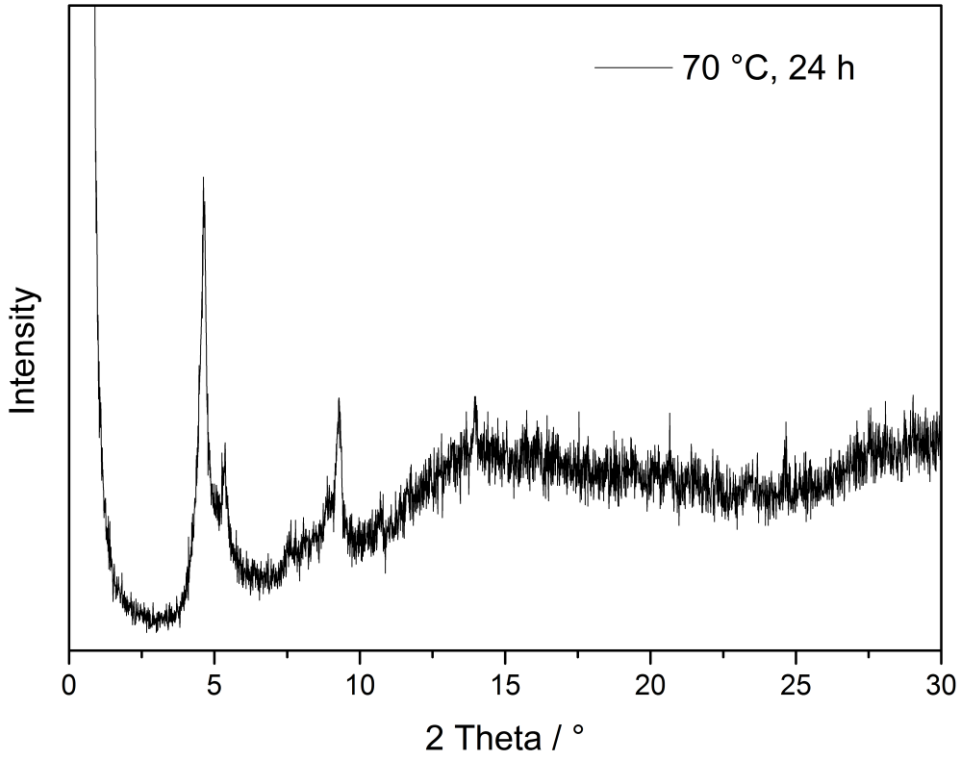

Figure 138. XRD spectrum of UiO-68-NH_2 obtained after 24 h at 70°C.

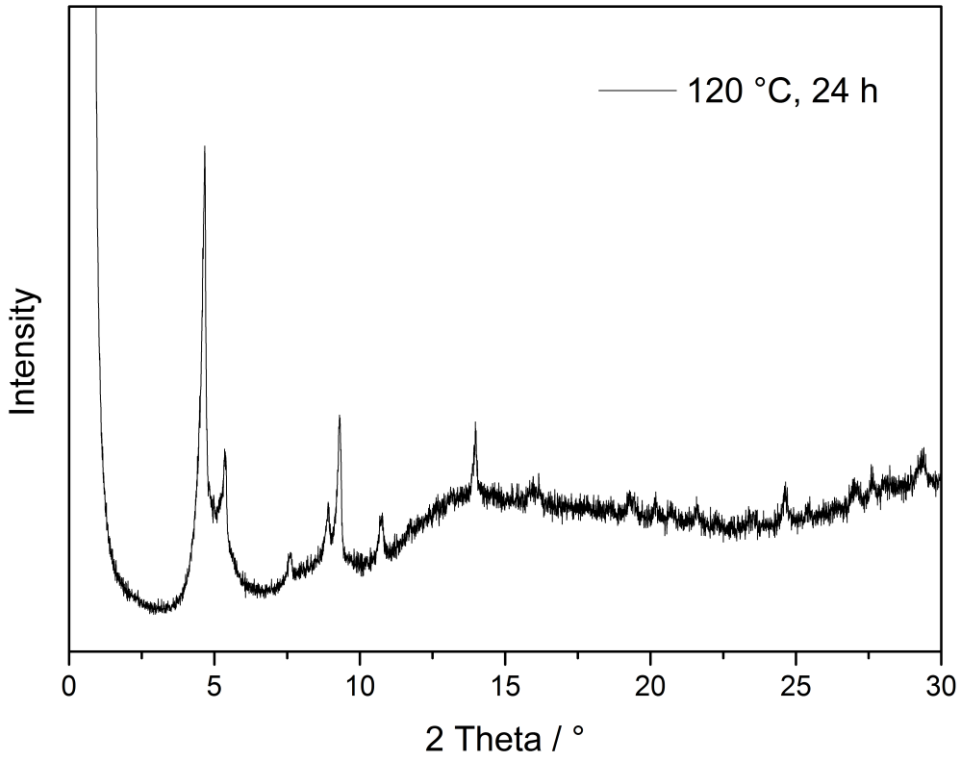

Figure 139. XRD spectrum of UiO-68-NH_2 obtained after 24 h at 120°C.

The initial results show that high temperatures at short reaction time seem to promote crystallinity. Both spectra display characteristic peaks at 2θ = 4.67°, 5.42° and 9.36°. A comparison with the calculated diffraction pattern of UiO-68 (Figure 140) reveal that a majority of reflexes disappear in the background noise from XRD pattern, which is mainly due to the amorphous nature of the samples. Although high temperatures are often preferred to increase the solubility of the reactants, the resulting fast crystallization from the reaction solution leads to the formation of irregular crystals with low internal surface areas.

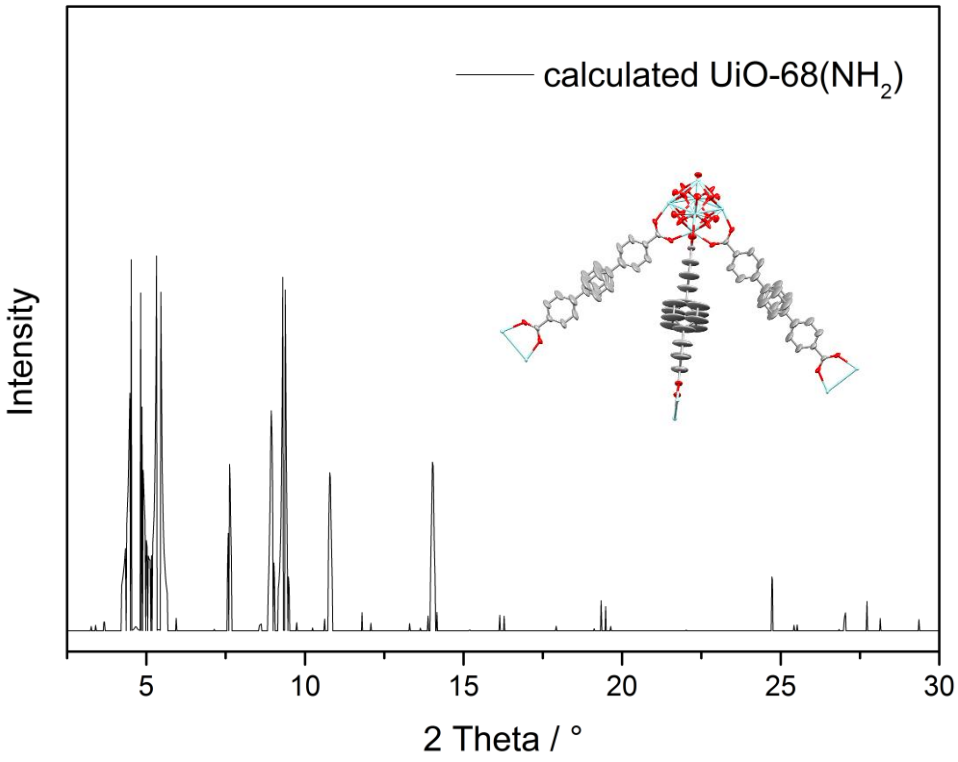

Figure 140. XRD spectrum of UiO-68-NH_2 obtained after 24 h at 120°C.

Hence, MOF syntheses were performed at low reaction temperature by varying the reaction time. The first experiment was conducted at 70 °C for 72 hours, the corresponding diffraction pattern is illustrated in Figure 141, while Figure 142 shows the XRD spectrum obtained when reaction time was increased up to 6 days. In addition, the XRDs were measured at different counting time and step size. The results are in good line with the observations before, proving that soft heating (70 °C) at longer reaction times (3 d to 6 d) significantly changed the crystalline state of UiO-68. Against this backdrop, it is not suprising that MOF precipitation after 24 h at 70 °C led to the formation of an amorphous solid with crystallinity. The overall intensity was found to increase with variation of counting time and step size. Furthermore, the intensity of the reflexes increased with longer reaction time, which is related to an increase in crystallinity.

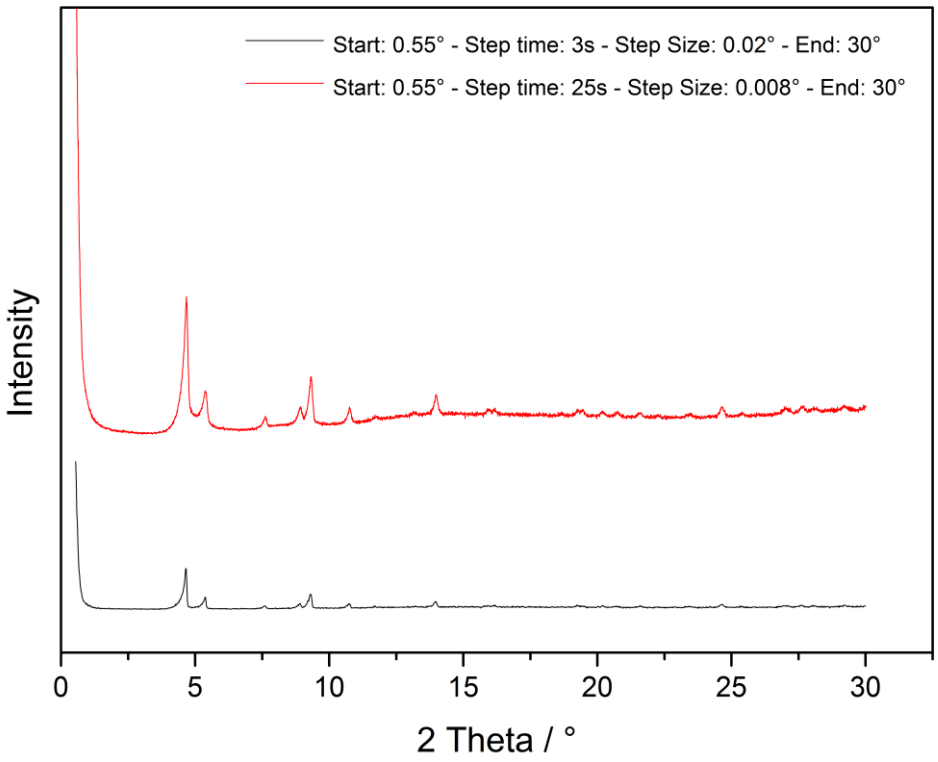

Figure 141. XRD spectra of UiO-68-NH_2 obtained after 3 days at 70°C.

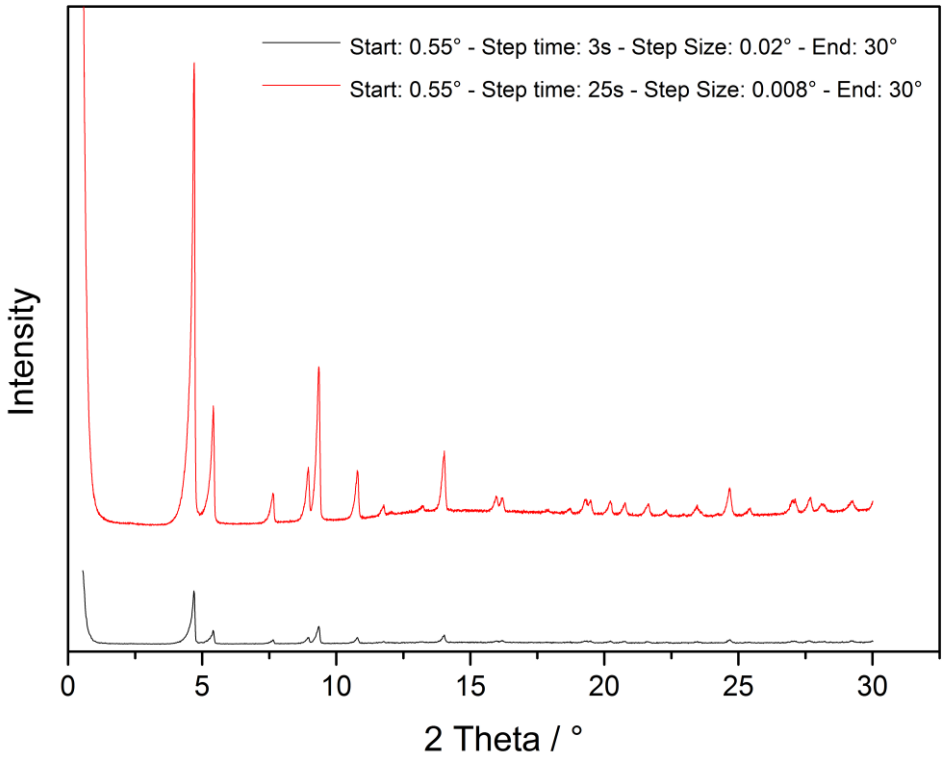

Figure 142. XRD spectra of UiO-68-NH_2 obtained after 6 days at 70°C.

Inspired by the diffraction pattern shown in Figure 142, several attempts have been made to improve the quality of this spectrum, while maintaining the temperature at 70 °C. Hence, further

investigations have been carried out on the effect of the reaction solvent volume, the corresponding XRD spectra are shown in Figure 143.

When the volume of the solvent was too large (20 mL, 24 mL), the process of crystallization of UiO-68(NH_2) was considerably slowed down, which was due to the low concentration of the reactants at high dilution. As a result, no precipitation was observed even after 72 h of reaction time. Upon increasing the temperature of the same sample to 120 °C, the MOF immediately crystallized within 24 h. Nevertheless, the XRD pattern shows only *'broad'* peaks which indicates the formation of a more amorphous material, but when the solvent volume was decreased to 12 mL and 10 mL, characteristic peaks with higher intensities could be obtained. Repeated experiments showed that best results in terms of XRD were achieved when using 12 mL of solvent volume instead of 10 mL due to the fact that increased concentration of reactants led to less solubility and therefore to an uncomplete conversion.

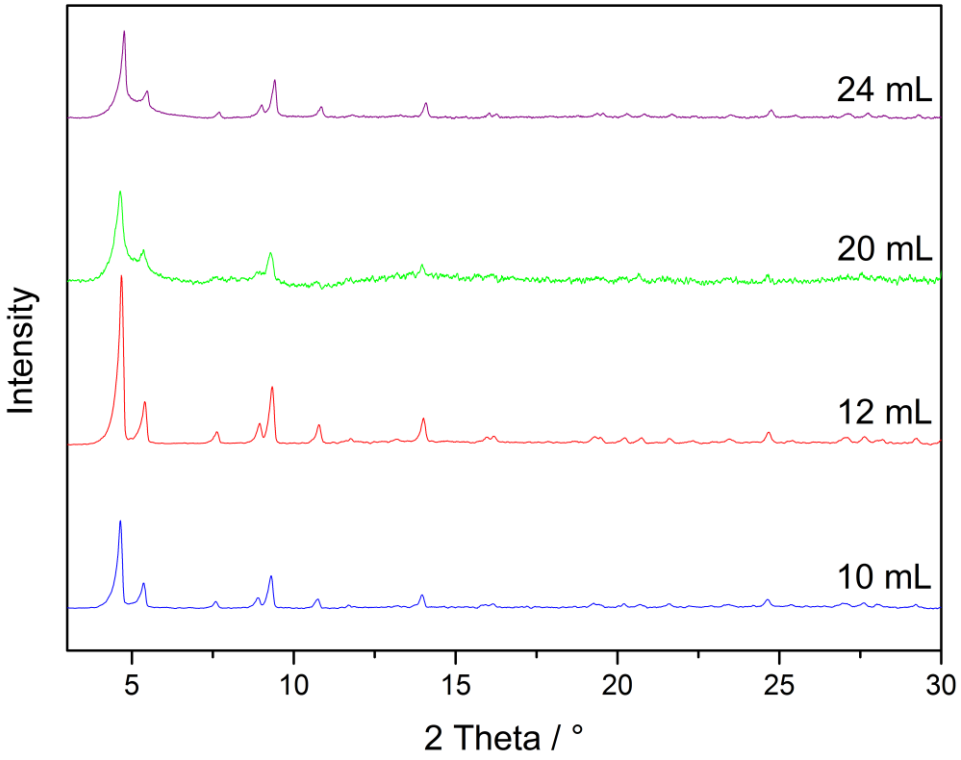

Figure 143. XRD spectra obtained by variation of the solvent volume.

The next step was to investigate the effect of the modulator. Inspired by the advantageous reported in literature, benzoic acid (BzOH) was used in the aforementioned syntheses as modulator. This is primarily due to its ability to reversibly bind to the zirconium nodes during MOF formation, which allows a controlled crystallization of the product. Although its precise role during synthesis is unknown, without BzOH more amorphous prodcuts were obtained.

Nevertheless, it is possible that BzOH irreversibly binds to the SBUs and builds defects into the MOF structure, which cannot be removed by simply washing the MOF. Thus, syntheses were also performed with liquid modulators such as HCl or HAc (30 eq.), in the hope that they will be rinsed more easily out of the pores. During reaction, it was observed that precipitation of the product occured within a few hours, indicating that the crystallization process occured too quickly. This was confirmed by XRD analysis, showing reflexes corresponding to amorphous materials (Figure 144).

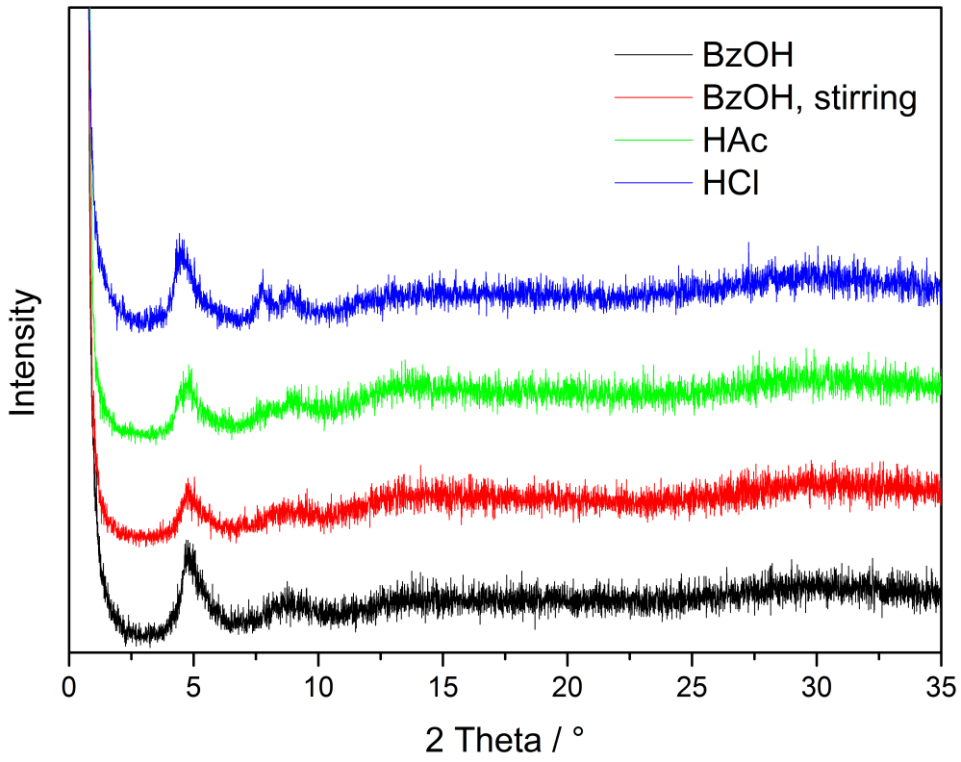

Figure 144. XRD spectra of UiO-68-NH_2 obtained by variation of the modulator.

These findings also underline that there is no common method for repeatedly producing highly crystalline MOFs. This time, the addition of BzOH gave an amorphous powder, showing that the MOF structure is affected by a variety of external factors, which are difficult to control. Therefore, the amino-functionalized UiO-68 synthesis was repeated several times and the resulting XRD spectra were compared with each other. The results provide information about the reproducibility of UiO-68.

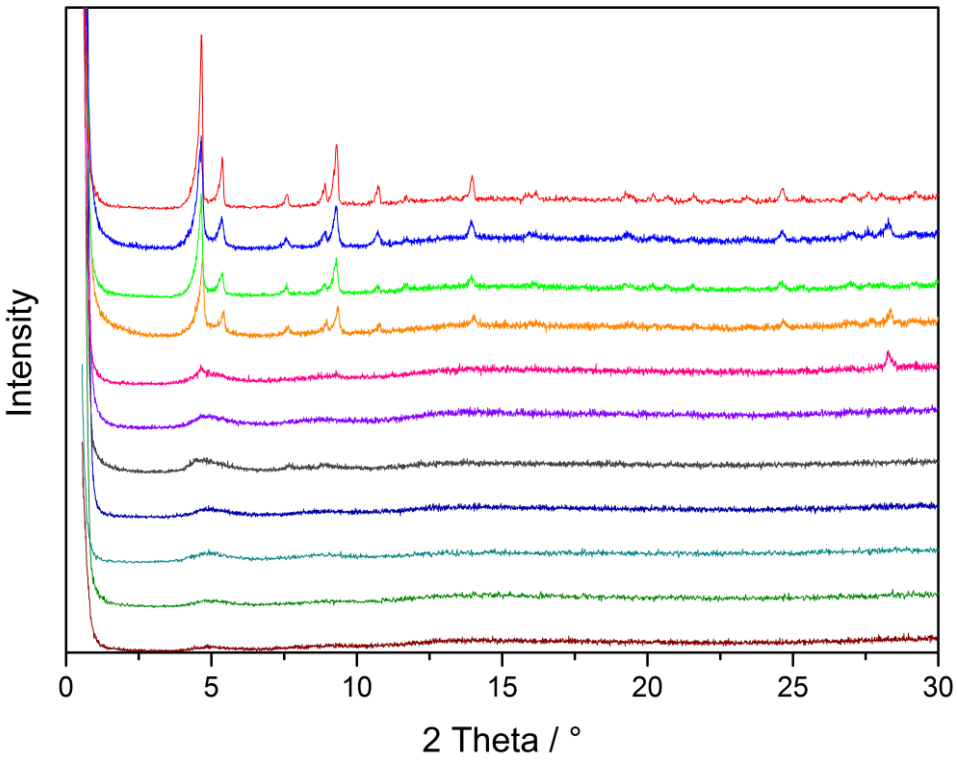

Figure 145. XRD spectra of UiO-68-NH_2 materials from different synthetic approaches.

As shown in Figure 145, experiments repeated under the same conditions not always gave the same PXRD pattern. Only 4 of 11 measured spectra correspond to the calculated diffraction pattern of UiO-68. Thus, the success rate for UiO-68 synthesis in this case is only 36 %.

In order to investigate the influence of the organic linker length on the MOF stability, UiO-67, which is one phenyl shorter in length than UiO-68, was synthesized under similar conditions using BzOH as modulator. Remarkably, the synthesis of UiO-67 was successful the first time and guaranteed a high reproducibility of crystallinity (Figure 146).

Based on these results, it could be concluded that the (non-)flexibility of the bridging ligand is also central for the development of more rigid and stable 3D network structures. It is believed that the rotation of the terminal phenyl rings around the central single bond in the terphenyl linker might break up the bonds to the SBUs, which is restricted in UiO-67. Furthermore, the use of a slightly longer linker can produce interpenetrated frameworks that can lead to partial or even total collapse of the pores. It can, therefore, be concluded that the more rigid the organic linker, the more stable the resulting MOF. All these factors explain why UiO-66 and UiO-67 have been widely studied over the past years, while there are only few publications in general dealing with UiO-68 and its derivatives.

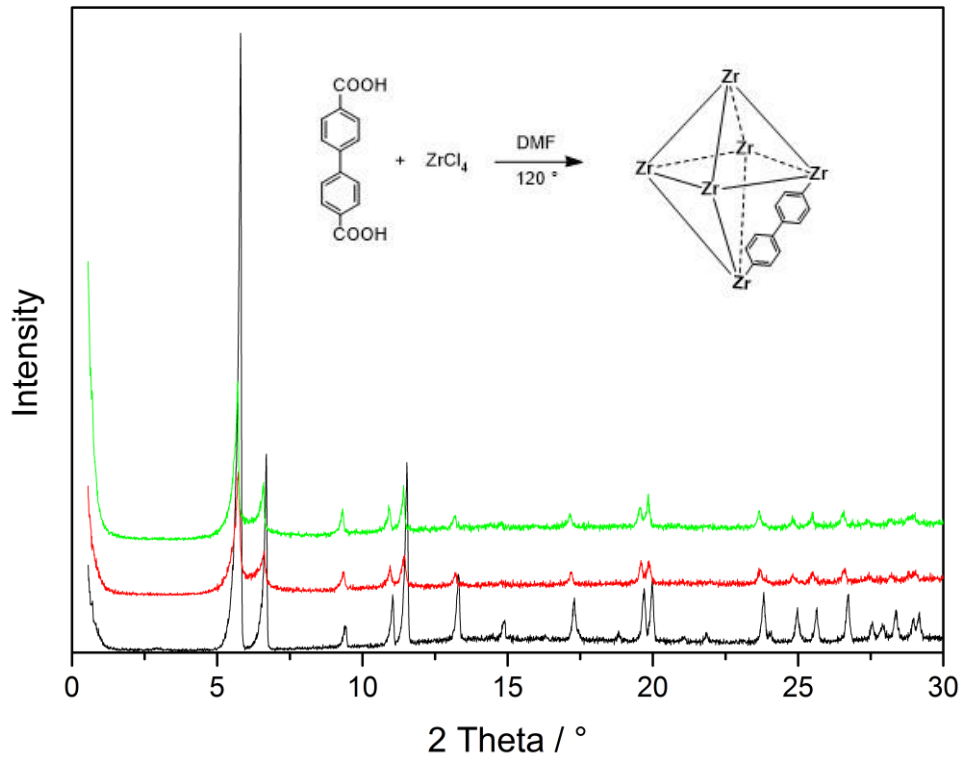

Figure 146. XRD spectra of UiO-67.

Inspired by the large-scale production of UiO-66, the concentration of the reactants was doubled while the volume of the reaction solvent was increased from 12 to 24 mL for better solubility. Hereby, it is expected to improve the yield of UiO-68 to get enough material for further experiments. The corresponding XRD spectra obtained from differet large-scale syntheses are presented in Figure 147.

As expected, this task was also very challenging since only MOFs with low crystallinity were produced by this method, which is again due to difficulties in reproducibility. This is mainly due to the fact that the organic linker molecules collide much more frequently with the zirconium ions at high concentrations and react at faster rates, thus inducing a fast crystallization of amorphous UiO-68. This was also indicated by an intense fluffy precipitation of the product which occurred very rapid. In summary, conventional methods appear to be useful only for small scale syntheses.

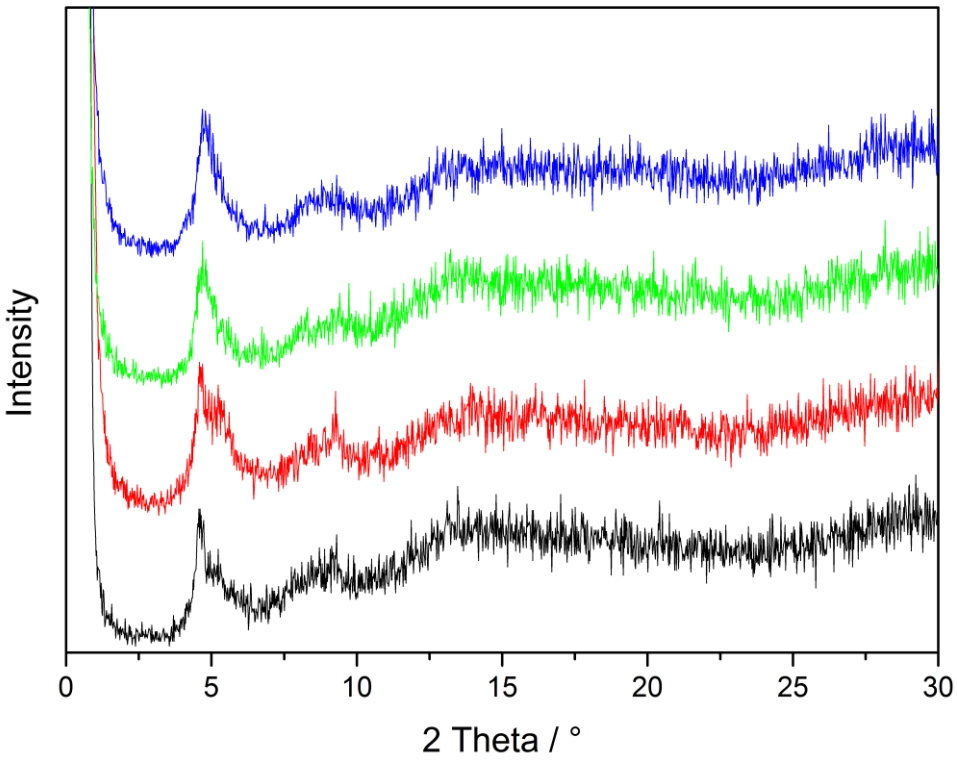

Figure 147. XRD spectra of UiO-68-NH_2 obtained from large-scale syntheses.

All syntheses described before were performed in a glass vessel of 50 mL solvent volume. However, glass vessels are not very stable towards high pressure that is build up inside during heating. To investigate how the crystallinity was influenced by the material of the reaction vessel, experiments were carried out in stainless steel vessels with a volume of 45 mL in a preheated oven at a selected temperature (Figure 148). Based on all previous results, syntheses carried out at 70 °C were heated for a longer period of time due to slow crystallization, while some were prepared at 120 °C for 24 h. Interestingly, here a reaction temperature of 120 °C was more advantageous than 70 °C, the latter preferred for hydrothermal MOF synthesis. Although both products appear as amorphous on XRD diffractogram, the degree of crystallinity vary considerably.

The diffraction pattern of UiO-68 generated in autoclave was compared to that obtained from Schott synthesis. As shown in Figure 149, the intensity of the reflexes show that MOF formation was not strongly influenced by the type of the reaction vessel. The only requirement seems to be that reactions are performed in closed vessels, which withstand the extremely high temperatures and vapor pressures.

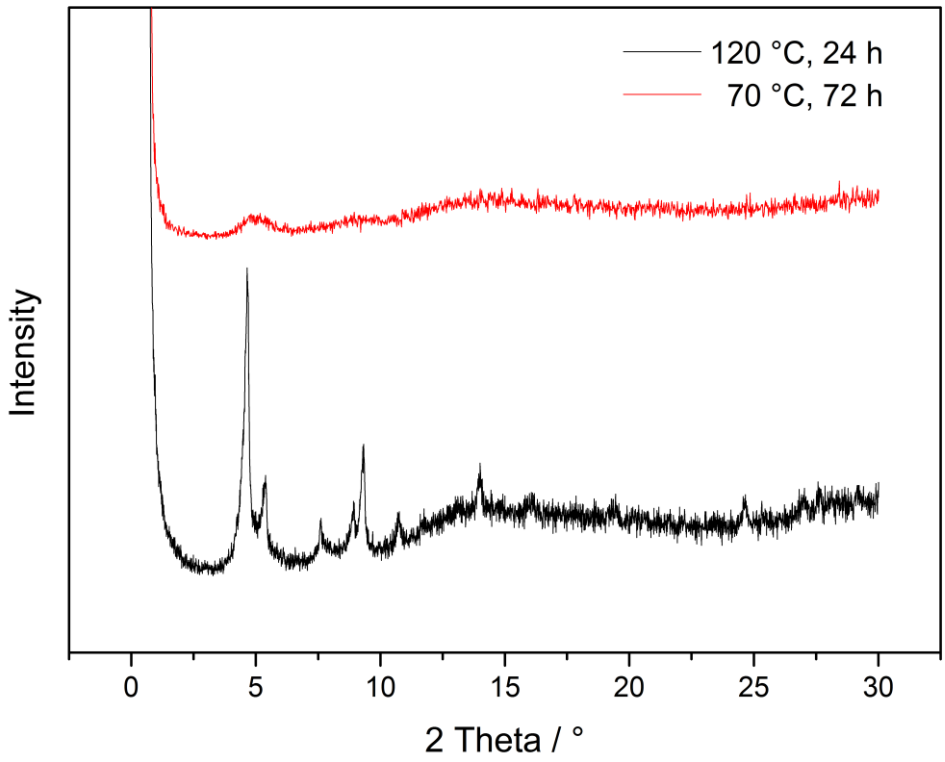

Figure 148. UiO-68-NH_2 MOF syntheses performed in stainless steel vessels at different temperatures.

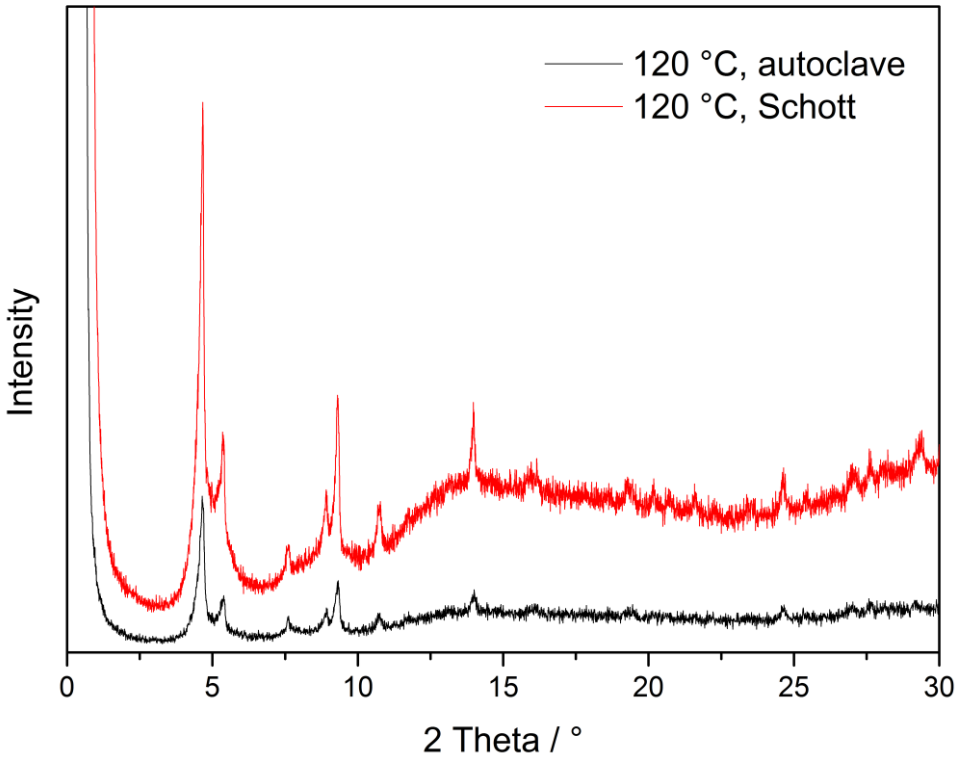

Figure 149. Comparison of XRD spectra generated at 120 °C in autoclave and Schott flask.

By comparison, preparation of UiO-68 in a simple glass flask under standard Schlenk techniques was unsuccessful. Powder diffraction analyses confirmed that the quality of the product strongly suffers under non-solvothermal conditions (Figure 150), which is due to the complexity of the UiO-68 architecture. Thus, it was concluded that highly crystalline UiO-68 and its derivatives could only be generated when using closed vessels and high internal pressures.

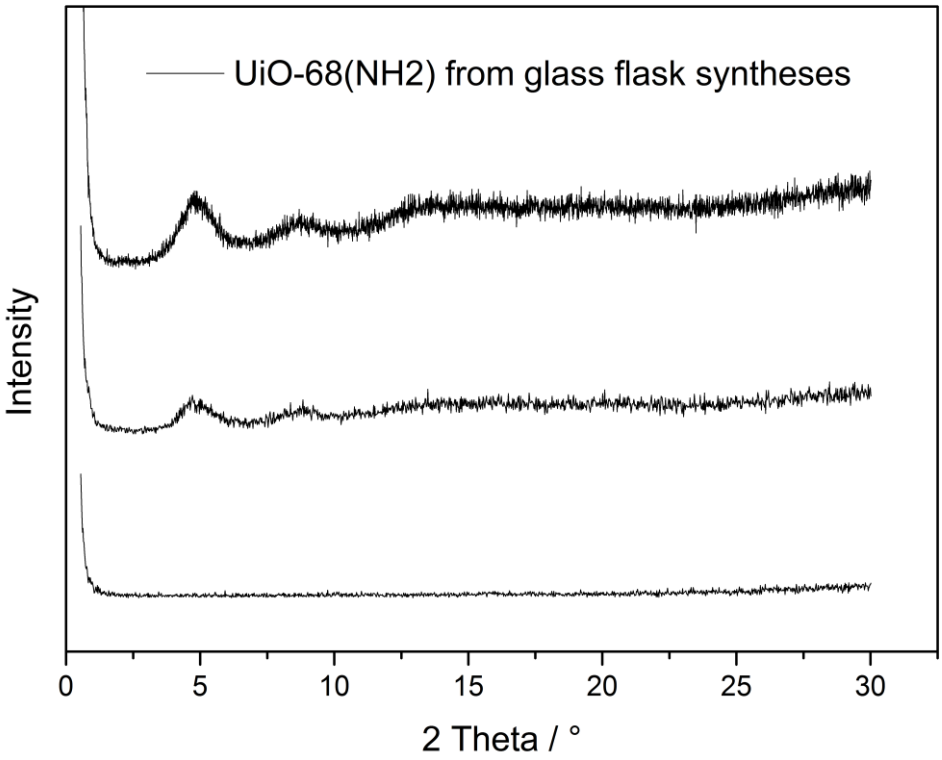

Figure 150. XRD spectra obtained from glass flask syntheses.

In order to analyze the property of a porous system, N_2 physisorption analyses were performed at 77 K on a Quantachrome Autosorb 6 instrument. The samples were degassed at 200 °C for 12 h prior measurement. Specific surface areas were assessed by multi-point Brunauer-Emmett-Teller (BET) analysis in the range of $0.1 \leq p/p_0 \leq 0.3$. Pore volumes were calculated at $p/p_0 = 0.99$. Pore size distributions were calculated by Barrett, Joyner, und Halenda (BJH) analysis from the desorption branches of the isotherms.[185]

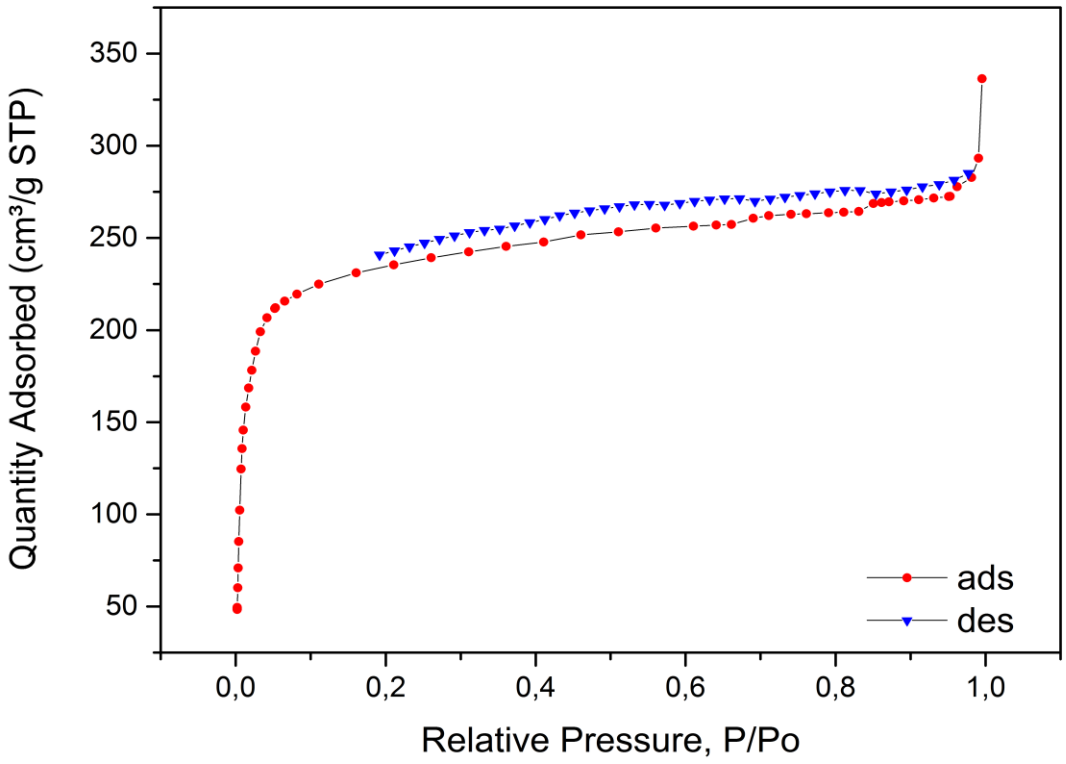

Figure 151. BET of UiO-68-NH_2 prepared in 10 mL.

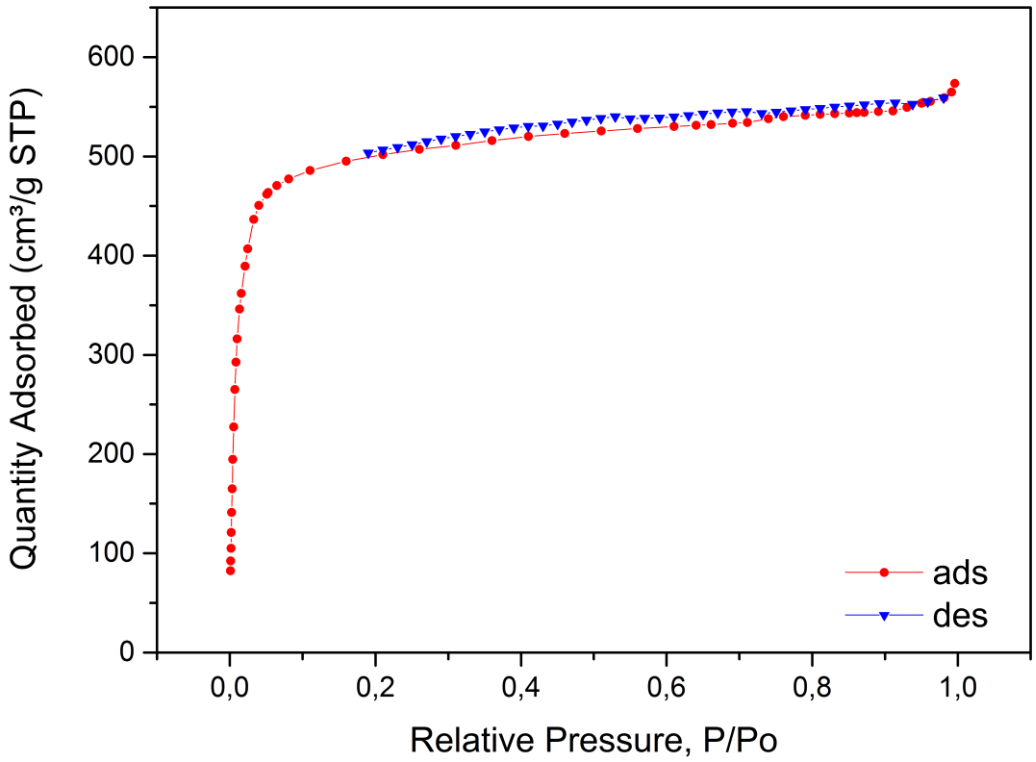

Figure 152. BET of UiO-68-NH_2 prepared in 12 mL.

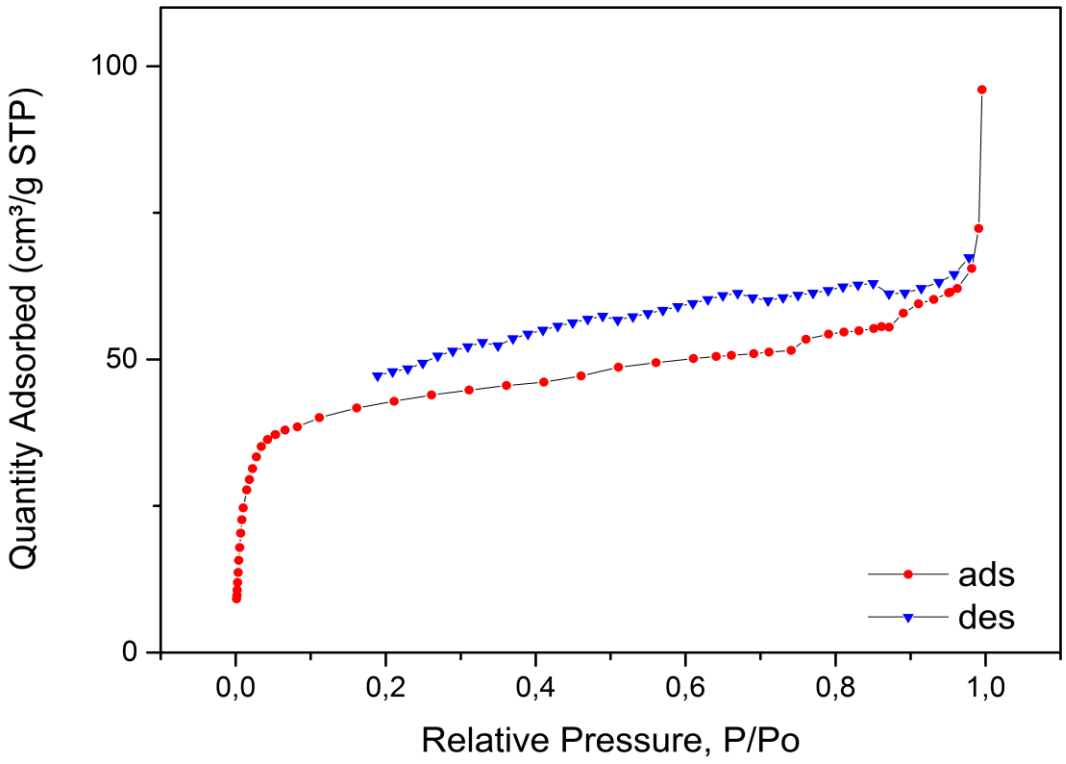

Figure 153. BET of UiO-68-NH_2 prepared in 20 mL.

The adsorption isotherms shown in Figures 151, 152 and 153 belong to products from experiments in solvent volumes of 20 mL to 12 mL and 10 mL, respectively. The results are consistent with the quality of the corresponding powder diffractograms.

Table 16. Area-volume summary.

Sample	**Solvent Volume [mL]**	**S_{BET} [m^2/g]**	**Pore Volume [cm^3/g]**	**Ø Pore Size [nm]**
MOF-1	20	129	0.11	3.48
MOF-2	12	2066	0.87	1.69
MOF-3	10	689	0.45	2.63

The highest surface area (2066 m^2/g) was determined for the reaction performed in 12 mL of DMF. To the best of our knowledge, this is the second highest value ever reported for UiO-68-NH_2. In order to distinguish this system from others, it will be called UiO-68-$NH_{2,opt}$ (opt = optimal). The first was reported by CARBONI et al.[204], who measured a BET surface area of 3730 m^2/g, indicating microporous structure. Considering that there is in general a lack of

scientific data available on surface properties of UiO-68, it is not surprising that there is no generally agreed method for the synthesis of this complex material. In Table 16, selected data are summarized for MOFs 1-3. As evident from the area-volume data, with decreasing pore size, the surface area and thus the capacity of the resulting porous materials increases. In addition, as the pore size decreases, the pore volume increases which is due to the presence of smaller pores and thus to an increase of the number of micropores. In the following, the data are compared to amine derivatives of the UiO MOF family.

Comparison of BET surface areas of pristine and modified UiO-MOFs revealed that incorporation of amino groups leads to a dramatic decrease in surface area (Table 17). This is not only limited to amines but can also be found for other functional groups and is due to the increasing sterical requirements of the substituents within the pores.

Table 17. Observed and calculated BET surface areas.

Sample	**Measured N_2 S_{BET} [m²/g]**	**Calculated N_2 S_{BET} [m²/g]**
UiO-66[205]	1580	800-1550
UiO-66-NH_2[205]	830/1200	700-1150
UiO-67[205]	2500	2700-3100
UiO-67-NH_2[205]	2080	2150
UiO-68[205]	n.rep.	4170
UiO-68-NH_2	2066/3730[204]	n.rep.

Interestingly, the surface area of UiO-68-$NH_{2,opt}$ decreased enormously (405 m²/g) when it was measured after exposure to ambient air, suggesting that the porous structure was instable towards air over longer periods of time. The corresponding XRD pattern is shown in Figure 154, in which the decrease of the peak intensity corresponds to the decrease of the surface area.

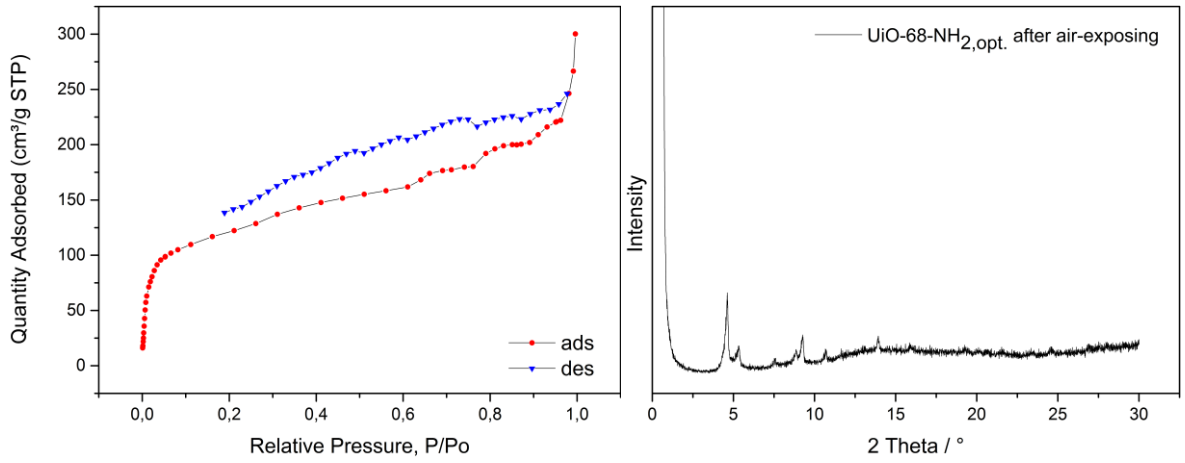

Figure 154. Left, BET of UiO-68-$NH_{2,opt}$ recorded after air exposing. Right, the corresponding XRD spectrum.

An interesting phenomenon was observed when the sample was removed from the adsorption isotherm instrument at the end of the measurement. The sample changed its color from white to yellow. Considering that the yellow color corresponds to the color of the unbound organic MOF linker (H_2)tpdc-NH_2, IR spectroscopy was performed with MOFs before and after thermal treatment and were compared to the IR spectrum of tpdc-NH_2 .

Figure 155 shows the FT-IR spectra of UiO-68-NH_2 and the amino-tagged MOF linker. The FT-IR spectrum of the linker shows that the O-H stretch of the carboxylic acid groups appears as a very broad band in the region 2500-3100 cm^{-1}, overlapping the sharp vibrations of C-H stretching. The carbonyl C=O stretch is located at 1686 cm^{-1}, while the O-H bend appears at the region around 1419 cm^{-1}. Furthermore, the sharp band at 1290 cm^{-1} was assigned to stretching of the C-O moiety, supporting the existence of carboxylic acid groups within the molecule. The band at 1607 cm^{-1} was attributed to N-H bending vibration of NH_2, while the peak located at 768 cm^{-1} could be assigned to wagging vibration of N-H.

Comparing these results with the IR spectrum of the MOF, a significant difference was found concerning the vibration frequencies of the carboxylic acid groups. First, the C=O band previously observed at around 1700 cm^{-1} completely dissapeared after being attached to the zirconium nodes within the framework, instead appearance of an intense band at 1408 cm^{-1} was recorded which was due to the presence of C-O stretches. Same was observed for the broad O-H region, being fully removed from the spectrum and thus indicating the coordination of the -COOH groups to the metal ions. To find out the reason for the decrease of the surface area, infrared spectroscopy of the MOF was recorded after undergoing heat treatment of BET analysis (Figure 156). The most intensive peaks appear in the region of 1400-1600 cm^{-1}. Two absorption bands located at 1599 and 1549 cm^{-1} can be assigned to the ν_{as}(COO) asymmetric

stretching of the carboxylic functions, whereas the band at 1408 cm^{-1} can be assigned to the corresponding stretching vibration. Due to the small transition moment, the N-H stretching transition is only very weak and attributed to the large size of the MOF.

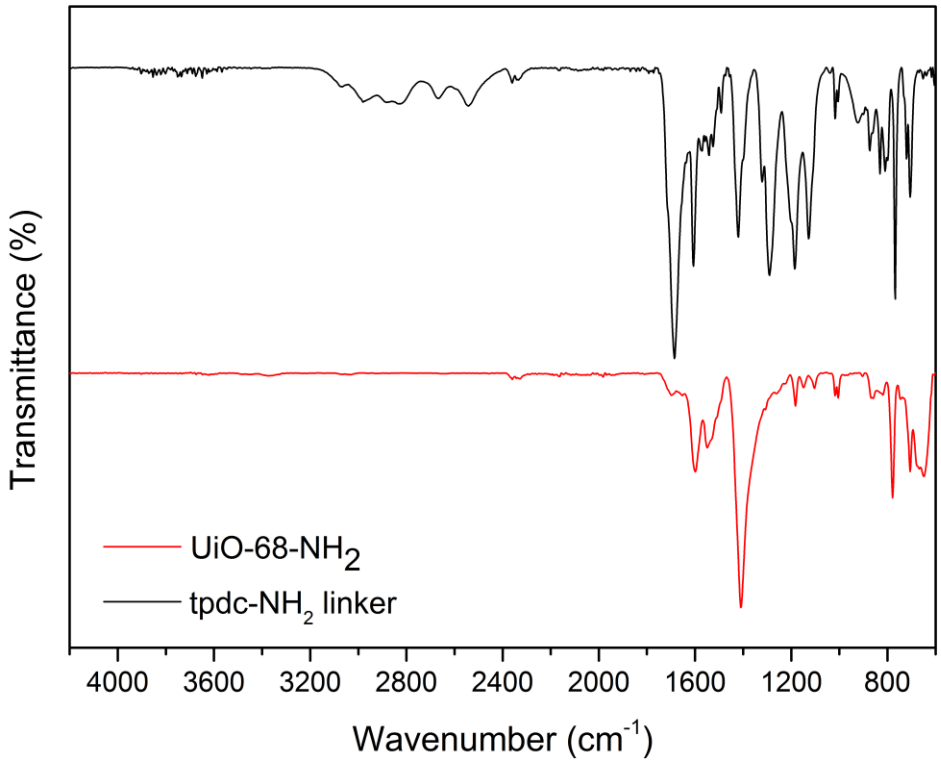

Figure 155. IR spectrum of (H_2)tpdc-NH_2 and UiO-68-NH_2.

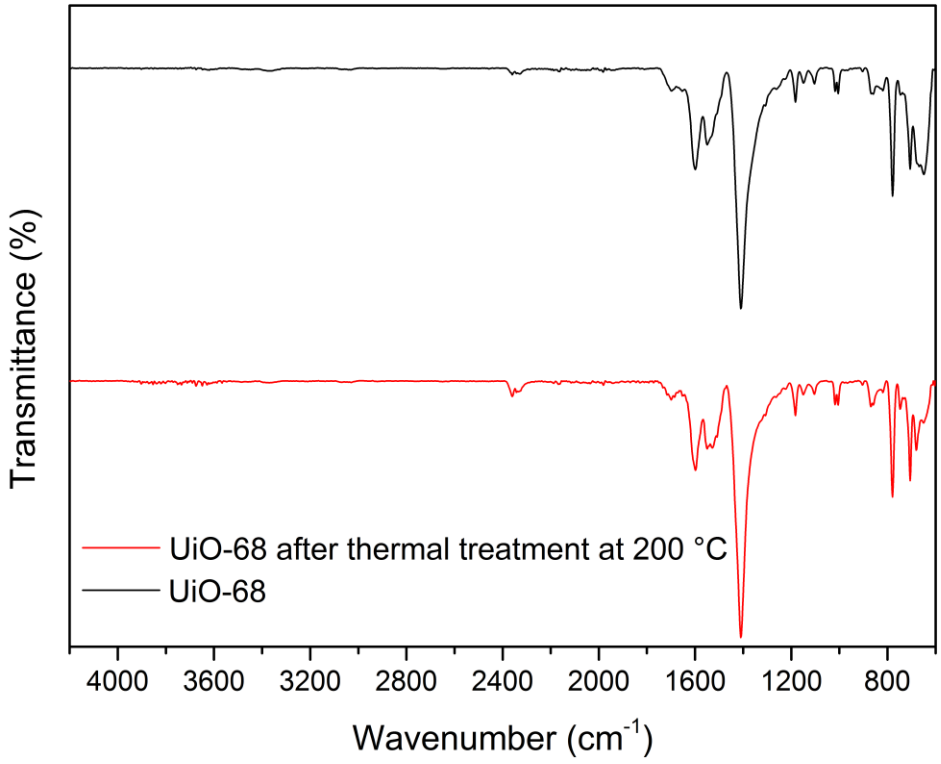

Figure 156. IR spectrum of UiO-68-NH_2 after thermal treatment.

By comparison, there is no significant change between the samples before and after thermal treatment. The only but slight difference is that at the low adsorption region, the peaks became sharper and similar to those obtained for the free organic linker. In addition, the surface area after heat treatment shows an enormous decrease, which might indicate partial framework decomposition.

As described previously for some MOF samples, a yellow solid was obtained after final BET analysis. A comparison of the IR spectra of these materials with that recorded for the unbound organic linker confirmed decomposition of the MOF structure due to the re-appearance of O-H bands, which is fairly identical to the infrared range of the free linker, thus suggesting that decoordination of the bridging linkers from the SBUs was the main source of color change after thermal treatment (Figure 157). This finding was remarkable since it was possible to predict the stability of the resulting MOF based on its color.

When comparing the BET analyses of MOFs of different color (Figure 158), it could be found that the higher surface area of 959 m^2/g belonged to the *'white'* product, while the decrease in surface area (556 m^2/g), despite being synthesized under the same experimental conditions, was related to partially decomposed amino-functionalized UiO-68, as indicated by its pale yellow color.

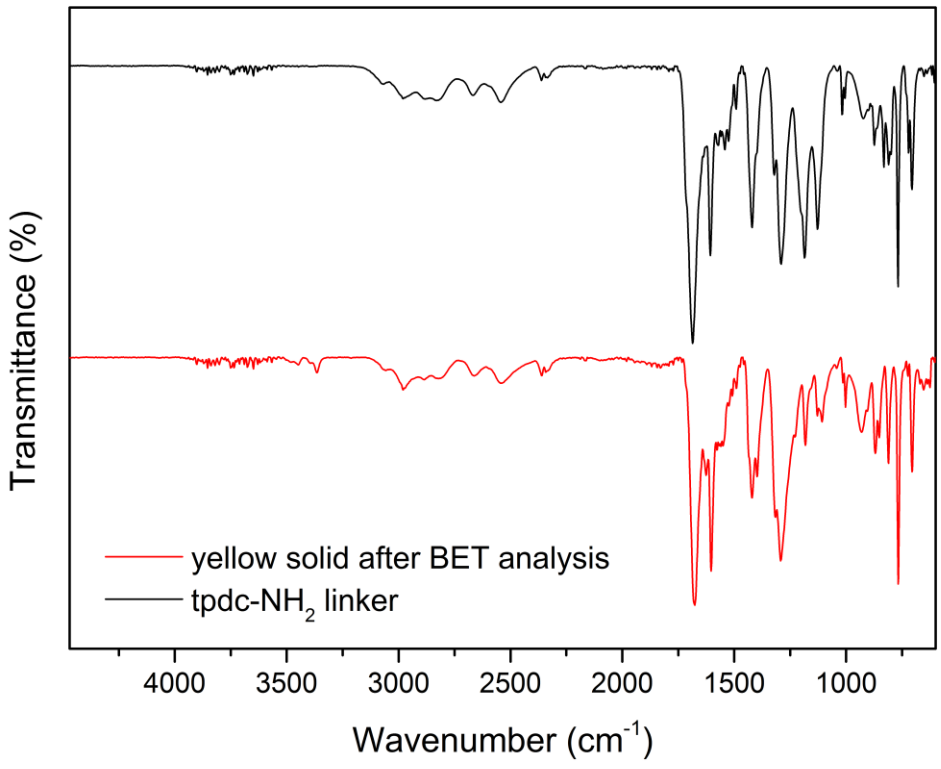

Figure 157. IR spectrum of yellow solid.

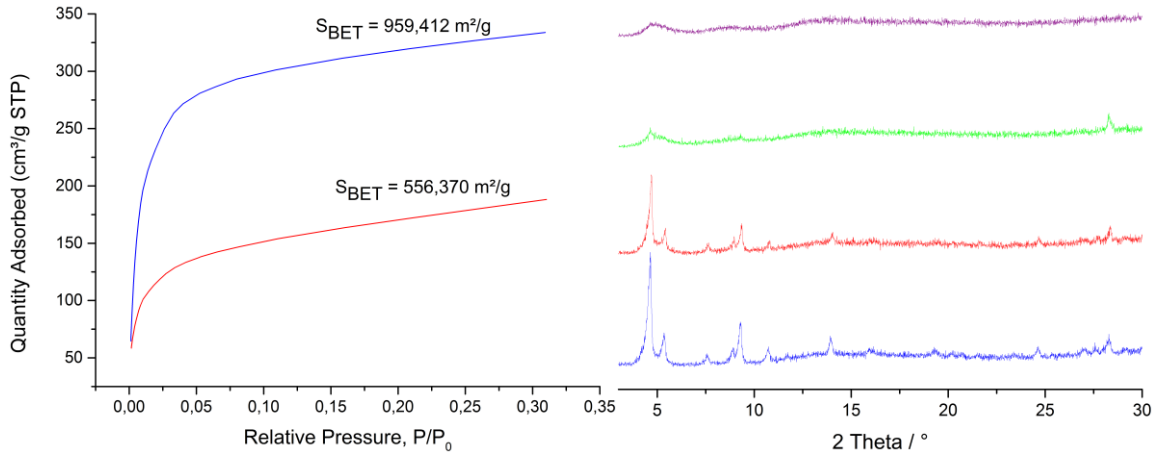

Figure 158. Comparison of XRD (right) and BET (left) results belonging to *'white'* and *'yellow'* MOFs.

Inspired by the color change of the MOF after BET measurements, TGA was performed using MOF material with the highest BET surface area in order to study the thermal stability. As evident from Figure 159, UiO-68(NH_2) was stable up to 723 K.

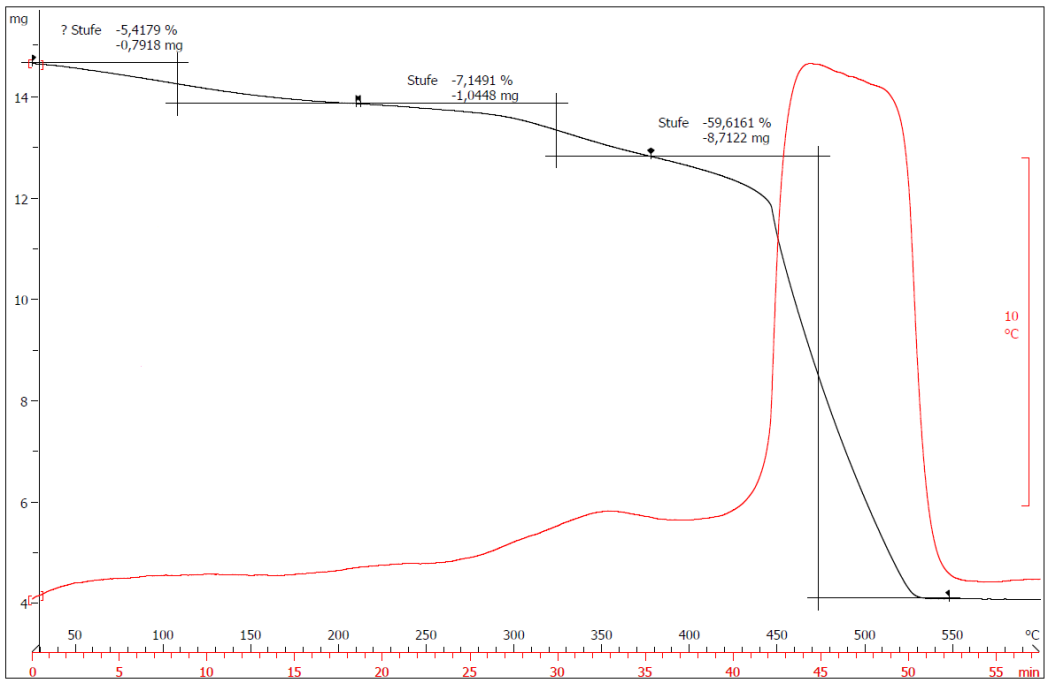

Figure 159. TGA of UiO-68-NH_2.

The TGA spectrum is characterized by three weight loss steps. The first weight loss of 5.4 wt% occurred between 303 K and 373 K and is attributed to the vaporization of water, while the second weight loss of 7.1 wt% arises at 373-593 K and is due to vaporization of enclosed DMF molecules within the pores. The third step of weight loss was 59.6 wt% above 713 K due to decomposition of material.

Typically, MOF products were dried under vacuum pressure to remove enclosed guest molecules from the pores. In order to exclude that rapid vaporization was a source of structural damage, MOF products were dried by slow evaporation at room temperature until their weight remains constant. Subsequently, the porosity was investigated by XRD.

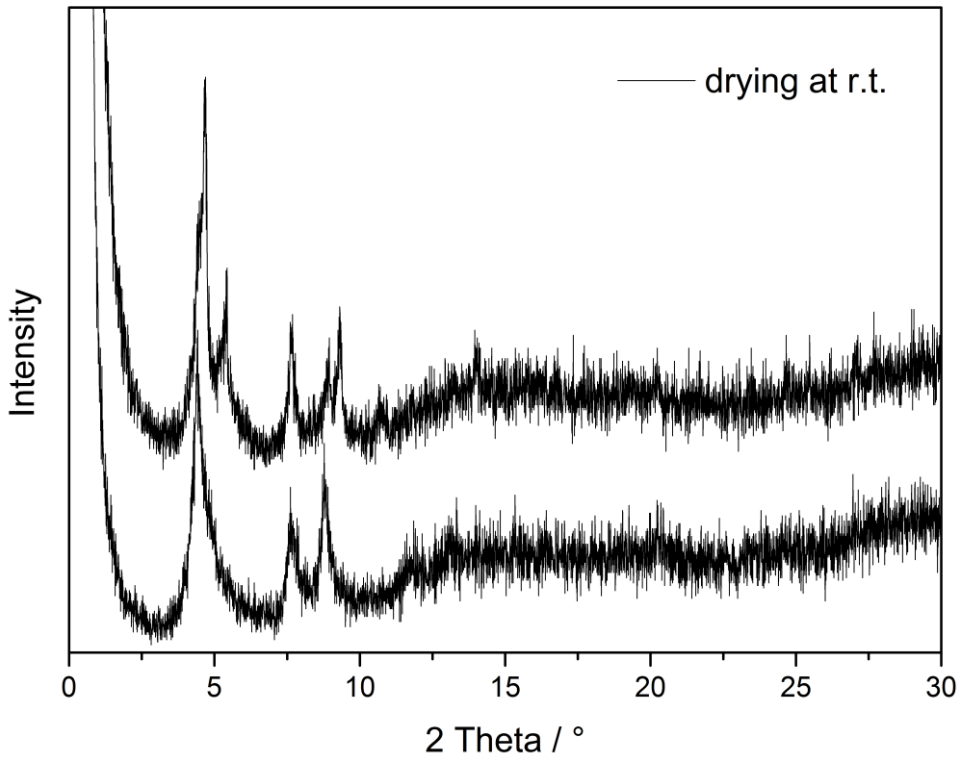

Figure 160. XRD pattern of UiO-68-NH_2 MOFs dried under air.

The XRD pattern in Figure 160 confirmed that UiO-68-NH_2 was synthesized with characteristic peaks but the amorphous quality of these materials cannot be ignored. This can in part be attributed to incomplete and irregular precipitation of the products during MOF synthesis but also to the sensitivity of the MOFs towards air. Although UiO-68-NH_2 was successfully synthesized in small scale, it is quite difficult to give a fair comparison between the different synthetic approaches since extent of factors such as temperature, reaction time, MOF activation and the presence of certain substances influencing MOF formation can strongly differ from synthesis to synthesis. However, reproducibility was found to be the key limiting factor of UiO-68-NH_2 and its large-scale production.

Finally, post-synthetic modification were carried out with crystalline amino-tagged UiO-68 including the transformation of the amine moiety to amide and imine by a wide range of acid anhydrides and aromatic aldehydes in order to study the degree of conversion with increasing chain length, which is essential when incorporating large-sized ruthenium catalysts into the pores of the MOFs.

10.3 Post-synthetic modification on UiO-68-NH_2.

Generally, a typical MOF modification is carried out in chloroform or dichloromethane due to their volatileness at ambient conditions.[206] Herein, high conversions rates were obtained by heating in acetonitrile or toluene (Figure 161). Each transformation was supported by NMR spectroscopy and mass spectrometry (ESI-MS). The incorporation of the bridging ligands was confirmed after MOF digestion in a solution of CsF/D_2O/DMSO-d_6, while ESI-MS analysis in negative mode was used to confirm the digested MOF linkers (Figure 162).

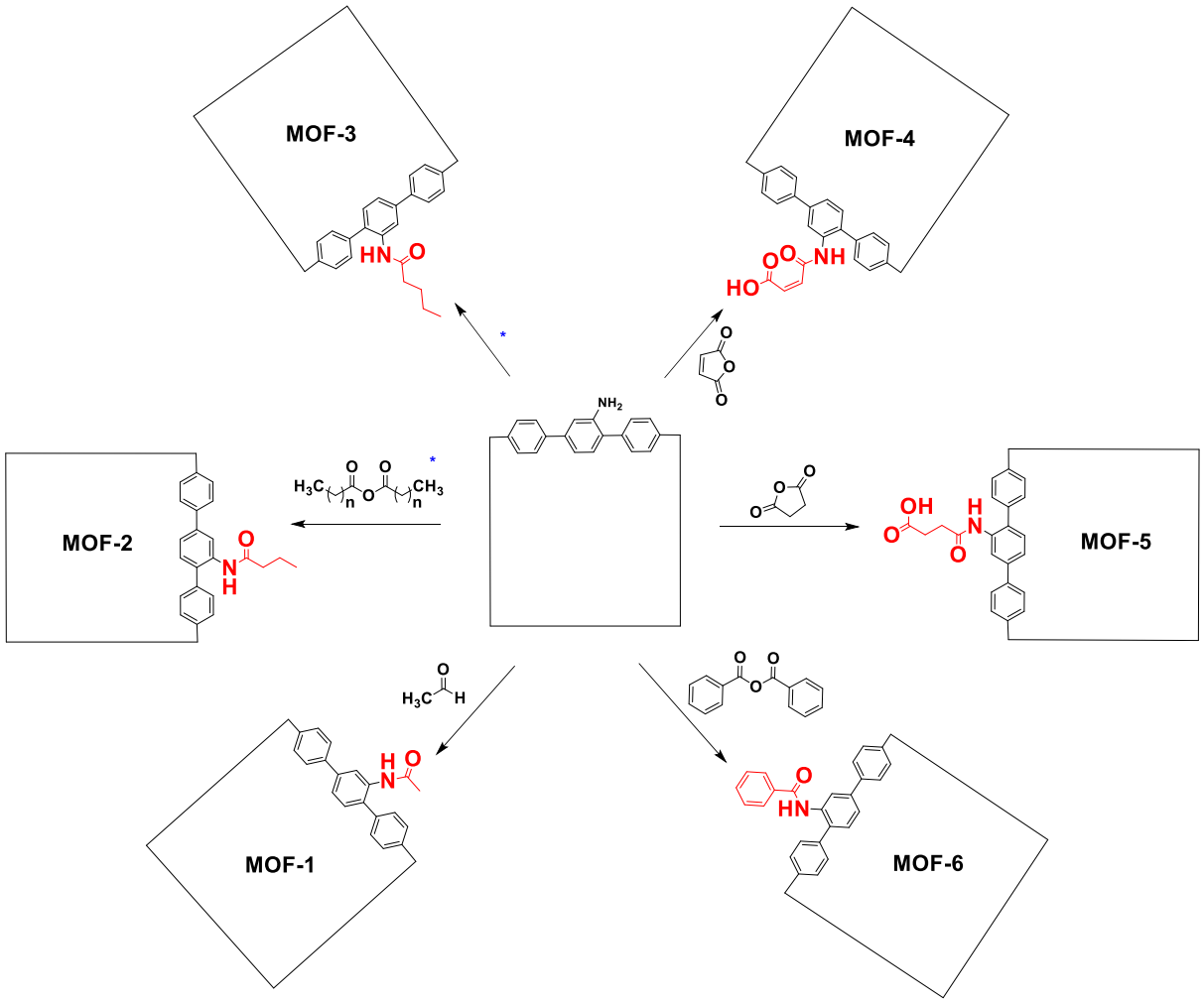

Figure 161. Post-synthetic modification on amino-tagged UiO-68.

The results of different synthesis approaches have shown that the degree of the conversion decreased with increasing chain length, while the degree of acylation was increased by increasing the duration of the MOF syntheses from 24 h to 3 days and by varying the equivalents from 6 up to 20 with yields of 96 %, 86 %, 47 %, 68 %, 64 %, 34 % for acetaldehyde, buteric

anhydride, valeric anhydride, succinic anhydride, maleic anhydride and benzoic anhydride, respectively.

As expected, the smallest acetic anhydride molecule was fully converted to UiO-66-$NHCOCH_3$ resulting from non-hindered diffusion into the pores, while sterically more demanding anhydrides react preferentially at the surface which prevents the entry of larger molecules into the pore cavity. Since characterization of MOF structures are limited due to their insolubility in organic and inorganic solutions, only the results of the most common methods for material identification of digested UiO-68 derivatives will be introduced in the following.

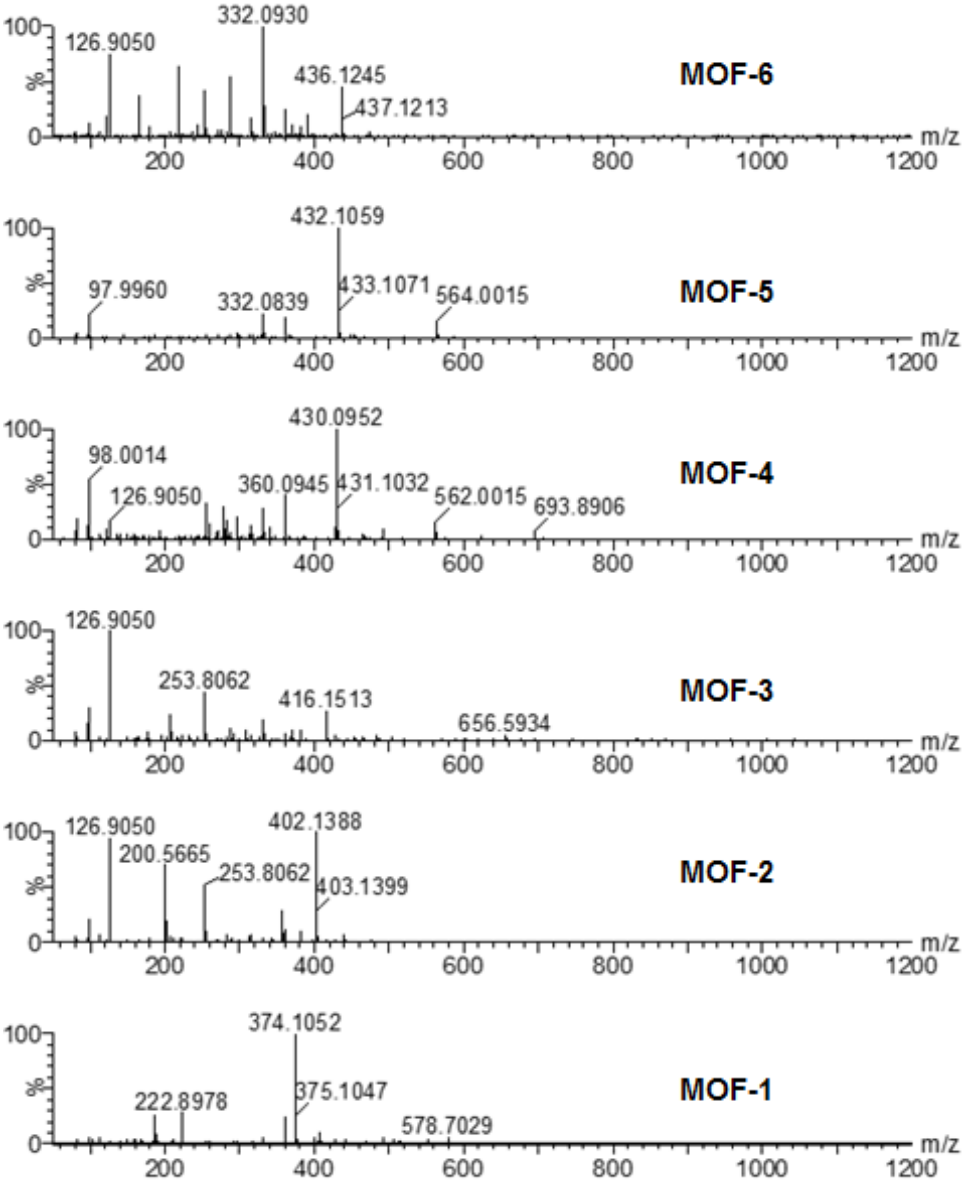

Figure 162. ESI-MS recorded for digested UiO-68 derivatives.

As evident from mass spectra, a mass peak is observed at *m/z* = 332 which is attributed to the unmodified UiO-68 linker, indicating that not all linker molecules could be converted most

probably due to diffusion problems. The corresponding diffraction patterns are shown in Figure 163. Unfortunately, none of the modified UiO-68 MOFs could maintain their crystallinity after work-up involving repeated washing of the resulting MOFs in order to remove excess of reactants. Therefore, BET analysis could not be performed with these materials.

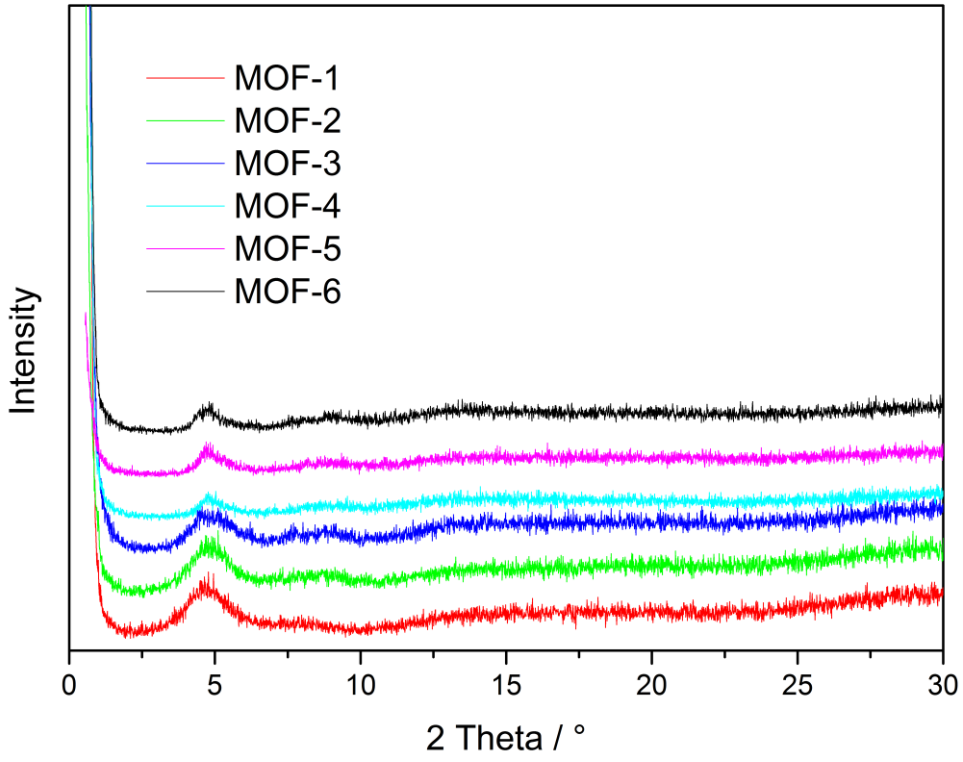

Figure 163. XRD pattern of MOFs 1-6.

Based on these findings, there was no doubt that the synthesis of the ruthenium-doped MOFs, K1@MOF and K4@MOF, would probably give rise to similar diffraction patterns. MOF syntheses carried out with $ZrCl_4$ and K1 or K4 at different temperatures revealed that precipitation of the desired products were limited by the excellent solubility of the homogeneous catalysts in DMF. ESI-MS of red DMF solutions gave a parent peak at *m/z* = 771, corresponding to the starting ruthenium complex. Although MOFs exhibit a large breathing behaviour, a phenomenon, which avoids rapid collapse of the framework, the immobilization of K1 or K4 is believed to produce defects due to the length and sterical bulkiness of the ligands, which might cause structural collapse during MOF formation.

Hence, a new but facile immobilization strategy was developed to incorporate metal catalysts being capable of water oxidation. Due to the high effectiveness, robustness and activity of Cp* iridium complexes for catalytic water oxidation in both, homogeneous and heterogeneous systems[52-67], $(IrCp^*Cl_2)_2$ was used as precursor at different stages of sal(IrCp*Cl) synthesis, as shown in Figure 164.

First, the iridium dimer was prepared in a one-pot synthesis[207] by refluxing hydrated iridium trichloride and pentamethylcyclopentadiene in methanol, from which the product precipitated as an orange solid. In the second step, 2'-amino-[1,1';4',1"-terphenyl]-4,4"-dicarboxylic acid was modified with excess of salicylaldehyde, which is capable of coordinating the iridium precursor *via* its lone pairs on the nitrogen and oxygen atom. All reaction intermediates were fully characterized by NMR spectroscopy and mass spectrometry.

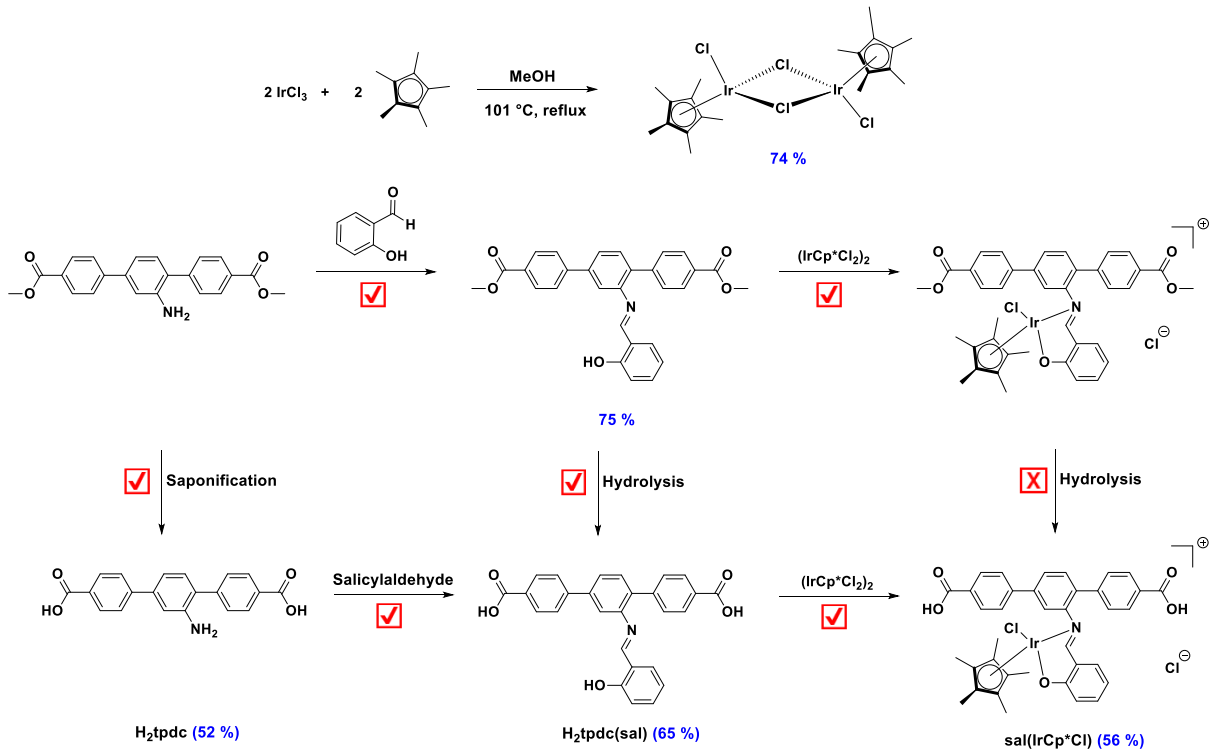

Figure 164. Synthetic route of sal(IrCp*Cl).

In general, the coordination of iridium to the salphen ligand (H_2tpdc(sal)) was performed in DMF which is due to the better solubility of the carboxylic acid at room temperature. Fortunately, replacing DMF by MeCN and increasing the reaction temperature from 25 to 60 °C for 48 h led to a significant increase of the product yield (Figure 167).

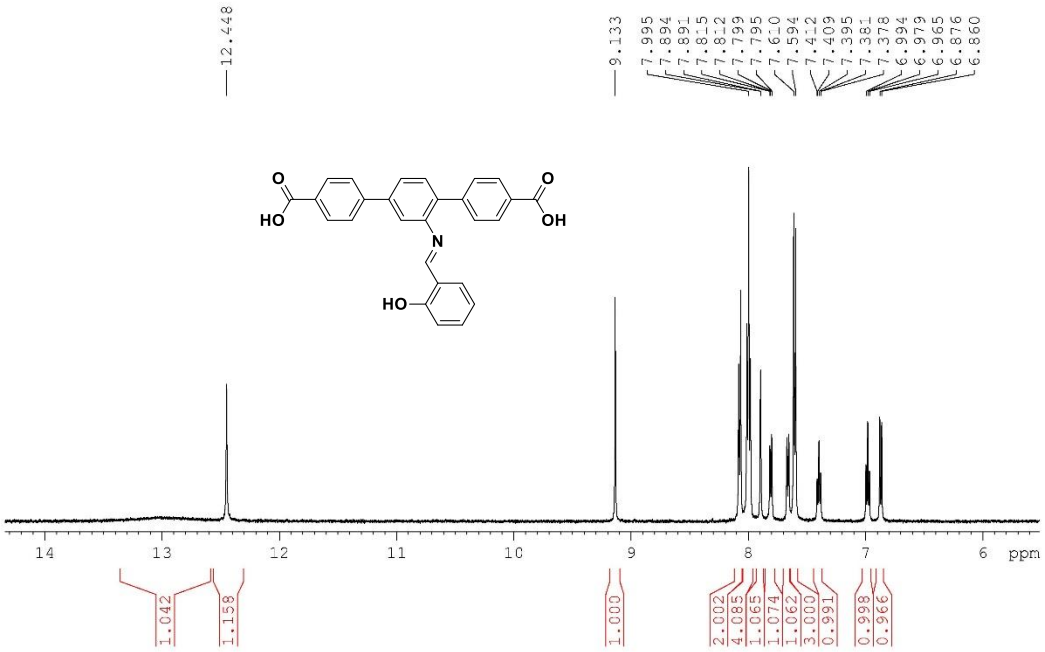

Figure 165. ^{1}H NMR of H_2tpdc(sal).

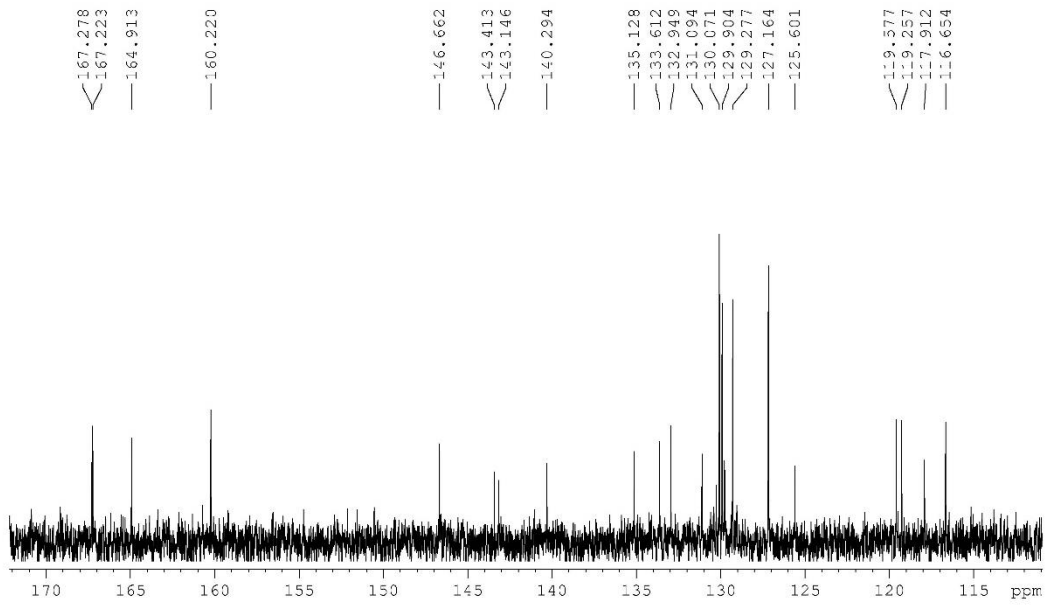

Figure 166. ^{13}C NMR of H_2tpdc(sal).

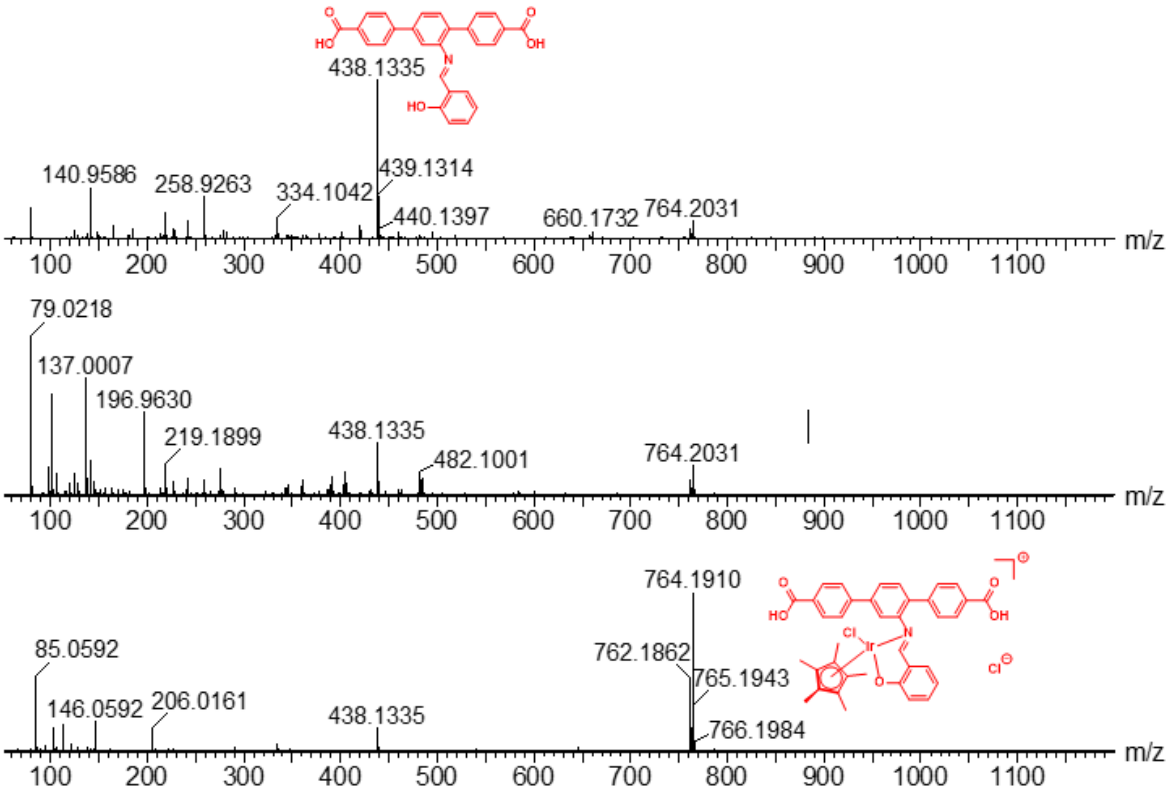

Figure 167. ESI-mass spectra of H_2tpdc(sal) and sal(IrCp*Cl). The isotope pattern of the iridium complex correspond to $[M–Cl]^+$.

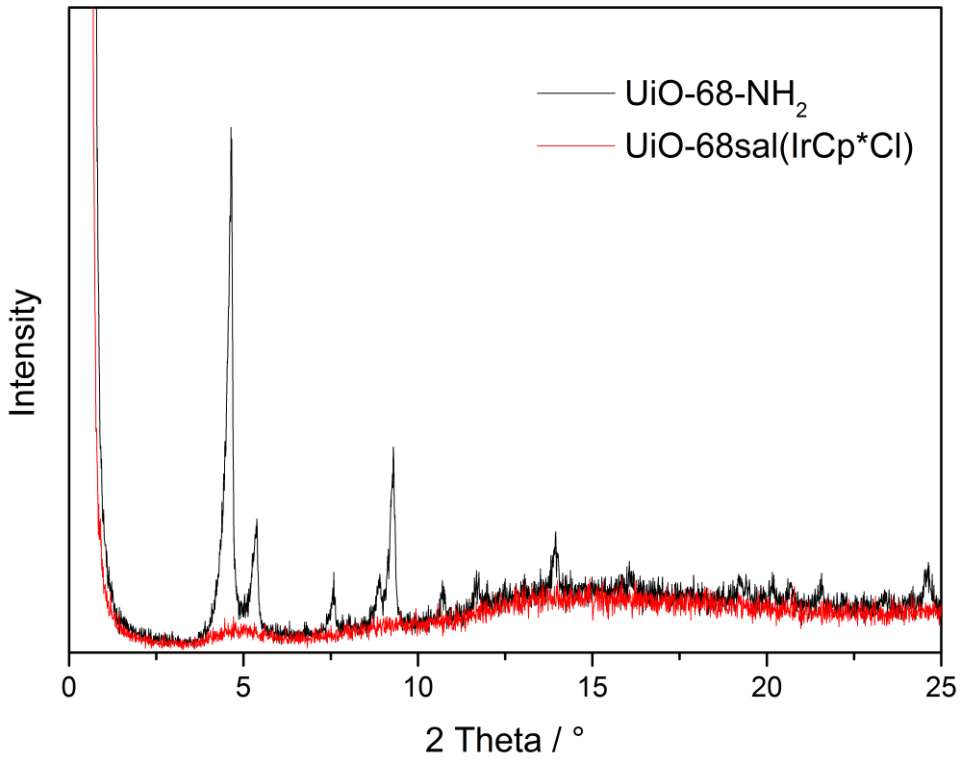

Figure 168. XRD pattern of pristine UiO-68-NH_2 and UiO-68sal(IrCp*Cl).

To the best of our knowledge, this is the first iridium complex based on UiO-68, in which the amine moiety is modified by an aldehyde group. Future works will focus on the large-scale production and incorporation of this catalyst into the UiO-68 framework since first attempts resulted in loss of crystallinity of pristine UiO-68-NH_2, as shown in Figure 168. The incorporation can be done in a mixed linker strategy using the amino-functionalized MOF linker and the iridium linker with a stoichiometric ratio of 1:1. Thanks to the similar linker length and the compactibility of the iridium rest, the novel linker is supposed to readily fit into the large pores of UiO-68, while the resulting MOF is expected to be highly stable and active towards catalytic water oxidation.

CHAPTER 11

Conclusion

The conversion of energy production from fossil fuels to renewable energy is currently a major problem, which is expected to continue over the next years. In this context, chemically-driven water-splitting is one alternative to overcome this problem, which is preferred over light-driven chemical reactions due to the easy variation of the reaction partners.

A significant focus of the work of this thesis was the preparation and characterization of ligands containing carboxylic acid functionalities. Especially the synthesis of π-extended ligands used for the synthesis of K1 and K4 was complex, which was primarily due to the increased aromaticity and sensitivity of the polar groups towards thermal and chemical decomposition.
First, a short summary about the main motivational factors concerning motivation and design of the complexes was given in **Chapter 5**. Synthetic steps and purification steps were optimized, thereby increasing the overall yield. In particular through variation of the cross-coupling reaction conditions, a general synthetic route was designed for the preparation of ligands with increased ligand-size in high yields. Following characterization of all ligands provided molecular symmetry. A generally accepted method (**Chapter 7**) was applied for the synthesis of the carboxylate- and carboxamide ruthenium complexes, while purification revealed one common by-product, which was due to the reaction of the ruthenium precursor $Ru(DMSO)_4Cl_2$ with excess of axial ligands resulting in the formation of $Ru(L)_4Cl_2$ (L = 4-picoline, isoquinoline), as confirmed by ^1H NMR and mass spectroscopic analysis. As desired, by introducing carboxylic acid groups into the ligands, it was possible to generate ruthenium(II) complexes which were completely soluble in water. The increased solubility enabled water oxidation to get triggered in pure water without the addition of any organic co-solvent, which is essential in terms of catalytic water oxidation.

(Spectro-)electrochemical and UV/Vis redox titrations with cerium(IV) ammonium nitrate confirmed that oxidation of Ru^{2+} to Ru^{3+} took place in ruthenium WOCs of the type K1 and K4 over time even in the absence of oxidizing agent, giving rise to broad bands at 708 nm and 704 nm for K1 and K4, respectively. ^1H NMR in acidic aqueous solutions revealed broad

resonance signals between -6 and 33 ppm, which confirmed the presence of paramagnetic interactions. This could be also confirmed by mass spectrometric analysis, revealing a mass peak around *m/z* = 770, which goes along with the oxidation of the ruthenium center to Ru^{3+} as evident from the mass peak at *m/z* = 771. Contrary to the generally accepted idea, it could be concluded that water coordination did not require ligand exchange to produce the active species for water oxidation. Instead, addition of water took place at the Ru(III) state resulting in the appearance of the mass signal around *m/z* = 787, which indicates the formation of the seven-coordinated intermediate $[Ru^{IV}\text{-}OH]^{+}$. Moreover, the central ruthenium at the oxidation state +3 could only be oxidized by subsequent addition of cerium(IV) ammonium nitrate to the ruthenium oxidation stage +IV before oxygen evolution occured (**Chapter 8**).

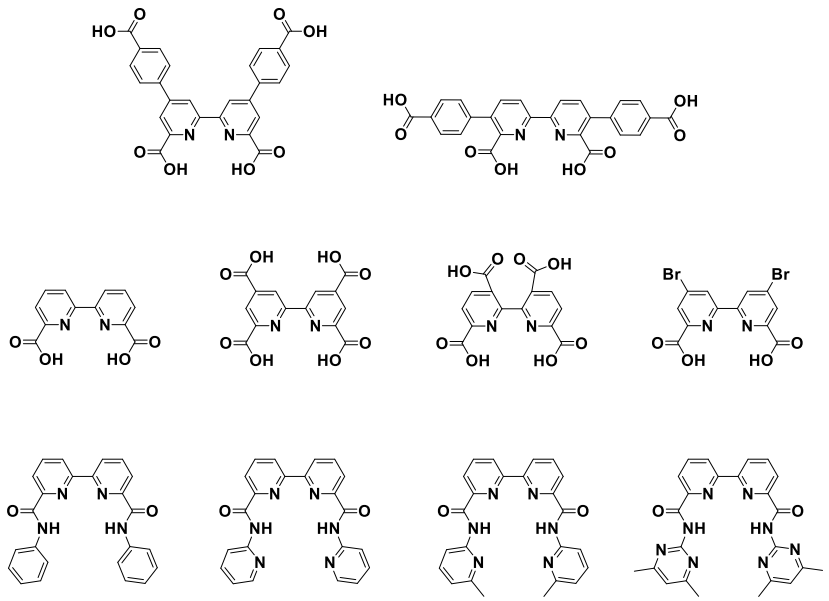

Figure 169. Molecular structures of ligands prepared in this work for complex synthesis.

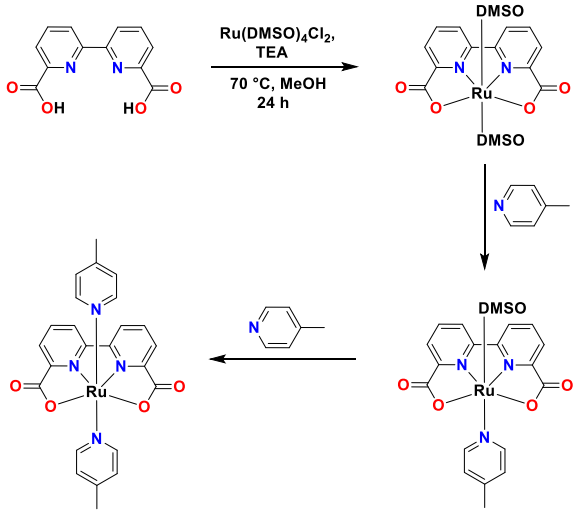

Figure 170. General synthesis scheme for the preparation of Ru(II) WOCs.

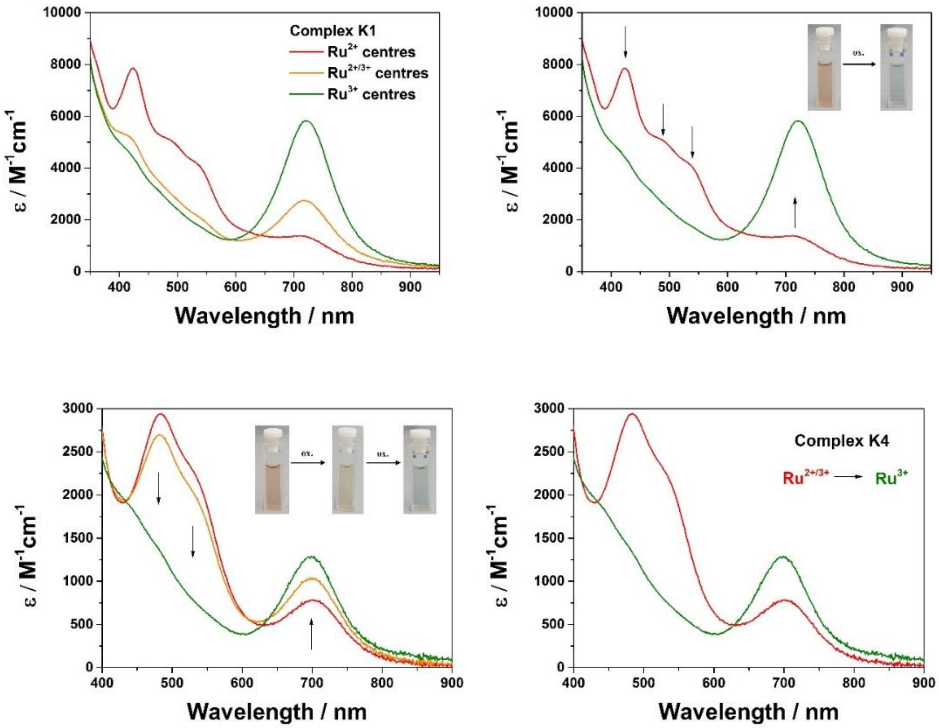

Figure 171. Results of UV-vis spectroscopy recorded for K1 and K4 in pure water.

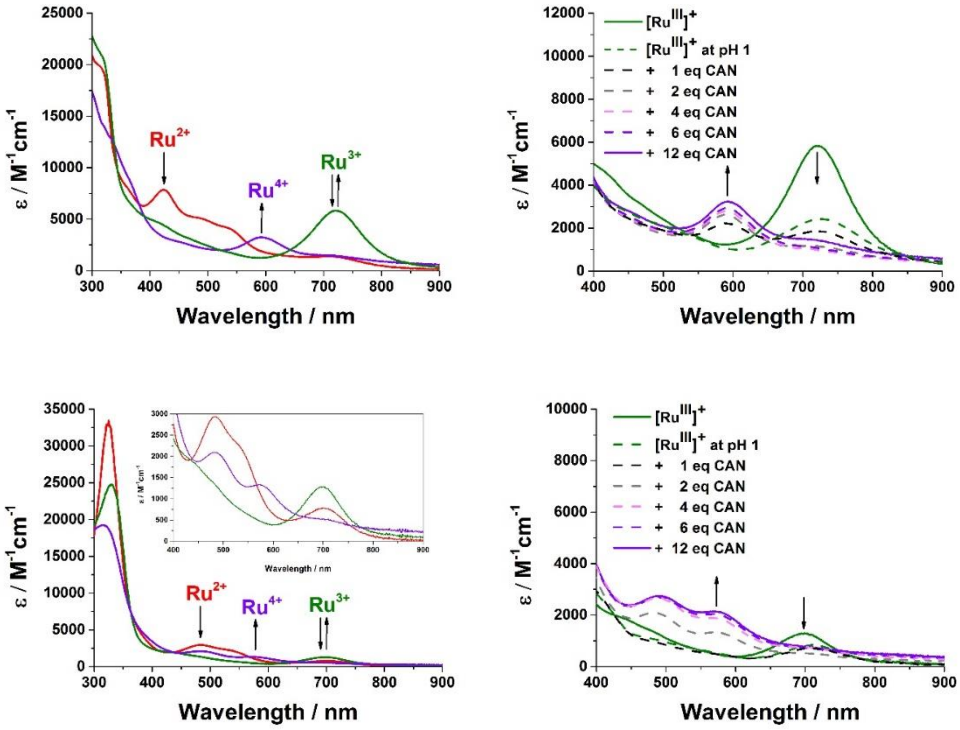

Figure 172. Results of UV-vis redox titration with K1 and K4 using cerium(IV) ammonium nitrate as oxidant.

Similar redox events were found for ruthenium WOCs modified with bromo- and carboxylic acid groups at the 3,3' and 4,4'-positions of the original bda-ligand. By comparison, the characterization of the ruthenium WOCs consisting of carboxamide moieties displayed complex behaviour, which is proposed to deliver from the stability of the bonds at the equatorial plane, preventing the intramolecular decoordination of the nitrogen atom from the ruthenium center and thus the attachment of water to initiate the oxygen evolution process. Hence, the results of this work confirmed that ruthenium complexes containing negatively charged carboxylate groups were able to drive the electrochemical water oxidation process by decreasing the redox potentials.

In the next step, the ability of K1 and K4 to drive the water oxidation chemically using CAN under highly acidic conditions (pH 1) was studied by oxygen evolution experiments (**Chapter 9**). During these experiments it could be observed that the color of the reaction solution, switching from orange-yellow (large excess of CAN) to colorless (termination of catalysis), was directly related to catalytic performance of the respective system. By tuning the catalyst concentration to an optimal and catalyst specific value, the catalytic activity could be successfully increased. From these results, it could be concluded that the water oxidation activity was depending on [cat.] and independent on CAN at high concentrations. Cerium(IV)-induced water oxidation of K1 and K4 revealed a strong correlation between catalytic performance and ligand topology.

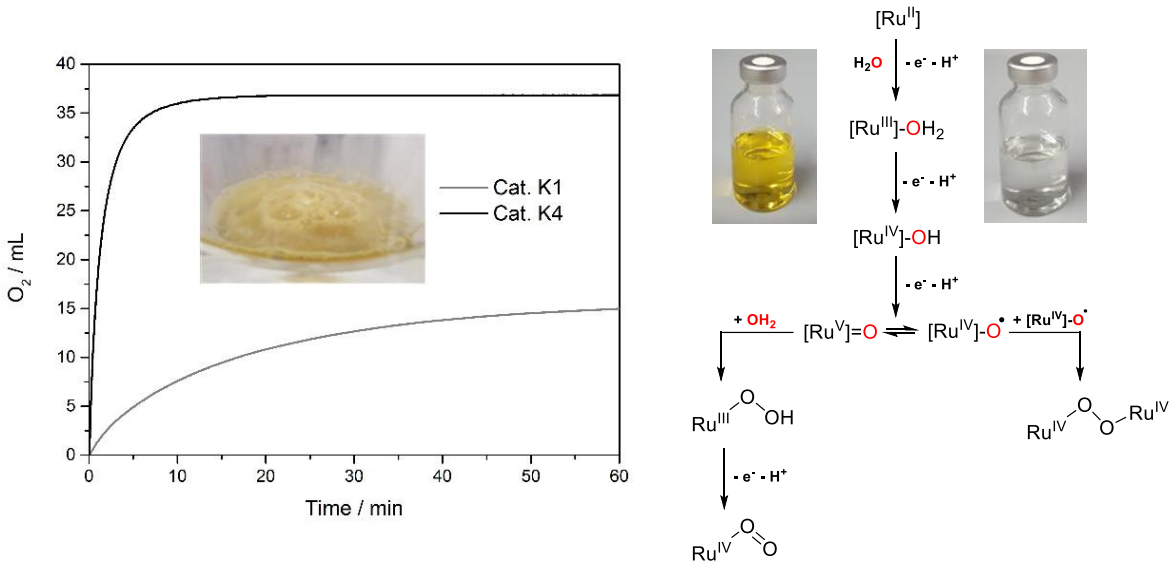

Figure 173. Oxygen evolution experiments with K1 and K4 and the proposed mechanism based on DFT calculation. Mechanism path reprinted from [131].

Contrary to previous findings in which the non-flexibility of substituted bda-ligands have been assumed to force catalysts towards the competing WNA pathway, the results of this work could show that the change in kinetic behaviour of the long-linker ruthenium water oxidation catalysts compared to the reference Ru-bda system was primarily induced by increased number of conjugated π-systems at the equatorial plane of the ligand backbone. In this context, a relatively high turnover frequency of 6 s^{-1} was obtained for the linear catalyst K4, while K1 displayed a TOF of 0.2 s^{-1}.

Kinetic studies on K4 showed a linear dependence on catalyst concentration, resulting in a slope value of ~1.1, being lower than that obtained for K1 with a slope value of ~1.4. These findings supposed that the geometrical arrangement of substituents on the equatorial ligand plane have a strong influence on the reaction path of water oxidation. While K4 shows a higher propensity to proceed *via* a mononuclear water nucleophilic attack reaction for the O-O bond formation, the kinetic results of K1 implie a mechanistic switch between the simple mononuclear and the bimolecular coupling pathway. Supporting evidence was given by computational simulations, which confirmed that addition of the terminal phenyl rings at the 5,5' positions led to a decrease of the activation barrier for the water nucleophilic attack. According to DFT, K1 produced an activation energy of 81,75 kJ/mol, while extending the π-conjugated system of the bipyridine at the 5,5'-positions appear to reduce the overall reorganization energy of forming the transition state enabling a lower activation barrier of 67,84 kJ/mol for the water nucleophilic attack. By comparison, the reference complex Ru-bda exhibited an activation energy of 83,50 kJ/mol, which is quite similar to that of K1. These results are in good agreement with kinetic water oxidation experiments performed with K1. Variation of the reference Ru-bda catalyst revealed that substitution at the equatorial plane led to an overall slowdown of O_2 release, while intramolecular H-bonding interactions between neighboring polar groups appear to strongly influence the catalyst stability. By comparison, the isoquionoline-substituted analogues showed better catalytic stability and higher catalytic activity, which is in excellent agreement with the literature and due to π-stacking interactions of the isoquinolines. DFT calculations confirmed that full removal of the carboxylic acid groups generally ended up in higher transition state energies, showing that introducing electron-withdrawing groups was essential to reduce the barrier for WNA by decreasing the redox potentials.

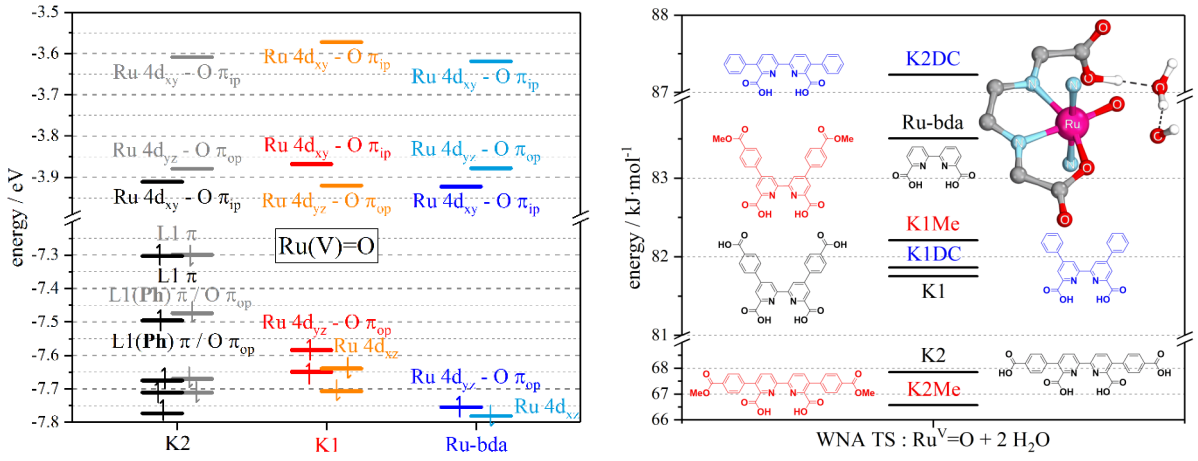

Figure 174. Results of theoretical calculations.

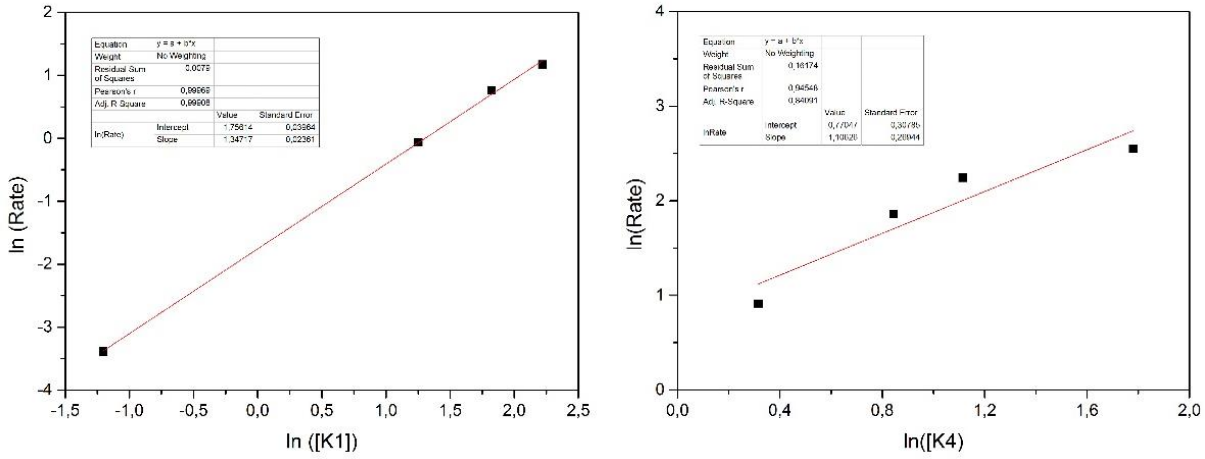

Figure 175. Results of kinetic experiments for K1 and K4.

In addition, increasing the steric demands of the surrounding ligands near both, the equatorial and axial plane, appear to blockade the catalyst's active site, thus making the coordination of water to the aqua complex more difficult or even impossible. Furthermore, it is proposed that the phenomenon of dangling carboxylate groups plays an important role in crucial O-O bond formation step, which seems to be inhibited within the complexes K16-K19 due to the increased stability of the Ru-N bonds located in the equatorial ligand backbone, at which the critical catalytic steps of water oxidation generally take place. Interestingly, this dangling effect is also observed in the Mn_4Ca^{2+} cluster of PSII, which seems to have beneficial effects on the catalytic features of metal catalysts.

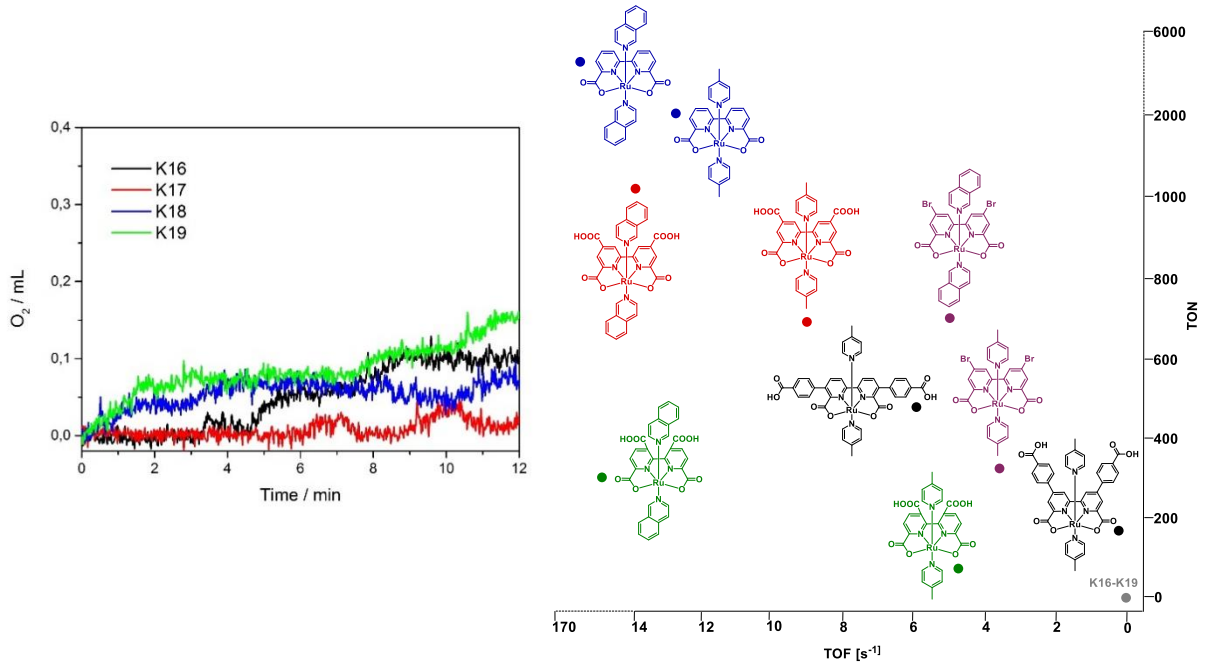

Figure 176. Left, results of oxygen evolution experiments performed with complexes based on carboxamide ligands. Left, overview of TON and TOF values of title compounds.

The final part of this thesis was the synthesis and characterization of highly porous metal-organic frameworks based on the UiO-68 type by varying a number of synthetic conditions. The results revealed that no general rule could be applied for the synthesis of UiO-68-NH_2. Nevertheless, a high BET surface area of 2066 m^2/g was obtained from nitrogen adsorption analysis, which is, to the best of our knowledge, the second highest value reported for UiO-68 since 2013. It posessess a large pore volume of 0.87 cm^3/g, while its average pore size was calculated to be 1.69 nm. Its thermal stability is around 450 °C.

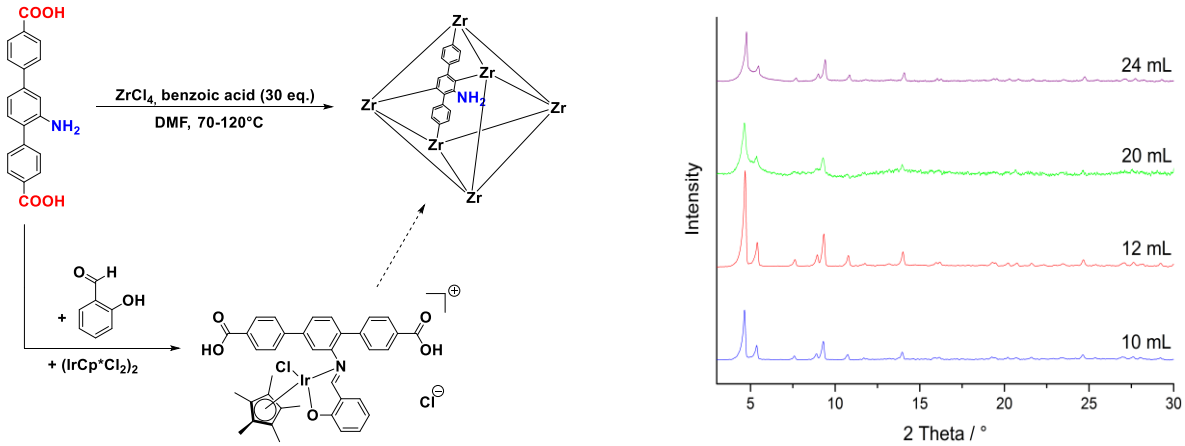

Figure 177. Left, general synthesis scheme of sal(IrCp*Cl). Right, XRD spectra of UiO-68-NH_2 under optimized conditions.

However, reproducibility was found to limit the synthesis of MOFs with increased pore size (**Chapter 10**). Initial modification steps on amino-tagged UiO-68 showed that the crystallinity drastically suffers from work-up procedures. The incorporation of pre-synthetically modified MOF linkers containing metal complexes that are capable of catalyzing water oxidation is believed to be an alternative for the development of MOFs for water-splitting. Hence, the first iridium-doped UiO-68 MOF linker was prepared on a moderate scale, whose large-scale production and immobilization into UiO-68 remain the main goals to be followed up in the future.

In summary, the present work shows that the construction of novel π-conjugated systems gave spectroscopic access to high-valent ruthenium-oxo species, which are typically difficult to detect. Considering that the linear catalyst K4 bearing 4-picoline at the axial positions exhibited an excellent TOF of 6 s^{-1} in organic-free medium, the large-scale production and isolation of its isoquinoline K5 and phthalazine K6 analogues is certainly of major interest since these ligands are well-known to enhance the catalytic features of a given catalyst. Moreover, the introduction of carboxylic acid groups gives the complexes the solubility they need for water oxidation. Additionally, it could be shown that the shift from light-driven water oxidation to chemical (CAN) conditions brings new levels of agility and simplicity to the catalytic reaction, while under photocatalytic conditions many more parameters must be optimized, and all of them are known to significantly influence the reaction. The large-scale production of energy from renewable sources is a long-term strategy, which is economically not very easy to realize. Nevertheless, if this could be done in future, their would be a chance to survive even after the total consumption of the world's total coal reserves, by only using water and sunlight as the only needed natural sources to produce clean energy.

CHAPTER 12

Analytical Methods and Instrumental Details

12.1 Analytical and spectroscopic equipment

NMR-Experiments: NMR spectra were recorded using a *Bruker Avance* spectrometer at 125 MHz for ^{13}C, 500 MHz for ^{1}H and 50 MHz for ^{15}N. The solvents and temperatures are noted for every substance. All chemical shifts refer to the δ scale and are given in ppm. Reference substances (δ = 0 ppm) are TMS (^{1}H, ^{13}C) and ammonia (^{15}N). ^{1}H- and ^{13}C-spectra are calibrated according to the chemical shifts of the solvent peaks. Two-dimensional NMR spectra, like COSY, HMBC and HMQC were used to ensure correct nuclei correlations, if possible. To paramagnetic ruthenium species, small smounts of ascorbic acid was added to ensure reduction of the central ruthenium atom, which reduced the quality of the resulting NMR spectra. Moreover, due to the limited solubility of the prepared ruthenium(II) carboxylate complexes in organic solvents, the recording of ^{13}C-, DEPT- and two-dimensional NMR spectra was difficult, if not impossible, for some cases. Hence, structural assignment was then achieved only by ^{1}H-NMR, mass spectrometric analysis, FT-IR and UV-vis.

Mass Spectroscopy: Electron ionization spectra were recorded with a *Synapt* G2 *QTOF* instrument of Waters. The solvents are noted for every substance. Mass spectra with EI as ionisation method were performed at 200 °C source temperature and 70 eV electron impact energy in connection with a *Thermo Scientific DFS* sector field mass spectrometer.

Infrared Radiation (IR) Measurements: FT-IR measurements were performed on a FT-IR spectrometer from *Bruker Vertex 70*.

UV/Vis- spectroscopy: UV-vis absorption spectra of catalysts (6×10^{-5} mol/L) were recorded at 298 K between 190 and 1100 nm in either freshly freeze-pumped water or acetonitrile/water

mixtures on a *Varian Cary 50* UV/Vis spectrophotometer. Any visible change of the solution color was recorded instantly to document any change in oxidation state. Redox titration experiments were performed by adding different equivalents of cerium(IV) ammonium nitrate (CAN) to freshly prepared solutions containing the respective catalyst (6×10^{-5} mol/L) at pH 1.

Elemental Analysis: Elemental analyses were performed on an *Elementar vario Micro Cube* instrument.

Electrochemistry: Electrochemical properties were investigated using cyclic- (CV) and square wave voltammetry (SWV) at room temperature, which were performed with the *PAR101* potentiostat from *Metrohm* in a solution of double distilled H_2O/ 0.1 M KPF_6 with the following three electrode arrangement: GC working electrode (1.6 mm diameter), Ag/AgCl / 3 M KCl reference electrode and Pt wire as counter electrode. The water solutions with concentrations between 1 and 2 mmole/L of dissolved Ru-complex were vented three times via the freeze-pump technique. All measurements were carried out under argon atmosphere in both, neutral (pH 7) and acidic (pH 1, HOTf) medium to electrochemically simulate at close-to-real water oxidation conditions. Electrochemical experiments carried out in organic solvent were conducted using 0,1 M NBu_4PF_6. A measured amount of ferrocene was added as an internal standard after the measurements to calibrate redox potentials, which were given with respect to the redox pair ferrocene/ferrocenium couple (Fc/Fc^+). The solvents are noted for every substance. Spectroelectrochemical measurements were performed with 10 mL aqueous solutions containing K2 (10^{-5} mol/L) in a bulk electrolysis cell consisting of a platinum gauze as working electrode, platinum wire as counter electrode and a Ag / 0.01 M $AgNO_3$ / MeCN reference electrode. A cuvette (1 mm optical path length) from *Hellma* was introduced to follow the electrolysis spectroscopically.

Single crystal X-ray diffraction: Intensity data were collected on a *Bruker AXS SMART APEX* diffractometer with graphite monochromated MoK radiation (λ = 0.71073 Å) at 1302 K. Data reduction and absorption correction were performed with SAINT and SADABS. The structures were solved with direct and conventional Fourier methods. All non-hydrogen atoms were refined anisotropically with full-matrix least-squares procedures based on F^2 by SHELXL. Hydrogen atom positions were derived from different Fourier maps and then refined at idealised

positions, riding on their parent C atoms with isotropic displacement parameters $U_{iso}(H) = 1.2\ U_{eg}(C)$.

Catalytic Experiments: Catalytic experiments were performed at room temperature in a 100 mL double-walled temperature controlled glass reactor which was connected to an automatic gas burette *(GASMESS-5-CONT)*. In a typical catalytic experiment, the reaction vessel was evacuated and flushed with argon for several times to remove any other gases. The catalytic activity of the complexes were tested by dissolving CAN (~ 5000 equiv.) in 0.1 M aqueous HOTf (14 mL, initial pH = 1), which was loaded into the reaction flask, followed by addition of a freshly prepared aqueous solution of the catalyst (10^{-4} mol/L) at a constant stirring rate. Oxygen evolution instanteuosly occured upon injecting the complex into the acidic CAN solution. The turnover numbers (TONs) are calculated from moles of produced O_2/moles of catalyst. Kinetic studies were performed to determine the order of reaction. In a typical kinetic experiment, the concentration of CAN was kept constant due to the large excess used in catalytic oxidation reactions, while the concentration of the Ru water oxidation catalyst was varied in the range of 20-600 µM. Rates of O_2 evolution were calculated from the slopes of linearly fitted O_2 evolution plots through the first 90 s. From the slopes of the linear plots of ln(Rate) *vs*. ln([Catalyst]), the order of the catalytic reaction was determined.

Gas chromatography: Gas chromatographic analyzes were performed with the following arrangement: a) Headspace *Agilent* 6890 with TCD-detectors (Thermal Conductivity Detector), ShinCarbon ST 100/120 (molecular sieve): 2 m; 1 mm ID, argon as carrier gas (14 ml/min). Program of temperature: 45 °C; 25 °C/min; 250 °C. Injector: 150 °C, 1:5. Injection of 1,5 ml from gas volume of the respective reaction solution, detector: 300 °C. b) *Inficon*. Micro GC Fusion with TCD detector, Et-Molsieve 5 Å: 10 m; 0,25 mm ID, argon as carrier gas. Injector: 90 °C, Backflush, sampling time, 60 seconds.

DFT studies: Density functional theory (DFT) calculations were performed by L. Burkhardt (working group of Prof. Dr. M. BAUER), which are essential to understand the catalytic behaviors of Ru-bda complexes. The purpose of the theoretical study here is to explore the configurations of intermediates and energetics of unit reactions involved in the catalytic water oxidation pathway. In order to describe the surroundings of the aqueous medium accurately, an explicit water molecule was included as an acceptor of hydrogen bonding for each polar

hydrogen (aqua or hydroxyl group) when the geometry of ruthenium intermediates was simulated.

All calculations presented here were performed with the ORCA package (version 4.0.1). Unconstrained geometry optimizations were conducted with the PBEh-3c method of the Grimme group. 10.1021/acs.jctc.7b00365 Minima structures were confirmed by analytical frequency calculations and the absence of negative frequencies.

Transition state (TS) search were performed by relaxed surface scans of the O-O coordinate, to find structures close to the particular transition state (TS). Afterwards, structures close to the TS were used as a starting point for TS geometry optimization. TSs were confirmed by presence of one negative frequency and the negative frequency has been verified to be localized on the O-O reaction coordinate.

Energies were calculated using the PBE0 10.1063/1.478522 functional in conjunction with the def2-TZVP Basisset 10.1039/B508541A, the def2-ecp for Ru 10.1016/0009-2614(96)00382-X with very tight SCF convergence criteria (energy change of 1.0 e-9 au). Dispersion correction has been performed via Becke-Johnson damping scheme 10.1063/1.3382344 10.1002/jcc.21759. Solvation by water is covered by the SMD solvation model 10.1021/jp810292n, as implemented in ORCA (version 4.0.1). All energies were correct for basis set superposition error (BSSE) 10.1063/1.3700154.

Thermogravimetric Analysis (TGA): Thermogravimetric analysis was performed with the Mettler Toledo TGA/SDTA851 with the following method parameters: MT-25-600-10 pm-Air, Δt 1 s, 25-600 °C, 10 °C/min, Air 85 ml/min.

P-XRD analysis: Powder XRD was performed with a *Bruker AXS D8 Advance* diffractometer with Cu-K_α (λ = 0.154 nm) radiation (40 kV, 40 mA), a step size of 0.02 °, and a counting time of 9 s per step.

N_2 physisorption: In order to analyze the property of a porous system, N_2 physisorption analyses were performed at 77 K on a *Quantachrome Autosorb 6* instrument. The samples were degassed at 200 °C for 12 h prior measurement. Specific surface areas were assessed by multi-point Brunauer-Emmett-Teller (BET) analysis in the range of $0.1 \leq p/p_0 \leq 0.3$. Pore volumes were calculated at $p/p_0 = 0.99$. Pore size distributions were calculated by Barrett, Joyner, und Halenda (BJH) analysis from the desorption branches of the isotherms.

12.2 Experimental section

12.2.1 Chemicals and synthetic techniques

All reactions carried out under anhydrous conditions were performed in dried glassware and under argon atmosphere using Schlenk and glove box techniques. All chemicals were reagent grade and were used without any further purification. If not marked otherwise, all solvents were purchased from commercial sources and used without further purification. Prior to use methanol was dried and distilled over Mg. Acetonitrile was pre-dried over 4Å mole sieves and distilled over calcium hydride. THF was distilled from sodium/benzophenone. Toluene was pre-dried over CaH_2 with 4Å mole sieves and then fractionally distilled from sodium. Triethylamine was dried over $CaSO_4$ followed by distillation from CaH_2. All solvents were de-oxygenated with three freeze-thaw cycles under reduced pressure and stored in air-free storage flasks in the dark. 6-amino-2-methylpyridine and dry DMSO were purchased from Sigma Aldrich Chemical Company, $RuCl_3 \cdot xH_2O$ was obtained from abcr GmbH. Compounds, which were prepared according to literature procedures are marked as such.

12.2.2 Synthesis and characterization of the organic ligands

12.2.2.1 Synthesis of ligand L1

6-bromo-2-methylpyridine.

The preparation of 6-bromo-2-methylpyridine was performed according to the method described in [208]. 48 % hydrobromic acid (147 mL) was cooled to -20 °C and 30.1 g (278 mmole) 6-amino-2-methylpyridine was added under stirring. Bromide (45.4 mL, 885 mmole) was added slowly through a dropping funnel. The obtained yellow solution turned to orange and a voluminous precipitate was formed. The reaction mixture was stirred at the same temperature for additional 30 min. 50.8 g sodium nitrite (737 mmole) was dissolved in water (75 mL) and then introduced dropwise into the reaction mixture over 30 min. The deep brown suspension was stirred at < 0 °C for 2 ½ h. When the reaction mixture reached pH 10 by adding 20 % NaOH, the color of the solution changed to pale yellow. After extraction with diethyl ether (3 x 150 mL) and evaporation with rotary evaporator, a dirtybrown oil was obtained. The residue was fractionally distilled (Lit. 87 °C, 13 mbar. exp 70 °C, 8 mbar) yielding a colorless to pale yellow liquid (Yield: 89 %, 42.5 g, 247 mmole).

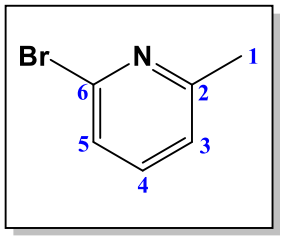

^{1}H NMR (500 MHz, $CDCl_3$): δ = 2.23 (s, 3H, H^1), 6.82 (d, ^{3}J = 7.7 Hz, H^3), 6.98 (d, ^{3}J = 8.0 Hz, H^5), 7.15 (t, ^{3}J = 7.7 Hz, ^{3}J = 8.0 Hz, H^4).

^{13}C NMR (125 MHz, $CDCl_3$): δ = 23.9 (C^1), 122.0 (C^3), 124.8 (C^5), 138.5 (C^4), 141.0 (C^6), 159.7 (C^2).

^{15}N NMR (500 MHz, $CDCl_3$): 276 ppm.

The spectroscopic data are in accordance with the literature.[208]

6,6'-dimethyl-2,2'-bipyridine.

6,6'-dimethyl-2,2'-bipyridine was prepared according to the procedure described by Duan et al.[190] By varying the reaction conditions, time of work-up could be succesfully reduced. 2.6 g (10.8 mmole) $NiCl_2$ x 6 H_2O in 431 mL of DMF was heated with stirring to 40 °C. Then 37.1 g (215.4 mmole) of 6-bromo-2-methylpyridine, anhydrous 9.1 g (215.4 mmole) lithium chloride and 17 g (258.4 mmole) zinc dust were added and the reaction mixture was heated to 70 °C. A few drops of acetic acid and gains of iodine were added to catalyze the reaction. Heating was continued for additional 3 hours. After cooling, an aqueous solution of 1N HCl (323 mL) was added to consume the remaining zinc dust, followed by the addition of aqueous ammonia (25%) to make alkaline (pH 12). After extraction with CH_2Cl_2 (3 x 150 mL), the organic phases were collected, dried over Na_2SO_4 and concentrated to give an orange oil. On standing at room temperature, the product crystallized out which was further purified from oily by-product by dissolving in *n*-Hexan (2 x 300 mL). After removing the organic solvent under reduced pressure, 6,6'-dimethyl-2,2'-bipyridine was isolated in 74 % (29.3 g, 159 mmole) as a pale yellow solid.

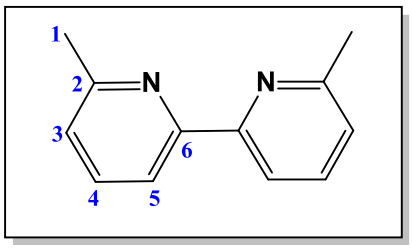

^{1}H NMR (500 MHz, $CDCl_3$): δ = 2.62 (s, 6H, H^1), 7.14 (d, ^{3}J = 7.7 Hz, 2H, H^5), 7.66 (t, ^{3}J = 7.7 Hz, ^{3}J = 8.0 Hz, 2H, H^4), 8.16 (d, ^{3}J = 8.0, 2H, H^3).

^{13}C NMR (125 MHz, $CDCl_3$): δ = 24.6 (C^1), 118.2 (C^5), 123.0 (C^3), 136.9 (C^4), 155.9 (C^6), 157.8 (C^2).

^{15}N NMR (500 MHz, $CDCl_3$): 305 ppm.

Anal. Found (calcd) for $C_{12}H_{12}N_2$: C, 77.60 (78.23); H, 6.57 (6.57); N, 15.10 (15.21).

ESI-MS: m/z (%): 185.10(95).

The spectroscopic data are in accordance with the literature.[190]

6,6'-dimethyl-2,2'-dipyridyl di-*N*-*N'*-oxide.

For the syntheses of the following steps, literature-known methods[209] were implemented by varying the experimental conditions with significant yield improvement. The desired compound was prepared by the reaction with peroxycarboxylic acid, which was generated *in-situ* from acetic acid and hydrogen peroxide. 16.7 g (90.6 mmole) 6,6'-dimethyl-2,2'-bipyridine was dissolved in glacial acetic acid (105 mL). Then the solution was heated to 80 °C and 31.6 mL of H_2O_2 (35 %) was added. Heating was continued for addtitional 7 hours in which time the color of the solution became clearer. After cooling to room temperature overnight, the solution was neutralized with 20 % NaOH and extracted with chloroform. After vacuum evaporation, a yellow oil was obtained, from which product was precipitated by adding diethyl ether as off-white solid in 91 % (17.83 g, 82 mmole) yield.

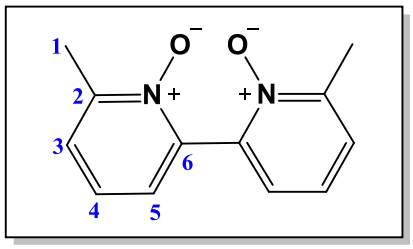

^{1}H NMR (500 MHz, $CDCl_3$): δ = 2.55 (s, 6H, H^1), 7.20 (t, ^3J = 7.7 Hz, ^3J = 8.0 Hz, 2H, H^4), 7.34 (d, ^3J = 7.7 Hz, 4H, H^3, H^5).

^{13}C NMR (125 MHz, $CDCl_3$): δ = 17.9 (C^1), 124.1 (C^3), 125.4 (C^5), 126.8 (C^4), 143.6 (C^2), 149.7 (C^6).

^{15}N NMR (500 MHz, $CDCl_3$): 280 ppm.

Anal. Found (calcd) for $C_{12}H_{12}N_2O_2$: C, 55.08 (66.60); H, 5.17 (5.59); N, 10.13 (12.96).

ESI-MS $[M + Na]^+$: m/z (%): 239.08(04).

The spectroscopic data are in accordance with the literature.[209]

6,6'-dimethyl-4,4'-dinitro-2,2'-dipyridyl di-*N*,*N'*-oxide.

The introduction of nitro groups was achieved by nitration with nitrating acid. Therefore, a three-necked flask was loaded with concentrated sulphuric acid (123 mL) with cooling in an ice bath and constantly stirring, following by the slowly addition of fuming nitric (41 mL) from

a syringe. Then 17.5 g (81 mmole) 6,6‘-dimethyl-4,4‘-2,2‘-dipyridyl di-*N,N‘*-oxide was added in portions to avoid strong nitrous gases which were initiated in a wash-bottle filled with aqueous sodium hydroxide. The nitration was carried out at 70°C for 6 h. After cooling to 0°C, the clearly yellow solution was poured into ice water (584 mL). A yellow solid was precipitated. After cooling overnight, the suspension was neutralized with 16 M NaOH whereupon precipitation occurred, which was filtered off, washed with water and dichloromethane and dried under vacuum. The product was isolated in 93 % (23.1 g, 75 mmole) as a yellow solid.

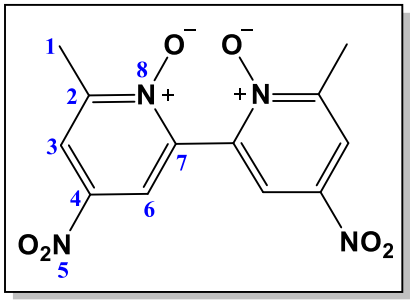

^{1}H NMR (500 MHz, DMSO-d$_6$): δ = 2.49 (s, 6H, H^1), 8.53 (d, ^4J = 3.2 Hz, 2H, H^3), 8.60 (d, ^4J = 3.2 Hz, 2H, H^6).

^{13}C NMR (125 MHz, DMSO-d$_6$): δ = 17.6 (C^1), 121.3 (C^3), 121.8 (C^6), 140.6 (C^7), 142.9 (C^4), 150.5 (C^2).

^{15}N NMR (500 MHz, DMSO-d$_6$): 301 ppm (s, N^8), 364 ppm (s, N^5).

Anal. Found (calcd) for $C_{12}H_{12}N_4O_6$: C, 44.73 (47.07); H, 3.39 (3.29); N, 17.70 (18.30).

ESI-MS $[M + Na]^+$: m/z (%): 329.05(06).

6,6'-dimethyl-4,4'-dibromo-2,2'-dipyridyl di-*N,N'*-oxide.

10 g (32.66 mmole) 6,6'-dimethyl-4,4'-dinitro-2,2'-dipyridyl di-*N,N'*-oxide was suspended in 131 mL (2286 mmole) acetyl bromide and the reaction mixture was heated to 95 °C overnight. After completion of the reaction, the mixture was cooled to room temperature and ice water (1650 g) was added, followed by neutralization with 25 % sodium carbonate and extraction with dichloromethane (3 x 200 mL). The organic phases were collected, dried over anhydrous Na_2SO_4 and concentrated under reduced pressure to give a pale yellow solid. To increase the purity of the solid product, the crude product was washed with a small quantity of cold acetone. 6,6'-dimethyl-4,4'-dibromo-2,2'-dipyridyl di-*N,N'*-oxide was obtained in 60 % (7.3 g, 19.6 mmole) and used without further purification for the next step.

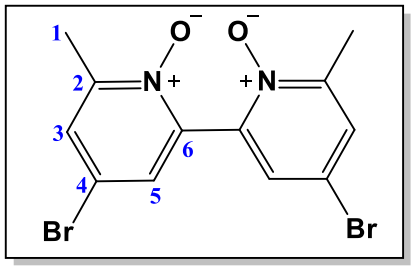

^{1}H NMR (500 MHz, DMSO-d_6): δ = 2.36 (s, 6H, H^1), 7.83 (d, ^{4}J = 3.0 Hz, 2H, H^3), 7.92 (d, ^{4}J = 3.0, 2H, H^5).

^{13}C NMR (125 MHz, DMSO-d_6): δ = 17.5 (C^1), 115.7 (C^4), 129.0 (C^5), 130.1 (C^3), 143.4 (C^6), 150.1 (C^2).

^{15}N NMR (500 MHz, DMSO-d_6): 286 ppm.

Anal. Found (calcd) for $C_{12}H_{10}Br_2N_2O_2$: C, 36.61 (38.53); H, 2.72 (2.69); N, 7.05 (7.49).

ESI-MS: m/z (%): 374.92(15).

4,4'-dibromo-6,6'-dimethyl-2,2'-bipyridine.

The removal of the oxygen atoms was performed with PBr_3. Under an argon atmosphere, 9 g (24.02 mmole) 6,6'-dimethyl-4,4'-dibromo-2,2'-dipyridyl di-*N*,*N*'-oxide was loaded into a Schlenk flask and dissolved in anhydrous dichloromethane (225 mL). After addition of 45 mL PBr_3 (473 mmole), the reaction mixture was heated to reflux for 2 hours, followed by stirring at room temperature overnight. The mixture was poured on ice (135 mL) and made neutral with 20 % NaOH at 0 °C, whereupon an off-white precipitate fell out of solution which was filtered off and washed with a small quantity of water. The aquoeus phase was made alkaline (pH 10) and extracted with dichloromethane (3 x 50 mL) to get a second crop of product. Sublimation was performed to produce pure white 4,4'-dibromo-6,6'-dimethyl-2,2'-bipyridine in 86 % (7.1 g, 20.6 mmole) yield.

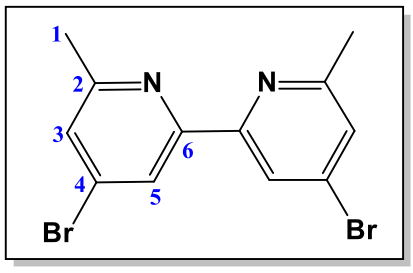

^{1}H NMR (500 MHz, $CDCl_3$): δ = 2.60 (s, 6H, H^1), 7.33 (d, ^{4}J = 1.2 Hz, 2H, H^3), 8.38 (d, ^{4}J = 1.2, 2H, H^5).

^{13}C NMR (125 MHz, $CDCl_3$): δ = 24.3 (C^1), 121.8 (C^5), 126.6 (C^3), 133.9 (C^4), 155.6 (C^6), 159.3 (C^2).

^{15}N NMR (500 MHz, $CDCl_3$): 289 ppm.

Anal. Found (calcd) for $C_{12}H_{10}Br_2N_2$: C, 41.89 (42.14); H, 3.15 (2.95); N, 8.10 (8.19).

ESI-MS: m/z (%): 342.92(72).

4,4-dibromo-2,2-dipyridyl-6,6-dicarboxylic acid.

4,4-dibromo-2,2-dipyridyl-6,6-dicarboxylic acid was prepared according to the procedure described in [210]. The methyl groups were transferred to acid groups by oxidation with CrO_3. The starting 4,4-dibromo-6,6-dimethyl-2,2-dipyridyl (1.23 g, 3.59 mmole) was dissolved at 50 °C in concentrated sulfuric acid (17 mL) and heated to 70 °C. Upon addition of 1.80 g (18 mmole) chromium trioxide in small portions, the yellow color of the reaction mixture turned green and the mixture was heated for additional 2 hours, controlling the temperature increase not higher than 75 °C. After completion of reaction, the mixture was poured into ice-water (72 g), whereupon a white precipitate separated. The reaction flask was left for stirring overnight to ensure complete precipitation. The product was collected by filtration and washed with small amounts of water, ethanol, and diethyl ether, and left under high-vacuum for several hours. 4,4-dibromo-2,2-dipyridyl-6,6-dicarboxylic acid was obtained in 58 % (0.84 g, 2.1 mmole) yield as white powder.

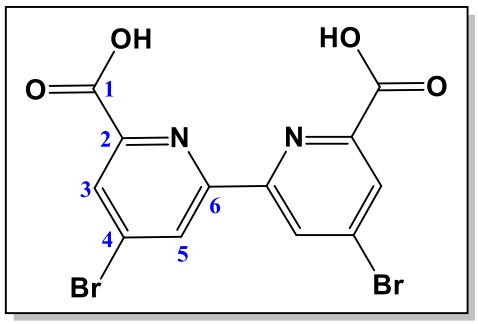

^{1}H NMR (500 MHz, DMSO-d_6): δ = 8.29 (br.s, 2H, H^3), 8.92 (br.s, 2H, H^5).

^{13}C NMR (125 MHz, DMSO-d_6): δ = 125.0 (C^3), 132.8 (C^5), 137.6 (C^4), 150.9 (C^2), 157.6 (C^6), 168.3 (C^1).

^{15}N NMR (500 MHz, DMSO-d_6): 164 ppm.

Anal. Found (calcd) for $C_{12}H_6Br_2N_2O_4$: C, 35.77 (35.85); H, 1.86 (1.50); N, 7.09 (6.97).

IR (KBr, cm^{-1}): 1779 (w), 1714 (s), 1699 (sh), 1652 (sh), 1562 (sh), 1548 (m), 1473 (w), 1386 (w), 1353 (w), 1313 (w), 1280 (w), 1267 (m), 1242 (sh), 1209 (sh), 1168 (m), 1118 (w), 1039 (w), 987 (w), 908 (w), 883 (m), 846 (m), 786 (m), 715 (s), 676 (s), 580 (sh), 549 (w), 511 (m), 470 (w), 418 (w), 397 (w), 352 (m), 327 (sh), 302 (w), 283 (sh), 279 (w), 268 (sh), 246 (w), 227 (w), 204 (m).

The spectroscopic data are in accordance with the literature.[210]

Dimethyl-4,4'-dibromo-2,2'bipyridine-6,6'-dicarboxylate.

The desired dibromodicarboxylate was synthesized by esterification. The diacid compound (0.9 g, 2.22 mmole) was dissolved in 22 mL dry methanol and 2.2 mL concentrated sulphuric acid was added stirring at 70 °C overnight. The reaction mixture was cooled to room temperature and evaporated under vacuum resulting in a colorless solution. A small quantity of water (15 ml) was poured on the residue before adding 25 % Na_2CO_3 at room temperature in order to bring the pH to about 9. The product, produced in 61 % (0.58 g, 1.4 mmole), was separated by filtration and dried to dryness at high vacuum.

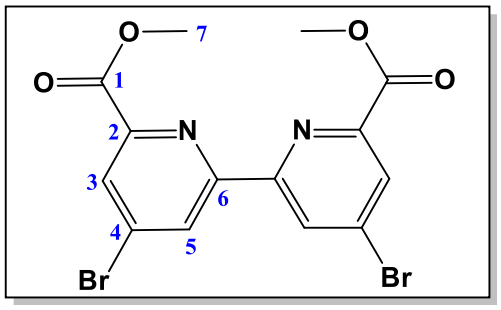

^{1}H NMR (500 MHz, $CDCl_3$): δ = 4.05 (s, 6H, H^1), 8.31 (d, ^4J = 1.7 Hz, 2H, H^3), 8.82 (d, ^4J = 1.7 Hz, 2H, H^5).

^{13}C NMR (125 MHz, $CDCl_3$): δ = 53.2 (C^7), 128.1 (C^3), 129.2 (C^5), 135.1 (C^4), 148.6 (C^2), 155.3 (C^6), 164.4 (C^1).

^{15}N NMR (500 MHz, $CDCl_3$): 337 ppm.

Anal. Found (calcd) for $C_{14}H_{10}Br_2N_2O_4$: C, 37.36 (39.10); H, 2.45 (2.34); N, 6.36 (6.51).

IR (KBr, cm^{-1}): 1747 (s), 1724 (sh), 1695 (sh), 1660 (w), 1627 (w), 1562 (s), 1548 (s), 1502 (w), 1494 (sh), 1442 (m), 1415 (w), 1388 (m), 1319 (w), 1276 (s), 1255 (s), 1188 (m), 1149 (s), 1087 (m), 1070 (sh), 1010 (w), 964 (m), 918 (w), 883 (m), 848 (w), 813 (w), 784 (s), 736 (s), 707 (w), 682 (s), 634 (w), 613 (w), 588 (w), 559 (w), 513 (m), 478 (w), 447 (w), 412 (w), 358 (m), 298 (w), 283 (sh), 260 (m), 237 (w), 221 (sh), 204 (sh).

ESI-MS $[M + Na]^+$: m/z (%): 452.88(84).

Dimethyl 4,4'-bis(4-(methoxycarbonyl)phenyl)-2,2'-bipyridine-6,6'-dicarboxylate.

1.19 g dimethyl-4,4'-dibromo-2,2'bipyridine-6,6'-dicarboxylate (2.76 mmole), 1.24 g (6.91 mmole) 4-methoxycarbonylphenylboronic acid, 1.51 g (7.07 mmole) K_3PO_4 and 0.24 g (0.2 mmole) $Pd(PPh_3)_4$ were charged into a flame-dried Schlenk flask under argon in a glove box and dissolved in 71 mL anhydrous DMF. Because of the light sensitive palladium catalyst, the reaction was carried out in darkness and heated to 100 °C for 72 hours. The product was precipitated during reaction time which was filtered off and recrystallized from chloroform.

The solution was filtered off from the undissolved white residue and evaporated under vacuum, yielding an off-white solid in 70 % (1.04 g, 1.93 mmole). To remove DMF from the product, the crude product was stirred in petrolether (150 mL) overnight and filtered off.

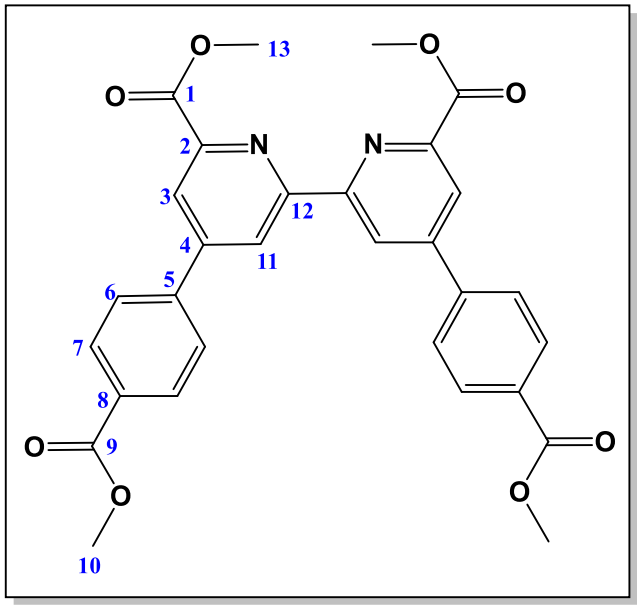

^{1}H NMR (500 MHz, $CDCl_3$): δ = 4.00 (s, 6H, H^{10}), 4.10 (s, 6H, H^{13}), 7.89 (d, ^{3}J = 8.2 Hz, 4H, H^{6}), 8.20 (d, ^{3}J = 8.2 Hz, 4H, H^{7}), 8.45 (d, ^{4}J = 1.7 Hz, 2H, H^{3}), 9.00 (d, ^{4}J = 1.7 Hz, 2H, H^{11}).

^{13}C NMR (125 MHz, $CDCl_3$): δ = 52.3 (C^{10}), 53.0 (C^{13}), 122.9 (C^{11}), 123.7 (C^{3}), 127.4 (C^{6}), 130.4 (C^{7}), 131.1 (C^{8}), 141.6 (C^{5}), 148.5 (C^{2}), 149.8 (C^{4}), 156.2 (C^{12}), 165.6 (C^{1}), 166.5 (C^{9}).

^{15}N NMR (500 MHz, $CDCl_3$): 302 ppm.

Anal. Found (calcd) for $C_{30}H_{24}N_2O_8$: C, 64.46 (66.66); H, 4.92 (4.48); N, 4.07 (5.18).

IR (KBr, cm^{-1}): 1768 (br), 1718 (s), 1593 (s), 1540 (w), 1512 (sh), 1471 (w), 1446 (w), 1431 (m), 1417 (w), 1377 (w), 1313 (m), 1294 (m), 1247 (m), 1186 (w), 1155 (w), 1103 (m), 1078 (sh), 1064 (m), 1014 (w), 991 (sh), 954 (w), 906 (w), 854 (m), 827 (w), 810 (sh), 788 (w), 767 (s), 723 (w), 709 (m), 698 (sh), 661 (m), 642 (sh), 622 (sh), 597 (w), 545 (w), 526 (w), 499 (sh), 476 (m), 435 (w), 420 (w), 399 (sh), 351 (m), 312 (w), 281 (sh), 239 (w), 212 (w).

ESI-MS: m/z (%): 541.16(09).

6,6'-dimethyl-2,2'-bipyridine-4,4'-dibenzoic acid.

1.03 g (1.9 mmole) of dicarboxylate was dissolved in 274 mL THF under vigorous stirring at 40 °C. Then 136.6 mL KOH in MeOH (5.5 mol/L) was added and stirred for 2 days at the same temperature. A purple solid was formed during reaction time which was filtered and suspended

in THF (109 mL), followed by addition of trifluoracetic acid (13.6 mL, 178 mmole). After stirring 1.5 h at room temperature, water (273 mL) was added whereupon a white solid precipitated. The reaction flask was left for stirring overnight to ensure complete precipitation. 6,6'-dimethyl-2,2'-bipyridine-4,4'-dibenzoic acid was obtained in 63 % (0.58 g, 1.2 mmole) yield.

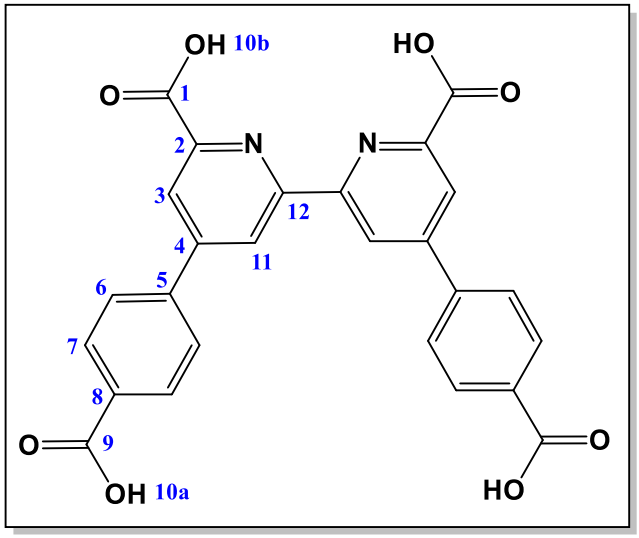

^{1}H NMR (500 MHz, DMSO-d_6): δ = 8.11 (d, ^{3}J = 8.4 Hz, 4H, H^{6}), 8.17 (d, ^{3}J = 8.4 Hz, 4H, H^{7}), 8.47 (d, ^{4}J = 1.6 Hz, 2H, H^{3}), 9.12 (d, ^{4}J = 1.6 Hz, 2H, H^{11}), 13.24 (br.s, 4H, COOH, $H^{10a/b}$).

^{13}C NMR (125 MHz, DMSO-d_6): δ = 122.4 (C^{11}), 123.5 (C^{3}), 128.0 (C^{6}), 130.7 (C^{7}), 132.3 (C^{8}), 141.1 (C^{5}), 149.5 (C^{4}), 149.6 (C^{2}), 155.6 (C^{12}), 166.1 (C^{1}), 167.3 (C^{9}).

^{15}N NMR as well as elemental analysis could not be applied for $C_{26}H1_6N_2O_8$ due to strong H-bonding interactions.

IR (KBr, cm^{-1}): 3097 (w), 3066 (w), 2980 (w), 2970 (m), 2920 (m), 2850 (m), 1770 (m), 1697 (s), 1686 (s), 1653 (sh), 1637 (sh), 1595 (s), 1578 (sh), 1558 (w), 1541 (m), 1520 (sh), 1508 (sh), 1489 (w), 1473 (w), 1458 (m), 1419 (s), 1375 (w), 1362 (w), 1321 (m), 1296 (m), 1271 (m), 1236 (sh), 1217 (m), 1169 (br), 1101 (br), 1076 (sh), 1061 (m), 1016 (w), 991 (w), 935 (w), 906 (m), 856 (s), 797 (w), 771 (s), 746 (sh), 719 (m), 698 (m), 669 (m), 656 (sh), 606 (w), 590 (w), 545 (m), 527 (sh).

ESI-MS: m/z (%): 483.08(34).

12.2.2.2 Synthesis of ligand L2

5-bromo-6-methyl-2-pyridinamine.

5-bromo-6-methyl-2-pyridinamine was synthesized according to the method described in [211]. To a solution of 10 g (92.5 mmole) 6-methyl-2-pyridinamine in methanol (284 mL) was slowly added 16.8 g (94.5 mmole) NBS in portions. The color of the solution turned from colorless to yellow. After a reaction time of 30 min at room temperature, the solvent was removed under reduced pressure. The reaction mixture was quenched with water (200 mL), diluted with ethyl acetate (100 mL) and washed with aqueous $NaHCO_3$ (3 x 100 mL) and brine (3 x 100 mL). The organic phases were collected amd dried over Na_2SO_4. After removal of the solvent in vacuo the product was obtained in 99 % (17.1 g, 91.6 mmole) as an off-white solid.

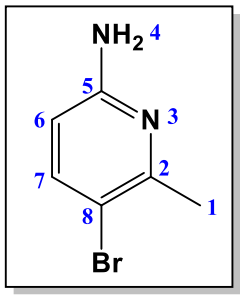

^{1}H NMR (500 MHz, $CDCl_3$): δ = 2.49 (s, 3H, H^1), 4.37 (s, 2H, H^4), 6.21 (dd, ^{3}J = 8.6 Hz, ^{5}J = 0.6 Hz, 1H, H^6), 7.46 (d, ^{3}J = 8.6 Hz, 1H, H^7).

^{13}C NMR (125 MHz, $CDCl_3$): δ = 24.4 (C^1), 107.6 (C^6), 108.7 (C^8), 141.3 (C^7), 155.1 (C^2), 156.7 (C^5).

^{15}N NMR (500 MHz, $CDCl_3$): 271 ppm (s, N^3).

Anal. Found (calcd) for C_6H_7BrN: C, 38.60 (38.53); H, 3.86 (3.77); N, 14.79 (14.98).

EI-MS: m/z (%): 187.94(49).

The spectroscopic data are in accordance with the literature.[211]

3,6-dibromo-2-methyl-pyridine.

The desired compound is synthesized according to the method described in [208]. 17.2 g (92 mmole) 2-amino-5-bromo-6-methypyridine were dissolved in 89 mL aqueous HBr at -10 °C. Bromine (9.5 mL, 184 mmole) was added dropwise. After 30 minutes stirring, aqueous $NaNO_2$ (15.9 g in 18 mL water, 232 mmole) was added in portions and the reaction mixture was stirred for 2 hours at room temperature. To stop the reaction, the mixture was poured onto ice-water (92 mL), followed by neutralization to pH 10 with sodium hydroxide (20 %). The solution was extracted with dichlormethane (3 x 150 mL) and evaporated under reduced pressure. A brown solution was obtained which was washed with *n*-hexane. The undissolved

brown solid was separated from the organic phase. The *n*-hexane phase was evaporated producing a red solution which was dried under high vacuum. During this time, the product crystallized out of the solution. After purification by vacuum sublimation, the product was isolated as pure white solid in 65 % (15.1 g, 59.8 mmole).

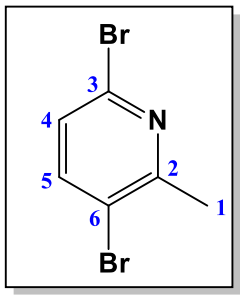

^{1}H NMR (500 MHz, $CDCl_3$): δ = 2.63 (s, 3H, H^1), 7.18 (d, ^{3}J = 8.3 Hz, 1H, H^4), 7.59 (d, ^{3}J = 8.3 Hz, 1H, H^5).

^{13}C NMR (125 MHz, $CDCl_3$): δ = 24.1 (H^1), 120.5 (C^6), 126.7 (C^4), 139.4 (C^3), 142.0 (C^5), 158.8 (C^2).

^{15}N NMR (500 MHz, $CDCl_3$): 318 ppm.

Anal. Found (calcd) for $C_6H_5Br_2N$: C, 28.26 (28.72); H, 2.10 (2.01); N, 5.51 (5.58).

EI-MS: m/z (%): 251.88(58).

3-bromo-6-iodo-2-methylpyridine.

3-bromo-6-iodo-2-methylpyridine was synthesized according to the method described in [212]. Under an argon atmosphere, sodium iodide 14.4 g (96 mmole) was loaded into a reaction flask and completely dissolved in dry acetonitrile (120 mL). Upon addition of 3,6-dibromo-2-methylpyridine (6 g, 24 mmole), a brown reaction mixture was formed, followed by addition of acetyl chloride (2.5 mL, 36 mmole). While heating at reflux, an orange suspension was formed. Heating was continued over 2 days. After cooling to room temperature, the mixture was quenched with water and basified with saturated sodium bicarbonate (pH = 10). Then the dark solution was extracted with ethyl acetate (3 x 150 mL) and the combined organic extracts were washed with brine and dried over sodium sulfate. The solvent was removed in vacuo to obtain a red oil. The residue was washed with *n*-hexane (250 mL), while the undissolved solid was separated from the organic phase. The *n*-hexane solution was evaporated under reduced pressure. An oil was obtained from which product crystallized out on standing at room temperature in 89 % (6.4 g, 21.4 mmole) yield.

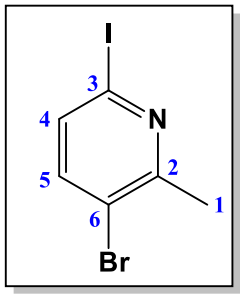

^{1}H NMR (500 MHz, $CDCl_3$): δ = 2.62 (s, 3H, H^1), 7.40 (s, 2H, H^4, H^5).

^{13}C NMR (125 MHz, $CDCl_3$): δ = 24.7 (C^1), 114.6 (C^3), 121.9 (C^6), 133.5 (C^4), 141.1 (C^5), 159.4 (C^2).

^{15}N NMR (500 MHz, $CDCl_3$): 333 ppm.

Anal. Found (calcd) for C_6H_5BrIN: C, 24.88 (24.19); H, 1.95 (1.69); N, 4.87 (4.70).

ESI-MS: m/z (%): 299.87(04).

5,5‘-dibromo-6,6‘-dimethyl-2,2‘-bipyridine.

The preparation of 5,5‘-dibromo-6,6‘-dimethyl-2,2‘-bipyridine was performed according to the method described in [213]. Under an argon atmosphere, 4.8 g (16.4 mmole) 3-bromo-6-iodo-2-methylpyridine and $Pd(PPh_3)_4$ (0.5 g, 0.43 mmole) were loaded into a 2-neck Schlenk flask. Anhydrous toluene (176 mL) and *n*-Bu_6Sn_2 (5 mL, 8.8 mmole) were added and the resulting solution was refluxed (115 °C) for 2 days. After cooling to room temperature, the solvent was evaporated under vacuum. The residue was dissolved in dichloromethane (100 mL) and the organic phase was washed with water (3 x 100 mL) and brine (3 x 100 mL), dried over Na_2SO_4 and concentrated under reduced pressure. After precipitation from methanol, the product was obtained in 73 % (4 g, 12 mmole) as fine white solid.

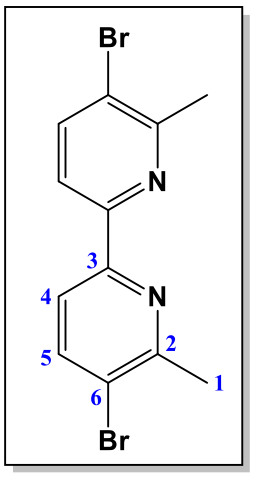

^{1}H NMR (500 MHz, $CDCl_3$): δ = 2.69 (s, 3H, H^1), 7.91 (d, ^{3}J = 8.4 Hz, 1H, H^5), 8.10 (dd, ^{3}J = 8.4 Hz, ^{5}J = 0.4 Hz, 1H, H^4).

^{13}C NMR (125 MHz, $CDCl_3$): δ = 25.1 (C^1), 119.7 (C^4), 121.8 (C^3), 140.5 (C^5), 153.6 (C^2), 156.6 (C^6).

^{15}N NMR (500 MHz, $CDCl_3$): 310 ppm.

Anal. Found (calcd) for $C_{12}H_{10}Br_2N_2$: C, 44.53 (42.14); H, 2.14 (3.68); N, 7.68 (8.19).

ESI-MS: m/z (%): 342.92(83).

The spectroscopic data are in accordance with the literature.[213]

Dimethyl-4,4‘-(6,6‘-dimethyl-[2,2‘-bipyridine]-5,5‘-diyl)dibenzoate.

0.17 g (0.5 mmole) 5,5‘-dibromo-6,6‘-dimethyl-2,2‘-bipyridine, 0.23 g (1.3 mmole) 4-methoxycarbonylphenylboronic acid, 0.27 g (1.3 mmole) K_3PO_4 and 0.04 g (0.04 mmole) $Pd(PPh_3)_4$ were charged into a flame-dried Schlenk flask under argon in a glove box and dissolved in 6 mL anhydrous DMF. Because of the light sensitive palladium catalyst, the reaction was cariied out in darkness and was heated to 100 °C for 72 hours. The product was precipitated during reaction time which was filtered off and recrystallized from chloroform. The solution was filtered off from the undissolved white residue and evaporated under vacuum, yielding a white solid in 53 % (0.12 g, 0.26 mmole). To remove DMF from the product, the crude product was stirred in petrolether (50 mL) overnight and filtered off.

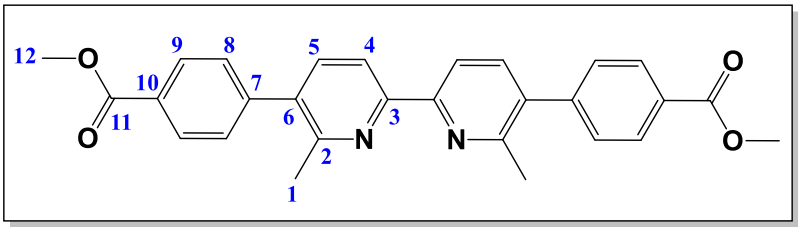

^{1}H NMR (500 MHz, $CDCl_3$): δ = 2.58 (s, 3H, H^1), 3.95 (s, 3H, H^{12}), 7.46 (d, ^3J = 8.5 Hz, 4H, H^8), 7.67 (d, ^3J = 8.0 Hz, 2H, H^5), 8.13 (d, ^3J = 8.5 Hz, 4H, H^9), 8.36 (d, ^3J = 8.0 Hz, 2H, H^4).

^{13}C NMR (125 MHz, $CDCl_3$): δ = 23.7 (CH_3, C^1), 52.2 (CH_3, C^{12}), 118.5 (C^4), 129.1 (C^8), 129.3 (C^{10}), 129.7 (C^9), 135.9 (C^6), 137.9 (C^5), 144.8 (C^7), 154.9 (C^3), 155.1 (C^2), 166.8 (C^{11}).

^{15}N NMR (500 MHz, $CDCl_3$): 308 ppm.

Anal. Found (calcd) for $C_{28}H_{24}N_2O_4$: C, 73.81 (74.32); H, 5.79 (5.35); N, 6.19 (6.07).

IR (KBr, cm^{-1}): 3101 (w), 3060 (w), 2997 (w), 2964 (sh), 2944 (sh), 2923 (m), 2850 (w), 1866 (sh), 1836 (sh), 1791 (sh), 1770 (br.s), 1718 (s), 1654 (sh), 1635 (sh), 1608 (m), 1575 (w), 1556 (w), 1535 (m), 1508 (sh), 1488 (sh), 1452 (sh), 1436 (m), 1404 (m), 1373 (w), 1350 (w), 1311 (w), 1270 (m), 1247 (sh), 1193 (w), 1180 (m), 1108 (sh), 1099 (s), 1031 (w), 1024 (w), 1002 (m), 982 (sh), 973 (sh), 869 (w), 850 (m), 840 (sh), 819 (m), 815 (sh), 769 (s), 752 (m), 727

(w), 703 (s), 671 (w), 653 (w), 634 (sh), 576 (w), 530 (m), 497 (w), 466 (w), 439 (w), 416 (w), 401 (sh), 362 (w), 331 (s), 304 (sh), 287 (sh), 279 (w), 246 (w), 227 (sh), 212 (m).

ESI-MS: m/z (%): 453.18(46).

4,4‘-(6,6‘-dimethyl-[2,2‘-bipyridine]-5,5’diyl)dibenzoic acid.

The oxidation of the ester groups were performed in THF in two steps. 0.12 g (0.26 mmole) dimethyl 4,4‘-(6,6‘-dimethyl-[2,2‘-bipyridine]-5,5‘-diyl)dibenzoate was suspended in 18 mL THF and heated to 40 °C. KOH in MeOH (5.5 mol/L, 9.5 mL, 1.38 mole) was added and the reaction mixture was stirred for 24 h at 40 °C. After cooling to room temperature, the precipitate was filtered off and again suspended in THF (7.5 mL). Upon addition of 1 mL (13 mmole) trifluoroacetic acid, the solution was stirred for additional 1.5 h at room temperature. The reaction was stopped by adding water (18.5 mL), whereupon immediate precipitation occurred, which was filtered off and dried at high-vacuum. The product was obtained in 62 % (0.07 g, 0.16 mmole) as fine white solid.

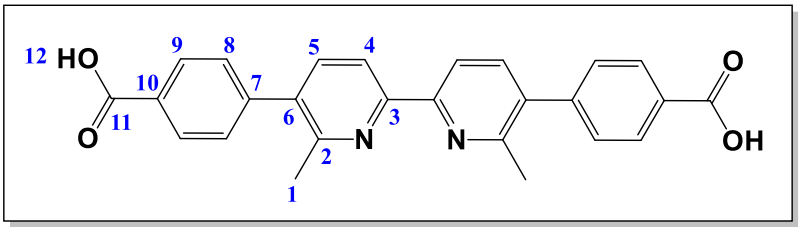

^{1}H NMR (500 MHz, DMSO-d$_6$): δ [ppm] = 2.61 (s, 6H, H^{1}); 7.64 (d, ^{3}J = 8.5 Hz, 4H, H^{8}), 7.93 (d, ^{3}J = 8.1 Hz, 2H, H^{5}), 8.08 (d, ^{3}J = 8.5 Hz, 4H, H^{9}), 8.41 (d, ^{3}J = 8.1 Hz, 2H, H^{4}), 13.0 (br.s, 2H, H^{12}).

^{13}C NMR (125 MHz, DMSO-d$_6$): δ = 23.6 (C^{1}), 118.2 (C^{4}), 129.4 (C^{8}), 129.5 (C^{9}), 130.0 (C^{6}), 135.7 (C^{10}), 138.4 (C^{5}), 143.7 (C^{7}), 153.6 (C^{3}), 154.7 (C^{2}), 167.1 (C^{11}).

^{15}N NMR (500 MHz, DMSO-d$_6$): 309 ppm.

Elemental analysis could not be applied for $C_{28}H_{24}N_2O_4$ due to strong H-bonding interactions.

Mass spectrometric analysis (ESI-MS) was unsuccesful in positive and negative mode, but the structure could be clearly confirmed by ^{1}H NMR.

5,5‘-bis(4-carboxyphenyl)-[2,2‘-bipyridine]-6,6‘-dicarboxylic acid.

0.61 g (1.4 mmole) of 4,4‘-(6,6‘-dimethyl-[2,2‘-bipyridine]-5,5’diyl)-dibenzoic acid were suspended in 17 ml of water. The reaction mixture was heated to 75 °C and 1.5 g of potassium permanganate (10 mmole) was added in small portions. The mixture was heated up to 90 °C and kept stirring at this temperature overnight. Manganese dioxide was formed which was removed by filtration of the hot solution over celite. The filter cake was washed several times with excess of distilled water. Upon acidification with 37 % HCl to pH 1-2, a white solid (55 %, 0.37 g, 0.77 mmole) precipitated which was recrystallized from hot water to obtain the product in pure form.

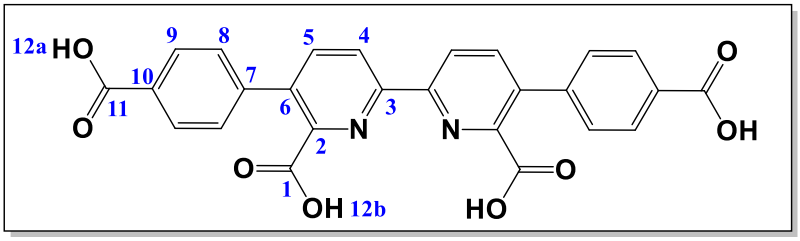

^{1}H NMR (500 MHz, DMSO-d$_6$): δ [ppm] = 7.65 (d, ^{3}J = 8.2 Hz, 4H, H^{8}), 8.08 (d, ^{3}J = 8.2 Hz, 4H, H^{9}), 8.18 (d, ^{3}J = 8.5 Hz, 2H, H^{5}), 8.62 (d, ^{3}J = 8.5 Hz, 2H, H^{4}), 13.1 (br.s, 2H, H$^{12a\ or\ 12b}$), 13.6 (br.s, 2H, H$^{12a\ or\ 12b}$).

^{13}C NMR (125 MHz, DMSO-d$_6$): δ [ppm] = 122.1 (C^{4}), 128.6 (C^{11}), 129.5 (C^{9}), 129.6 (C^{8}), 130.6 (C^{9}), 134.7 (C^{6}), 139.9 (C^{5}), 141.8 (C^{7}), 150.1 (C^{2}), 152.7 (C^{3}), 167.0 (C^{1}), 167.9 (C^{11}).

Anal. Found (calcd) for $C_{26}H_{16}N_2O_8$: C, 64.47 (63.38); H, 3.85 (3.33); N, 5.88 (5.78).

^{15}N NMR could not be applied due to strong H-bonding interactions.

IR (KBr, cm^{-1}): 3099 (w), 3062 (w), 2966 (w), 2927 (w), 2848 (w), 1768 (m), 1734 (sh), 1695 (s), 1652 (sh), 1637 (sh), 1608 (m), 1587 (m), 1556 (w), 1539 (w), 1519 (sh), 1508 (sh), 1488 (w), 1471 (w), 1456 (w), 1410 (br), 1361 (w), 1300 (br), 1267 (sh), 1245 (sh), 1225 (m), 1178 (m), 1159 (sh), 1114 (sh), 1103 (m), 1080 (w), 1043 (sh), 1024 (m), 986 (sh), 966 (br), 874 (w), 847 (m), 827 (sh), 794 (s), 775 (s, 723 (sh), 704 (m), 671 (s), 646 (m), 615 (w), 600 (w), 553 (w), 530 (m).

ESI-MS: m/z (%): 483.08(61).

12.2.2.3 Synthesis of ligand [2,2'-bipyridine]-6,6'-dicarboxylic acid.

The preparation of [2,2'-bipyridine]-6,6'-dicarboxylic acid was prepared according to the procedure described in [210]. The methyl groups were transferred to acid groups by oxidation with CrO_3. 6,6'-dimethyl-2,2'-bipyridine (2.5 g, 10.2 mmole) was dissolved at 50 °C in concentrated sulfuric acid (50 mL) and heated to 70 °C. Upon addition of 5.1 g (51 mmole) chromium trioxide in small portions, the yellow color of the reaction mixture turned green and the mixture was heated for additional 2 hours, controlling the temperature increase not higher than 75 °C. After completion of reaction, the mixture was poured into ice-water (200 g), whereupon a white precipitate separated. The reaction flask was left for stirring overnight to ensure complete precipitation. The product was collected by filtration and washed with small amounts of water, ethanol, and diethyl ether, and left under high-vacuum for several hours. [2,2'-bipyridine]-6,6'-dicarboxylic acid was obtained in 91 % yield (2.7 g, 9.3 mmole) as white powder.

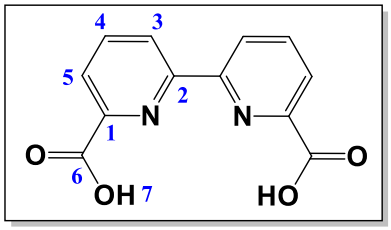

^{1}H NMR (500 MHz, DMSO-d_6): δ = 8.14 (d, ^3J = 7.9 Hz, 2H, H^5); 8.19 (t, ^3J = 7.8 Hz, 2H, H^4); 8.75 (d, ^3J = 7.9 Hz, 2H, H^3), 13.24 (br.s, 2H, H^7).

^{13}C NMR (125 MHz, DMSO-d_6): δ = 124.2 (C^5), 125.3 (C^3), 139.0 (C^4), 148.2 (C^1), 154.5 (C^2), 166.0 (C^6).

ESI-MS $[M + Na]^+$: m/z (%): 267.03(92).

IR (KBr, cm^{-1}): 3091 (w), 2981 (w), 2840 (w), 2624 (w), 2555 (w), 1699 (s), 1583 (m), 1452 (w), 1423 (m), 1319 (m), 1265 (s), 1157 (m), 1080 (m), 993 (m), 939 (m), 831 (m), 761 (s), 692 (s), 630 (m), 574 (w), 547 (w), 468 (w), 416 (m), 324 (m).

The spectroscopic data are in accordance with the literature.[210]

12.2.2.4 Synthesis of ligand [2,2'-bipyridine]-4,4',6,6'-tetracarboxylic acid.

4,4',6,6'-tetramethyl-2,2'-bipyridine.

4,4',6,6'-tetramethyl-2,2'-bipyridine was prepared exactly to the method described by Fu et al.[193]. Differently from literature, after cooling the resulting yellow solution was allowed to

dry in air over the weekend, producing large colourless crystals in moderate yield (43 %, 4.26 g, 20.1 mmole).

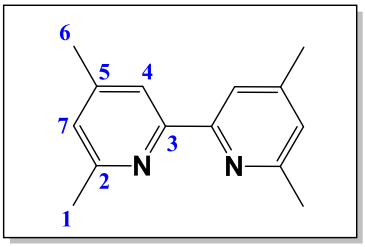

^{1}H NMR (500 MHz, $CDCl_3$): δ = 2.36 (s, 2H, H^6), 2.57 (s, 2H, H^1), 6.94 (s, 2H, H^7), 7.96 (s, 2H, H^4).

^{13}C NMR (125 MHz, $CDCl_3$): 21.0 (C^6), 24.4 (C^1), 119.2 (C^7), 123.9 (C^4), 147.9 (C^5), 155.9 (C^3), 157.5 (C^2).

^{15}N NMR (500 MHz, $CDCl_3$): 297 ppm.

The spectroscopic data are in accordance with the literature.[193]

[2,2'-bipyridine]-4,4',6,6'-tetracarboxylic acid.

0.51 g (2.40 mmole) 4,4',6,6'-tetramethyl-2,2'-bipyridine was loaded into a 45 mL stainless steel bomb, followed by addition of 16 mL H_2O and 1 mL concentrated HNO_3. The bomb was heated at 160 ℃ for 36 h and then slowly cooled to room temperature. Upon exposure to air, yellow needles (34 %, 0.27 g, 0.82 mmole) were produced which were washed with water to remove any water-soluble impurities and dried under air.

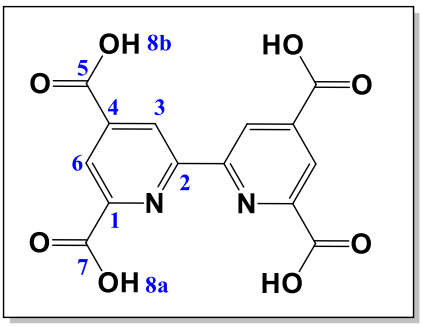

^{1}H NMR (500 MHz, DMSO-d_6): δ = 8.43 (d, ^{4}J = 1.4 Hz, 2H, H^6), 8.98 (d, ^{4}J = 1.4 Hz, 2H, H^3), 14.15 (br.s, 4H, $H^{8a/b}$).

^{13}C NMR (125 MHz, DMSO-d_6): δ = 123.4 (C^6), 124.1 (C^3), 126.4 (C^1), 141.3 (C^2), 149.7 (C^4), 165.7 (C^7), 165.8 (C^5).

The spectroscopic data are in accordance with the literature.[193]

12.2.2.5 Synthesis of ligand 2,2'-bipyridine-3,3',6,6'-tetracarboxylic acid.

The synthesis of 2,2'-bipyridine-3,3',6,6'-tetracarboxylic acid was followed a simple method described in [194]. 4.17 g (20 mmole) 2,9-dimethyl-1,10-phenanthroline was charged into a flask and 1.6 g (40 mmole) NaOH in 150 mL water was added. A cloudy suspension was obtained. Then 21.35 g (135 mmole) $KMnO_4$ was added in small portions. An exothermic reaction occurs by forming a black reaction mixture. The mixture was heated under reflux

overnight and the precipitate formed was filtered off. The filtrate was heated with active coal for an hour and filtered. The colorless liquid was evaporated to the half of the beginning volume. The solution was acidified to pH = 1.5 with concentrated hydrochloric acid forming a white solid of product. The solid was filtered off and recrystallized from water, yielding 2,2'-bipyridine-3,3',6,6'-tetracarboxylic acid as white powder in 86 % (5.7 g, 17.2 mmole) yield.

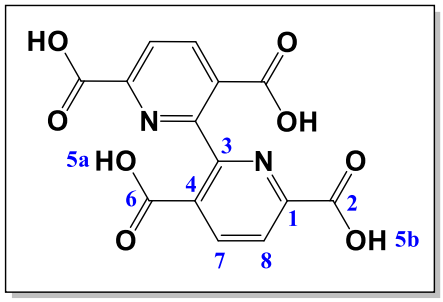

^{1}H NMR (500 MHz, DMSO-d$_6$): δ = 8.19 (d, ^{3}J = 8.1 Hz, 2H, H^{8}); 8.49 (d, ^{3}J = 8.1 Hz, 2H, H^{7}), 13.44 (s, 4H, H$^{5a/b}$).

^{13}C NMR (125 MHz, DMSO-d$_6$): δ = 124.3 (C^{8}), 129.2 (C^{4}), 139.8 (C^{7}), 149.8 (C^{3}), 158.9 (C^{1}), 165.9 (C^{6}), 166.4 (C^{2}).

^{15}N NMR could not be applied due to strong H-bonding interactions.

Anal. Found (calcd) for $C_{14}H_8N_2O_8$: C, 49.26 (50.61); H, 2.80 (2.43); N, 8.20 (8.43).

IR (KBr, cm^{-1}): 3477 (s), 3091 (w), 2858 (w), 2638 (w), 2528 (w), 1726 (sh), 1689 (s), 1581 (m), 1415 (m), 1475 (m), 1456 (m), 1371 (s), 1344 (m), 1257 (s), 1215 (m), 1162 (m), 1139 (s), 1091 (s), 1066 (s), 1049 (s), 964 (m), 898 (s), 877 (s), 825 (m), 750 (s), 690 (s), 626 (s), 568 s, 560 s, 475 m, 430 m, 402 (m).

MS-ESI: m/z (%): 331.02(04).

The spectroscopic data are in accordance with the literature.[194]

12.2.2.6 Synthesis of ligands based on carboxamide.

All tetradentate bipyridine carboxamide ligands were prepared according to a similar method reported in [214].

***N*$_6$, *N*$_6$'-diphenyl-[2,2'-bipyridine]-6,6'-dicarboxamide.**

Under an argon atmosphere, to 0.50 g (2.06 mmole) [2,2'-bipyridine]-6,6'-dicarboxylic acid was added thionyl chloride (9.5 mL) and the mixture solution was refluxed until the carboxylic acid was completely dissolved and the color of the reaction mixture turned green. Then, excess of thionyl chloride was removed under reduced pressure. The slight yellow residue was dissolved in 13 mL dry CH_2Cl_2 followed by addition of stochiometric amount of triethylamine (0.29 ml, 2.06 mmole). Aniline (0.44 g, 4.68 mmole) was added slowly to the above-mentioned cold mixture solution, stirred for overnight at room temperature and finally poured into saturated sodium bicarbonate solution (100 mL). The product was filtered and washed with water to give 57 % (0.46 g, 1.17 mmole) pure white solid.

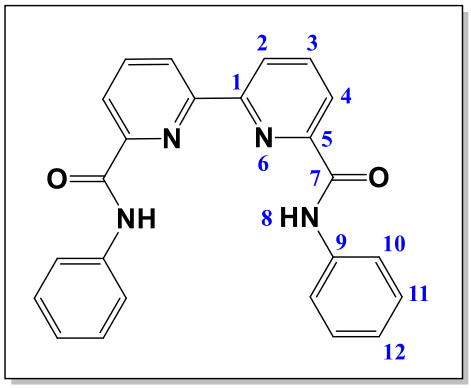

^{1}H NMR (500 MHz, $CDCl_3$): δ = 7.20 (t, ^3J = 7.4 Hz, ^4J = 1.0 Hz, 2H, H^{12}), 7.42 (t, ^3J = 7.9 Hz, 4H, H^{11}), 7.83 (d, ^3J = 7.4 Hz, 4H, H^{10}), 8.15 (t, ^3J = 7.7 Hz, 2H, H^3), 8.43 (d, ^3J = 7.5 Hz, 2H, H^4), 8.63 (d, ^3J = 7.7 Hz, ^4J = 1.0 Hz, 2H, H^2), 10.01 (s, 2H, H^8).

^{13}C NMR (125 MHz, $CDCl_3$): δ = 120.3 (C^4), 123.5 (C^{10}), 124.2 (C^2), 125.1 (C^{12}), 129.6 (C^{11}), 137.9 (C^9), 139.4 (C^3), 150.1 (C^5), 154.0 (C^1), 162.1 (C^7).

^{15}N-NMR (50.7 MHz, $CDCl_3$): δ = 122.3 (s, N^8), 291.6 (s, N^6).

IR (KBr, cm^{-1}): 3344 (w), 1662 (m), 1600 (w), 1581 (sh), 1567 (sh), 1527 (s), 1494 (sh), 1448 (m), 1431 (m), 1390 (sh), 1324 (w), 1301 (sh), 1243 (w), 1207 (w), 1186 (w), 1134 (w), 1076 (m), 1033 (w), 993 (w), 933 (w), 894 (w) ,840 (sh), 817 (w), 756 (s), 707 (w), 688 (s), 663 (s), 630 (m), 588 (w), 516 (w), 493 (m), 439 (w), 352 (w), 304 (m), 271 (w), 223 (m).

ESI-MS $[M + Na]^+$: m/z (%): 417.14(37).

***N*$_6$, *N*$_6$'-di(pyridin-2-yl)-[2,2'-bipyridine]-6,6'-dicarboxamide.**

Under an argon atmosphere, to 0.50 g (2.06 mmole) [2,2'-bipyridine]-6,6'-dicarboxylic acid was added thionyl chloride (9.5 mL) and the mixture solution was refluxed until the carboxylic acid

was completely dissolved and the color of the reaction mixture turned green. Then, excess of thionyl chloride was removed under reduced pressure. The slight yellow residue was dissolved in 13 mL dry CH_2Cl_2 followed by addition of stochiometric amount of triethylamine (0.29 ml, 2.06 mmole). Pyridine-2-amine (0.44 g, 4.68 mmole) was added slowly to the above-mentioned cold mixture solution, stirred for overnight at room temperature and poured into saturated sodium bicarbonate solution (100 mL), filtered and washed with water to give 32 % (0.26 g, 0.65 mmole) pure off-white solid.

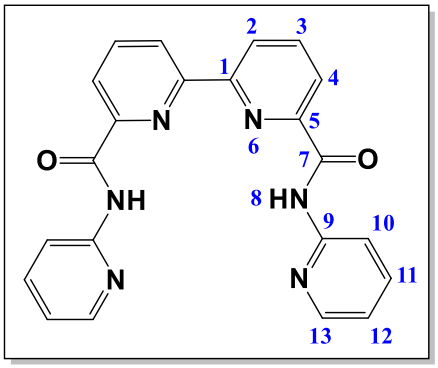

^{1}H NMR (500 MHz, $CDCl_3$): δ = 7.15 (m, 2H, H^{12}), 7.84 (t, ^3J = 7.2 Hz, ^4J = 1.1 Hz, 2H, H^{11}), 8.18 (t, ^3J = 7.8 Hz, ^4J = 0.9 Hz, 2H, H^3), 8.44 (dd, ^3J = 6.7 Hz, ^4J = 0.7 Hz, 4H, H^4, H^{10}), 8.53 (dd, ^3J = 8.3 Hz, ^4J = 0.8 Hz, 2H, H^{13}), 8.86 (dd, ^3J = 7.9 Hz, ^4J = 1.1 Hz, 2H, H^2), 10.51 (s, 2H, H^8).

^{13}C NMR (125 MHz, $CDCl_3$): δ = 114.3 (C^{10}), 120.3 (C^{12}), 123.5 (C^4), 124.7 (C^2), 138.7 (C^{11}), 139.2 (C^3), 148.4 (C^{13}), 149.3 (C^5), 151.3 (C^9), 153.8 (C^1), 162.5 (C^7).

IR (KBr, cm^{-1}): 3363 (w), 2921 (m), 2844 (w), 1697 (m), 1623 (m), 1535 (m), 1544 (s), 1326 (w), 1299 (w), 1245 (w), 1161 (w), 1128 (w), 1101 (w), 1068 (w), 1053 (w), 993 (m), 904 (w), 823 (m), 777 (m), 757 (m), 713 (sh), 682 (s), 632 (m), 603 (m), 597 (sh), 518 (w), 470 (w), 410 (m), 368 (w), 356 (w), 312 (m), 279 (w), 248 (w), 223 (m).

ESI-MS: m/z (%): 397.13(94).

***N*$_6$, *N*$_6$'-bis(6-methylpyridin-2-yl)-[2,2'-bipyridine]-6,6'-dicarboxamide.**

Under an argon atmosphere, to 0.50 g (2.06 mmole) [2,2'-bipyridine]-6,6'-dicarboxylic acid was added thionyl chloride (9.5 mL) and the mixture solution was refluxed until the carboxylic acid was completely dissolved and the color of the reaction mixture turned green. Then, excess of thionyl chloride was removed under reduced pressure. The slight yellow residue was dissolved in 13 mL dry CH_2Cl_2 followed by addition of stochiometric amount of triethylamine (0.29 ml, 2.06 mmole). 6-methylpyridin-2-amine (0.51 g, 4.68 mmole) was added slowly to the above-mentioned cold mixture solution, stirred for overnight at room temperature and poured

into saturated sodium bicarbonate solution (100 mL), filtered and washed with water to give 67 % (0.58 g, 1.38 mmole) pure off-white solid.

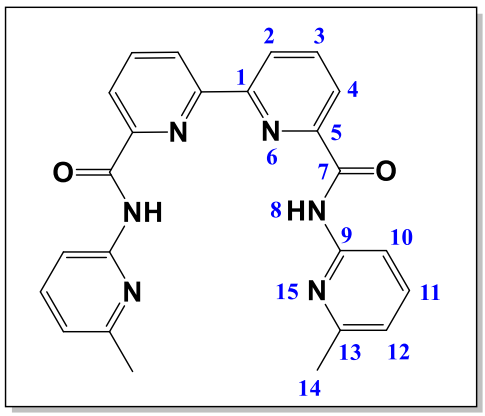

^{1}H NMR (500 MHz, $CDCl_3$): δ = 2.56 (s, 6H, H^{14}), 6.98 (d, ^{3}J = 7.3 Hz, 2H, H^{12}), 7.69 (t, ^{3}J = 7.8 Hz, 2H, H^{11}), 8.17 (t, ^{3}J = 7.6 Hz, 2H, H^{3}), 8.29 (d, ^{3}J = 8.1 Hz, 2H, H^{10}), 8.41 (d, ^{3}J = 7.7 Hz, 2H, H^{4}), 8.83 (d, ^{3}J = 7.8 Hz, 2H, H^{2}), 10.39 (s, 2H, H^{8}).

^{13}C NMR (125 MHz, $CDCl_3$): δ = 24.2 (C^{14}), 111.1 (C^{3}), 119.7 (C^{4}), 123.3 ($C1^{2}$), 124.6 (C^{2}), 138.7 (C^{10}), 139.0 (C^{11}), 149.2 (C^{5}), 150.4 (C^{13}), 153.7 (C^{1}), 157.3 (C^{9}), 162.4 (C^{7}).

^{15}N-NMR (50.7 MHz, $CDCl_3$): δ = 132.9 (s, N^{8}), 283.1 (s, N^{15}), 293.1 (s, N^{6}).

IR (KBr, cm^{-1}): 3334 (w), 2921 (m), 2850 (w), 1731 (w), 1701 (s), 1602 (w), 1579 (s), 1529 (s), 1456 (s), 1438 (sh), 1396 (m), 1378 (sh), 1292 (w), 1238 (w), 1162 (w), 1132 (w), 1101 (w), 1076 (w), 1056 (sh), 995 (m), 933 (w), 891 (w), 827 (w), 783 (m), 754 (m), 732 (w), 684 (m), 630 (w), 611 (m), 547 (w), 468 (w), 418 (w), 335 (m), 266 (w), 221 (w).

ESI-MS: m/z (%): 425.17(30).

Synthesis of *N*$_6$, *N*$_6$'-bis(4,6-dimethylpyrimidin-2-yl)-[2,2'-bipyridine]-6,6'-dicarboxamide.

4,6-dimethylpyrimidin-2-amine.

The synthesis of 4,6-dimethylpyrimidin-2-amine was performed according to the method described in [215]. A suspension of 4.5 g (37 mmole) guanidine nitrate, 8.4 g Na_2CO_3, 25 mL H_2O and 6 mL pentanedione (58.1 mmole) was heated to 100 °C for 24 h. After cooling, the resulting brown mixture was poured on H_2O (150 mL), followed by extraction with DCM (3 x 100 mL) and brine (3 x 150 mL). After evaporation under reduced vacuum, 4,6-dimethylpyrimidin-2-amine was obtained in 78 % (3.5 g, 28.7 mmole) yield.

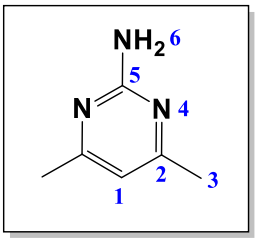

^{1}H NMR (500 MHz, $CDCl_3$): δ = 2.28 (s, 6H, H^3), 5.03 (br.s, 2H, H^6), 6.32 (s, 1H, H^1).

^{13}C NMR (125 MHz, $CDCl_3$): 23.8 (C^3), 110.71 (C^1), 162.9 (C^5), 167.9 (C^2).

^{15}N-NMR (50.7 MHz, $CDCl_3$): δ = 75 (N^6) ppm, 241 ppm (N^4).

ESI-MS: m/z (%): 124.08(81).

The spectroscopic data are in accordance with the literature.[215]

***N*$_6$, *N*$_6$'-bis(4,6-dimethylpyrimidin-2-yl)-[2,2'-bipyridine]-6,6'-dicarboxamide.**

Under an argon atmosphere, to 0.50 g (2.06 mmole) [2,2'-bipyridine]-6,6'-dicarboxylic acid was added thionyl chloride (9.5 mL) and the mixture solution was refluxed until the carboxylic acid was completely dissolved and the color of the reaction mixture turned green. Then, excess of thionyl chloride was removed under reduced pressure. The slight yellow residue was dissolved in 13 mL dry CH_2Cl_2 followed by addition of stochiometric amount of trimethylamine (0.29 ml, 2.06 mmole). 4,6-dimethylpyrimidin-2-amine (0.58 g, 4.68 mmole) was added slowly to the above-mentioned cold mixture solution, stirred for overnight at room temperature and poured into saturated sodium bicarbonate solution (100 mL), filtered and washed with water to give 86 % (0.8 g, 1.77 mmole) pure white solid.

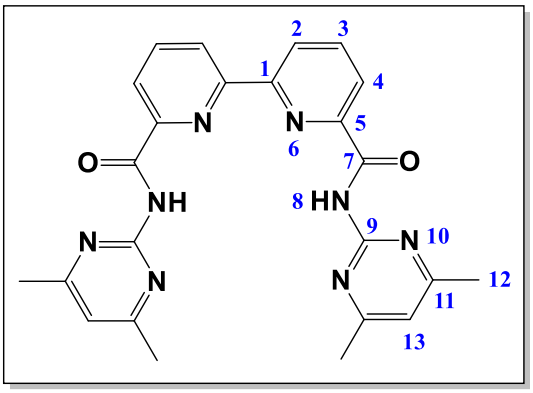

^{1}H NMR (500 MHz, $CDCl_3$): δ = 2.52 (s, 12H, H^{12}), 6.84 (s, 2H, H^{13}), 8.12 (t, ^3J = 7.7 Hz, 2H, H^3), 8.47 (d, ^3J = 7.5 Hz, 2H, H^4), 8.79 (d, ^3J = 7.7 Hz, 2H, H^2), 10.52 (s, 2H, H^8).

^{13}C NMR (125 MHz, $CDCl_3$): δ = 24.4 (C^{12}), 116.6 (C^{13}), 124.0 (C^4), 125.0 (C^2), 139.4 (C^3), 149.6 (C^5), 153.9 (C^1), 157.4 (C^9), 161.8 (C^7), 168.9 (C^{11}).

^{15}N-NMR (50.7 MHz, $CDCl_3$): δ = 132.2 (s, N^8), 265.3 (s, N^{10}), 295.2 (s, N^6).

IR (KBr, cm^{-1}): 3367 (br), 1718 (w), 1598 (w), 1510 (m), 1432 (s), 1386 (sh), 1342 (sh), 1286 (sh), 1242 (w), 1135 (w), 1105 (sh), 1074 (w), 1029 (w), 995 (w), 865 (w), 844 (sh), 823 (sh), 784 (w), 756 (w), 686 (w), 655 (w), 632 (w), 565 (w), 545 (w), 505 (sh), 474 (sh), 420 (sh), 337 (w), 297 (sh), 256 (w), 244 (sh), 221 (sh), 216 (w).

ESI-MS: m/z (%): 455.19(46).

12.2.2.7 Synthesis of MOF linker, UiO-68-NH_2 and post-synthetic modification.

Both, the preparation of the MOF linker and the UiO synthesis follows the same procedure described in [33].

12.2.2.7.1 Synthesis of MOF linker.

Dimethyl 2'-amino-[1,1'-4',1''-terphenyl]-4,4''-dicarboxylate.

Under an argon atmosphere, 2,5-dibromoaniline (0.82 g, 3.26 mmole), 4-(methoxycarbonyl)-phenylboronic acid (3.12 g, 17.32 mmole) and paladium acetate (5.20 mg, 0.023 mmole) were dissolved in 9 mL DMF. An aqueous solution of sodium carbonate (1.23g, 11.60 mmole, 10 mL) was added and the resulting yellow solution was heated at 60 °C for 24 h. After cooling, H_2O (200 mL) was added to the greenish reaction mixture, followed by repeated extraction with ethyl acetate (3 x 50 mL). The organic phases were collected, dried over Na_2SO_4 and concentrated under reduced pressure. Dimethyl 2'-amino-[1,1'-4',1''-terphenyl]-4,4''-dicarboxylate was isolated in 75 % (0.87 g, 2.42 mmole) as a pale yellow solid.

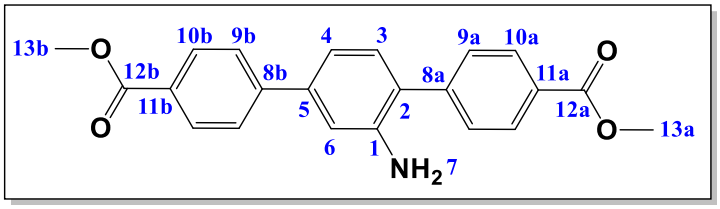

^{1}H NMR (500 MHz, $CDCl_3$): δ = 3.84 (br.s, 2H, H^7), 3.94, 3.95 (s, 6H, H^{13a}, H^{13b}), 7.05 (d, ^4J = 1.7 Hz, 1H, H^6), 7.12 (dd, ^3J = 7.9 Hz, ^4J = 1.7 Hz, 1H, H^4), 7.25 (d, ^3J = 7.9 Hz, 1H, H^3), 7.62 (d, ^3J = 8.4 Hz, 2H, H^{9a}), 7.69 (d, ^3J = 8.4 Hz, 2H, H^{9b}), 8.12 (d, ^3J = 8.4 Hz, 2H, H^{10b}), 8.16 (d, ^3J = 8.4 Hz, 2H, H^{10a}).

^{13}C NMR (125 MHz, $CDCl_3$): δ = 52.1, 52.2 (C^{13a}, C^{13b}), 114.5 (C^6), 117.8 (C^4), 126.3 (C^2), 126.9 (C^{9b}), 129.0 (C^{9a}), 129.1 ($C^{11a/11b}$), 130.1 (C^{14}), 130.2 ($C^{10a/10b}$), 130.9 (C^3), 141.0 (C^5), 143.9 (C^{8a}), 145.3 (C^{8b}), 166.8, 167.0 (C^{12a}, C^{12b}).

ESI-MS: m/z (%): 362.13(92).

Anal. Found (calcd) for $C_{22}H_{19}NO_4$: C, 70.01 (73.12); H, 5.36 (5.30); N, 3.89 (3.88).

The spectroscopic data are in accordance with the literature.[33]

2'-amino-[1,1':4',1''-terphenyl]-4,4''-dicarboxylic acid, H_2tpdc.

Dimethyl 2'-amino-[1,1'-4',1"-terphenyl]-4,4"-dicarboxylate (1.91 g, 5.29 mmole) was added to 380 mL THF. The yellow suspension was heated to 40 °C, followed by addition of a solution of solid KOH in methanol (5.5 M/L, 190 mL, 1.05 mole). The mixture was maintained at 40 °C for additional 24 h. After cooling to room temperature, the reaction mixture was filtered and the resulting residue was re-dissolved in 152 mL THF. 19.8 mL trifluoroacetic acid was added and the reaction was stirred for further 1.5 h at room temperature. Upon addition of 380 mL destilled H_2O, a fine yellow powder immediately precipitated, which was washed with water and dried under high vacuum. 2'-amino-[1,1':4',1"-terphenyl]-4,4"-dicarboxylic acid was isolated in 52 % (0.9 g, 2.7 mmole) yield.

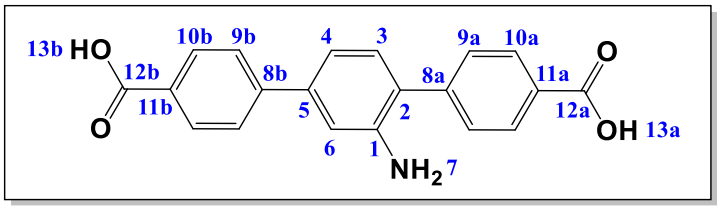

^{1}H NMR (500 MHz, DMSO-d_6): δ = 5.20 (s, 2H, H^7), 7.11 (d, ^3J = 7.8 Hz, ^4J = 1.1 Hz, 1H, H^4), 7.18 (d, ^3J = 7.8 Hz, 1H, H^3), 7.20 (d, ^4J = 1.1 Hz, 1H, H^6), 7.62 (d, ^3J = 8.2 Hz, 2H, H^{9b}), 7.75 (d, ^3J = 8.2 Hz, 2H, H^{9a}), 8.04 (d, ^3J = 8.2 Hz, 4H, $H^{10a/10b}$), 12.91 (s, 2H, $H^{13a/13b}$).

^{13}C NMR (125 MHz, DMSO-d_6): δ = 114.6 (C^6), 116.4 (C^4), 125.5 (C^5), 127.0 (C^{9a}), 129.2 (C^{9b}), 130.0 ($C^{12a/12b}$), 130.3, 130.4 (C^{10a}, C^{10b}), 131.3 (C^3), 140.0 (C^{8a}), 144.1 (C^{8b}), 144.9 (C^1), 145.7 (C^2), 167.6 ($C^{12a/12b}$).

ESI-MS: m/z (%): 334.10(87).

Anal. Found (calcd) for $C_{20}H_{15}NO_4$: C, 61.12 (72.06); H, 4.03 (4.54); N, 3.35 (4.20).

The spectroscopic data are in accordance with the literature.[33]

12.2.2.7.2 Synthesis of UiO-68-NH_2.

In a typical procedure, 0.06 g $ZrCl_4$ and 0.97 g benzoic acid were fully dissolved in 10-24 mL DMF by sonicating. Then 0.10 g of the pre-prepared organic linker was added and treated by sonication, followed by the addition of 0.021 mL of water. The reaction mixture was sealed and transferred into a pre-heated oil bath at 70-120 °C. After MOF precipitation was finished, the white solid was first washed with DMF, then with ethanol to remove all unreacted linker molecules or solvent molecules from the pores. All synthesized MOFs have been dried under high vacuum prior to chemical and physical analysis. The structural formula of UiO-68-NH_2 is $Zr_6O_4(OH)_4(tpdc)_6$.

12.2.2.7.3 Post-synthetic modification of UiO-68-NH_2.

MOF 1: MOF 1 was prepared by suspending 0.1 g (0.34 mmole) UiO-68-NH_2 in 5 mL dry MeCN, followed by the addition of 10 equivalents (0.32 mL) acetaldehyde. The reaction mixture was heated to 80 °C overnight, during which time a colorless precpipitate was formed. The product was filtered, washed with small portions of acetonitrile and dried under vacuum. MOF 1 was isolated in 96 % yield.

ESI-MS: m/z (%): 374.10(52).

MOF 2 and MOF 3: MOFs 2-3 were prepared by suspending 0.1 g (0.34 mmole) UiO-68-NH_2 in 1.73 mL (10.6 mmole) buteric anhydride (MOF 2) or 2.09 mL (10.6 mmole) valeric anhydride (MOF 3). The reaction mixture was heated to reflux for 2h. The anhydride was evaporated in vacuo and the residue was washed with *n*-Hexan to give the products (86 % and 47 % for MOF $2_{buteric}$ and MOF $3_{valeric}$, respectively) as off-white solids.

ESI-MS (MOF 2): m/z (%): 402.13(88).

ESI-MS (MOF 3): m/z (%): 416.15(13).

MOF 4: MOF 4 was prepared by suspending 0.1 g (0.34 mmole) UiO-68-NH_2 in 5 mL dry MeCN, followed by addition of 1.39 g (14.2 mmole) maleic anhydride. The reaction mixture was stirred 24 h at room temperature, during which time a colorless precpipitate was formed. The product was filtered, washed with small portions of acetonitrile and dried under vacuum. MOF 4 was isolated in 64 % yield.

ESI-MS: m/z (%): 430.09(52).

MOF 5: MOF 5 was prepared by suspending 0.1 g (0.34 mmole) UiO-68-NH_2 in 5 mL dry MeCN, followed by addition of 1.42 g (14.2 mmole) succinic anhydride. The reaction mixture was stirred 24 h at room temperature, during which time a yellow precpipitate was formed. The product was filtered, washed with small portions of acetonitrile and dried under vacuum. MOF 5 was isolated in 68 % yield.

ESI-MS: m/z (%): 432.10(59).

MOF 6: MOF 6 was prepared by suspending 0.1 g (0.34 mmole) UiO-68-NH_2 in 5 mL dry MeCN, followed by addition of 3.21 g (14.2 mmole) benzoic anhydride. The reaction mixture was stirred 24 h at room temperature, during which time a pale yellow precpipitate was formed. The product was filtered, washed with small portions of acetonitrile and dried under vacuum. MOF 5 was isolated in 34 % yield.

ESI-MS: m/z (%): 436.12(45).

Protocol for MOF digestion: To post-synthesized MOF material was added DMSO-d_6 and saturated CsF in D_2O. After shaking, MOF was totally dissolved and the organic phase was analyzed by ^1H NMR.

12.2.2.8 Synthesis of Sal(IrCp*Cl).

Pentamethylcyclopentadienyl iridium dichloride dimer

$Ir(Cp^*Cl_2)_2$ was prepared according to [207]. 0.6 g $IrCl_3$ (2 mmole) and 0.5 mL Cp* (2.9 mmole) was heated to 101 °C in 6.5 mL dry MeOH. The resulting precipitate was filtered, washed with cold MeOH (10 mL), cold *n*-Hexan (15 mL) and dried under high-vacuum.

Pentamethylcyclopentadienyl iridium dichloride dimer was obtained in 74 % (0.59 g, 1.48 mmole) as a shiny orange solid.

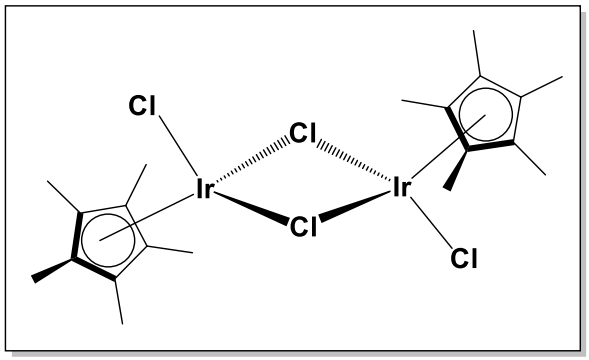

^{1}H NMR (500 MHz, $CDCl_3$): δ = 1.61 (s, 15H, CH_3).

ESI-MS $[M - Cl]^{2+}$: m/z (%): 363.04(80).

The spectroscopic data are in accordance with the literature.[207]

Dimethyl-2'-((2-hydroxybenzylidene)amino)-[1,1':4',1''-terphenyl]-4,4''-dicarboxylate.
Under air and moisture sensitive conditions, 0.67 g (1.86 mmole) dimethyl 2'-amino-[1,1'-4',1''-terphenyl]-4,4''-dicarboxylate was dissolved in 30 mL dry $CHCl_3$, followed by addition of salicylaldehyde (40 eq., 7.8 mL, 74.4 mmole). The resulting yellow suspension was stirred overnight at room temperature. Subsequently, the reaction mixture was heated to reflux for 2 h, after which time a clear yellow reaction solution was obtained. After vacuum evaporation, the residue was stirred in diethylether (50 mL) overnight to remove undissolved impurities. The organic ether phase was concentrated under reduced pressure. Dimethyl-2'-((2-hydroxy-benzylidene)amino)-[1,1':4',1''-terphenyl]-4,4''-dicarboxylate was isolated in 75 % (0.65 g, 1.39 mmole) as a yellow solid.

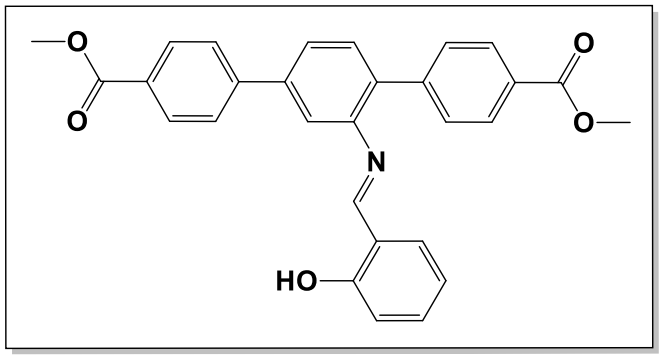

^{1}H NMR (500 MHz, $CDCl_3$): δ = 3.93, 3.96 (s, 6H, H^{20a}, H^{20b}), 6.95 (d, ^{3}J = 7.7 Hz, 2H), 7.36 (d, ^{3}J = 8.2 Hz, ^{4}J = 1.4 Hz, 2H), 7.49 (d, ^{4}J = 1.6 Hz, 1H, H^{6}), 7.56 (d, ^{3}J = 8.3 Hz, 3H), 7.65 (dd, ^{3}J = 7.9 Hz, ^{4}J = 1.6 Hz, 1H), 7.77 (d, ^{3}J = 8.3 Hz, 2H), 8.12 (d, ^{3}J = 8.3 Hz, 2H), 8.19 (d, ^{3}J = 8.3 Hz, 2H), 8.71 (s, 1H, CH), 12.43 (s, 1H).

^{13}C NMR (125 MHz, $CDCl_3$): δ = 52.4, 52.6 (C^{20a}, C^{20b}), 117.7, 118.2, 119.5, 126.1, 129.5, 129.9, 131.6, 132.8, 133.9, 135.7, 141.6, 143.8, 144.8, 147.4, 161.3, 164.1, 167.2 and 167.3 (2 x C=O).

^{15}N-NMR (50.7 MHz, $CDCl_3$): δ = 296 ppm.

ESI-MS $[M + Na]^+$: m/z (%): 488.14(68).

2'-((2-hydroxybenzylidene)amino)-[1,1':4',1''-terphenyl]-4,4''-dicarboxylic acid, H_2tpdc(sal).

H_2tpdc(sal) can be prepared by hydrolysis *via* the method described in [33]. Herein, the product was synthesized exactly to the method reported in literature[204b]. After drying under high-vacuum, 2'-((2-hydroxy-benzylidene)amino)-[1,1':4',1"-terphenyl]-4,4"-dicarboxylic acid was isolated in 65 % (0.09 g, 0.2 mmole).

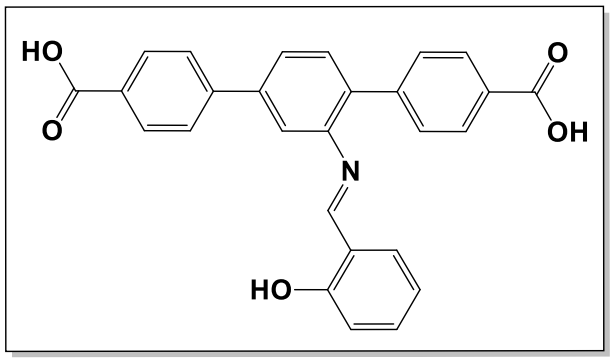

^{1}H NMR (500 MHz, DMSO-d_6): δ = 6.87 (d, ^3J = 8.4 Hz, 1H), 6.98 (t, 1H, ^3J = 7.6 Hz, 1H), 7.39 (t, ^3J = 7.7 Hz, ^4J = 1.4 Hz, 1H), 7.60 (d, ^3J = 8.1 Hz, 3H), 7.66 (dd, ^3J = 7.8 Hz, ^4J = 1.4 Hz, 1H), 7.80 (dd, ^3J = 8.0 Hz, ^4J = 1.5 Hz, 1H), 7.90 (d, ^4J = 1.4 Hz, 1H), 7.99 (t, ^3J = 7.5 Hz, 4H), 8.06 (d, ^3J = 8.3 Hz, 2H), 9.12 (s, 1H, CH), 12.44, 13.00 (s, 2H, 2 x OH).

^{13}C NMR (125 MHz, DMSO-d_6): δ = 116.6, 117.9, 119.2, 119.5, 125.6, 127.1, 129.2, 129.9, 130.0, 131.0, 132.9, 133.6, 135.1, 140.2, 143.1, 143.4, 146.6, 160.2, 164.9, 167.2 and 167.3 (2 x C=O).

ESI-MS: m/z (%): 438.13(35).

The spectroscopic data are in accordance with the literature.[204b]

Sal(IrCp*Cl).

Under an argon atmosphere, 0.06 g H_2tpdc(sal) (0.125 mmole) and 0.01 g sodium acetate (0.132 mmole) were loaded into a round bottom flask, to which 10 mL of dry MeOH was added and the resulting yellow suspension was gently heated to 65 °C. Subsequently, 0.05 g (0.063 mmole) iridium dimer was added to the reaction mixture, whereupon the color of the reaction turned shiny yellow to give an orange precipitate. The reaction was continued for 48 h. The collected orange solid was washed with small portions of methanol and dried under vacuum to give sal(IrCp*Cl) in 56 % yield (0.06 g, 0.07 mmole).

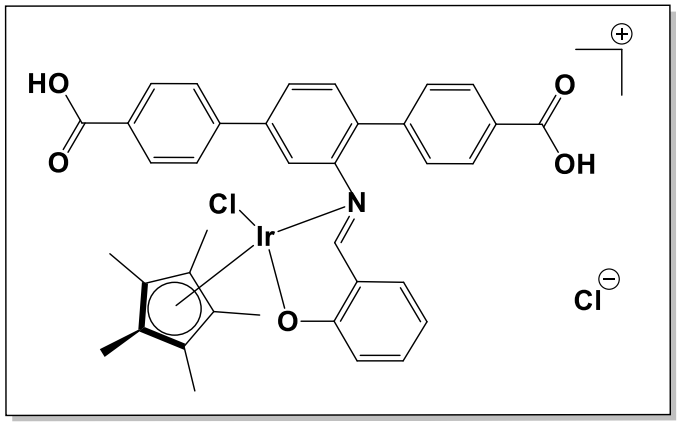

^{1}H NMR (500 MHz, DMSO-d_6): δ = 1.25, 6.89, 6.98, 7.40, 7.60, 7.67, 7.81, 7.91, 8.00, 8.08, 9.12, 12.42, 13.01. *Similar to H_2tpdc(sal) with an additional signal at 1.25 corresponding to the methyl groups of the Cp* group.*

ESI-MS $[M-Cl]^+$: m/z (%): 764.21(51).

12.2.3 Synthesis of ruthenium complexes.

$Ru(DMSO)_4Cl_2$ was prepared according to [197], while the synthesis of all ruthenium(II) complexes refer to [216]. Structural assignment of prepared Ru(II) complexes was limited in large part due to the easy oxidation of the metal center from Ru^{2+} to Ru^{3+}, the high molecular weight of the complexes and the limited solubility in deuterated solvent. Addition of ascorbic acid resulted in sharp peaks in the ^{1}H spectra, nevertheless, recording ^{13}C, DEPT and 2D NMR was not possible for each substance. Thus, structural identification was made by ^{1}H NMR and mass spectrometric analysis.

Dichlorotetrakis(dimethyl) sulfoxide)ruthenium(II), $Ru(DMSO)_4Cl_2$.

$Ru(DMSO)_4Cl_2$ was prepared exactly to the method described in literature[197]. After addition of acetone (20 mL), a yellow crystalline powder was formed which was washed with acetone (3 x 10 mL) and diethyl ether (1 x 10 mL). After drying at high vacuum, the pure compound was obtained in 93 % yield (9 g, 18.6 mmole).

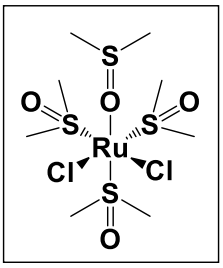

^{1}H NMR (500 MHz, $CDCl_3$): δ = 2.63 (Me of free DMSO), 2.74 (Me of DMSO, O-Ru linked), 3.34, 3.45, 3.51, 3.54 (Me of DMSO, S-Ru linked).

The molecular structure of $Ru(DMSO)_4Cl_2$ was confirmed by X-ray analysis.

Anal. Found (calcd) for $C_8H_{24}Cl_2O_4RuS_4$: C, 19.98 (19.83); H, 4.99 (4.99).

IR (KBr, cm^{-1}): 3022 (w), 3002 (w), 2919 (w), 1440 (sh), 1396 (w), 1303 (w), 1286 (w), 1112 (s), 1083 (s), 1037 (sh), 1020 (m), 991 (m), 960 (m), 931 (s), 715 (m), 675 (m), 607 (w).

ESI-MS: m/z (%): 485.89(62).

The spectroscopic data are in accordance with the literature.[208]

Synthesis of K1-K3.

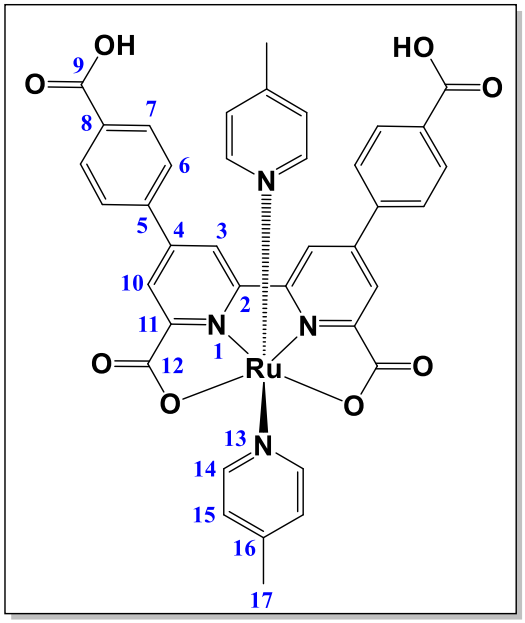

Complex K1: A mixture of ligand L1 (0.16 g, 0.32 mmole), $[Ru(DMSO)_4Cl_2]$ (0.16 g, 0.32 mmole), and Et_3N (1.26 mL, 9.1 mmole) in dry CH_3OH (10 mL) was degassed by Ar and refluxed for 4 h. Subsequently, an excess of 4-methyl-pyridine (0.42 mL, 4.3 mmole) was added and the solution was refluxed for additional 48 h. The solution was evaporated under vacuum to give dark-red solid residue, the resulting residue was purified by column chromatography (water/methanol: 2/1, *v/v*) to afford K1 as dark red solid in 73 % (0.18 g, 0.23 mmole) yield.

^{1}H NMR (500 MHz, Me_3OD-d_4): δ = 2.27 (s, 6H, H^{17}), 7.08 (dd, ^{3}J = 6.6 Hz, ^{5}J = 0.6 Hz, 4H, H^{15}), 7.76 (dd, ^{3}J = 7.6 Hz, ^{4}J = 1.5 Hz, 4H, H^{14}), 8.02 (dd, ^{3}J = 8.4 Hz, ^{4}J = 1.9 Hz, 4H, H^{6}), 8.15 (dd, , ^{3}J = 8.4 Hz, ^{4}J = 1.9 Hz, 4H, H^{7}), 8.40 (d, ^{4}J = 1.7 Hz, 2H, H^{10}), 9.18 (d, ^{4}J = 1.7 Hz, 2H, H^{3}).

^{13}C NMR (125 MHz, Me_3OD-d_4): δ = 19.2 (C^{17}), 122.9 (C^3), 123.3 (C^{10}), 125.7 (C^{15}), 126.3 (C^6), 129.9 (C^7), 138.3 (C^5), 139.2 (C^8), 144.2 (C^4), 149.4 (C^{16}), 151.1 (C^{14}), 156.1 (C^{11}), 160.6 (C^2), 173.1 (C^9), 173.8 (C^{12}).

^{15}N-NMR (50.7 MHz, $CDCl_3$): δ = 235 ppm (s, N^{13}), 266 ppm (s, N^1).

IR (KBr, cm^{-1}): 3647-3130 (br), 2980 (w), 2943 (sh), 1600 (s), 1475 (m), 1445 (sh), 1383 (sh), 1333 (br), 1279 (w), 1215 (w), 1173 (m), 1074 (br), 1035 (m), 1013 (sh), 962 (w), 872 (w), 831 (m), 808 (sh), 752 (br), 723 (w), 681 (w), 638 (w), 611 (w).

ESI-MS: m/z (%): 771.10(45).

Complex K2: Complex K2 was produced in a way quite similar to K1 by displacing the axial ligand with isoquinoline. After pre-washing with diethylether and purification by column chromatography (water/methanol: 3/1, *v/v*), K2 was obtained in 43 % (0.11 g, 0.13 mmole) yield as dark red solid.

^{1}H NMR (500 MHz, Me_3OD-d_4): δ = 7.70 (m, 4H), 7.81 (m, 4H), 7.90 (d, ^3J = 8.3 Hz, 2H), 7.98 (d, ^3J = 7.8 Hz, 2H), 8.10 (d, ^3J = 8.3 Hz, 4H), 8.21 (d, ^3J = 8.4 Hz, 4H), 8.43 (d, ^4J = 1.6 Hz, 2H), 8.82 (s, 2H), 9.33 (d, ^4J = 1.6 Hz, 2H).

ESI-MS: m/z (%): 843.09(74).

Complex K3: Complex K3 was produced in a way quite similar to K1 by displacing the axial ligand with phthalazine. After pre-washing with chloroform and purification by column chromatography (water/methanol: 3/1, *v/v*), K3 was obtained in 17 % (0.04 g, 0.05 mmole) yield as dark red solid.

ESI-MS: m/z (%): 845.0914.

Synthesis of K4-K6.

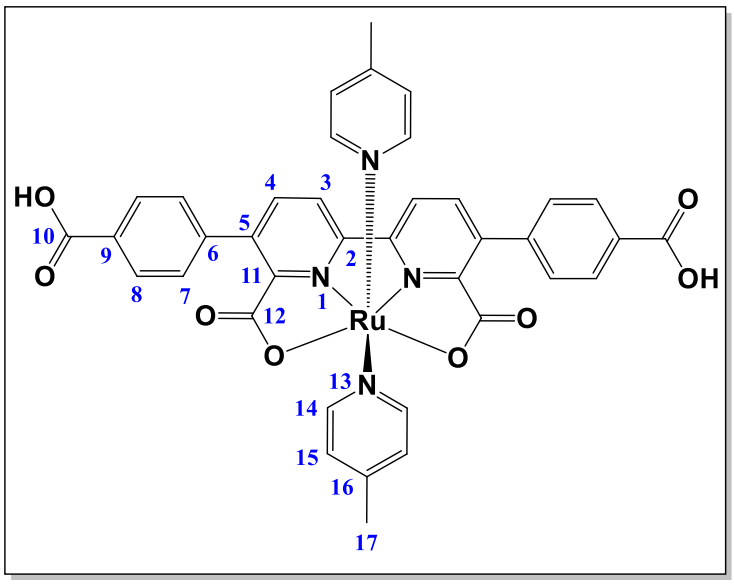

Complex K4: A mixture of ligand L2 (0.09 g, 0.18 mmole), $[Ru(DMSO)_4Cl_2]$ (0.10 g, 0.18 mmole), and Et_3N (0.97 mL, 7 mmole) in dry CH_3OH (10 mL) was degassed by Ar and refluxed for 4 h, an excess of 4-methylpyridine (0.95 mL, 10.7 mmole) was added and the solution was refluxed for 48 h. After cooling to room temperature, the solution was evaporated under vacuum. The resulting residue was purified by column chromatography (water/methanol: 2/1, *v/v*) to afford K4 as dark red solid in 85 % (0.12 g, 0.15 mmole) yield.

^{1}H NMR (500 MHz, Me_3OD-d_4): δ = 2.28 (s, 6H, H^{17}), 7.06 (d, ^3J = 6.4 Hz, 4H, H^{15}), 7.46 (d, ^3J = 8.3 Hz, 4H, H^7), 7.71 (d, ^3J = 8.3 Hz, 2H, H^4), 7.82 (d, ^3J = 6.4 Hz, 4H, H^8), 8.02 (d, ^3J = 8.2 Hz, 4H, H^{14}), 8.49 (d, ^3J = 8.4 Hz, 2H, H^3).

^{13}C NMR (125 MHz, Me_3OD-d_4): δ = 19.2 (C^{17}), 123.2 (C^3), 125.6 (C^{15}), 128.2 (C^7), 128.3 (C^{14}), 134.6 (C^4), 138.1, 138.4 and 149.2 (C^5, C^6, C^9, C^{11} and C^{16}), 151.4 (C^8), 158.9 (C^2), 166.2 (C^{10}), 173.4 (C^{12}).

IR (KBr, cm^{-1}): 3676-2775 (br), 1616 (sh), 1587 (s), 1500 (sh), 1379 (s), 1296 (sh), 1230 (w), 1209 (w), 1144 (w), 1097 (w), 1060 (m), 1013 (m), 916 (w), 843 (m), 787 (m), 714 (m), 685 (sh), 611 (w).

ESI-MS: m/z (%): 771.11(71):

Complex K5: Complex K5 (synthesis approach 0.20 mmole) was produced in a way quite similar to K4 by displacing the axial ligand with isoquinoline. The crude product was washed with diethylether to remove excess of axial ligand. After purification by column chromatography (water/methanol: 3/1, *v/v*), K5 was obtained in 15 % (0.02 g, 0.03 mmole) yield as dark red solid.

ESI-MS: m/z (%): 843.11(00).

Complex K6: Complex K6 (synthesis approach 0.15 mmole) was produced in a way quite similar to K4 by displacing the axial ligand with phthalazine. After pre-washing with chloroform and purification by column chromatography (water/methanol: 3/1, *v/v*), K6 was obtained in 13 % (0.02 g, 0.02 mmole) yield as dark red solid.

ESI-MS: m/z (%): 845.0959.

Synthesis of K7-K9.

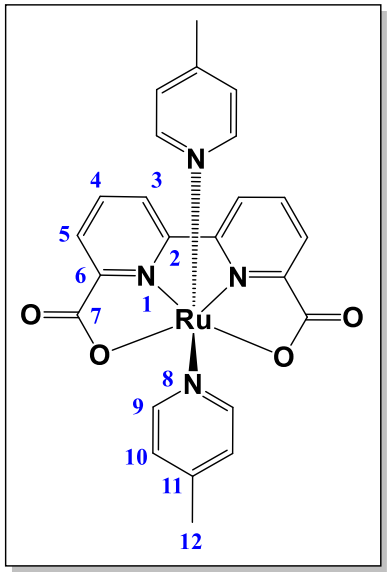

Complex K7: A mixture of [2,2'-bipyridine]-6,6'-dicarboxylic acid (0.5 g, 2 mmole), equimolar quantity of $[Ru(DMSO)_4Cl_2]$ (0.99 g, 2 mmole) and triethylamine (0.7 mL, 4.9 mmole) in MeOH (20 mL) was refluxed for 24 h. Then, a 10-fold excess of 4-picoline was added (1.9 mL, 20 mmole) and the reflux was continued for additional 48 h, producing the corresponding mononuclear ruthenium(II) complex. After purification by column chromatography (DCM/MeOH: 3/1, *v/v*), K7 was obtained in 88 % (0.93 g, 1.76 mmole) yield as dark red solid.

^{1}H NMR (500 MHz, Me_3OD-d_4): δ = 2.27 (s, 6H, H^{12}), 7.05 (d, 4H, ^{3}J = 6.6 Hz, H^{10}), 7.64 (d, ^{3}J = 6.6 Hz, 4H, H^{9}), 7.89 (t, ^{3}J = 7.8 Hz, 2H, H^{4}), 8.05 (dd, ^{3}J = 7.8 Hz, 2H, H^{3}), 8.58 (dd, ^{3}J = 8.1 Hz, 2H, H^{5}).

^{13}C NMR (125 MHz, Me_3OD-d_4): δ = 19.2 (C^{12}), 124.7 (C^{3}, C^{5}), 125.6 (C^{10}), 131.4 (C^{4}), 149.4 (C^{11}), 150.9 (C^{9}), 153.3 (C^{2}), 156.1 (C^{6}), 160.2 (C^{7}).

^{15}N-NMR (50.7 MHz, Me_3OD): δ = 236 ppm (s, N^{8}), 271 ppm (s, N^{1}).

ESI-MS: m/z (%): 531.06(59).

Complex K8: Complex K8 (synthesis approach 2 mmole) was produced in a way quite similar to K7 by displacing the axial ligand with isoquinoline. After purification by column chromatography (DCM/MeOH: 7/1, *v/v*), K8 was obtained in 67 % (0.81 g, 1.34 mmole) yield as dark red solid.

^{1}H NMR (500 MHz, Me_3OD-d_4): δ = 7.60 (d, ^{3}J = 6.4 Hz, 2H), 7.66 (d, ^{3}J = 6.4 Hz, 4H), 7.75 (m, ^{3}J = 8.0 Hz, 2H), 7.84 (d, ^{3}J = 8.1 Hz, 2H), 7.88 (d, ^{3}J = 8.1 Hz, 2H), 7.95 (t, ^{3}J = 7.8 Hz, 2H), 8.05 (dd, ^{3}J = 7.8 Hz, ^{4}J = 0.9 Hz, 2H), 8.66 (s, 2H), 8.69 (dd, ^{3}J = 7.8 Hz, ^{4}J = 0.9 Hz, 2H).

^{13}C NMR (125 MHz, Me_3OD-d_4): δ = 121.7, 125.1, 125.2, 126.5, 127.3, 127.9, 128.7, 131.5, 132.2, 134.1, 142.8, 156.0, 159.6, 171.8.

^{15}N-NMR (50.7 MHz, Me_3OD): δ = 244 ppm (s, N^8), 270 ppm (s, N^1).

ESI-MS: m/z (%): 603.05(71).

Complex K9: Complex K9 (synthesis approach 0.18 mmole) was produced in a way quite similar to K7 by displacing the axial ligand with phthalazine. After purification by column chromatography (DCM/MeOH: 10/1, *v/v*), K9 was obtained in 47 % (0.51 g, 0.85 mmole) yield as dark red solid.

ESI-MS: m/z (%): 605.05(30).

Synthesis of K10-K11.

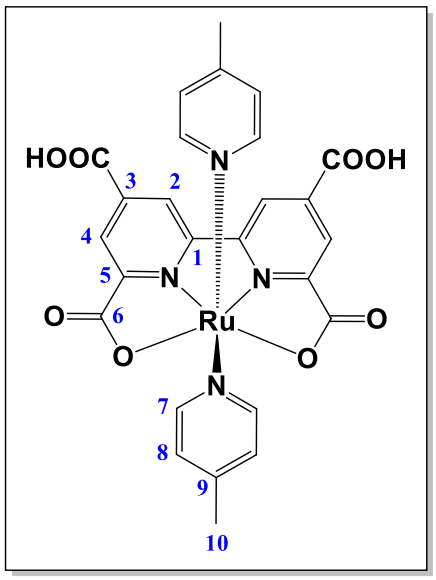

Complex K10. A mixture of [2,2'-bipyridine]-4,4',6,6'-tetracarboxylic acid (0.25 g, 0.75 mmole), $[Ru(DMSO)_4Cl_2]$ (0.36 g, 0.75 mmole), and Et_3N (0.52 mL, 3.7 mmole) in CH_3OH (10 mL) was degassed by Ar and refluxed for 24 h. Subsequently, an excess of 4-picoline (1.2 mL, 12 mmole) was added and the solution was refluxed for further 48 h. The solution was evaporated under vacuum to give dark-red solid residue. After purification by column chromatography (MeOH/H_2O: 3/1, v/v), K10 was obtained in 44 % (0.20 g, 0.33 mmole) yield.

^{1}H NMR (500 MHz, Me_3OD-d_4): δ = 2.25 (s, 6H, H^{10}), 7.03 (d, ^3J = 5.9 Hz, 4H, H^7 or H^8), 7.58 (d, ^3J = 5.7 Hz, 4H, H^7 or H^8), 8.52 (s, 2H, H^2 or H^4), 9.05 (s, 2H, H^2 or H^4).

ESI-MS: m/z (%): 619.03(93).

Complex K11. Complex K11 (synthesis approach 0.78 mmole) was produced in a way quite similar to K10 by displacing the axial ligand with isoquinoline. After pre-washing with diethylether, dichloromethane and purification by column chromatography (MeOH/ H_2O: 5/1, *v/v*), K11 was obtained in 37 % (0.20 g, 0.29 mmole) yield as dark red solid.

ESI-MS: m/z (%): 691.05(55).

Synthesis of K12-K13.

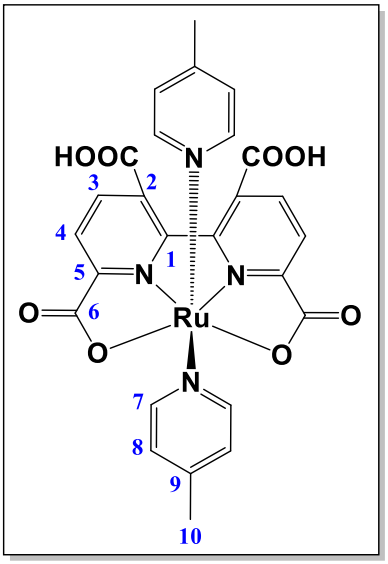

Complex K12: A mixture of 2,2'-bipyridine-3,3',6,6'-tetracarboxylic acid (0.50 g, 1.5 mmole), $[Ru(DMSO)_4Cl_2]$ (0.71 g, 1.5 mmole), and Et_3N (1 mL, 7.2 mmole) in CH_3OH (20 mL) was degassed by Ar and refluxed for 24 h. Subsequently, an excess of 4-picoline (2 mL, 20.6 mmole) was added and the solution was refluxed for further 48 h. The solution was evaporated under vacuum to give dark-red solid residue. After purification by column chromatography (MeOH/DCM: 10/1, *v/v*), K12 was obtained in 17 % (0.16 g, 0.26 mmole) yield as dark red solid.

^{1}H NMR (500 MHz, Me_3OD-d_4): δ = 2.23 (s, 6H, H^{10}), 6.70 (d, 4H, ^3J = 5.6 Hz, H^7 or H^8), 7.64 (d, 4H, ^3J = 4.7 Hz, H^7 or H^8), 8.00 (s, 2H, H^3 or H^4), 8.06 (s, 2H, H^3 or H^4).

ESI-MS: m/z (%): 619.03(93).

Complex K13: Complex K13 (synthesis approach 1.5 mmole) was produced in a way quite similar to K12 by displacing the axial ligand with isoquinoline. After pre-washing with diethylether and purification by column chromatography (MeOH/DCM: 10/1, *v/v*), K13 was obtained in 6 % (0.06 g, 0.09 mmole) yield as dark red solid.

ESI-MS: m/z (%): 691.04(41).

Synthesis of K14-K15.

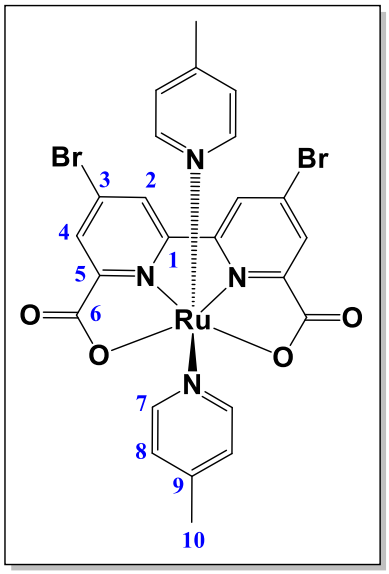

Complex K14. A mixture of 4,4-dibromo-2,2-dipyridyl-6,6-dicarboxylic acid (0.5 g, 1.3 mmole), equimolar quantity of $[Ru(DMSO)_4Cl_2]$ (0.6 g, 1.3 mmole) and trimethylamine (0.22 mL, 1.6 mmole) in MeOH (10 mL) was refluxed for 24 h. Then, a 10-fold excess of 4-picoline was added (1.3 mL, 13 mmole) and the reflux was continued for additional 48 h, producing the corresponding mononuclear ruthenium(II) complex. After purification by column chromatography (MeOH/DCM: 10/1, *v/v*), K14 was obtained in 52 % (0.47 g, 0.67 mmole) yield as dark red solid.

^{1}H NMR (500 MHz, Me_3OD-d_4): δ = 2.27 (s, 6H, H^{10}), 7.06 (d, ^3J = 6.0 Hz, 4H, H^8), 7.62 (d, ^3J = 6.7 Hz, 4H, H^7), 8.20 (d, ^4J = 1.8 Hz, 2H, H^4), 8.89 (d, ^4J = 1.8 Hz, 2H, H^2).

^{13}C NMR (125 MHz, Me_3OD-d_4): δ = 19.2 (C^{10}), 125.8 (C^8), 126.2 (C^4), 128.8 (C^2), 129.2 (C^3), 149.7 (C^7), 150.9 (C^9), 156.8 (C^5), 160.4 (C^1), 172.3 (C^6).

ESI-MS: m/z (%): 688.87(38).

Complex K15. Complex K15 (synthesis approach 1.3 mmole) was produced in a way quite similar to K14 by displacing the axial ligand with isoquinoline. After purification by column chromatography (MeOH/DCM: 10/1, *v/v*), K15 was obtained in 49 % (0.48 g, 0.64 mmole) yield as dark red solid.

ESI-MS: m/z (%): 760.89(54).

Synthesis of K16-K19.

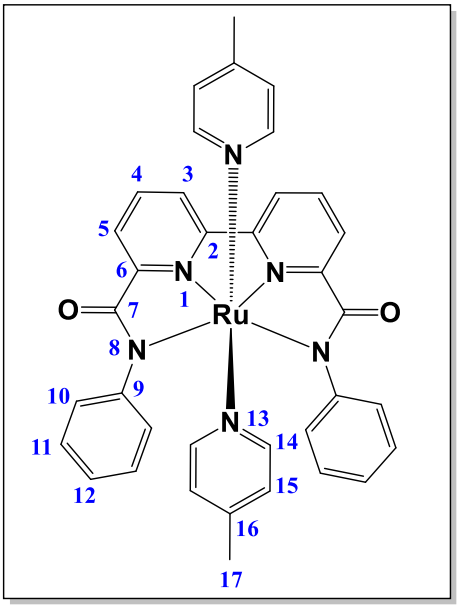

Complex K16. Under air and moisture sensitive conditions, a mixture of ligand N_6, N_6'-di(pyridin-2-yl)-[2,2'-bipyridine]-6,6'-dicarboxamide (0.07 g, 0.19 mmole), $[Ru(DMSO)_4Cl_2]$ (0.1 g, 0.19 mmole), and Et_3N (0.29 mL, 2.1 mmole) in dry CH_3OH (10 mL) was degassed by Ar and refluxed for 24 h. After adding an excess of 4-methylpyridine (0.28 mL, 2.9 mmole), the deeply red reaction mixture was refluxed for further 48 h. The reaction was evaporated under vacuum to give dark-red solid residue, which was purified by column chromatography (H_2O/MeOH: 3/1, *v/v*) to afford dark red solid in 43 % (0.06 g, 0.08 mmole) yield.

^{1}H NMR (500 MHz, Me_3OD-d_4): δ = 2.21 (s, 6H, H^{17}), 6.88 (d, ^3J = 6.0 Hz, 4H, H^{15}), 7.03 (m, 10H, H^{10}, H^{12}, H^{14}), 7.55 (d, ^3J = 6.4 Hz, 4H, H), 7.84 (t, ^3J = 8.1 Hz, 2H, H^4), 8.10 (dd, ^3J = 7.7 Hz, ^3J = 0.8 Hz, 2H, H^5), 8.34 (dd, ^3J = 8.1 Hz, ^4J = 0.9 Hz, 2H, H^3).

^{13}C NMR (125 MHz, Me_3OD-d_4): δ = 20.6 (C^{17}), 123.7 (C^3), 124.4 (C^{10}), 126.3 (C^5), 126.6 (C^{12}), 126.7 (C^{15}), 129.5 (C^{11}), 133.1 (C^4), 150.4 (C^{16}), 151.6 (C^9), 152.6 (C^{14}), 160.7 (C^2), 161.1 (C^1), 172.3 (C^7).

^{15}N-NMR (50.7 MHz, Me_3OD-d_4): δ = 167.5 (s, N^8), 232.9 (s, N^{13}), 276.6 (s, N^1).

IR (KBr, cm^{-1}): 202 (w), 246 (m), 279 (m), 393 (s), 457 (s), 692 (m), 756 (s), 815 (m), 867 (w), 950 (m), 1058 (s), 1207 (m), 1299 (w), 1357 (m), 1485 (m), 1560 (s), 1652 (w), 1749 (w), 1793 (w), 2360 (m), 2981 (w), 3274 (w), 3363 (w).

ESI-MS: m/z (%): 680.15(56).

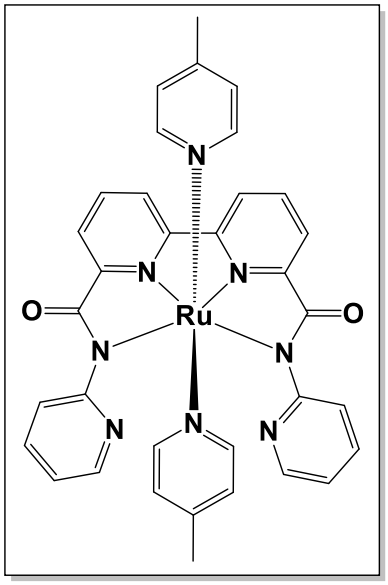

Complex K17. Under air and moisture sensitive conditions, a mixture of ligand N_6, N_6'-bis(6-methylpyridin-2-yl)-[2,2'-bipyridine]-6,6'-dicarboxamide (0.19 g, 0.48 mmole), $[Ru(DMSO)_4Cl_2]$ (0.23 g, 0.48 mmole), and Et_3N (0.75 mL, 5.4 mmole) in dry CH_3OH (20 mL) was degassed by Ar and refluxed for 24 h. After adding an excess of 4-methylpyridine (0.67 mL, 6.9 mmole), the deeply red reaction mixture was refluxed for further 48 h. The reaction was evaporated under vacuum to give dark-red solid residue, which was purified by column chromatography (DCM/MeOH: 10/1, *v/v*) to afford dark red solid in 16 % (0.05 g, 0.07 mmole) yield.

IR (KBr, cm^{-1}): 246 (w), 354 (m), 412 (m), 501 (m), 615 (m), 665 (m), 700 (m), 765 (s), 910 (w), 1002 (m), 1080 (m), 1184 (m), 1367 (s), 1425 (s), 1458 (m), 1569 (s), 1733 (w), 2360 (w), 2852 (w), 2921 (m), 3367 (br).

ESI-MS: m/z (%): 683.14(59).

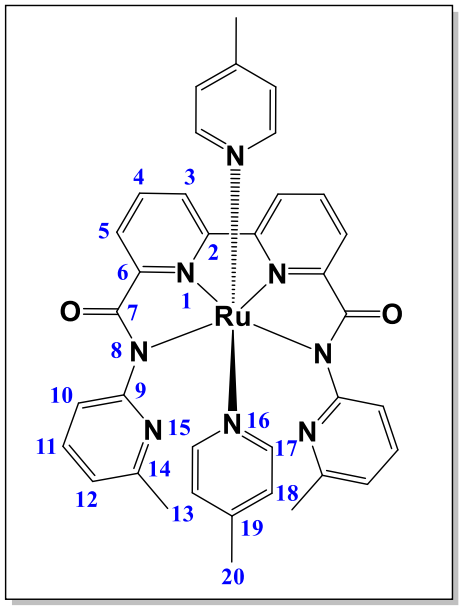

Complex K18. Under air and moisture sensitive conditions, a mixture of ligand N_6, N_6'-bis(6-methyl-pyridin-2-yl)-[2,2'-bipyridine]-6,6'-dicarboxamide (0.21 g, 0.49 mmole), $[Ru(DMSO)_4Cl_2]$ (0.24 g, 0.49 mmole), and Et_3N (0.75 mL, 5.4 mmole) in dry CH_3OH (20 mL) was degassed by Ar and refluxed for 24 h. After adding an excess of 4-methylpyridine (0.74 mL, 7.6 mmole), the deeply red reaction mixture was refluxed for further 48 h. The reaction was evaporated under vacuum to give dark-red solid residue, which was purified by column chromatography (DCM/MeOH: 1/2, *v/v*) to afford dark red solid in 56 % (0.20 g, 0.27 mmole) yield.

^{1}H NMR (500 MHz, Me_3OD-d_4): δ = 2.21 (s, 6H, H^{20}), 2.60 (s, 6H, H^{13}), 6.92 (d, ^3J = 6.9 Hz, 6H), 7.17 (d, ^3J = 7.3 Hz, 2H), 7.63 (t, ^3J = 7.9 Hz, 2H), 7.73 (dd, ^3J = 6.7 Hz, ^4J = 1.4 Hz, 4H), 8.00 (t, ^3J = 7.9 Hz, 2H), 8.20 (d, ^3J = 7.4 Hz, 2H), 8.59 (d, ^3J = 8.0 Hz, 2H).

IR (KBr, cm^{-1}): 227 (w), 279 (w), 397 (m), 503 (m), 549 (w), 711 (m), 765 (s), 810 (m), 865 (w), 950 (w), 1020 (m), 1087 (m), 1149 (m), 1207 (m), 1303 (m), 1330 (m), 1365 (s), 1438 (s), 1558 (s), 1575 (s), 1683 (w), 1733 (w), 2360 (w), 2852 (w), 2921 (m), 3049 (w), 3394 (br), 3648 (w), 3749 (w).

ESI-MS: m/z (%): 711.17(74).

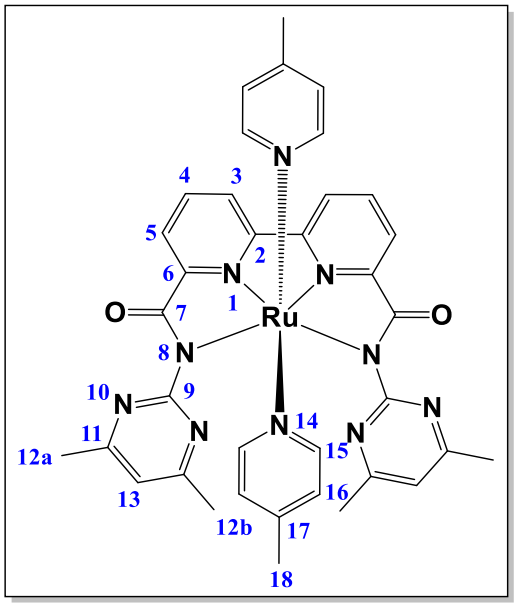

Complex K19. Under air and moisture sensitive conditions, a mixture of ligand N_6, N_6'-bis(4,6-dimethylpyrimidin-2-yl)-[2,2'-bipyridine]-6,6'-di-carboxamide (0.44 g, 0.97 mmole), $[Ru(DMSO)_4Cl_2]$ (0.41 g, 0.85 mmole), and Et_3N (1.37 mL, 9.9 mmole) in dry CH_3OH (20 mL) was degassed by Ar for 20 min and refluxed for 24 h. After adding an excess of 4-methylpyridine (1.35 mL, 13.9 mmole), the deeply red reaction mixture was refluxed for further 48 h. The reaction was evaporated under vacuum to give a dark solid residue, which was purified by column chromatography (DCM/MeOH: 1/2, *v/v*) to afford dark red solid in 79 % (0.57 g, 0.77 mmole) yield.

^{1}H NMR (500 MHz, Me_3OD-d_4): δ = 2.18 (s, 6H, H^{18}), 2.26 (s, 12H, H^{12a}, H^{12b}), 6.78 (dd, ^3J = 6.8 Hz, ^4J = 0.7 Hz, 4H, H^{16}), 6.93 (s, 2H, H^{13}), 7.85 (t, ^3J = 7.9 Hz, 2H, H^5), 7.93 (dd, ^3J = 6.8 Hz, ^4J = 1.4 Hz, 4H, H^{15}), 7.98 (dd, ^3J = 7.7 Hz, ^4J = 0.9 Hz, 2H, H^5), 8.55 (dd, ^3J = 8.2 Hz, ^4J = 0.9 Hz, 2H, H^4).

^{13}C NMR (125 MHz, Me_3OD-d_4): δ = 20.6 (C^{18}), 23.7 (C^{13}), 116.4 (C^{14}), 124.9 (C^4), 125.9 (C^{16}), 126.0 (C^6), 132.6 (C^5), 149.7 (C^7), 153.9 (C^{15}), 160.8 (C^2), 161.2 (C^3), 169.2 (C^{12}), 170.5 (C^8), 173.4 (C^{10}).

^{15}N-NMR (50.7 MHz, Me_3OD-d_4): δ = 234 ppm (s, N^{14}), 271 ppm (s, N^{10}), 279 ppm (s, N^1).

IR (KBr, cm^{-1}): 3087 (w), 3039 (w), 2971 (w), 2916 (w), 1575 (s), 1529 (sh), 1502 (sh), 1436 (m), 1400 (sh), 1371 (s), 1342 (sh), 1311 (sh), 1236 (w), 1207 (w), 1186 (w), 1155 (w), 1108 (w), 1022 (w), 973 (w), 946 (w), 918 (w), 846 (w), 810 (m), 784 (w), 765 (m), 756 (sh), 711 (w), 686 (w), 661 (w), 615 (w), 592 (w), 563 (w), 530 (w), 507 (m), 460 (w), 414 (sh), 399 (m), 325 (w), 302 (w), 281 (w), 254 (w), 231 (w), 221 (w).

ESI-MS: m/z (%): 741.19(99).

REFERENCE LIST

[1] Jules Verne, *The Myterious Island*, **1874**.

[2] R. S. Burn, *The Steam Engine – Its History and Mechanism: Being Descriptions and Illustrations of the Stationary, Locomotive and Marine Engine*, University of Toronto **1964**, pp. 30-35.

[3] iea.org > statistics > statisticssearch > report > China > electricity & heat, **2013**, accessed on 18.09.2018.

[4] greenpeace.org > india > Global > india > docs > Boom & Bust, **2017**, accessed on 18.09.2018.

[5] AIMU Technical Services Committee, January **2012**, pp. 1-24, accessed on 18.09.2018.

[6] IRENA Renewable Energy Technologies: Cost Analysis Series, June **2012**, pp. 1-44, accessed on 18.09.2018.

[7] MIT Massachusetts Institute of Technology, *The Future of Geothermal Energy* **2006**, pp. 1-372, accessed on 18.09.2018.

[8] M. Wasfi, JRSE, *Solar Energy and Photovoltaic Systems*, February **2011**, accessed on 18.09.2018.

[9] eesi.org > topics > bioenergy-biofuels-biomass > description, accessed on 18.09.2018.

[10] renewableenergyworld.com > hydrogen > tech, accessed on 18.09.2018.

[11] R. A. Williamson, *Chapter Two: Developing the Space Shuttle*, pp. 161-192.

[12] P. Kurzweil, *Brennstoffzellentechnik: Grundlagen, Komponenten, Systeme, Anwendungen*, Springer **2012**.

[13] D. L. Trimm, M. S. Wainwright, ScienceDirect **1990**, *Catalysis Today*, pp. 261-278.

[14] N. Kamiya, From Suiso Enerugi Shisutemu **2016**, *Overview of hydrogen production by electrolysis of water*, 41, pp. 2-6.

[15] Sutin et al., *J. Am. Chem. Soc.* **1979**, 101, pp. 1298-1300.

[16] Hong et al., *Eur. J. Inorg. Chem*. **2014**, 4, pp. 645-659.

[17] Basu et al., Current Opinion in Electrochemistry **2017**, 5, pp. 56-62.

[18] S. Romain, L. Vigara, A. Llobet, *Acc. Chem. Res.* **2009**, 42, pp. 1944-1953.

[19] J. J. Concepcion, J. W. Jurss, M. K. Brennaman, P. G. Hoertz, A. O. T. Patrocinio, N. Y. Murakami Iha, J. L. Templeton, T. J. Meyer, *Acc. Chem. Res.* **2009**, 42, pp. 1954-1965

[20] L. Duan, F. Bozoglian, S. Mandal, B. Stewart, T. Privalov, A. Llobet, L. Sun, *Nature Chemistry* **2012**, 4, pp. 418-423.

[21] Zouni et al., *Nature* **2001**, 409, pp. 739-743.

[22] Kamiya et al., *Proc. Natl. Acad. Sci. USA* **2003**, 100, pp. 98-103.

[23] Ferreira et al., *Science* **2004**, 303, pp. 1831-8.

[24] Loll et al., *Nature* **2005**, 438, pp. 1040-1044.

[25] Guskov et al., *Nature Structural & Molecular Biology* **2009**, 16, pp. 334-342.

[26] Kamiya et al., *Nature* **2011**, 473, pp. 55-60.

[27] B. A. Johnson, A. Bhunia, S. Ott, *Dalton Trans.* **2017**, 46, pp. 1382-1388.

[28] A. M. Ploskonka, J. B DeCoste, *ACS applied materials & interfaces* **2017**, 9, pp. 21579-21585.

[29] S. Gökpinar, T. Diment, C. Tatyana, *Dalton Trans.* **2017**, 46, pp. 9895-9900.

[30] S. Andersson, P.-E. Larsson, *From Abstracts of Papers* **2014**, 247th ACS National Meeting & Exposition.

[31] Lillerud et al., *Inorg. Chem*. **2016**, 55, pp. 1986-1991.

[32] Dolbecq et al., *Chem. Commun.* **2015**, 51, pp. 2972-2975.

[33] Behrens et al., *Chem. Eur. J.* **2011**, 17, pp. 6643-6651.

[34] R. Haldar, N. Sikdar, T. KumarMaji, *Materials Today* **2015**, 18, pp. 97-116.

[35] R. U. Shahzad, *Durreesamin Journal* **2015**, 1.

[36] livescience.com > greenhouse effect, accessed on 23.05.2015.

[37] bgs.ac.uk > discoveringGeology > climateChange > CCS > consequencesOFTemperatureIncrease, accessed on 23.05.2015.

[38] livescience.com > greenhousegases, accessed on 23.05.2015.

[39] climatehotmap.org > global-warmingeffects > health, 29.05.2015.

[40] Meyer et al., *Angew. Chem. Int. Ed.* **2014**, 53, pp. 12226-12230.

[41] L. Li., Doctoral Thesis, *Functional Photo-electrochemical Devices for Solar Cells and Solar Fuels Based on Molecular Components*, Stockholm **2012**, p. 7.

[42] R. H. Garrett, C. M. Grisham, *Biochemistry*, 5th Edition, Wadsworth Publishing Co Inc. **2012**.

[43] K. Hasegawa et al., *Chem. Phys. Lett.* **1999**, 300, pp. 9-19.

[44] J. M. Peloquin, *J. Am. Chem. Soc. 2000*, 122, pp. 10926-10942.

[45] E. M. Sproviero, *J. Chem. Theory Comput.* **2006**, 2, pp. 1119-1134.

[46] E. M. Sproviero, *Curr. Opin. Struct. Biol.* **2007**, 17, pp. 173-180.

[47] R. J. Debus, *Biochim. Biophys. Acta.* **2001**, 1503, pp. 164-186.

[48] B. A. Diner, *Biochim. Biophys. Acta.* **2001**, 1503, 147-163.

[49] B. A. Diner, *Advances in photosynthesis* **1996**. pp. 213-247.

[50] B. A. Diner, *Curr. Opin. Struct. Biol.* **1991**, 1, pp. 546-554.

[51] J. Barber, *Phil. Trans. R. Soc. A* **2007**, 365, pp. 1007-1023.

[52] J. Barber, *Phil. Trans. R. Soc. Lond. B. Biol. Sci.* **2008**, 363, pp. 2665-2674.

[53] Brudvig et al., *Dalton Trans.* **2015**, 44, pp. 12452-12472.

[54] Brudvig et al., *J. Am. Chem. Soc.* **2011**, 133, p. 10473.

[55] Macchioni et al., *Green Chem.* **2011**, 13, p. 3360.

[56] Crabtree et al., *J. Am. Chem. Soc.* **2010**, 132, p. 16017.

[57] Crabtree et al., *J. Am. Chem. Soc.* **2009**, 131, p. 8730.

[58] Crabtree et al., *Chem. Sci.* **2011**, 2, p. 94.

[59] Brudvig et al., *Inorg. Chem.* **2013**, 52, p. 1860.

[60] Brudvig et al., *Inorg. Chem.* **2012**, 51, p. 7749.

[61] Crabtree et al., *Organometallics* **2012**, 31, p. 7158.

[62] Crabtree et al., *Organometallics* **2013**, 32, p. 5384.

[63] Macchioni et al., *Chem. Commun.* **2010**, 46, p. 9218.

[64] Macchioni et al., *J. Organomet. Chem.* **2014**, 24, p. 771.

[65] Papish et al., *Inorg. Chem.*, 2013, **52**, 9175.

[66] Fukuzumi et al., *Energy Environ. Sci.* **2012**, 5, 5708.

[67] Sun et al., *Inorg. Chem*. **2009**, 48, pp. 2717-2719.

[68] Sun et al., *Angew. Chem. Int. Ed.* **2010**, 49, pp. 8934-8937.

[69] Sun et al., *Acc. Chem. Res*. **2015**, 48, pp. 2084-2096

[70] Sun et al., *Dalton Trans.* **2017**, 46, p. 1304.

[71] Sun et al., *Dalton Trans.* **2013**, 46, pp. 1304-1310.

[72] Sun et al., *Inorg. Chem*. **2013**, 52, pp. 2505-2518.

[73] Sun et al., *JACS* **2012**, 134, pp. 18868-18880.

[74] Sun et al., *Chem. Commun*. **2014**, 50, p. 12947.

[75] Sun et al., *Inorg. Chem*. **2013**, 52, pp. 7844-7852.

[76] Sun et al., *Angew. Chem. Int. Ed.* **2011**, 50, pp. 445−449.

[77] Sun et al. *Chem. Commun*. **2014**, 50, p. 13948.

[78] Allakhverdiev et al., Chem. Rev. 2016, 116, pp. 2886-2936.

[79] Nocera et al., *J. Am. Chem. Soc.* **2010**, 132, pp. 13692-13701.

[80] Gamelin et al., *J. Am. Chem. Soc.*, **2010**, 132, pp. 4202-4207.

[81] Hill et al., *J. Am. Chem. Soc.*, **2014**, 136, pp. 9268-9271.

[82] Anwander et al., *Chem. Commun.* **2014**, 50, p. 14763.

[83] Vasca et al., *Polyhedron* **1988**, 7, pp. 135-1361.

[84] Kohler et al., *Phys Chem Chem Phys.* 2017, 19, pp. 3523-3531.

[85] Brudvig et al., *Chem. Soc. Rev.* **2013**, 42, pp. 247-252.

[86] LloretFillol et al., *Nat. Commun.* **2015**, 6, pp. 5865-5873.

[87] T. J. Wydrzynski, W. Hillier, *Molecular Solar Fuels*, Royal Society of Chemistry **2011**, p. 65.

[88] Meyer et al., *J. Am. Chem. Soc.* **1982**, 104, pp. 4029-4030.

[89] Meyer et al., *J. Am. Chem. Soc.* **1985**, 107, pp. 3855-3864.

[90] Thummel et al., *J. Am. Chem. Soc.* **2005**, 127, pp. 12802-12803.

[91] Brudvig et al., *Science* **1999**, 283, pp. 1524-1527.

[92] McKenzie et al., *Angew. Chem. Int. Ed.* **2005**, 44, p. 6916.

[93] McKenzie et al., *Dalton Trans.*, **2003**, p. 1765.

[94] Berlinguette et al., *Chem. Sci.* **2013**, 4, p. 734.

[95] Sakai et al., *Chem Commun.* **2013**, 49, pp. 6325-6327.

[96] Costas et al., *Nature Chemistry* **2011**, 3, pp. 807-813.

[97] Mayer et al., *Nature Chemistry* **2012**, 4, pp. 498-502.

[98] Bernhard et al., *J Am Chem Soc*. **2008**, 130, pp. 210-217.

[99] Albrecht et al., *Angewandte Chemie International Edition* **2010**, 49, pp. 9765-9768.

[100] Thummel et al., *J. Am. Chem. Soc.* **2005**, 127, p. 12802.

[101] Åkermark et al., *Angew. Chem. Int. Ed.* **2012**, 51, p. 11589.

[102] Meyer et al., *J. Am. Chem. Soc.* **2008**, 130, p. 16462.

[103] S. Masaoka, K. Sakai, *Chem. Lett.* **2009**, 28, p. 182.

[104] Meyer et al., *J. Am. Chem. Soc.* **2010**, 132, p. 1545.

[105] Meyer et al., *Inorg. Chem.* **2010**, 49, p. 1277.

[106] Meyer et al., *Proc. Natl. Acad. Sci. U.S.A.* **2010**, 107, p. 7225.

[107] Meyer et al., *Proc. Natl. Acad. Sci. U.S.A.* **2012**, 109, p. 15669.

[108] Meyer et al., *J. Am. Chem. Soc.* **2014**, 136, p. 6854.

[109] Berlinguette et al., *Inorg. Chem.* **2010**, 49, p. 2202.

[10] Berlinguette et al., *J. Am. Chem. Soc.* **2010**, 132, p. 16094.

[11] Yagi et al., *Dalton Trans.* **2011**, 40, p. 3802.

[112] Sakai et al., *Chem. Lett.* **2009**, 28, p. 182.

[113] Llobet et al., *Angew. Chem. Int. Ed.* **2010**, 19, p. 7745.

[114] Thummel et al., *Inorg. Chem.* **2012**, 51, p. 2930.

[115] Llobet et al., *Inorg. Chem.* **2013**, 52, p. 3591.

[116] Thummel et al., *Dalton Trans.* **2017**, 46, pp. 12901-12907.

[117] Thummel et al., *Inorg. Chem.* **2008**, 47, p. 990.

[118] Åkermark et al., *Dalton Trans.* **2016**, 45, pp. 3272-3276

[119] Richmond et al., *Dalton Trans.* **2016**, 45, p. 19361

[120] Sun et al., *Dalton Trans.* **2017**, 46, pp. 1304-1310.

[121] Hannon et al., *Dalton Trans.* **2006**, 22, pp. 2635-2642.

[122] Fujita et al., *J. Am. Soc.* **2011**, 133, p. 14649.

[123] Meyer et al., *J. Am. Chem. Soc.* **2014**, 136, p. 6854.

[124] Thummel et al., *Inorg. Chem.* **2008**, 47, p. 11763.

[125] Åkermark et al., *Chem. Eur. J.* **2015**, 21, pp. 10039-10048.

[126] Concepcion et al., *Chem. Soc. Rev.* **2017**, 46, p. 6170-6193.

[127] Llobet et al., *Acc Chem Res.* **2009**, 42, pp. 1944-1953.

[128] Llobet et al., *J. Am. Chem. Soc.,* **2004**, 126, p. 7798.

[129] Llobet et al., *J. Am. Chem. Soc.,* **2009**, 131, p. 15176.

[130] Wu et al., *Angew. Chem. Int. Ed.* **2016**, 55, pp. 6229-6234.

[131] a) Würthner et al., *Energy Environ. Sci.,* **2017**, 10, pp. 2137-2153. b) Würthner et al., *Nat. Chem.* **2016**, 8, pp. 576-583. c) M. Schulze, *'Ruthenium Complexes as Water Oxidation Catalysts and Photosensitizers'*, Dissertation, Julius-Maximilians-Universität Würzburg **2016**.

[132] Concepcion et al., *Chem. Commun.* **2015**, 51, pp. 4105-4108.

[133] Li et al., *New J. Chem.* **2018**, 42, pp. 2526-2536.

[134] Liu et al., *Chin. J. Catal.* **2015**, 36, pp. 1742-1749.

[135] Yaghi et al., *Science **2013***, 341, p. 1230444.

[136] Yaghi et al., *J. Am. Chem. Soc.* **1995**, 117, pp. 10401-10402.

[137] Yaghi et al., *Nature* **1999**, 402, pp. 276-279

[138] O'Keeffe et al., *CrystEngComm.* **2012**, 14, pp. 3001-3004.

[139] Yaghi et al., *J. Am. Chem. Soc.* **2005**, 127, pp. 17998-17999.

[140] Hupp et al., *J. Am. Chem. Soc.*, **2012**, 134, pp 15016-15021.

[141] Farha et al., *J. Am. Chem. Soc.*, **2015**, 137, pp 3585-3591.

[142] Zhou et al. , *J. Phys. Chem. Lett.* **2013**, 4, pp. 925-930.

[143] Chen et al., J. *Phys. Chem. Lett.*, **2014**, 5, pp. 3468-3479.

[144] Zhoub et al., Chem. Commun., **2010**, 46, pp. 44-53.

[145] Yaghi et al., *Inorg. Chem.* **2011**, 50, pp. 6853-6855.

[146] Gubbins et al., *J. Chem. Phys.* **2013**, 138, p. 034102.

[147] Karwacki, *J. Phys. Chem. C*. **2009**, 113, pp. 13906-13917.

[148] Bandosz et al., *Langmuir* **2011**, 27, pp. 13043-13051.

[149] Bandosz et al., *Langmuir* **2010**, 26, pp. 15302-15309.

[150] Lu et al., *CrystEngComm.* **2016**, 18, p. 2596.

[151] Maji et al., *Materials Today* **2015**, 18, pp. 97-116.

[152] Lillerud et al., *Inorg. Chem.* **2016**, 55, pp 1986–1991.

[153] Cohen et al., *CrystEngComm.* **2012**, 14, pp. 4096-4104.

[154] Bordiga et al., *Phys. Chem. Chem. Phys.* **2012**, 14, pp. 1614-1626.

[155] Rabenau et al., *Angew. Chem. Int. Ed. Engl.* **1985**, 24, p. 1026.

[156] Biswas et al., *Chem. Rev.* **2012**, 112, pp. 933-969.

[157] Yan et al., *Microporous Mesoporous Mater.* **2003**, 58, p.105.

[158] Yaghi et al., *Tetrahedron* **2008**, 64, p. 8553.

[159] Wiebcke et al., *Chem. Mater.* **2009**, 21, p. 1410.

[160] Zhou et al., *Inorg. Chem. Commun.* **2013**, 36, pp. 241-244.

[161] Fan et al., *Trans. Nonferrous Met. Soc. China* **2015**, 25, pp. 3987-3994.

[162] Ahn et al., *Korean J. Chem. Eng.* **2013**, 30, pp. 1667-1680.

[163] Fischer et al., *Chem. Rev.* **2012**, 112, pp. 1055-1083.

[164] Mueller et al., *J. Mater. Chem.* **2006**, 16, pp. 626-636.

[165] James et al., *CrystEngComm.* **2006**, 8, pp. 211-214.

[166] Nair et al.,*Cryst. Growth Des.* **2011**, 11, pp 4505-4510.

[167] Ahn et al., *Chem. Commun.* **2008**, pp. 6336-6338.

[168] Deng et al., *Tsinghua Science & Technology*, **2010**, 15, pp. 363-376.

[169] Korposh et al., *Sensors and Actuators B: Chemical* **2015**, 221, pp. 891-899.

[170] plasmachem.com > HKUST, accessed on 18.09.2018.

[171] Yaghi et al., *Chemical Engineering Science* **2011**, 66, pp. 163-170.

[172] metal-organic-frameworks.eu > adsorbentien > MOF-5, accessed on 18.09.2018.

[173] Yaghi et al., *J. Phys. Chem. C.* **2012**, 116, pp. 13307-13312.

[174] M. Birkholz, *Thin Film Analysis by X-Ray Scattering*, Wiley **2006**.

[175] T. T. Steven, A. Rex, *Modern Physics for Scientists and Engineers*, Saunders College Publishing **1993**.

[176] H. Saisho, Y. Gohshi, *Applications of Synchrotron Radiation to Materials Analysis*, Elsevier Science **1996**.

[177] R. J. Hemley, *Ed. Reviews in Mineralogy & Geochemistry* **1998**, 37, MSA Series, Washington, DC.

[178] Struzhkin et al., *J. Synch. Rad.* **2005**, 12, pp. 135-154.

[179] Mao et al., Nuovo Cimento 20D **1998**, 114, pp. 539-551.

[180] D. L. Andrews, *in Encyclopedia of Spectroscopy and Spectrometry* **1999**.

[181] R. Schoch, '*Active species identification of iron-based homogeneously and heterogeneously catalyzed reactions'*, Dissertation, Universität Paderborn **2017**.

[182] Holý et al., *J. Appl. Crystallogr.* **2015**, 48, pp. 613-618.

[183] prism.mit.edu > xray > Basics of X-Ray > Powder Diffraction, accessed on 18.09.2018.

[184] B. B. He, *Two-dimensional X-ray Diffraction*, Wiley **2009**.

[185] a) C. Weinberger, '*Kohlenstoff-basierte Wirt-Gast-Komposite für Anwendungen als Sorbentien und Elektrodenmaterialien'*, Dissertation, Universität Paderborn **2016**. b) Thommes et al., *Pure Appl. Chem.* **2015**, p. 9.

[186] Snurr et al., *Langmuir* **2010**, 26, pp. 5475-5483.

[187] Deng et al., *J. Phys. Chem. Lett.* **2010**, 1, pp. 73-78.

[188] S. Nielsen, Food Analysis, 5th Edition, Springer **2017**.

[189] nptel.ac.in > courses > 115103030 > module4 > lec23 > 4, accessed on 18.09.2018.

[190] Duan et al., *J. Org. Chem.* **2014**, 79, pp. 777-782.

[191] Parmar et al., *Catalysts* **2017**, 7, p. 1-23.

[192] Pattenden et al., *J. Chem. Soc., Perkin Trans. I* **1999**, 10, pp. 1235-1246.

[193] Fu et al., *Chem. Eur. J.* **2014**, 20, pp. 13957-13964.

[194] Pruchnik et al., *Dalton Trans.* **2009**, pp. 3348-3353.

[195] openchemistryhelp.blogspot.com > 2013 > 02 > making-acid-chlorides-from-carboxylic, accessed on 18.09.2018.

[196] orgchemboulder > Spectroscopy > irtutor > aminesir, accessed on 18.09.2018.

[197] Santana et al., *J. Brazil. Chem. Soc.* **2010**, 21, pp. 279-287.

[198] Granger et al., *Inorg. Chem.* **1983**, 22, pp 532-535.

[199] Llobet et al., *Chem. Eur. J.* **2018**, 24, pp. 1-11.

[200] Saricifici et al., *Electrocatalysis* **2015**, 6, pp. 185-197.

[201] B. E. Tropp, *Molecular Biology*, 4th Edition, JustTheFacts101 **2017**.

[202] Scheinost et al., *Inorg. Chem.* **2013**, 52, pp. 11734-11743.

[203] Sun et al., *ACS Catal.* **2017**, 7, 4, pp. 2956-2966.

[204] a) Lin et al., *Chemical Science* **2013**, 4, p. 2396. b) Lin et al., *J. Am. Chem. Soc.*, **2014**, 136, pp. 13182-13185.

[205] Farha et al., *Chem.Commun*. **2013**, 49, p. 9449.

[206] Tilset et al., *J. Mater. Chem.* **2010**, 20, pp. 9848-9985.

[207] Shen et al., *Org. Chem. Front.* **2018**, 5, pp. 46-50.

[208] Schubert et al., *Org. Letters* **2000**, 2, pp. 3373-3376.

[209] Kirsanov et al., *Russ.Chem.Bull.* **2012**, 61, pp. 881-890.

[210] Liao et al., *J. of Org. Chem.* **2014**, 792, pp. 777-782.

[211] Cheung et al., PCT Int. Appl. **2016**.

[212] Yang et al., PCT Int. Appl. **2015**.

[213] Shouwey et al., *Angew. Chem.* **2014**, 53, pp. 11261-11265.

[214] Shao et al., *J. Incl. Phenom. Macrocycl. Chem*. **2008**, 62, pp. 99-103.

[215] Liu et al., *Bioorg. Med. Chem.* **2018**, 26, pp. 2621-2631.

[216] Duan et al., *J. Am. Chem. Soc.* **2009**, 131, pp. 10397-10399.

TABLE OF FIGURES

LIST OF TABLES

APPENDIX

NMR spectra

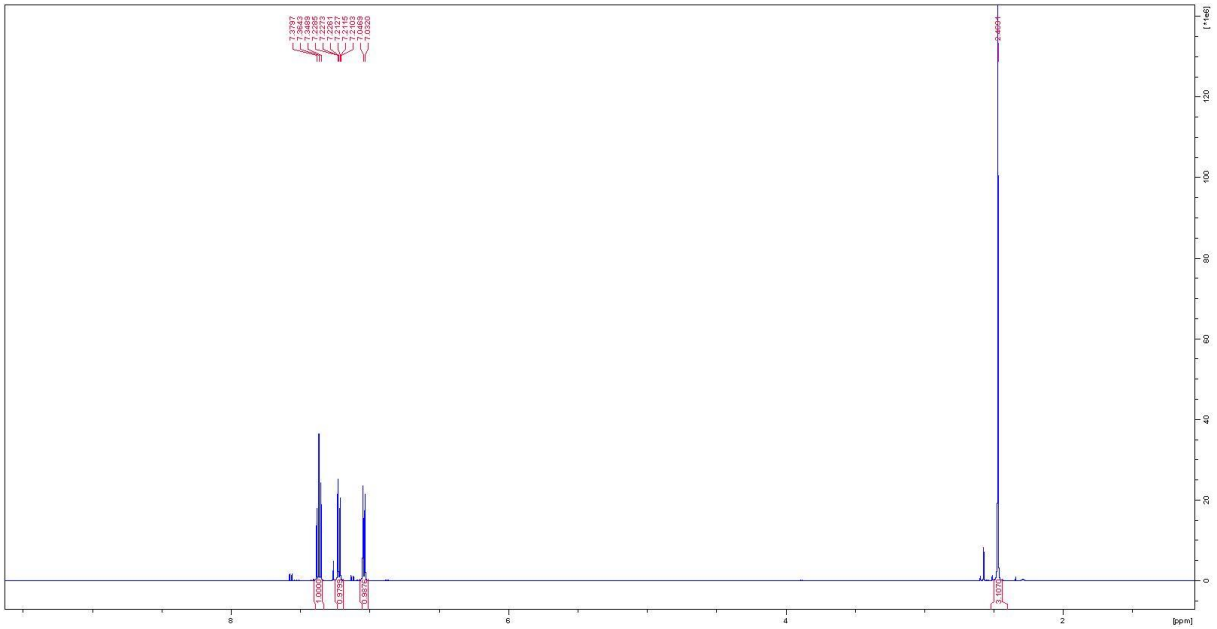

Figure 178. ^{1}H spectrum of 6-bromo-2-methylpyridine.

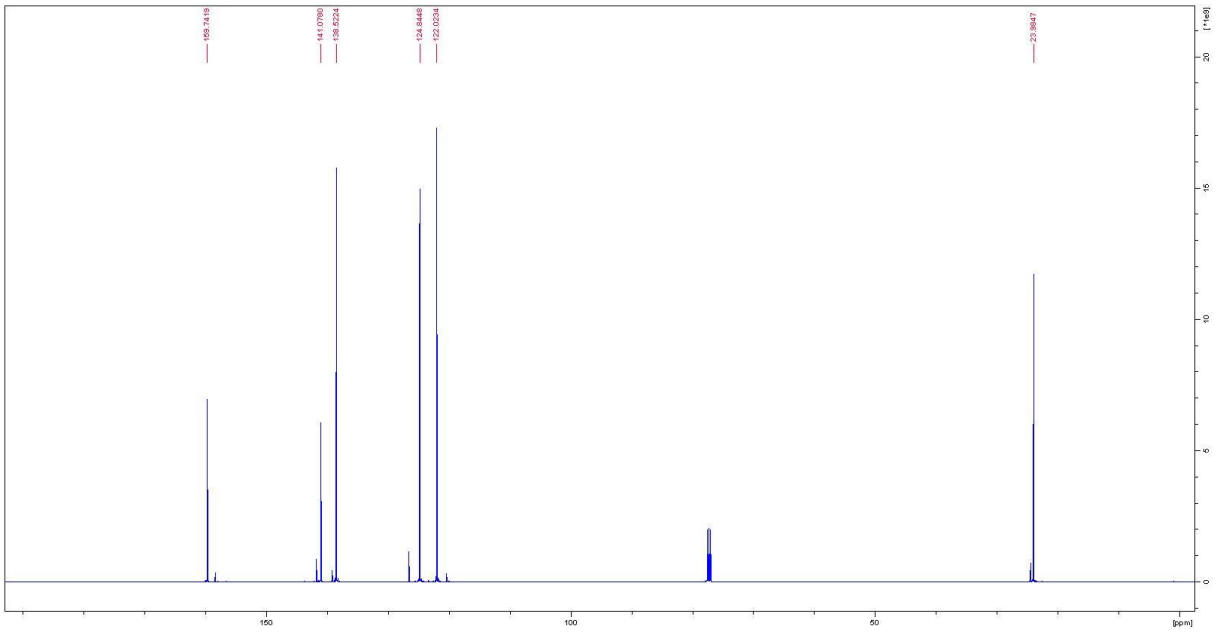

Figure 179. ^{13}C spectrum of 6-bromo-2-methylpyridine.

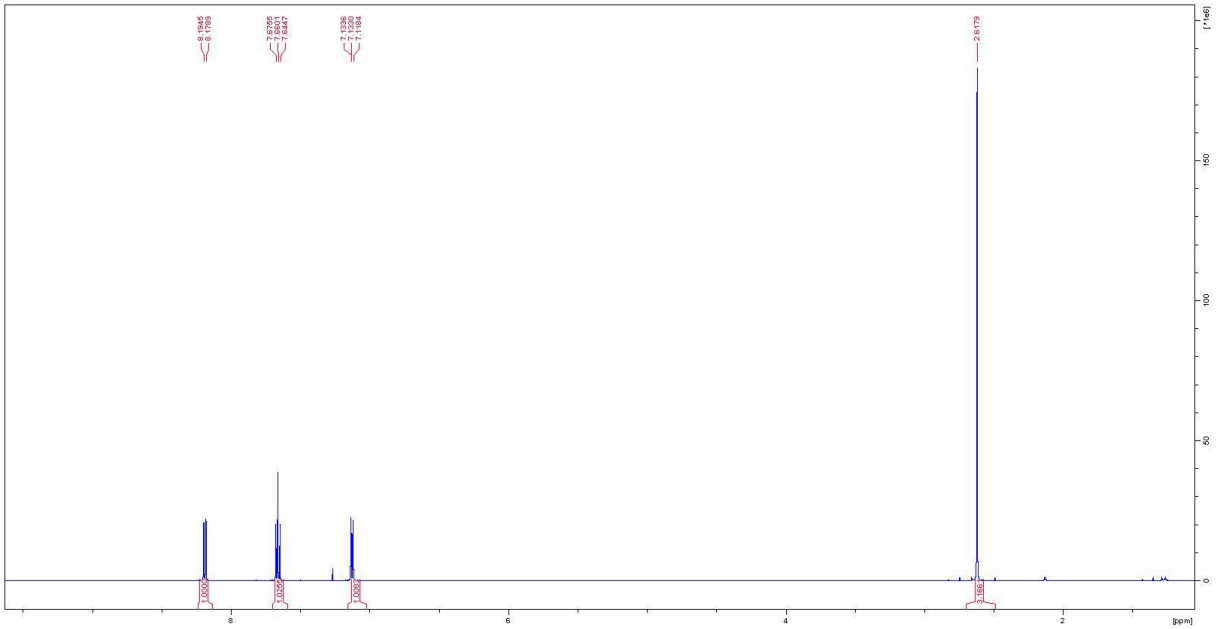

Figure 180. ^{1}H spectrum of 6,6'-dimethyl-2,2'-bipyridine.

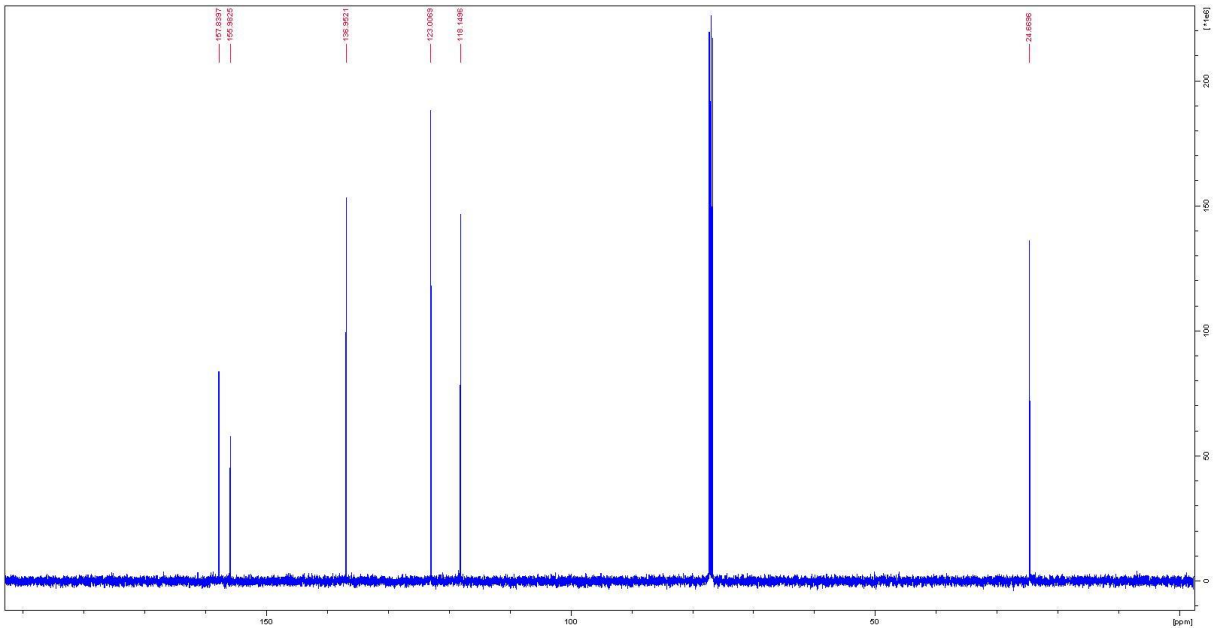

Figure 181. ^{13}C spectrum of 6,6'-dimethyl-2,2'-bipyridine.

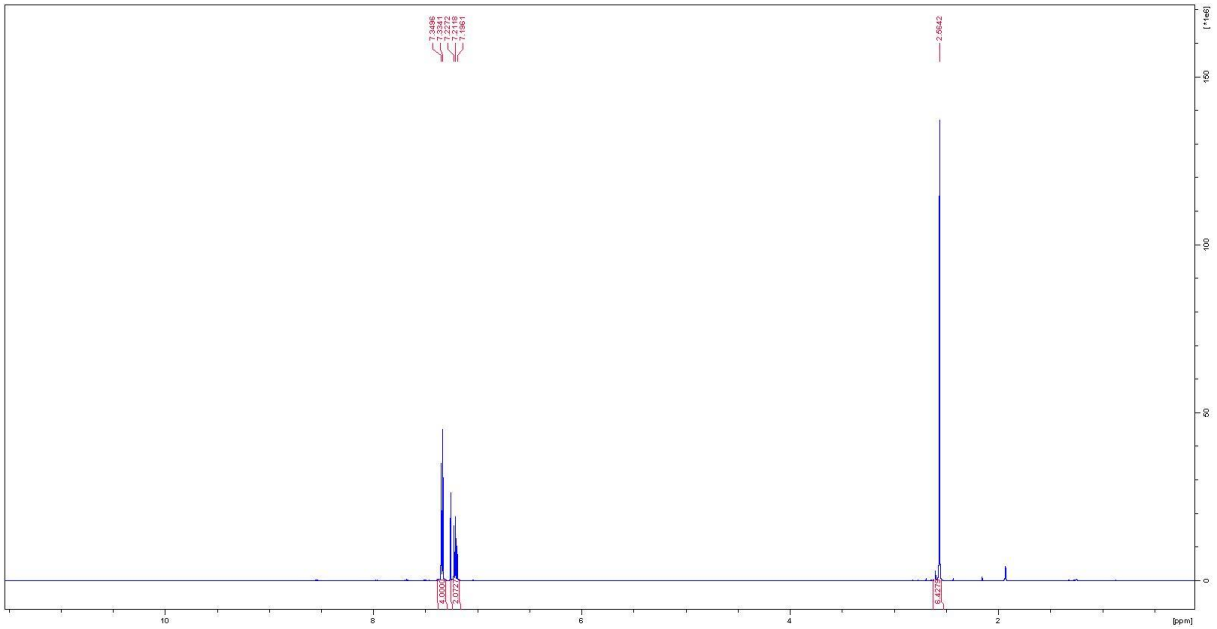

Figure 182. ^{1}H spectrum of 6,6'-dimethyl-2,2'-dipyridyl di-*N*-*N'*-oxide.

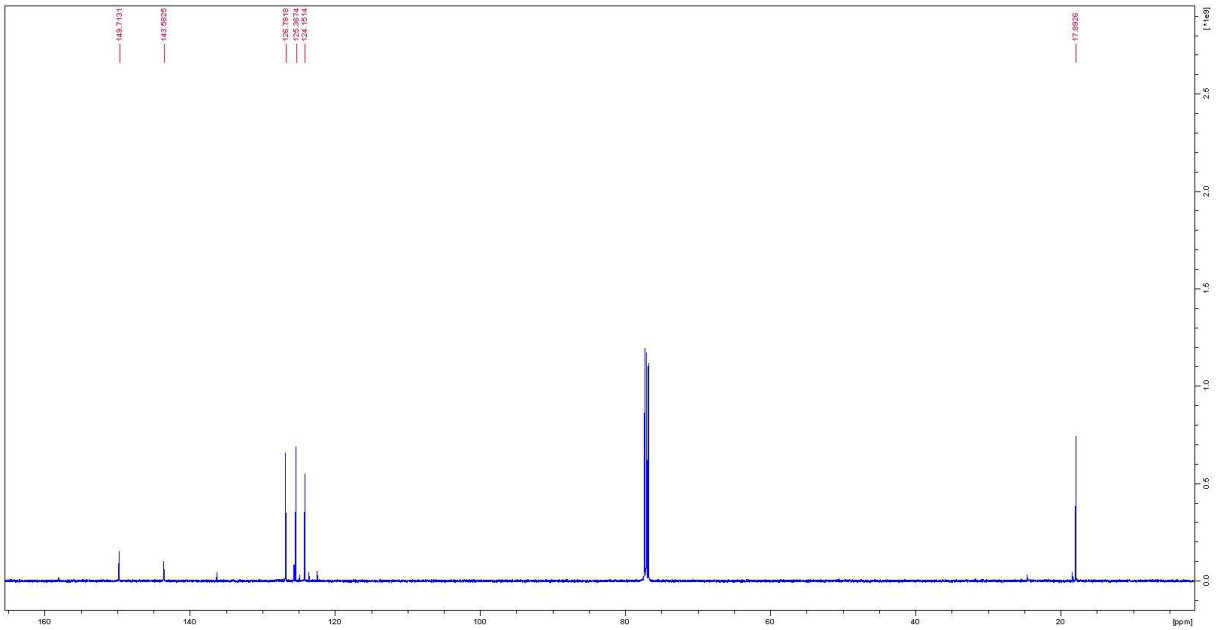

Figure 183. ^{13}C spectrum of 6,6'-dimethyl-2,2'-dipyridyl di-*N*-*N'*-oxide.

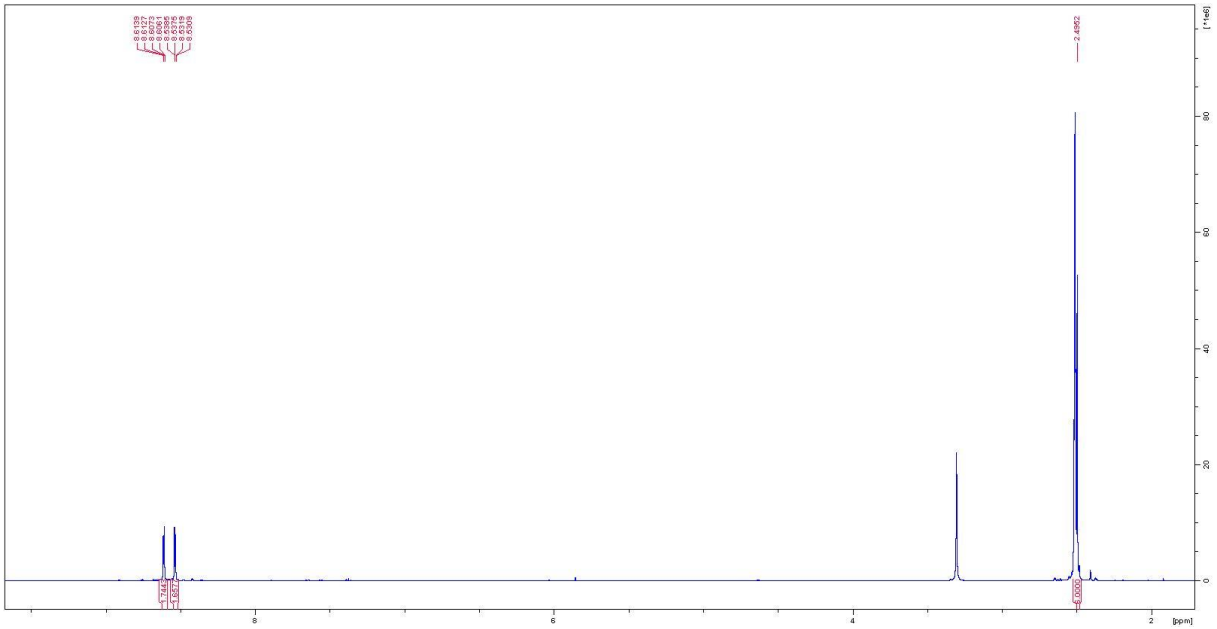

Figure 184. ^{1}H spectrum of 6,6'-dimethyl-4,4'-dinitro-2,2'-dipyridyl di-*N*,*N'*-oxide.

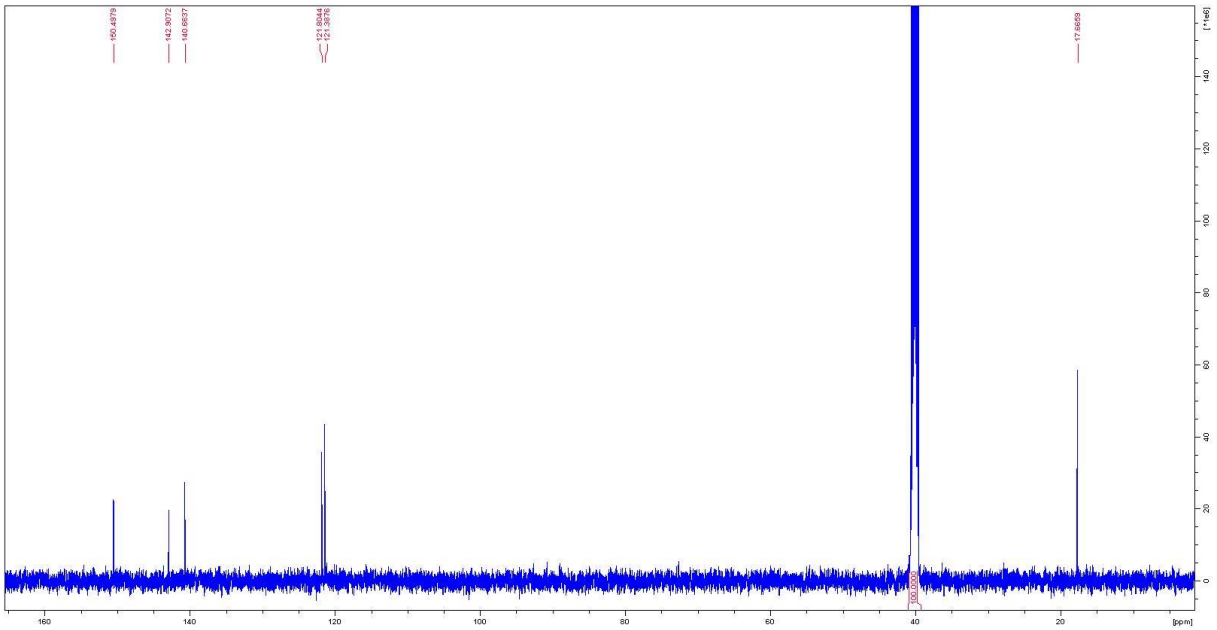

Figure 185. ^{13}C spectrum of 6,6'-dimethyl-4,4'-dinitro-2,2'-dipyridyl di-*N*,*N'*-oxide.

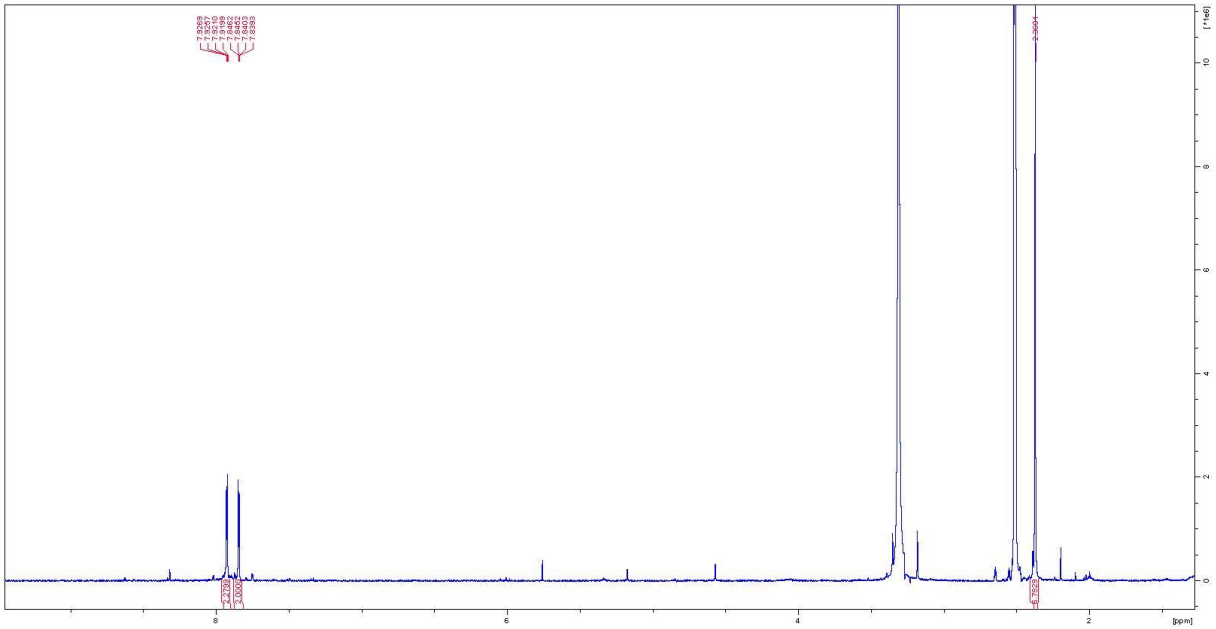

Figure 186. ^{1}H spectrum of 6,6'-dimethyl-4,4'-dibromo-2,2'-dipyridyl di-*N*,*N'*-oxide.

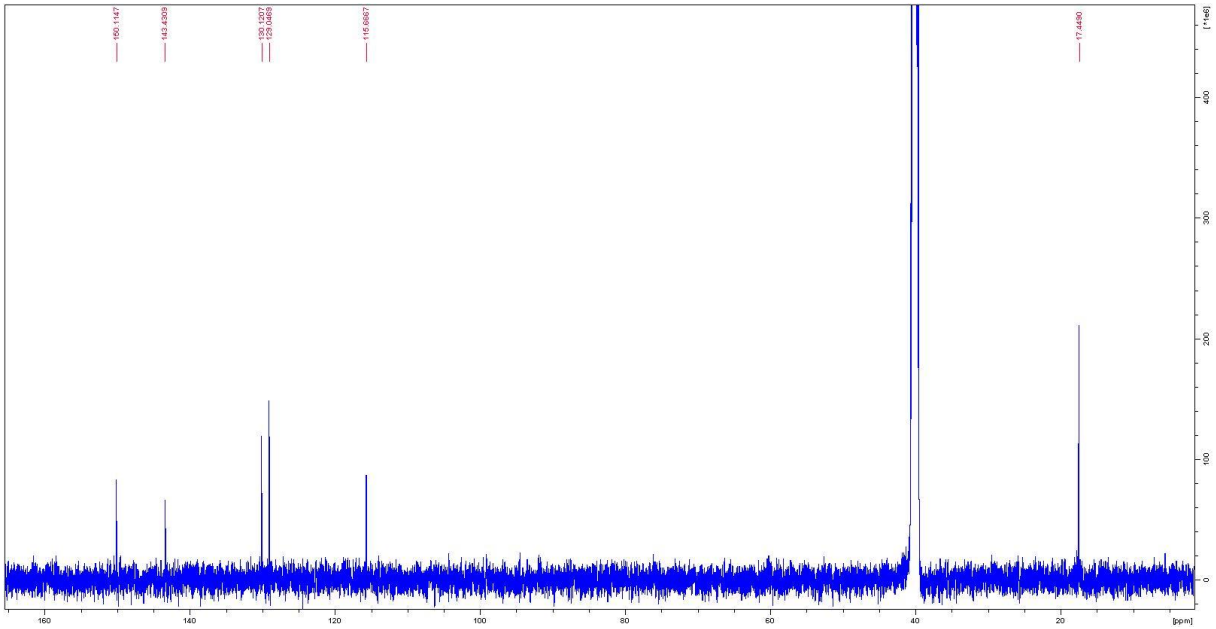

Figure 187. ^{13}C spectrum of 6,6'-dimethyl-4,4'-dibromo-2,2'-dipyridyl di-*N*,*N'*-oxide.

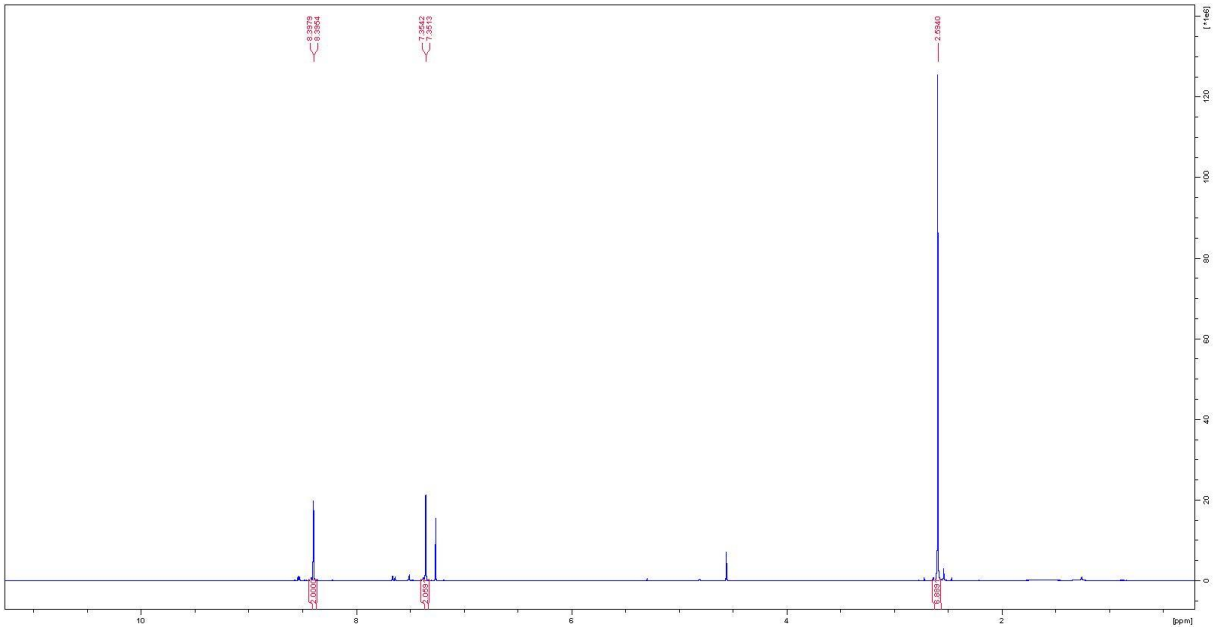

Figure 188. ^{1}H spectrum of 4,4'-dibromo-6,6'-dimethyl-2,2'-bipyridine.

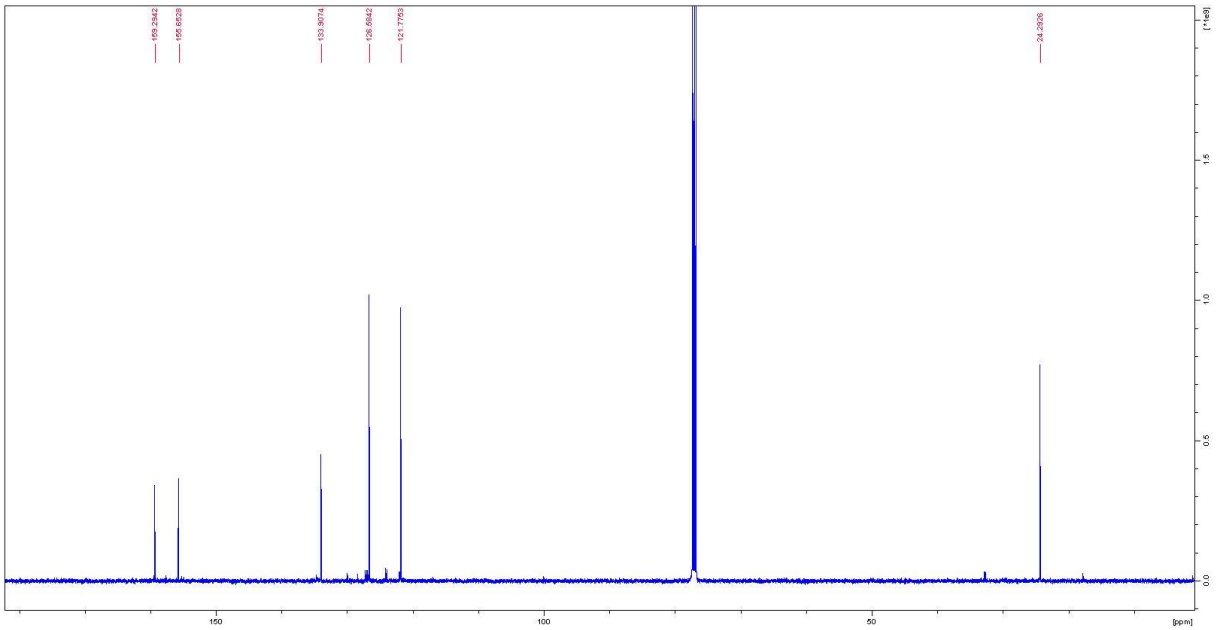

Figure 189. ^{13}C spectrum of 4,4'-dibromo-6,6'-dimethyl-2,2'-bipyridine.

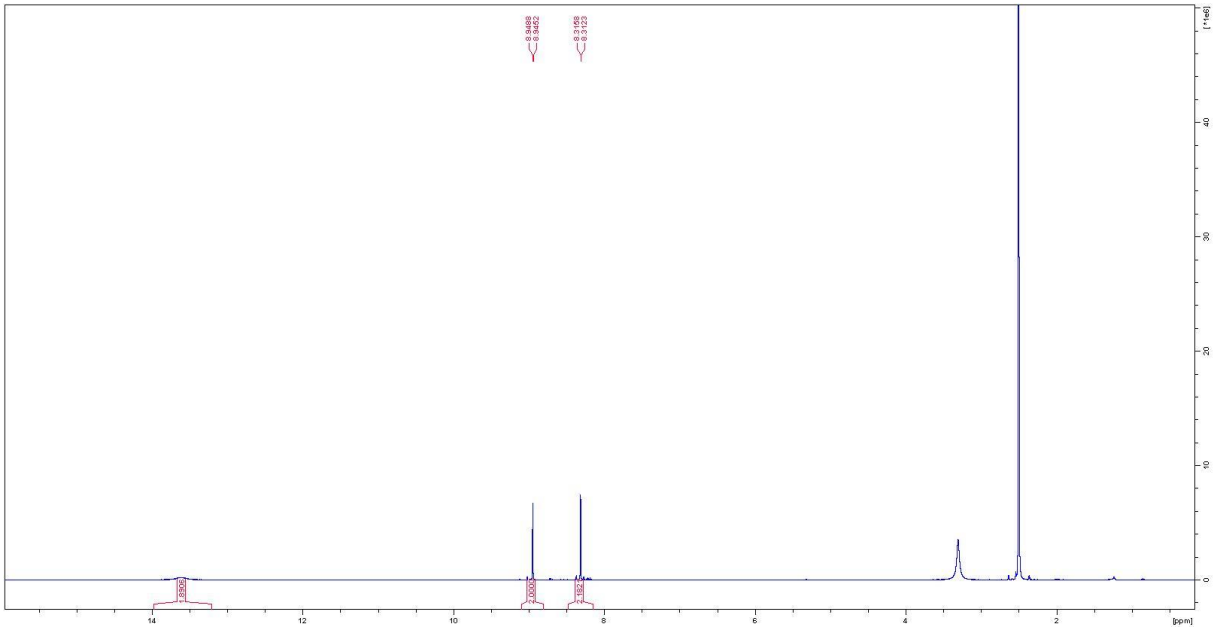

Figure 190. ^{1}H spectrum of 4,4-dibromo-2,2-dipyridyl-6,6-dicarboxylic acid.

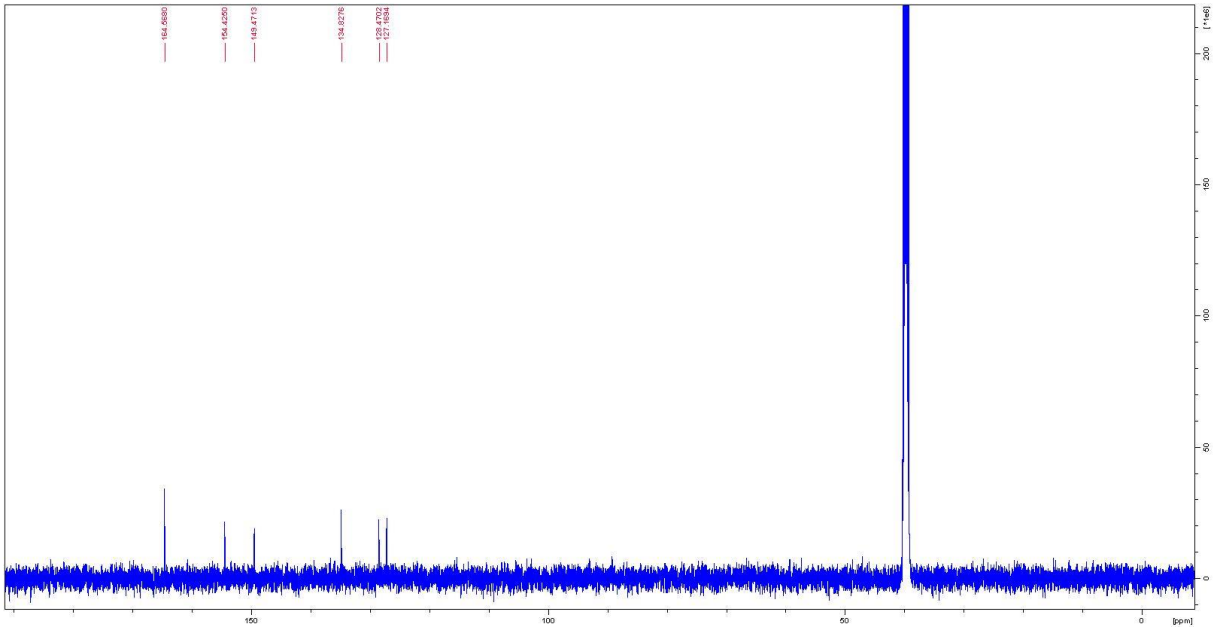

Figure 191. ^{13}C spectrum of 4,4-dibromo-2,2-dipyridyl-6,6-dicarboxylic acid.

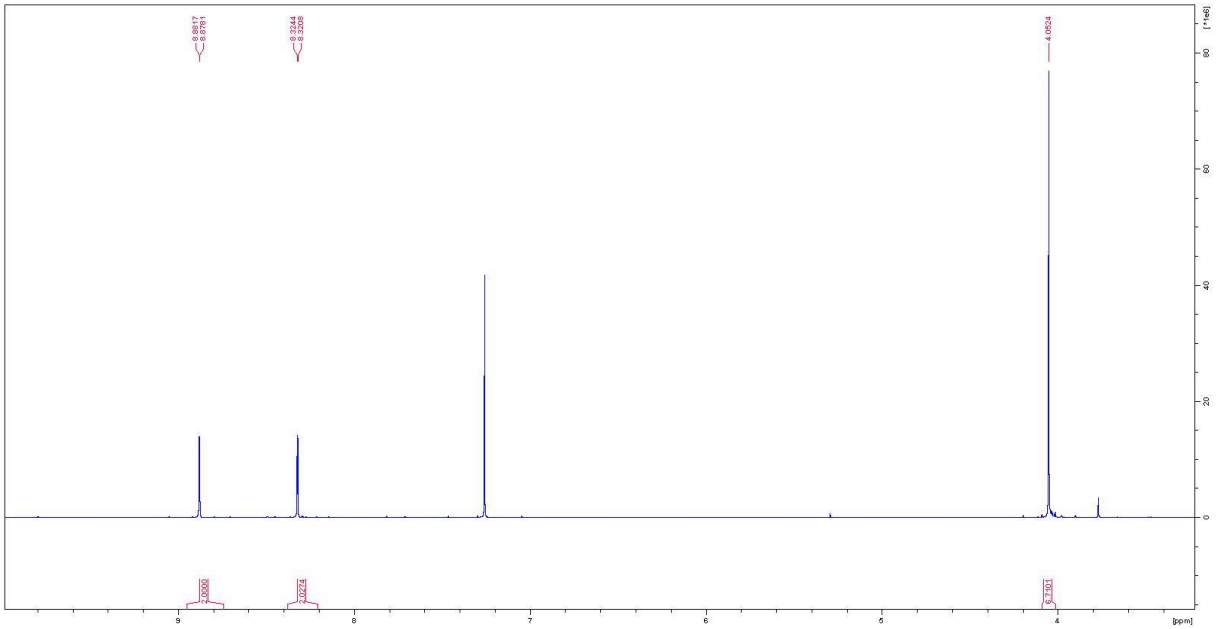

Figure 192. ^{1}H spectrum of dimethyl-4,4’-dibromo-2,2’bipyridine-6,6’-dicarboxylate.

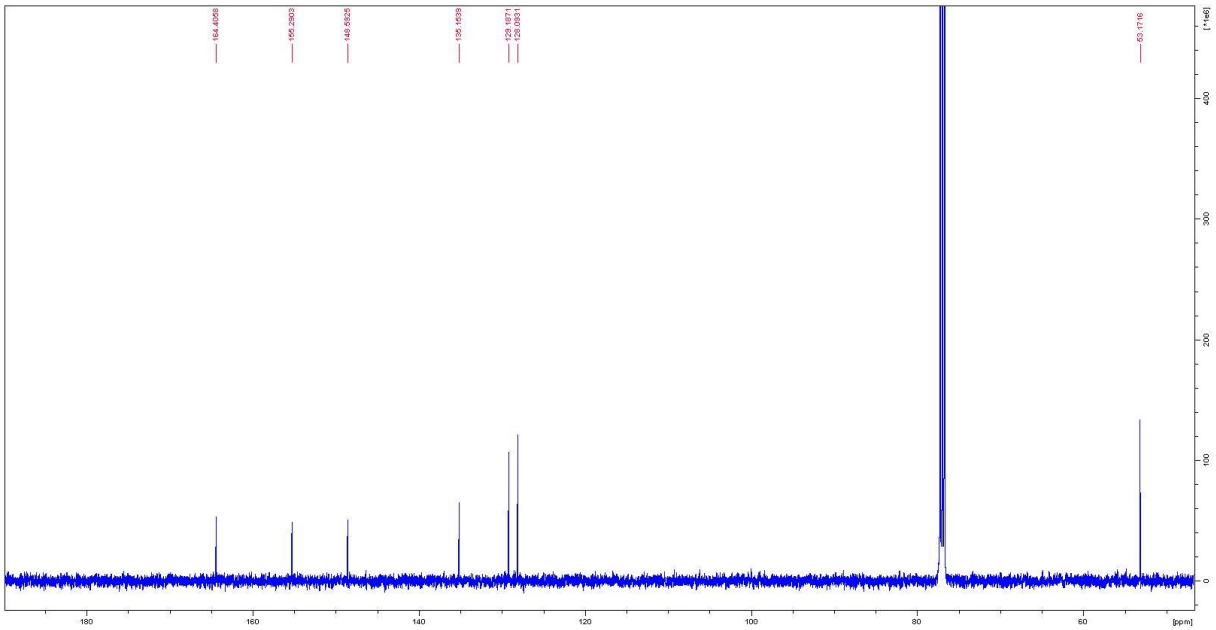

Figure 193. ^{13}C spectrum of dimethyl-4,4’-dibromo-2,2’bipyridine-6,6’-dicarboxylate.

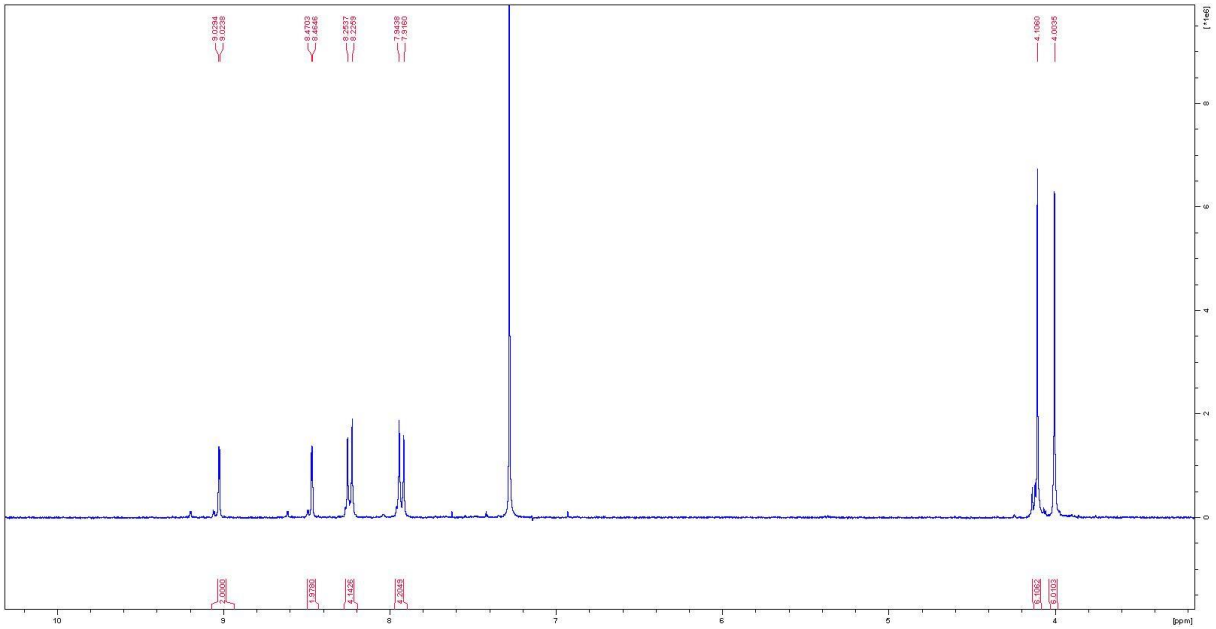

Figure 194. ^{1}H spectrum of dimethyl 4,4‘-bis(4-(methoxycarbonyl)phenyl)-2,2‘-bipyridine-6,6‘-dicarboxylate.

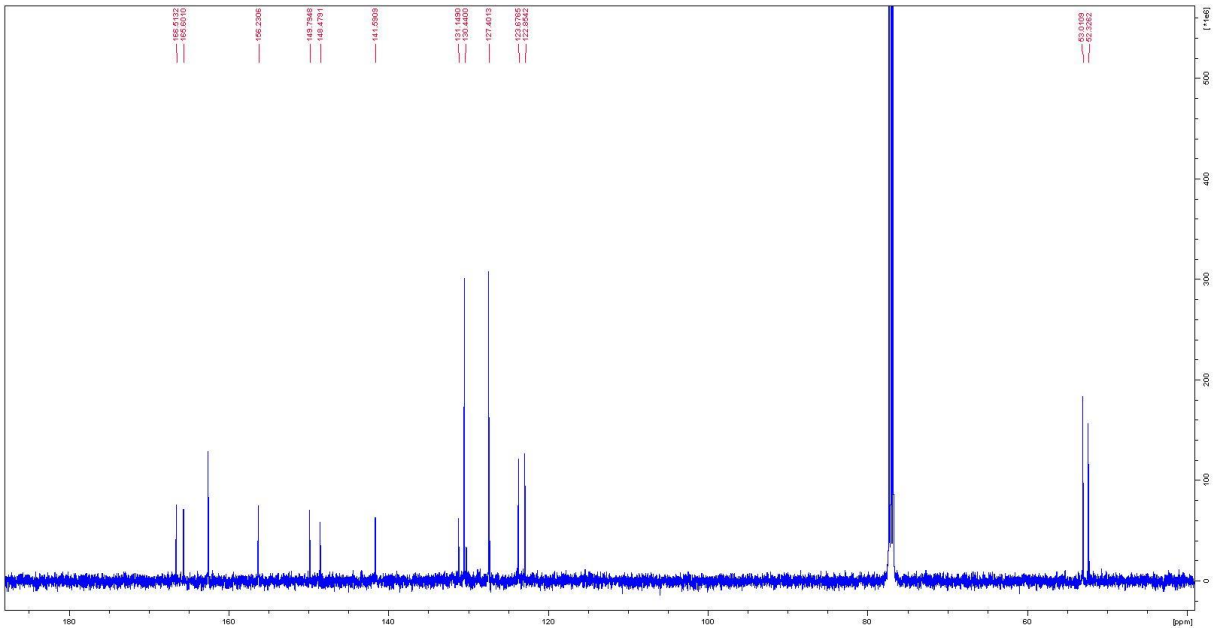

Figure 195. ^{13}C spectrum of dimethyl 4,4‘-bis(4-(methoxycarbonyl)phenyl)-2,2‘-bipyridine-6,6‘-dicarboxylate.

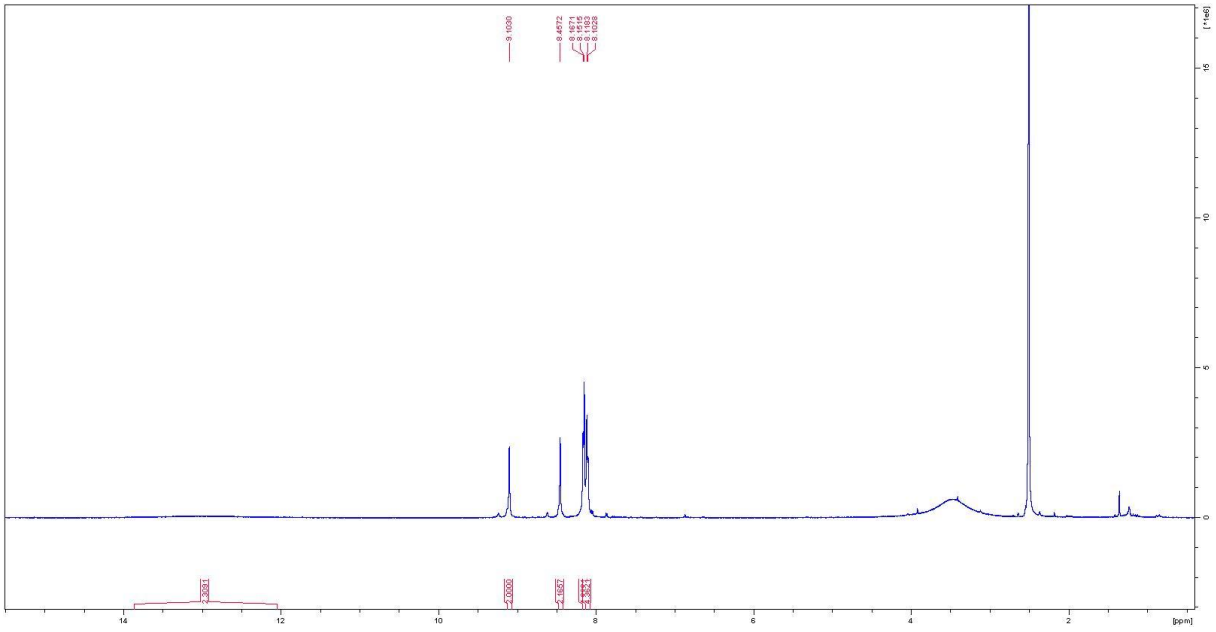

Figure 196. ^{1}H spectrum of 6,6'-dimethyl-2,2'-bipyridine-4,4'-dibenzoic acid.

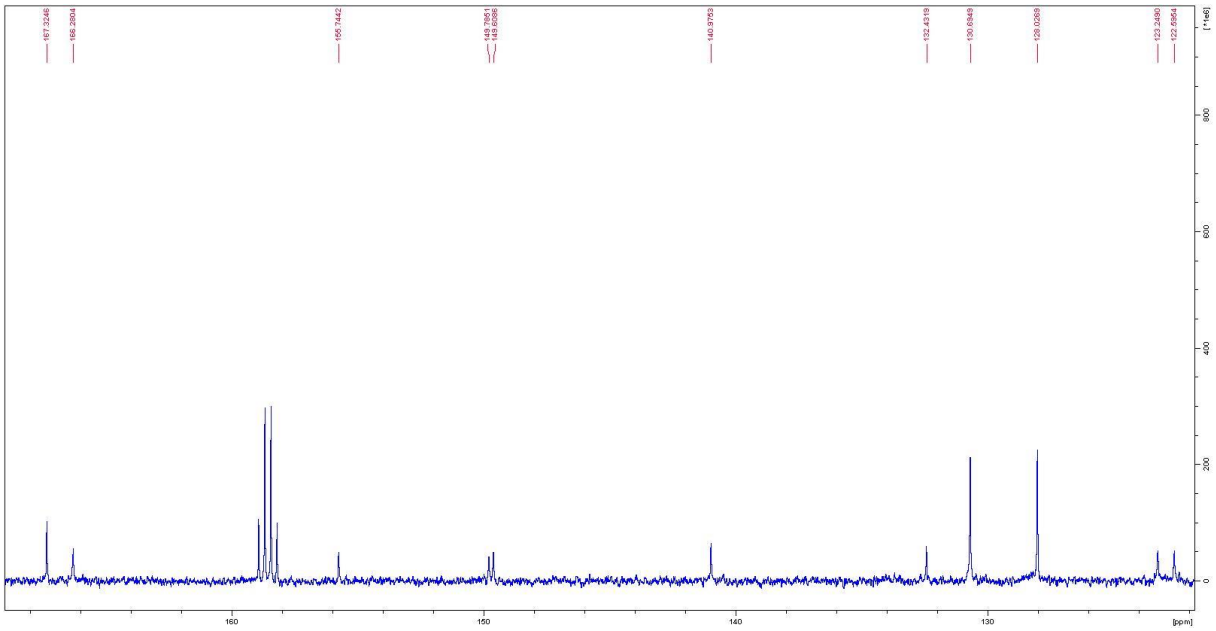

Figure 197. ^{13}C spectrum of 6,6'-dimethyl-2,2'-bipyridine-4,4'-dibenzoic acid.

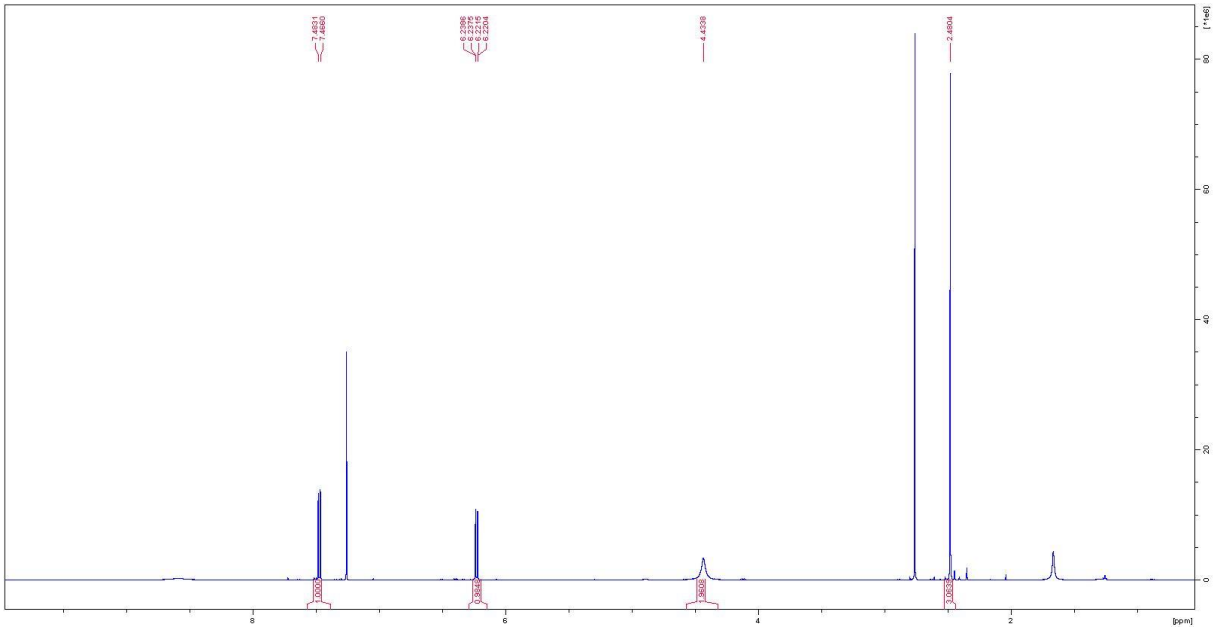

Figure 198. ^{1}H spectrum of 5-bromo-6-methyl-2-pyridinamine.

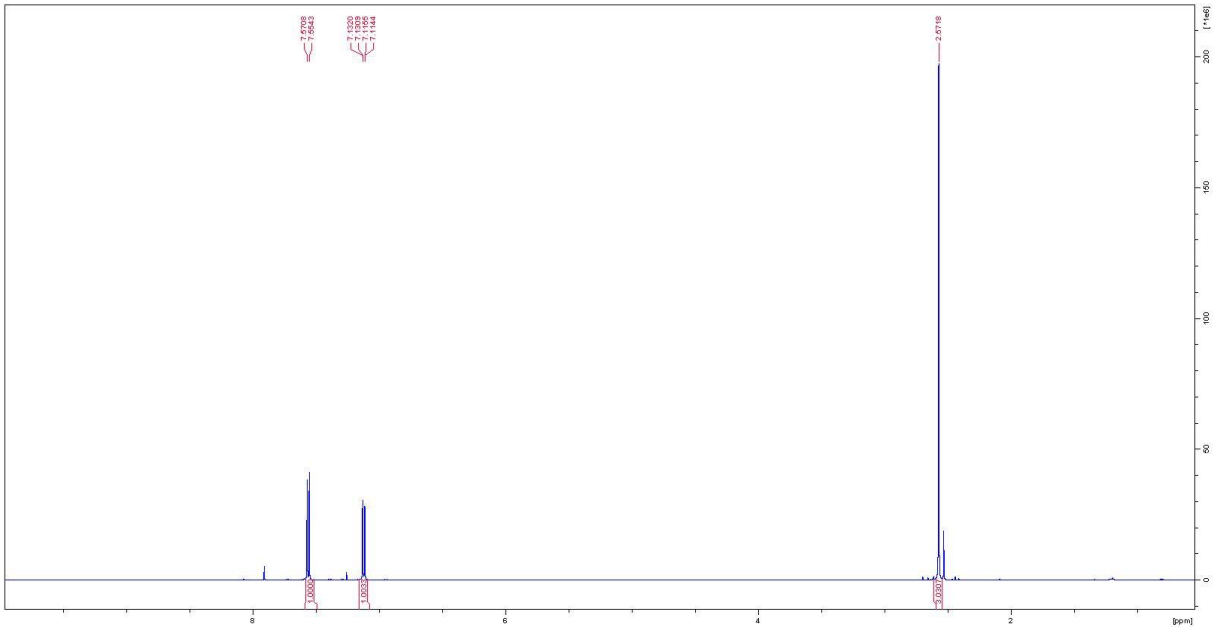

Figure 199. ^{1}H spectrum of 3,6-dibromo-2-methyl-pyridine.

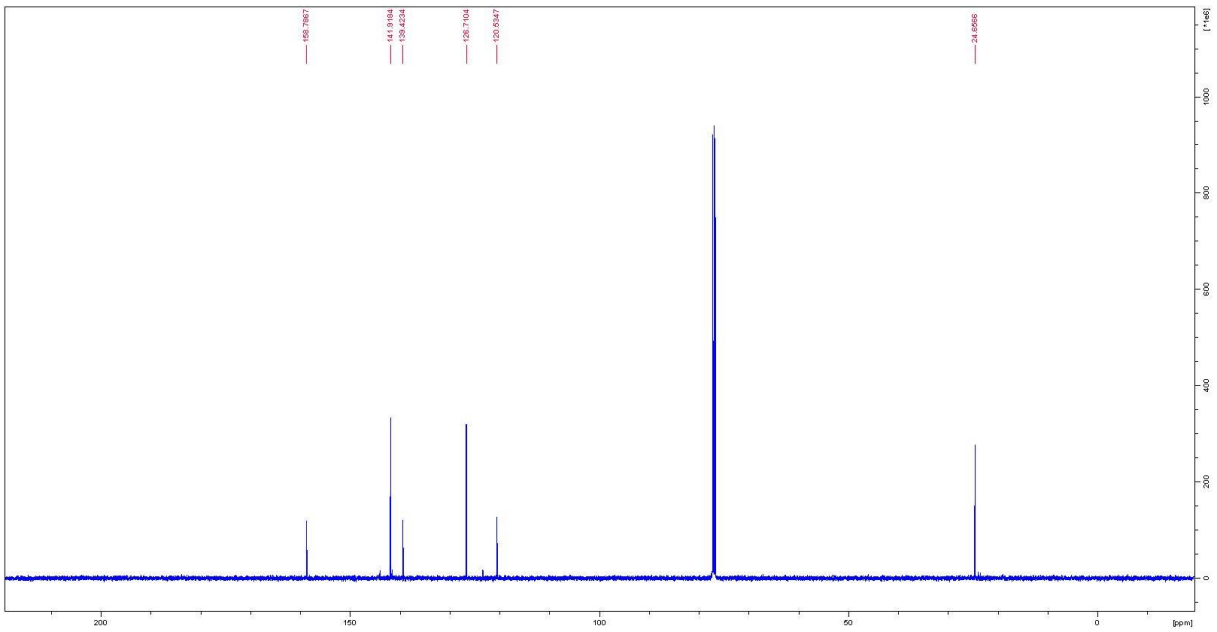

Figure 200. ^{13}C spectrum of 3,6-dibromo-2-methyl-pyridine.

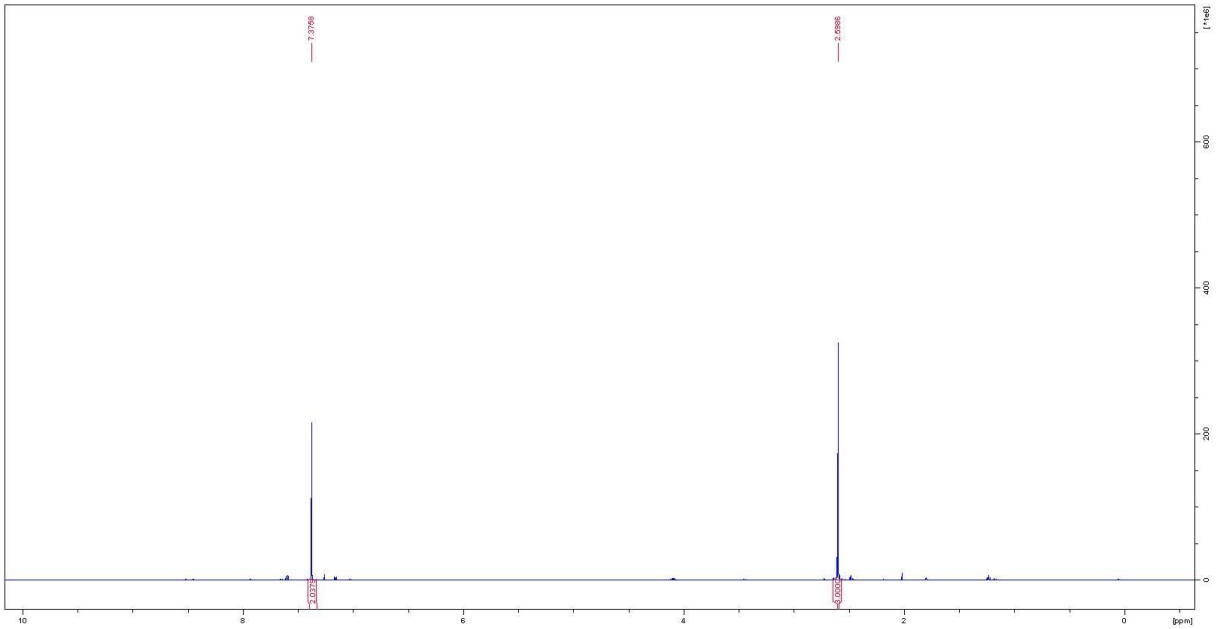

Figure 201. ^{1}H spectrum of 3-bromo-6-iodo-2-methylpyridine.

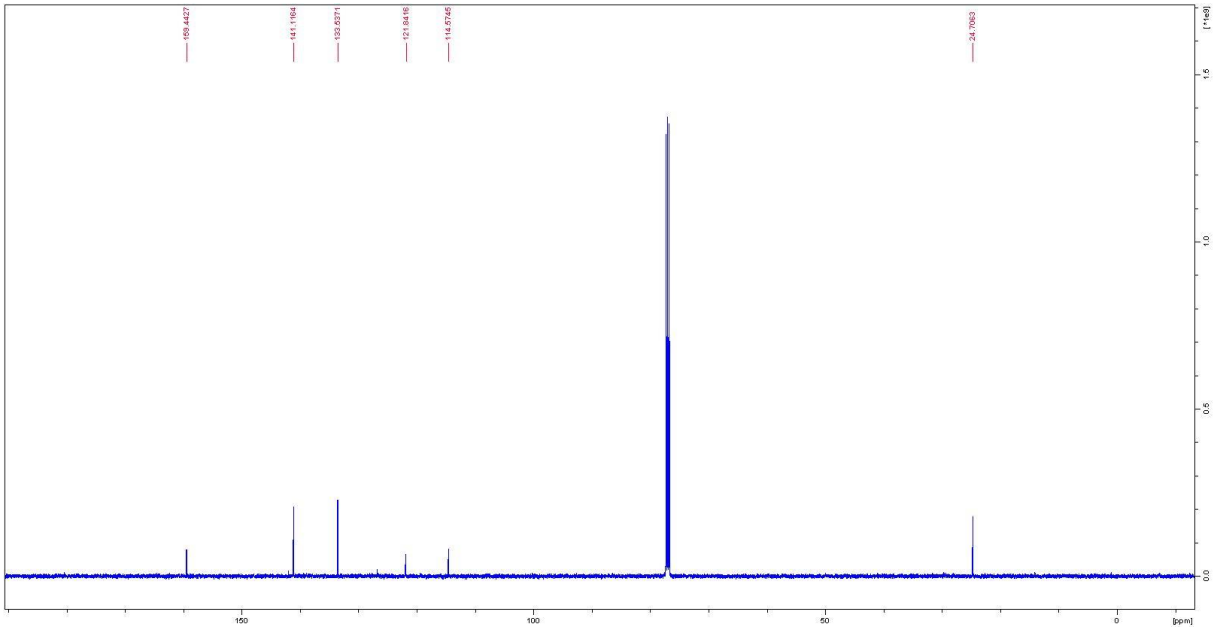

Figure 202. ^{13}C spectrum of 3-bromo-6-iodo-2-methylpyridine.

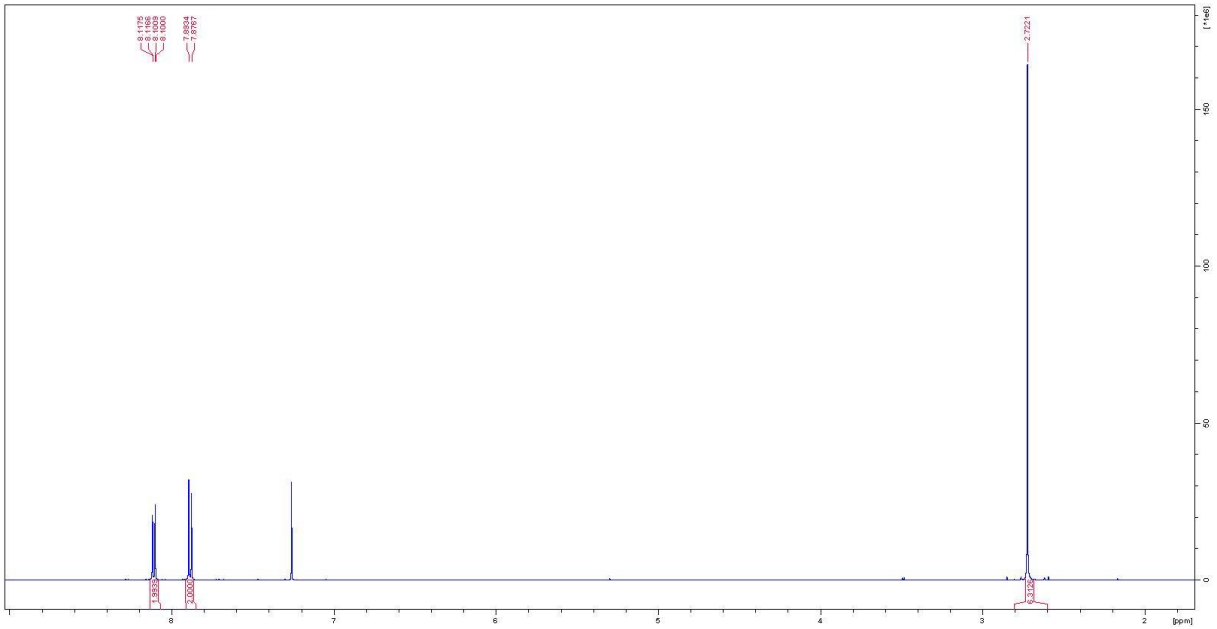

Figure 203. ^{1}H spectrum of 5,5‘-dibromo-6,6‘-dimethyl-2,2‘-bipyridine.

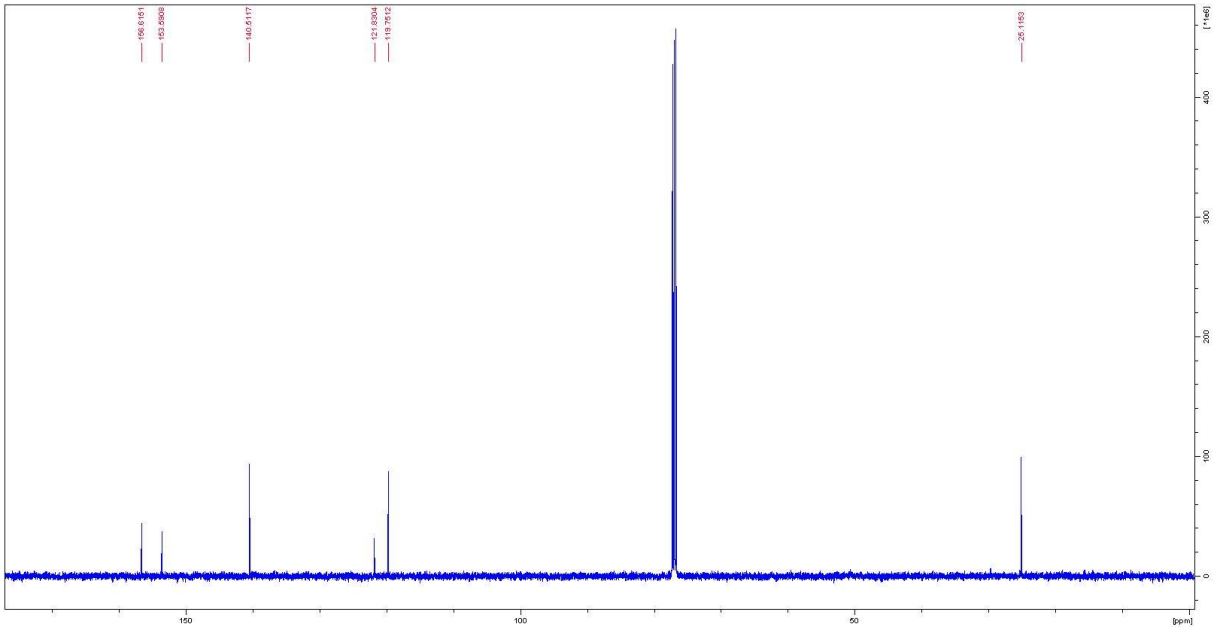

Figure 204. ^{13}C spectrum of 5,5‘-dibromo-6,6‘-dimethyl-2,2‘-bipyridine.

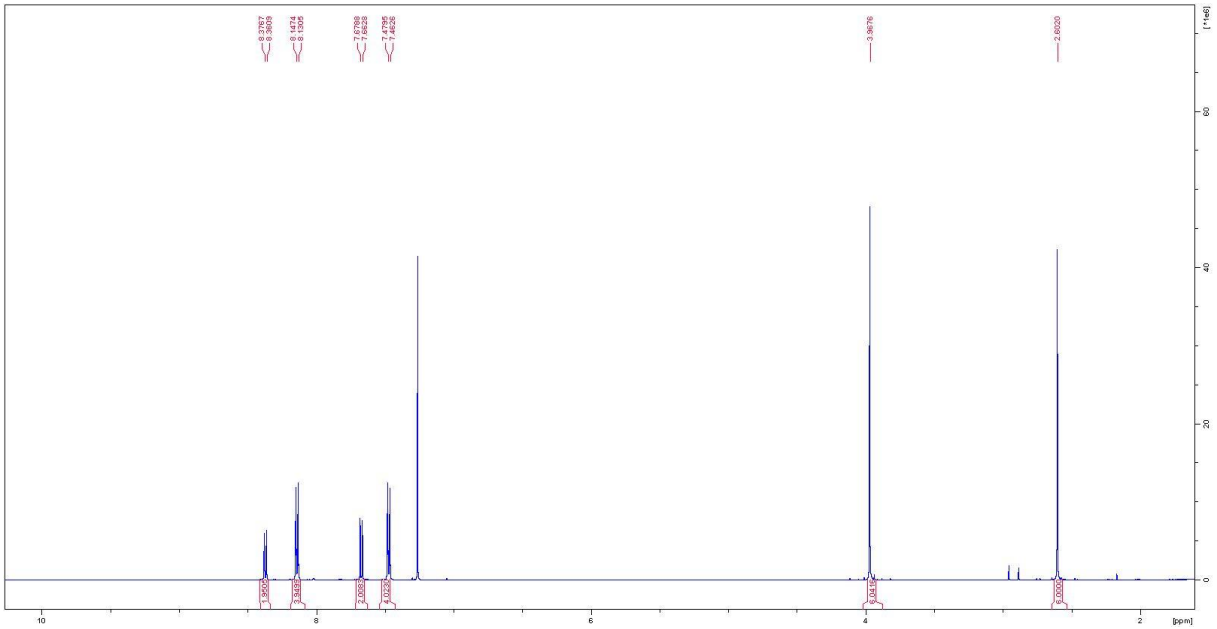

Figure 205. ^{1}H spectrum of dimethyl-4,4‘-(6,6‘-dimethyl-[2,2‘-bipyridine]-5,5‘-diyl)-dibenzoate.

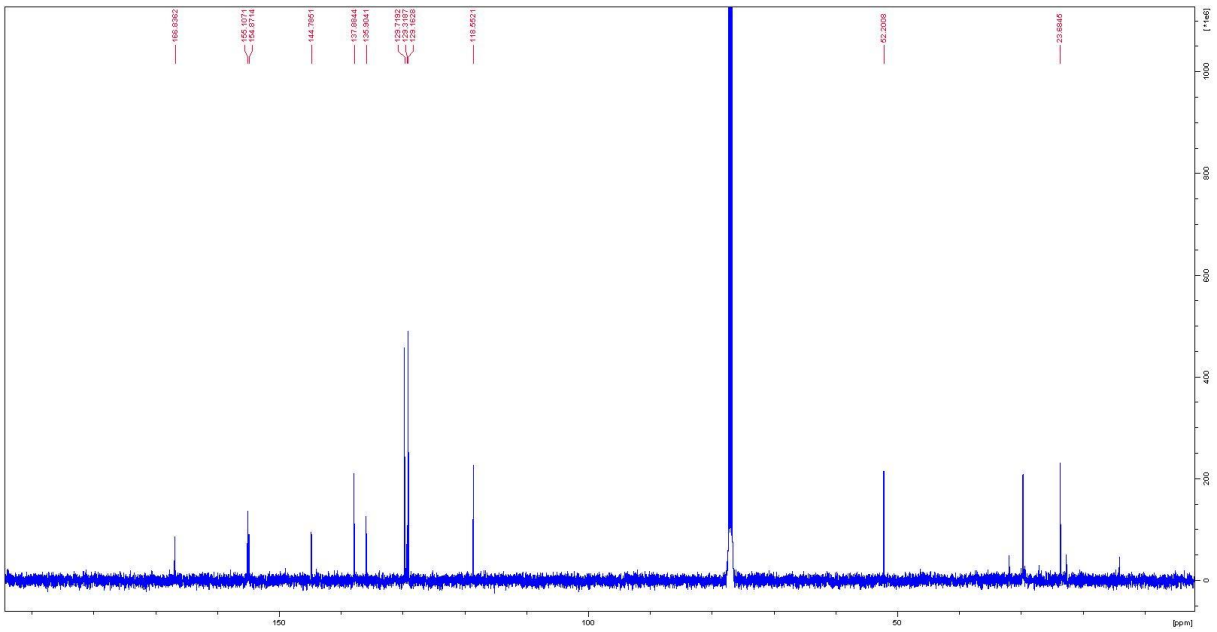

Figure 206. ^{13}C spectrum of dimethyl-4,4‘-(6,6‘-dimethyl-[2,2‘-bipyridine]-5,5‘-diyl)-dibenzoate.

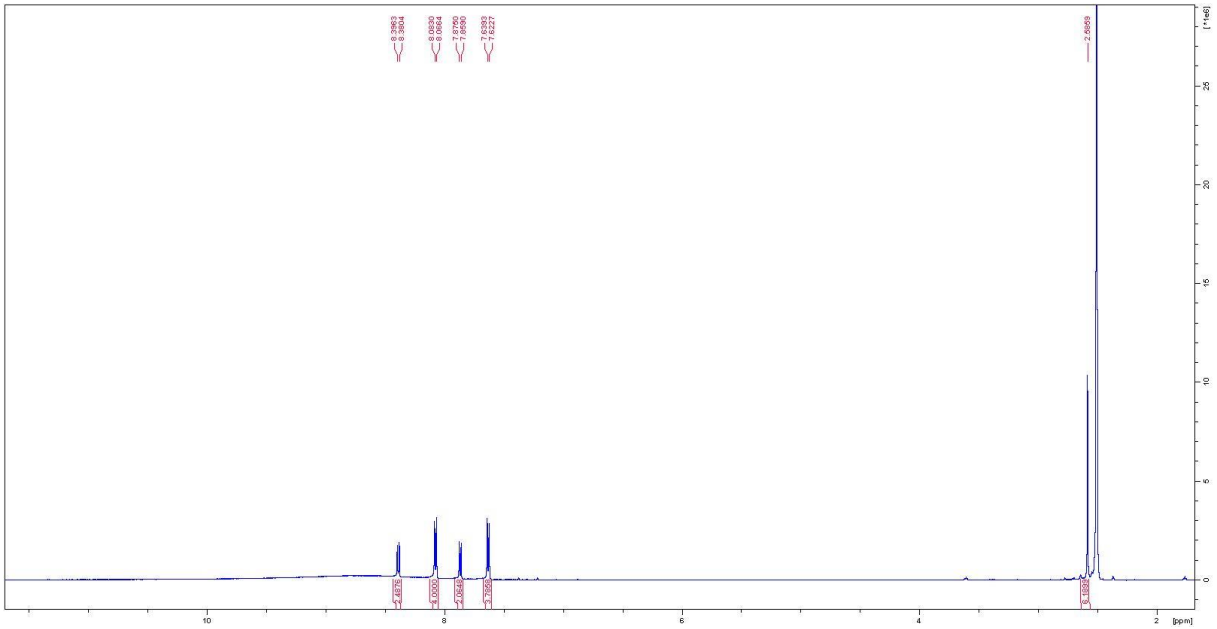

Figure 207. ^{1}H spectrum of 4,4‘-(6,6‘-dimethyl-[2,2‘-bipyridine]-5,5’diyl)dibenzoic acid.

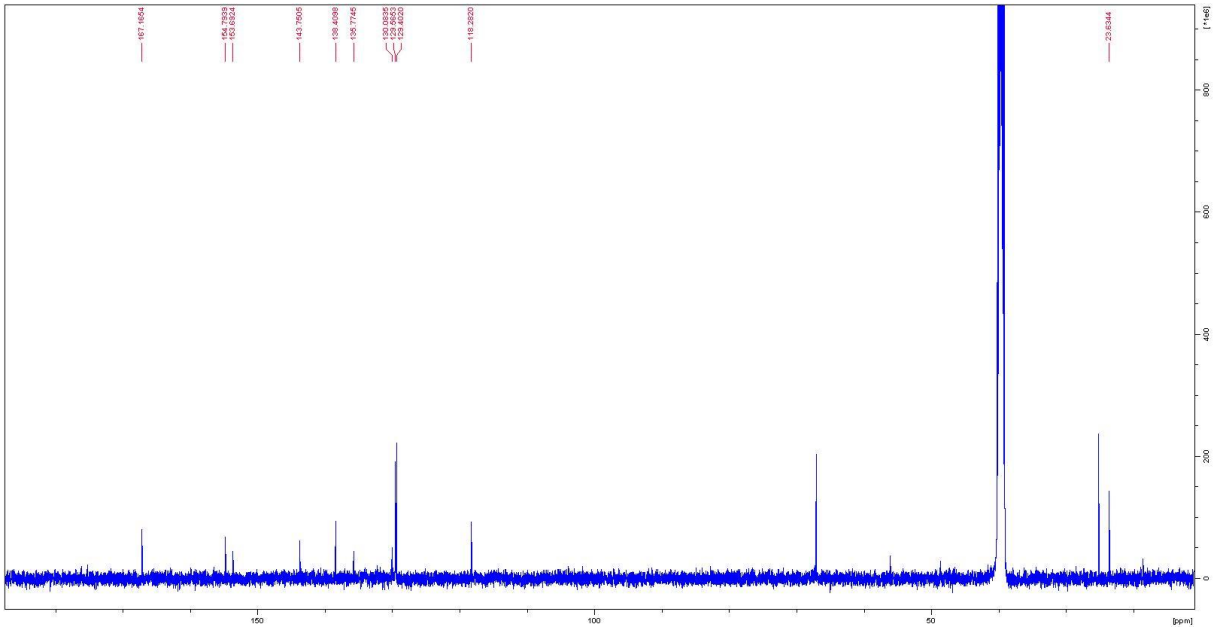

Figure 208. ^{13}C spectrum of 4,4‘-(6,6‘-dimethyl-[2,2‘-bipyridine]-5,5’diyl)dibenzoic acid.

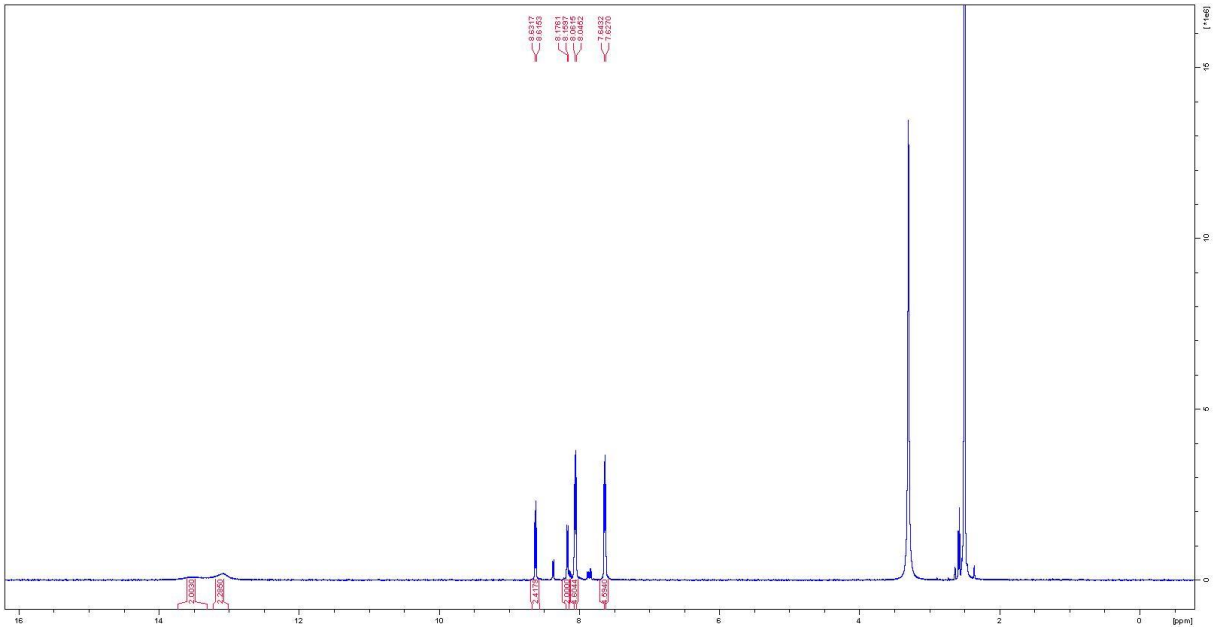

Figure 209. ^{1}H spectrum of 5,5‘-bis(4-carboxyphenyl)-[2,2‘-bipyridine]-6,6‘-dicarboxylic acid.

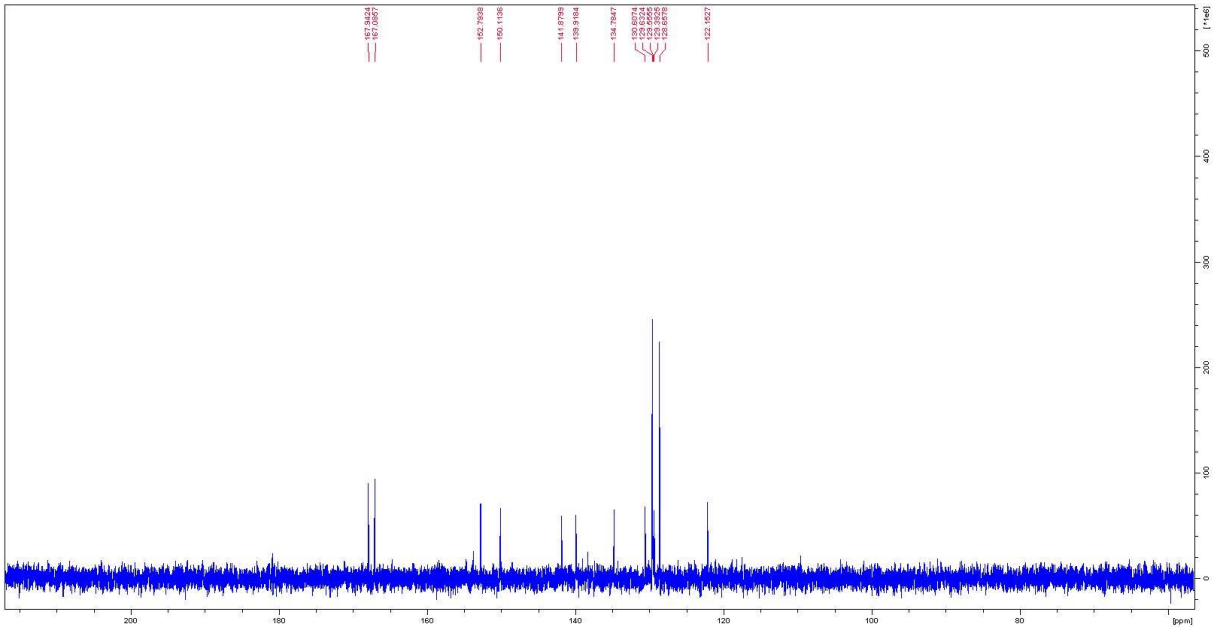

Figure 210. ^{13}C spectrum of 5,5‘-bis(4-carboxyphenyl)-[2,2‘-bipyridine]-6,6‘-dicarboxylic acid.

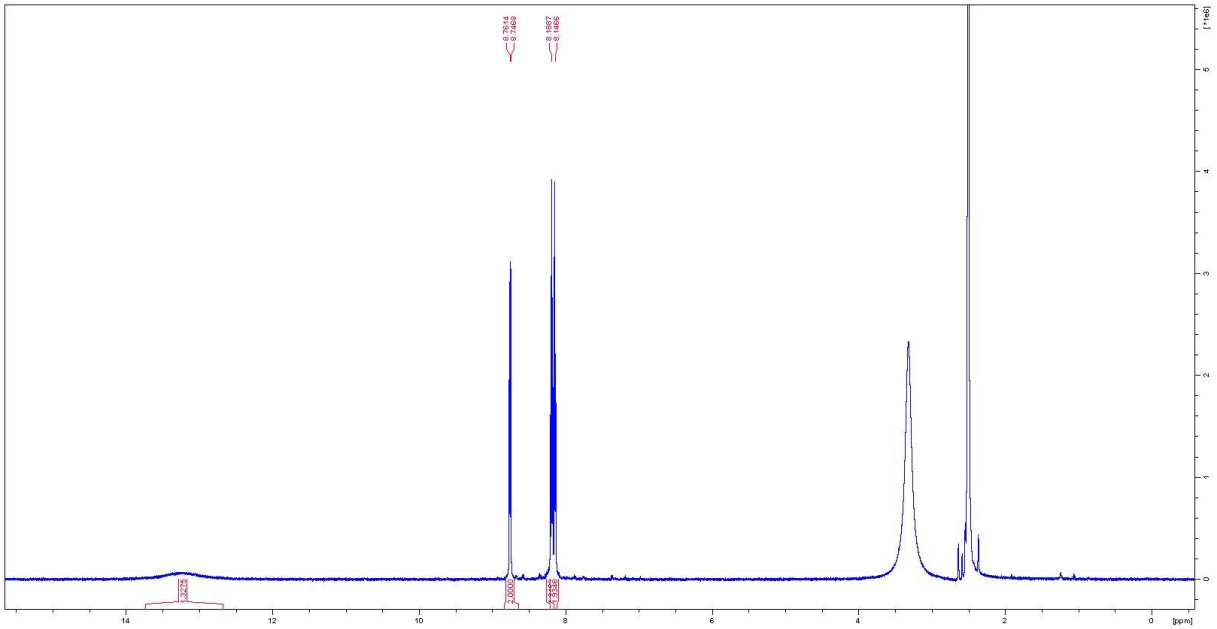

Figure 211. ^{1}H spectrum of [2,2'-bipyridine]-6,6'-dicarboxylic acid

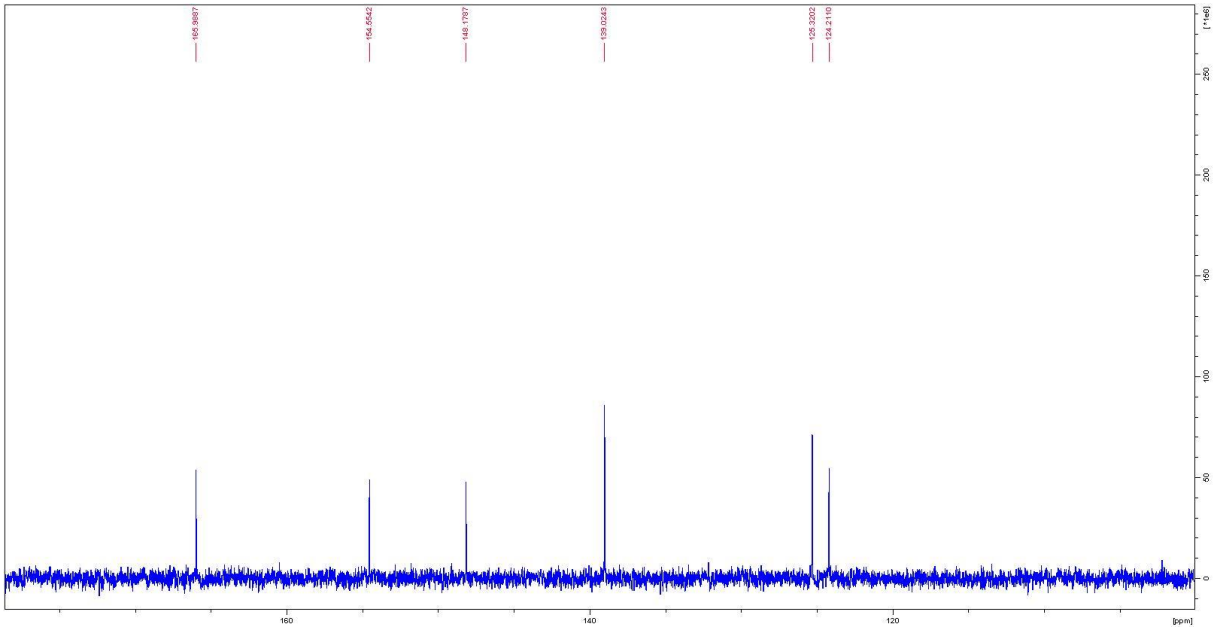

Figure 212. ^{13}C spectrum of [2,2'-bipyridine]-6,6'-dicarboxylic acid

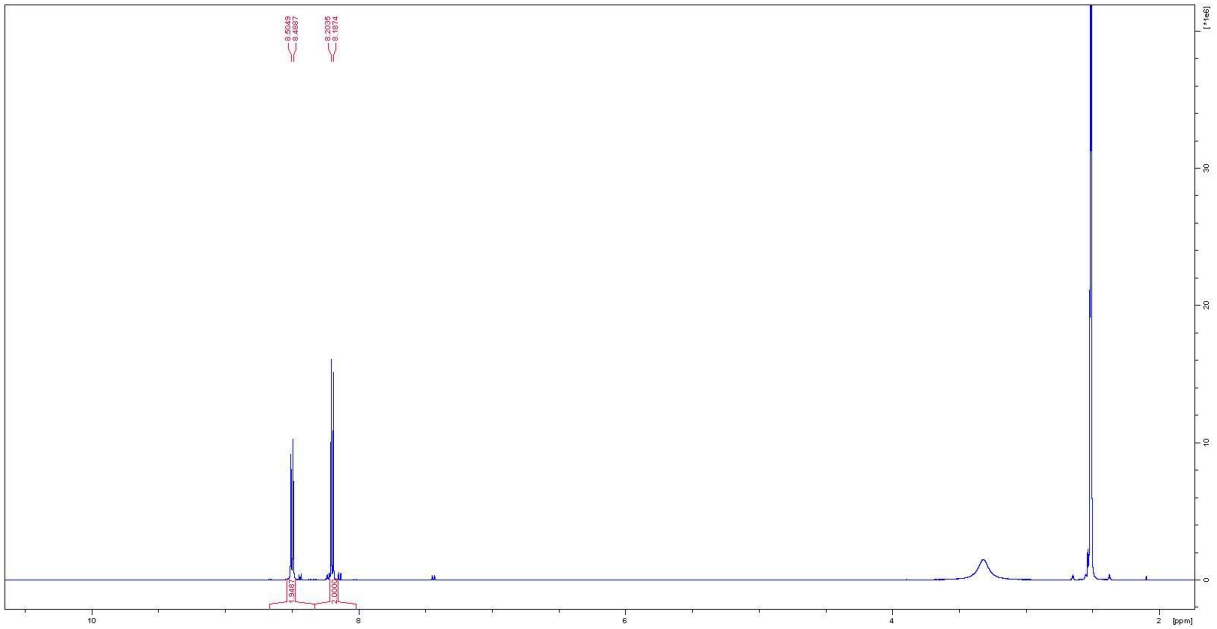

Figure 213. ^{1}H spectrum of 2,2'-bipyridine-3,3',6,6'-tetracarboxylic acid.

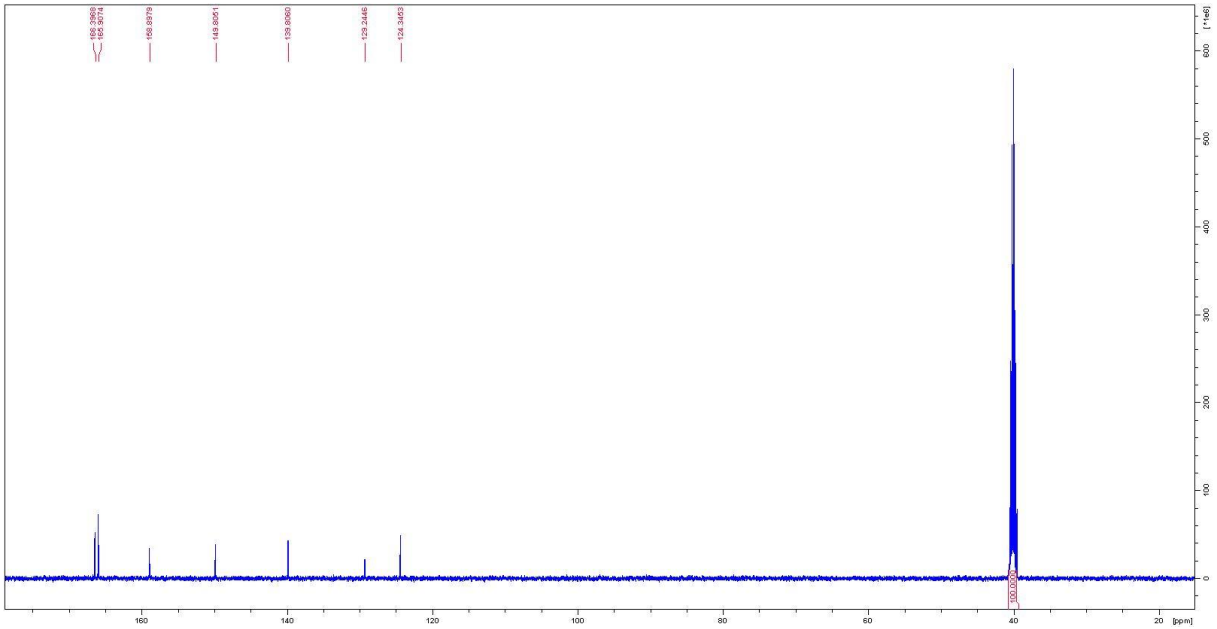

Figure 214. ^{13}C spectrum of 2,2'-bipyridine-3,3',6,6'-tetracarboxylic acid.

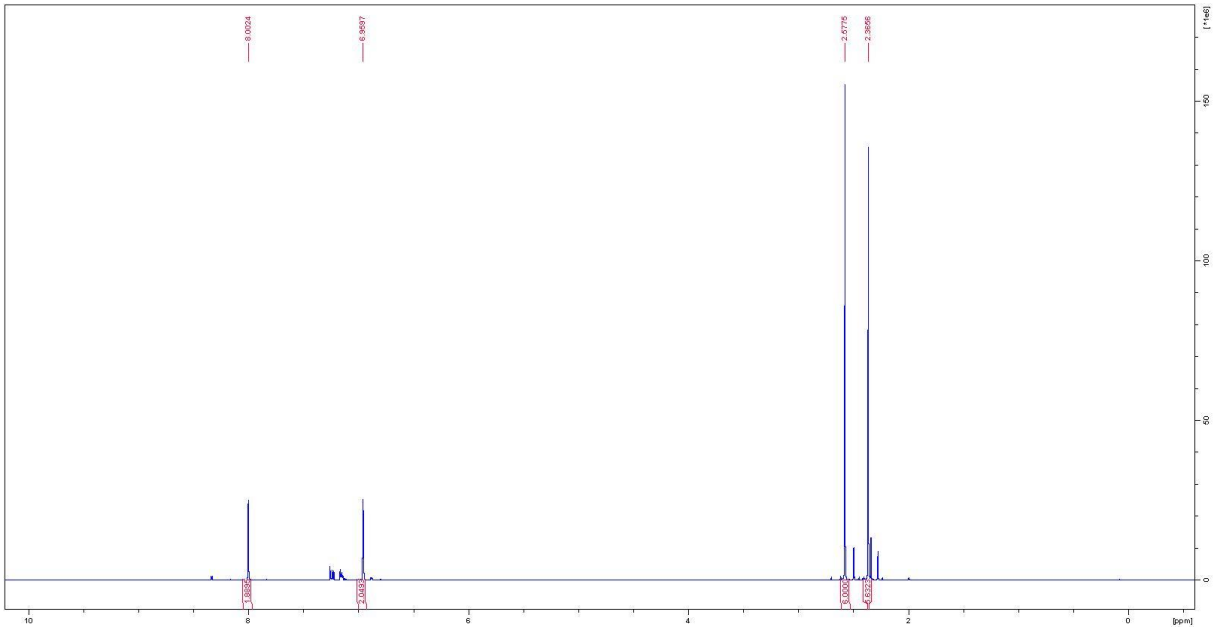

Figure 215. ^{1}H spectrum of 4,4',6,6'-tetramethyl-2,2'-bipyridine.

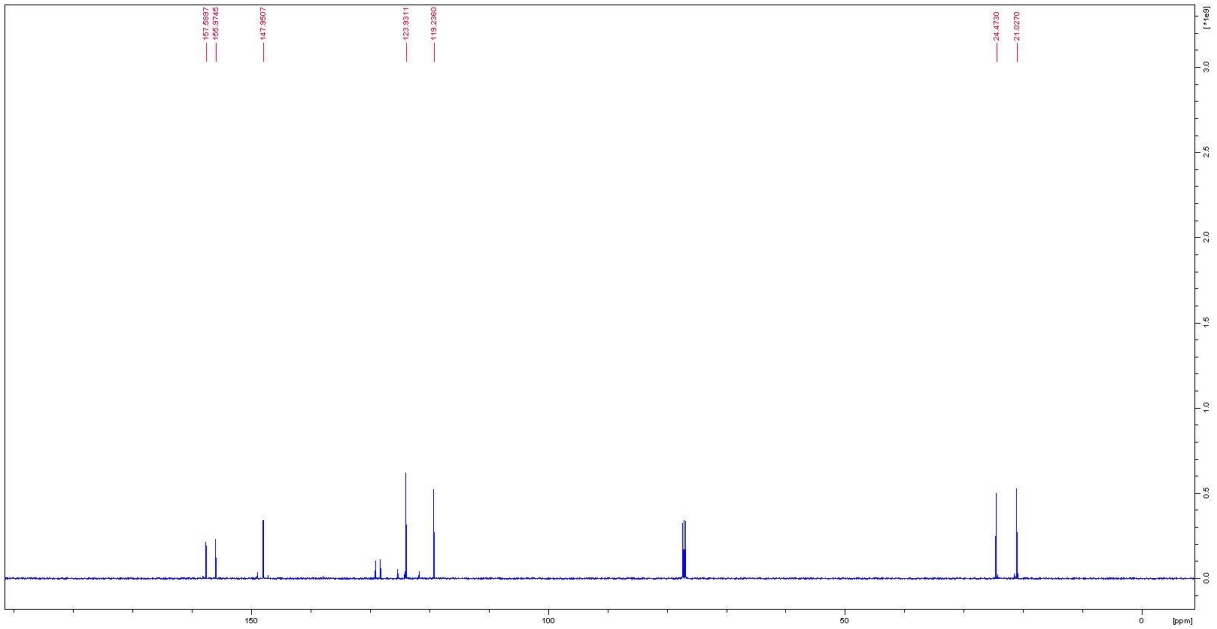

Figure 216. ^{13}C spectrum of 4,4',6,6'-tetramethyl-2,2'-bipyridine.

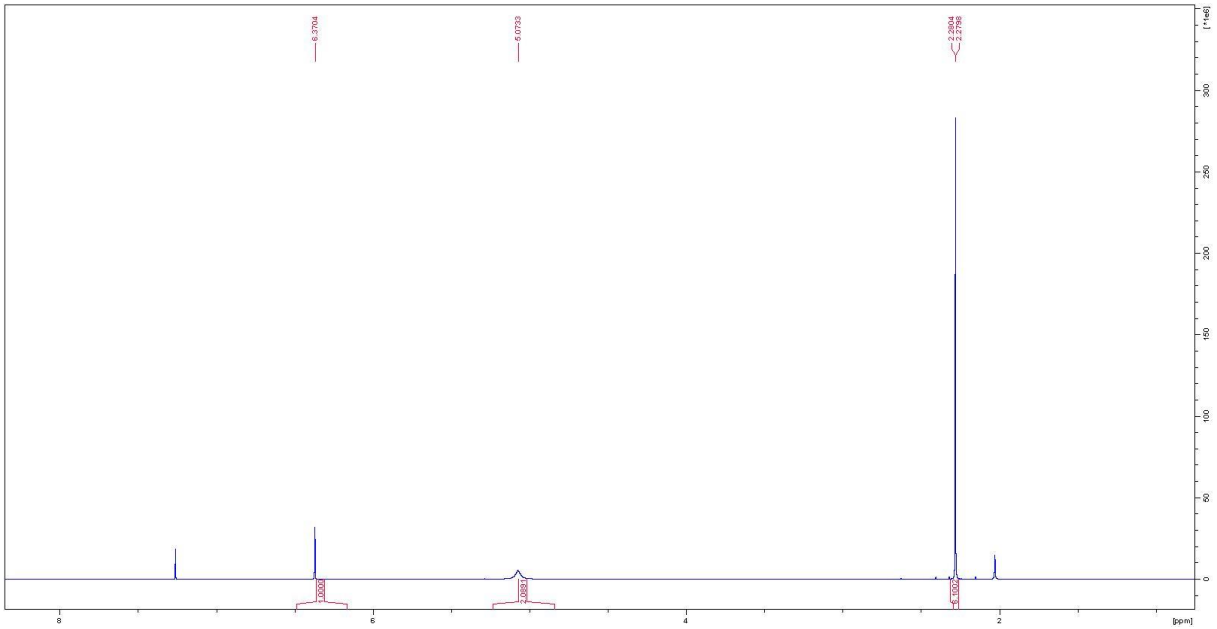

Figure 217. ^{1}H spectrum of 4,6-dimethylpyrimidin-2-amine.

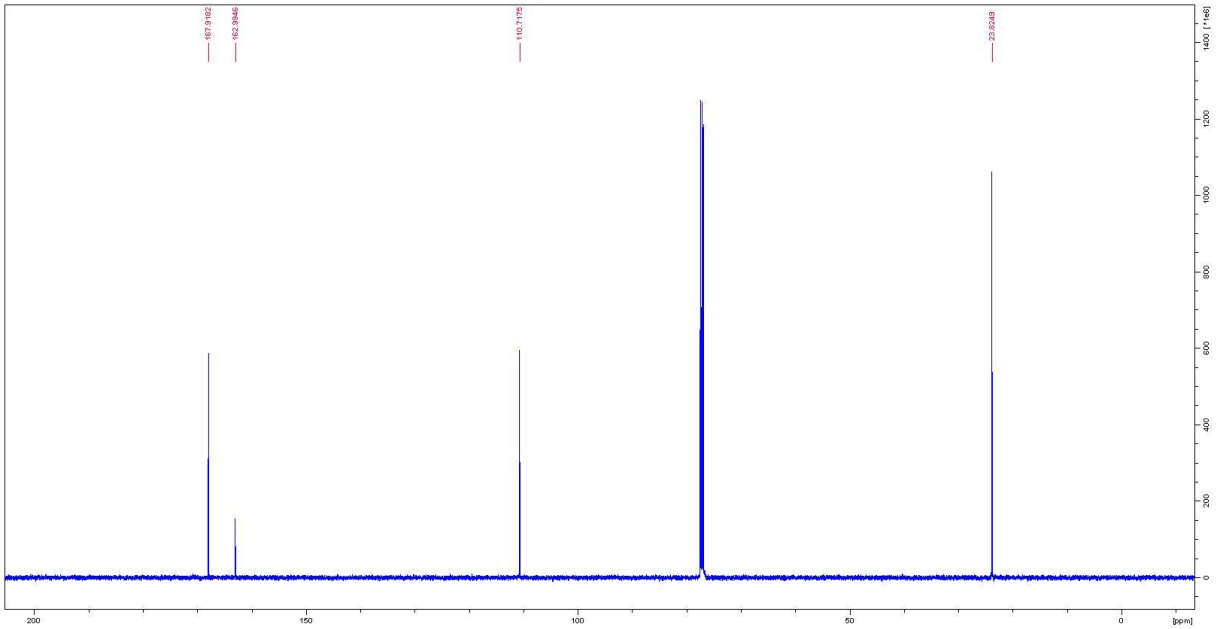

Figure 218. ^{13}C spectrum of 4,6-dimethylpyrimidin-2-amine.

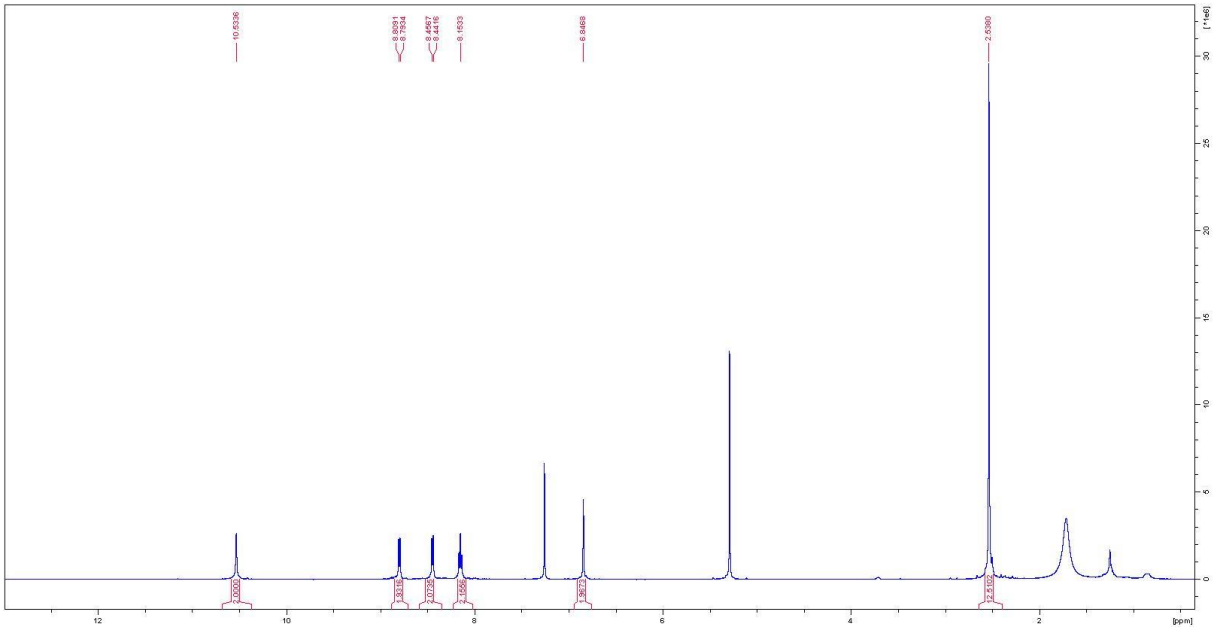

Figure 219. ^{1}H spectrum of N_6, N_6'-bis(4,6-dimethylpyrimidin-2-yl)-[2,2'-bipyridine]-6,6'-dicarboxamide.

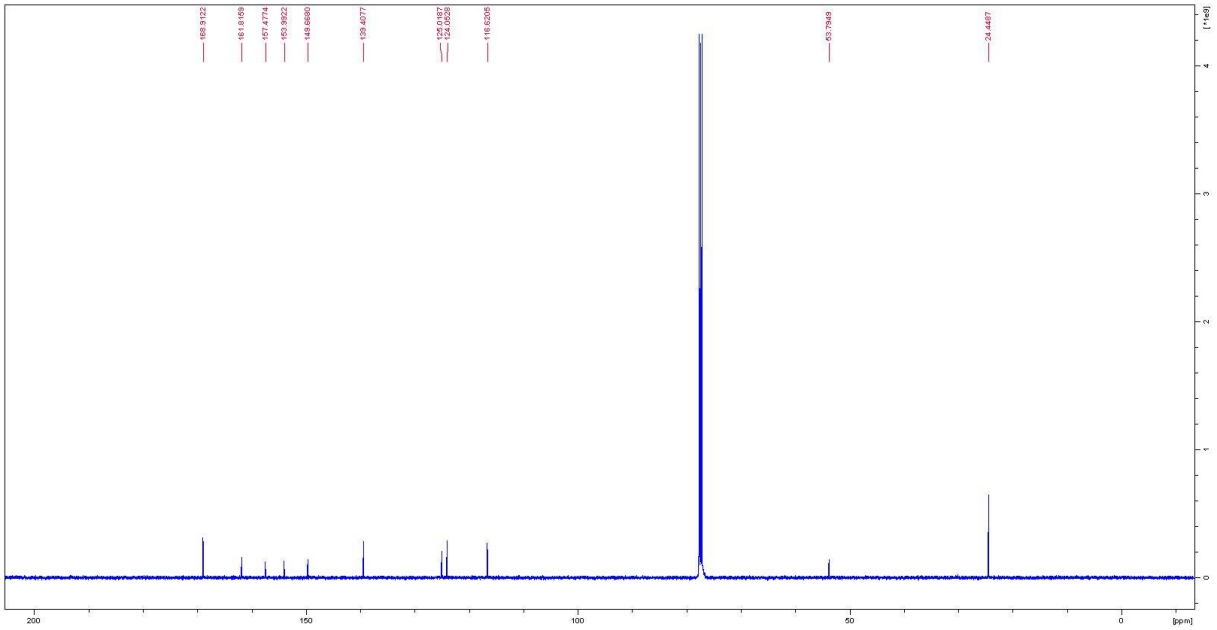

Figure 220. ^{13}C spectrum of N_6, N_6'-bis(4,6-dimethylpyrimidin-2-yl)-[2,2'-bipyridine]-6,6'-dicarboxamide.

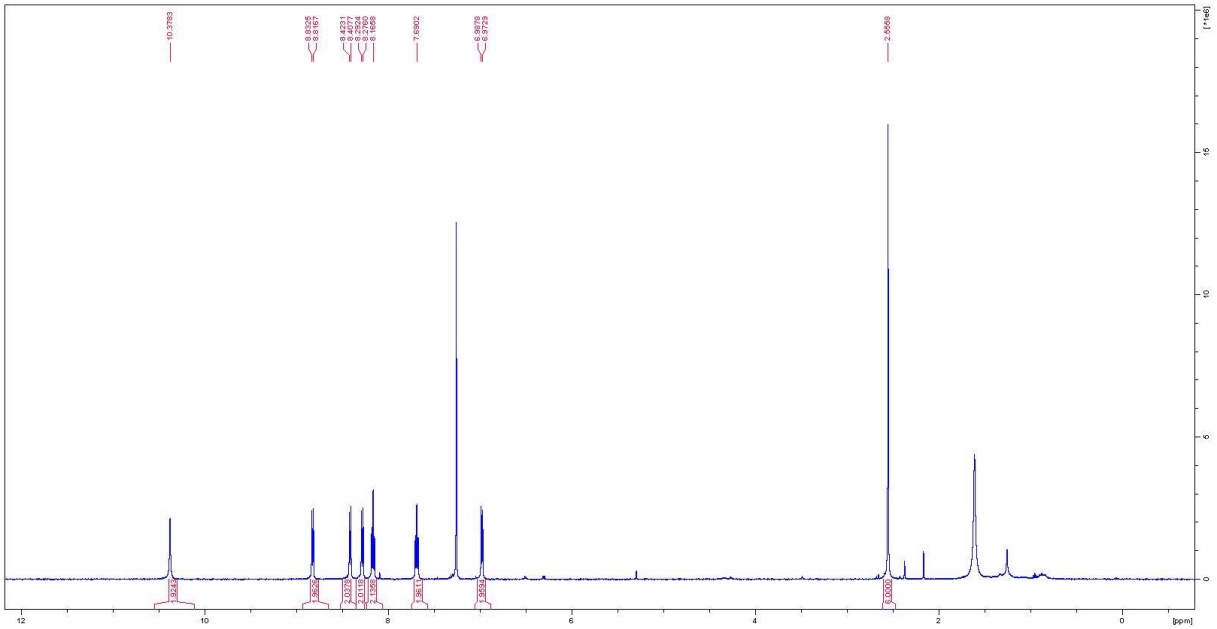

Figure 221. ^{1}H spectrum of N_6, N_6'-bis(6-methylpyridin-2-yl)-[2,2'-bipyridine]-6,6'-di-carboxamide.

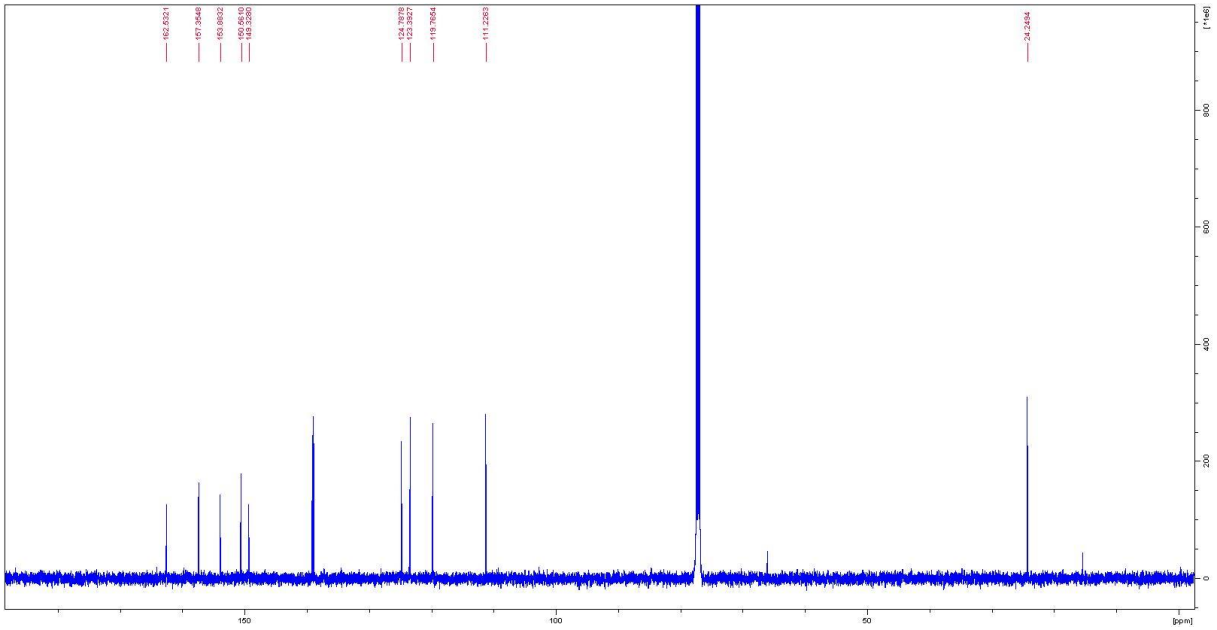

Figure 222. ^{13}C spectrum of N_6, N_6'-bis(6-methylpyridin-2-yl)-[2,2'-bipyridine]-6,6'-di-carboxamide.

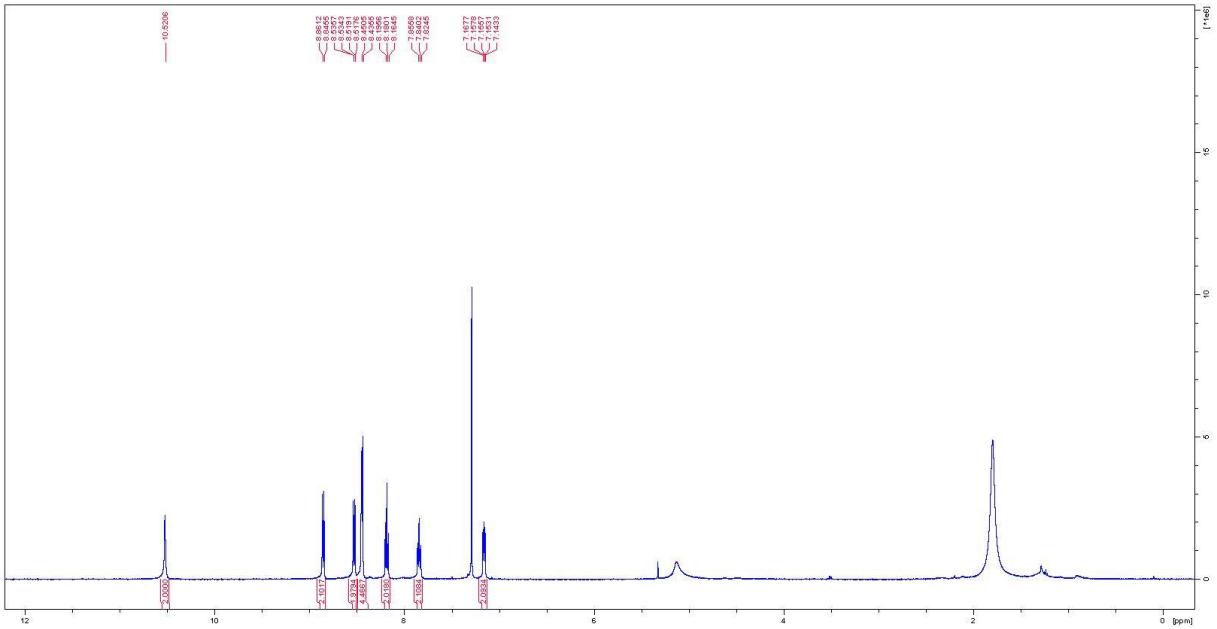

Figure 223. ^{1}H spectrum of N_6, N_6'-di(pyridin-2-yl)-[2,2'-bipyridine]-6,6'-dicarboxamide.

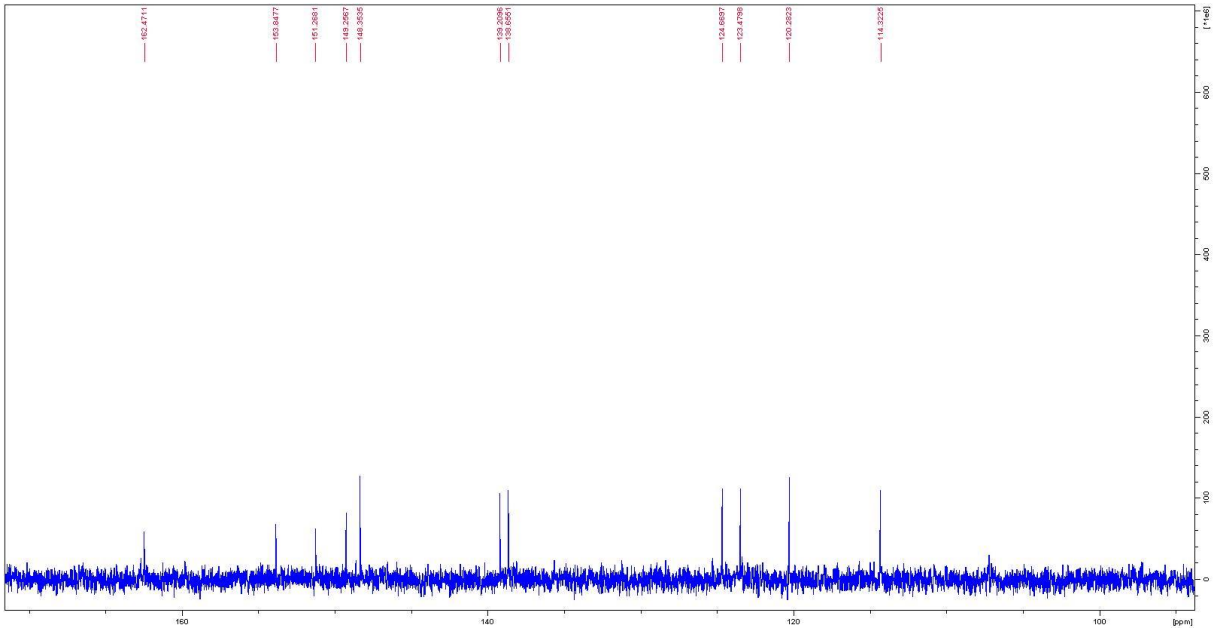

Figure 224. ^{1}H spectrum of N_6, N_6'-di(pyridin-2-yl)-[2,2'-bipyridine]-6,6'-dicarboxamide.

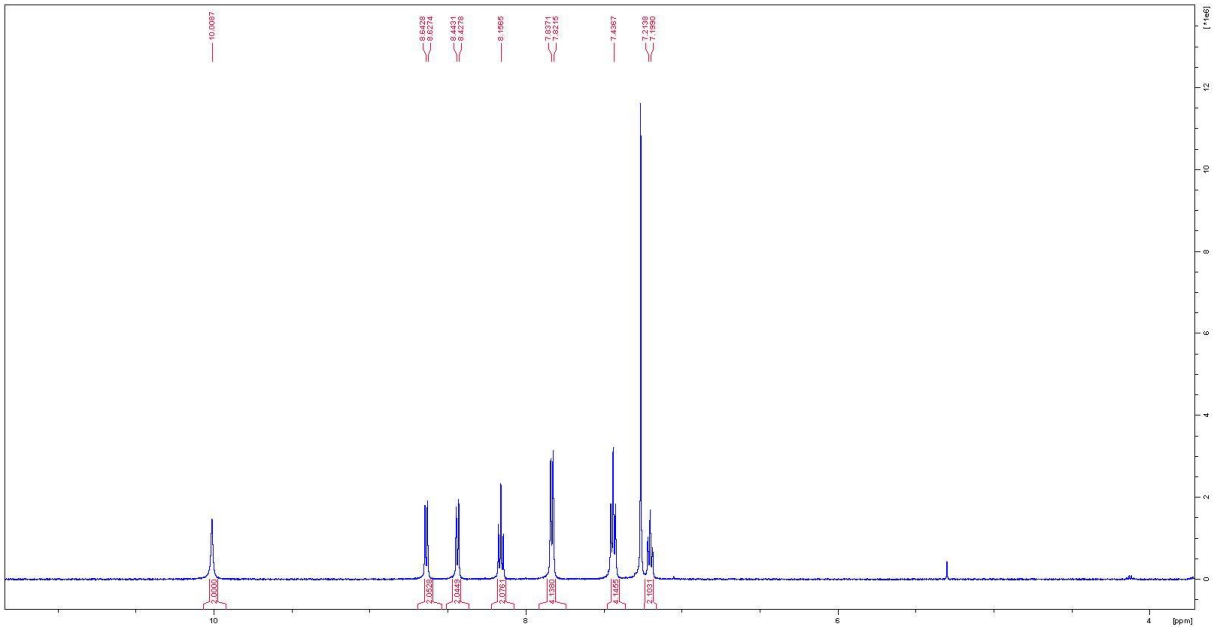

Figure 225. ^{1}H spectrum of N_6, N_6'-diphenyl-[2,2'-bipyridine]-6,6'-dicarboxamide.

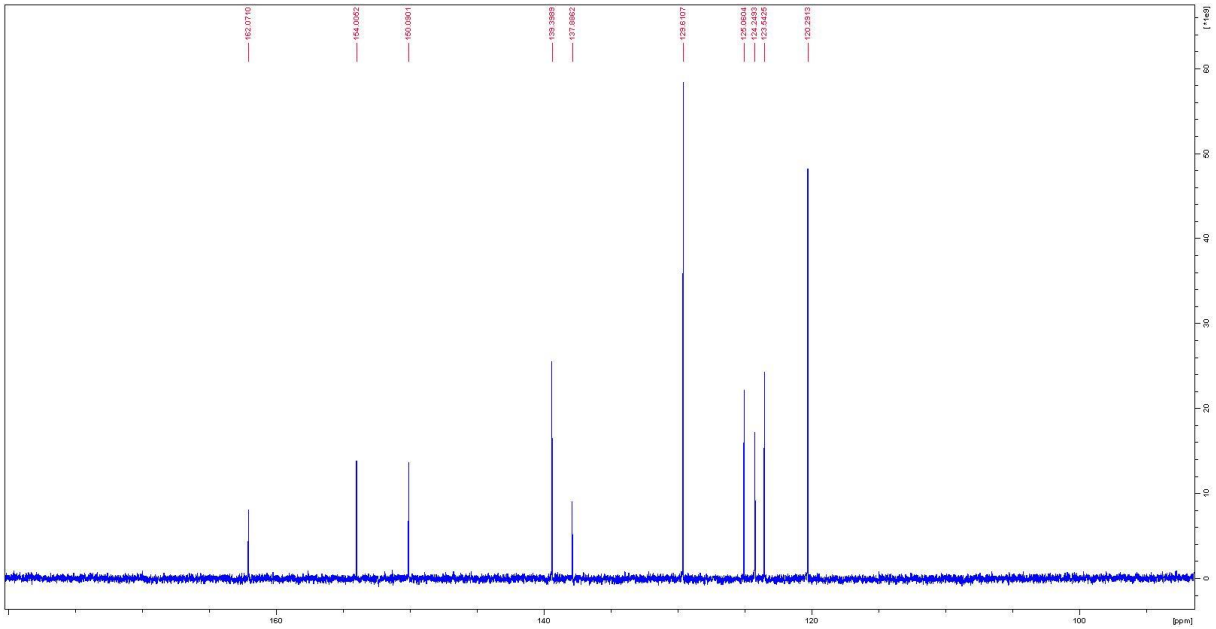

Figure 226. ^{13}C spectrum of N_6, N_6'-diphenyl-[2,2'-bipyridine]-6,6'-dicarboxamide.

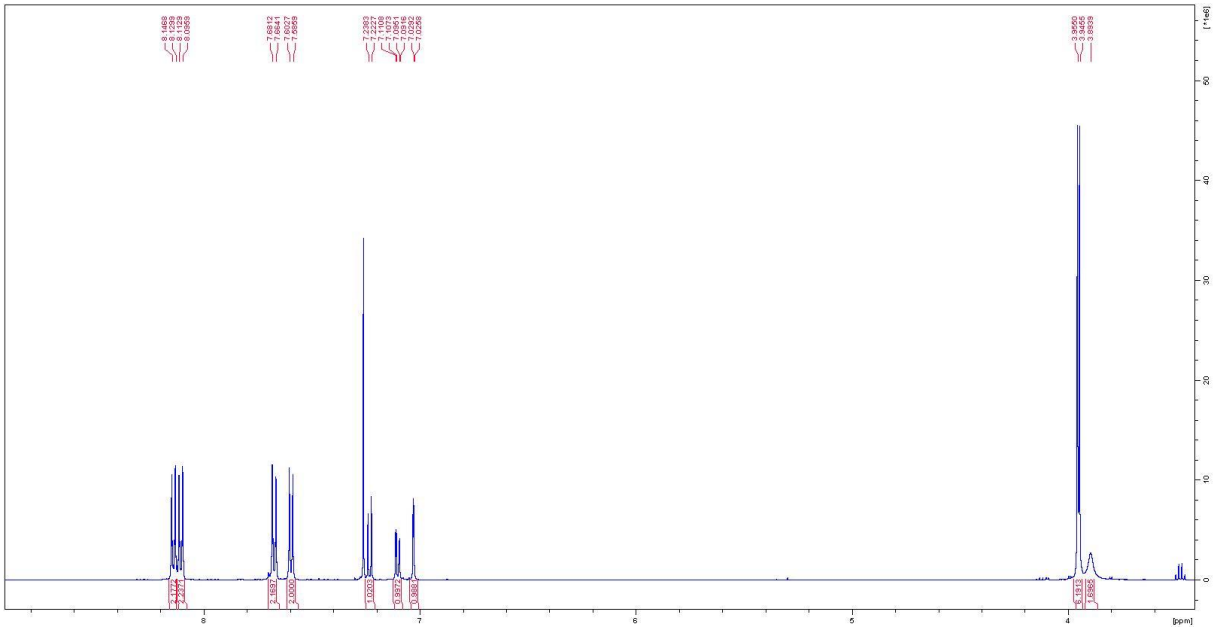

Figure 227. ^{1}H spectrum of dimethyl 2'-amino-[1,1'-4',1"-terphenyl]-4,4"-dicarboxylate.

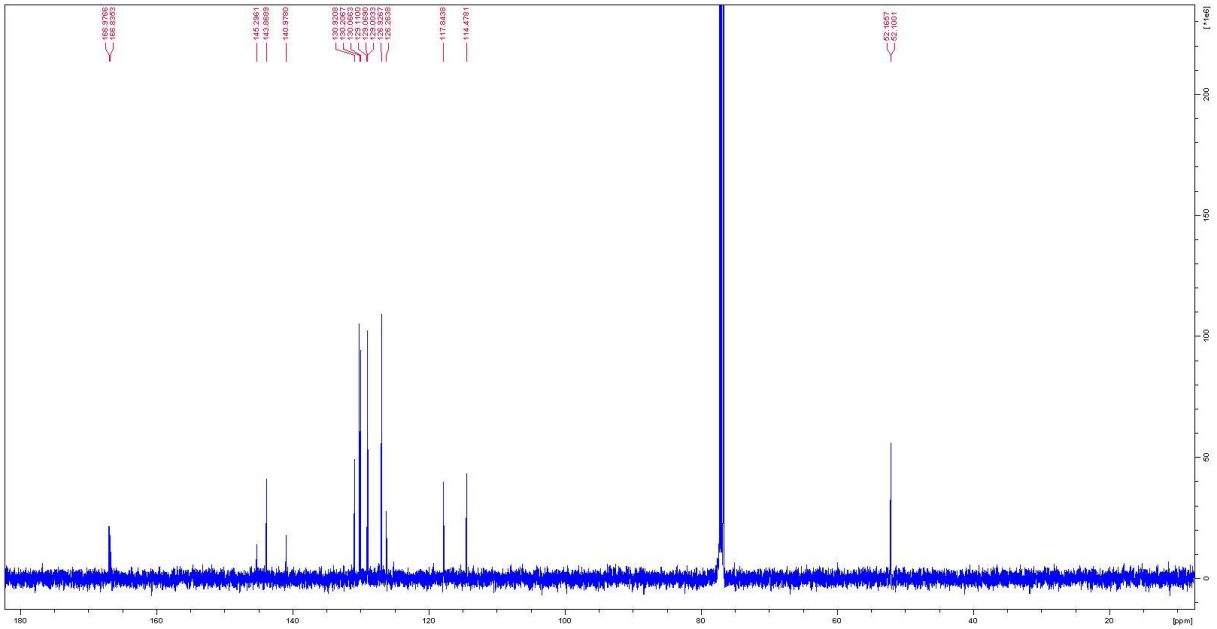

Figure 228. ^{13}C spectrum of dimethyl 2'-amino-[1,1'-4',1"-terphenyl]-4,4"-dicarboxylate.

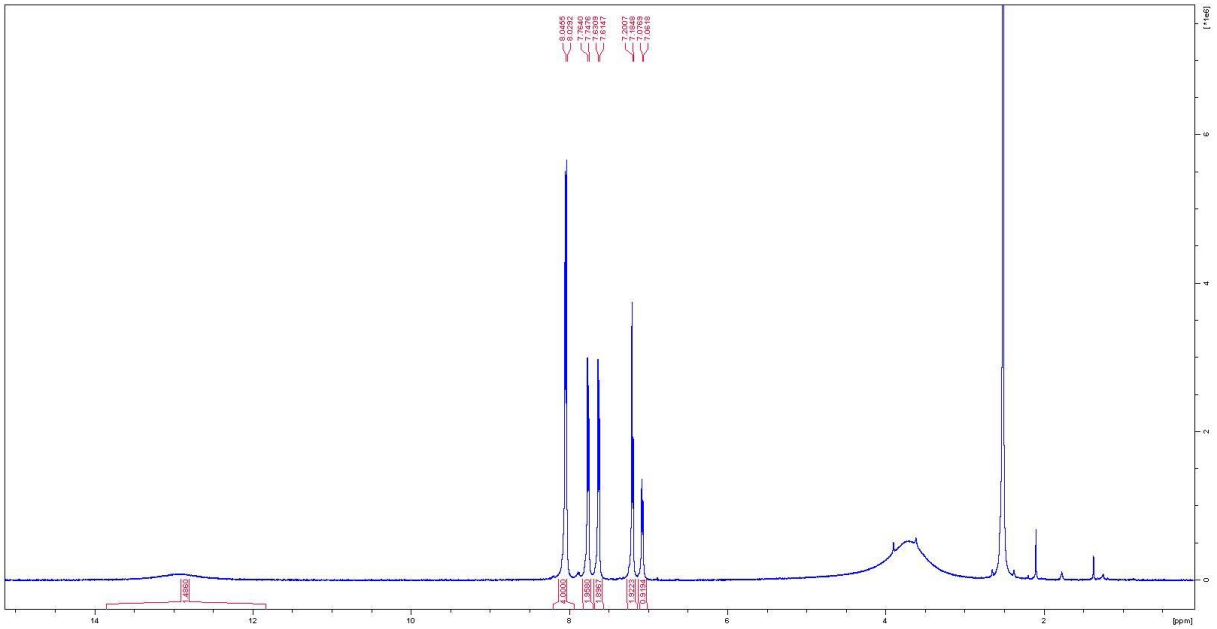

Figure 229. ^{1}H spectrum of 2'-amino-[1,1':4',1"-terphenyl]-4,4"-dicarboxylic acid

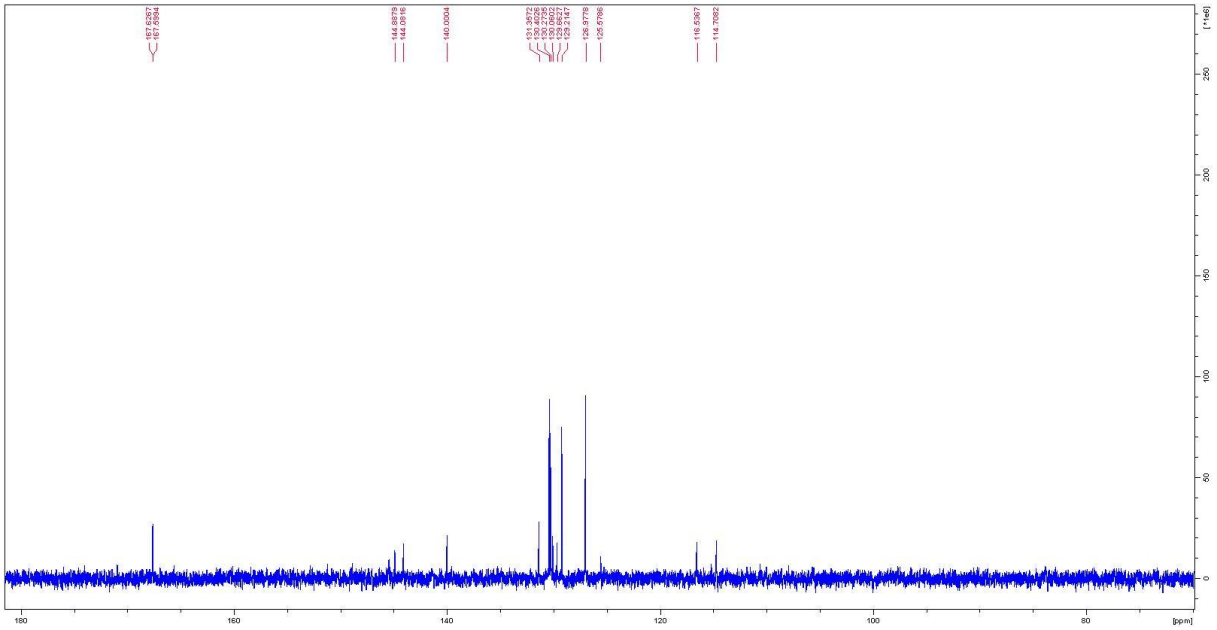

Figure 230. ^{13}C spectrum of 2'-amino-[1,1':4',1"-terphenyl]-4,4"-dicarboxylic acid

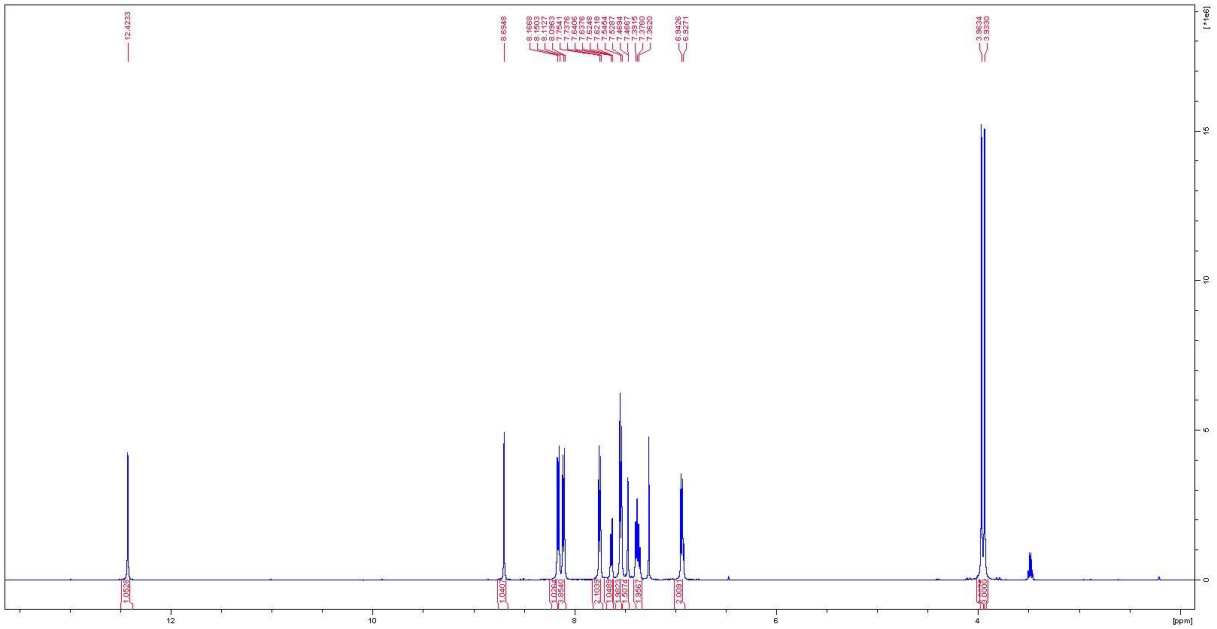

Figure 231. ^{1}H spectrum of dimethyl-2'-((2-hydroxybenzylidene)amino)-[1,1':4',1''-terphenyl]-4,4''-dicarboxylate.

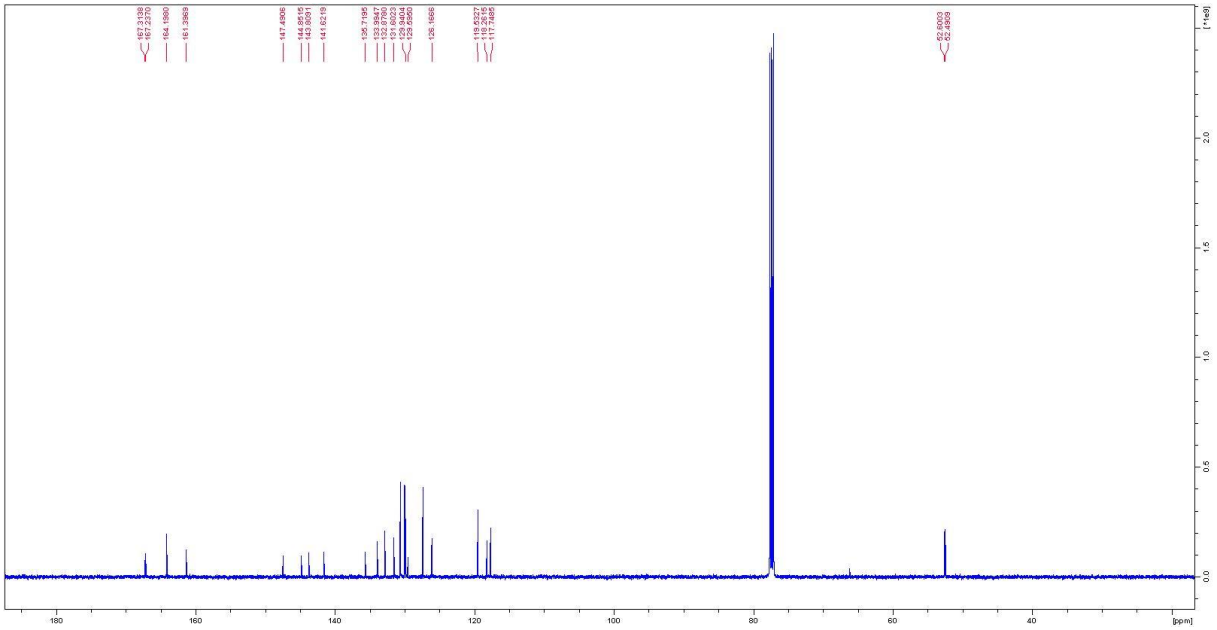

Figure 232. ^{13}C spectrum of dimethyl-2'-((2-hydroxybenzylidene)amino)-[1,1':4',1''-terphenyl]-4,4''-dicarboxylate.

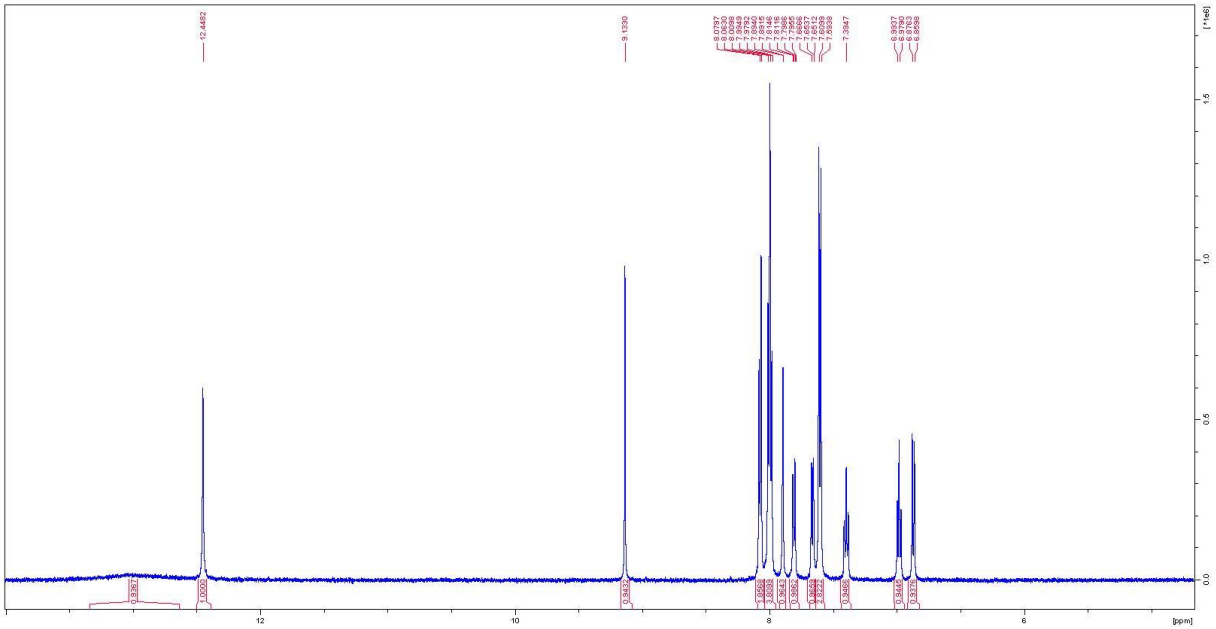

Figure 233. ^{1}H spectrum of 2'-((2-hydroxybenzylidene)amino)-[1,1':4',1"-terphenyl]-4,4"-di-carboxylic acid.

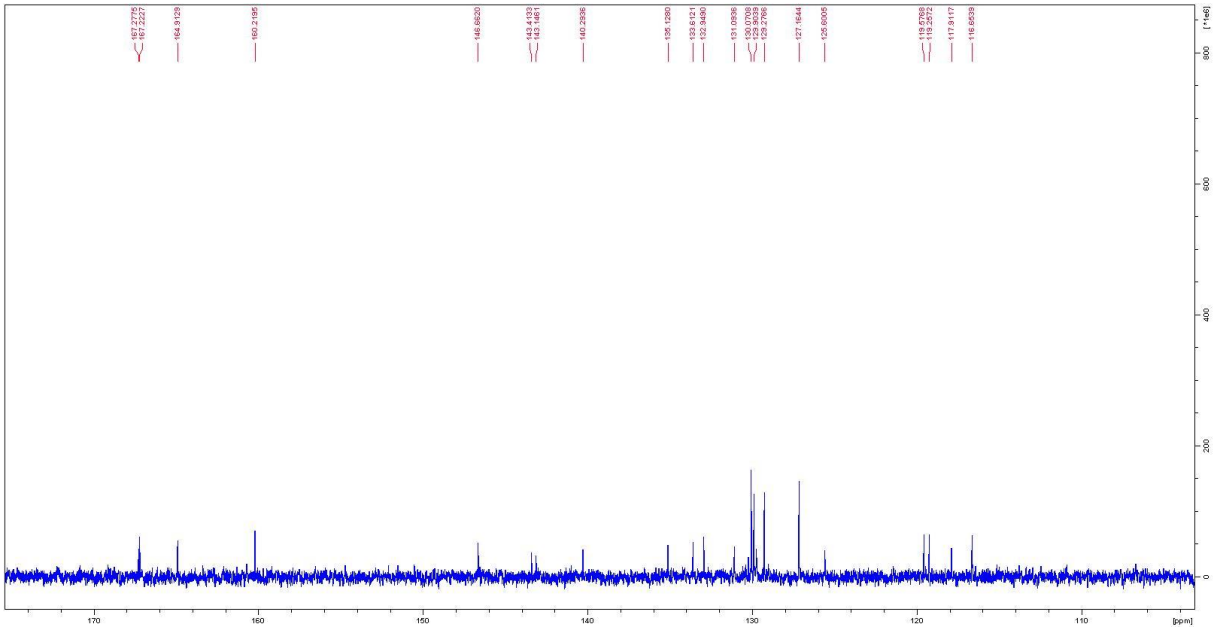

Figure 234. ^{13}C spectrum of 2'-((2-hydroxybenzylidene)amino)-[1,1':4',1"-terphenyl]-4,4"-di-carboxylic acid.

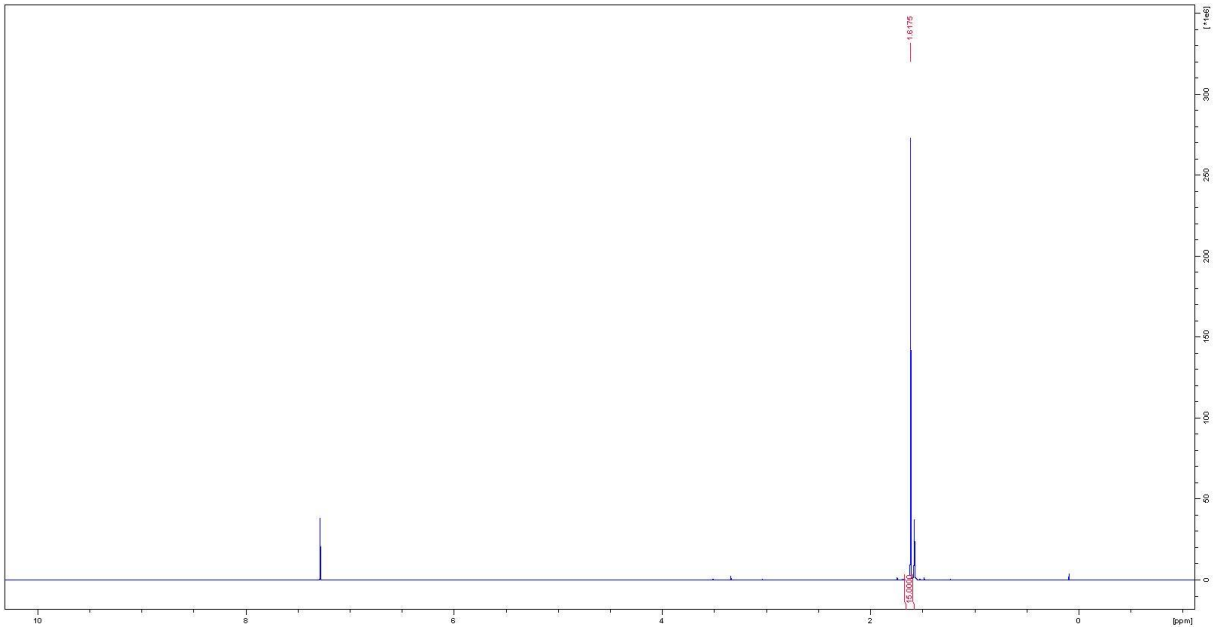

Figure 235. ^{1}H spectrum of pentamethylcyclopentadienyl iridium dichloride dimer.

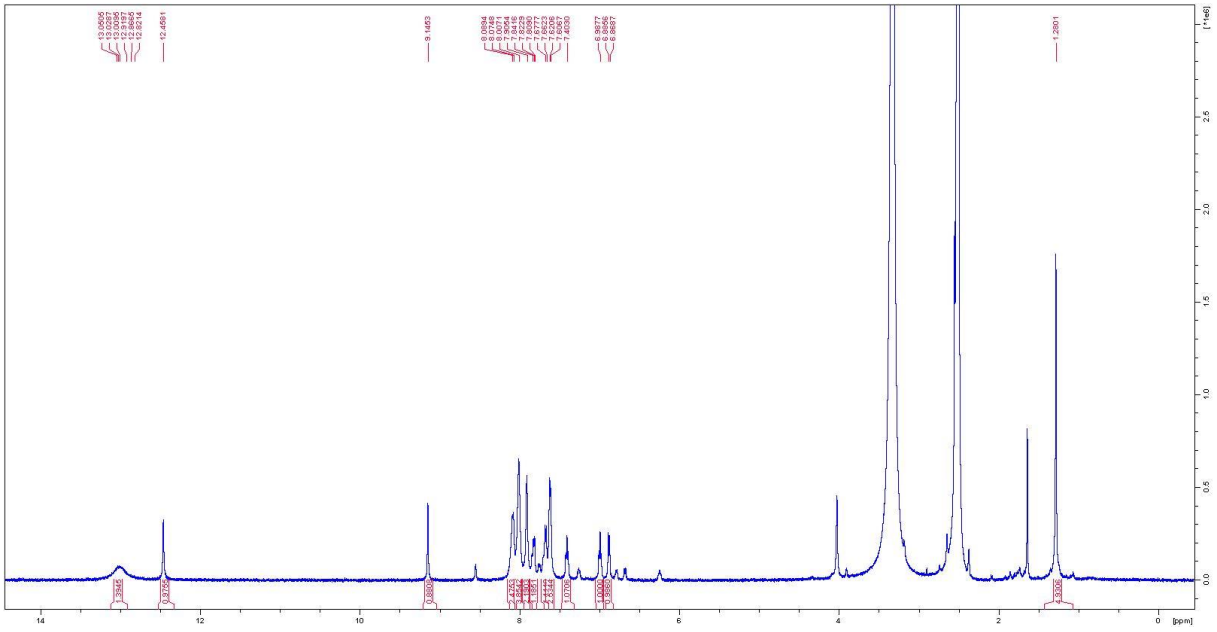

Figure 236. ^{1}H spectrum of sal(IrCp*Cl).

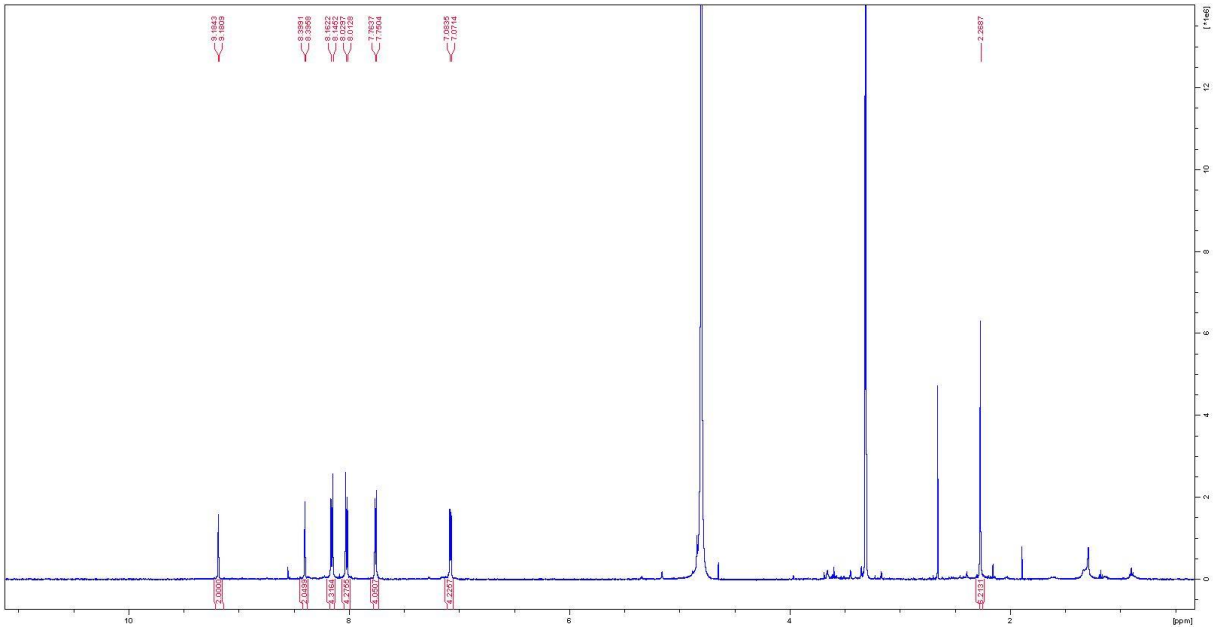

Figure 237. ^{1}H spectrum of K1.

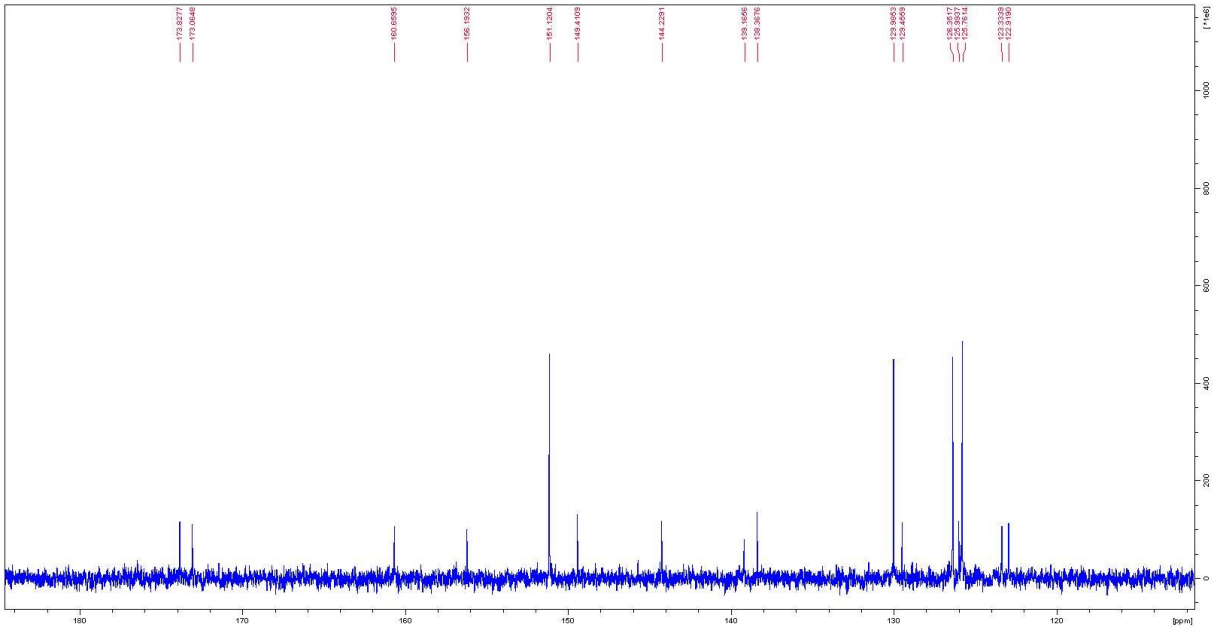

Figure 238. ^{13}C spectrum of K1.

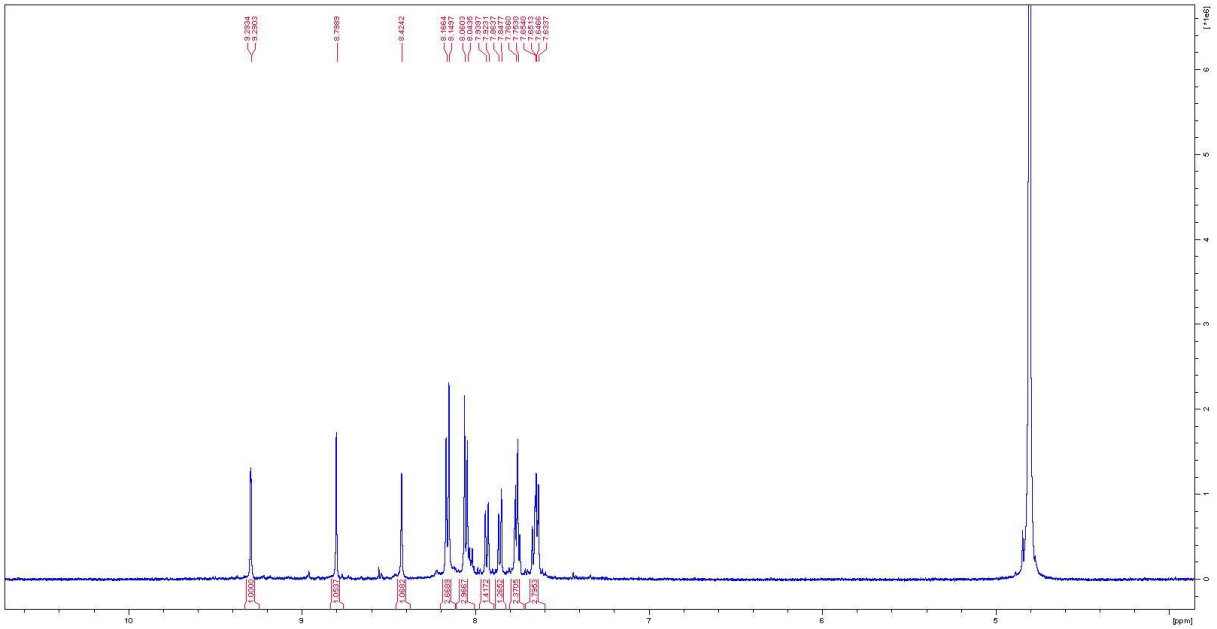

Figure 239. ^{1}H spectrum of K2.

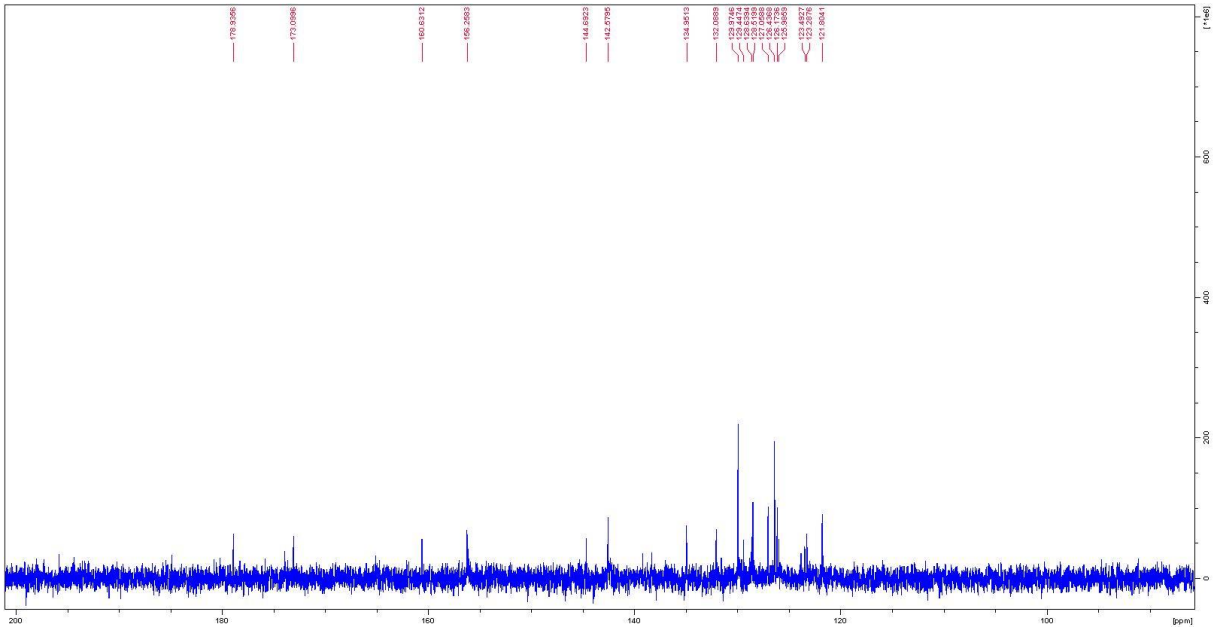

Figure 240. ^{13}C spectrum of K2.

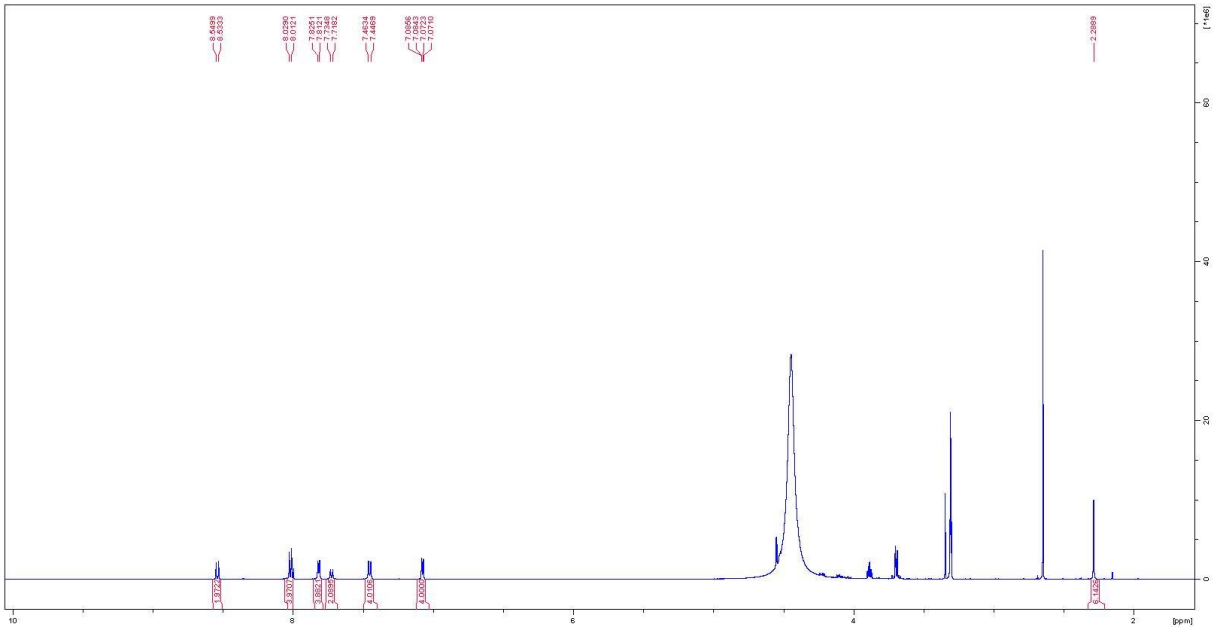

Figure 241. ^{1}H spectrum of K4.

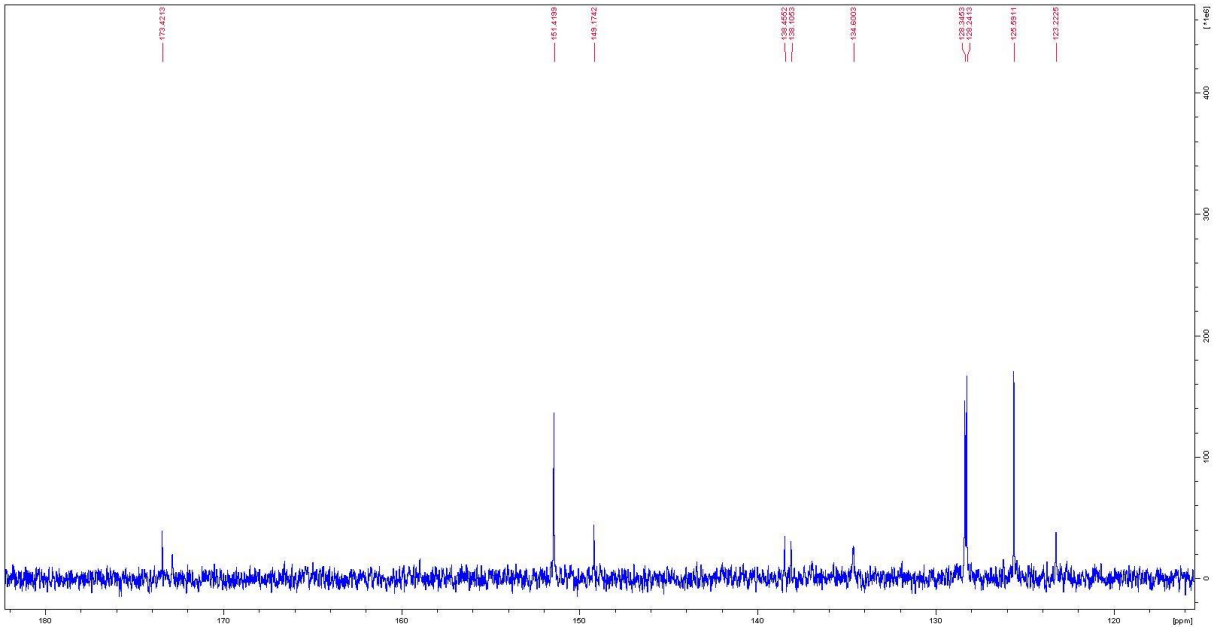

Figure 242. ^{13}C spectrum of K4.

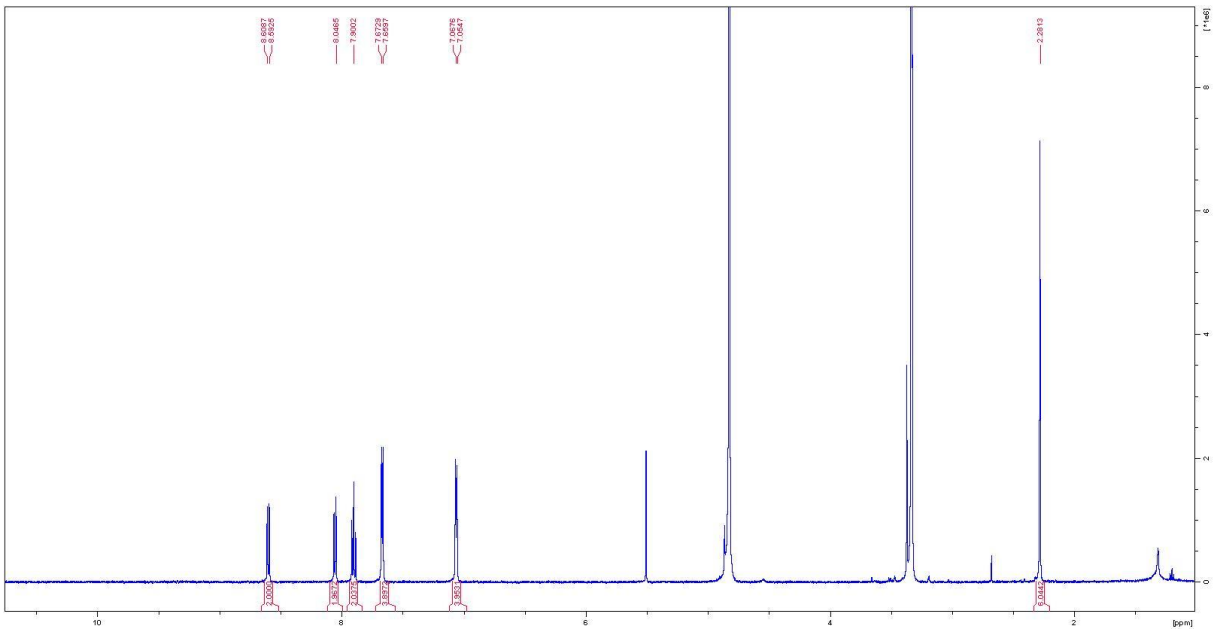

Figure 243. ^{1}H spectrum of K7.

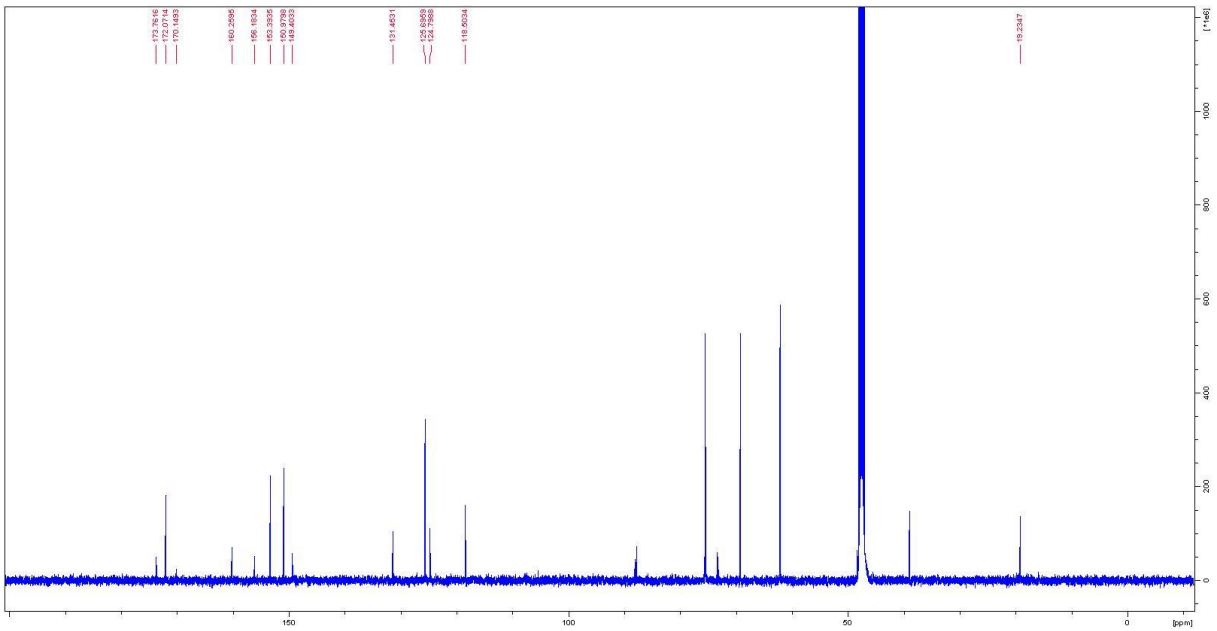

Figure 244. ^{13}C spectrum of K7.

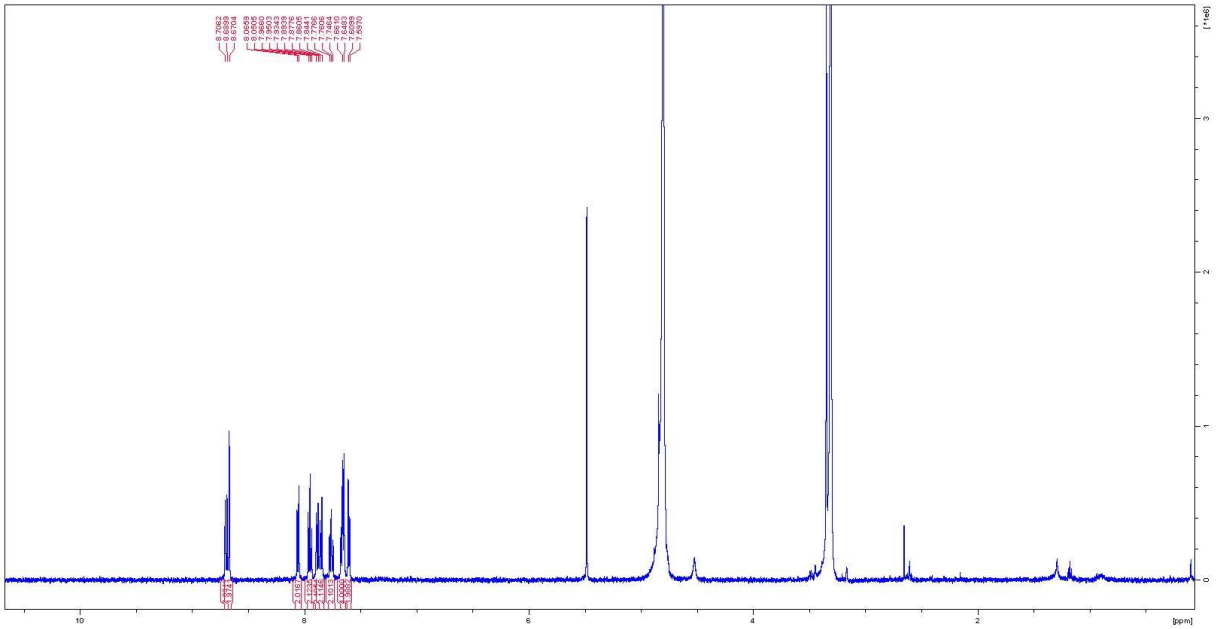

Figure 245. ^{1}H spectrum of K8.

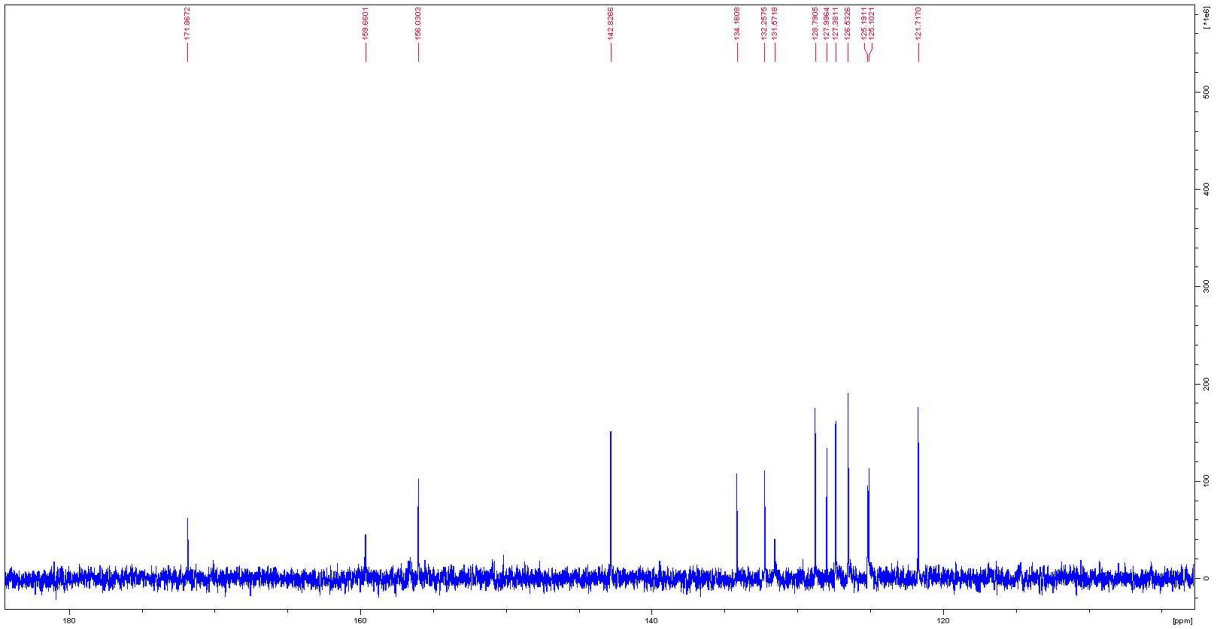

Figure 246. ^{13}C spectrum of K8.

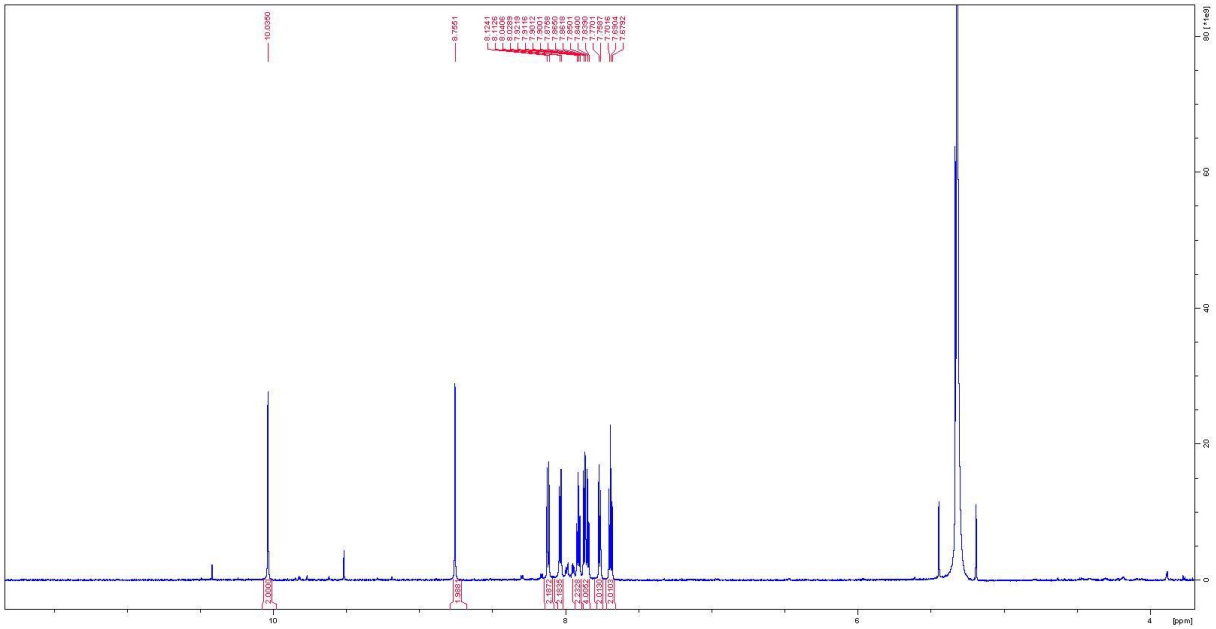

Figure 247. ^{1}H spectrum of K9.

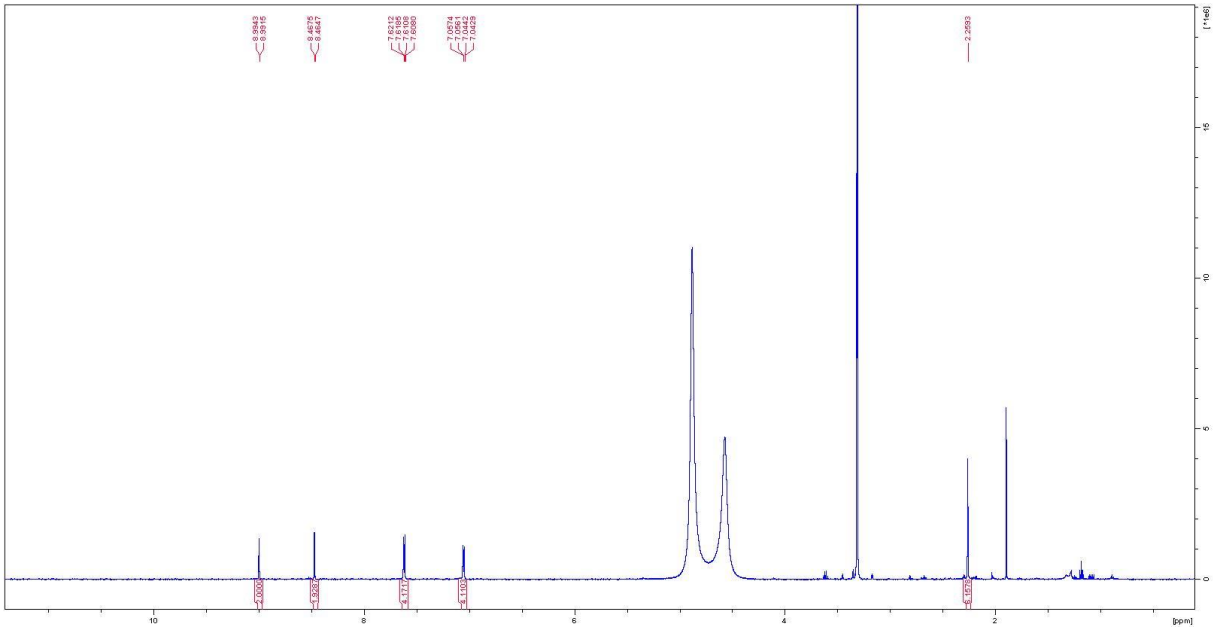

Figure 248. ^{1}H spectrum of K10.

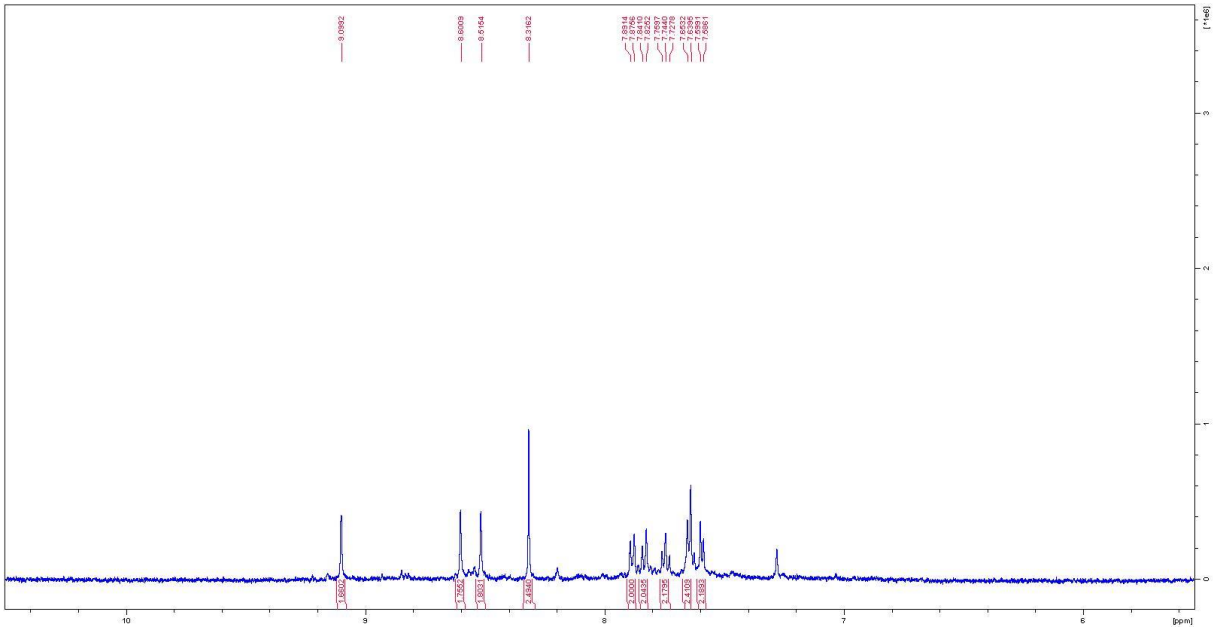

Figure 249. ^{1}H spectrum of K11.

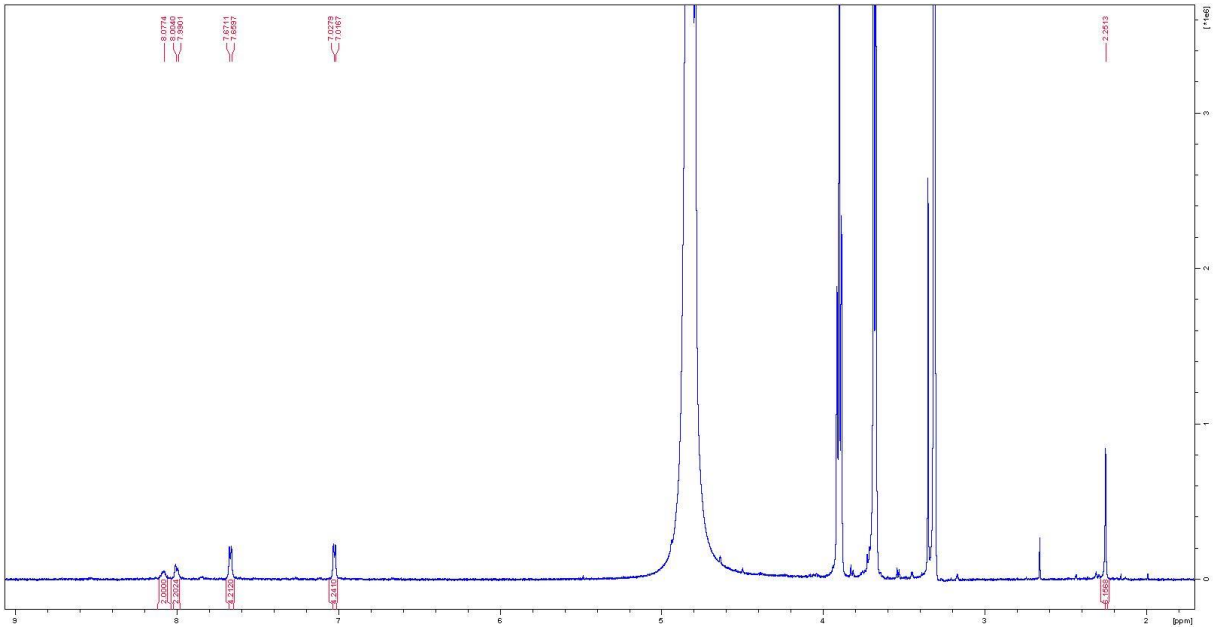

Figure 250. ^{1}H spectrum of K12.

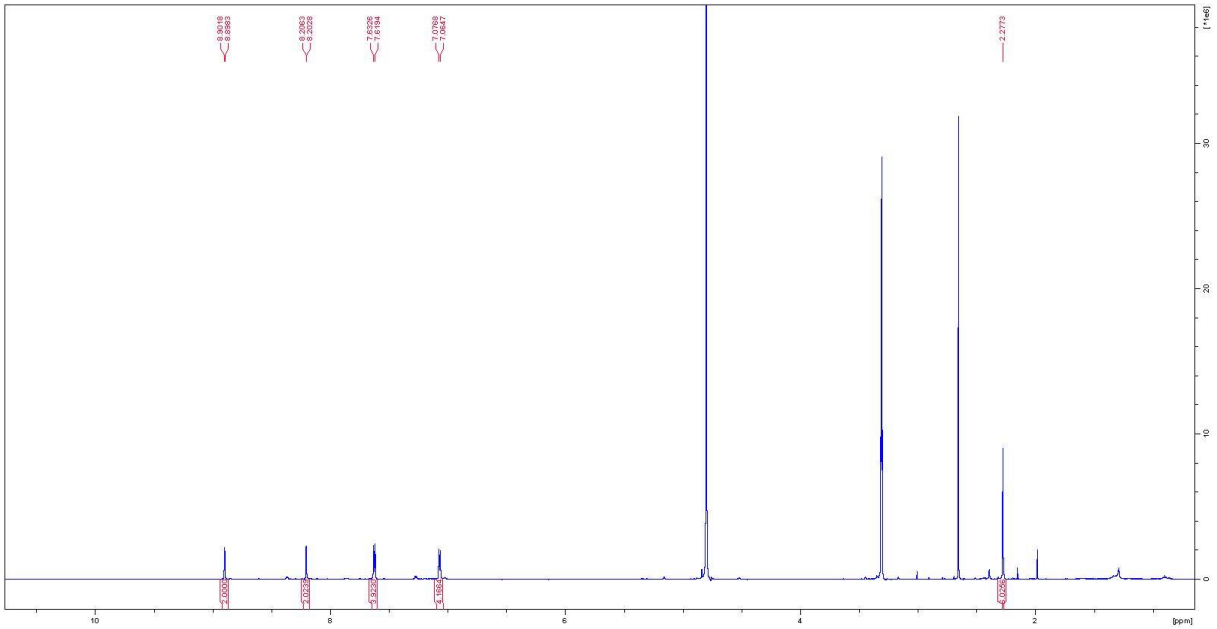

Figure 251. ^{1}H spectrum of K14.

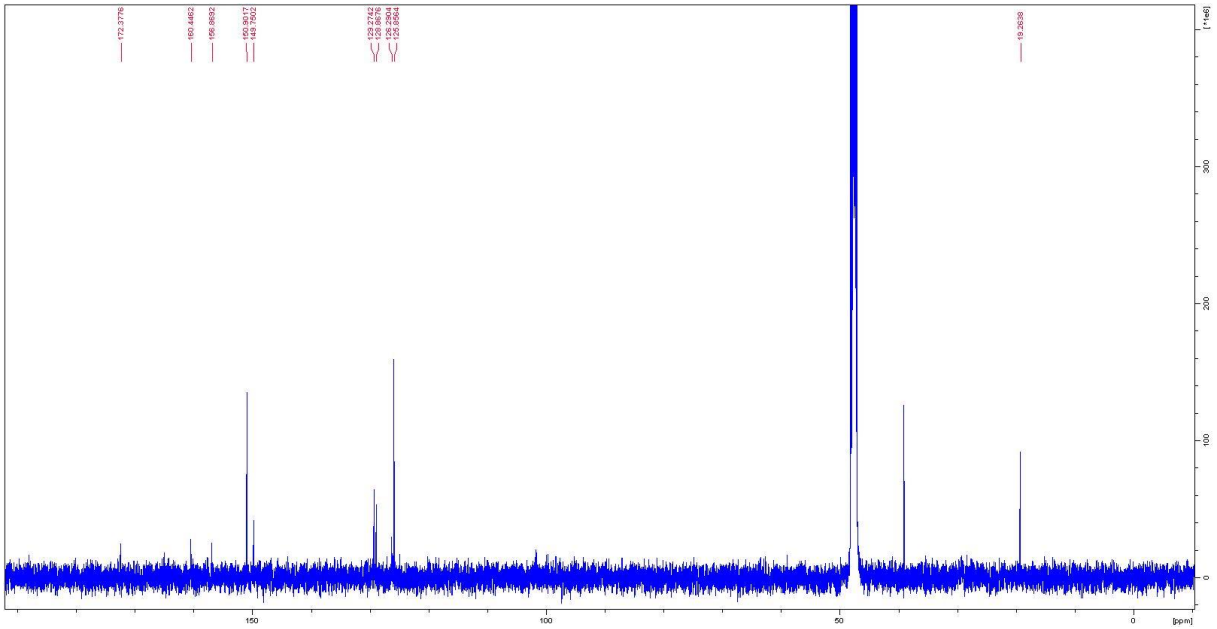

Figure 252. ^{13}C spectrum of K14.

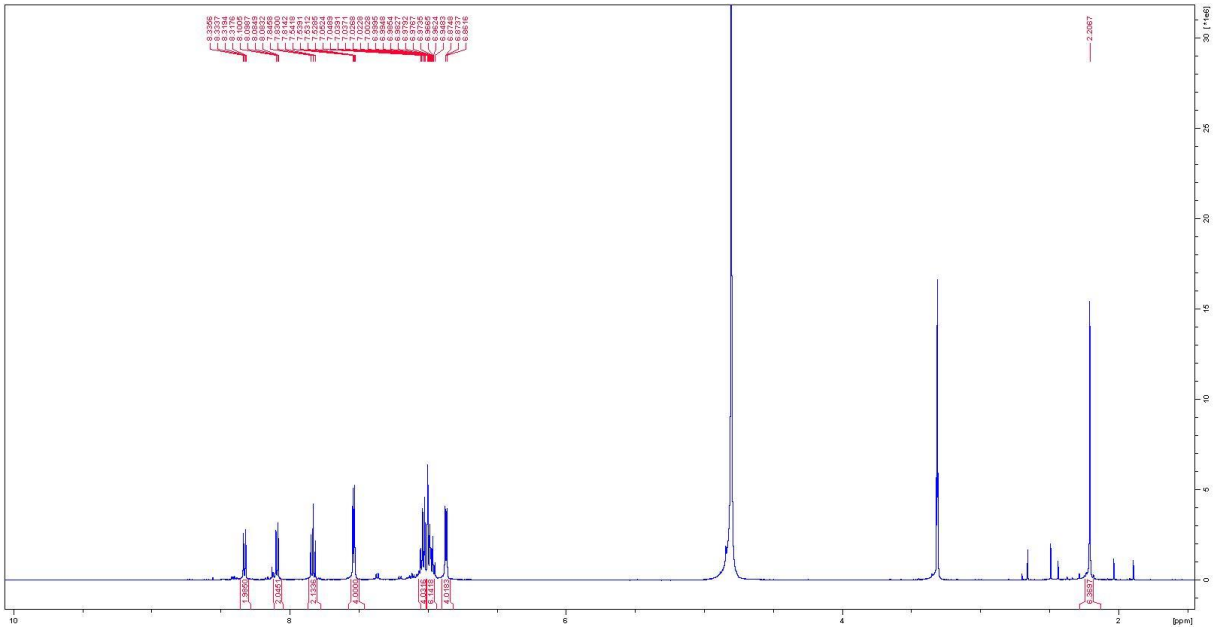

Figure 253. ^{1}H spectrum of K16.

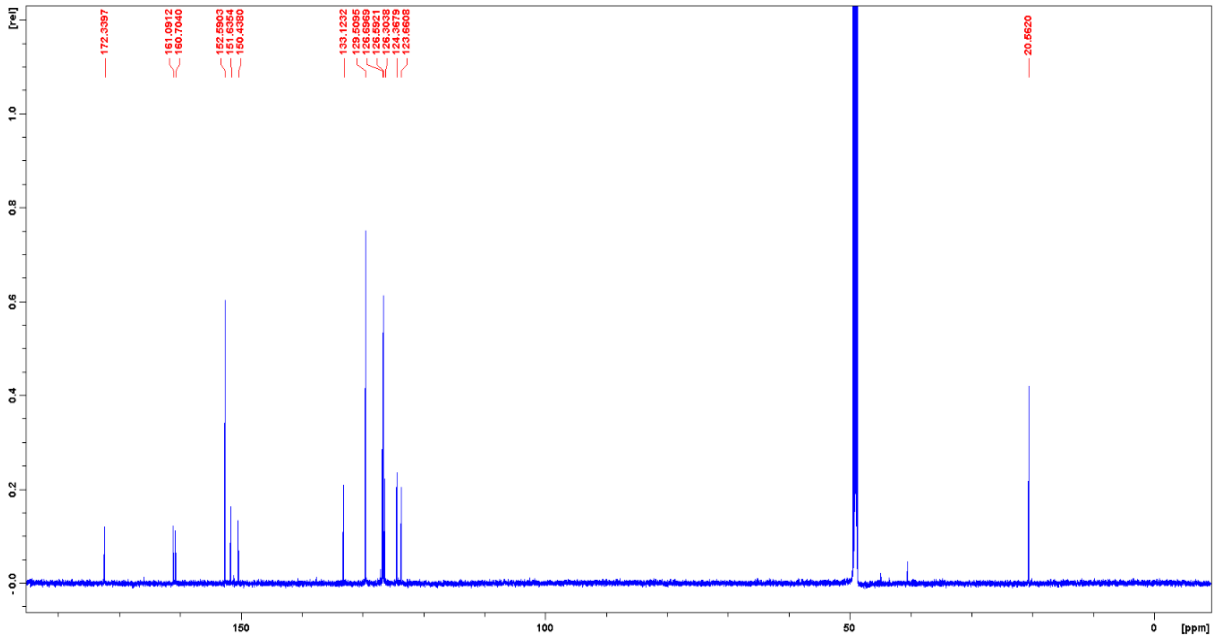

Figure 254. ^{13}C spectrum of K16.

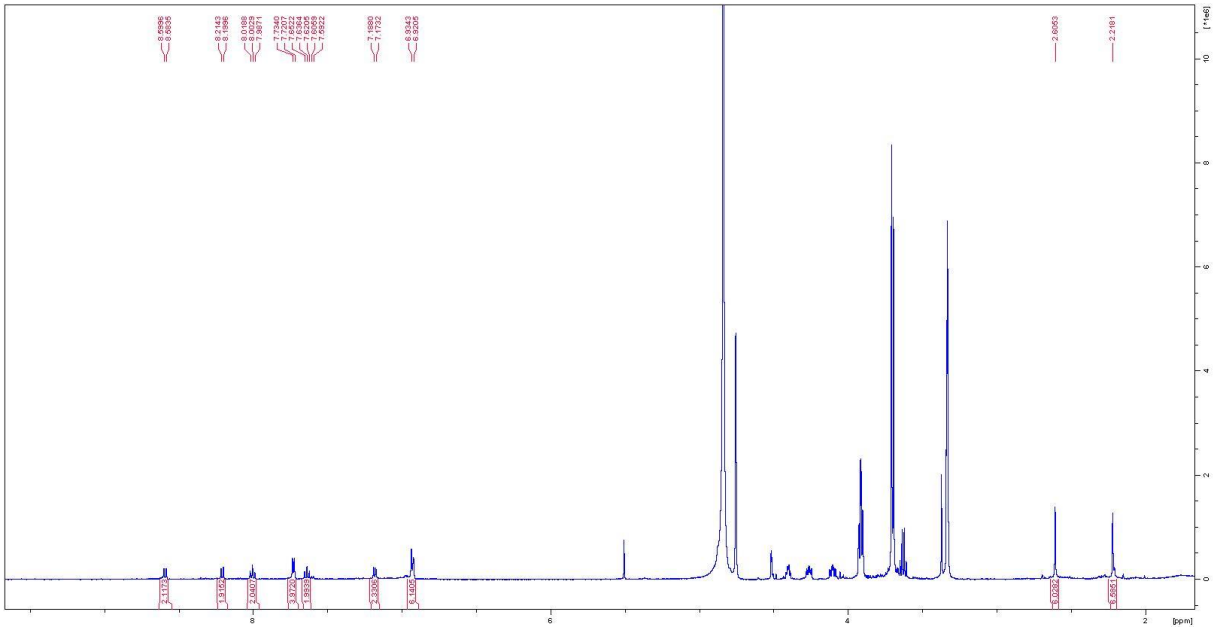

Figure 255. ^{1}H spectrum of K18.

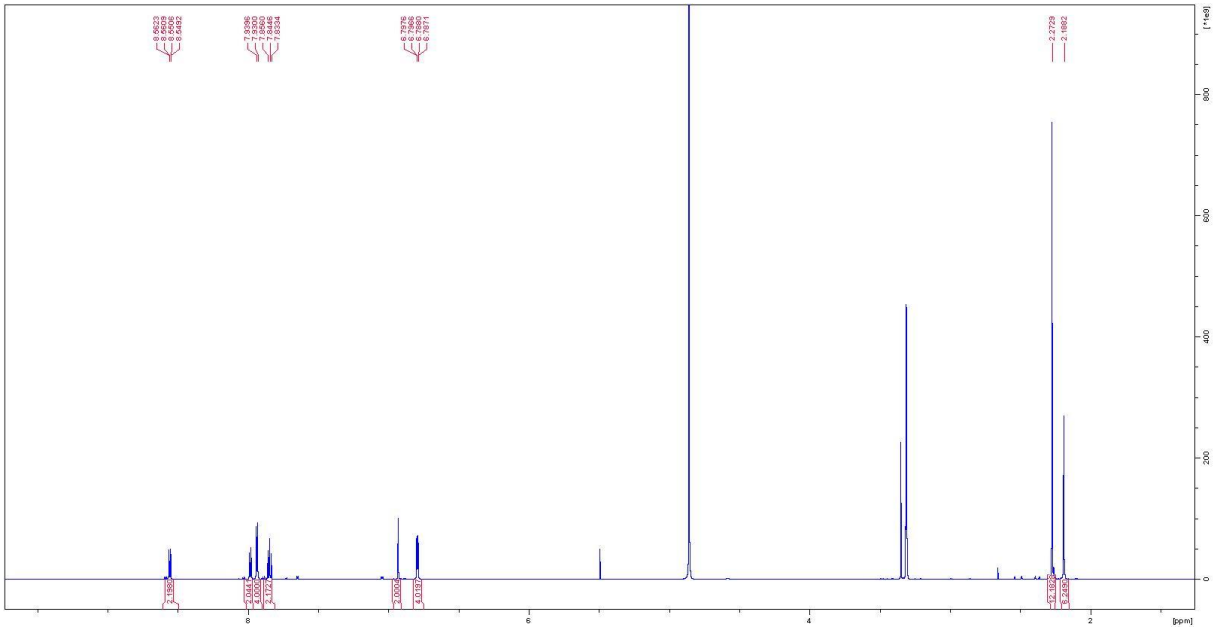

Figure 256. ^{1}H spectrum of K19.

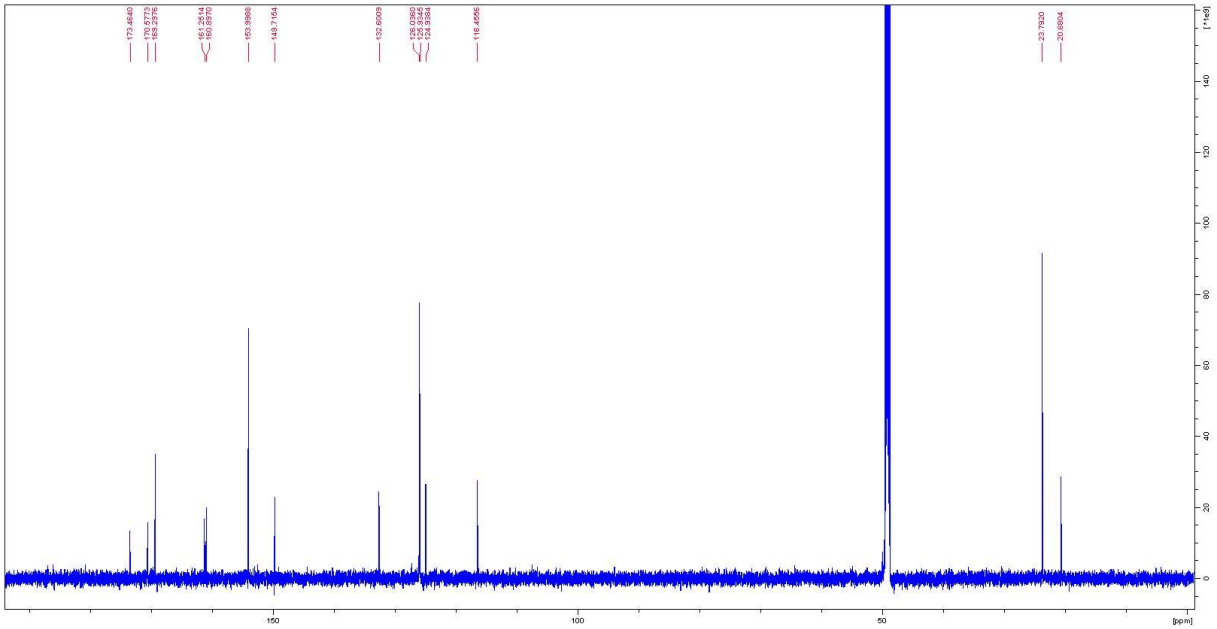

Figure 257. ^{13}C spectrum of K19.

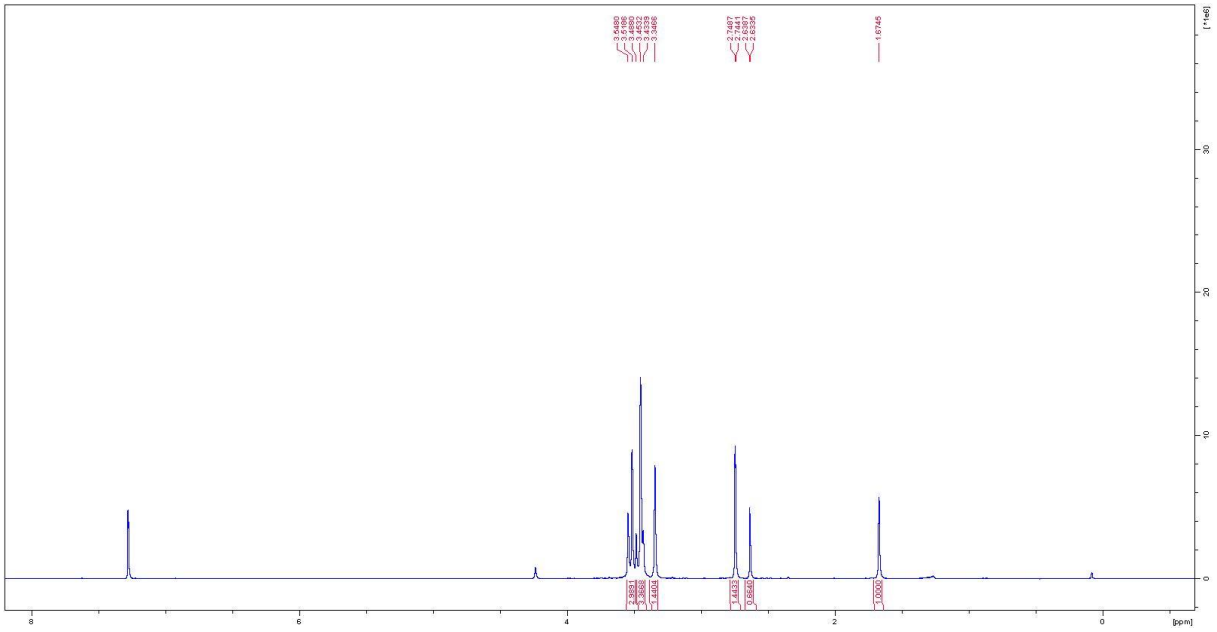

Figure 258. ^{1}H spectrum of $Ru(DMSO)_4Cl_2$.

MeOH

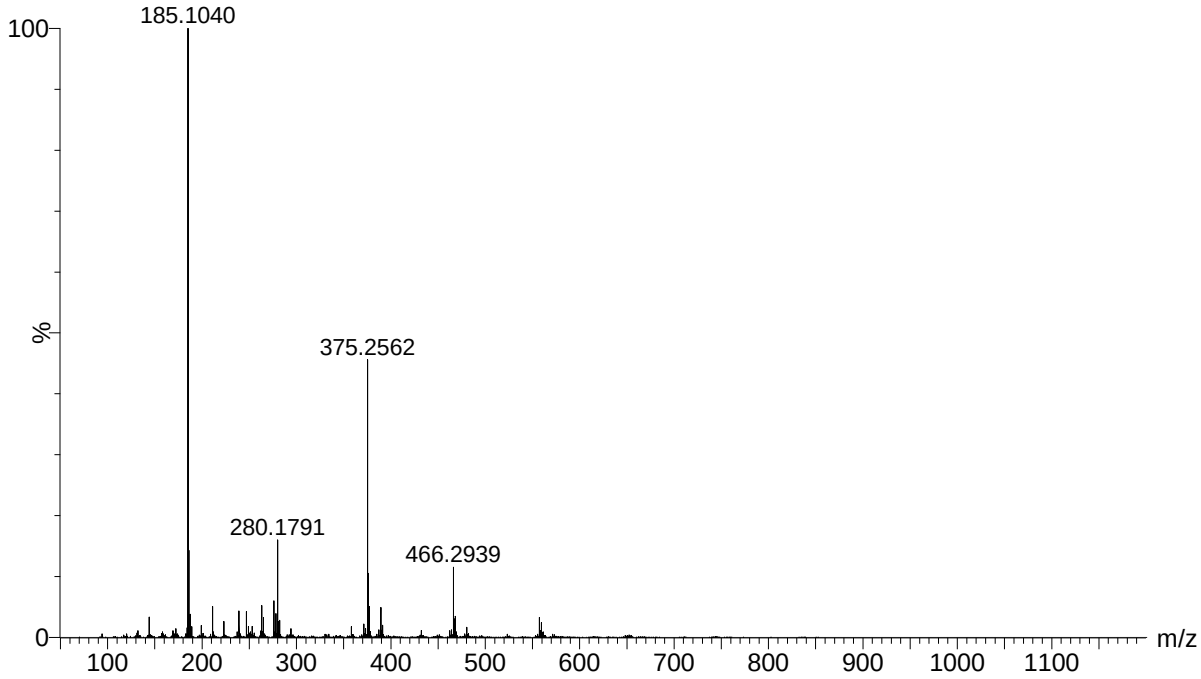

Figure 259. ESI-MS spectrum of 6,6'-dimethyl-2,2'-dipyridine.

H2O

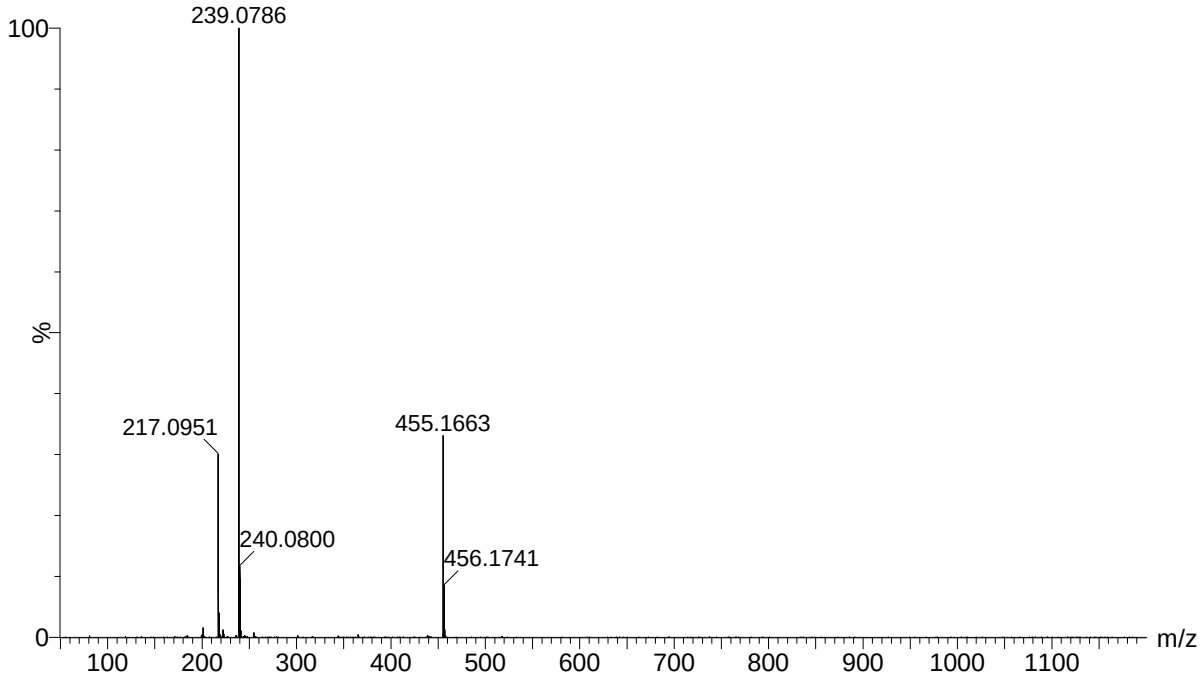

Figure 260. ESI-MS spectrum of 6,6'-dimethyl-2,2'-dipyridyl di-*N*-*N'*-oxide.

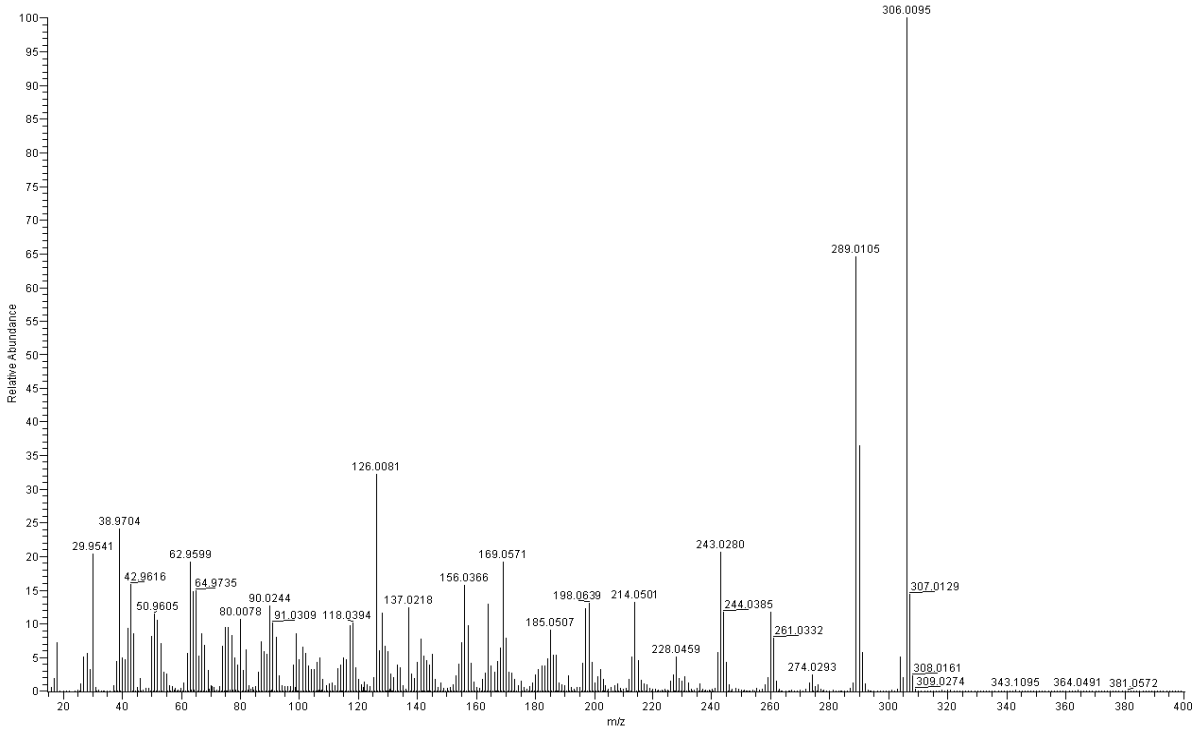

Figure 261. EI-MS spectrum of 6,6'-dimethyl-4,4'-dinitro-2,2'-dipyridyl di-*N*,*N'*-oxide.

MeCN

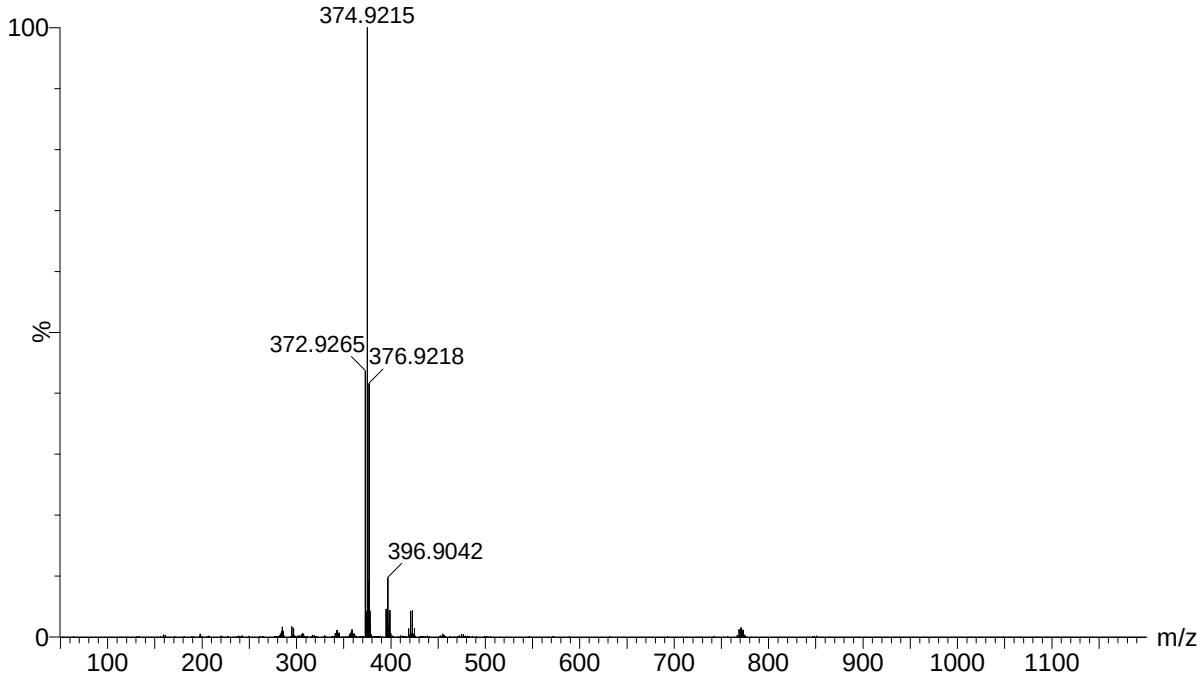

Figure 262. ESI-MS spectrum of 6,6'-dimethyl-4,4'-dibromo-2,2'-dipyridyl di-*N*,*N'*-oxide.

MeOH

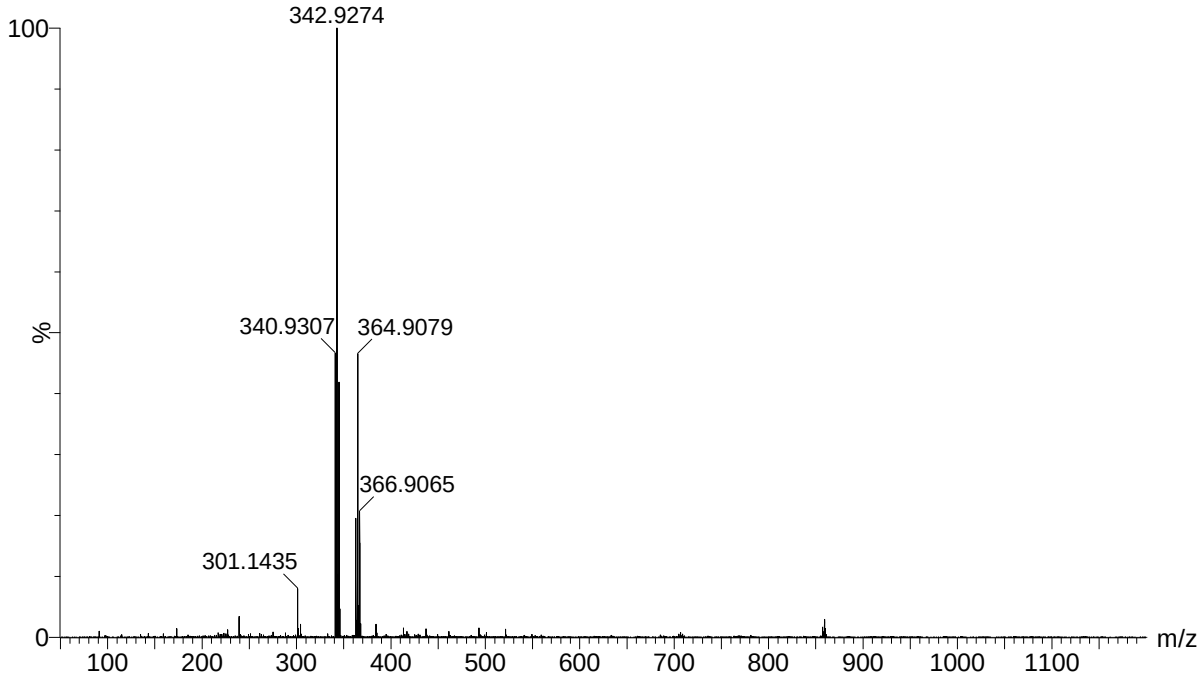

Figure 263. 4,4'-dibromo-6,6'-dimethyl-2,2'-bipyridine.

ACN

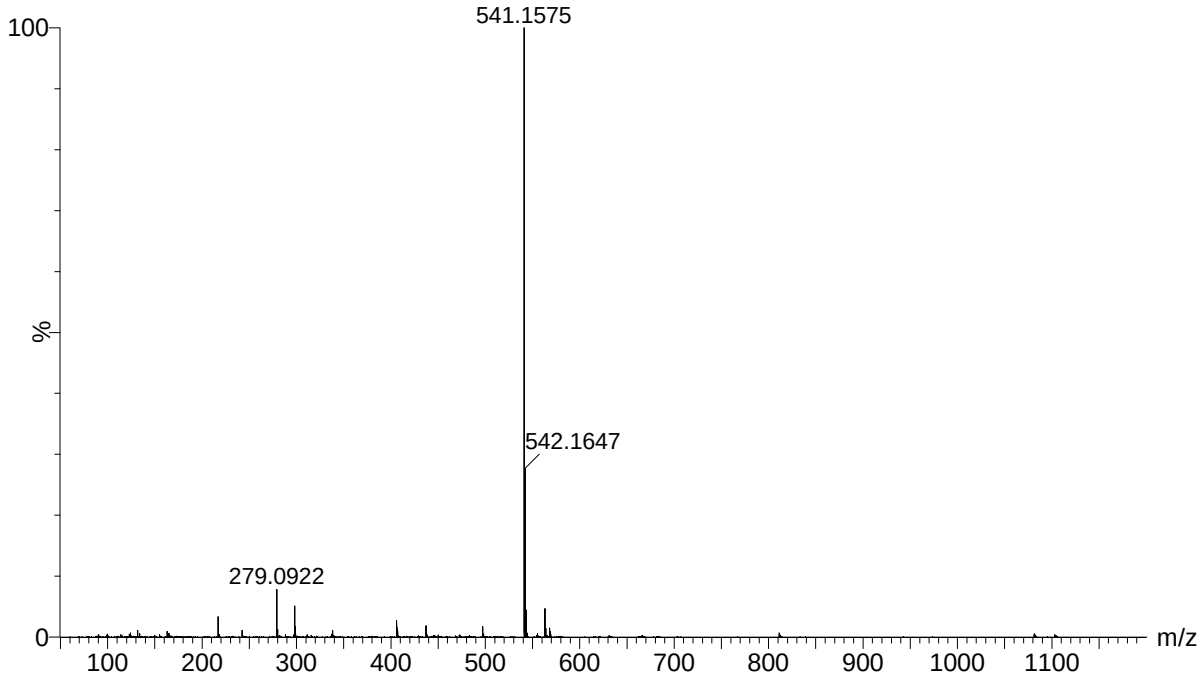

Figure 264. ESI-MS spectrum of dimethyl 4,4‘-bis(4-(methoxycarbonyl)phenyl)-2,2‘-bi-pyridine-6,6‘-dicarboxylate.

MeCN+NH4OH

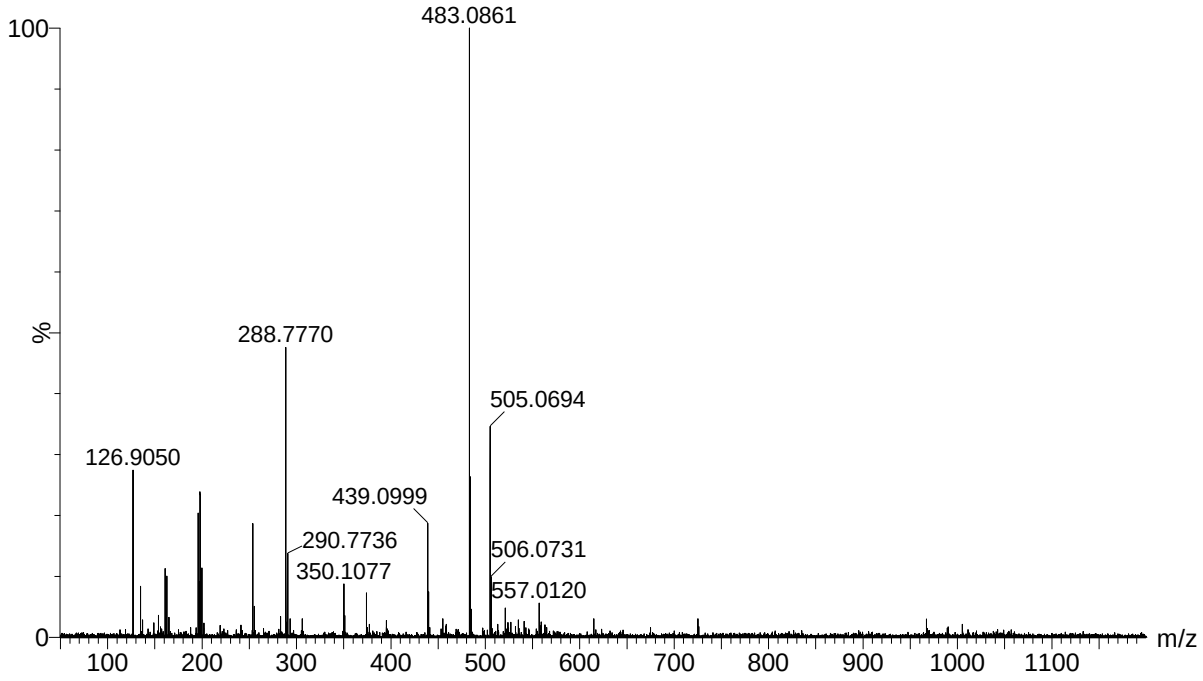

Figure 265. ESI-MS spectrum of 6,6'-dimethyl-2,2'-bipyridine-4,4'-dibenzoic acid.

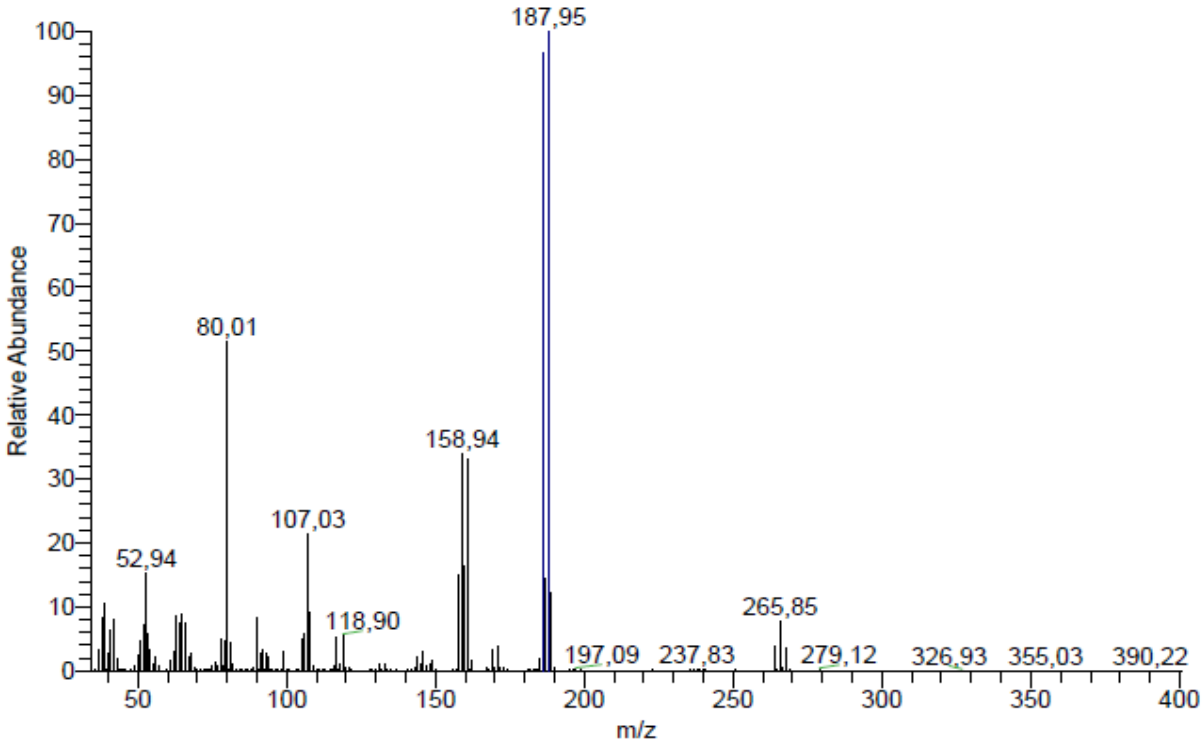

Figure 266. EI-MS spectrum of 5-bromo-6-methyl-2-pyridinamine.

MeCN

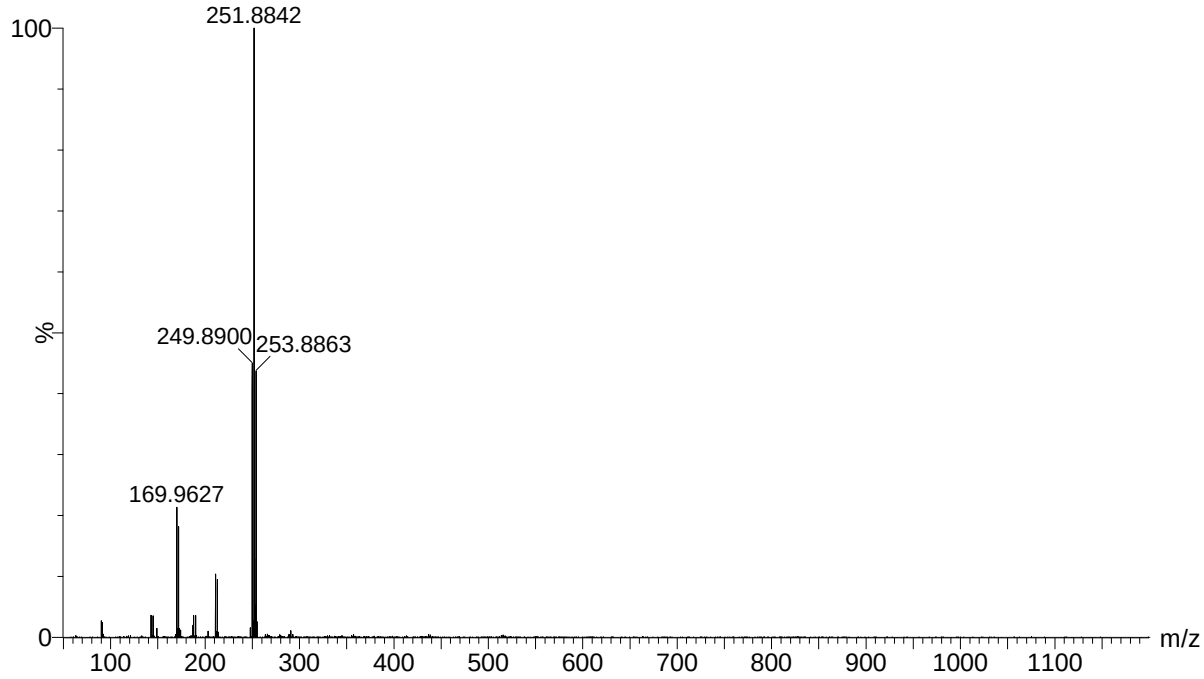

Figure 267. ESI-MS spectrum of 3,6-dibromo-2-methyl-pyridine.

MeOH+Acid

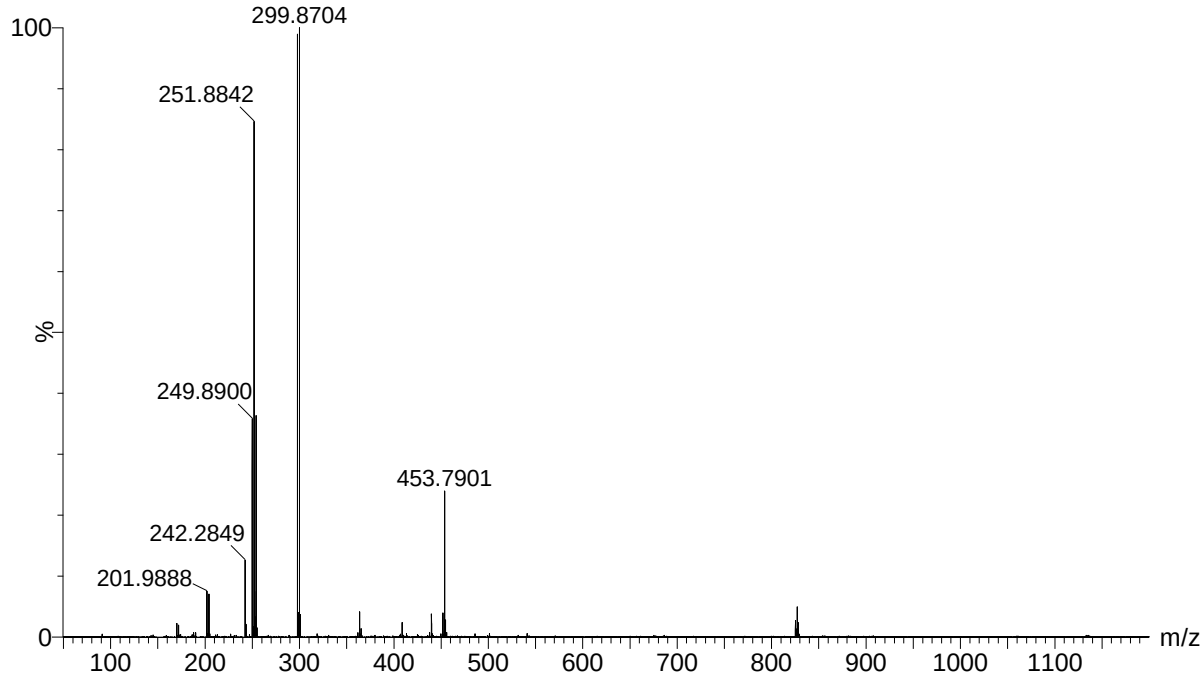

Figure 268. ESI-MS spectrum of 3-bromo-6-iodo-2-methylpyridine.

MeCN

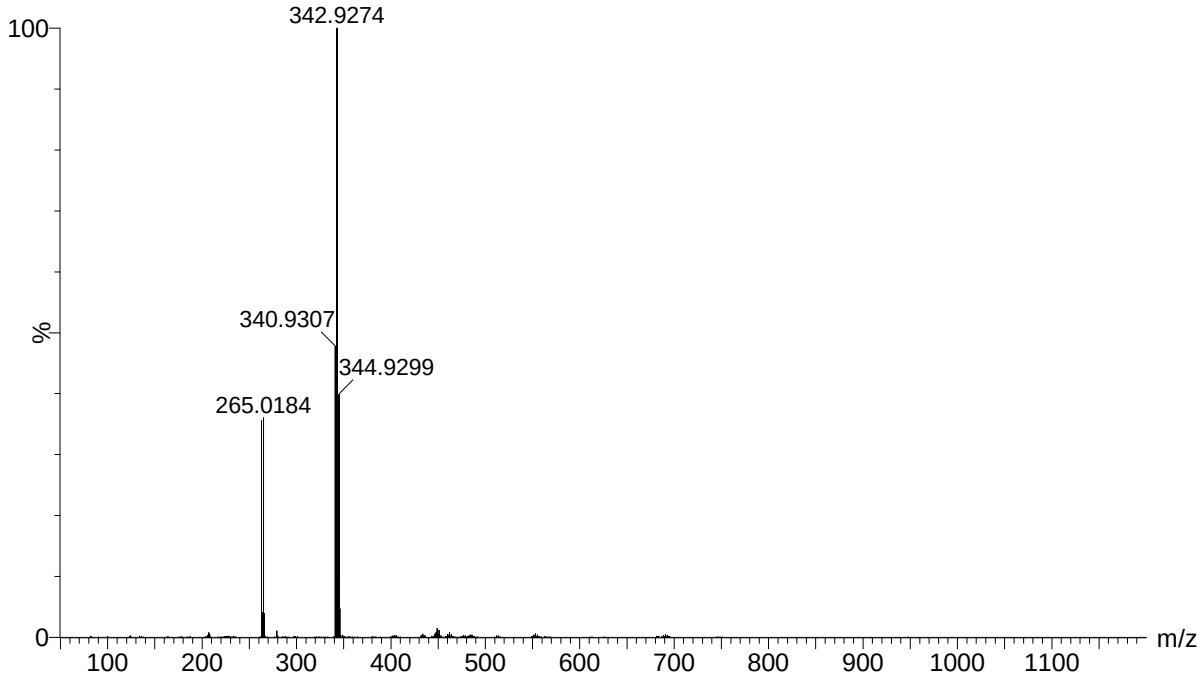

Figure 269. ESI-MS spectrum of 5,5‘-dibromo-6,6‘-dimethyl-2,2‘-bipyridine.

MeOHueber Cloroform

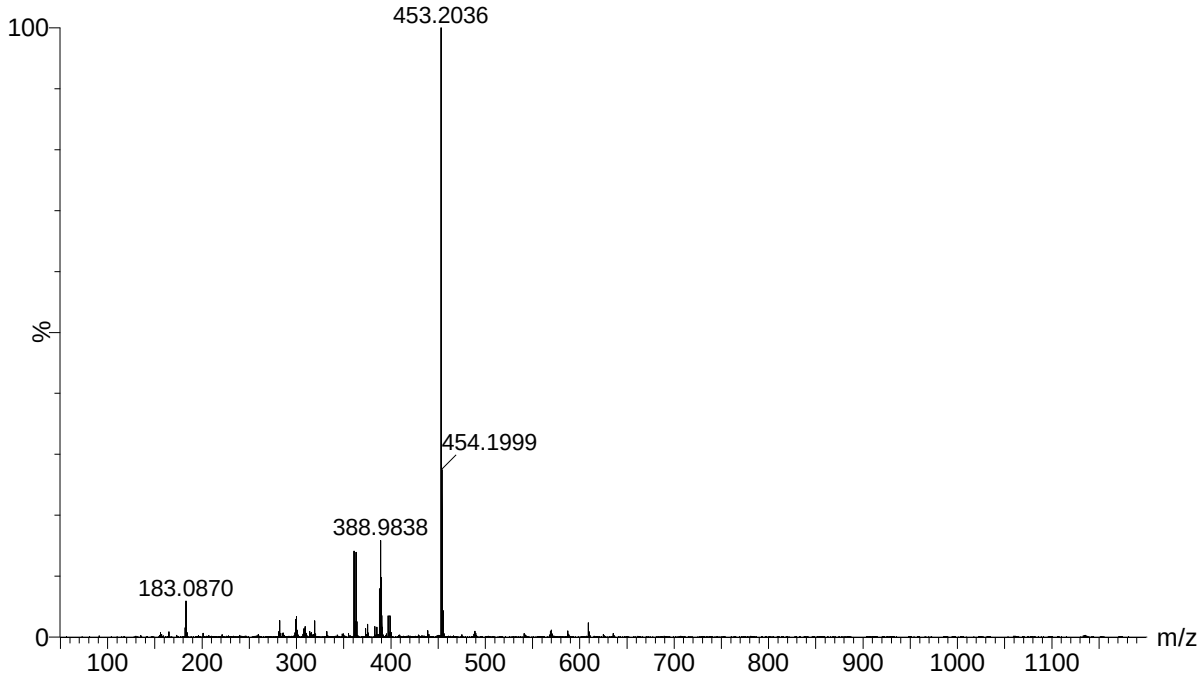

Figure 270. ESI-MS spectrum of dimethyl-4,4‘-(6,6‘-dimethyl-[2,2‘-bipyridine]-5,5‘-diyl)-dibenzoate.

DMSO / H2O + NH4OH

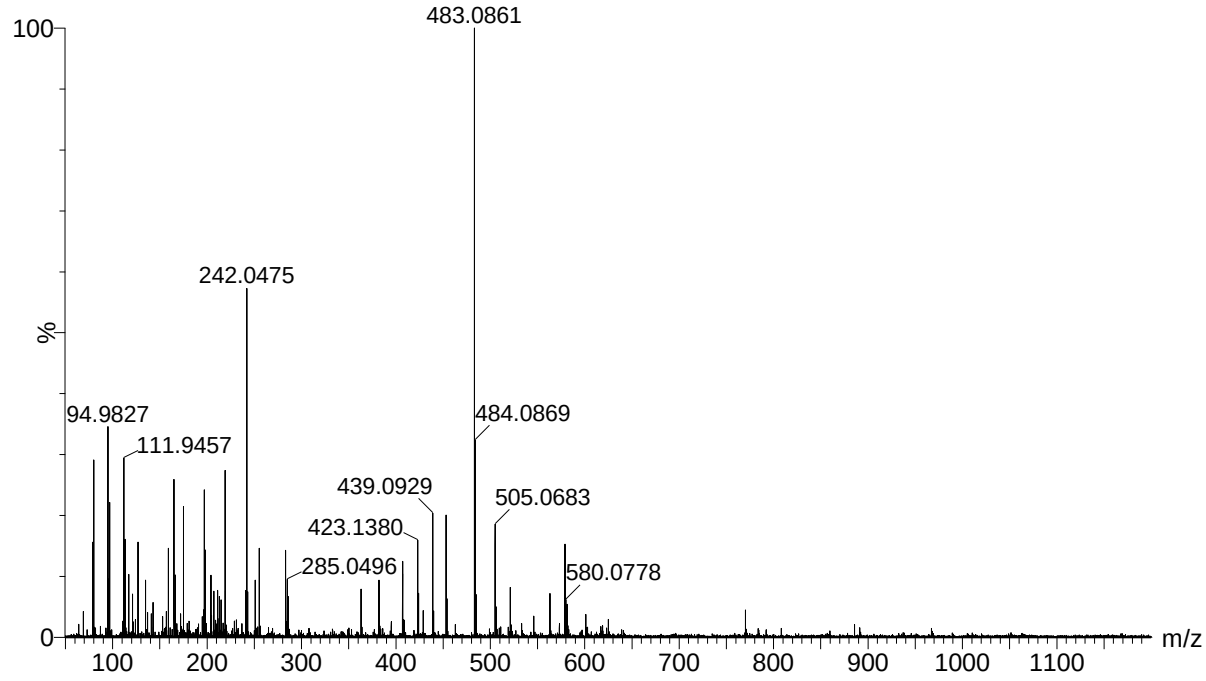

Figure 271. ESI-MS spectrum of 5,5‘-bis(4-carboxyphenyl)-[2,2‘-bipyridine]-6,6‘-di-carboxylic acid.

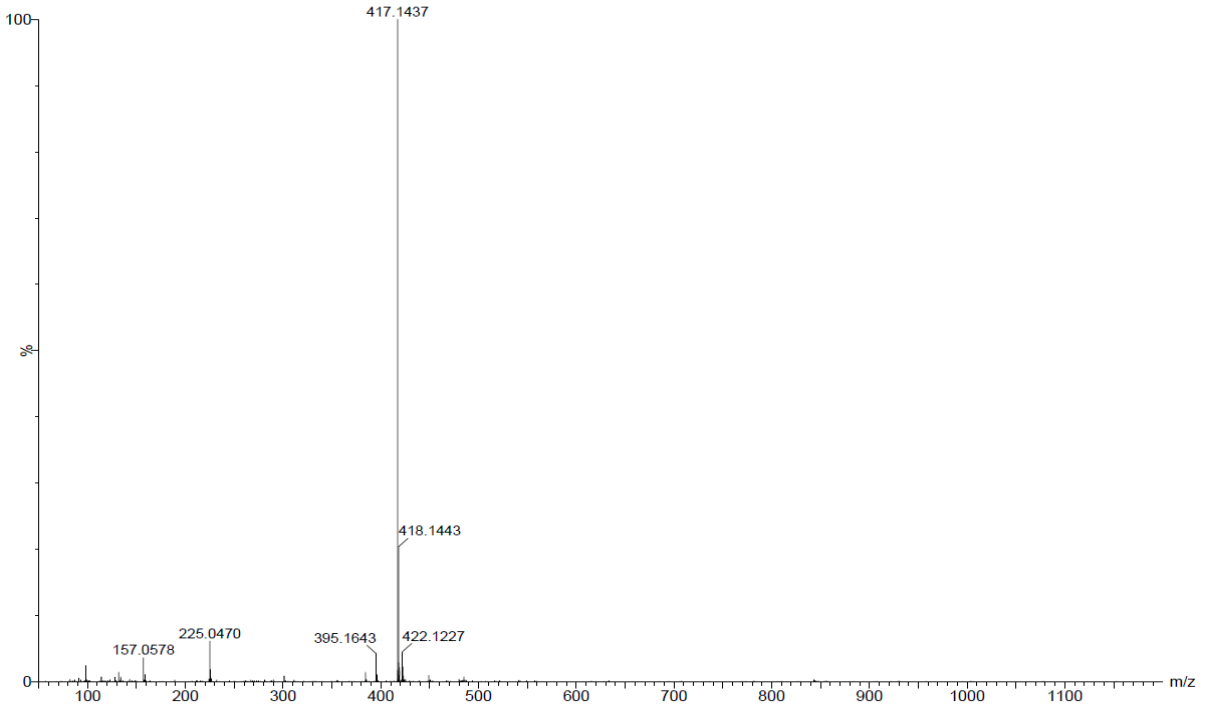

Figure 272. ESI-MS spectrum of L7.

MeCN ueber Chloroform

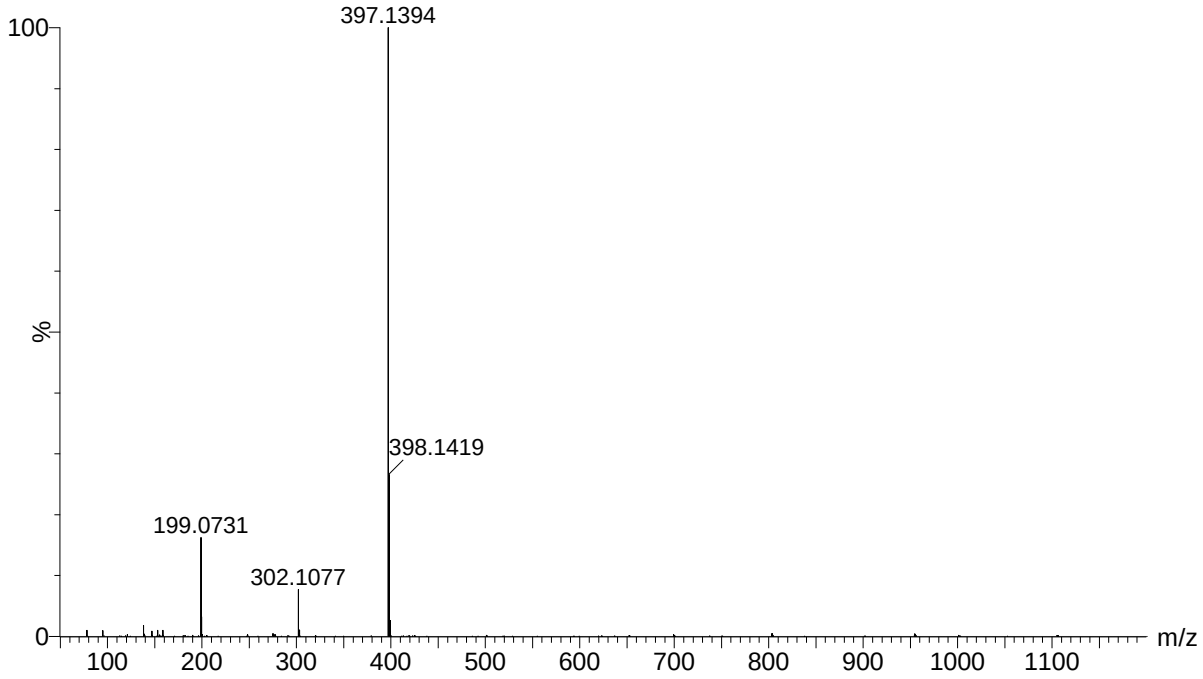

Figure 273. ESI-MS spectrum of L8.

MeCN

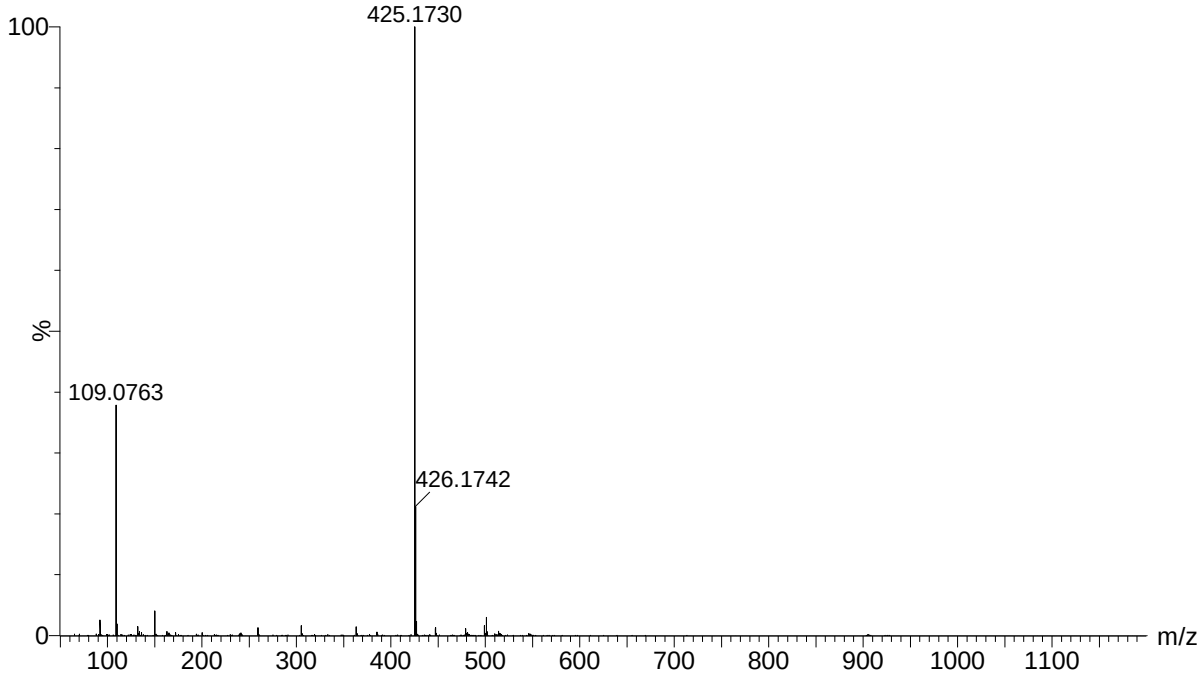

Figure 274. ESI-MS spectrum of L9.

MeCN

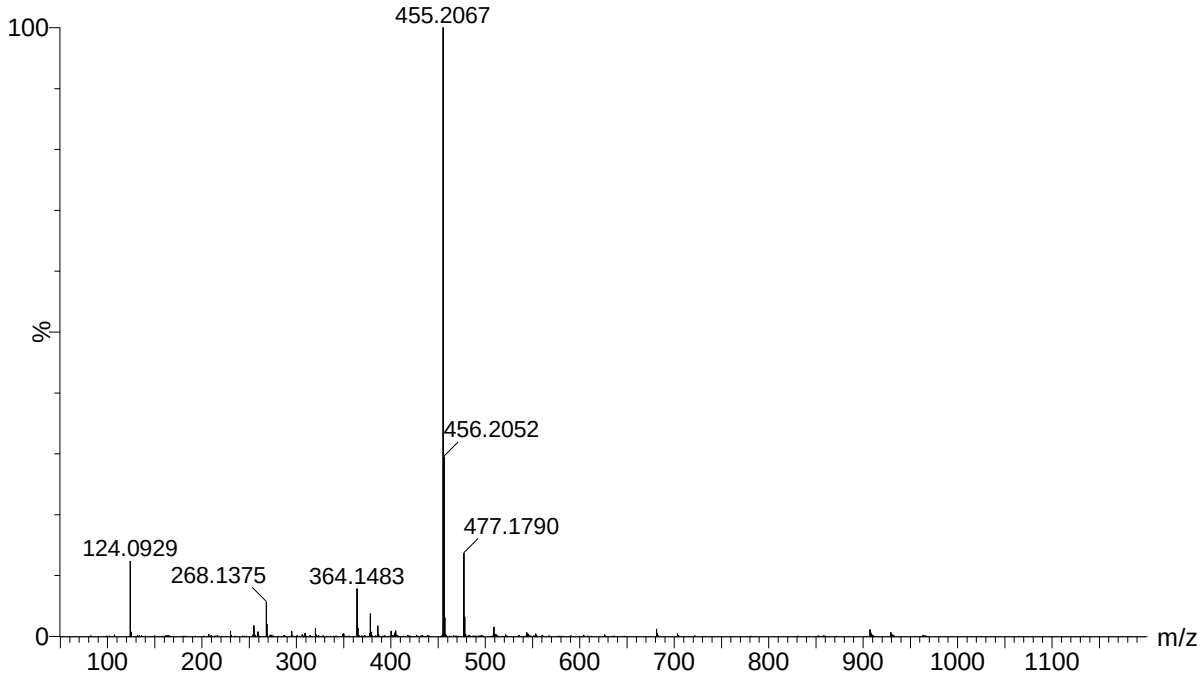

Figure 275. ESI-MS spectrum of L10.

MeOH+H2O

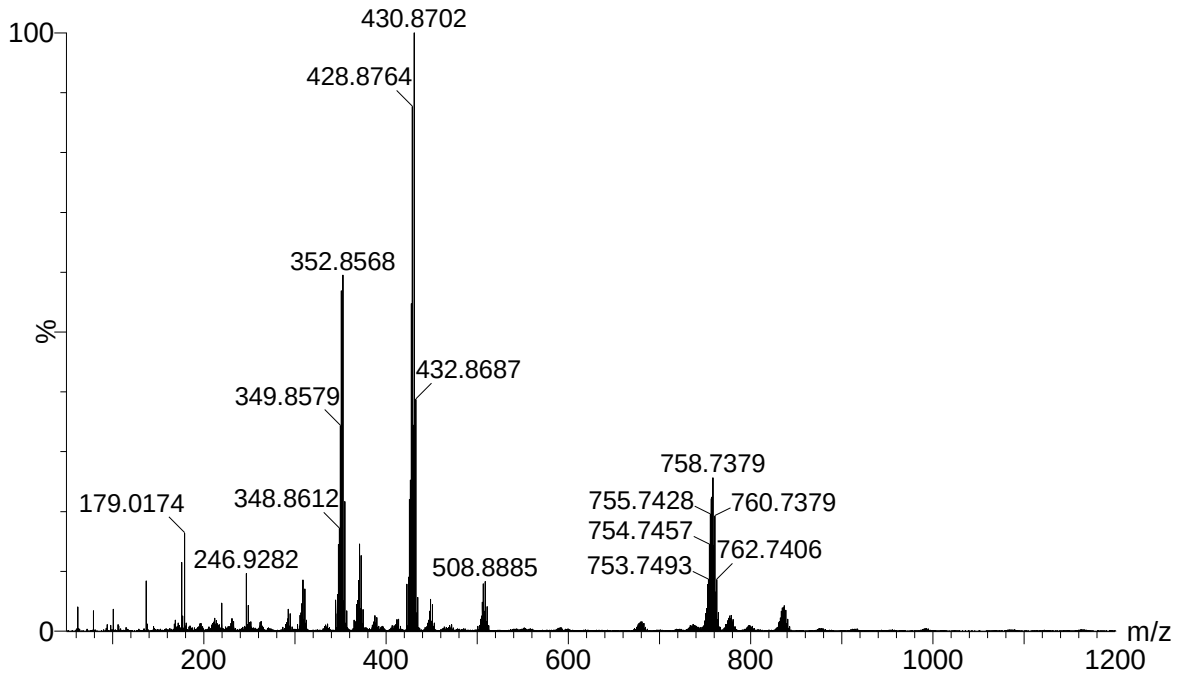

Figure 276. ESI-MS spectrum of $Ru(DMSO)_4Cl_2$.

MeOH

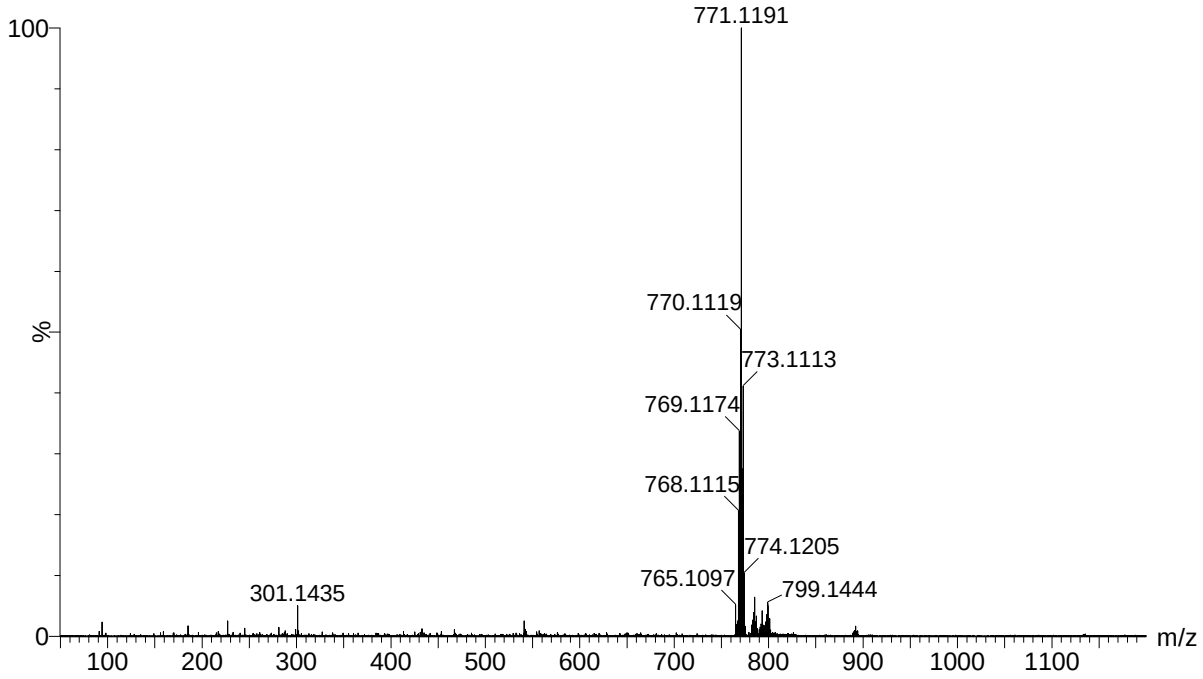

Figure 277. ESI-MS spectrum of K1.

MeOH:H2O

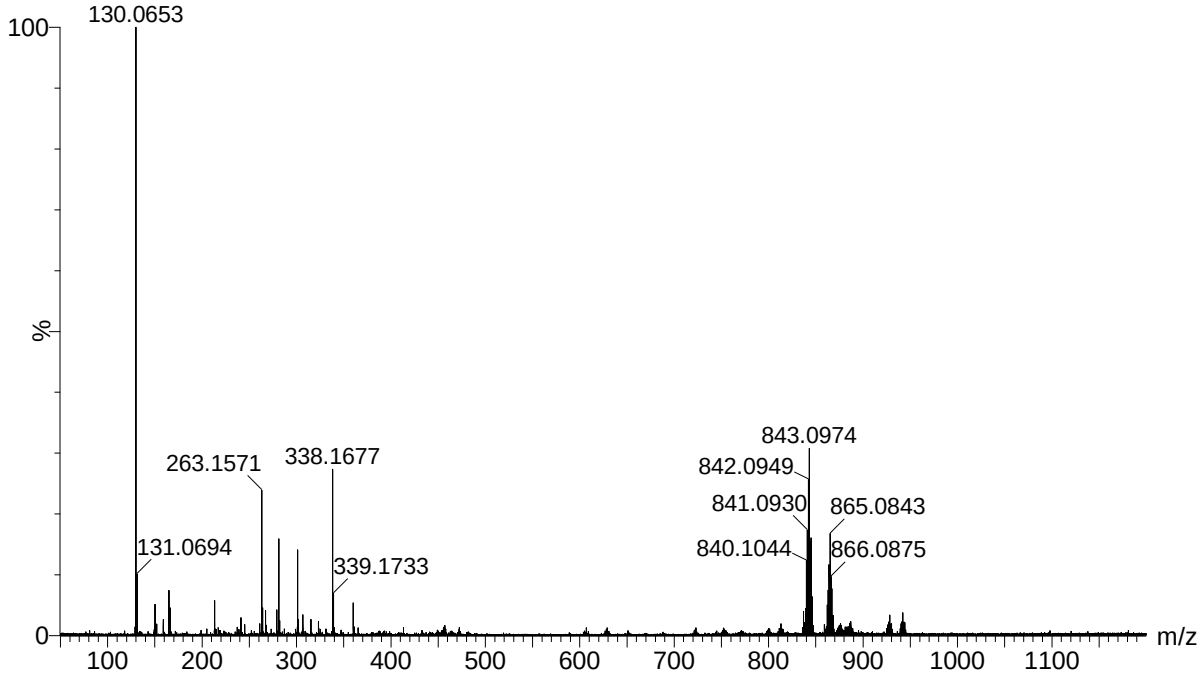

Figure 278. ESI-MS spectrum of K2.

H2O

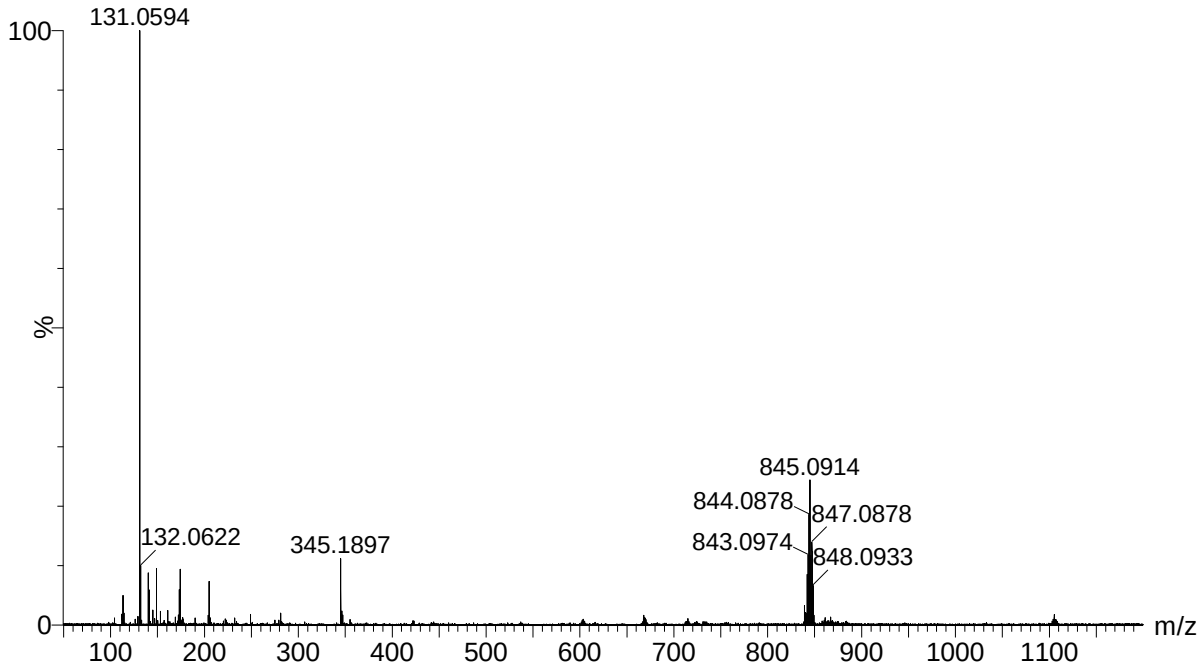

Figure 279. ESI-MS spectrum of K3.

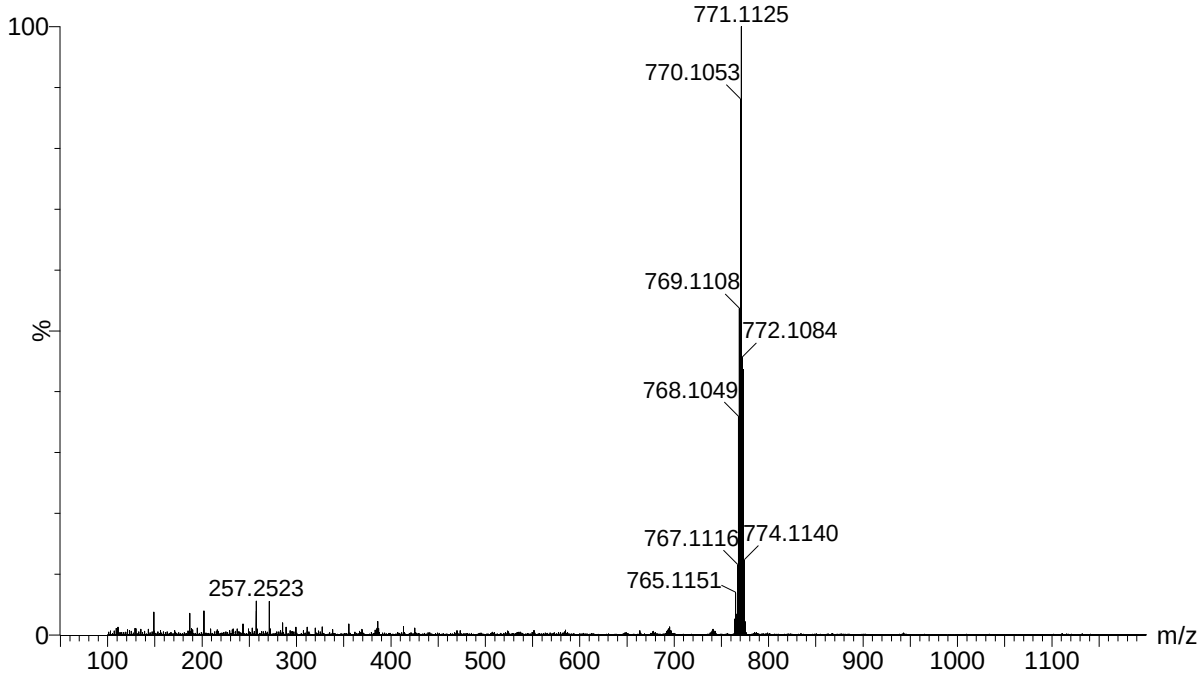

Figure 280. ESI-MS spectrum of K4.

MeOH+H20+Acid

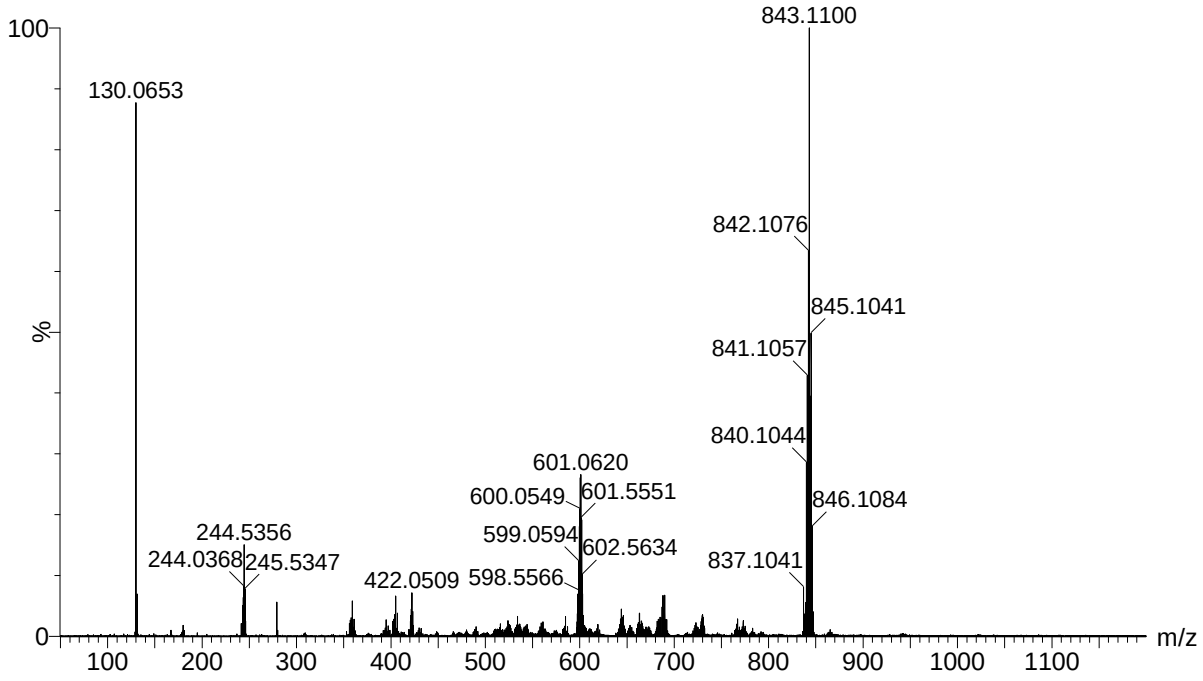

Figure 281. ESI-MS spectrum of K5.

MeCN

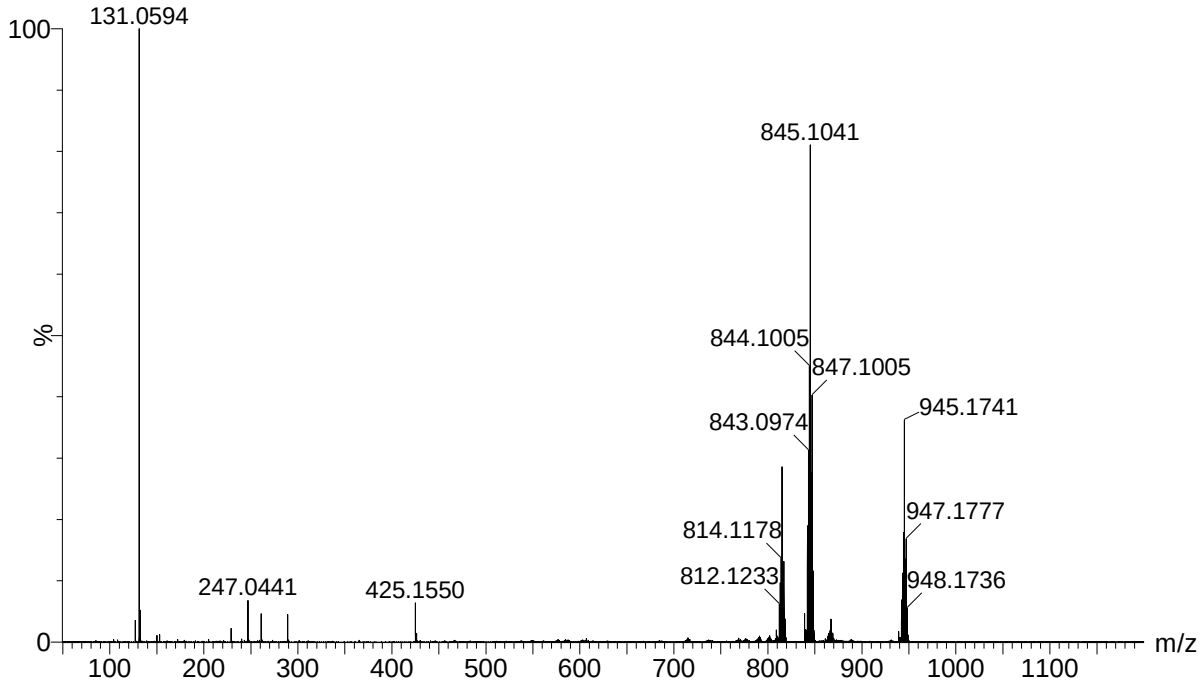

Figure 282. ESI-MS spectrum of K6.

MeOH +H+

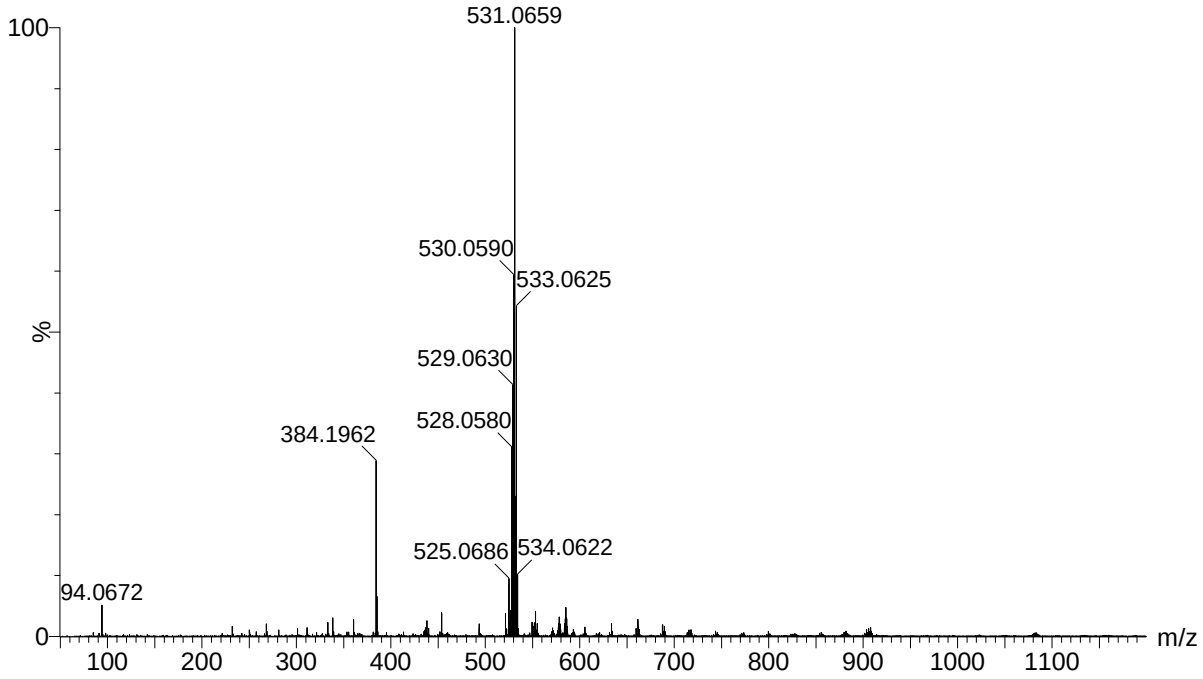

Figure 283. ESI-MS spectrum of K7.

MeOH/H2O

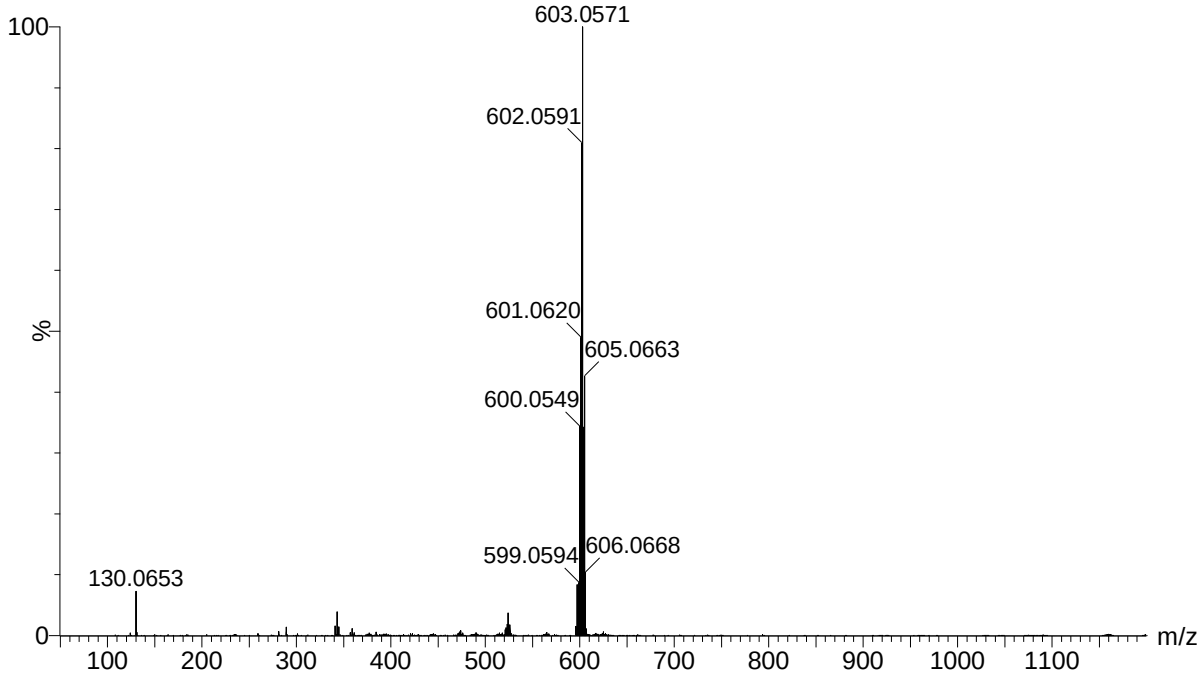

Figure 284. ESI-MS spectrum of K8.

MeCN + H+

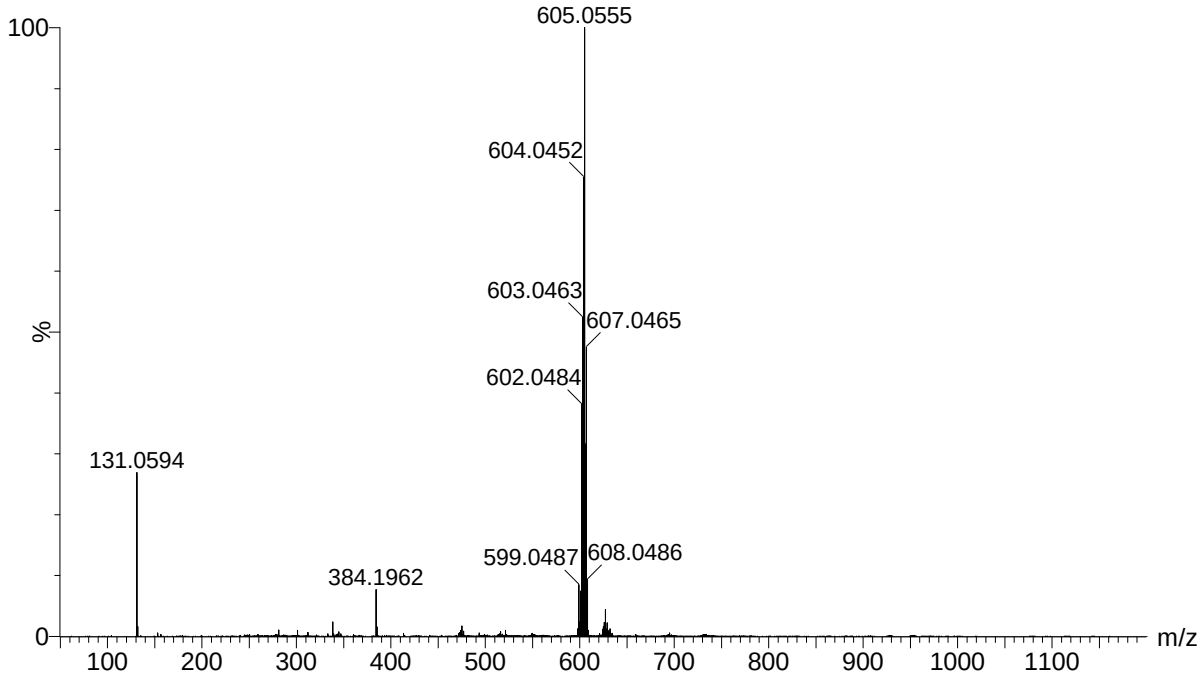

Figure 285. ESI-MS spectrum of K9.

MeOH/H2O +H+

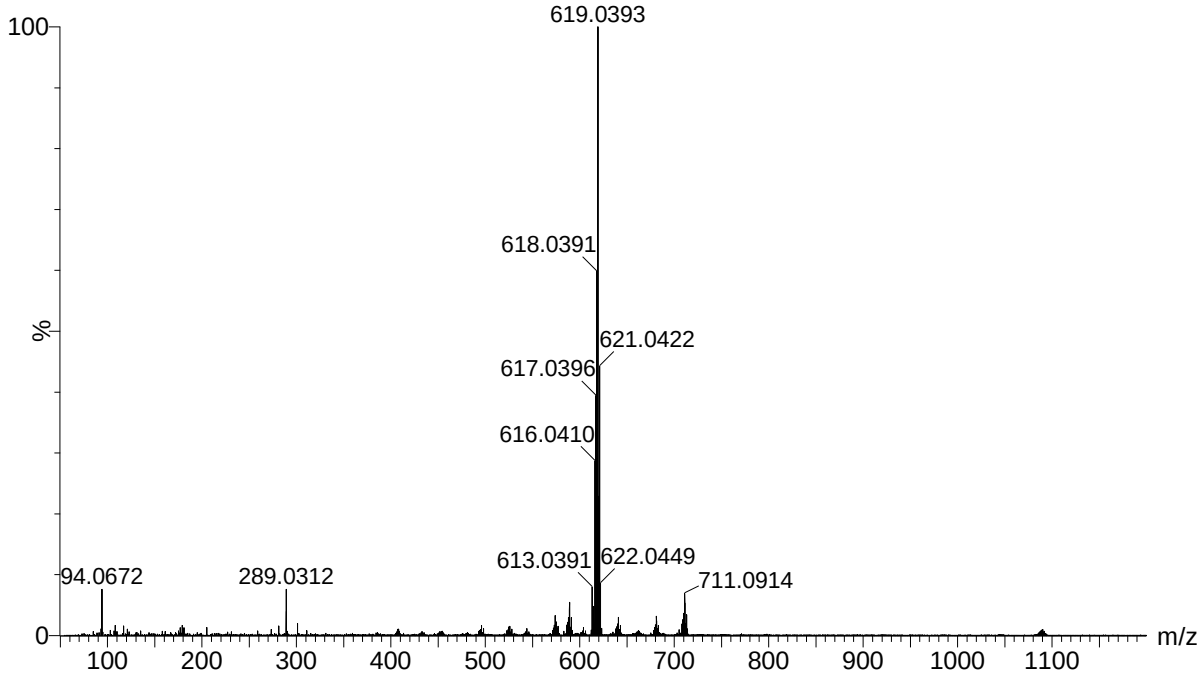

Figure 286. ESI-MS spectrum of K10.

MeOH:H2O/1:1 + H+

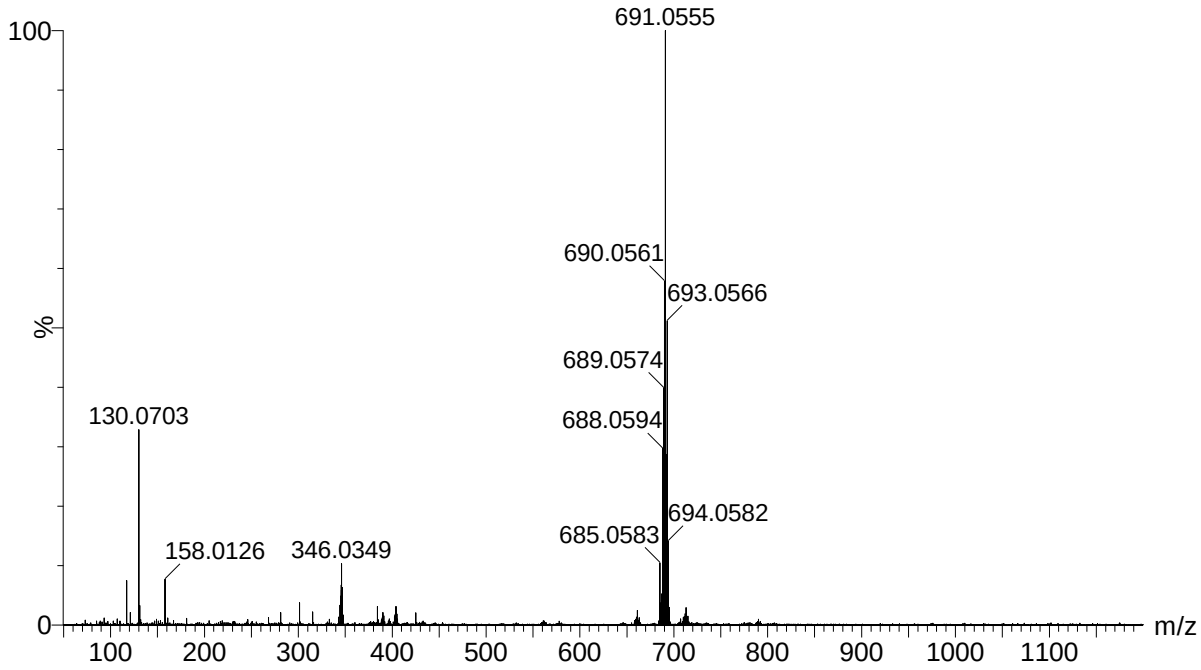

Figure 287. ESI-MS spectrum of K11.

MeOH

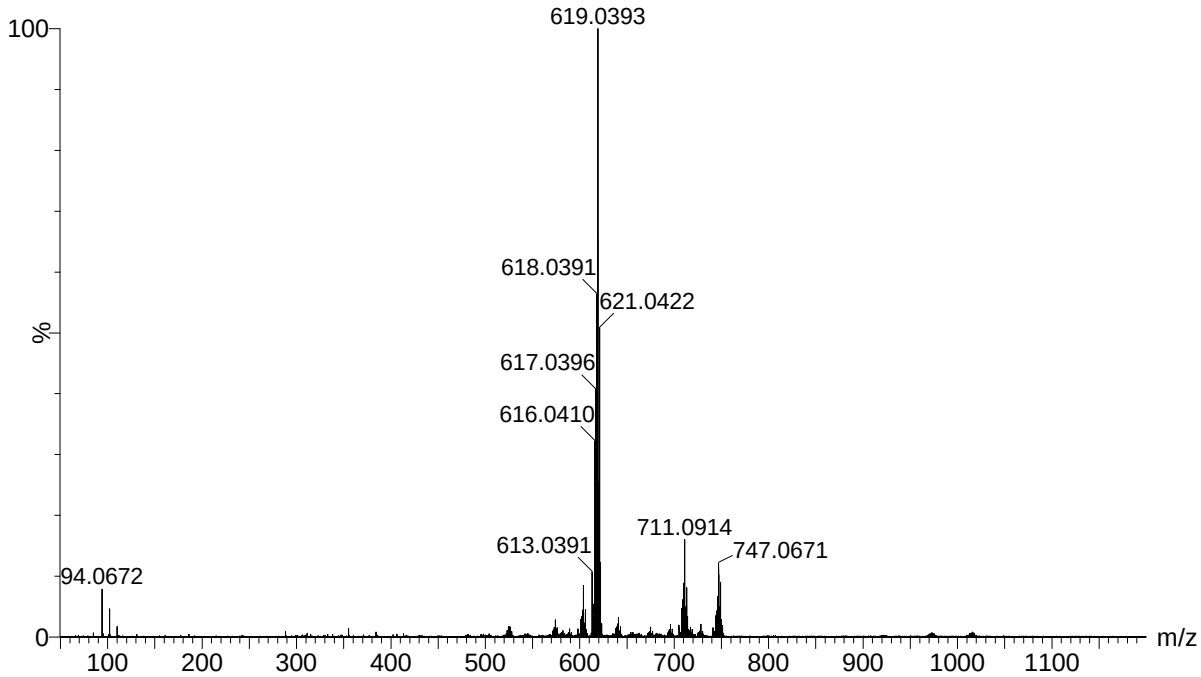

Figure 288. ESI-MS spectrum of K12.

MeOH:H2O + H+

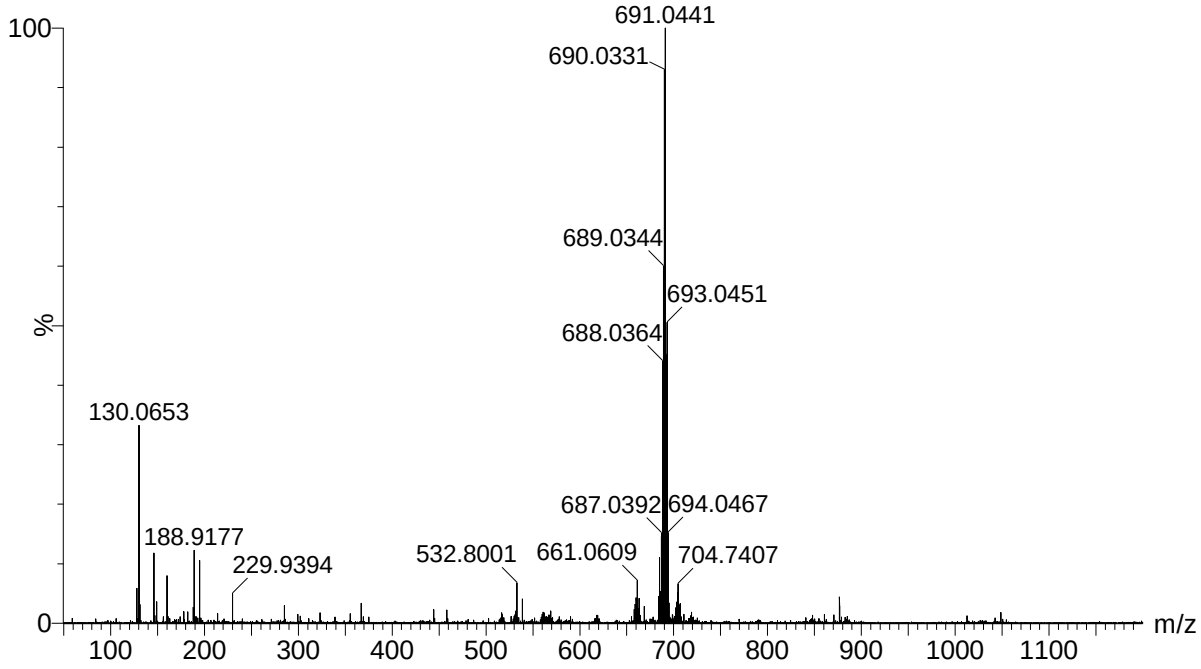

Figure 289. ESI-MS spectrum of K13.

MeOH

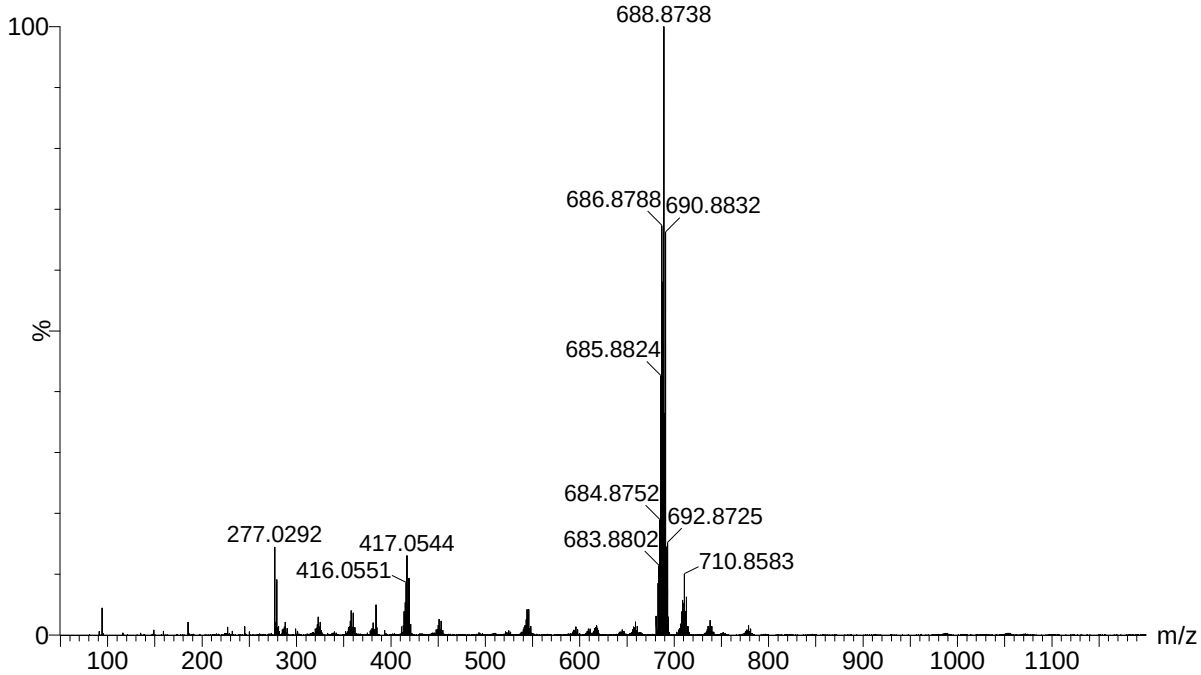

Figure 290. ESI-MS spectrum of K14.

MeOH:H2O

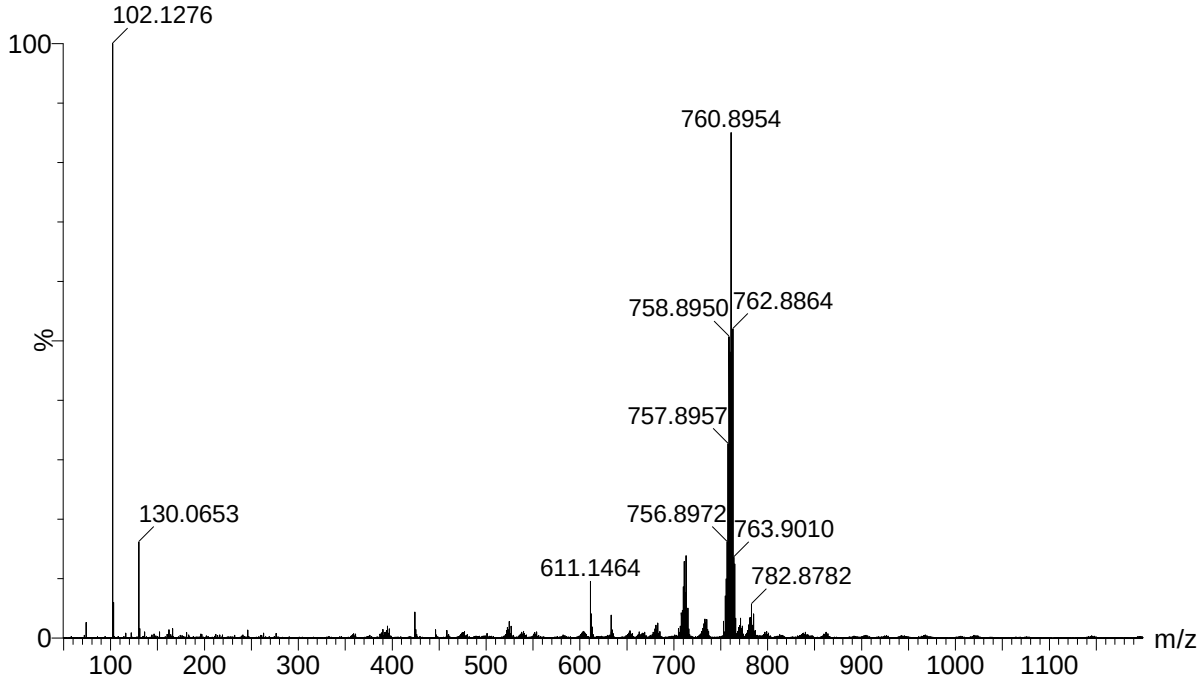

Figure 291. ESI-MS spectrum of K15.

MeOH+H+

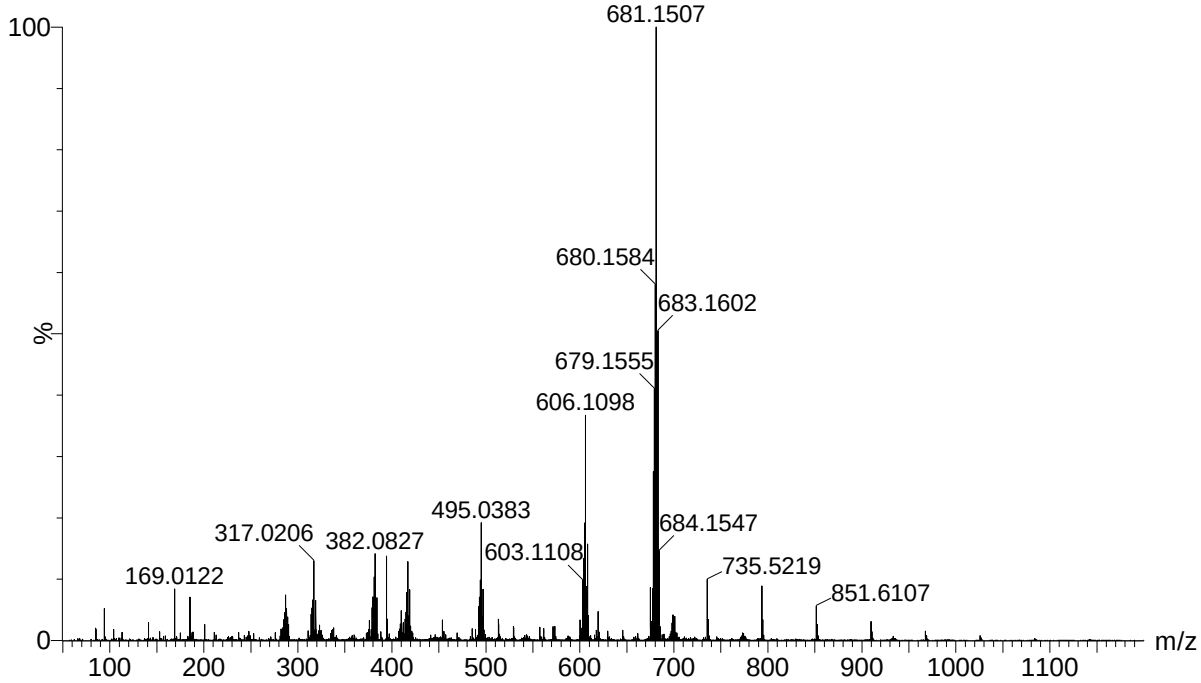

Figure 292. ESI-MS spectrum of K16.

MeOH

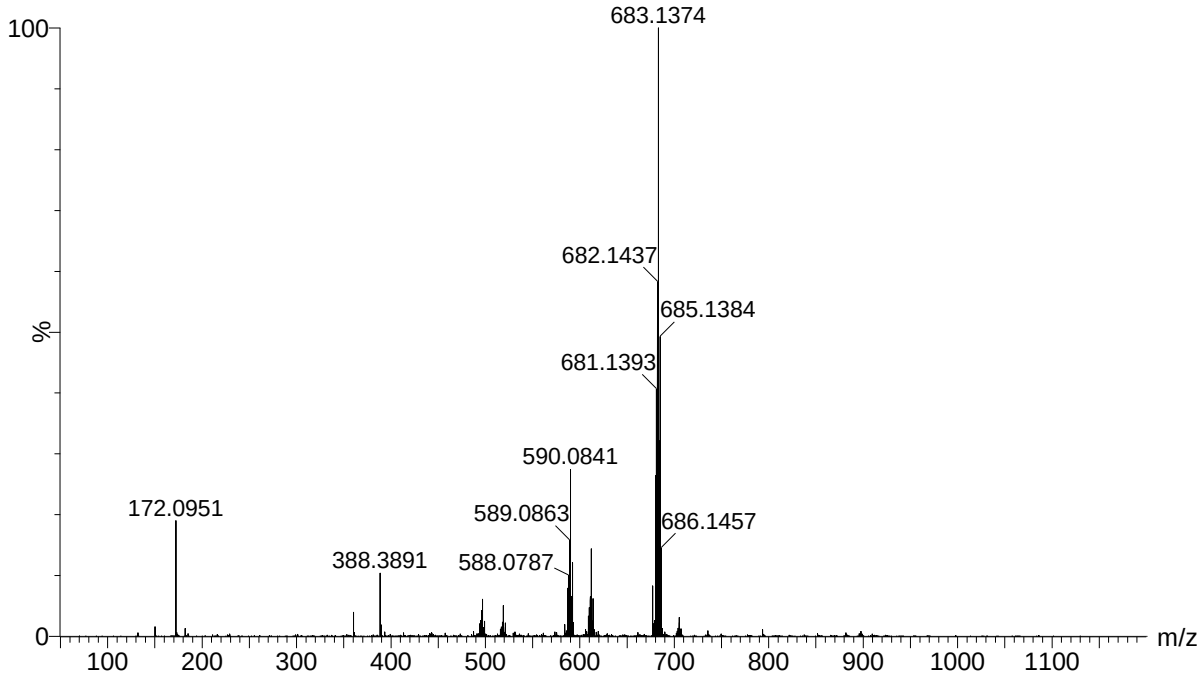

Figure 293. ESI-MS spectrum of K17.

MeOH

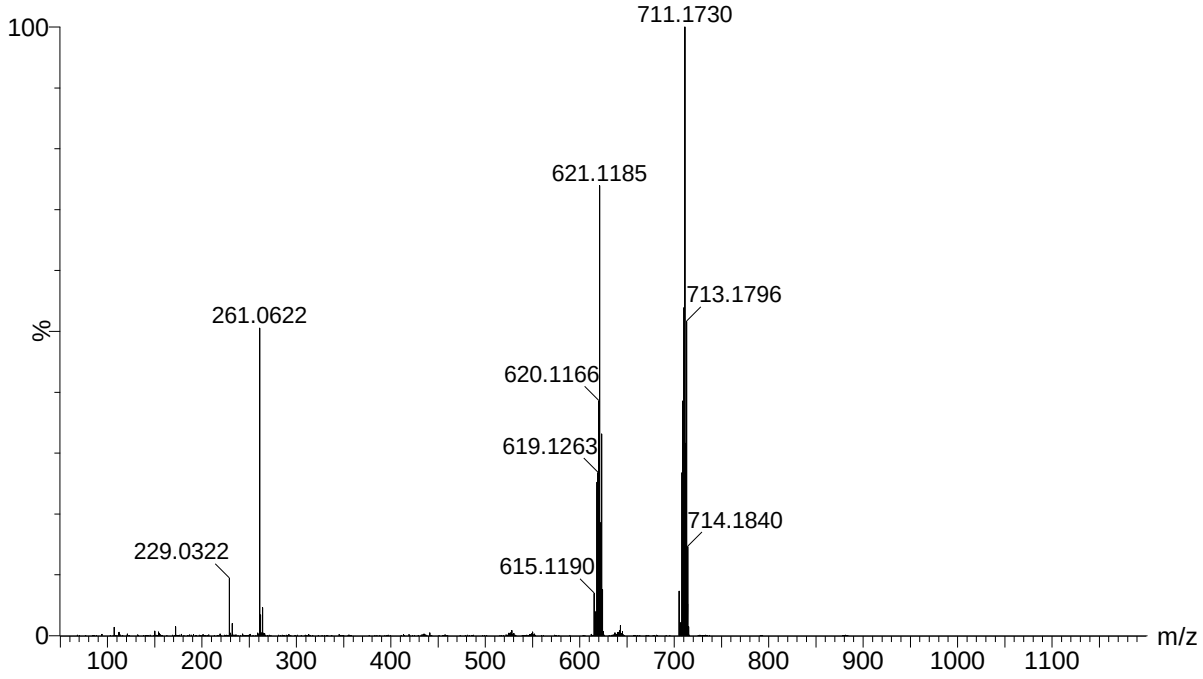

Figure 294. ESI-MS spectrum of K18.

MeCN

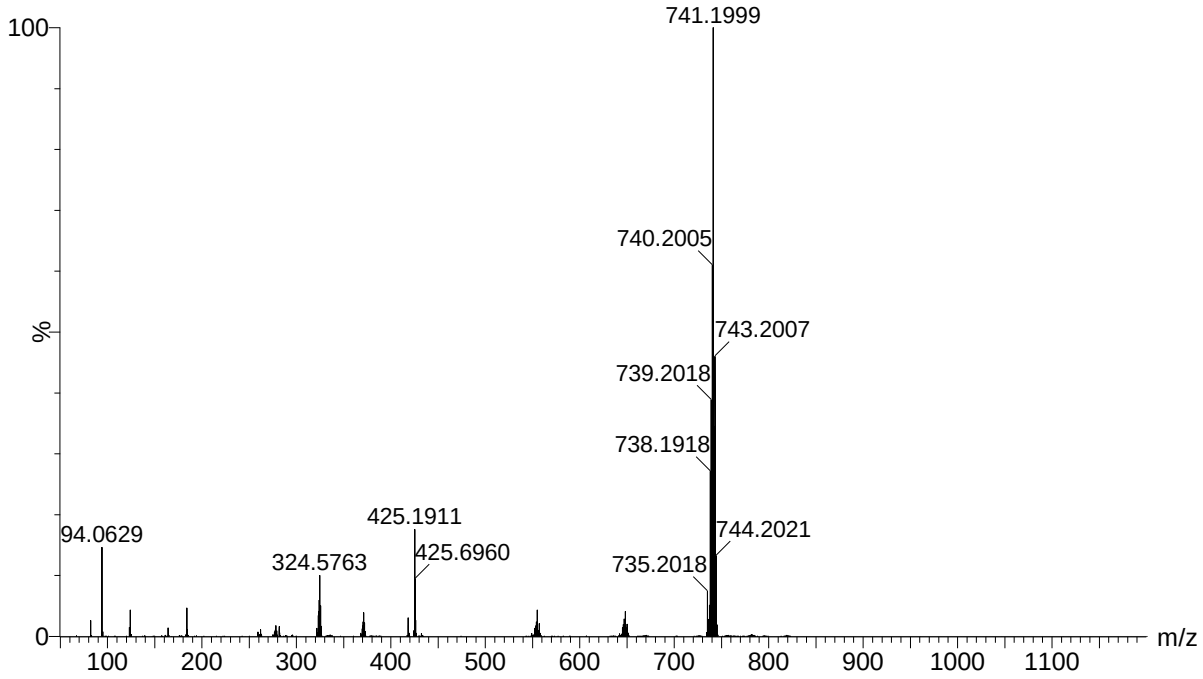

Figure 295. ESI-MS spectrum of K19.

ACN

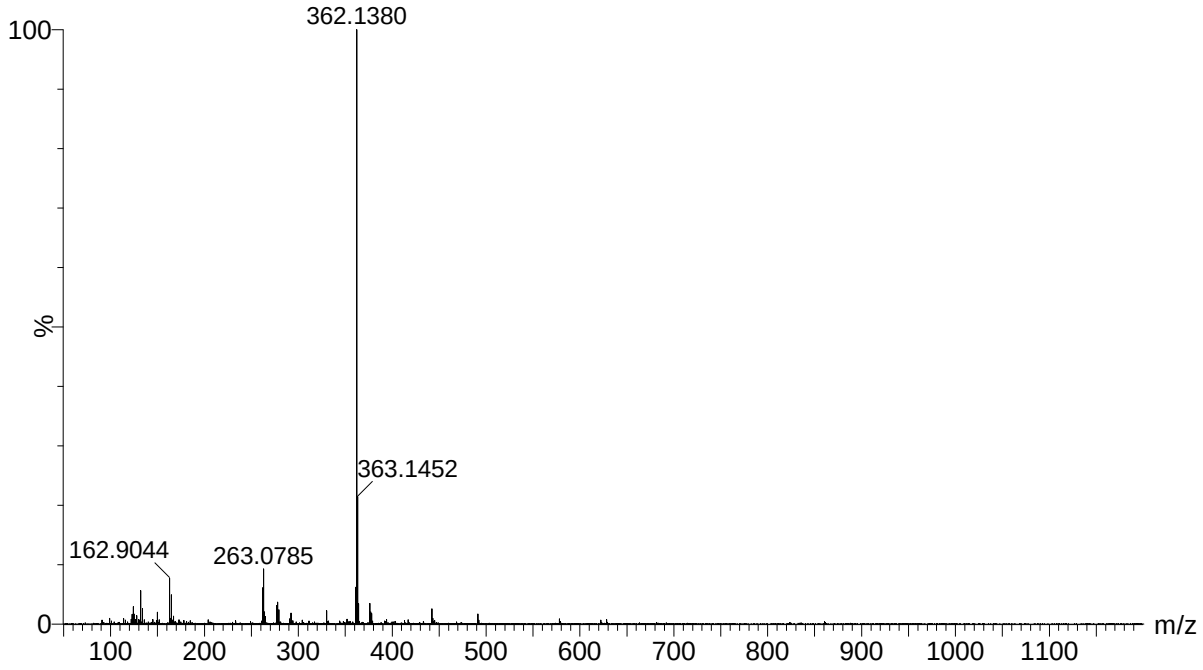

Figure 296. ESI-MS spectrum of dimethyl 2'-amino-[1,1'-4',1"-terphenyl]-4,4"-dicarboxylate.

MeOH+H2O+Acid

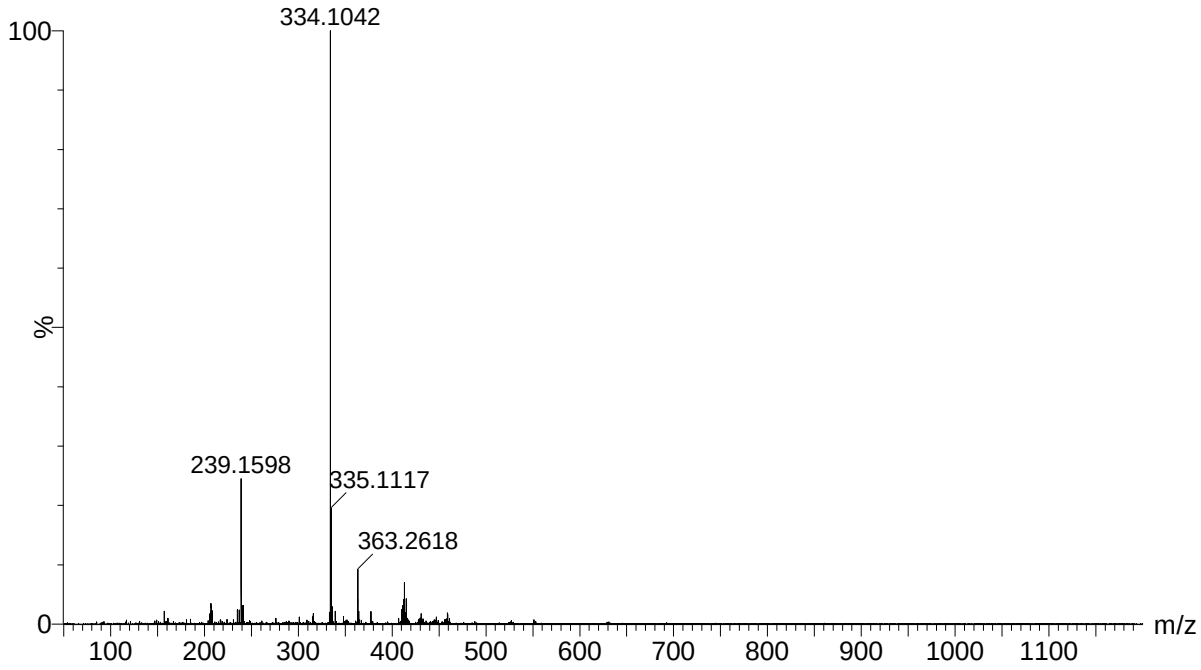

Figure 297. ESI-MS spectrum of 2'-amino-[1,1':4',1''-terphenyl]-4,4''-dicarboxylic acid.

MeCN

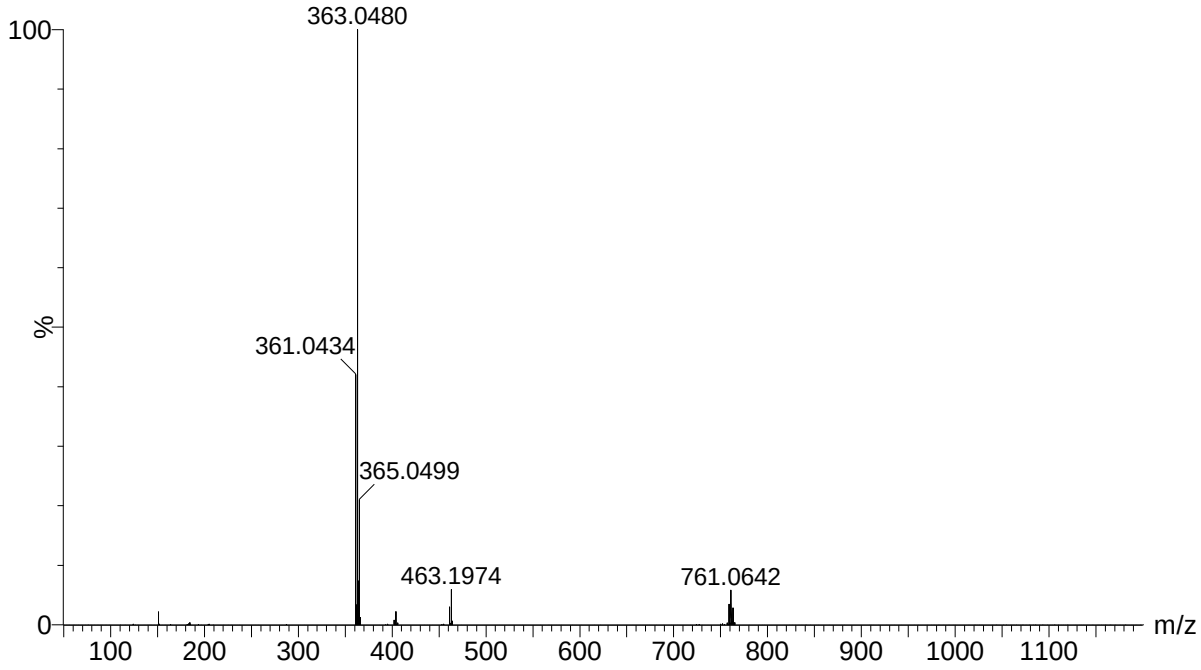

Figure 298. ESI-MS spectrum of pentamethylcyclopentadienyl iridium dichloride dimer.

MeOH

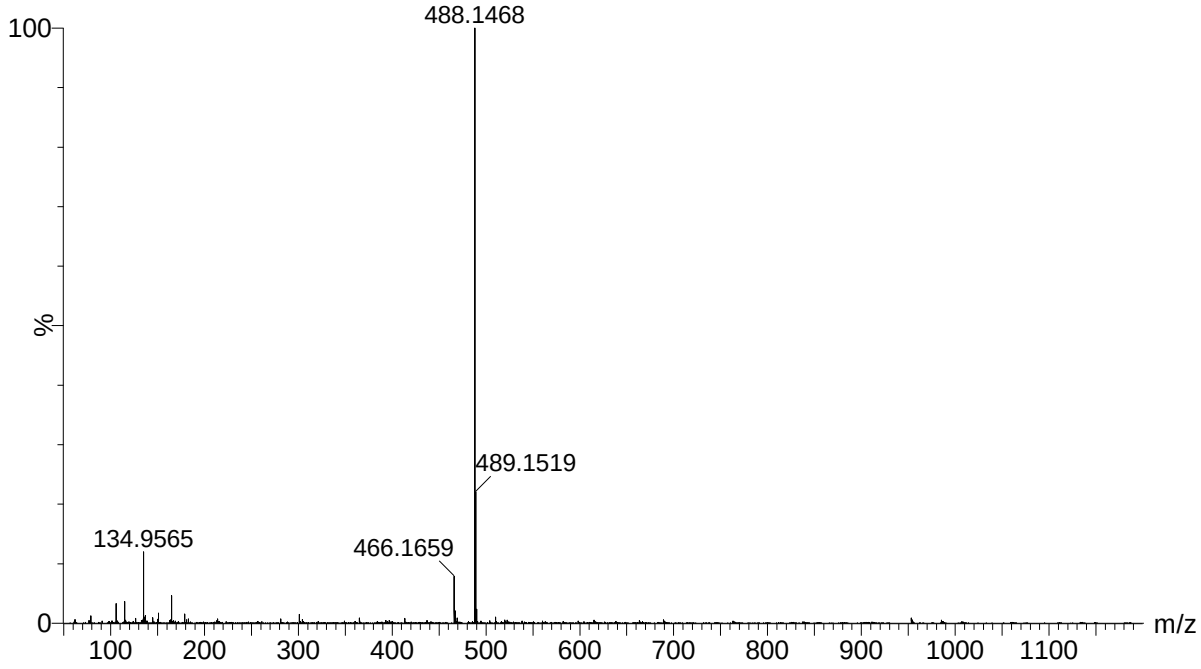

Figure 299. ESI-MS spectrum of dimethyl-2'-((2-hydroxybenzylidene)amino)-[1,1':4',1"-terphenyl]-4,4"-dicarboxylate.

MeOH

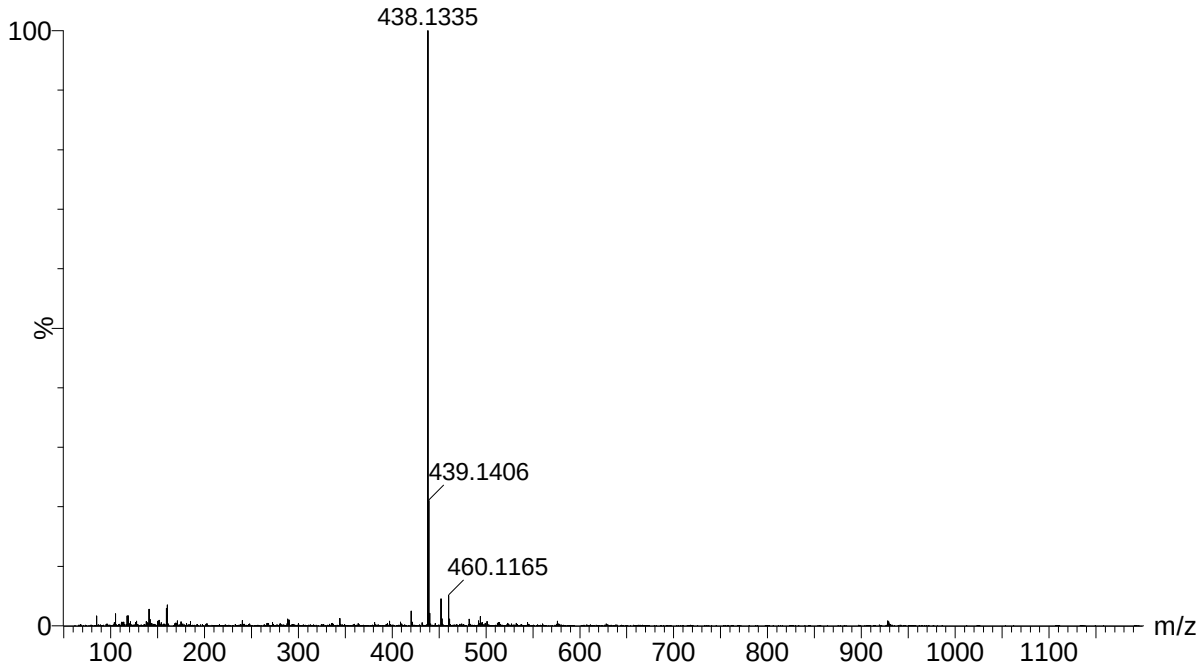

Figure 300. ESI-MS spectrum of 2'-((2-hydroxybenzylidene)amino)-[1,1':4',1"-terphenyl]-4,4"-dicarboxylic acid.

H2O ueber DMSO

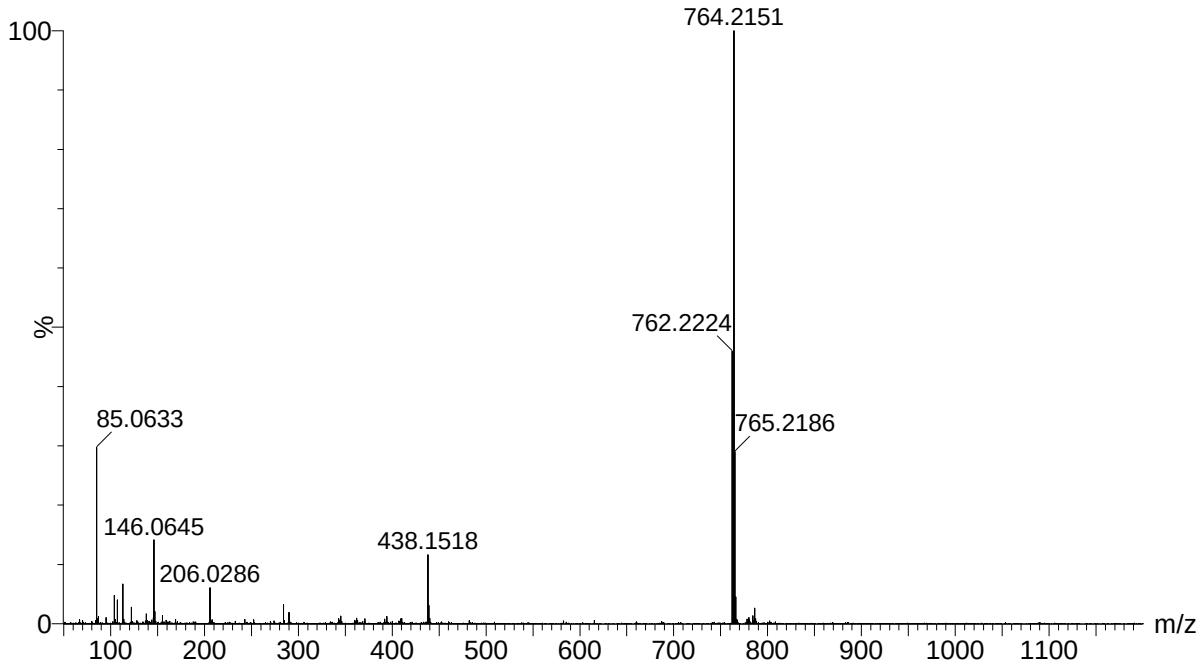

Figure 301. ESI-MS spectrum of sal(IrCp*Cl).

Crystal data

Table 18. Crystal data and structure refinement for **$Ru(DMSO)_4Cl_2$**.

Identification code	$Ru(DMSO)_4Cl_2$	
Empirical formula	$C_8H_{24}Cl_2O_4RuS_4$	
Formula weight	484.48	
Temperature	130(2) K	
Wavelength	0.71073 Å	
Crystal system	Monoclinic	
Space group	P2(1)/n	
Unit cell dimensions	a = 8.8613(14) Å	α = 90°.
	b = 17.816(3) Å	β = 127.113(7)°.
	c = 14.1109(17) Å	γ = 90°.
Volume	1776.5(5) $Å^3$	
Z	4	
Density (calculated)	1.811 Mg/m^3	
Absorption coefficient	1.657 mm^{-1}	
F(000)	984	
Crystal size	0.21 x 0.10 x 0.09 mm^3	
Theta range for data collection	2.14 to 27.87°.	
Index ranges	-11<=h<=11, -23<=k<=23, -15<=l<=18	
Reflections collected	16725	
Independent reflections	4231 [R(int) = 0.0438]	
Completeness to theta = 27.87°	99.9 %	
Absorption correction	Semi-empirical from equivalents	
Max. and min. transmission	0.8652 and 0.7222	
Refinement method	Full-matrix least-squares on F^2	
Data / restraints / parameters	4231 / 0 / 180	
Goodness-of-fit on F^2	1.009	
Final R indices [I>2sigma(I)]	R1 = 0.0324, wR2 = 0.0710	
R indices (all data)	R1 = 0.0430, wR2 = 0.0756	
Largest diff. peak and hole	1.319 and -0.490 e.$Å^{-3}$	

Table 19. Crystal data and structure refinement for **dimethyl 4,4'-(6,6'-dimethyl-[2,2'-bipyridine]-5,5'-diyl)dibenzoate**.

Identification code	dimethyl 4,4'-(6,6'-dimethyl-[2,2'-bipyridine]-5,5'-diyl)dibenzoate.	
Empirical formula	$C_{28}H_{24}N_2O_4$	
Formula weight	452.49	
Temperature	130(2) K	
Wavelength	0.71073 Å	
Crystal system	Triclinic	
Space group	P -1	
Unit cell dimensions	a = 7.268(2) Å	α = 99.056(5)°.
	b = 7.280(2) Å	β = 95.820(6)°.
	c = 11.022(3) Å	γ = 108.743(5)°.
Volume	538.1(3) $Å^3$	
Z	1	
Density (calculated)	1.396 Mg/m^3	
Absorption coefficient	0.094 mm^{-1}	
F(000)	238	
Crystal size	0.470 x 0.250 x 0.200 mm^3	
Theta range for data collection	1.896 to 27.878°.	
Index ranges	-9<=h<=9, -9<=k<=9, -14<=l<=14	
Reflections collected	5055	
Independent reflections	2548 [R(int) = 0.0252]	
Completeness to theta = 25.242°	99.7 %	
Absorption correction	Semi-empirical from equivalents	
Max. and min. transmission	1.0000 and 0.5094	
Refinement method	Full-matrix least-squares on F^2	
Data / restraints / parameters	2548 / 0 / 156	
Goodness-of-fit on F^2	1.063	
Final R indices [I>2sigma(I)]	R1 = 0.0517, wR2 = 0.1200	
R indices (all data)	R1 = 0.0709, wR2 = 0.1333	
Extinction coefficient	n/a	
Largest diff. peak and hole	0.374 and -0.231 $e.Å^{-3}$	

Table 20. Crystal data and structure refinement for **L9**.

Identification code	L9.	
Empirical formula	$C_{24}H_{20}N_6O_2$	
Formula weight	424.46	
Temperature	126(2) K	
Wavelength	0.71073 Å	
Crystal system	Monoclinic	
Space group	$P2_1/n$	
Unit cell dimensions	a = 11.569(2) Å	α = 90°.
	b = 6.0900(11) Å	β = 106.076(3)°.
	c = 15.107(3) Å	γ = 90°.
Volume	1022.7(3) $Å^3$	
Z	2	
Density (calculated)	1.378 Mg/m^3	
Absorption coefficient	0.092 mm^{-1}	
F(000)	444	
Crystal size	0.600 x 0.300 x 0.250 mm^3	
Theta range for data collection	1.975 to 28.318°.	
Index ranges	-15<=h<=14, -8<=k<=8, -20<=l<=20	
Reflections collected	9845	
Independent reflections	2541 [R(int) = 0.0377]	
Completeness to theta = 25.242°	100.0 %	
Refinement method	Full-matrix least-squares on F^2	
Data / restraints / parameters	2541 / 0 / 150	
Goodness-of-fit on F^2	1.032	
Final R indices [I>2sigma(I)]	R1 = 0.0491, wR2 = 0.1215	
R indices (all data)	R1 = 0.0666, wR2 = 0.1308	
Extinction coefficient	n/a	
Largest diff. peak and hole	0.336 and -0.187 $e.Å^{-3}$	

Table 21. Crystal data and structure refinement for **L7**.

Identification code	L7	
Empirical formula	$C_{24}H_{18}N_4O_2$	
Formula weight	394.42	
Temperature	200(2) K	
Wavelength	0.71073 Å	
Crystal system	Orthorhombic	
Space group	Pbca	
Unit cell dimensions	a = 9.2391(11) Å	α = 90°.
	b = 9.9400(11) Å	β = 90°.
	c = 21.809(2) Å	γ = 90°.
Volume	2002.9(4) $Å^3$	
Z	4	
Density (calculated)	1.308 Mg/m^3	
Absorption coefficient	0.086 mm^{-1}	
F(000)	824	
Crystal size	0.650 x 0.400 x 0.200 mm^3	
Theta range for data collection	1.867 to 28.299°.	
Index ranges	-12<=h<=12, -13<=k<=13, -26<=l<=29	
Reflections collected	18966	
Independent reflections	2480 [R(int) = 0.0333]	
Completeness to theta = 25.242°	100.0 %	
Refinement method	Full-matrix least-squares on F^2	
Data / restraints / parameters	2480 / 0 / 140	
Goodness-of-fit on F^2	1.024	
Final R indices [I>2sigma(I)]	R1 = 0.0435, wR2 = 0.1102	
R indices (all data)	R1 = 0.0524, wR2 = 0.1174	
Extinction coefficient	n/a	
Largest diff. peak and hole	0.314 and -0.281 $e.Å^{-3}$	

Table 22. Crystal data and structure refinement for **K10**.

Identification code	K10	
Empirical formula	$C_{36}H_{34}N_{10}O_2Ru$	
Formula weight	739.80	
Temperature	130(2) K	
Wavelength	0.71073 Å	
Crystal system	Orthorhombic	
Space group	$P2_12_12_1$	
Unit cell dimensions	a = 11.4607(12) Å	α = 90°.
	b = 16.0350(17) Å	β = 90°.
	c = 19.139(2) Å	γ = 90°.
Volume	3517.1(6) $Å^3$	
Z	4	
Density (calculated)	1.397 Mg/m^3	
Absorption coefficient	0.493 mm^{-1}	
F(000)	1520	
Crystal size	0.50 x 0.20 x 0.10 mm^3	
Theta range for data collection	1.657 to 28.310°.	
Index ranges	-15<=h<=15, -21<=k<=21, -25<=l<=23	
Reflections collected	35948	
Independent reflections	8748 [R(int) = 0.0522]	
Completeness to theta = 25.242°	100.0 %	
Refinement method	Full-matrix least-squares on F^2	
Data / restraints / parameters	8748 / 0 / 449	
Goodness-of-fit on F^2	1.087	
Final R indices [I>2sigma(I)]	R1 = 0.0462, wR2 = 0.1103	
R indices (all data)	R1 = 0.0512, wR2 = 0.1125	
Absolute structure parameter	0.24(4)	
Extinction coefficient	n/a	
Largest diff. peak and hole	1.873 and -0.775 $e.Å^{-3}$	